JAERI-Conf
2001-006

INDC(JPN)-188/U

PROCEEDINGS OF THE 2000 SYMPOSIUM ON NUCLEAR DATA NOVEMBER 16-17, 2000, JAERI, TOKAI, JAPAN

March 2001

(Eds.) Naoki YAMANO* and Tokio FUKAHORI

日本原子力研究所
Japan Atomic Energy Research Institute

本レポートは，日本原子力研究所が不定期に公刊している研究報告書です。
入手の問合わせは，日本原子力研究所研究情報部研究情報課（〒319－1195 茨城県那珂郡東海村）あて，お申し越しください。なお，このほかに財団法人原子力弘済会資料センター（〒319－1195 茨城県那珂郡東海村日本原子力研究所内）で複写による実費頒布をおこなっております。

This report is issued irregularly.
Inquiries about availability of the reports should be addressed to Research Information Division, Department of Intellectual Resources, Japan Atomic Energy Research Institute, Tokai-mura, Naka-gun, Ibaraki-ken 〒319－1195, Japan.

編集兼発行　日本原子力研究所

JAERI-Conf 2001-006 INDC(JPN)-188/U

Proceedings of the 2000 Symposium on Nuclear Data
November 16-17, 2000, JAERI, Tokai, Japan

(Eds.) Naoki YAMANO* and Tokio FUKAHORI

Japanese Nuclear Data Committee
Tokai Research Establishment
Japan Atomic Energy Research Institute
Tokai-mura, Naka-gun, Ibaraki-ken

(Received February 9, 2001)

The 2000 Symposium on Nuclear Data was held at Tokai Research Establishment, Japan Atomic Energy Research Institute (JAERI), on 16th and 17th of November 2000. Japanese Nuclear Data Committee and Nuclear Data Center, JAERI organized this symposium. In the oral sessions, presented were 18 papers on topics of recent experiments, status of JENDL-3.3 and JENDL High Energy File, benchmark tests of JENDL-3.2, international activities and other subjects. In the poster session, presented were 40 papers concerning experiments, evaluations, benchmark tests and on-line database on nuclear data. Those presented papers are compiled in the proceedings.

Keywords: Nuclear Data, Symposium, Proceedings, Nuclear Reaction, JENDL, Experiment, Evaluation, Benchmark Test, Cross Section.

*Sumitomo Atomic Energy Industries, Ltd.

2000年核データ研究会報文集
2000年11月16日～17日，東海研究所，東海村

日本原子力研究所東海研究所
シグマ研究委員会
（編）山野　直樹*・深堀　智生

(2001年2月9日受理)

2000年核データ研究会が、2000年11月16日と17日の両日、日本原子力研究所東海研究所において開催された。この研究会は、日本原子力研究所のシグマ研究委員会と核データセンターが主催して開いたものである。口頭発表では、最近の実験に関するトピックス、JENDL-3.3及びJENDL High Energy Fileの現状、JENDL-3.2の積分テスト、国際セッション、その他のトピックスについての18件の報告があった。ポスター発表では、40件の発表があり、それらは、核データの測定、評価や評価済核データのベンチマークテスト、オンラインデータベース等に関するものであった。本報文集は、それらの論文をまとめたものである。

東海研究所：〒319-1195 茨城県那珂郡東海村白方白根2-4
* 住友原子力工業㈱

Program Committee

Naoki YAMANO(Chairman)	Sumitomo Atomic Energy Industries, Ltd.
Satoshi CHIBA	Japan Atomic Energy Research Institute
Tokio FUKAHORI	Japan Atomic Energy Research Institute
Tetsuo IGUCHI	Nagoya University
Makoto ISHIKAWA	Japan Nuclear Cycle Development Institute
Osamu IWAMOTO	Japan Atomic Energy Research Institute
Tomohiko IWASAKI	Tohoku University
Shigeaki OKAJIMA	Japan Atomic Energy Research Institute
Yoshihisa TAHARA	Mitsubishi Heavy Industries, Ltd.

プログラム委員会

山野　直樹（委員長）	住友原子力工業（株）
千葉　敏	日本原子力研究所
深堀　智生	日本原子力研究所
井口　哲夫	名古屋大学
石川　眞	核燃料サイクル開発機構
岩本　修	日本原子力研究所
岩崎　智彦	東北大学
岡嶋　成晃	日本原子力研究所
田原　義壽	三菱重工業（株）

PLEASE BE AWARE THAT
ALL OF THE MISSING PAGES IN THIS DOCUMENT
WERE ORIGINALLY BLANK

Contents

目 次

1. Introduction

The 2000 symposium on nuclear data was held at Tokai Research Establishment, Japan Atomic Energy Research Institute (JAERI), on 16th and 17th of November 2000, with about 150 participants. Japanese Nuclear Data Committee and Nuclear Data Center, JAERI organized the symposium.

The program of the symposium is listed below. In the oral sessions, presented were 18 papers on topics of recent experiments, status of *JENDL-3.3* and *JENDL High Energy File*, benchmark tests of JENDL-3.2, international activities and other related subjects. In the poster session, presented were 40 papers concerning experiments, evaluations, benchmark tests and on-line database on nuclear data. Those presented papers are compiled in the proceedings.

Program of 2000 Symposium on Nuclear Data

Nov. 16 (Thr.)

10:00-10:25

1. Opening Session — Chairman: N. Yamano (SAE)

1.1 Opening Address — Chief of JNDC (JAERI)

1.2 Memorial Address for Prof. R. Nakajima — T. Yoshida (Musashi Tech.)

10:25-12:00

2. Topics for Recent Experiments — Chairman: N. Koori (Tokushima U.)

2.1 A Systematic Radiochemical Study of Photopion Nuclear Reactions of Complex Nuclei at Intermediate Energies [25+5] — K. Sakamoto (Kanazawa U.)

2.2 Heavy Element Nuclear Chemistry Research in JAERI [25+5] — Y. Nagame (JAERI)

2.3 New Magic Number, N=16, near the Neutron Drip Line[30+5] — A. Ozawa (RIKEN)

12:00-13:00 Taking Photo + Lunch

13:00-14:00

3. Poster Session 1

14:00-16:00

4. Producing JENDL-3.3 Chairman: A. Zukeran (Hitachi)

4.1 Status of JENDL-3.3 [30+10] K. Shibata (JAERI)

4.2 Integral Test for Reactors [30+10] H. Takano (JAERI)

4.3 Integral Test for Shielding [30+10] N. Yamano (SAE)

16:00-16:20 Coffee Break

16:20-17:40

5. International Session Chairman: A. Hasegawa (JAERI)

5.1 Application of ENDF Data for Testing a Monte-Carlo Neutron and Proton Transport Code [15+5] Pariwat Siangsanan (OAEP)

5.2 Uranium-fuel Thermal Reactor Benchmark Testing of CENDL-3 [15+5] Liu Ping (CIAE)

5.3 Evaluation of the significance of Zr Bound in ZrHx for its Possible Inclusion in the WIMSD-5 Cross Section Library [15+5] T.K. Chakrobortty (BAEC)

5.4 Measurement of Photoneutron Spectrum at Pohang Neutron Facility [15+5] Kim Guinyun (PAL)

18:00-20:00 Reception

Nov. 17 (Fri.)

9:00-10:00

6. Integral Test Chairman: T. Iwasaki (Tohoku U.)

6.1 JENDL-3.2 Performance in Analyses of MISTRAL Critical Experiments for High-Moderation MOX Cores [25+5] N. Takada (NFI)

6.2 Integral Test of JENDL-3.2 Data by Reanalysis of Sample Reactivity Measurements at SEG and STEK Facilities [25+5] K. Dietze (JNC)

10:00-10:20 Coffee Break

10:20-12:00

7. Topics Chairman: K. Ishibashi (Kyushu U.)

7.1 OKLO Reactor and Nuclear Physics Constant [40+10] A. Iwamoto (JAERI)

7.2 Analysis of Nuclear Radii form Reaction-Cross Sections in Various Energy Regions Using the QMD Approach [20+5] T. Maruyama (Nihon U.)

7.3 Data for Radiation Protection and Nuclear Data [20+5] Y. Yamaguchi (JAERI)

12:00-13:00 Lunch

13:00-14:00
8. Poster Session 2

14:00-16:00
9. JENDL High Energy File Chairman: M. Baba (Tohoku U.)
9.1 Present status of JENDL High Energy File [30+10] Y. Watanabe (Kyushu U.)
9.2 Integral Test for JENDL High Energy File [30+10] F. Maekawa (JAERI)
9.3 Integral Test for JENDL High Energy File [30+10] N. Yoshizawa (MRI)

16:00-16:30
10. Closing Session
10.1 Poster Award Presentation [5] N. Yamano (SAE)
10.2 Summary Talk [20] Y. Tahara (MHI)

Poster Presentations
Odd-Number: Poster Session 1 (Nov. 16 (Thr.) 12:10-14:00)
Even-Number: Poster Session 2 (Nov. 17 (Fri.) 12:00-14:00)

P1. Decay Heat Measurement of Minor Actinides at YAYOI Y. Ohkawachi (JNC)
P2. Measurement of the Resonance Integral of the ^{90}Sr(n, gamma)^{91}Sr Reaction
S. Nakamura (JNC)
P3. Measurement of the Thermal Neutron Capture Cross Section and the Resonance Integral of the ^{109}Ag(n, gamma)^{110m}Ag Reaction S. Nakamura (JNC)
P4. Evaluation of Neutron Cross Sections for Er-Isotopes
A.K.M. Harun-ar-Rashid (U. of Chittagong)
P5. Neutron Capture Cross Section Measurement of Np-237 below 10 keV by the Linac Time-of-Flight Method Lee Sam Yol (KUR)
P6. Projectile Dependency of Radio Activities of Spallation Products Induced in Copper
H. Yashima (Tohoku U.)
P7. Measurement of Neutron Production Cross Sections by High Energy Heavy Ions
H.Sato (Tohoku U.)

P8. New Evaluation of Prompt Neutron Spectra of U-235 and Pu-239 for JENDL-3.3
T. Ohsawa (Kinki U.)

P9. Nuclear Data Evaluation up to 3GeV for Fe-54,56,57,58 N. Yoshizawa (MRI)

P10. Reactor Kinetics Calculated in the Summation Method and Key Delayed-neutron Data
K. Oyamatsu (Aichi Shukutoku U.)

P11. Measurement of γ -ray Emission Probabilities of Tc-100
K. Furutaka (JNC)

P12. Measurement of Secondary Gamma-ray Spectra from Structural and Blanket Materials Bombarded by D-T Fusion Neutrons T. Nishio (Osaka U.)

P13. Measurement of Double Differential Cross Section for Proton Emission Reactions of Silicon and Fluorine by Incident DT Neutrons Y. Terada (Osaka U.)

P14. (n,2n) Reaction Cross Section Measurement with A Beam DT Neutron Source — Establishment of the Measurement Method — I. Murata (Osaka U.)

P15. Activation Cross Section Measurement for Short-lived Products Less than 10 s at Neutron Energy between 13.5 and 14.9 MeV Y. Kasugai (JAERI)

P16. Measurement of Activation Cross Sections with d-D Neutrons in the 2 – 6 MeV Energy Region S. Furuichi (Nagoya U.)

P17. Measurements of Li-d, Be-d Nuclear Reaction Cross Sections at Low Energy
K. Ochiai (JAERI)

P18. Precise Determination of Gamma-ray Emission Probabilities and Beta-ray Intensities for some Nuclides with Relatively Short Half-lives Nada Marnada (Nagoya U.)

P19. Short Comments to ^{56}Fe of FENDL/MG-2.0 C. Konno (JAERI)

P20. DORT Analysis of Iron and Concrete Shielding Experiments at JAERI/TIARA with P7 and P9 Approximated LA150 Multigroup Libraries C. Konno (JAERI)

P21. Measurements of Spectra of Neutron Produced from a Thick Iron Target Bombarded with 1.5 GeV Protons S. Meigo (JAERI)

P22. Recoil Properties of Radionuclides Formed in Photospallation Reactions on Complex Nuclei at Intermediate Energies H. Haba (JAERI)

P23. Analysis of activation yields by INC/GEM S. Furihata (MRI)

P24. Production of Charged Particles by Proton-induced Reaction at Intermediate Energy
F. Saiho (Kyushu U.)

P25. Evaluation of Neutron and Proton Nuclear Data of Si-28 for Energies up to 200 MeV
Sun Weili (Kyushu U.)

P26. Calculation of Neutron- and Proton-induced Cross Sections on W up to 3 GeV
H. Kitsuki (Kyushu U.)

P27. A Program for Optical Model Potential Search with Simulated Annealing and Nonlinear Least Squares Fitting Young-Ouk Lee (KAERI)

2. Papers Presented at Oral Sessions

JP0150645

2.1

A Systematic Radiochemical Study of Photopion Nuclear Reactions of Complex Nuclei at Intermediate Energies

Koh Sakamoto[1], Hiromitsu Haba[2], Samir Ranjan Sarkar[1], Yasuji Oura[3], Hiroshi Matsumura[1], Yutaka Miyamoto[1], Seiichi Shibata[4], Michiaki Furukawa[5], and Ichiro Fujiwara[6]

[1]Department of Chemistry, Faculty of Science, Kanazawa University,
Kanazawa-shi, Ishikawa 920-1192, Japan
e-mail: kohsakamoto@par.odn.ne.jp
[2]Research Group for Nuclear Chemistry of Heavy Elements,
Advanced Science Research Center, Japan Atomic Energy Research Institute,
Tokai, Naka-gun, Ibaraki 319-1195, Japan
[3]Department of Chemistry, Graduate School of Science, Tokyo Metropolitan University,
Hachioji-shi, Tokyo 192-0397, Japan
[4]Research Reactor Institute, Kyoto University, Sennan-gun, Osaka 590-0494, Japan
[5]Faculty of Environmental and Information Sciences, Yokkaichi University,
Yokkaichi-shi, Mie 512-8512, Japan
[6]Department of Economics, Faculty of Economics, Otemon-Gakuin University,
Ibaraki-shi, Osaka 567-8502, Japan

A short review is given on our systematic studies of photopion nuclear reactions, in which the product yields from (γ,π^+) and (γ,π^-xn) reactions for x = 0–9 have been measured radiochemically as functions of bremsstrahlung end-point energy (E_0) from 30 to 1200 MeV and of target mass, ^{27}Al–^{181}Ta for (γ,π^+) and ^{7}Li–^{209}Bi for (γ,π^-xn) reactions. Yield variations as a function of the number of the emitted neutrons (x) for each target at $E_0 \geq 400$ MeV were found to be typical of (3,3) resonance. The reactions for neutron multiplicities as large as $x \geq 6$ are notable for targets of mass $A_t \geq 100$, while only the reactions for smaller x are measurable for the lighter targets. The yields for both (γ,π^-) and (γ,π^+) are A_t-independent for targets heavier than $A_t > 30$–40, while much smaller yields are reported for targets with A_t = 7–14. The yield ratio $(\gamma,\pi^-)/(\gamma,\pi^+)$ becomes as high as 5.5 and such a high value suggests that the neutron density in the surface region of nucleus is higher than that expected from the neutron-to-proton ratio for the entire nucleus. The observed yields for individual (γ,π^-xn) reactions having equal x were also found to be a smoothly varying function of the neutron-to-proton ratio of the target, $(N/Z)_t$, not of the target mass A_t or number of target neutrons N_t. This implies that the reactions are initiated via competitive photoabsorptions by neutrons and protons in the target nucleus. The smooth variation of the profile changes its characteristics at $(N/Z)_t$ = 1.30~1.40, corresponding to A_t = 100–130; this implies higher excitation energies due to progressively larger medium effects in nuclei with $A_t > 100$. The results are compared with theoretical calculations made using the photon-induced intranuclear cascade and evaporation analysis program by Gabriel and Alsmiller.

1. Introduction

At energies above the pion production thresholds, the Δ isobar is expected to be produced through (3,3) resonance absorption of an incoming photon by a single nucleon (N) in the target nucleus. The isobar decays immediately (10^{-24} s) into a stable nucleon and a pion: $\gamma + n \rightarrow \Delta^0 \rightarrow p + \pi^-$, $\gamma + p \rightarrow \Delta^+ \rightarrow n + \pi^+$, and $\gamma + N \rightarrow \Delta^0 \rightarrow N + \pi^0$. After these initial processes, pion and/or nucleon may escape from the nucleus or develop a cascade-evaporation process inside the nucleus. The probability of the escape may depend on the location of the formation of Δ, thence on the size of the nucleus. Especially, when photoabsorption occurs at the surface region of the nucleus, the chance of an escape would be high. A systematic measurement of photopion reaction yields as functions of photon energy and target mass has, therefore, been of our current interest [1–4].

Radiochemical methods are useful for identifying individual (γ,π^-xn) reactions for different x. It is possible to isolate the product nuclides chemically as a series of radioisotopes with mass numbers (A_t-x) belonging to (Z_t+1) element from a target with mass number A_t of an element with atomic number Z_t and also from the dominant spallation products of $A_p < A_t$ and $Z_p \leq Z_t$. The (γ,π^+) reaction leads to a product nucleus of $A_p = A_t$ and $Z_p = Z_t-1$ that is also distinguishable from those of other competitive reaction paths, though the (γ,π^+xn)

products are not separable from the (γ,px'n) products. The information obtained from the activation method is integral with respect to the energy and angle of the final products, but forgoes a detailed theoretical analysis of the final states involved. However, the complete picture concerning competitive reaction paths opened by Δ-resonance such as photopion reactions different in x, photospallation, photofragmentation and photofission in cases of heavy complex nuclei can be clarified. A series of radiochemical measurements of photonuclear reactions of complex nuclei in the Δ region has been performed and systematized with respect to photon energy and target mass during the last 25 years. The present paper is a concise review of the part of photopion reactions among the various reaction paths opened by the Δ-resonance. Our study of the (γ,π⁻xn) reactions emphasizes the yield variations for individual x with respect to a wide range of photon energies and target compositions, A_t and $(N/Z)_t$. The (γ,π⁺) yields relative to the (γ,π⁻) yields over the same range of photon energies and target compositions are another concern in the present work. The results are also discussed in conjunction with a theoretical calculations based on the photon-induced intranuclear cascade analysis code (PICA) by Gabriel and Alsmiller [5].

2. Experimental

All of the data included in this paper were obtained from bremsstrahlung irradiations of targets (^{7}Li–^{209}Bi) in suitable chemical forms using the 1.3 GeV electron synchrotron of the High Energy Accelerator Research Organization (KEK) at Tanashi in the bremsstrahlung end-point energies E_0 range of 250–1200 MeV, and the 300 MeV electron linac of the Laboratory of Nuclear Science, Tohoku University in the E_0 range of 30–270 MeV, both using steps of 50 MeV or less. For the experimental detail and the data analysis, see Ref. [1–4].

3. Results and Discussion

3.1. Mass Yield Distribution

Measured (secondary-corrected) yields as a function of E_0, $Y(E_0)$, in unit of μb per equivalent quanta (μb/eq.q.), show steep rises above E_0 = 140 MeV, the photopion threshold, and attain plateaus around E_0 = 300–500 MeV, which are characteristic of the resonance process. Typical examples of the yield curves $Y(E_0)$ and of the cross sections per photon of energy, k, σ(k), obtained by unfolding of $Y(E_0)$ were reported for ^{51}V [1] and ^{133}Cs [2] targets. In the following the energy-integrated $Y(E_0)$ values are presented to characterize their target dependent features. The E_0-dependence of the (γ,π⁻xn) yields is shown in Fig. 1, where the measured yield values at E_0 = 800, 400 and 250 MeV from ^{51}V, ^{59}Co, ^{75}As, ^{89}Y, ^{109}Ag, ^{115}In, ^{127}I, ^{133}Cs, ^{139}La, ^{175}Lu, ^{197}Au and ^{209}Bi targets are plotted as a function of the number of neutrons emitted (x), i.e., isotopic mass yield curves. The solid, broken and dotted curves are drawn through the data points for E_0 = 800, 400 and 250 MeV, respectively, taking the target mass-dependent variations of all the yield values into consideration. The mass yields at E_0 = 400 and 800 MeV are almost the same and higher than those at E_0 = 250 MeV. The difference between the yield patterns for 250 MeV and 400 (and 800) MeV increases with the increasing A_t, and it becomes more prominent at larger x in the A_t region from 127 to 209. An important feature of the isotopic mass yield curves is that the reactions of high neutron multiplicities become progressively more possible as A_t increases, and the reaction probabilities for x = 2–7 (and even more) at $E_0 \geq$ 400 MeV are nearly comparable for a heavy target such as ^{175}Lu, ^{197}Au or ^{209}Bi, though not at E_0 = 250 MeV. On the other hand, reactions with such high neutron multiplicities are not possible for the lighter targets (A_t < 100). For the region of targets having A_t = 51–115, as shown in the upper half of Fig. 1, the difference between the 250 MeV and the 400 (and 800) MeV yields is more prominent at x = 1–3. The neutron multiplicity reflects primarily the excitation energy left after pion emission, while the energy spectrum of neutrons is to be known. Also noteworthy is that the yields for (γ,π⁻) reactions are almost the same for all of the studied targets at E_0 = 800, 400 and 250 MeV.

The widths of the mass yield distributions at E_0 = 400 and 250 MeV, defined here as the x values of the (γ,π⁻xn) reaction for which the yield is equal to that of the (γ,π⁻) reaction, 78 μb/eq.q. for E_0 = 400 MeV and 51 μb/eq.q. for E_0 = 250 MeV (see subsection 3.2 below), are read from the fit curves in Fig. 1 and plotted as a function of the neutron-to-proton ratio of the target, $(N/Z)_t$, in Fig. 2. The target dependence of the yields from the (γ,π⁻xn) reactions for $x \geq 1$ is not parameterized by target mass A_t, nor by the number of target neutrons N_t, because the (γ, π⁻2n) and (γ, π⁻3n) reaction yields from ^{51}V are higher by an order of magnitude than those from ^{59}Co, as seen in the upper left corner of Fig. 1. As noted above qualitatively, the range of neutron multiplicity is larger for heavier targets. However, the degree of the increase of the width is not monotonic, but changes largely at $(N/Z)_t$ = 1.3–1.4 (^{109}Ag-^{127}I), and the rate of increase becomes smaller at $(N/Z)_t$ = 1.30–1.35 (^{109}Ag–^{115}In) and at 1.48–1.52 (^{197}Au–^{209}Bi) in the case of E_0 = 400 MeV. The change of the width at E_0 = 250 MeV is small, but the rate of increase also changes at $(N/Z)_t \approx$1.35. The peak positions also increase with an increasing of $(N/Z)_t$ in a manner similar to the widths (see the discussion on (γ,π⁻xn) yields below).

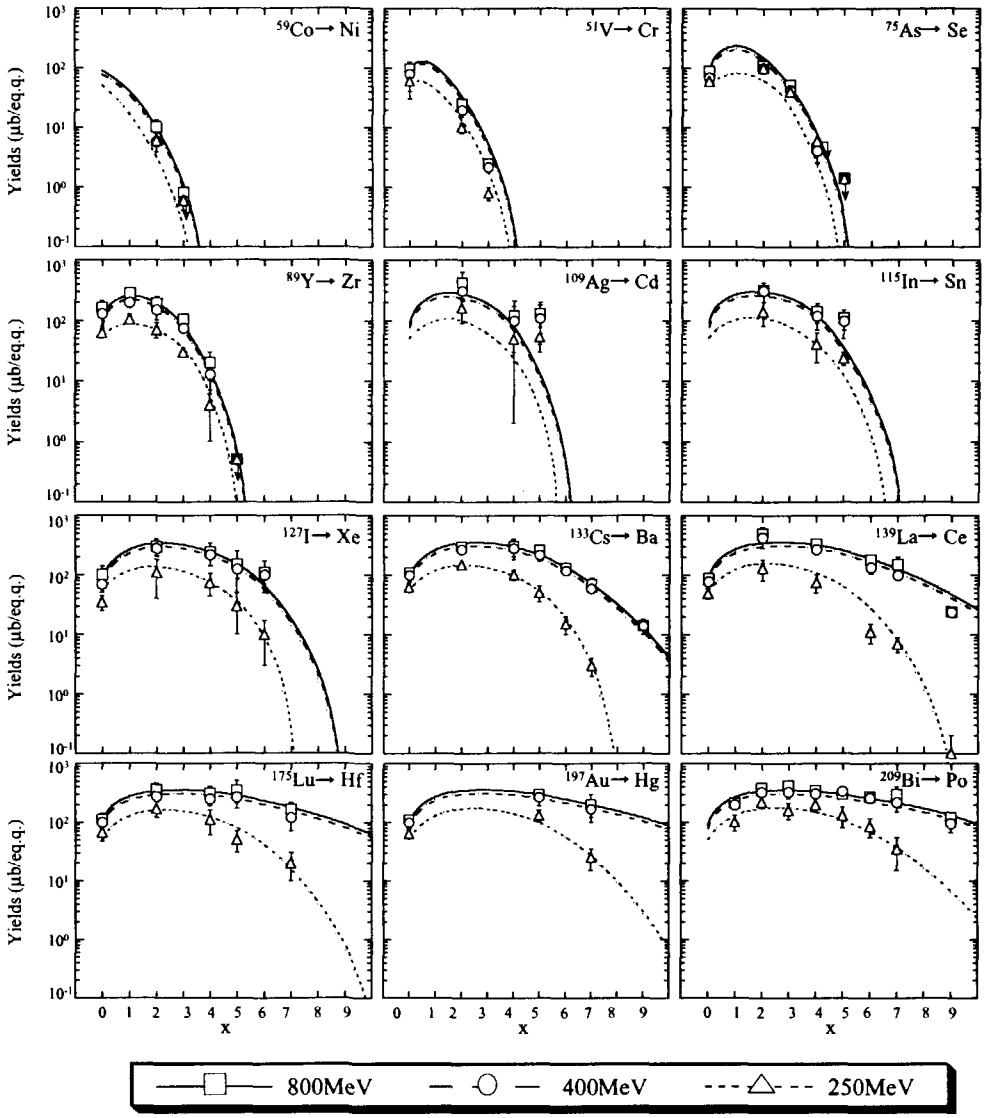

Fig. 1. Variations for (γ,π^{-}xn) reaction yields in unit of μb/eq.q. as a function of number of emitted neutrons, x, isotopic mass yield curves, at E_0=800, 400, and 250 MeV.

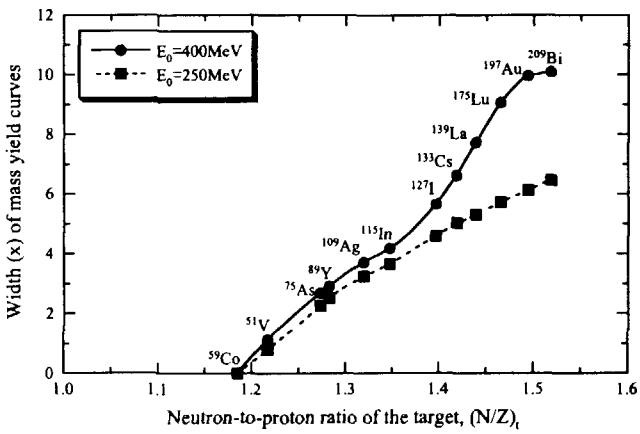

Fig. 2. Widths of the isotopic mass yield curves as a function of $(N/Z)_t$ at E_0=400 and 250 MeV.

3.2. $(\gamma,\pi^{\pm})$ Yields

Figure 3 shows the measured yields (large symbol) of (γ,π^{+}) and (γ,π^{-}) reactions at E_0 = 400 MeV as a function of A_t, together with the literature data (small symbols) [4]. Open squares are for the (γ,π^{+}) yields from ^{9}Be, ^{27}Al, ^{37}Cl, ^{41}K, ^{51}V, ^{59}Co, ^{60}Ni, ^{65}Cu, ^{75}As, ^{87}Rb, ^{88}Sr, ^{109}Ag, ^{115}In, ^{133}Cs, ^{138}Ba, ^{139}La and ^{181}Ta, and closed circles for the (γ,π^{-}) yields from ^{7}Li, ^{11}B, ^{12}C, ^{14}N, ^{44}Ca, ^{51}V, ^{65}Cu, ^{75}As, ^{88}Sr, ^{89}Y, ^{127}I, ^{130}Te, ^{133}Cs, ^{139}La, ^{175}Lu, and ^{197}Au, and they are connected by solid lines, respectively. Dotted lines are the corresponding ones calculated by the PICA code. Both the (γ,π^{+}) yields are A_t-independent except for light targets, irrespective of E_0. The yields for (γ,π^{-}) reactions on lighter targets such as ^{7}Li, ^{11}B, ^{12}C, ^{14}N are anomalously small compared with those for the heavier targets. The low values for the ^{7}Be and ^{14}O yields up to E_0 = 1200 MeV were confirmed in the present work, and the low yields are explained as due to small numbers of particle stable states (two in ^{7}Be, ten in ^{11}C, one in ^{12}N and ^{14}O) [6]. Also, it is well known that the anomalously slow transition rates in the A = 14 isobars are observed in $^{14}\mathrm{C} \rightarrow {}^{14}\mathrm{N} + e^{-} + \bar{\nu}_e$ and $^{14}\mathrm{O} \rightarrow {}^{14}\mathrm{N} + e^{+} + \nu_e$ as well as in radiative pion and muon captures [7]. On the other hand, many bound states leading to (γ,π^{-}) reactions exist for the heavy nuclei. This manifests the A_t-independence in the heavy target region; the weighted means of the yield values of (γ,π^{-}) reactions on targets having $A_t \geq 44$ are 91±6, 78±6 and 51±5 μb/eq.q. for E_0 = 800, 400 and 250 MeV, respectively (horizontal solid lines in Fig. 3). The PICA calculations for the corresponding reactions on these heavy targets at E_0 = 400 MeV are smaller than the measured values by 35 % on average, though the calculations also indicate A_t-independence. The (γ,π^{+}) reaction yields are also A_t-independent for $A_t \geq 27$, and their weighted means are 18±2, 14±2, 7.3±1.1μb/eq.q. for E_0 = 800, 400 and 250 MeV, respectively. The yield values reported for $^{9}\mathrm{Be}(\gamma,\pi^{+})^{9}\mathrm{Li}$ in the energy range of E_0 = 100-800 MeV by Nilsson *et al.* [8] are definitely smaller than the trend, probably because there are only two bound states in ^{9}Li. Although both the (γ,π^{+}) and (γ,π^{-}) reactions on the light nuclei have been of interest from a theoretical point of view [9], they are not included in our discussions with those of the heavier complex nuclei which allow for statistical treatments. The PICA calculation for (γ,π^{+}) reactions in the heavy target region also reproduces the A_t-independence, but the average values obtained from the calculations are two times those of the measurements. Thus, the measured yields in the A_t-independent region at E_0 = 400 MeV give a yield ratio of $Y(\gamma,\pi^{-})/Y(\gamma,\pi^{+})$ = 5.6±1.0, while the corresponding PICA value at E_0 = 400 MeV is 1.8±0.3.

The high observed yield ratios compared with the calculated ones may imply new nuclear structure effects that are not taken into consideration in the theoretical foundation of the PICA code. The nuclear model used in the theoretical calculations is exactly the same as the one used in the Bertini calculations [10]. The continuous charge density distribution inside the nucleus, $\rho(r) = \rho_0/\{1+\exp(r-c)/z_1\}$, c and z_1 being the relevant parameters, obtained by electron scattering data [11] was approximated by dividing the nucleus into three concentric spheres: a central sphere and two surrounding spherical annuli having the uniform densities of 0.9, 0.2, and 0.01 of $\rho(0)$ at the center of the nucleus. The neutron to proton density ratios were assumed to be equal to the ratio of neutrons to protons for the entire nucleus. Cross sections for the photoabsorption by a nucleon in the (3,3) resonance region were taken from those for elementary processes for free nucleon-photon interactions, by assuming $\sigma(\gamma p \rightarrow n\pi^{+}) = (\gamma n \rightarrow p\pi^{-})$ from charge-symmetry considerations. And the intranuclear cascade calculation of Bertini [10] was then used to account for the secondary effect of nucleon- and pion-interactions with the remaining nucleus following the initial photon interaction. Pion absorption is assumed to occur via a two-nucleon mechanism with a cross section for the absorption of a charged pion by a nucleon with isobaric spin projection of the opposite sign (i.e., a pair of nucleons must contain at least one proton to absorb a negative pion and at least one neutron to absorb a positive pion).

The higher yields of the (γ,π^{-}) reactions and the lower ones of the (γ,π^{+}) reactions relative to those expected from the PICA calculation could possibly be understood if the neutron density in nuclear surface region is higher than the inner density of the nucleus. An initial production of negative pions by way of $\gamma + n \rightarrow \Delta^{0} \rightarrow p + \pi^{-}$ would be more probable than those of positive pions by way of $\gamma + p \rightarrow \Delta^{+} \rightarrow n + \pi^{+}$, and the secondary absorption of negative pions by way of π^{-} + pp or π^{-} + pn would be less than those for positive pions by way of π^{+} + np or π^{+} + nn in the neutron-rich surface region.

These processes which lead to (γ,π^{-}) and (γ,π^{+}) reactions are, therefore, considered here to occur in the surface region of the nucleus, but experimental observations seem to show that the cross sections are not proportional to $A_t^{2/3}$ but A_t-independent. This A_t-independence may be explained as due to a compensation for the increase in pion production with increasing nuclear size (surface) by the competitive increase of neutron emissivity associated with pion emission (see subsection 3.3). The available final transitions are, therefore, limited to a certain number of levels below the particle separation energy which is set equal to 7 MeV in PICA. While the number of the bound states and the strength of transitions to these states are unknown, they must be statistically significant, as the A_t-independence from the PICA calculation also suggests. There has been no

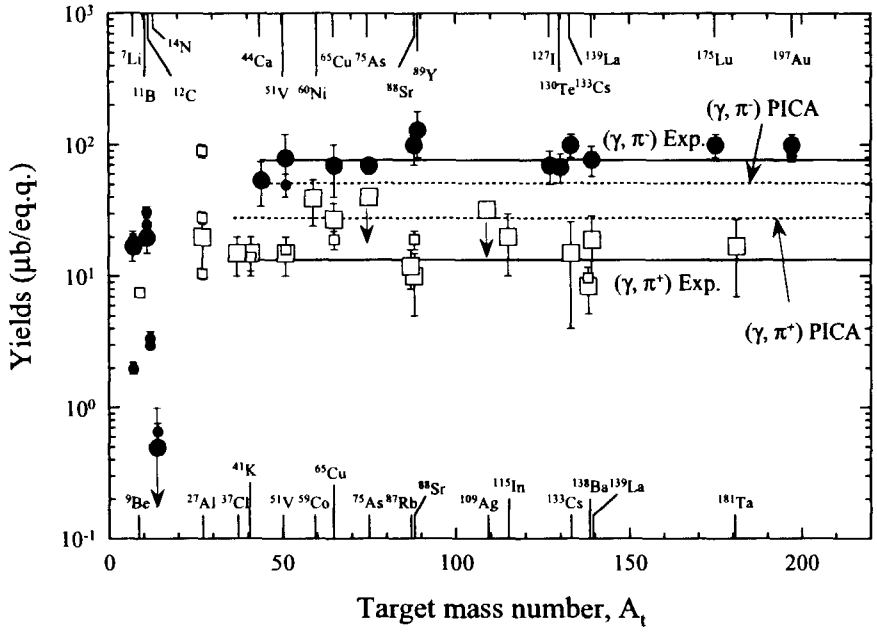

Fig. 3. Variations of the measured and calculated yields for the (γ,π^+) and (γ,π^-) reactions as a function of A_t at E_0 = 400 MeV. See the text for explanation.

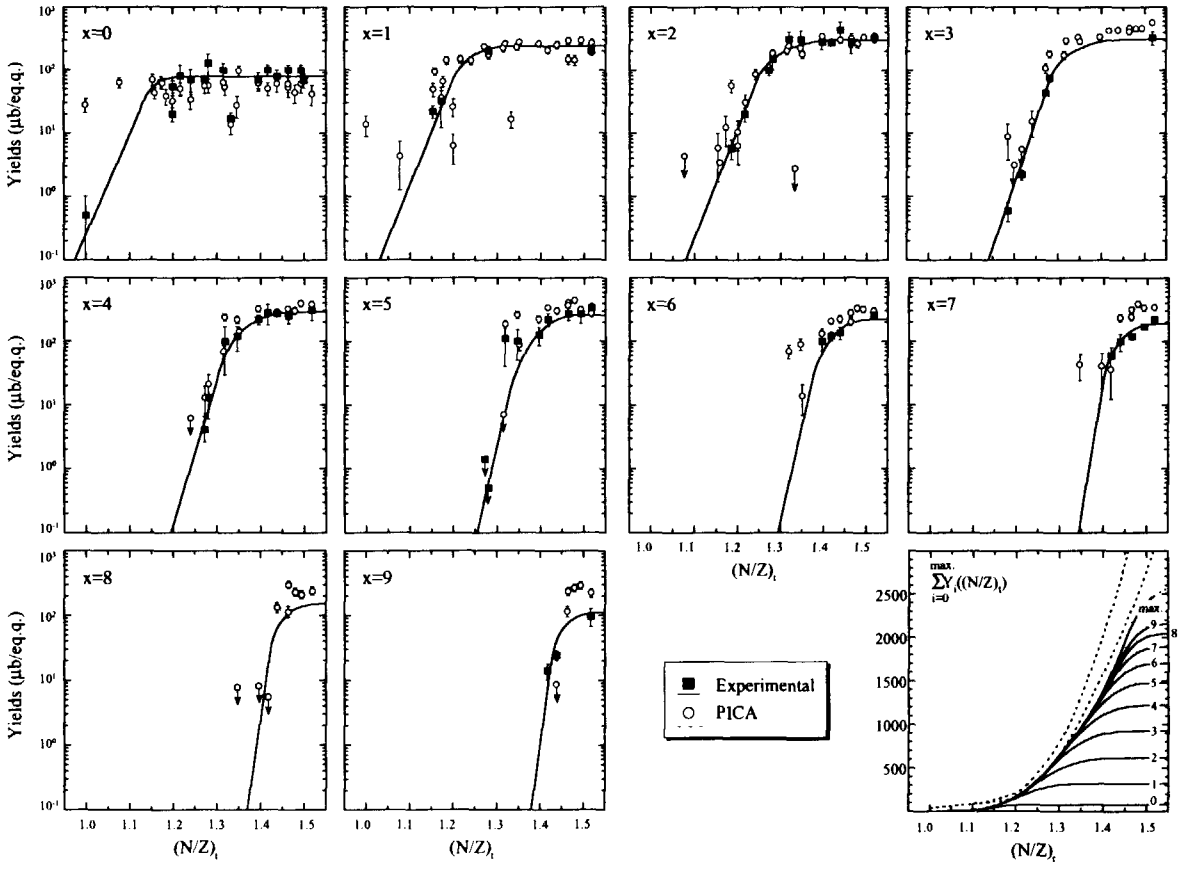

Fig. 4. Variations of the measured and calculated yields for the (γ,π^-xn) reactions as a function of $(N/Z)_t$ at E_0 = 400 MeV. See the text for explanation.

evidence for the density difference between protons and neutrons in the stable nucleus, but neutron skin and neutron halo structures have been discovered in very neutron-rich light nuclei near the drip line [12, 13]. Further study of structural changes in nuclei closer to the stability line is required; the present work suggests photonuclear processes may cause such effects.

3.3. ($\gamma,\pi^- x$n) Yields

In order to reveal the target-dependent changes of the ($\gamma,\pi^- x$n) reaction yields for each x of $x \geq 0$, the yield values at E_0 = 400 MeV (closed squares) are plotted in Fig. 4 as a function of the neutron-to-proton ratio of the entire target nucleus, $(N/Z)_t$. Solid lines representing x = 0–9 are drawn through the observed points with the aid of the smoothed mass yield curves in Fig. 1. Also plotted in Fig. 4 are the yield values calculated for E_0 = 400 MeV (open circles) by the PICA code [4].

The yield values of the ($\gamma,\pi^- x$n) reactions at a given E_0 change systematically with respect to the neutron multiplicity x and $(N/Z)_t$. Both the observed and the calculated values for the individual reactions begin at a certain $(N/Z)_t$, increase rapidly with an increase of $(N/Z)_t$, and reach a plateau. The PICA calculations approximate the observed profiles as a whole. Notably, the positive slope regions of the $Y(E_0)$ vs. $(N/Z)_t$ curves are well reproduced, with some exceptions at $(N/Z)_t$ = 1.18 (^{59}Co), 1.32 (^{109}Ag), 1.35 (^{115}In), whereas the plateau values are largely discrepant. The PICA results underestimate by 35% the (γ,π^-) yields as noted above, but increasingly overestimate by factors of 1.5–2.0 the ($\gamma,\pi^- x$n) reaction yields for $x \geq 3$. The deviation increases with the increasing x. The calculations for light targets such as ^{7}Li, ^{11}B, ^{12}C, ^{14}N and ^{27}Al, for which observed values for either the (γ,π^-) or (γ,π^+) reactions are available, show small yields for reactions with x = 1–2, but show large deviations from the smooth trends of the yields for the heavier targets. Also it was found that the start values of $(N/Z)_t$, the slopes of the rising part, and the plateau values indicate smooth variations with respect to x, but all change their variations at $x \geq 5$. Also the sums of the yields of the reactions of x = 0 to 1, 2,$\cdots$,9 and the maximum possible x (max), $\sum^{x}_{i=0} Y_i(N/Z)_t$, increase sigmoidally with an increase of $(N/Z)_t$, showing that the $\sum^{max}_{i=0} Y_i(N/Z)_t$ curve consists of two sigmoides; one from $(N/Z)_t$ = 1.01 to 1.35 and the other from 1.35 to 1.55. The second sigmoid is steep, reflecting the rapid increase in the ($\gamma,\pi^- x$n) yields for $x \geq 5$ for the targets with $(N/Z)_t \geq 1.35$. All of these changes in the yield profiles for targets heavier than A_t = 100 might be associated with pronounced nuclear medium effects giving rise to more excessive excitation as compared with medium-heavy targets of $A_t \leq 100$. A more advanced theoretical model concordant with the present findings needs to be developed in order to better quantify the results.

Acknowledgement

The authors would like to express their gratitude to Drs. H. Okuno and K. Masumoto, and the ES crew members of the High Energy Accelerator Research Organization at Tanashi, for their invaluable cooperations in the course of experiments. This work was supported in part by the Grant-in-Aid for Scientific Research (07304077) of the Ministry of Education, Science and Culture of Japan.

References

[1] Sakamoto, K., Yoshida, M., Kubota, Y., Fukasawa, T., Kunugise, A., Hamajima, Y., Shibata, S., and Fujiwara, I.: Nucl. Phys. **A501**, 693 (1989).
[2] Sakamoto, K., Hamajima, Y., Soto, M., Kubota, Y., Yoshida, M., Kunugise, A., Masatani, M., Shibata, S., Imamura, M., Furukawa, M., and Fujiwara, I.: Phys. Rev. C**42**, 1545 (1990).
[3] Oura, Y., Yazawa, A., Yoshida, M., Sarkar, S. R., Sakamoto, K., Shibata, S., Fujiwara, I., and Furukawa, M.: Radiochim. Acta **68**, 27 (1995).
[4] Sakamoto, K., Sarkar, S. R., Oura, Y., Haba, H., Matsumura, H., Miyamoto, Y., Shibata, S., Furukawa, M., and Fujiwara, I.: Phys. Rev. C **59**, 1497 (1999).
[5] Gabriel, T. A. and Alsmiller, Jr., R. G.: Phys. Rev. **182**, 1035 (1969).
[6] Oura, Y., Kawaguchi, K., Sarkar, S. R., Haba, H., Miyamoto, Y., Sakamoto, K., Shibata, S., Fujiwara, I., and Furukawa, M.: Res. Rept. Lab. Nucl. Sci. Tophoku Univ. **27**, 133 (1994).
[7] Blomqvist, I., Nydahl, G., and Forkman, B.: Nucl. Phys. **A162**, 193 (1971).
[8] Nilsson, M., Schroder, B., Bulow, B., Grintals, J., Jonsson, G. G., Lindner, B., Srinivasa Rao, K., and Susila, S.: Z. Physik **A294**, 253 (1980).
[9] Nagl, A., Devanathan, V., and Uberall, H.: *Nuclear Pion Photoproduction* (Springer-Verlag, Berlin 1991).
[10] Bertini, H. W.: Phys. Rev. **131**, 1801 (1963).
[11] Hofstadter, R.: Rev. Mod. Phys. **28**, 214 (1956).
[12] Hansen, P. G., Jensen, A. S., and Jonson, B.: Ann. Rev. Nucl. Part. Sci., **45**, 591 (1995).
[13] Tanihata, I.: J. Phys. G: Nucl. Part. Phys. **22**, 157 (1996).

JP0150646

2.2

Heavy Element Nuclear Chemistry Research in JAERI *

Yuichiro NAGAME, Masato ASAI, Hiromitsu HABA, Kazuaki TSUKADA,
Minoru SAKAMA†, Shin-ichi GOTO, Ichiro NISHINAKA and Shin-ichi ICHIKAWA
Advanced Science Research Center, Japan Atomic Energy Research Institute
Tokai-mura, Ibaraki 319-1195, Japan
e-mail: nagame@popsvr.tokai.jaeri.go.jp

Abstract

Heavy element nuclear chemistry research in JAERI is reviewed. Recent experimental results on decay studies of neutron deficient actinide nuclei using the gas-jet coupled JAERI-ISOL are presented. Successful production of the transactinide nuclei, ^{261}Rf and ^{262}Db, and the present status of studies of chemical properties on the transactinide elements are introduced.

1 Introduction

Nuclear chemistry study of heavy elements in JAERI is currently being performed at the JAERI tandem accelerator facility. Nuclear decay studies of neutron deficient actinide nuclei are conducted using the gas-jet coupled JAERI-ISOL system and recently the new isotopes ^{233,236}Am and ^{237}Cm have been successfully identified. Quite recently, the transactinide nuclei ^{261}Rf and ^{262}Db have been produced for the first time in Japan via the reactions of ^{248}Cm(^{18}O,5n) and ^{248}Cm(^{19}F,5n), respectively. In this report, the present status of nuclear chemistry studies of heavy elements in JAERI is briefly summarized.

2 EC/α decay studies of neutron deficient actinides

There still remain many unknown isotopes to be discovered in the region of neutron deficient actinides which predominantly decay through the electron capture (EC). Decay properties of these nuclides lead to considerable advances in the understanding of proton excess heavy nuclei: verification of the proton drip line, nuclear structure of large deformed nuclei such as hexadecapole deformation, and fission barrier heights of neutron deficient nuclei far from stability.

To search for new isotopes and study EC/α decay properties of neutron deficient actinides, we have developed a composite system consisting of a gas-jet transport apparatus and a thermal ion source in the on-line isotope separator (JAERI-ISOL) [1]. This gas-jet coupled JAERI-ISOL system enables us to determine simultaneously mass number via the isotope separator and atomic number by the measurement of x rays associated with the EC/$\beta^{\pm}$ decay of a nucleus. Some new neutron rich rare-earth isotopes produced in the proton-induced fission of ^{238}U were identified

*In collaboration with Tokyo Metropolitan University, Nagoya University, Hiroshima University, Niigata University, Osaka University, Gesellschaft für Schwerionenforschung (GSI), Mainz University, Paul Scherrer Institut (PSI) and Bern University

†Permanent address: Department of Radiological Technology, Tokushima University, Tokushima 770-8509, Japan

with this system [2-5]. In the following, the EC/α decay studies of the neutron deficient actinides are summarized.

The experimental setup is schematically drawn in Fig. 1. The ^{6}Li beams delivered from the JAERI tandem accelerator bombarded the ^{233,235}U and ^{237}Np targets set in a multiple target chamber. The used reaction systems are ^{233}U(^{6}Li,xn)$^{233-235}$Am, ^{235}U(^{6}Li,5n)^{236}Am and ^{237}Np(^{6}Li,xn)^{237,238}Cm. Reaction products recoil out of the targets were thermalized in He gas loaded with PbI_2 aerosol clusters. The products attached to the aerosols were swept out of the target chamber and transported to the thermal ion source of ISOL through a capillary (1.5 mm i.d. and 8 m length). The transported nuclides were ionized in the thermal ion source, and mass-separated atoms were collected on an aluminum coated Mylar tape in a tape transport system or a rotating catcher foil apparatus. In the tape transport system, we use Ge detectors for the x/γ-ray measurement and the Si photodiode detectors set in the rotating catcher foil apparatus were employed for the measurement of α-rays. Detailed experimental procedures are described in [6, 7].

As a typical example, the identification of the new isotope ^{233}Am produced in the ^{233}U(^{6}Li,6n) reaction is described [7]. The isotope ^{233}Am was identified through an $\alpha-\alpha$ correlation analysis. The α decay of ^{233}Am is followed by the five successive α decays starting from ^{229}Np as shown in Fig. 2: ^{229}Np ($t_{1/2}$=4.0 min) $\rightarrow$ ^{225}Pa ($t_{1/2}$=1.7 s) $\rightarrow$ ^{221}Ac ($t_{1/2}$=52 ms) $\rightarrow$ ^{217}Fr ($t_{1/2}$=22 μs) $\rightarrow$ ^{213}At ($t_{1/2}$=125 ns) $\rightarrow$ ^{209}Bi (stable). Since the last four nuclides decay via α particle emission with the short half-lives, the α-α correlation events among these nuclides can be unambiguously identified. Figure 2 shows an α-particle spectrum constructed from the observed α-α correlation events in the mass-separated A=233 fraction. The α-ray energies of ^{233}Am and ^{229}Np are clearly observed and those corresponding to the decays of the other nuclides are also seen. The α-ray energy of ^{233}Am was determined to be 6780$\pm$17 keV, and from the decay curve of the intensity of this α-line, the half-life was 3.2$\pm$0.8 min. Since no Pu Kx-rays following the EC-decay of ^{233}Am was observed, the α-decay branching ratio was estimated as I_α >3% based on the detection efficiency of the Pu Kx-rays.

In Table 1, the half-lives, α decay energies and α-decay branching ratios measured in the present study and those compared with the literature data are shown. In the case of ^{235}Am, we first observed the α-decay process and the α branching intensity was derived from the ratio between the observed α and Pu Kx-ray intensities. The half-life value of ^{235}Am has been determined to be 10.3$\pm$0.6 min based on the decay curve of the α line of 6457 keV and that of Pu K_αx-rays following the EC decay of ^{235}Am. With the γ-γ coincidence technique, it is found that there are two EC-decaying states in ^{236}Am [8]. The α-decay processes in ^{234}Am and ^{236}Am were not observed in the preset experiments, although those were reported by Hall *et al.* [9] as shown in Table 1.

Table 1. EC/α decay properties of the neutron-deficient Am and Cm isotopes measured in the present work and those compared with the literature data.

Nuclide	Half-life (min)		α-energy (keV)		α branching ratio (%)	
	Present	Ref.	Present	Ref.	Present	Ref.
^{233}Am	3.2$\pm$0.8	(1.72)*	6780$\pm$17	(7100)*	> 3	
^{234}Am		2.32$\pm$0.08	-	6460	< 0.04	0.039$\pm$0.012
^{235}Am	10.3$\pm$0.6	15$\pm$5	6457$\pm$14	6700	0.40$\pm$0.05	
^{236g}Am	3.6$\pm$0.2	4.4$\pm$0.8	6150	6410	< 0.004	0.042$\pm$0.006
^{236m}Am	2.9$\pm$0.2					
^{237}Cm	$\approx$10	(15)*	6660$\pm$10	(6800)*		
^{238}Cm			6560$\pm$10	6520$\pm$50		

* Predicted

3 Nuclear chemistry studies of the transactinide elements

Studies of chemical properties of the transactinide elements - starting with element 104 (Rf) - offer the unique opportunity to obtain information about trends in the Periodic Table at the limits of nuclear stability and to assess the magnitude of the influence of relativistic effects on chemical properties. According to the calculations of the electron configurations of the transactinide elements, it is predicted that sudden changes in the structure of electron shells may appear due to the relativistic effects which originate from the increasing strong Coulomb field of the highly charged atomic nucleus. Thus, it is expected that the transactinide elements show a drastic rearrangement of electrons in their atomic ground states and as the electron configuration is responsible for the chemical behavior of the element, such relativistic effects can lead to surprising chemical properties. Increasing deviations from the periodicity of chemical properties based on extrapolation from lighter homologues in the Periodic Table are predicted. The main objective of the present group is to explore experimentally the influence of the relativistic effects on the electron shell structure by studying the chemical properties of the transactinide elements. The comparison studies of such fundamental chemical properties as the most stable oxidation states, complex ability and ionic radii with those of lighter homologues, and with results of relativistic molecular orbital calculations are invaluable in evaluating the role of the relativistic effects.

The transactinide elements must be produced by bombarding heavy radioactive actinide targets with high-intensity heavy ion beams and must be identified by the measurement of their decay or that of their known daughter nuclei with unambiguous detection techniques. Detailed studies of nuclear decay properties of transactinide nuclides are also the important subject.

Since 1998, we have developed some experimental apparatus for the transactinide nuclear chemistry study, *i.e.* a beam-line safety system for the usage of the gas-jet coupled radioactive ^{248}Cm target chamber, a rotating wheel catcher apparatus for the measurement of the α and SF decays of the transactinides and an automated rapid chemical separation apparatus based on the high performance liquid chromatography.

Quite recently, we have successfully produced the transactinides, ^{261}Rf and ^{262}Db, by using the ^{248}Cm(^{18}O,5n) and ^{248}Cm(^{19}F,5n) reactions, respectively. Figure 3 shows the schematic of the experiment for the production and identification of ^{261}Rf and ^{262}Db: the target chamber coupled to the gas-jet transport and the rotating wheel catcher apparatus. The ^{248}Cm target of 590 μg/cm^2 thickness was bombarded by the ^{18}O and ^{19}F beams with the intensity of 200-300 pnA. The recoiling products were stopped in He gas, attached to a KCl aerosol, and were continuously transported through a Teflon capillary to the rotating wheel catcher apparatus. The transported nuclei were deposited on polypropylene foils of 240 μg/cm^2 thickness and 20 mm diameter at the periphery of an 80-position stainless steel wheel of 80 cm diameter. The wheel was stepped at 30 s time intervals to position the foils between six pairs of Si PIN photodiode detectors. The details of the experimental procedures are described elsewhere [10].

The sum of α-particle spectra measured in the six top detectors in a 3.9 h irradiation for the production of ^{261}Rf is shown in Fig. 4(a). In the α energy range of 8.12-8.36 MeV, α lines from 78-s ^{262}Rf (8.28 MeV) and its daughter 26-s ^{257}No (8.22, 8.27, 8.32 MeV) are clearly shown. No contributions from other nuclides in this energy window are observed, although there exit several α lines originating from the Pb impurities in the ^{248}Cm target. A total of 98 events in the singles measurement and 28 α-α correlation events were registered. The production cross section of ^{261}Rf in this reaction was evaluated to be about 6 nb at the ^{18}O energy of 99 MeV.

Figure 4(b) shows the sum of α-particle spectra for the production of ^{262}Db in the 100 MeV ^{19}F-induced reaction of ^{248}Cm. From the mother-daughter correlation of α-energies between ^{262}Db-mother and ^{258}Lr-daughter, the cross section of this reaction was about 1 nb.

Because of the short half-lives and the low production rate of the transactinides, each atom produced decays before a new atom is synthesized. This means that any chemistry to be per-

formed must be done on an *atom-at-a-time* basis. Therefore rapid, very efficient and selective chemical procedures are indispensable to isolate the desired transactinides.

We have developed the gas-jet coupled automated chemical separation apparatus to perform rapid, repetitive and high performance liquid chromatography separations on the second time scale. It is equipped with two magazines, each containing twenty micro-columns (1.6 mm in diameter and 8 mm long). A series of chromatographic pumps, valves, mechanical sliders, and micro-columns are all controlled by a personal computer. The performance is almost the same as that of ARCA developed by the GSI-Mainz group [11]. On-line ion exchange experiments with the above apparatus are being carried out using the Rf homologues Zr and Hf produced via the ^{89}Y(p,n)^{89m}Zr and ^{152}Gd(^{18}O,xn)^{165,167}Hf reactions. The Rf chemistry experiments based on the ion exchange behavior will be started in the beginning of 2001.

Acknowledgements

We wish to acknowledge the crew of the JAERI tandem accelerator for providing the stable and intense ^{6}Li, ^{18}O and ^{19}F beams. This work was supported in part by the JAERI-University Collaboration Research Project and the Program on the Scientific Cooperation between JAERI and GSI in Research and Development in the Field of Ion Beam Application.

References

[1] Ichikawa S. *et al.*: Nucl. Instrum. Meth. Phys. Res. A **374**, 330 (1996).

[2] Asai M. *et al.*: J. Phys. Soc. Japan, **65**, 1135 (1996)

[3] Ichikawa S. *et al.*: Phys. Rev. C **58**, 1329 (1998).

[4] Asai M. *et al.*: Phys. Rev. C **59**, 3060 (1999).

[5] Ichikawa S. *et al.*: *Proceedings of the 2nd International Conference on Fission and Properties of Neutron-rich Nuclei*, St. Andrews, Scotland, June 28-July 3, 1999, World Scientific, Singapore, 2000, p. 203.

[6] Tsukada K. *et al.*: Phys. Rev. C **57**, 2057 (1998).

[7] Sakama M. *et al.*: Eur. Phys. J. A **9** 303 (2000).

[8] Asai M. *et al.*: to be published.

[9] Hall H. *et al.*: Phys. Rev. C **41**, 618 (1990) and LBL-27878 (1989).

[10] Haba H. *et al.*: *Extended Abstracts of the 5th International Conference on Nuclear and Radiochemistry*, Pontresina, Switzerland, September 3-8, 2000, p. 195.

[11] Schädel M. *et al.*: Radiochim. Acta **48**, 171 (1989).

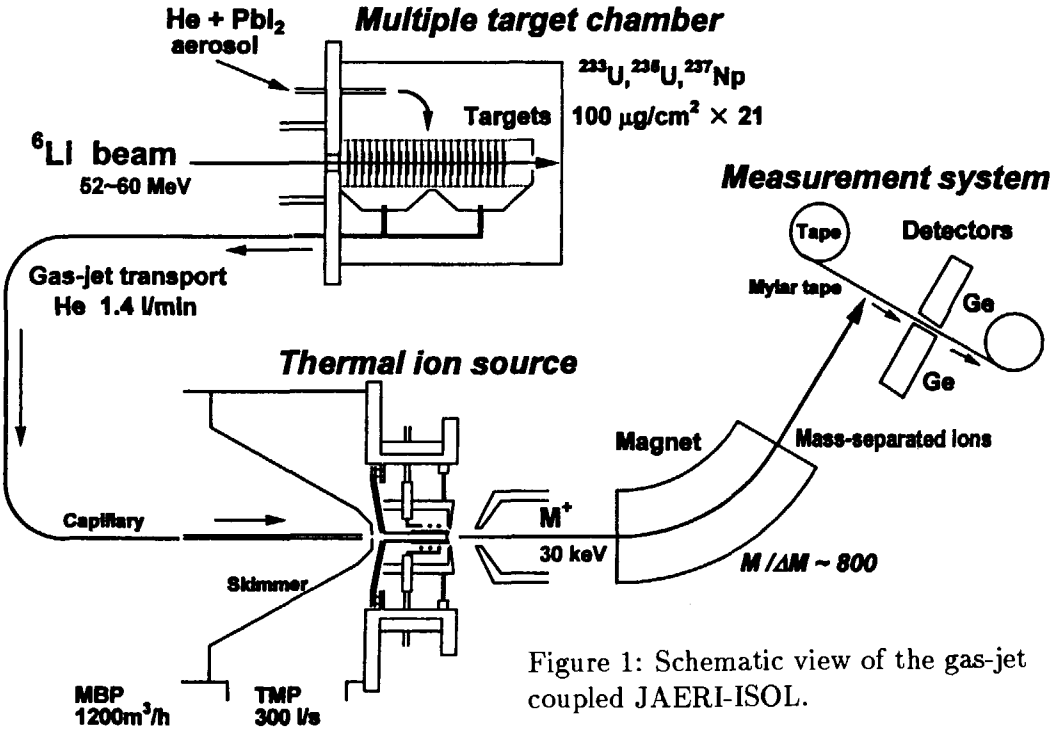

Figure 1: Schematic view of the gas-jet coupled JAERI-ISOL.

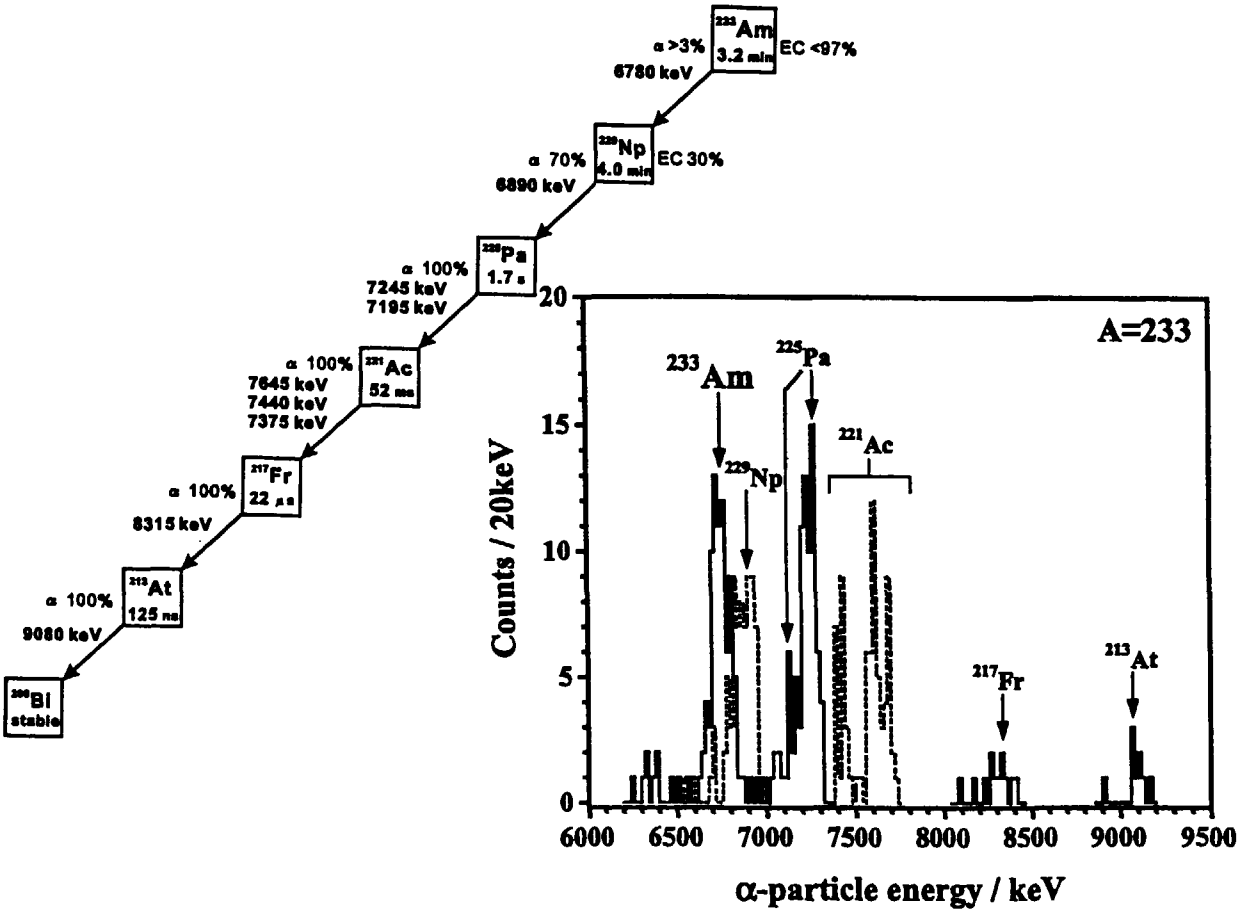

Figure 2: α-decay chain originating from the α decay of ^{233}Am, and α-particle spectrum constructed from the measured α-α correlation events associated with the α-decay of ^{233}Am.

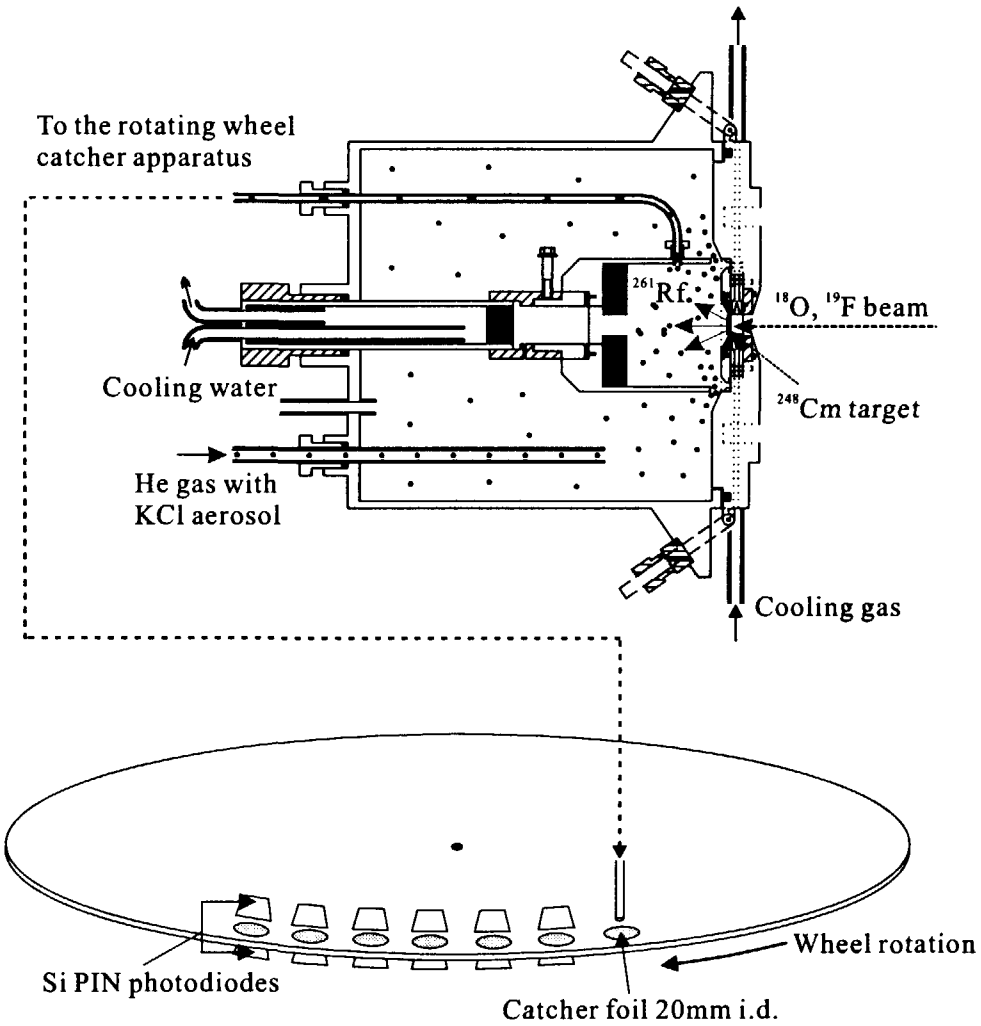

Figure 3: Schematic of the experiment for the production of ^{261}Rf and ^{262}Db.

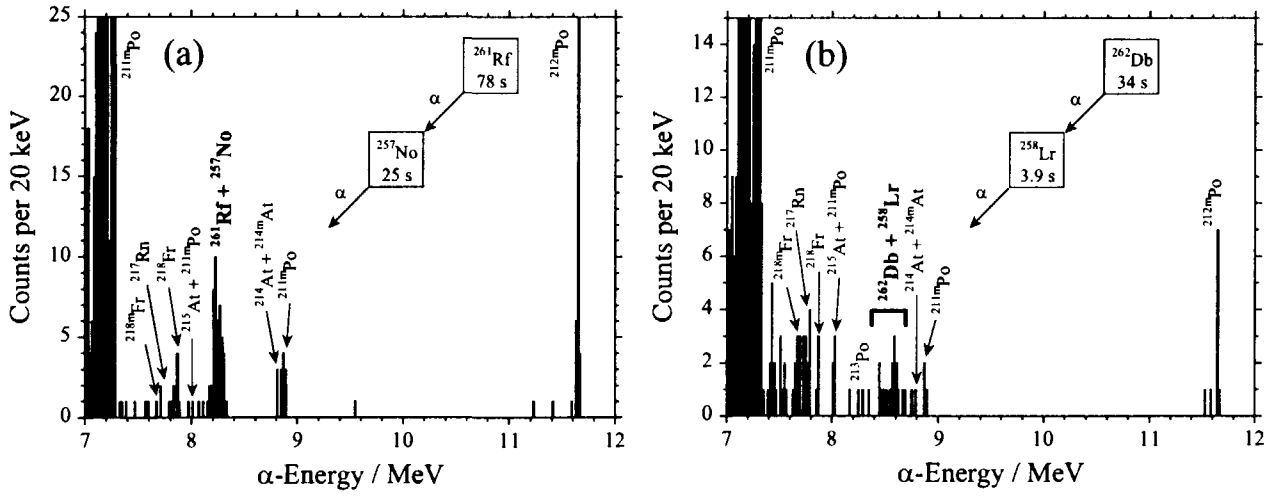

Figure 4: (a) Sum of α-particle spectra measured in the bombardment of the ^{248}Cm target with 99 MeV ^{18}O ions, and (b) that in the bombardment of the ^{248}Cm target with 100 MeV ^{19}F ions.

JP0150647

2.3

New Magic Number, N = 16, near the Neutron Drip-Line

Akira Ozawa
The Institute of Physical and Chemical Research (RIKEN),
Hirosawa 2-1, Wako-shi, Saitama 351-0198, Japan
e-mail: ozawa@rarfaxp.riken.go.jp

The neutron separation energies (S_n) and the interaction cross-sections (σ_I) for the neutron-rich *p-sd* and *sd* shell region have been surveyed in order to search for a new magic number. Very recently, both measurements have reached up to the neutron drip-line, or close to the drip-line, for nuclei of Z • 8. The neutron-number (N) dependence of S_n shows clear breaks at N=16 near to the neutron drip-line, which shows the creation of a new magic number. A neutron number dependence of σ_I shows a large increase of σ_I for N=15, which supports the new magic number. The origin and influence of the new magic number are also discussed.

1. Introduction

The shell structure is one of the very important quantities concerning nuclear structure. Nuclei show a closed shell structure for the following neutron (N) and proton (Z) numbers: 2, 8, 20, 28, 50, 82 and 126. They are called nuclear magic numbers. The appearance of magic numbers has been explained by Mayer and Jensen at 1949, introducing a spin-orbit coupling.

Recent improvements of radioactive beam (RI beam) technology allow measurements of the mass, half-life, size and other properties of unstable nuclei. Furthermore, nuclear reactions using RI beams have been studied very much [1]. Thus, based on the results, some interesting characteristics of unstable nuclei, such as a halo and a skin, have been revealed. In the points of nuclear magic numbers, the disappearance of some traditional magic numbers has been studied both experimentally and theoretically. For example, the disappearance of the N = 20 closed shell was shown in ^{32}Mg experimentally in terms of a low-lying 2^+ level [2] and a large $B(E2;0^+_1 \rightarrow 2^+_1)$ value [3]. Direct evidence for a breakdown of the N = 8 shell closure

was shown for ^{12}Be by studying the one-neutron knockout reaction (^{12}Be, ^{11}Be+γ) on a ^{9}Be target at 78 *A* MeV [4]. Although the disappearance of magic numbers has been discussed, as shown above, no appearance of a magic number has been shown experimentally so far.

From theoretical points of view, the appearance of new magic numbers in a neutron-rich region has been predicted within the framework of the energy-density formalism [5]. The authors in Ref. [5] predicted the appearance of N = 16, 34 and 58 as neutron magic numbers for unstable nuclei, together with a weakening of the shell closure at N = 20 and 28.

2. Search for new magic numbers

Recent improvements of secondary-beam techniques allow us to now measure the mass and the interaction cross-sections (σ_I) for nuclei on the neutron drip-line or close to the drip-line. One of the powerful mass measurements is a direct time-of-flight mass determination. The principle of this technique requires only a determination of the magnetic rigidity and velocity of an ion. That is, for a particle of mass m and charge q traversing through an achromatic system, the magnetic rigidity ($B\rho$) is related to the velocity (v) as $B\rho = mv/q$. Thus, a precise measurement of the rigidity and velocity would allow the mass of an ion to be deduced. Direct mass measurements have reached to the drip-line and near to the drip-line for $Z \bullet 8$ in a recent mass evaluation [6]. On the other hand, measurements of σ_I can be performed by the transmission method, which have been extensively measured at the projectile fragment separator facility (FRS) at GSI. FRS is the only available RI beam facility for relativistic energies (~1 *A* GeV). Recently, σ_I measurements have reached to the drip-line for $Z \bullet 8$, except for ^{22}C [7].

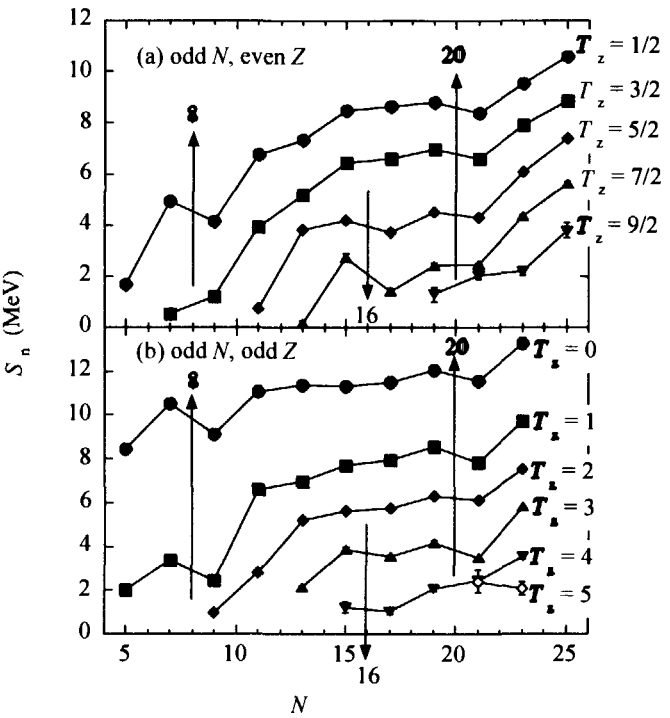

Fig. 1 Neutron-number (N) dependence for experimentally observed neutron separation energies (S_n).

The neutron-number dependence of experimentally observed S_n for nuclei with

odd N and even Z (odd N and odd Z) is shown in Fig. 1 (a) (Fig. 1 (b)), respectively. S_n is defined by the difference of the binding energies (BE) ($S_n(N,Z) = BE(N,Z) - BE(N-1,Z)$), where BE are determined by recent mass measurements. In Fig. 1, a magic number appears as a decrease of S_n along with an increase of N [8]. The traditional magic numbers (N=8, 20) are clearly seen close to stable nuclei as breaks in the small isospin numbers (T_z) lines. However, the break at N = 8 (N = 20) disappears at neutron-rich T_z= 3/2 (T_z= 4), which is also known concerning other experimental quantities, as discussed above. On the other hand, a break in the S_n line appears at N = 16 for T_z• 3, as clearly shown in Fig. 1, which indicates the creation of a new magic number in N = 16 near to the neutron drip-line.

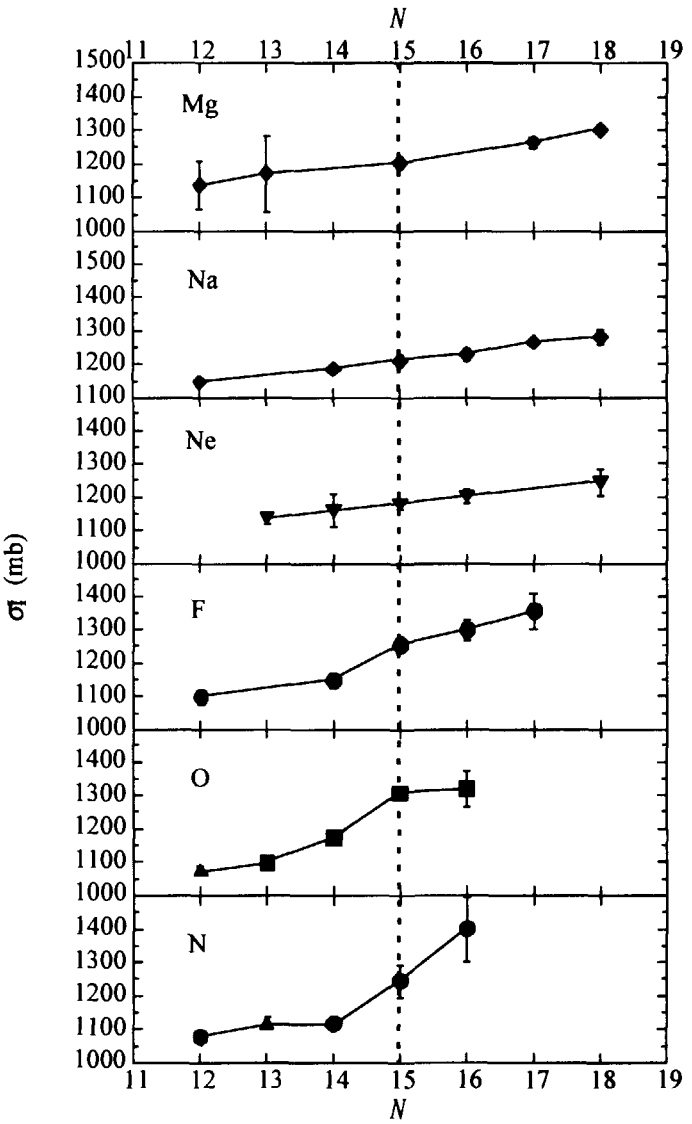

Fig. 2 Neutron-number (N) dependence for experimentally observed interaction cross-sections (σ_I) for N to Mg isotopes on C targets.

In Fig. 2, a neutron-number dependence of experimentally observed σ_I for N to Mg isotopes is shown. A steep increase of σ_I from N = 14 to N = 15 for N to F isotopes, is shown in Fig. 2. On the other hand, for Ne to Mg isotopes, no steep increase of σ_I is shown in Fig. 2, although some σ_I have large error bars. It is noted that a clear difference occurs at T_z= 3, which suggests some correlation for the new magic number N = 16, as shown in S_n. The recent development of a Glauber model analysis for few-body systems allows one to distinguish the single-particle wave-functions for the valence nucleon ($2s_{1/2}$ or $1d_{5/2}$ orbitals) [7]. The results of an analysis show a dominance of the $2s_{1/2}$ orbital for the valence neutron in ^{22}N, ^{23}O and ^{24}F.

On the other hands, in ^{25}Ne, ^{26}Na and ^{27}Mg, the nature of a mixing of $2s_{1/2}$ and $1d_{5/2}$ orbitals is shown. Thus, a valence neutron in the N = 15 chain shows the following tendency: the purity of the $2s_{1/2}$ orbital is larger when T_z is larger. This conclusion supports the creation of a new magic number at N = 16 near to the neutron drip-line, since a clear single-particle structure is suggested for N = 15 nuclei near to the neutron drip-line.

3. The origin of the new magic number

The origin of this new magic number may be due to neutron halo formation. Fig. 3 shows the single-particle orbitals of a neutron in the normal spherical Woods-Saxon potential. The single-particle orbitals were calculated for A/Z = 3 nuclei just to show the effect of neutron excess (A is the mass number). Normal shell gaps N=8, 20, 28 are seen in the region for a binding energy of about 6 to 8 MeV, as expected. However, for a weakly bound system in A/Z = 3 nuclei, the spacing, and even the ordering, of the orbitals changes. The most pronounced is the s orbital for N = 9, 10. In the region of a binding energy below 1 MeV, the $2s_{1/2}$ orbital is below the $1d_{5/2}$ orbital. This fact is clearly observed as an abnormal ground-state spin-parity of ^{15}C (J^{π}=1/2$^+$). It is also observed as a strong contribution of the $2s_{1/2}$ orbital to the formation of a neutron halo in ^{11}Li, ^{11}Be and ^{14}Be (the mixing of $(2s_{1/2})^2$ and $(1p_{1/2})^2$ in the halo wave function). The lowering of the s orbitals is due to halo formation. A neutron halo is formed since the orbital with a low angular momentum gains energy by extending the wave function. This effect is largest in the s orbital and next in the p orbital. The effect for the p orbitals is also seen in Fig. 3.

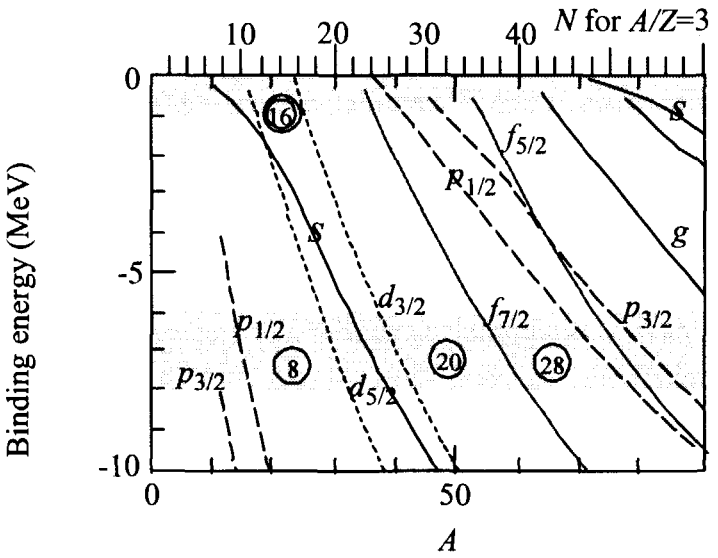

Fig. 3 Spectrum of single-neutron orbitals, obtained by the Woods-Saxon potential, for A/Z = 3 nuclei.

When the neutron number increases for a weakly bound system, strong mixing between $2s_{1/2}$ and $1d_{5/2}$ orbitals appears. Thus, the energy gap between these two orbitals and $1d_{3/2}$ become much larger. At weakly bound N = 16, the $2s_{1/2}$ and $1d_{5/2}$

orbitals are filled by neutrons leaving a large gap to the $1d_{3/2}$ orbital, as shown in Fig. 3. Thus, the mechanism that forms a neutron halo and makes the lowering of low-angular momentum orbitals, for weakly bound neutrons, is also essential for the appearance of the magic number N=16 near to the neutron drip-line. This mechanism may be common in nuclei near to the neutron drip-line. It therefore may destroy or produce other magic numbers in heavier elements, too.

4. Influence of the new magic number

Here, two aspects concerning the influence of the new magic numbers are pointed out. One is that the traditional nuclear shell model will be modified. A new modified shell model should explain the disappearance of magic numbers at neutron-rich N = 8 and 20, and the appearance of a magic number at N = 16 near to the neutron drip line. Another aspect is an influence on the *r*-process path. One of characteristics of the path is that the *r*-process goes through neutron magic numbers. Thus, if new magic numbers appear in the heavier neutron-rich region, such as near to N=82 and 126, the *r*-process path may be modified. Such a modification would solve any inconsistencies between calculations and observations for the *r*-process abundance [9].

5. Summary

In summary, a new magic number, N = 16, near to the neutron drip-line is introduced in this paper [10]. The new magic number has been surveyed by the neutron separation energies (S_n) and the interaction cross-sections (σ_I) for the neutron-rich *p-sd* and *sd* shell region. The neutron-number dependence of S_n shows clear breaks at N = 16 near to the neutron drip-line. The neutron-number dependence of σ_I shows a large increase in neutron-rich N = 15 nuclei, which shows that the purity of the $2s_{1/2}$ orbital is larger when the isospin number is larger in our analysis. These two facts indicate the appearance of a new magic number at N = 16 near to the drip-line. The origin of this new magic number may be due to neutron halo formation. The mechanism to form a new magic number may be common in nuclei near to the neutron drip-line. Other magic numbers in heavier elements may be produced. The new magic number may require modification of the traditional nuclear shell model and may change the possible *r*-process path.

References

[1] I.Tanihata, Experimental Techniques in Nuclear Physics, p.343 (Walter de Gruyter, 1997).

[2] D.Guillemaud-Mueller et al., Nucl. Phys. A 426, 37 (1984).
[3] T.Motobayashi et al., Phys. Lett. B 346, 9 (1995).
[4] A.Navin et al., Phys. Rev. Lett. 85, 266 (2000).
[5] M.Beiner et al., Nucl. Phys. A 249, 1 (1975).
[6] G.Audi and A.H.Wapstra, Nucl. Phys. A 595, 409 (1995).
[7] A.Ozawa et al., submitted to Nucl. Phys. A .
[8] A.Bohr and B.R.Mottelson, Nuclear Structure vol. 1, p.192 (W.A.Benjaming, 1969).
[9] S.E.Woosley et al., Astrophys. J. 433, 229 (1994).
[10] A. Ozawa et al., Phys. Rev. Lett. 84, 5493 (2000).

JP0150648

2.4
Present Status of JENDL-3.3

Tsuneo NAKAGAWA and Keiichi SHIBATA
Nuclear Data Center, Japan Atomic Energy Research Institute
Tokai-mura, Naka-gun, Ibaraki-ken 319-1195
e-mail: shibata@ndc.tokai.jaeri.go.jp

The latest version of JENDL General Purpose Library, JENDL-3.3, is being compiled. The evaluations for JENDL-3.3 have been performed mainly by the Medium-Heavy Nuclide Data Evaluation WG, the Heavy Nuclide Data Evaluation WG and the Delayed Neutron WG in the Japanese Nuclear Data Committee. The main objective of the evaluations is to solve the problems that were pointed out in JENDL-3.2.

1. Introduction

The library JENDL-3.2 [1] was released in 1994, and it has been used in various fields. This library was examined [2] by considering the feedback from users. As a result, we found several problems in JENDL-3.2: overestimation of k_{eff} for thermal reactors, inadequate neutron spectra for heavy nuclides, neglect of direct and semi-direct processes in capture cross sections, and inconsistency between natural and isotopic data. Two Working Groups, Medium-Heavy Nuclide Data Evaluation WG and Heavy Nuclide Data Evaluation WG, were organized to solve these problems in the Japanese Nuclear Data Committee. The two WGs carefully looked into the JENDL-3.2 data by comparing with differential and integral measurements. After that, the evaluated data have been improved.

This paper describes how the evaluation was performed in the heavy and medium-heavy mass regions.

2. Evaluation

2.1 Heavy Nuclides

2.1.1 Resonance Parameters of ^{235}U

The biggest problem of JENDL-3.2 is that the k_{eff} values are overestimated by 0.3~1% for thermal reactors as compared with those of JENDL-3.1. We adopted the resonance parameters obtained by Leal et al. [3] for JENDL-3.3. These parameters were recommended to use by the NEANSC Working Party on Evaluation Cooperation Subgroup 18. Figures 1

and 2 show the fission and capture cross sections of ^{235}U, respectively. Smaller fission cross sections below 0.3 eV lead to decreasing the k_{eff} values. One can see a large difference in the capture cross section between JENDL-3.3 and JENDL-3.2 in the energy region from several hundreds of eV to 2 keV.

2.1.2 Fission Cross Sections of U and Pu Isotopes

Fission cross sections of $^{233, 235, 238}$U and $^{239, 240, 241}$Pu were simultaneously evaluated [4] by taking account of ratio measurements as well as absolute measurements in the energy region from 30 keV to 20 MeV, as was done in the JENDL-3.2 evaluation. About 170 sets of measurements (4560 data points) were used in the evaluation. The evaluated ^{233}U(n,f) and ^{235}U(n,f) cross sections are shown in Figs. 3 and 4, respectively. It is found from Fig 3 that the presently evaluated ^{233}U(n,f) cross sections are lower than those of JENDL-3.2 above 300 keV. As for ^{235}U, the present values are different from the JENDL-3.2 cross sections above 14 MeV, which comes from the fact that the experimental data measured by Lisowski et al. [5] were employed in the present evaluation above 12 MeV. The change in the fission cross section of ^{235}U influenced other cross sections through their ratios.

2.1.3 Neutron Emission Spectra

Fission neutron spectra from ^{235}U and ^{239}Pu were re-evaluated by the multi-modal analyses. The ratio of JENDL-3.3 to JENDL-3.2 is illustrated in Fig. 5 at thermal energy. As for ^{235}U, the JENDL-3.3 spectrum is harder than that of JENDL-3.2.

Unphysical continuum neutron spectra from the (n,n') reaction are contained for some nuclides in JENDL-3.2. These spectra were replaced with the calculations using the EGNASH code [6]. In JENDL-3.3, we use the ENDF interpolation law INT=22 for neutron spectra, leading to appropriate interpolation of the spectra between the adjacent incident energies given in the library.

Concerning delayed neutron spectra, we adopted those values calculated by Brady and England [7] which were recommended to use by the Delayed Neutron WG.

2.2 Medium-Heavy Nuclides

2.2.1 Outline of Evaluations

Resonance parameters of V, Cr, Fe, Co and W isotopes were updated. The Reich-Moore formula was used for these nuclei except W.

The data for natural elements were contained in JENDL-3.2. However, there is inconsistency between the natural and isotopic data. In JENDL-3.3, we did not make elemental data for structural-material nuclei. In the case where experimental data on total cross sections were available for a natural element, isotopic data were evaluated so that the

sum of the isotopic data reproduced the measurements of the natural element.

The EGNASH code was rigorously used to evaluate the cross sections for the threshold reactions such as (n,2n) and (n,p). The neutron emission spectra were taken from the DDX data in JENDL/F-99 [8] for many nuclides.

2.2.2 Iron Data

The resonance parameters of $^{54, 56}$Fe were taken from ENDF/B-VI and JEF-2.2, respectively. As a result, the upper limit of the resolved resonance region turned out to be 700 keV for ^{54}Fe and 850 keV for ^{56}Fe, while those of JENDL-3.2 is 250 keV for both nuclei.

The total cross sections of $^{54, 56}$Fe were revised above the resonance region. As for ^{54}Fe, the evaluation is based on the experimental data measured by Carlton et al. [9] and Conelis et al. [10] Three sets of the measurements [11-13] were used to estimate the total cross sections of elemental iron. The total cross section of ^{56}Fe was obtained by subtracting the contribution of other isotopes from the elemental data. It is found from Fig. 6 that the presently evaluated cross sections are higher than those of JENDL-3.2 in the energy region from 1 keV to 1 MeV on the average.

3. Concluding Remarks

The evaluation for JENDL-3.3 was described with an emphasis on heavy-nuclide data. The number of nuclides, whose data are revised, would be about 90. It is expected that 18 new evaluations are compiled into JENDL-3.3 such as Hg, Er and a few minor actinides. We are going to release the library in the spring of 2001.

Acknowledgment

The members of the Japanese Nuclear Data Committee have made great efforts to carry out the JENDL-3.3 evaluations, which were briefly described in this paper. The authors would like to appreciate their cooperation.

References

[1] Nakagawa T., et al.: *J. Nucl. Sci. Technol.*, **32**, 1259 (1995).

[2] Japanese Nuclear Data Committee: Private communication (1998).

[3] Leal L.C., et al.: *Nucl. Sci. Eng.*, **131**, 230 (1999).

[4] Kawano T., et al.: *J. Nucl. Sci. Technol.*, **37**, 327 (2000).

[5] Lisowski P.W., et al: Proc. Specialists' Meeting on Neutron Cross Section Standards above 20 MeV", Uppsala 1991, p.177 (1991).

[6] Yamamuro N.: JAERI-M 90-006 (1990).

[7] Brady M.C. and England T.R.: *Nucl. Sci. Eng.*, **103**, 129 (1989).

[8] Chiba S., et al.: *Fusion Eng. Design*, **37**, 175 (1997).

[9] Carlton R.F., et al.: *Bull. Am. Phys. Soc.*, **30**, 1252 (1985).

[10] Cornelis E., et al.: Proc. Int. Conf. Nuclear Data for Science and Technology, Antwerp 1982, p.135 (1983).

[11] Berthold K., et al.: Taken from EXFOR (1995).

[12] Carlson A.D. and Cerbone R.J.: *Nucl. Sci. Eng.*, **42**, 28 (1970).

[13] Perey F.G., et al.: ORNL-4823 (1972).

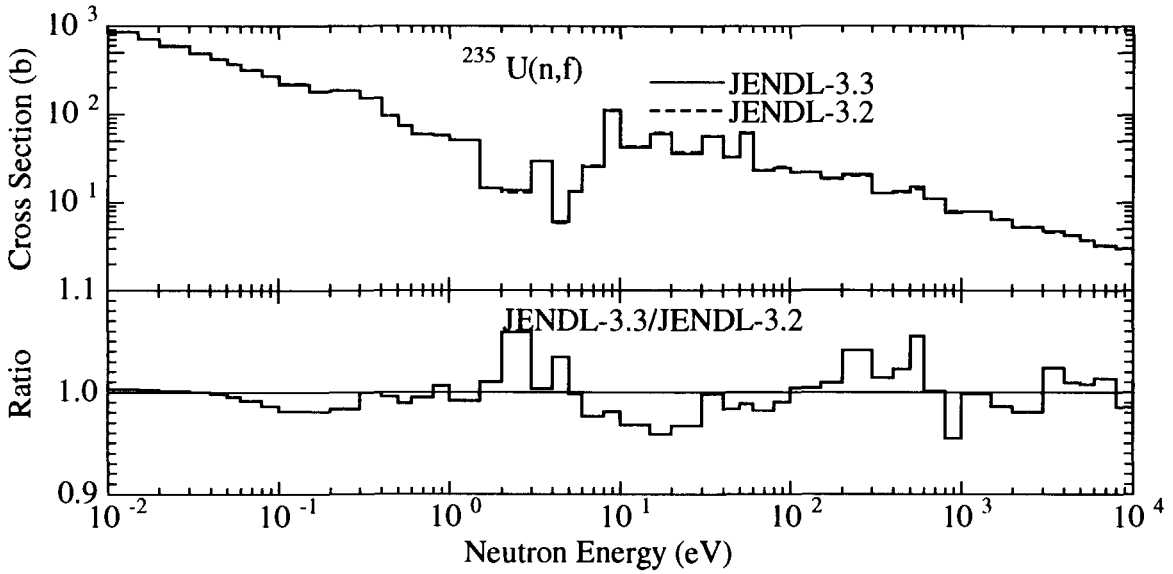

Fig. 1 Fission cross sections of ^{235}U.

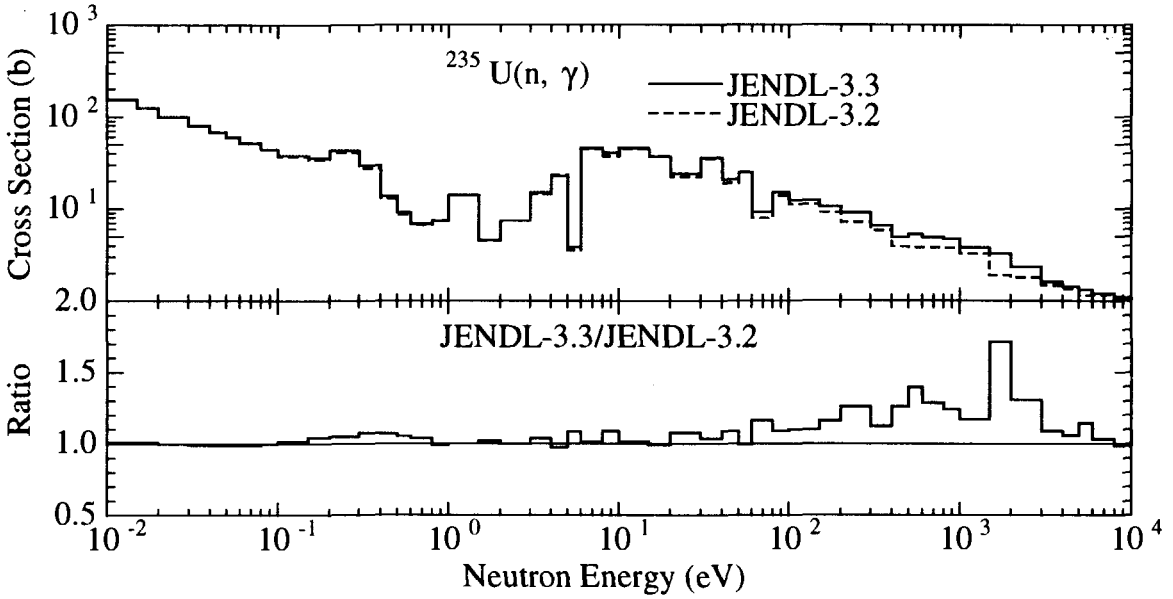

Fig. 2 Capture cross section of ^{235}U.

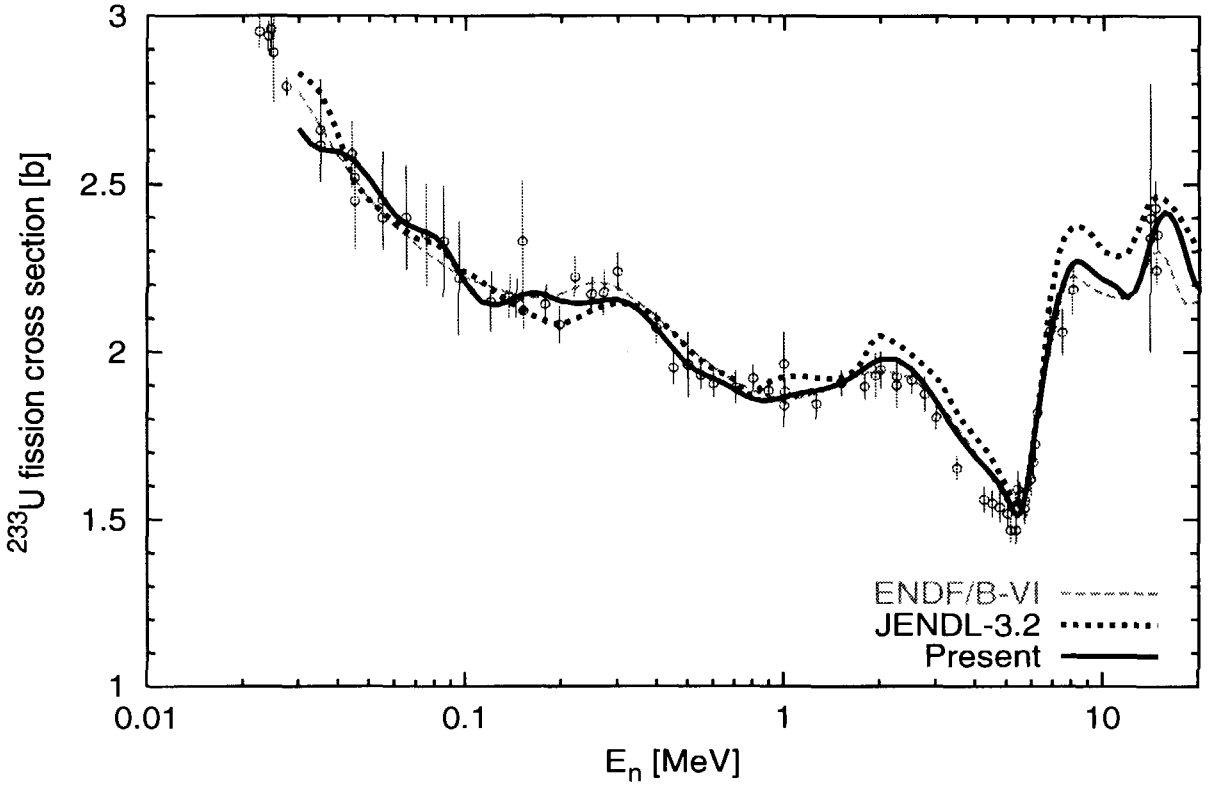

Fig. 3 Fission cross section of ^{233}U.

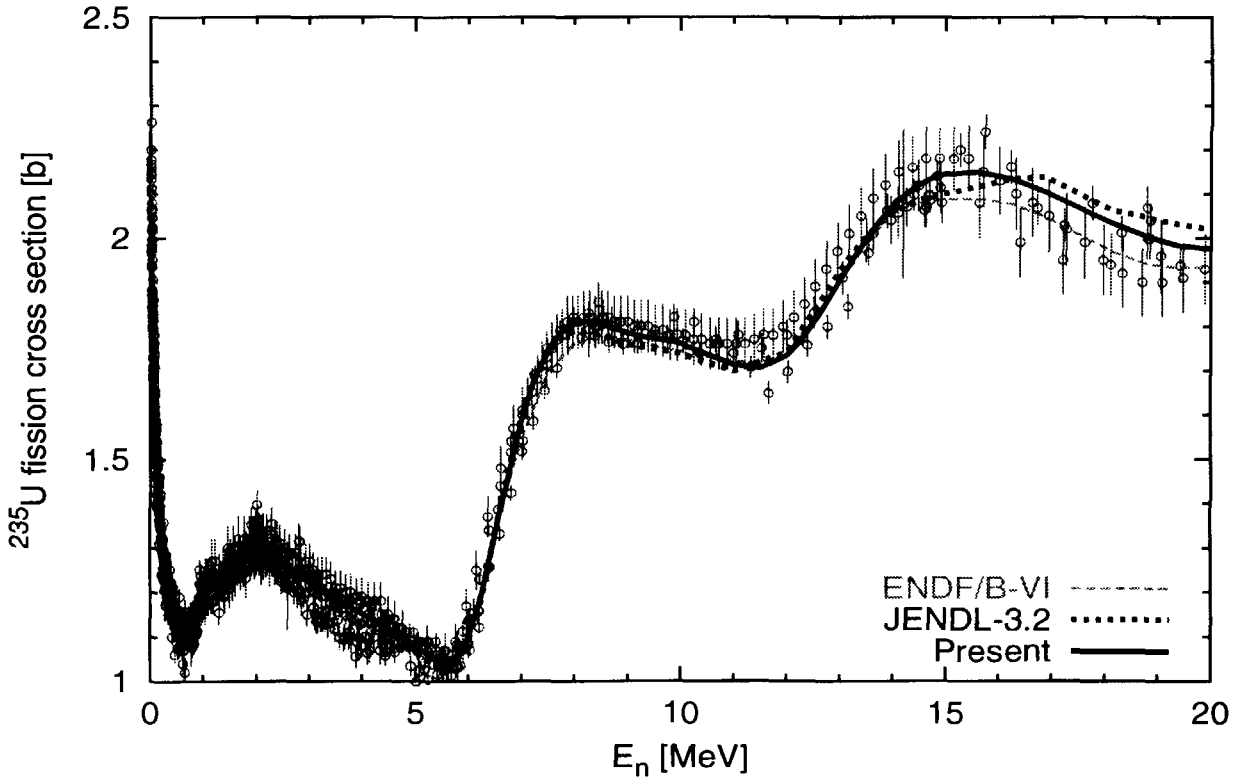

Fig. 4 Fission cross section of ^{235}U.

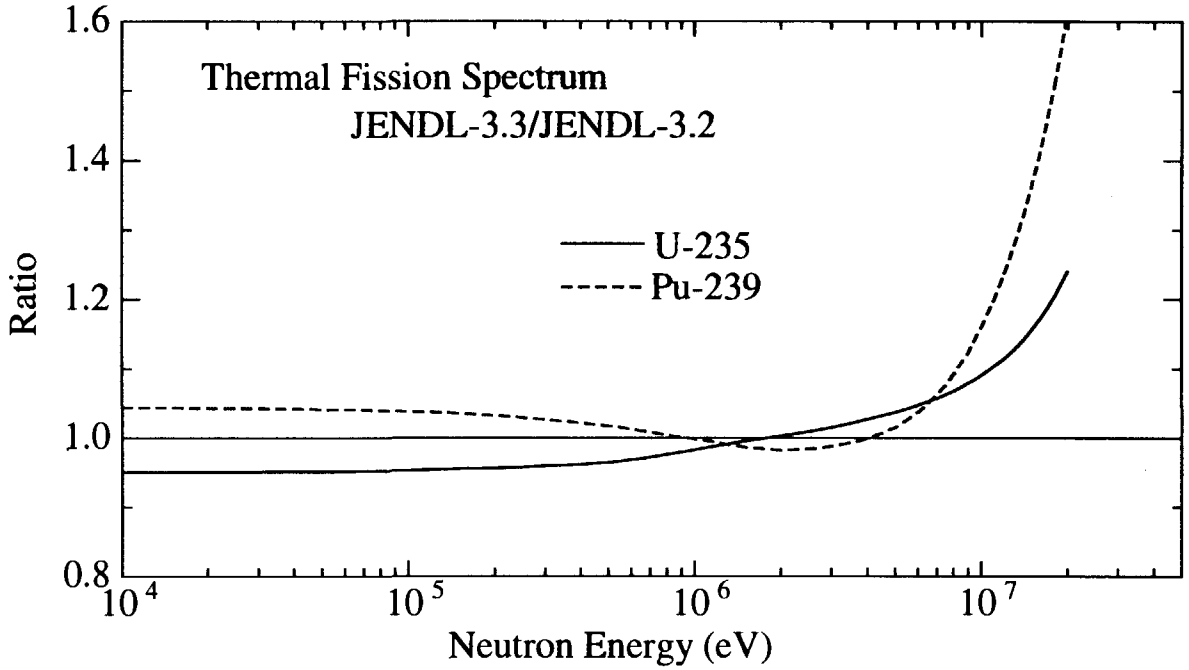

Fig. 5 Thermal fission spectra from ^{235}U and ^{239}Pu.

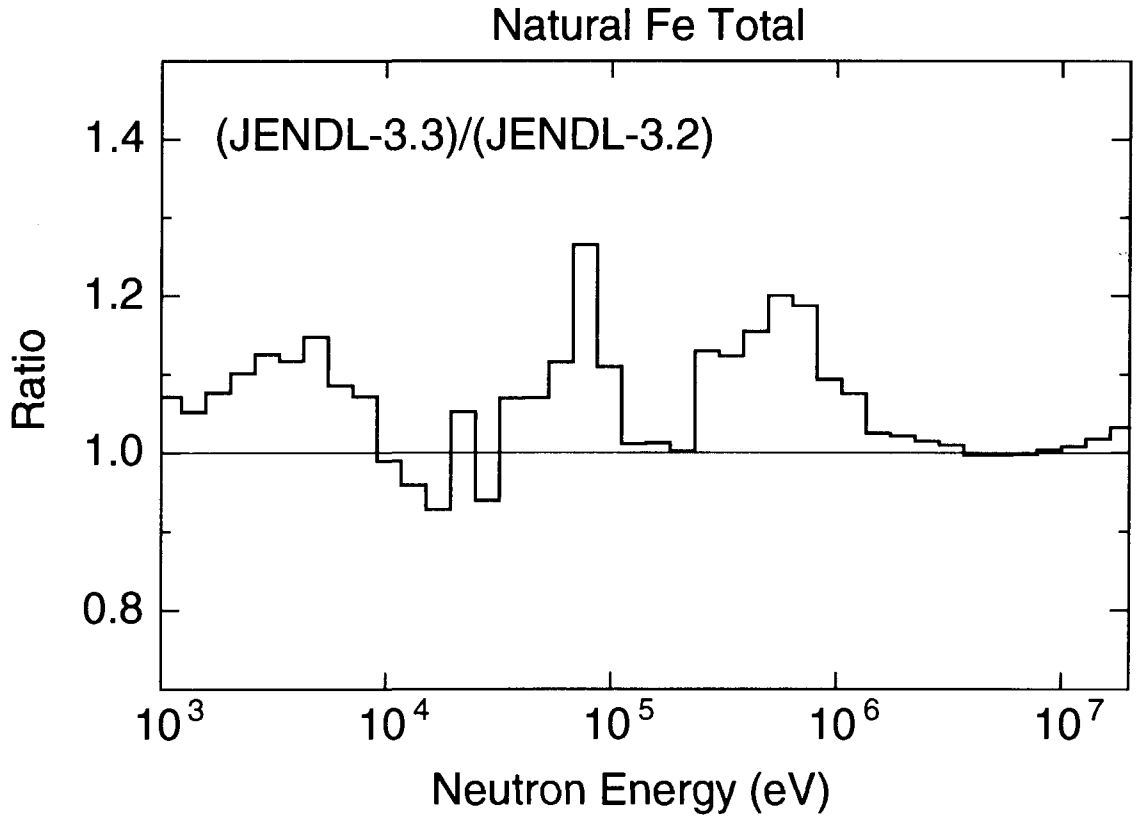

Fig. 6 Total cross section of elemental iron.

JP0150649

2.5

Validation of JENDL-3.3 by Criticality Benchmark Testing

Hideki TAKANO, Tsuneo NAKAGAWA and Kunio KANEKO*

Japan Atomic Energy Research Institute,

Tokai-mura, Naka-gun, Ibaraki-ken, 319-11, Japan

Takano@cens.toaki.jaeri.go.jp, nakagawa@ndc.tokai.jaeri.go.jp, kanekoku@can.bekkoame.ne.jp

In the thermal uranium core, the keff-values of STACY, TRACY and JRR-4 overestimated with JENDL-3.2 were improved significantly by decreasing of about 0.6 % with JENDL-3.3. This is due to modification of the fission spectrum and thermal fission cross section of ^{235}U from JENDL-3.2 to JENDL-3.3 data. For the uranium fast cores, the discrepancies of keff values between JENDL-3.2 and 3.3 were very small. In the thermal Pu cores of TCA, the keff-values calculated with JENDL-3.3 were in good agreement with the experimental values. For Pu fuel cores of ZPPR-9 and FCA-XVII, the keff values calculated with JENDL-3.3 became larger 0.2 % than those for JENDL-3.2. In small fast cores with U-233 fuel, the keff-values overestimated with JENDL-3.2 were improved considerably with JENDL-3.3, due to reevaluation of U-233 fission cross sections in the high energy region.

1. INTRODUCTION

In order to accurately assess neutronic behavior of various types of reactors, it is necessary to validate both calculation methods and nuclear data by analyzing integral experimental data. On the nuclear data development, the updated version of JENDL-3 nuclear data library, JENDL-3.3, has been tentatively released to test the validation in early 2000.

In fast reactor benchmark calculations, the selected cores are LMFBR mock-up cores ZPPR-9 and FCA-XVII-1, and small fast reactor cores such as JEZEBEL, GODIVA and FLATTOP with hard neutron spectrum. For thermal reactors, the JRR-4, TRX and TCA cores with water moderated lattice of U or Pu fuel, and furthermore the STACY and TRACY with uranyl nitrate solution were selected.

All the benchmark calculations were performed with the continuous energy Monte Carlo code MVP to reduce the uncertainties of core geometrical modeling and data processing for multigroup cross sections production.

The objective of this benchmark calculations is validation of JENDL-3.3 released tentatively to

assess neutronic behavior of various types of reactors, to validate both calculation methods and nuclear data by analyzing integral experimental data. We confirmed the JENDL-3.3 shows the best results based on the comparative studies with the other nuclear data; JENDL-3.2, ENDF/B-VI and JEF-2.2.

2. BENCHMARK CORES AND ITS CHARACTERISTICS

Thermal neutron cores: For the thermal reactors, JRR-4, TCA and TRX as the water moderated lattice cores of U or Pu fuel, and STACY and TRACY as the critical cores with uranyl nitrate solution were selected. In the uranium fueled cores, TCA-150U, -183U, -248U, -300U are low-enriched UO_2 lattice, and TRX-1 and 2 are uranium-metal hexagonal lattice. And STACY, TRACY and JRR-4 are high-enriched research reactors with 10 and 20%EU. For these high-enriched cores, JENDL-3.2 overpredicted significantly the keff-values. As the plutonium fueled cores, TCA-242Pu, -298Pu, -424Pu and -555Pu are PuO_2 lattice with low Pu contents. U enrichment and Pu content in the thermal cores are as follows: TCA-UO2 is 2.6%EU, TRX-U 1.3%EU, JRR-4 20%EU, STACY and TRACY the uranyl solution of 10%EU, and TCA-MOX 3%Pu content.

Fast neutron cores: For the fast reactors, we selected JEZEBEL, GODIVA, FLATTOP and BIGTEN of small and very hard neutron spectrum cores with U-235, Pu and U-233, and ZPPR-9, ZPPR-13A and FCA-XVII-1 of large FBR mock-up cores. Table 1 shows the geometrical sizes for the small cores. In the U-235 cores, GODIVA is the bare sphere of highly enriched U, FLATTOP-25 the bare sphere of highly enriched U with U-reflector and BIGTEN the cylinder of 10%EU with U-reflector. In the U-233 cores, JEZEBEL-23 is the bare sphere of 98% enriched U-233 fuel and FLATTOP-23 the bare sphere of U-233 fuel with U-reflector. In the Pu cores, JEZEBEL is the bare sphere of Pu fuel, JEZEBEL-Pu the bare sphere of Pu fuel with 20%Pu-240, FLATTOP-Pu the bare sphere of Pu fuel with U-reflector and THOR the bare sphere of Pu fuel with Th-reflector. As large size LMFBR cores, ZPPR-9 is the reference core of MOX-FBR in JUPITER program, ZPPR-13A the radial heterogeneous core and FCA-XVII-1 the MOX-FBR mockup core with a highly-enriched uranium driver region.

Table1 Geometrical sizes of small fast reactors

Core	sphere radius(cm)	reflector thicness(cm)
GODIVA	8.741	
FLATTOP-25	6.116	24.13
JEZEBEL	6.385	
JEZEBEL-Pu	6.660	
FLATTOP-Pu	4.533	24.13
JEZEBEL-23	5.983	
FLATTOP-23	4.317	24.13
THOR	sphere:r=5.310, cylinder-radius:26.65, Height:53.30	
BIG10	cylinder radius: 41.91, Height: 96.428	

3. BENCHMARK CALCULATION

In this calculation, the continuous energy Monte Carlo code, MVP[1] is used from the point of view to reduce the uncertainties of core geometrical modeling and data processing for multigroup cross sections production, and as the calculation time is the shortest. All the benchmark cores are calculated with MVP library generated based on JENDL-3.3.

The calculation conditions are as follows: Statistical error of keff is 0.02%. The calculation CPU time is 10 h for TCA, 1-6h for small fast cores and 18h for large FBRs, respectively. History No. per one batch is 20,000. Initial batch No. is 400,000. The highest energy is 20 MeV. The lowest energy is 10^{-5} eV. Thermal cut energy is below 4.5 eV, and S(α,β) of ENDF/B-III data is used. Furthermore, the unresolved resonance region is treated by the probability table method.

We studied that the difference between keff-values calculated with MVP and MCNP4B using JENDL-3.2 data. The preliminary results of the ratios of MVP to MCNP4B for the keff-values are as follows: 1.0013 for the cell calculation of UO_2 pin, 0.99998 for STACY, 1.0008 – 1.0021 for TCA-UO2, 1.0003 – 1.00224 for TCA-PuO_2, 1.002 for GODIVA and 0.99936 for JEZEBEL. That is, the results of MVP become larger 0.1 – 0.2 % for U-cores and smaller 0.1 % for small fast neutron Pu core. As this causes, we can consider the differences between both codes for unresolved resonance PT method, S(α,β), pointwise cross section production error, fission spectrum and inelastic scattering cross sections.

4. RESULTS AND DISCUSSIONS

The calculated results are shown in Tables 2, 3, 4 and 5. In these tables, the results calculated with JENDL-3.3 are compared with those calculated with JENDL-3.2, ENDF/B-VI.5 and JEF-2.2. We

Table 2 Comparison of the C/E(keff)-values for U-fuel thermal cores

Core	JENDL-3.3	JENDL-3.2	ENDF/B-VI.5	JEF-2.2
TCA150U	0.9960	1.0005	0.9921	1.0005*
TCA183U	0.9960	1.0011	0.9925	1.0014*
TCA248U	0.9967	1.0017	0.9935	1.0004*
TCA300U	0.9966	1.0011	0.9940	0.9983*
TRX-1	0.9920	0.9951	0.9902	0.9958*
TRX-2	0.9922	0.9954	0.9905	0.9937*
STACY	1.0036	1.0079	1.0002	*without U234: 0.15%
TRACY	1.0034	1.0082		

can see that the keff-values of STACY, TRACY[2] and JRR-4 in the highly enriched U fuel cores overestimated with JENDL-3.2 are improved significantly by decreasing of about 0.6 % with

JENDL-3.3. This is due to modification of the fission spectrum and thermal fission cross sections from JENDL-3.2 to JENDL-3.3 data. The keff-values of TRX cores are underestimated by all the nuclear data libraries, especially ENDF/B-VI.5. The keff-values for PuO_2 fuel cores of TCA calculated with all the nuclear data libraries are in very good agreement with the experiments.

Table 3 Comparison of the C/E-values (keff) for Pu-fuel thermal cores

Core	JENDL-3.3	JENDL-3.2	ENDF/B-VI.5	JEF-2.2
TCA242Pu	0.9966	0.9959	0.9946	0.9952
TCA298Pu	0.9975	0.9968	0.9948	0.9977
TCA424Pu	0.9985	0.9978	0.9954	
TCA555Pu	0.9988	0.9987	0.9967	

Table 4 Comparison of the C/E(keff)-values calculated for small cores

Cores	JENDL-3.3	JENDL-3.2	ENDF/B-VI.5	JEF-2.2
U-235 fuel				
GODIVA	1.0032	1.0030	0.9965	0.9953
FLATTOP-25	0.9983	0.9986	1.0037	0.9917
BIGTEN	0.9976	0.9984	1.0149	1.0044
Pu fuel				
JEZEBEL	0.9972	0.9972	0.9972	0.9970
JEZEBEL-Pu	1.0020	1.0015	0.9987	0.9990
FLATTOP-Pu	0.9923	0.9928	1.0041	0.9889
THOR	1.0068	1.0061	1.0059	0.9800
U-233 fuel				
JEZEBEL-23	1.0039	1.0129	0.9933	0.9641
FLATTOP-23	1.0003	1.0069	1.0028	0.9710

Table 5 Comparison of the keff and C/E-values for the ZPPR-9 and FCA-XVII-1 cores. The experimental keff-values are 1.00106 for ZPPR-9 and 0.9992 for FCA-XVII-1, respectively.

Nuclear data	Keff		C/E-value	
	ZPPR-9	FCA-XVII-1	ZPPR-9	FCA-XVII-1
JENDL-3.3	0.9976	1.0029	0.9965	1.0037
JENDL-3.2	0.9953	1.0011	0.9942	1.0019
ENDF/B-VI.5	1.0040	1.0104	1.0029	1.0112
JEF-2.2	0.9964	1.0073	0.9953	1.0081

The keff-values calculated for the fast neutron cores are shown in Tables 4 and 5. In the U-235 fuel cores, the keff-values for JENDL-3.3 and 3.2 show very good agreement with the experiments. For ZPPR-9 of large Pu FBR mock up core, JENDL-3.3 improves by 0.2 % the keff-value underestimated with JENDL-3.2. The causes are investigated by a sensitivity analysis with changing the nuclides from JENDL-3.2 to JENDL-3.3 as shown in Fig. 1. From this figure, the most important effect on keff is due to Iron of which total cross sections become large at the MeV to 100 keV region in JENDL-3.3, comparing with JENDL-3.2 data described in the previous paper by Nakagawa and Shibata. For the U-233 core, JENDL-3.3 shows the best estimation for keff-values in all the libraries.

5. CONCLUDING REMARKS

Thermal neutron spectrum core

U235-fuel: the keff-values of STACY, TRACY and JRR-4 overestimated with JENDL-3.2 were improved significantly by decreasing of about 0.6 % with JENDL-3.3. This is due to modification of the fission spectrum and thermal fission cross sections from JENDL-3.2 to JENDL-3.3 data. In TCA, the keff-values calculated from JENDL-3.3 were in good agreement with the experiments.

Pu-Fuel: the keff-values of TCA calculated from JENDL-3.3 were in good agreement with the experimental values.

Fast neutron spectrum cores

U235-fuel: the keff-values for JENDL-3.3 were in good agreement with the experimental values and the discrepancies between JENDL-3.2 and 3.3 were very small.

Pu-fuel: in ZPPR-9 and FCA-XVII-1, the keff values calculated with JENDL-3.3 became larger 0.2 % than those for JENDL-3.2.

U233-fuel: the keff-values overestimated with JENDL-3.2 were improved considerably with JENDL-3.3, due to reevaluation of U-233 fission cross sections in the high energy region.

Comparison of the results for JENDL-3.3 with those for ENDF/B-VI.5

For thermal and fast cores, and U-235, Pu and U-233 fuel cores, the keff-values for JENDL-3.3 showed better agreement with the experiments than those for ENDF/B-VI.5 as shown in Fig. 2.

Future works: Remained Benchmark calculations are as follows:

Reaction rate ratios and distributions. Reactivities for void, control rod and Doppler for FBRs.

Estimation of buildup nuclides by burnup calculation.

Comparative study between the discrepancies of keff-values calculated with MVP and MCNP.

Production of the multigroup cross section libraries for SRAC-J3.3 and JFS3-J3.3

REFERENCES

(1) Mori T. et al.: J. Nucl. Sci. Technol., 29, 325 (1992).

(2) Miyoshi Y., Kaneko K., Nakamura et al.: private communication.

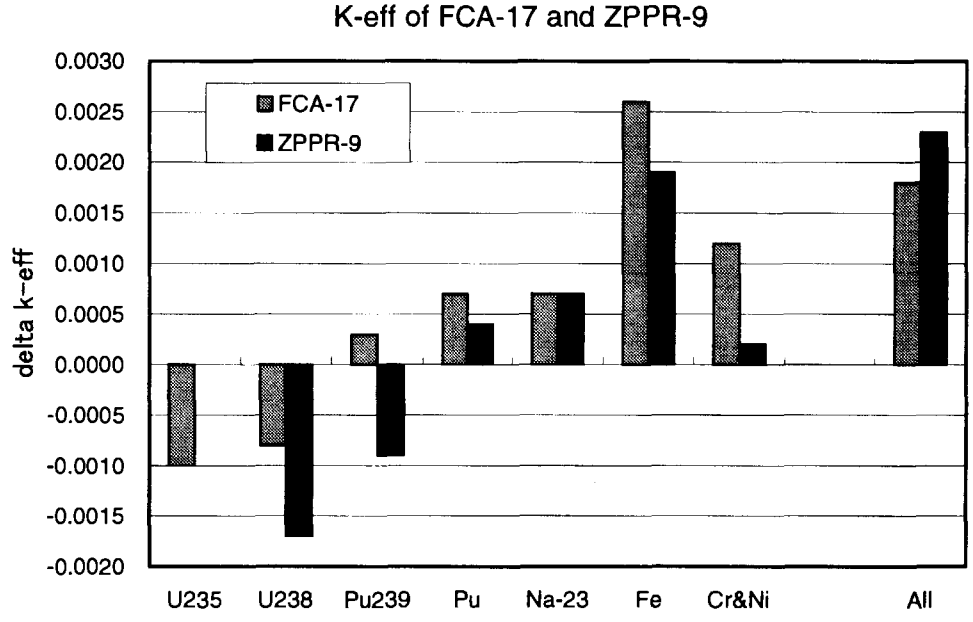

Fig. 1 Sensitivity analysis of nuclear data of nuclides changed from JENDL-3.2 to 3.3 in large FBR mockup cores of ZPPR-9 and FCA-XVII-1

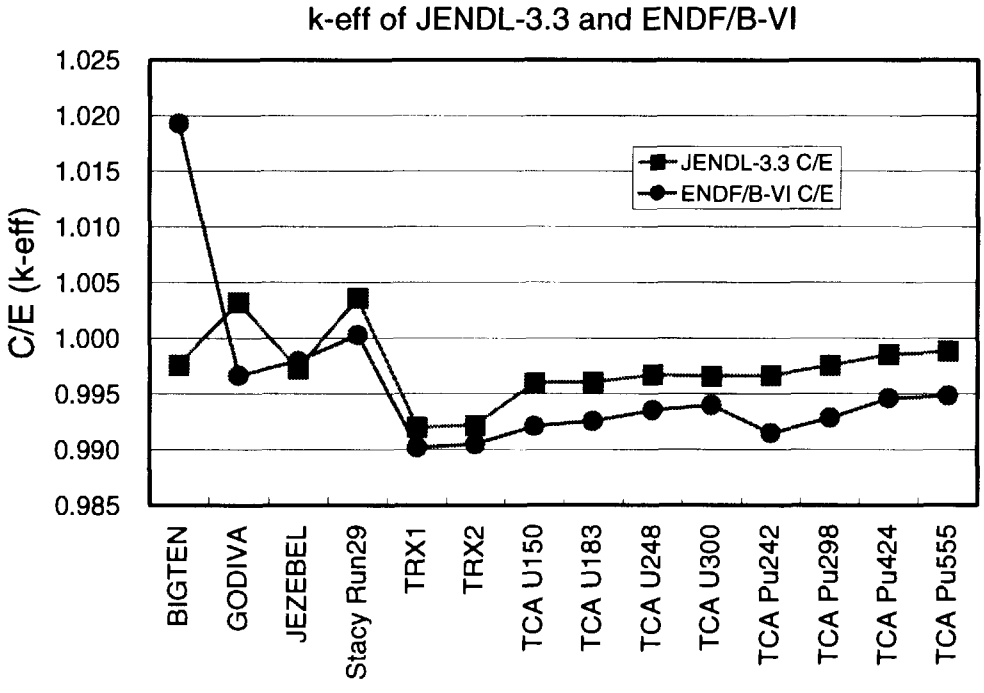

Fig. 2 Comparison of the (C/E-1) values for thermal cores calculated with JENDL-3.3 and ENDF/B-VI.5

JP0150650

2.6

Status on Testing of JENDL-3.3 with Shielding Benchmarks

Naoki YAMANO*†

* *Shielding Integral Test Working Group, Japanese Nuclear Data Committee*

† *Department of Nuclear Design, Sumitomo Atomic Energy Industries, Ltd.*

2-10-14 Ryogoku, Sumida-ku, Tokyo 130-0026

e-mail: yamano@sae.co.jp

Integral test of neutron and gamma-ray production data for the latest version of Japanese Evaluated Nuclear Data Library, Version 3.3 (JENDL-3.3) has been performed by using shielding benchmarks. An evaluation scheme for shielding benchmark analyses established in Japanese Nuclear Data Committee is applied to the integral test for Sodium, Titanium, Vanadium, Chromium, Iron, Nickel, Niobium and Tungsten. Calculations are made based on a continuous-energy Monte Carlo code MCNP4B/4C, and deterministic multi-group codes ANISN and DORT. The latest version of NJOY99 is employed to generate cross-section libraries for these transport codes. The status of the integral test activity is reviewed, and some benchmark results for medium-heavy nuclei are presented.

1. Introduction

The latest version of Japanese Evaluated Nuclear Data Library, Version 3.3 (JENDL-3.3) is the final stage of evaluation. Japanese Nuclear Data Committee (JNDC) is responsible for accuracy of the evaluation and showing applicability on shielding applications. Shielding Integral Test Working Group (WG) in JNDC has charge of validation work for JENDL-3.3 through shielding benchmark tests. An evaluation scheme [1] for shielding benchmark analyses established in JNDC has been applied to the integral tests for medium-heavy nuclei such as Aluminum, Sodium, Titanium, Vanadium, Chromium, Iron, Cobalt, Nickel, Copper, Niobium and Tungsten. In the present study, some benchmark results of neutron and gamma-ray production data are shown for Sodium, Iron, Vanadium, Tungsten, Nickel, Titanium, Niobium and Chromium.

2. Evaluation Scheme

For the integral test of cross sections by using shielding benchmarks, we should select appropriate integral measurements of different types, that are generally characterized as having good geometry, well-description of experimental method and result, and high sensitivity to the nuclear data of interest. In the present study, we selected a number of spectrum measurements listed in Table 1 to derive a general conclusion for energy-dependent data accuracy. For calculation, two comprehensive systems should be applied based on different approximations between cross-section processing and transport methods to evaluate errors due to each calculation process. We used a continuous-energy Monte Carlo code MCNP4B/4C,[2] and multi-group discrete ordinates codes ANISN [3] and DORT.[4] The latest version of NJOY99 [5] was employed to generate cross-section libraries for these transport codes. Then, a systematic analysis procedure was introduced to specify the accuracy and definite problems for typical reactions of nuclear data when discrepancy was found between calculation result and measurement. Calculations with JENDL-3.2,[6] JENDL-FF,[7] ENDF/B-VI,[8] FENDL-1 [9] and FENDL-2 [10] were also made for comparison.

3. Results and Discussions

3.1 Sodium

SDT4 benchmark called the Broomstick experiment, which was performed to investigate the effect of minima in the neutron total cross sections in the MeV energy range was analyzed. The results for 60.56 cm thick sodium are shown in Fig. 1.

---

* C. Ichihara, K. Ueki, Y. Matsumoto, F. Maekawa, C. Konno, Y. Hoshiai, K. Sasaki, M. Takemura, S. Suzuki, M. Kawai and A. Hasegawa

The neutron spectrum calculated with JENDL-3.3 showed a good agreement with experiment, and it was comparable to that of JENDL-3.2 except below 1 MeV. The difference is not a problem, since the absolute fluxes are relatively small in the energy region. Figures 2 and 3 show the results of JASPER IVFS-IC/Pb.9 (197.4 cm thick sodium) and JASPER IHX-IB/Pb (231.3 cm thick sodium) configurations, respectively. The results with JENDL-3.3 indicated a good agreement with both measurements, while these results showed slightly larger than those of JENDL-3.2 in the energy range below 1.5 MeV. The differences are within calculation errors and the same order of the experimental errors.

3.2 Iron

For relatively thin neutron transmission benchmarks, we selected KfK and NIST-ROSPEC experiments from iron spheres with a ^{252}Cf source in the center. Two calculations with ANISN and MCNP4B were employed in the KfK benchmark. The result is shown in Fig. 4 for the KfK iron sphere of 35 cm in diameter. Neutron spectra calculated by using two codes agreed with each other except for resonance minima below 300 keV, but good agreement was obtained between calculation and experiment. Figure 5 shows the result of the NIST-ROSPEC iron sphere of 50.7 cm in diameter. The result with JENDL-3.3 was comparable to that with JENDL-3.2. However, JENDL-3.3 indicated slightly smaller than that with ENDF/B-VI and measurement in the energy range between 2 and 5 MeV in the NIST benchmark, while the tendency did not appear in the KfK configuration. In this energy region, experimental error is relatively large compared with another energy range, and the shape of the source spectrum of ^{252}Cf much affects the calculated result, so that we cannot infer which evaluation is appropriate.

For relatively thick neutron transmission benchmarks, we adopted WINFRITH-ASPIS and JAERI-FNS experiments. Figures 6 and 7 show comparisons between calculated results with MCNP4C and the ASPIS measurements at 85.41 and 113.98 cm-depth in iron slabs, respectively. Figures 8 and 9 indicate comparisons between calculated results with MCNP4C and the FNS measurement at 81 cm-depth in large iron cylinder. In these benchmarks, neutron fluxes calculated with JENDL-3.3 in the energy range between 0.7 and 1 MeV were slightly underestimated compared with experiments. On the contrary, calculations with ENDF/B-VI were much better in this energy region. Two calculation methods with DORT and MCNP4C showed the same flux profile, so that we recommended improvement should be made in the energy range.

For lower energy region below the 24 keV s-wave resonance, we analyzed the FNS benchmark as shown in Fig. 9. JENDL-3.3 slightly showed overestimation compared with experiment. The calculation to experimental (C/E) ratio integrated over between 1 and 1000 eV was relatively large for JENDL-3.3, while the C/E deviations with JENDL-3.3 at each measured position were relatively smaller than those with another libraries.

For gamma-ray production benchmarks, we employed KfK and JAERI-FNS measurements. The results with JENDL-3.3 indicated good agreement with measurements as shown in Figs. 10 through 12, and improvement was generally obtained compared with JENDL-3.2.

3.3 Vanadium

We analyzed neutron and gamma-ray production benchmarks of JAERI-FNS experiments. In Fig. 13, neutron fluxes calculated with JENDL-3.3 showed underestimation below 1 keV, while some improvements were obtained compared with JENDL-3.2. In the energy region above 20 keV, a good agreement was generally obtained except for between 0.1 and 1 MeV. For gamma-ray production data, improvement from JENDL-3.2 was generally obtained as shown in Fig. 14.

3.4 Tungsten

For Tungsten benchmarks, JAERI-FNS and OKTAVIAN measurements were adopted. In Fig. 15, neutron spectrum above 100 keV was slightly underestimated compared with the FNS experiment. For leakage gamma-ray measurements of FNS and OKTAVIAN, photon spectrum profile was generally acceptable but improvement was still required in the energy range above 1 MeV as shown in Figs. 16 through 18.

3.5 Nickel, Titanium, Niobium and Chromium

Figure 19 shows the comparison between calculation with MCNP4C and measurement for the IPPE Nickel sphere experiment. The result was generally acceptable, and no problem was found. For Titanium, comparison of calculated neutron fluxes with ANISN and MCNP4B was shown in Fig. 20 together with the OKTAVIAN measurement. Two calculation methods indicated the same spectrum profile, and overestimation was shown below 3 MeV. Gamma-ray flux

calculated with JENDL-3.3 was overestimated in the energy range between 2 and 5 MeV as shown in Fig. 21. Comparisons between calculation and the OKTAVIAN measurement for Niobium and Chromium are shown in Figs. 22 and 23, respectively. Two calculations with ANSIN and MCNP4B showed the same flux profile. Chromium was generally acceptable, however Niobium indicated overestimation below 1 MeV.

4. Conclusion

Integral tests based on various shielding benchmarks were performed for Sodium, Iron, Vanadium, Tungsten, Nickel, Titanium, Niobium and Chromium for JENDL-3.3. The results were generally satisfactory and the new evaluation would be acceptable for shielding applications. However, some recommendations were given, and improvements should be made before official release of JENDL-3.3. A number of calculation results are being frequently informed to the Medium-Heavy Nuclide Data Evaluation WG of JNDC to assess data accuracy and consistency for their evaluation, so that the results in the present study may be changed hereafter until JENDL-3.3 is officially released scheduled in 2001.

Acknowledgments

Authors are indebted to M. Wada of Startcom Co. Ltd. and T. Nishio of Osaka University for their information concerning calculations of the FNS benchmarks. The work was performed as an activity of the Shielding Integral Test WG of JNDC.

References

(1) Yamano, N.: Ann. Nucl. Energy, **24**, 1085 (1997).
(2) Briesmeister, J.F. (ed.): "MCNP-A General Monte Carlo N-Particle Transport Code, Version 4C," LA-13709-M (2000).
(3) Engle Jr., W.W.: "A USER'S MANUAL FOR ANISN: A One Dimensional Discrete Ordinates Transport Code with Anisotropic Scattering," K-1693 (1967).
(4) Rhodes, W.A. and Mynatt, F.R.: Nucl. Sci. Eng., **99**, 88 (1988).
(5) MacFarlane, R.E. and Muir, D.W.: "The NJOY Nuclear Data Processing System, Version 91," LA-12740-M (1994).
(6) Nakagawa, T., et al.: J. Nucl. Sci. Technol., **32**, 1259 (1995).
(7) Chiba, S., et al.: "Evaluation of the Double-Differential Cross Sections of Medium-Heavy Nuclei for JENDL Fusion File," Proc. 3rd Specialists' Meeting on Nuclear Data for Fusion Reactors, Nov. 29-30, 1995, Tokai, Japan, JAERI-Conf 96-005, pp.45-54 (1996).
(8) Rose, P.F. (ed.): "ENDF-201 ENDF/B-VI Summary Documentation," BNL-NCS-17541 (1991).
(9) Ganesan, S. and McLaughin, P.K.: "FENDL/E Evaluated Nuclear Data Library of Neutron Nuclear Interaction Cross-Sections and Photon Production Cross-Sections and Photon-Atom Interaction Cross Sections for Fusion Applications Version 1.0 of May 1994," IAEA-NDS-128 (1995).
(10) Pashchenko, A.B., et al.: "FENDL-2: An Improved Nuclear Data Library for Fusion Applications," Proc. Int. Conf. on Nuclear Data for Science and Technology, May 19-24, Trieste, Italy, 1150 (1997 Italian Physical Society, Vol. 59, Part II).

Table 1 Candidates for Shielding Benchmark Test of JENDL-3.3

Nuclide	Benchmark Experiments
Sodium	SDT4, SDT12, JASPER(IVFS-IC/Pb.9, IHX-IB/Pb)
Aluminum	OKTAVIAN
Silicon	OKTAVIAN
Titanium	OKTAVIAN
Vanadium	FNS
Chromium	OKTAVIAN
Iron	SDT1, FNS, ASPIS, KfK, IPPE, NIST
Cobalt-59	OKTAVIAN
Nickel (include SS316)	IPPE, ORNL, FNS
Copper	OKTAVIAN, FNS
Niobium	OKTAVIAN
Tungsten	OKTAVIAN, FNS

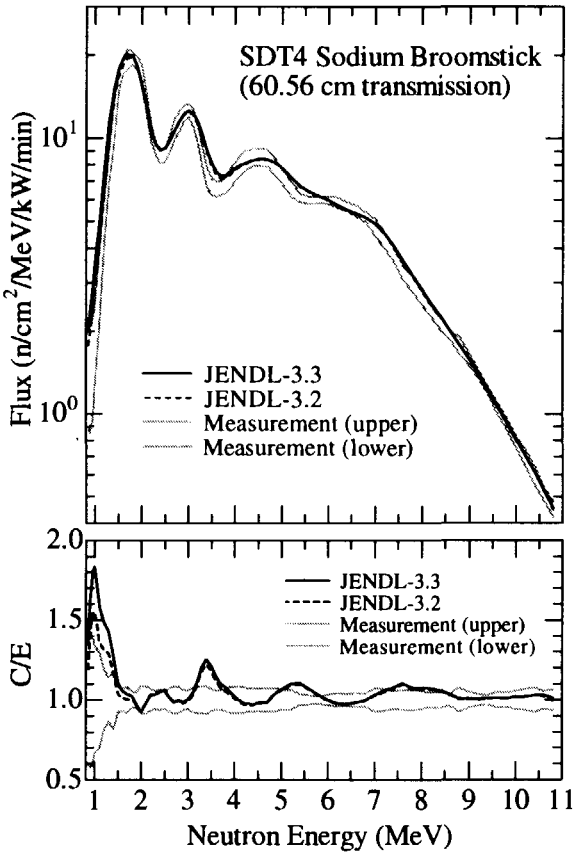

Fig. 1 Results of SDT4 Sodium benchmark.

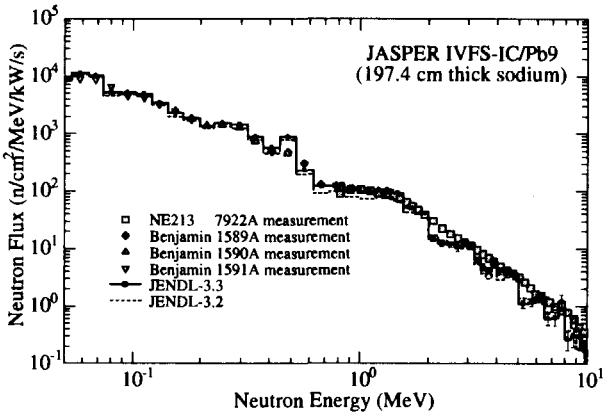

Fig. 2 Results of JASPER IVFS-IC/Pb benchmark.

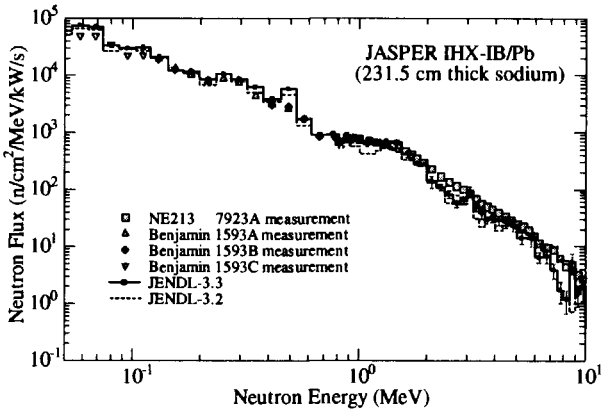

Fig. 3 Results of JASPER IHX-IB/Pb benchmark.

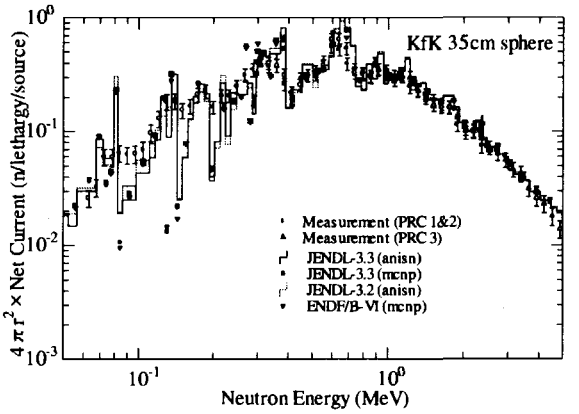

Fig. 4 Results of KfK Iron benchmark.

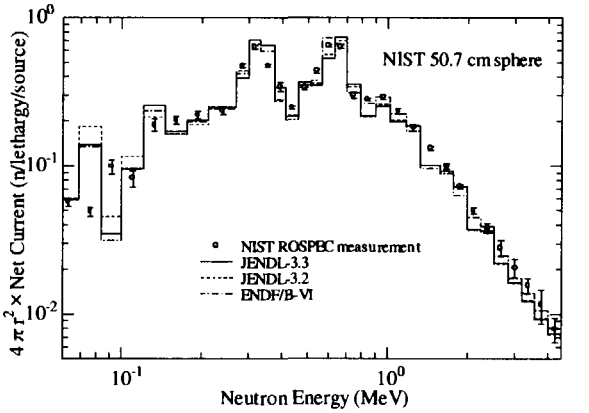

Fig. 5 Results of NIST-ROSPEC Iron benchmark.

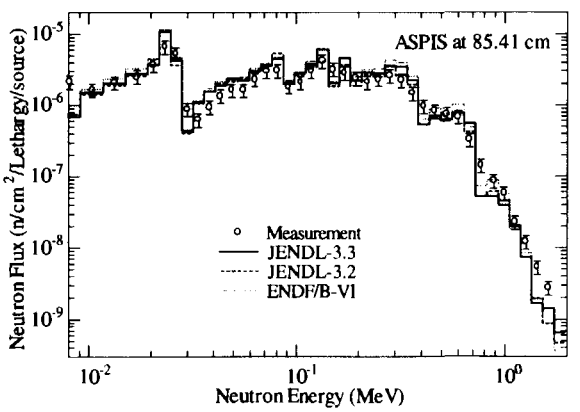

Fig. 6 Results of ASPIS Iron benchmark at 85.41 cm.

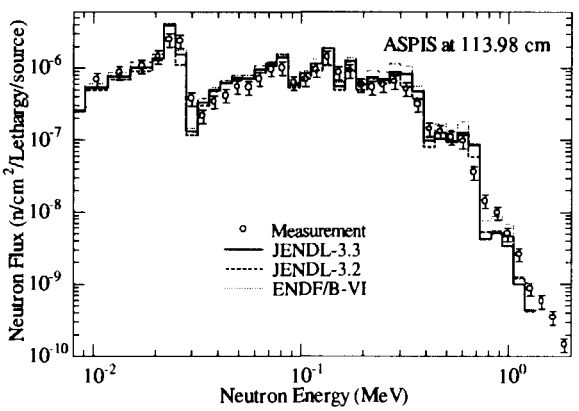

Fig. 7 Results of ASPIS Iron benchmark at 113.98 cm.

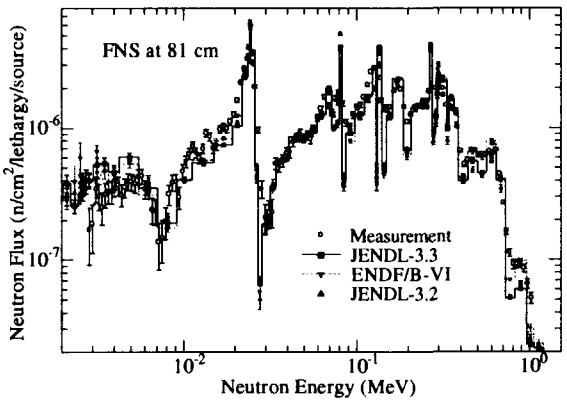

Fig. 8 Results of FNS Iron benchmark at 81 cm.

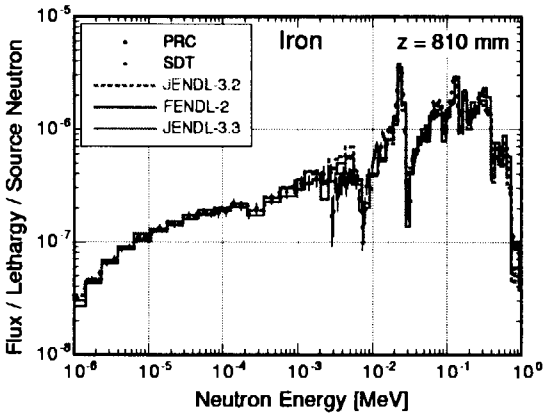

Fig. 9 Results of FNS Iron benchmark at 81 cm.

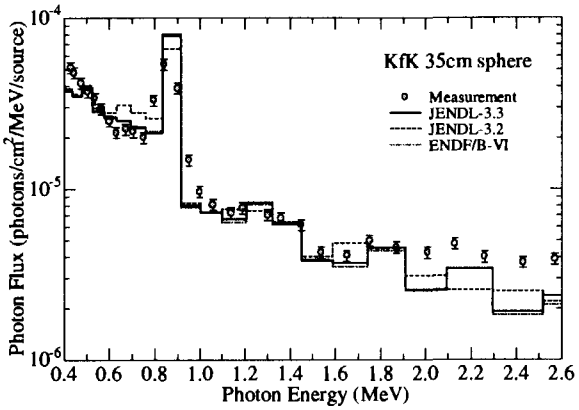

Fig. 10 Results of KfK Iron gamma-ray benchmark.

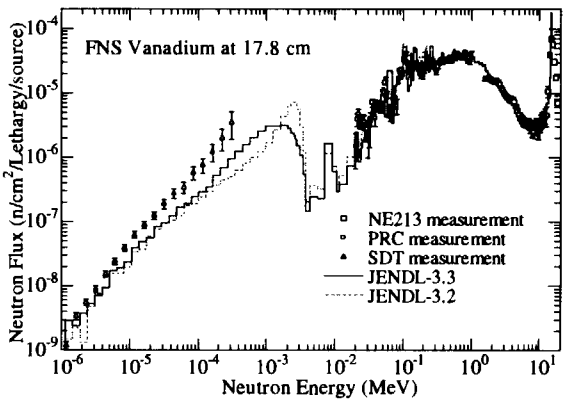

Fig. 13 Results of FNS Vanadium benchmark.

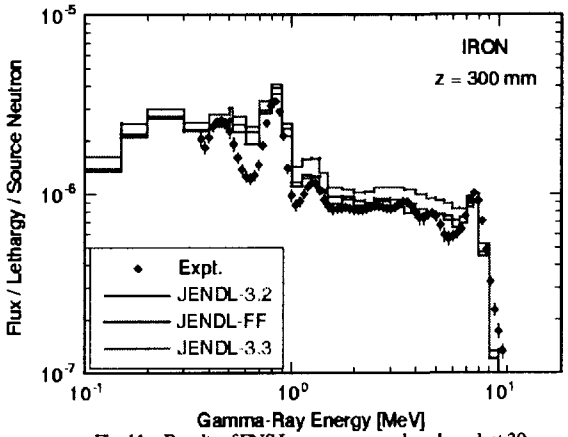

Fig. 11 Results of FNS Iron gamma-ray benchmark at 30 cm.

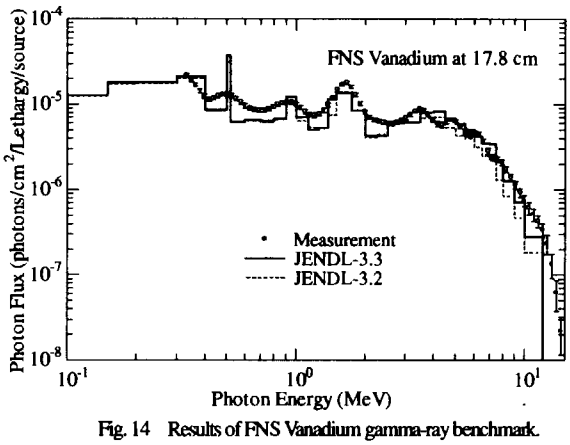

Fig. 14 Results of FNS Vanadium gamma-ray benchmark.

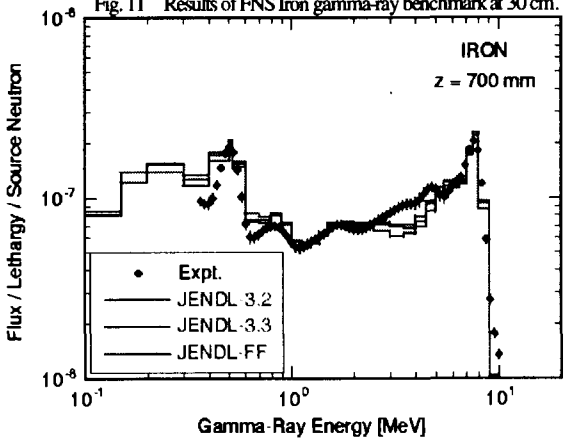

Fig. 12 Results of FNS Iron gamma-ray benchmark at 70 cm.

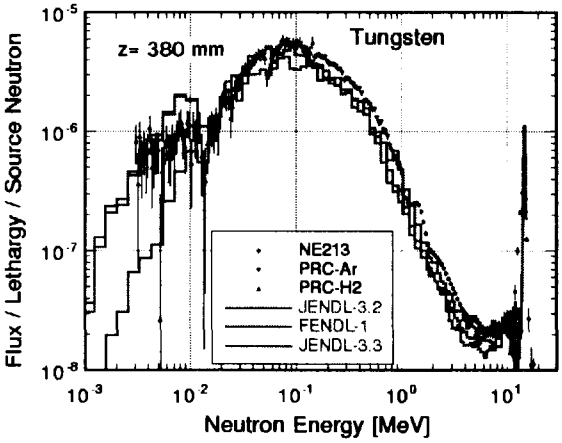

Fig. 15 Results of FNS Tungsten benchmark.

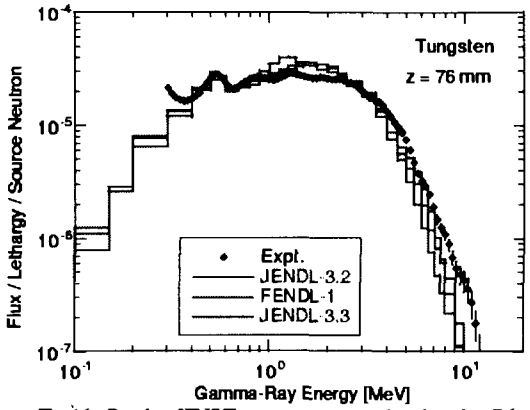

Fig. 16 Results of FNS Tungsten gamma-ray benchmark at 7.6 cm.

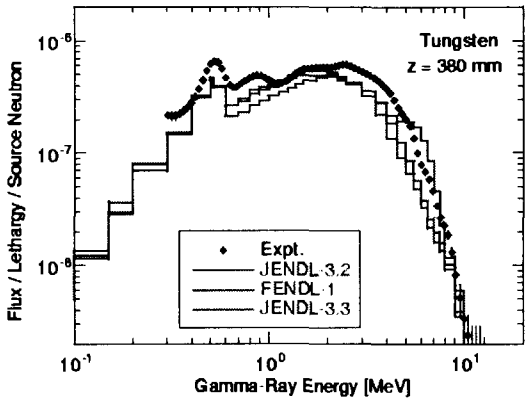

Fig. 17 Results of FNS Tungsten gamma-ray benchmark at 38 cm.

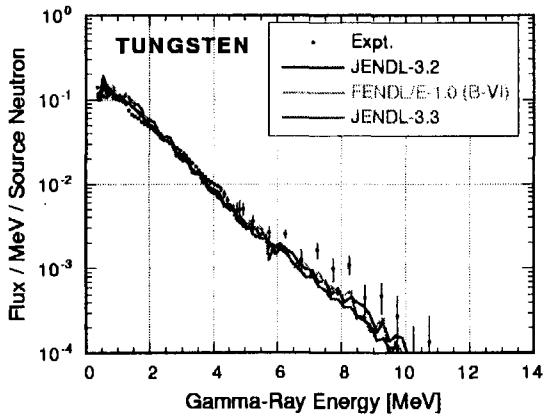

Fig. 18 Results of OKTAVIAN Tungsten gamma-ray benchmark.

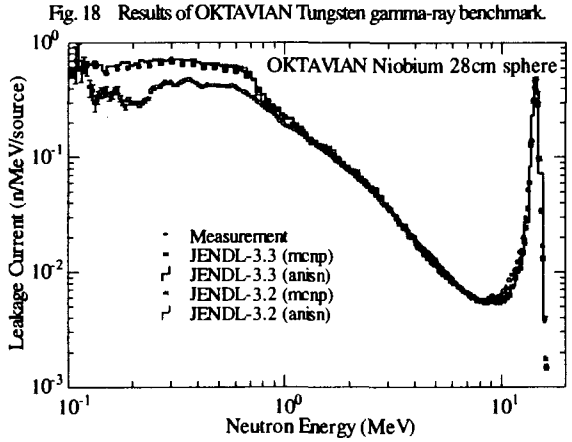

Fig. 22 Results of OKTAVIAN Niobium benchmark.

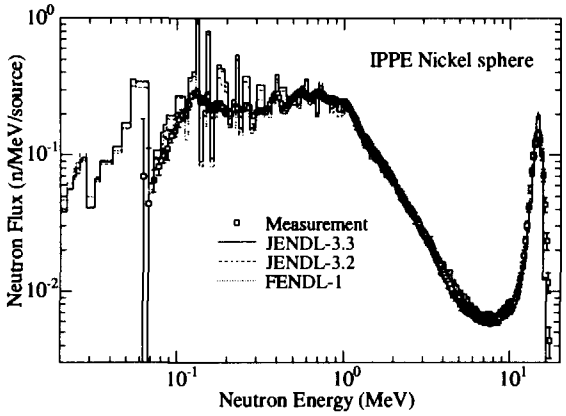

Fig. 19 Results of IPPE Nickel benchmark.

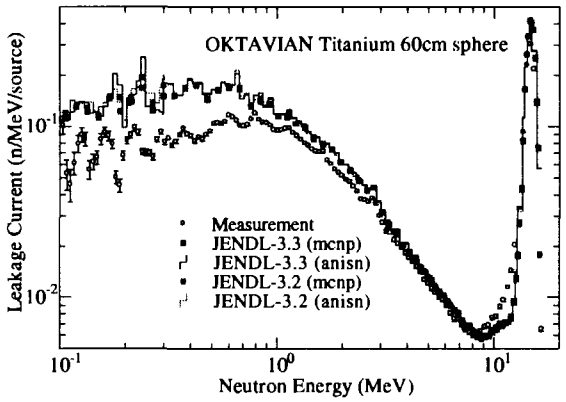

Fig. 20 Results of OKTAVIAN Titanium benchmark.

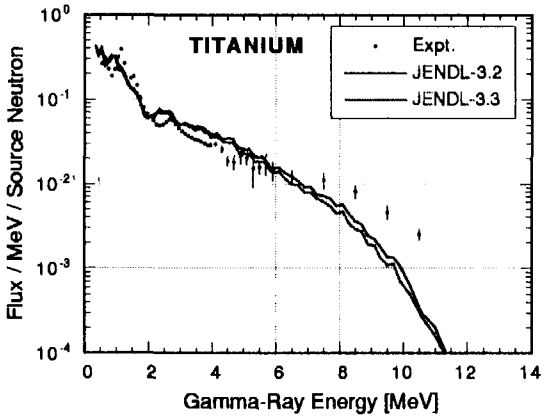

Fig. 21 Results of OKTAVIAN Titanium gamma-ray benchmark.

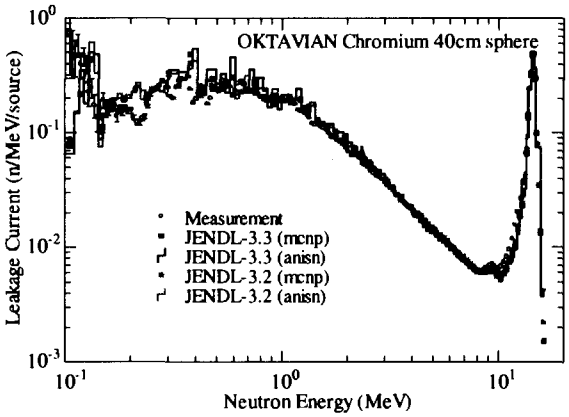

Fig. 23 Results of OKTAVIAN Chromium benchmark.

JP0150651

2.7

Application of ENDF Nuclear Data for Testing a Monte-Carlo Neutron and Photon Transport Code

P. Siangsanan, W.Dharmavanij and S. Chongkum
Physics Division, Office of Atomic Eneegy for Peace (OAEP),
Ministry of Science Technology and Environment, Thailand

A Monte-Carlo photon and neutron transport code was developed at OAEP. The code was written in C and C++ languages in an object-oriented programming style. Constructive solid geometry (CSG), rather than combinatorial, was used such that making its input file more readable and recognizable. As the first stage of code validation, data from some ENDF files, in the MCNP's specific format, were used and compared with experimental data. The neutron (from a 300 mCi Am/Be source) attenuation by water was chosen to compare the results. The agreement of the quantity $1/\Sigma$ among the calculation from SIPHON and MCNP, and the experiment—which are 10.39 cm, 9.71 cm and 10.25 cm respectively—was satisfactorily well within the experimental uncertainties. These results also agree with the 10.8 cm result of N.M., Mirza, et al.

1. Intrduction

We have developed our own Monte-Carlo particle transport code. The particles of our interest are neutron and photon, because they are available in our laboratory. We have used the reputed MCNP code, including its ACE nuclear data libraries, as our benchmark. Obviously, the MCNP is very long and complicated code because it was written in FORTRAN and has an old-style programming. It could have taken us much effort to study MCNP's source code directly. Instead, we have chosen to study the calculation method from other sources (including MCNP manual, of course) and developed our own code using MCNP as a guide. We chose C/C++ language because it has a neat structure, especially the OOP style of C++. Not only the enhanced speed of code development, its source code reuseability is also important. We can add new features to the code with much less effort–comparing to FORTRAN. Some people may worry about speed penalty to choosing C/C++ over FORTRAN, but we do not, because there are many good numerical libraries written in C/C++ that is comparable to that in FORTRAN. In our case we have chosen BLITZ++ (from http://oonumerics.org/blitz) because the vector operations are extensively used in our code.

2. The Code

The name of the code is Simple Implementation of PHOton and Neutron transport code (SIPHON). It is not final yet, but it has some major useful features. We have used the concept of Constructive Solid Geometry (CSG)[8] which define the geometry as a solid object. There are four basic shapes in SIPHON: cuboid, cylinder, sphere and cone. Objects of other shape could be obtained through Boolean operation between them. Some features of SIPHON are:

- User interface via text input file (an example input file in this benchmark is shown below)
- Repeated structure
- Fixed particle sources
- Neutron and photon transport
- Thermal neutron scattering treatment
- Photon energy deposition in a cell
- Track length estimate of particle flux in a cell

The flowchart of the code is shown in fig.1.

Table 1: An example of input file

```
object{ #declare srcwall = cylinder{<0,0,-.93>, <0,0,.93>, .87 } mat<0> }
#declare srcvial1 = cylinder{ <0,0,-1.13>, <0,0,1.97>,1.1 }
#declare srcvial2 = cylinder{ <0,0,-.93>, <0,0,1.77>,.9 }
object{ srcvial1 ~ srcvial2 mat<7> }
#declare srctube = object{ #declare srcvoid1 = cylinder{
<0,0,-15>, <0,0,32>, 2.3 } ~ #declare srcvoid2 = cylinder{
<0,0,-14.8>, <0,0,32>, 2.1 } mat<4> }
object{ srcvoid2 ~ srcvial1 mat<6> }
object{ srcvial2 ~ srcwall mat<6> }
#declare detvshroud = cylinder{ <16.2,0,-13.335>, <16.2,0,13.335>, 1.31 }
#declare upperCd1 = object{ #declare uCd1 = cylinder{
<16.2,0,-13.335>, <16.2,0,-1>, 1.49 } ~ cylinder{
<16.2,0,-13.335>, <16.2,0,-1>, 1.31 } mat<2> }
#declare lowerCd1 = object{ #declare lCd1 = cylinder{
<16.2,0,1>, <16.2,0,13.335>, 1.49 } ~ cylinder{
<16.2,0,1>, <16.2,0,13.335>, 1.31 } mat<2> }
#declare knifetool1 = cylinder{ <16.25,2,-14>, <16.25,2,14>, 2.1 }
#declare knifetool2 = cylinder{ <16.25,-2,-14>, <16.25,-2,14>, 2.1 }
#declare knifetool3 = cylinder{ <14.25,0,-14>, <14.25,0,14>, 2 }
#declare patchCd1 = object{ cylinder{ <16.2,0,-13.335>, <16.2,0,-1>, 1.58 } ~
uCd1 ~ knifetool1 ~ knifetool2 ~ knifetool3 mat<2> }
#declare patchCd2 = object{ cylinder{ <16.2,0,1>, <16.2,0,13.335>, 1.58 } ~
lCd1 ~ knifetool1 ~ knifetool2 ~ knifetool3 mat<2> }
#declare dettube = object{ #declare detvoid1 = cylinder{
<16.2,0,-15>, <16.2,0,32>, 1.9 } ~ #declare detvoid2 = cylinder{
<16.2,0,-14.8>, <16.2,0,32>, 1.7 } mat<4> }
object{ detvoid2 ~ upperCd1 ~ lowerCd1 ~ patchCd1
~ patchCd2 ~ detvshroud mat<6> }
#declare detwall = object{ detvshroud ~
#declare detel = cylinder{
<16.2,0,-9.8425>, <16.2,0,10.795>, 1.259 } mat<8> }
#declare detector = object{ detel mat<5> }
#declare splittank1 = cuboid{ <-55,-55,-55>, <5.25,55,55> }
#declare splittank2 = cuboid{ < 5.25,-55,-55>, <8.25,55,55> }
#declare splittank3 = cuboid{ < 8.25,-55,-55>, <11.25,55,55> }
#declare splittank4 = cuboid{ < 11.25,-55,-55>, <55,55,55> }
#declare tank = cylinder{ <0,0,-16>, <0, 0,16>, 35 }
#declare watertank1 = object{ (tank & splittank1) ~ srcvoid1 mat<1> }
#declare watertank2 = object{ tank & splittank2 mat<1> }
#declare watertank3 = object{ tank & splittank3 mat<1> }
#declare watertank4 = object{ (tank & splittank4) ~ detvoid1 mat<1> }
object{ #declare otank = cylinder{ tank mat<8> }
object{ #declare env = sphere{ <0,0,0>,50 } ~ otank ~ srcvoid1
~ detvoid1 mat<6> }
object{ sphere{ <0,0,0>,55 } ~ env mat<0> }
//+++Last(data) Section-++++++
mode = neutron
source={volume<1>, vect=<1,0,0>, dir=<0>, erg=<d 1> }
//Am/Be neutron energy distribution.
cdf 1{i=[ 0.0900 .1852 .3704 .5555 .7407 .9259 1.1111 1.2963
1.4815 1.6667 1.8518 2.0370 2.2222 2.4074 2.5926 2.7778
2.9630 3.1481 3.3333 3.5185 3.7037 3.8889 4.0741 4.2592
4.4444 4.6296 4.8148 5.0000 5.1852 5.3704 5.5555 5.7407
5.9259 6.1111 6.2963 6.4815 6.6667 6.8518 7.0370 7.2222
7.4074 7.5926 7.7778 7.9630 8.1481 8.3333 8.5185 8.7037
8.8889 9.0741 9.2592 9.4444 9.6296 9.8148 10.0000 10.1852
10.3700 10.5555 ],
p=[0.00000 .15314 .30671 .45185
```

```
-cont-
.57871 .69014 .78871 .87585 .96013 1.05370 1.15656 1.25942
1.36228 1.46656 1.58227 1.72798 1.90226 2.08226 2.24512 2.39583
2.53869 2.65726 2.78654 2.92654 3.07225 3.21939 3.37082 3.52368
3.65939 3.77867 3.88867 3.98467 4.06638 4.15066 4.24423 4.33637
4.41808 4.49522 4.57236 4.65879 4.74522 4.83450 4.92021 4.99449
5.05449 5.09663 5.12591 5.14591 5.16305 5.18019 5.20090 5.22733
5.25590 5.28233 5.30376 5.32162 5.33590 5.34661]}
mat 1[-1 1001.60 2 8016.60 1 lwtr.01t] //H2O
mat 2[-8.65 48000.35 1] //Cd
mat 3[1.236e-5 5010.60 1] //B-10
mat 4[-7.87 26000.50 1] // Fe
mat 5[1.2875e-5 5010.60 .96 5011.60 .04 9019.60 3] //BF-3
mat 6[-.0013 7014.60 4.348 8016.60 1.087] // Air
mat 7[-.97 6000.60 1 1001.60 2] // Polyethylene
mat 8[-7.92 26000.50 -.695 24000.50 -.19
28000.50 -.095 25055.60 -.02] // ss304
tally{ neutron flux within cell<detector> }
tally{ neutron flux within cell <detector> multiplier<1,3,107> }
run 500000 particles
imp[1 1 1 1 1 8 8 8 8 8 8 8 8 1 2 4 8 1 1 0]
```

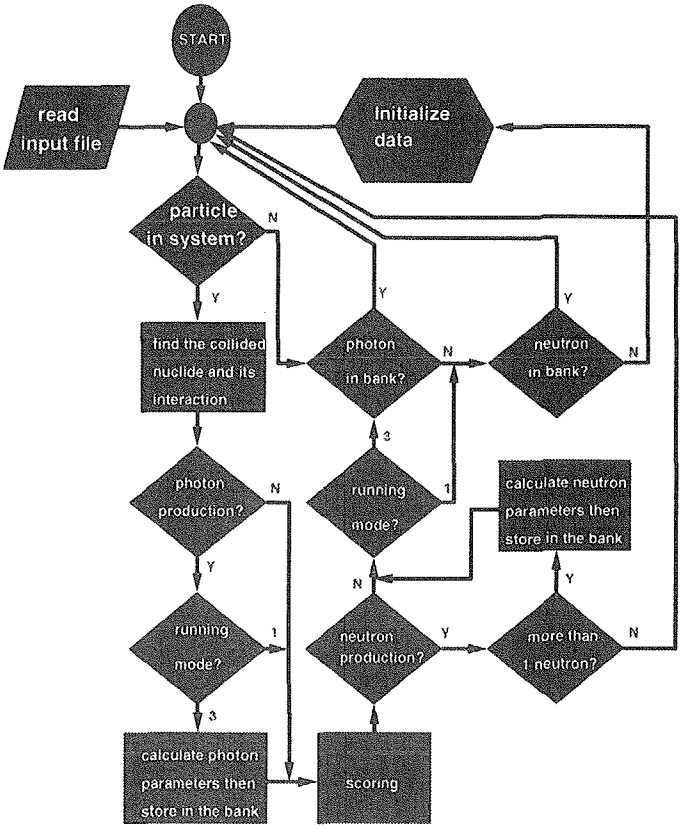

Figure 1: The flowchart of SIPHON

3. Experiment

The neutron attenuation in water was chosen to be the first validation scheme of the code. The experimental setup composed of a 300 mCi Am/Be neutron source installed in the middle of a 70-cm-diameter water tank. A cadmium-covered BF_3 detector was installed along side

of the source to measure the neutron activity. The distance of the detector to the source is allowed to vary from 2 cm to 26 cm with 2-cm-step increment. The thickness of cadmium is 1.8 mm and a 2-cm-wide window was provided at the middle of the detector. The window of the detector was aligned to the center of the source. The setup is shown in fig.2 and the detailed description of the detector is shown in fig.3

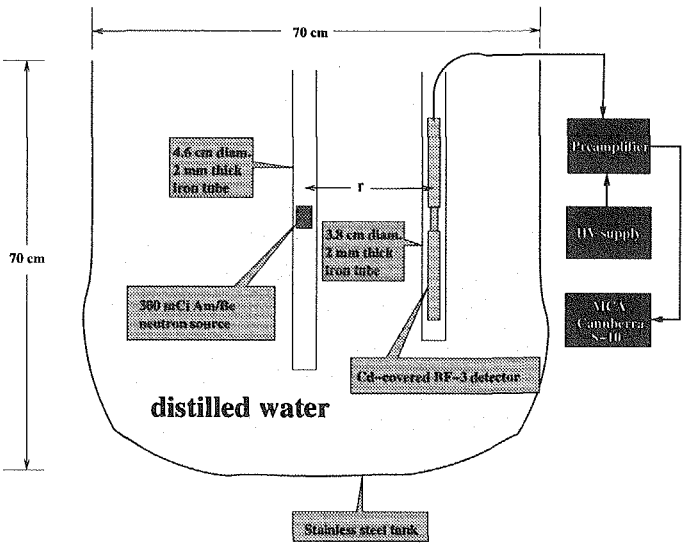

Figure 2: The experimental setup

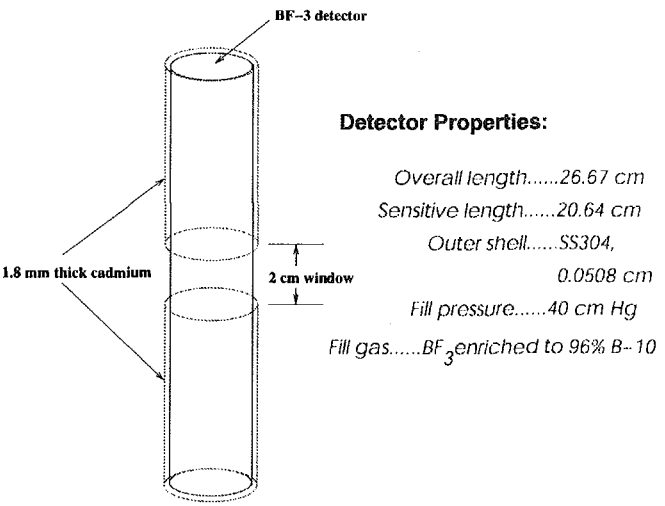

Figure 3: The detector description

4. Calculation

The model of the calculation at r = 16.2 cm is shown as the input file in table 1. In this calculation we have treat the implicit neutron capture, thermal neutron scattering and geometry splitting. At other r's the models are similar.

5. Results

The results from the experiment and the calculation are shown in table 2. The plot of $C^B \cdot r^2$ against r, where C^B is the activation of boron within the detector and can be

calculated from $C^B = \int_0^\infty \Sigma_{(n,\alpha)}(E)\phi(E)dE$, is also shown in fig.4. The source emission rate used was 96% of 6.6×10^5 n/s.

Table 2: The counting rate from measurements and calculations

r (cm)	counting rate (n/s) $C^B = \int_0^\infty \Sigma_{(n,\alpha)}(E)\phi(E)dE$				Experiment
	SIPHON		MCNP		
	C^B(rel.error)	fom	C^B(rel.error)	fom	mean(rel.error)
6.2	247.76(0.0015)	134.77	250.72(0.024)	13	304.47(0.0033)
8.2	209.75(0.013)	119.63	216.31(0.015)	10	249.36(0.0036)
10.2	155.97(0.013)	88.71	149.89(0.018)	7.3	182.84(0.0043)
12.2	114.11(0.011)	64.44	108.84(0.021)	5.2	129.04(0.0051)
14.2	81.13(0.013)	46.81	73.66(0.017)	3.6	87.87(0.0061)
16.2	55.37(0.0078)	59.96	52.27(0.015)	22	58.6(0.0075)
18.2	39.07(0.014)	41.72	34.39(0.016)	5.2	41.51(0.009)
20.2	26.83(0.016)	34.52	23.28(0.012)	13	28.00(0.01)
22.2	18.86(0.015)	24.61	16.00(0.013)	8.6	18.86(0.013)
24.2	12.89(0.024)	18.65	10.59(0.016)	6.6	12.88(0.016)
26.2	9.02(0.02)	12.38	7.67(0.02)	4.5	9.8(0.018)
28.2	6.18(0.02)	9.14	5.06(0.02)	3.4	6.35(0.023)
30.2	4.16(0.026)	4.17	3.36(0.029)	2.2	4.47(0.027)

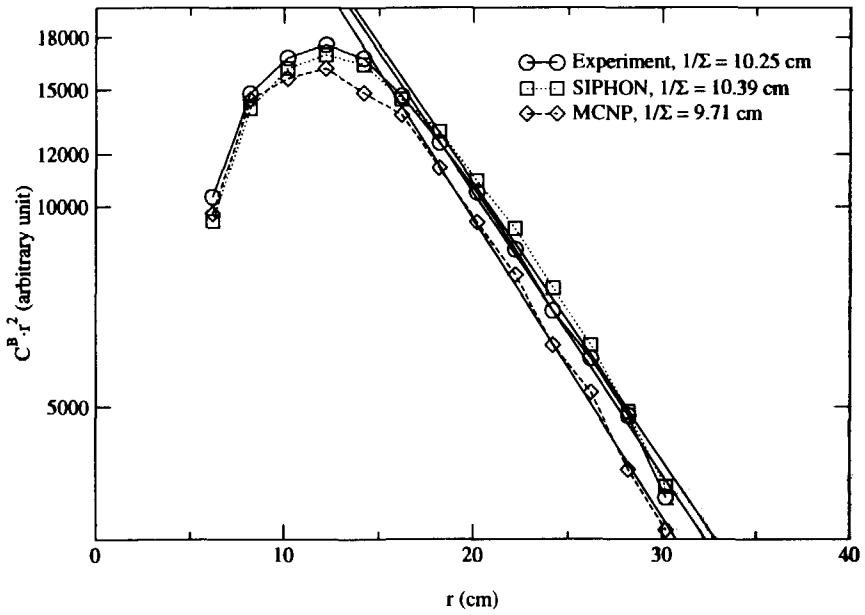

Figure 4: Plot of $C^B \cdot r^2$ against r to determine and compare $1/\Sigma$

6. Conclusion

It was seen from the plot in fig.4 that all curve have the same shape, though they are not exactly aligned. The determination of $1/\Sigma$ using the relation $C^B \sim e^{-\Sigma r}/r^2$ or

$r^2 \cdot C^B \sim e^{-\Sigma r}$ at r > 13 cm, was found to be 10.39 cm for SIPHON, 9.71 cm for MCNP and 10.25 cm for the experiment. These values agree with 10.8 cm from the work of Mirza, N.M., et al.[3].

It should be noted that the Monte-Carlo efficiency of SIPHON is rather good, as shown by the figure of merit (fom) in the third column of table 2. However, there are somewhat difference between the result of SIPHON and MCNP, which, unfortunately, we have not analysed in detail yet.

Acknowledgements

We would like to thank the free software community who contributed to every software we have used, especially BLITZ++, in our work.

References

[1] Lux, I. and L. Koblinger, "Monte Carlo Particle Transport Methods: Neutron and Photon calculations", CRC Press, Inc., Boca Raton, Florida. 517 p. (1990)

[2] Cashwell, E. D. and C. J. Everett, "Monte Carlo Method for Random Walk Problems", Pergamon Press, London. 153 p. (1959)

[3] Mirza, N. M., S. M. Mirza and M. Iqbal, "Determination of Mean Squared Slowing-down Distance for Am/Be Neutrons in Water using BF_3-Detector", *Radiat. Phys. Chem.* vol. 48 no. 4 pp. 413-417 (1995)

[4] Kludge, H. and K. Weise, "The Neutron Energy Spectrum of a ^{241}Am-Be(α,n) Source and Resulting Mean Fluence to Dose Equivalent Conversion Factors", Radiation Protection Dosimetry, vol. 2 No. 2 pp. 85-93 (1982)

[5] Briesmeister, J. F., "MCNP—A General Monte Carlo N-Particle Transport Code Version 4B", Radiation Information Computational Center (RSICC), Oak Ridge, U.S.A., 709 p. (1997)

[6] Eckel, B., "Thinking in C++", Prentice Hall, New Jersey, 813p. (1995)

[7] Goldstein, H., "Classical Mechanics", Addison-Wesley, U.S.A., pp.164-165. (1980 2nd Ed.)

[8] Foley, J. D., et al., "Computer Graphics: Priciples and Practice", Addison-Wesley, U.S.A., pp.712-714. (1992)

JP0150652

2.8
Uranium-fuel Thermal Reactor Benchmark Testing of CENDL-3

Liu Ping
China Nuclear Data Center
China Institute of Atomic Energy, P. O. Box 275(41),Beijing,102413, China.
e-mail: ping@iris.ciae.ac.cn

CENDL-3, the new version of China Evaluated Nuclear Data Library are being processed, and distributed for thermal reactor benchmark analysis recently. The processing was carried out using the NJOY[1]nuclear data processing system. The calculations and analyses of uranium-fuel thermal assemblies TRX-1,2, BAPL-1,2,3, ZEEP-1,2,3 were done with lattice code WIMSD5A. The results were compared with the experimental results, the results of the '1986'WIMS library and the results based on ENDF/B-VI.

I. INTRODUCTION

CENDL-3, the new version of China Evaluated Nuclear Data Library was started in 1996, it's now in progress. According to the plan, CENDL-3 will be completed by the year 2000, and will contain about 200 nuclides. Since then, the work has been done at CNDC (China Nuclear Data Center). So far, the present of CENDL-3 is shown in Table 1.

Table 1. The completed and planned nuclides of CENDL-3

Nuclides	Planned	Completed
Fissile nuclide	15	5(^{233,234,235,238}U, ^{239}Pu)
Structure material	24	15(^{90,91,92,96,0}Zr, ^{58,59,60,61,62,0}Ni, ^{63,65,0}Cu)
Fission products	91	73
Light nuclide	3	2(^{6}Li, ^{9}Be)
Total	133	95

In order to demonstrate the reliability of CENDL-3, it's necessary to subject the nuclear data library to benchmark testing against relevant integral experiments. The WIMS-D/4 lattices code [2] is widely used for thermal reactor and power reactor calculations, so it also was used to do the benchmark testing of CENDL-3.

This report gives the testing results of uranium-fuel thermal assemblies based on CENDL-3 and comparisons among CENDL-3, ENDF/B-VI and the '1986' WIMS library. The processing was carried out using NJOY nuclear data processing system and WIMSD5A code. The materials processed were hydrogen bound in water, oxygen, aluminum, uranium 235 and uranium 238.These materials are crucial components of light water reactor (LWR) and heavy water reactor (HWR).

II. Benchmark Calculations

1. Evaluated nuclear data processing

The CENDL-3 and ENDF/B-VI evaluated nuclear data libraries were selected as the source of basic data. The NJOY-97.0 modular system was applied for nuclear data processing.

The processing options consistently integrate the references[3-9]. A value of 0.2% was used for the resonance reconstruction tolerance, and a 0.2% maximum tolerance criterion for thinning was also applied.

A weighting spectrum for cross section averaging was derived for a PWR fuel cell according to the references [6,8,9]. At thermal energies the shape of the spectrum depends very strongly on the lattice geometry, composition and the operating parameters. In the resonance range between 4.0 and 9118 ev, a 1/E shape was applied to be consistent with the method of WIMS. Above the resonance range the EPRI-CELL LWR spectrum was adopted again.

Energy independent Goldstein-Cohen values were applied. They are shown in Table 2.

Table 2 List of applied Goldstein-Cohen λ values.

Materials	λ values
H	**1.0**
D	**1.0**
O	**1.0**
Al	**1.0**
U-235	**0.2**
U-238	**0.2**

Table 3. Brief Characteristics of TRX-1,2 and BAPL-1,2,3

Lattice	Fuel	Cladding	Moderator	Rod Radius(cm)	Pitch(cm)
TRX-1	1.3 wt. % U-metal	Al	H_2O	0.4915	1.8060
TRX-2	1.3 wt. % U-metal	Al	H_2O	0.4915	2.1740
BAPL-1	1.3 wt. % UO_2	Al	H_2O	0.4864	1.5578
BAPL-2	1.3 wt. % UO_2	Al	H_2O	0.4864	1.6528
BAPL-3	1.3 wt. % UO_2	Al	H_2O	0.4864	1.8057

2. Method of cell calculation

The cell calculations were used with WIMSD5A code. At first, according to real cell composition, intermediate approximation was used to calculate resonance self-shielding. The main transport equation was solved using Sn method, and the cylindrical cell approximation was used to simplify the geometry of the cell. Leakage calculations have been done with input buckling values and B1 method. The reaction rates of ^{235}U and ^{238}U were given in output files in two groups.

3. Benchmark calculations and analysis

All the integral parameters are defined as follows:

K_{eff} finite medium effective multiplication factor, -

ρ^{28} ratio of epithermal to thermal ^{238}U capture reaction rate,

δ^{25} ratio of epithermal to thermal ^{235}U fission reaction rate,

δ^{28} ratio of ^{238}U fission to ^{235}U fission reaction rate,

C^* ratio of ^{238}U capture to ^{235}U fission reaction rate.

RCR ratio of $C^*_{lattice}$ to $C^*_{Maxwellian}$

3.1 The calculations for TRX-1,2, BAPL-1,2,3

TRX-1,2 used Uranium metal fuel in ^{235}U enriched to 1.305 wt. %; BAPL-1,2,3 used Uranium oxide fuel enriched 1.311 wt. %; TRX and BAPL were water(H_2O)-moderated, Details of these lattices are given in Table 3. The comparisons are shown in Table4.

Table 4. Integral parameter comparison

Lattices	Integral parameter	Experiment	WIMS/D	CENDL-3	ENDF/B-VI
TRX-1	K-eff	1.0000(~.30)	1.0023	0.9975	0.98853
	ρ^{28}	1.32(~1.6)	1.279	1.3608	1.377
	δ^{25}	0.0987(~1.0)	0.099	0.09803	0.0977
	δ^{28}	0.0946(~4.3)	0.0965	0.09622	0.0974
	C^*	0.797(~1.0)	0.780	0.7922	0.808
TRX-2	K-eff	1.0000(~.10)	0.9965	0.9998	0.99113
	ρ^{28}	0.837(~1.9)	0.808	0.8530	0.863
	δ^{25}	0.0614(~1.3)	0.061	0.06201	0.0600
	δ^{28}	0.0693(~5.1)	0.0695	0.06811	0.0690
	C^*	0.647(~.93)	0.636	0.6387	0.650
BAPL-1	K-eff	1.0000(~.10)	1.0029	1.0016	0.99431
	ρ^{28}	1.390(~.72)	1.358	1.3923	1.429
	δ^{25}	0.084(~2.4)	0.084	0.08199	0.0824
	δ^{28}	0.078(~5.1)	0.0755	0.07362	0.0751
	C^*	0.0000	0.800	0.7972	0.819
BAPL-2	K-eff	1.0000(~.10)	1.0005	1.0003	0.99459
	ρ^{28}	1.120(~.89)	1.133	1.1602	1.188
	δ^{25}	0.068(~1.5)	0.0687	0.06695	0.0672
	δ^{28}	0.070(~5.7)	0.0652	0.06327	0.0645
	C^*	0.0000	0.732	0.7274	0.746
BAPL-3	K-eff	1.0000(~1.0)	0.9981	1.0007	0.99565
	ρ^{28}	0.906(~1.1)	0.894	0.9130	0.933
	δ^{25}	0.052(~1.9)	0.0529	0.0515	0.0516
	δ^{28}	0.057(~5.3)	0.0538	0.05184	0.0528
	C^*	0.0000	0.657	0.6511	0.666

The results show that the calculated results with CENDl-3are much better than those results with old WIMS library.

The K_{eff} values from CENDL-3 are in good agreement with experiments. Only the value of TRX-1 is lower than 0.1%. The values of ρ^{28} for TRX-2, BAPL-1 and 3 are well predicted within the uncertainty integral of the measurement values. For TRX-1 and BAPL-2, the results are higher than 3% (1.6% uncertainty in measurement) and 3.59% (0.89% uncertainty in measurement) respectively. All the values of δ^{25} are lower from 0.679% to 2.37% than experiment ones. For δ^{28}, the calculated results are generally within the uncertainty integral of the measurement values except for BAPL lattices, for which the prediction values are underestimated about 5.9% to 9% .The agreement for C^* is very good.

3.2 The calculations for ZEEP-1,2,3

ZEEP-1,2,3 used natural uranium fuel. ZEEP were heavy water(D_2O) -moderated. Details of these lattices are given in Table 5 and 6. The $C^*_{Maxwellian}$ given in the work is 0.654.

Table 5. Brief Characteristics of ZEEP-1,2,3

Region	Outer radius (mm)	Isotope	Concentration (10^{24} atoms / cm^2)
Fuel	16.285	^{235}U ^{238}U	3.454E-4 4.760E-2
Air Gap	16.470		5.0E-5
Cladding	17.490		6.025E-2
Moderator		^{1}H ^{2}H O	1.529E-4 6.633E-2 3.324E-2

Table 6. Integral parameter comparison for Heavy water reactor benchmarks

Lattices	Integral parameter	Experiment	WIMS/D4	CENDL-3	ENDF/B-VI
ZEEP-1	K_{eff}	1.0000	0.99398	1.0032	1.0036
	ρ^{28}	-----	0.26026	0.28687	0.282
	δ^{25}	-----	0.0258	0.0256	0.0263
		0.0675	0.06804	0.06785	0.0682
	δ^{28}	1.16	1.279	1.274	1.281
	RCR				
ZEEP-2	K_{eff}	1.0000	0.9993	0.99993	1.00161
	ρ^{28}	-----	0.4688	0.52713	0.516
	δ^{25}	-----	0.04891	0.048715	0.0502
		-----	0.07261	0.07192	0.0725
	δ^{28}	-----	1.464	1.489	1.491
	RCR				
ZEEP-3	K_{eff}	1.0000	1.00384	0.99752	1.00089
	ρ^{28}	----	0.62021	0.70397	0.688
	δ^{25}	----	0.06539	0.06538	0.0674
		----	0.07672	0.07583	0.0764
	δ^{28}	----	1.5968	1.6424	1.640
	RCR				

Although there are no quite enough experimental data with heavy water moderated lattices, the available data have shown that the calculated results based on CENDL-3 are within or close to the experimental uncertainty limits. All the lattice parameters calculated using CENDL-3 are in good agreement with those of experiments and ENDF/B-VI.

III. Conclusions

It is obvious that different evaluated nuclear data library is the cause of the difference of the results between old and new WIMS 69-group libraries. In general, the new library based on CENDL-3 or ENDF/B-VI is more reliable than the '1986' WIMS library.

In the benchmarks testing for both uranium metal fuel lattice assemblies and uranium oxide fuel lattice assemblies, the K_{eff} values calculated with ENDF/B-VI are underestimated. We can see that the excellent K_{eff} values for CENDL-3 are shown in the Table 4.

It is well-known that ^{238}U data affects strongly on the calculated results of reactor physics parameters and their trend, due to high concentration in the uranium fuel reactors. Through the comparisons of group cross sections between old and new library, no obvious difference was found for fission and absorption.

Through the comparisons of scattering cross sections between old and new library, a big difference was found. In the resonance energy region, the values of old library is much bigger than that of the new ones. The difference arises from the evaluation data and resonance self-shielding treatment for scattering cross sections as well. The bigger scattering cross section of old library caused relative lower possibility of absorption, higher slowdown power.

It is the same reason above mentioned, ^{238}U inelastic scattering effect of ENDF/B-VI makes assemblies spectrum harder and underestimates the fission contributions of ^{235}U, so that the K_{eff} values calculated with ENDF/B-VI are underestimated

It is obvious that ^{238}U data of CENDL-3 are better than that of ENDF/B-VI for thermal reactor calculations.

As shown in Table 4 and Table 6, the calculated results based on CENDL-3 are well consistent with the experimental results. It can be concluded that CENDL-3 is reliable for thermal reactor calculations.

References

[1]. Macfarlane,R., E., Muir, D,W., "The NJOY Nuclear Data Processing System", LA-12740, LANL, October 1994.

[2]. Askew, J. R., Fayers, F. J., Kemshell P. B., "A General Description of Lattices Code WIMS", J. British Nucl. Energy Soc., Vol. 5, No. 4, P. 564, October 1966

[3]. Ganesan, S. (compiler), "Update of the WIMS-D4 Nuclear Data Library ", (Status Report of the IAEA WIMS Library Update Project), INDC (NDS)-290, IAEA, Vienna, December 1993.

[4]. Trkov, A., Ravnik M., "Application of ENDF/B-VI Data for WIMS Lattices Code", Ann. Nucl. Energy, Vol. 20, No. 8, pp. 561-568, 1993.

[5]. Trkov, A., Aldama, D. L., "Parametric study of the NJOY input options in the frame of WIMS Library Update Project" Institute Jozef Stefan, Ljubljana, IJS-DP-7049, November 1994.

[6]. IAEA, "Proceeding of Consultants' Meeting on Planning for the final Stage of IAEA WIMS-D Library Update Project", 29-31 July 1996, IAEA Headquarters, Vienna.

[7]. Leszczynski F., "Goldstein-Cohen Parameters for Preparation of Multigroup Libraries", Private Communication, 1997.

[8]. Leszczynski F., "Neutron cross section Weighting Spectra for Preparation of Muligroup Libraries", PART 1, Private communication, 1997.

[9]. Trkov A., Ping L., "IAEA Interoffice Memorandum on review of Procedures for WIMS-D Library Update Project and Related CENDL-2.1 Processing in the IAEA Nuclear Data Section", IAEA, Vienna.

JP0150653

2.9

Evaluation of Significance of Zr Bound in ZrH_x for its Possible Inclusion in the WIMSD-5 Cross Section Library

S.I. Bhyuian, M.M. Sarker, T.K. Chakrobortty, M.J.H. Khan
Institute of Nuclear Science & Technology, AERE,
Ganakbari, savar, G.P.O. Box # 3787, Dhaka
Teresa Kulikowska
Institute of Atomic Energy, Swierk, 05-400 Otwock, Poland

Abstract

The principal objective of this study was to evaluate the significance of a separate data for Zirconium bound in Zirconium hydride rather than as a free atom and its possible inclusion in the WIMSD library. A TRIGA research reactor benchmark input specified for WIMSD-5 was prepared. The calculations have been performed by the WIMSD-5B code and the ANL version of WIMSD code. In the ANL version, two sets of data for Hydrogen were available: for Hydrogen bound in water and Hydrogen bound in Zirconium hydride. For Zirconium, the available data were for Zirconium natural and Zirconium bound in Zirconium hydride prepared without taking into account the P_1 correction. A separate data for Zirconium bound for Zirconium hydride with P_1 correction was prepared for the WIMSD-5B code at INST, AERE, Savar. The cross section data for all the elements of the benchmark input have been processed by NJOY94.10+ based on ENDF/B-VI library and incorporated in the 69-group WIMS library. All the calculations have been carried out applying 69 energy groups in the main transport routine with subsequent condensation to 7 group. Four cases namely (i) diffusion, (ii) B_1 with P_1 thermal scattering matrices for H and O in water only, (iii) as above but with a P_1 matrix also for H bound in ZrHx, (iv) as above but with a P_1 matrix also for Zr bound in ZrHx were studied. It is seen that the differences in cross sections are negligible although the overall effect in K-eff is up to 700 pcm in the case of ANL, and in our case, the effect is even stronger. The possible cause of this inconsistency could be the absence of P_1 matrices for all the principal materials for the benchmark input in the WIMSD library. The author of the WIMS recommends the usage of P_1 matrices only if they are available for all principal isotopes of a material. No material is treated separately on the level of leakage calculations and the contribution from the first order is weighted over spectra in materials, their volume and number densities.

Introduction

The principal objective of this study was to evaluate the significance of a separate data for zirconium bound in zirconium hydride rather than as a free atom and its possible inclusion in the WIMSD library. The influence of leakage and, in particular, P1 matrices on k-eff depends on the magnitude of the buckling, consequently might have a significant effect for a small reactor like TRIGA, so is the essence of performing this calculation. A Benchmark input specified for WIMSD-5 has been prepared. The calculations have been performed by the WIMSD-5B code developed at ANL[1]. Only two sets of data for hydrogen were available: for hydrogen bound in water and hydrogen bound in zirconium hydride. For zirconium, the available data were for zirconium natural and zirconium bound in zirconium hydride prepared without taking into account the P_1 correction. A separate data for zirconium bound in zirconium hydride with P_1 correction was prepared. The cross section data for all the elements of the benchmark input have been processed by NJOY [2] based on ENDF/B-VI library and incorporated in the 69-group WIMS library. All the calculations have been carried out applying 69 energy groups in the main transport routine with subsequent condensation to 7 group.

Significance of separate data for Zr bound in ZrH_x

The problem can be divided into two questions: (1) what is the effect of introduction of Zr bound in ZrH_x as a separate isotope with its own ID and the whole set of data?
(2) Is it necessary to introduce a P_1 scattering matrix for that new isotope?

Evaluation of the first effect is comparatively easy. It can be carried out by comparison of the computational results for a typical reactor with ZrH_x in its fuel, based on the free atom approach and those obtained with Zr bound in ZrH_x. Such a comparison has been done using the WIMS-ANL code and its standard library prepared on the basis of ENDFB-VI.

The second question is more complicated as it is connected with the specific algorithm applied in WIMSD in all its versions for B_1 calculations. This algorithm is described in detail below to give a theoretical basis for answering the second question.

Application of P1 matrices

The transport calculations in the WIMSD code are performed in consecutive steps. First, a detailed solution of the transport equation is carried out for the input case, treated as an infinite lattice of specified cells (macro-cells). Second, the code solves the transport equation once more using effective cross sections for a uniform infinite plate with given radial and axial bucklings. The first comparison shows the differences between calculations carried out on the basis of library data prepared separately for zirconium bound in the zirconium hydride (ID=2091) and those prepared for natural zirconium (ID=91) without taking into account the P_1 correction. The transport equation can be solved in the diffusion approximation written as:

$$\left(\sum^{g} - \sum_{s0}^{gg} + D_r^g . B_r^g + D_z^g . B_z^g \right) \Phi^g = \sum_{g' \neq g} \sum_{s0}^{g'g} . \Phi^{g'} + S_f^g \qquad (1)$$

Where:

Σ^g-total cross section in group g,

$\sum \frac{g'g}{so}$ –Scattering cross section, from group g' to g,

$D \frac{g}{x}$ –Diffusion coefficient in the direction x for group g,

$B \frac{g}{x}$ – buckling in the direction x for group g,

ϕ^g –Neutron flux in group g,

$S \frac{g}{f}$ – Fission source in group g.

P1 matrices for four light elements (H-1, H-2, O and C) are included in the WIMS library. The matrices are used only in the third part of WIMS calculations, so called, 'leakage correction'. The code solves transport equation for the whole system specified in input data before it performs any leakage correction. Thus the neutron flux values and macroscopic cross section are known for all regions in the infinite medium approximation. A leakage correction is then introduced through the application of input buckling given in input or bucklings calculated in the code and corresponding to the effective multiplication factor equal to unity. This is realised by flux volume weighting of macroscopic cross sections for all regions. Thus an artificial uniform medium is created in the form of an infinite slab and for that slab system once more the transport equation is solved but this time with a buckling correction. The transport equation for the uniform plate can be solved in the B1 approximationhere the notation of Eq. (1) has been kept, $B^2 = B\frac{2}{r} + B\frac{2}{z}$, and the neutron current is calculated as:

$$J^g = \frac{\sum\sum_{s1} \frac{g'g}{s1} J^{g'} + \frac{(B)^2}{|B^g|}\phi^g}{3a^g \Sigma^g - \sum_{s1} \frac{gg}{s1}} \qquad (3)$$

The quantities a are defined by the following formulas:

$$a^g = \left(\frac{B}{\Sigma^g}\right)^2 \cdot \frac{arctg\left(\frac{B}{\Sigma^g}\right)}{3\left(\frac{B}{\Sigma^g} - arctg\left(\frac{B}{\Sigma^g}\right)\right)}; for B^2 > 0, \qquad (4a)$$

$$a^g = \left(\frac{B}{\Sigma^g}\right)^2 \cdot \frac{in\left(\frac{\Sigma^g + |B|}{\Sigma^g - |b|}\right)}{\left(\frac{\Sigma^g + |B|}{\Sigma^g - |b|}\right) - \left(\frac{2|B|}{\Sigma^g}\right)}; \text{ For } B^2 > 0. \qquad (4b)$$

It should be noted that B=0 is not allowed in this approximation.

It should be kept in mind that as already stated, all material constants in both equations are properly weighted averages over respective regions of the whole system (cell or macro cell). In the second equation, beside the macroscopic cross-sections are calculated only now and only for the thermal energy diapason. In the present versions of the WIMSD-5 library there are only for 4 isotopes: hydrogen, deuterium, oxygen and carbon. Their application in calculations is activated by specification of the DNB cards in the third section of WIMS input. Their densities for each material are taken from the DNB cards and not from MATERIAL cards.

It should be kept in mind that the effect of P1 approach is meaningful only in the case of larger buckling values. It has no influence on the infinite lattice results and the leakage correction, expressed through Eqs. (1,2). The calculation of the effective spectrum and effective multiplication factor is a very rough one for a majority of reactors.

Numerical Results

The comparison is, therefore, done using the transport diffusion approximation. The difference in multiplication factors is shown on Table 1. For comparison, a case with hydrogen treated as bound in water (ID=2001) and not in zirconium hydride (ID=2191) has also been calculated

Table 1

Multiplication factors with different data for Zr and ZrH_x.

Library ID applied	Zr:91,H: 2001	Zr:91,H:2191	Zr:2091,H:2191
k-inf	1.400835	1.394566	1.393325
k-eff	1.087118	1.080440	1.079449

The differences in macroscopic cross sections can be observed Table 2,3 and 4

Table 2a
Broad group cross sections with ID (Zr)-91,ID (H)-2001 in ZrH_x

Broad Grp	Transport	Total	Capture	Fission	ν
1	2.14685E-01	3.56968E-01	4.76302E-04	9.34045E-04	2.72291E+00
2	5.67011E-01	1.05267E+00	1.84368E-03	8.45263E-04	2.43774E+00
3	6.57276E-01	1.41642E+00	2.05585E-02	8.88930E-03	2.43380E+00
4	8.12719E-01	1.49297E+00	1.63073E-02	2.11660E-02	2.43380E+00
5	1.15829E+00	1.84333E-00	4.17381E-02	4.65435E-02	2.43380E+00
6	1.81717E+00	2.49116E+00	3.16287E-02	6.54957E-02	2.43380E+00
7	3.02414E+00	3.71359E+00	5.17901E-02	9.90251E-02	2.43380E+00

Table 2b
Macroscopic scattering matrix with ID (Zr)=91, ID (H)=2001 in ZrH_x

To Grp	From Grp 1	From Grp 2	From Grp 3	From Grp 4	From Grp 5	From Grp 6	From Grp 7
1	2.59159E-01	0.00000E+00	0.00000E+00	0.00000E+00	0.00000E+00	0.00000E+00	0.00000E+00
2	9.61447E-02	9.20826E-01	0.00000E+00	0.00000E+00	0.00000E+00	0.00000E+00	0.00000E+00
3	2.53671E-04	1.29056E-01	1.29056E+00	2.99052E-03	1.88543E-12	0.00000E+00	0.00000E+00
4	0.00000E-00	4.48799E-05	6.84758E-02	6.35611E-01	2.81188E-03	2.44568E-10	3.53254E-11
5	0.00000E-00	4.36807E-05	6.32057E-02	6.87894E-01	1.18345E+00	6.61036E-02	8.77267E-03
6	0.00000E-00	8.08790E-06	9.95167E-03	9.95167E-02	4.47863E-01	1.76613E+00	4.26031E-01
7	0.00000E-00	4.09907E-06	4.41136E-03	3.53292E-02	1.15517E-01	5.61800E-01	3.12797E+00

Table 3a
Broad group cross sections with ID (Zr)=91, ID (H)=2191 in ZrHx

Broad grp	Transport	Total	Capture	Fission	ν
1	2.14681E-01	3.56967E-01	1.76306E-01	9.34029E-04	2.72291E+00
2	5.67011E-01	1.05267E+00	1.84369E-03	8.45266E-04	2.43774E+00
3	6.54964E-01	1.41615E+00	2.05852E-02	8.87959E-03	2.43380E+00
4	7.79528E-01	1.47625E+00	1.61477E-02	2.09255E-02	2.43380E+00
5	1.08664E-+00	1.76651E+00	4.67594E-02	4.80971E-02	2.43380E+00
6	1.68158E+00	2.37179E+00	3.33924E-02	7.22649E-02	2.43380E+00
7	3.05185E+00	3.73318E+00	4.77050E-02	8.37288E-02	2.43380E+00

Table 3b
Macroscopic scattering matrix with ID (Zr)=2091, ID(H)=2191 in ZrHx

To Grp	From Grp 1	From Grp 2	From Grp 3	From Grp 4	From Grp 5	From Grp 6	From Grp 7
1	2.59158E-01	0.00000E+00	0.00000E+00	0.00000E+00	0.00000E+00	0.00000E+00	0.00000E+00
2	9.61446E-02	9.20826E-01	0.00000E+00	0.00000E+00	0.00000E+00	0.00000E+00	0.00000E+00
3	2.53671E-04	1.29056E-01	1.24025E+00	2.37427-E03	3.52530E-11	0.00000E+00	0.00000E+00
4	0.00000E+00	4.48799E-05	6.79254E-02	6.09647E-01	2.03511E-03	2.47497E-09	1.16030E-10
5	0.00000E+00	4.36807E-05	6.34927E-02	6.87686E-01	1.14770E+00	4.80414E-02	1.07285E-02
6	0.00000E+00	8.08790E-06	1.03820E-02	1.04298E-01	3.81925E-01	1.82878E+00	3.51092E-01
7	0.00000E+00	4.09906E-06	4.63983E-03	3.51725E-02	1.39999E-02	3.89312E-01	3.23992E+00

Table 4a
Board group cross sections with ID(Zr)=2091,ID (H)=2191 in ZrH_x

Broad grp	Transport	Total	Capture	Fission	ν
1	2.14684E-01	3.56967E-01	4.76305E-04	9.34030E-04	2.72291E+00
2	5.67011E-01	1.05267E+00	1.84399E-03	8.45253E-04	2.43774E+00
3	6.54536E-01	1.41575 E+00	2.07270E-02	8.88149E-03	2.43380 E+00
4	7.76895E-01	1.47326 E+00	1.61458 E-02	2.09220E-02	2.43380 E+00
5	1.08406E+00	1.76369 E+00	4.67496 E-02	4.81209 E-02	2.43380 E+00
6	1.67920E+00	2.36922 E+00	3.33885 E-02	7.22503 E-02	2.43380 E+00
7	3.05072E+00	3.73194 E+00	4.76856 E-02	8.36562 E-02	2.43380 E+00

Table 4b
Macroscopic scattering matrix with ID (ZR)=2091,ID (H)=2191 in ZrH_x

To grp	From Grp 1	From Grp2	From Grp3	From Grp4	From Grp5	From Grp6	From Grp7
1	2.59158E-01	0.00000E+00	0.00000E+00	0.00000E+00	0.00000E+00	0.00000E+00	0.00000E+00
2	9.61446E-02	9.20826E-01	0.00000E+00	0.00000E+00	0.00000E+00	0.00000E+00	0.00000E+00
3	2.53671E-04	1.29056E-01	1.23978E+00	2.30089E-03	3.52186E-11	0.00000E+00	0.00000E+00
4	0.00000E+00	2.48800E-05	6.78838E-02	6.07055E-01	1.97060E-03	2.47870E-09	1.15843E-10
5	0.00000E+00	4.36807E-05	6.34668E-02	6.87369E-01	1.14641E+00	4.75525E-02	1.07271E-02
6	0.00000E+00	8.08791E-06	1.03777E-02	1.04299E-01	3.80434E-01	1.82882E+00	3.49182E-01
7	0.00000E+00	4.09907E-06	4.63792E-03	3.51736E-02	1.40005E-01	3.87203E-01	3.24069E+00

It is seen that the differences in cross sections are negligible although the overall effect in k-eff is up to 700 pcm.

Test for the effect of P_1 scatting matrices in WIMS-ANL.

The test included calculation if the TRIGA typical fuel under the B1 option with correct cross section for zirconium and hydrogen in zirconium hydride, ie. with ID (Zr)=2091 and ID(H)=2191,in 4 approximations:
(i) diffusion,
(ii) B_1 with P_1 thermal scattering matrices for H and O in water only,
(iii) as above but with a P_1 matrix also for H bound in ZrHx,
(iv) as above but with a P_1 matrix also for Zr bound in ZrHx.
The infinite and effective multiplication factors are shown in Table 5.

Table 5
Infinite and effective multiplication factors in various approximations of leakage calculations.

Case	(i)	(ii)	(iii)	(iv)
K-inf	1.393325	1.393204	1.393057	1.393056
k-eff	1.079449	1.080925	1.090408	1.068336
Φ_E/Φ_{th} in cell	3.42	3.44	3.46	3.46

It is seen that the effect on k-eff from (iii) to (iv) is even stronger than that from (ii) to (iii) but the P1 approximation in hydrogen increases the effective multiplication factor while for zirconium the trend goes in an opposite direction.

The flux spectrum obtained with P_1 matrices used in water and
(i) Without P_1 in ZrH_x,
(ii) P_1 matrix only for H bound in ZrH_x.
(iii) P_1 matrix for both H and Zr in ZrH_x

Table 6
7-group average cell flux values

Lower energy bound[eV]	P1 in H2O	P1 in H_2	P1 in Zr &H
5.0000E+05	3.2019E-01	3.2178E-01	3.2211E-01
1.4251E+03	2.5736E-01	2.5718 E-01	2.5717 E-01
1.1230Ei00	1.8302E-01	1.8254 E-01	1.8242 E-01
6.2500E-01	1.4331E-02	1.4289 E-02	1.4273 E-02
1.4000E-01	4.3202E-02	4.3018 E-02	4.2997 E-02
5.0000E-02	9.3432E-02	9.3048 E-02	9.2980 E-02
1.0000E-05	8.8171E-02	8.8148E-02	8.8016E-02

Conclusion

The results obtained for k-effective and k-infinity is opposite. Also, the values for k-effective given in table 3 increase from (i) to (ii) and (iii) and decrease for (iv). The possible cause of this inconsistency could be the absence of P1 matrices for all the principal materials in the WIMSD library. In description of the DNB[4] card, the author of the WIMS recommends the usage of P1 matrices only if they are available for all principal isotopes of a material. No material is treated separately on the level of leakage calculations and the contribution from the first order is weighted over spectra in materials, their volume and number densities. Therefore, the influence of P1 matrices should be considered only in the sense of its contribution to the whole first order scattering in the calculated cell.

References

1. J. R. Deen, W. L. Woodruff, C.I. Costescu, L. S. Leopando: WIMS-ANL USER MANUAL, Rev.2, ANL/RERTR/TM-23, June 1998.
2. R.E. MacFarlane et. Al., "NJOY94.10-Code System for Producing Pointwise and Multigroup Neutron and Photon Cross Section from ENDF Data" , PSR-355, RSIC, ORNL, Oak Ridge, TN 37830, USA.
3. J. R. Askew, F. J. Fayers, P.B. Kemshell: A General Description of the Lattice Code WIMS, Journ. BNES, Vol. 4, No. 4, P.564, 1966.
4. M. J. Halsall: A Summary of WIMSD4 Input Options, AEEW- M 1327, 1980.

JP0150654

2.10

Measurement of Photoneutron Spectrum at Pohang Neutron Facility

G. N. Kim[×], V. Kovalchuk[+], Y. S. Lee, V. Skoy[*], M. H. Cho, I. S. Ko, W. Namkung

Pohang Accelerator Laboratory, POSTECH, Pohang, Kyungbuk, 790-784, Korea

e-mail:gnkim@postech.ac.kr

Pohang Neutron Facility, which is the pulsed neutron facility based on the 100-MeV electron linear accelerator, was constructed for nuclear data production in Korea. The Pohang Neutron Facility consists of an electron linear accelerator, a water-cooled Ta target with a water moderator and a time-of-flight path with an 11 m length. The neutron energy spectra are measured for different water levels inside the moderator and compared with the MCNP calculation. The optimum size of the water moderator is determined on the base of this result. The time dependent spectra of neutrons in the water moderator are investigated with the MCNP calculation.

1. Introduction

Among the various kinds of neutron sources (reactors, accelerator-based neutrons, and radioisotopic neutron emitters), the accelerator-based neutron source is the most efficient one for high-resolution measurements of microscopic neutron cross sections. It produces short bursts of neutrons with a broad continuous energy spectrum by nuclear reactions of energetic photons or charged particles. Especially, an electron linear accelerator (linac) is a powerful tool to produce intense pulsed neutrons. Pulsed neutrons based on an electron linac are suited for measuring energy dependent cross sections with high resolution by the time-of-flight (TOF) technique covering the energy range from thermal neutrons to a few tens of MeV. The measurement of neutron cross sections gives basic information for the study of neutron interaction with nuclei. Precise measurements of neutron cross sections are of great importance for the safety design of nuclear reactors and for the evaluation of the neutron flux density and energy spectrum around a reactor.

The nuclear data project was initiated to construct the infrastructure for the nuclear data production by the Korea Atomic Energy Research Institute (KAERI) [1]. There was no activity for nuclear data production experiment until this project was launched. Since then, the collaboration group for nuclear data production was organized from several universities in Korea. The pulsed neutron facility using a 100-MeV electron linac was proposed in 1997 at the Pohang Accelerator Laboratory (PAL) [2]. The 100-MeV electron linac was designed and constructed based on experiences obtained from construction and operation of the 2-GeV electron linac at PAL [3].

The neutron energy spectra are measured for different water levels inside the moderator and compared with the results of the MCNP calculation. The optimum size of the water moderator is determined on the base of this result. Furthermore, the time dependent spectra of neutrons in the water moderator are investigated with the MCNP calculation.

2. Pohang Neutron Facility

The Pohang Neutron Facility (PNF) consists of a 100-MeV electron linac, a water-cooled Ta target, and an 11-m long TOF path. The 100-MeV electron linac consists of a thermionic RF-gun, an alpha magnet, four quadrupole magnets, two SLAC-type accelerating sections, a quadrupole triplet, and a beam-analyzing magnet. After the RF-conditioning of the accelerating structures and the wave-guide network, we tested the beam acceleration [3]. The maximum RF power from a SLAC 5045 klystron was up to 45 MW. The RF power fed to the RF-gun was 3 MW. The maximum energy is 75 MeV, and the measured beam currents at

---

[×] Joint appointment at the Center for High Energy Physics, Kyungpook Nat. Univ., Taegu 702-701, Korea

[+] Permanent address: Troitsk Institute for Innovation and Thermonuclear Research, Moscow, Russia

[*] Permanent address: Frank Laboratory of Neutron Physics, JINR, Dubna, Russia

the entrance of the first accelerating structure and at the end of linac are 100 mA and 40 mA, respectively. The length of electron beam pulses is 1.8 μs, and the pulse repetition rate is 12 Hz. The measured energy spread is ± 1% at its minimum. The energy spread was reduced by adjustment of the RF phase for the RF-gun and by optimization of the magnetic field for the alpha magnet.

As a photoneutron target, it is necessary to use a heavy mass material in order to produce an intense neutron source by way of Bremsstrahlung under the high beam power of electrons. We have chosen a tantalum as the target material, which has the advantage of high density (16.6 g/cm^3), high melting point (3,017°C) and high resistant against the corrosion by cooling water. The design of a water-cooled Ta target was done using the Monte Carlo simulation codes, EGS4 and MCNP version 4B. The Ta target as shown in Fig. 1 was composed of ten sheets of Ta plate, 4.9 cm in diameter and 7.4 cm in total length. There was 0.15-cm water gap between them in order to cool the target effectively [4]. The housing of the target was made of titanium. The conversion ratio obtained from MCNP code from a 100-MeV electron to neutrons was 0.032. The neutron yield per kW beam power at the target was 2.0×10^{12} n/sec, which was about 2.5% lower than the calculated value based on the Swanson's formula [5].

Since we have to utilize the space and the infrastructures of the PAL, an 11-m long TOF path and a detector room were constructed perpendicular to the electron linac. The TOF tubes were made by stainless steel with two different diameters of 15 and 20 cm.

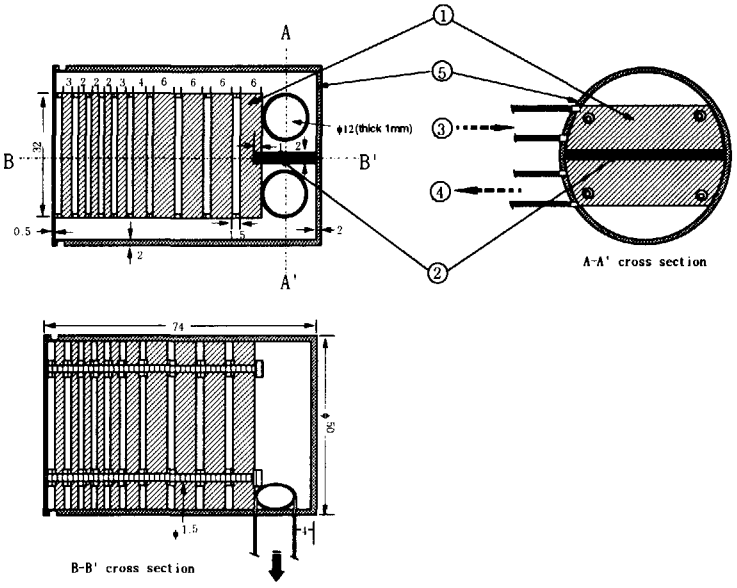

Fig. 1. Schematics of the water-cooled Ta target: Ã Ta plate, Ẽ Parting strip, Ĩ Cooling water (inlet), Ñ Colling water (outlet), Õ Ti housing. The numbers refer to dimensions in mm.

3. Experimental Arrangement

The experimental setup for the neutron TOF spectrum measurement is shown in Fig. 2. The Ta target is located in the position where the electron beam hits the center of the target. The target system consists of a Ta target and a water moderator. The water moderator is of a cylindrical shape with a diameter of 50 cm and a height of 30 cm, whose housing was made of aluminum with a thickness of 0.5 cm. The water moderator was mounted on an aluminum plate with a thickness of 2.5 cm and an iron table with a thickness of 2 cm as shown in Fig. 3. The rear part of the water moderator is covered by a 10 cm lead.

In order to reduce the gamma flash generated by the electron burst from the target and scattered high energy neutrons from the beam, a Pb block with a size of 20 x 20 x10 cm^3 was placed at the entrance of TOF tube with a diameter of 15 cm. Lead was chosen because of its low energy cross section which is about 3 barns at 0.007 eV and 11 barns above 0.2 eV; therefore the lead can serve as an effective low band filter removing more high energy neutrons than sub-thermal neutrons. There is 1.8 m thick concrete between the target room and the detector hall. The sample was placed at the midpoint of the TOF path.

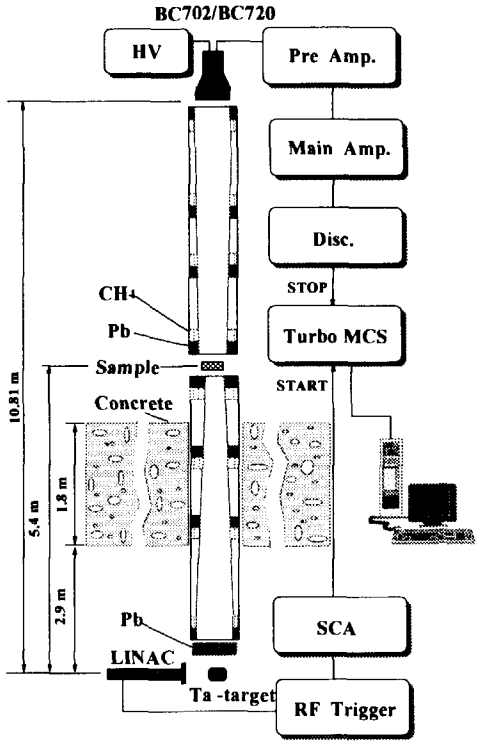

Fig. 2. Experimental setup and a block

As a neutron detector, a ^{6}Li-ZnS(Ag) scintillator BC702 with a diameter of 12.5 cm and a thickness of 1.5 cm mounted on an EMI-93090 photomultiplier was used. It was located at a distance of 10.8 m from the photoneutron target. The neutron detector was shielded by lead bricks and borated polyethylene plates.

In order to monitor the neutron intensity during the experiment, a BF_3 proportional counter with a diameter of 1.6 cm and a length of 5.8 cm was placed inside the target room at a distance of about 6 meters from the target as shown in Fig. 4. The polyethylene sphere with a diameter of 30.5 cm was used as a neutron moderator for the BF_3 counter. The neutron detector with polyethylene sphere has the maximal response for fast neutrons [6]. The lead shield with a thickness of 10 cm was used to protect gamma flash generated by the electron burst from the target. Additionally, a borated polyethylene plate with a thickness of 5 cm was used to cut the thermal neutrons generated from the moderator and walls inside the target room.

In order to investigate the neutron energy spectra for the different water levels in the moderator, we used four water levels as shown in Fig. 5. G1 represents the geometry without water inside the moderator. G2 corresponds to the half of water in the moderator in which water is around the target but no water above the target. G3 is the geometry with a water level of 5 cm above the target surface. Geometry G4 is a full of water in the moderator, which corresponds to 11 cm water level from the target surface. The cooling water inside the Ta target could not change significantly the spectral distribution of original photoneutrons.

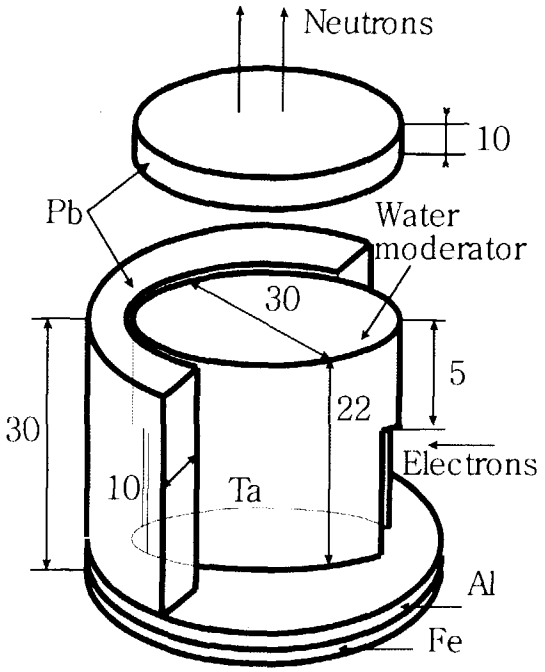

Fig. 3.Geometry for the target system used in the experiment and the MCNP calculation. The numbers in this figure refer to dimensions in cm.

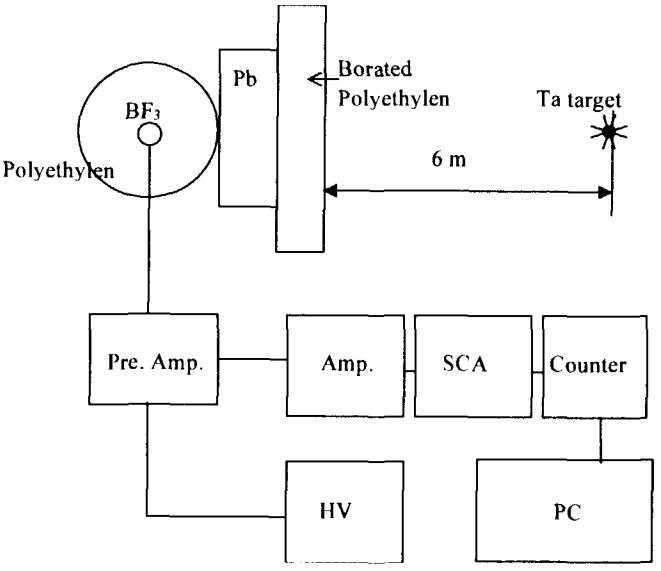

Fig. 4. Experimental arrangement for a BF_3 neutron monitor in the target room and block diagram for the data taking.

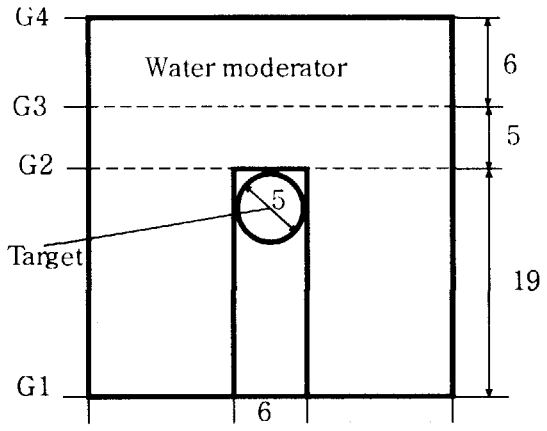

Fig. 5. The geometry used in MCNP for optimizing the water level: G1, G2, G3, and G4 indicate the water level in the moderator vessel. The numbers refer to dimensions in cm.

4. Data Taking

The neutron energy spectra produced from a tantalum target with a water moderator were measured by the TOF method. As shown in Fig. 2, the signal from the ^{6}Li_ZnS(Ag) scintillator was connected through an ORTEC-113 pre-amplifier (Pre. Amp.) to an ORTEC-571 amplifier (Main Amp.). The amplifier output was then fed a discriminator (Disc.) input, whose output was used as a stop signal of the 150 MHz time-digitizer (Turbo MCS). The lower threshold level of the discriminator was set to 30 mV. The Turbo MCS was operated as a 16384-channel time analyzer. The channel width of the time analyzer was set to 0.5 μs. The 12 Hz trigger signal (RF Trigger) for the modulator of the electron linac was connected to an ORTEC-550 single channel analyzer (SCA), the output signal was used as the start signal for the Turbo MCS. The Turbo MCS is connected to a personal computer. The data were collected, stored and analyzed on this computer.

The block diagram of the data acquisition system for the BF_3 neutron monitor is shown in Fig. 4. The signal from a BF_3 counter was connected through an ORTEC-142PC preamplifier (Pre. Amp.) to an ORTEC-590A spectrometric amplifier (Amp.). The amplifier output was fed to an ORTEC-SCA550 single channel analyzer (SCA), where the distance from the preamplifier to the amplifier is about 30 m. The single channel analyzer was used to create the standard signal and to cut noises originating from gamma rays and low-energy neutrons. The output signal from the single channel analyzer was fed into an ORTEC-996 timer and counter. The counter was connected with a personal computer. During the experiment, the electron linac was operated with a repetition rate of 12 Hz, a pulse width of 1.8 μs, a peak current of 30 mA, and electron energy of 60 MeV.

5. Data Analysis

The neutron energy spectra generated by the Ta target with a water moderator with different water levels of G1-G4 were measured with the TOF method at PNF. Fig. 6 shows a typical neutron TOF spectrum for the G3 geometry. The neutron energy spectrum mainly consists of fast neutrons with the mean energy of 0.92 MeV and thermal neutrons produced in the water moderator and scattered from the wall and other materials around the target. The TOF spectrum was only measured in the direction perpendicular to the incident electron beam. In order to estimate the background level, we took neutron TOF spectra for a Sm sample with a Cd filter of 0.5 mm in thickness and a run without any samples (blank run). The background level was estimated from the fitting function $F(I)=a+b\times I+c\times I^{2}$, where a, b, and c are constants and I is the channel number of the time digitizer, as shown in Fig. 7. The resonances in the neutron TOF spectrum for the blank run are related to Sb and W impurities inside the Pb block. The signal-to-background ratio defined as the neutron counts minus background counts divided by the background counts at a particular energy was about 10 to 1.

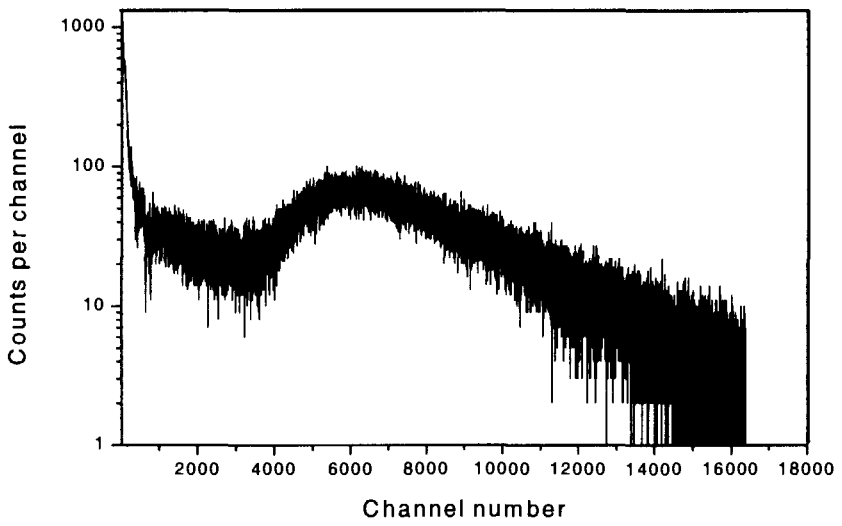

Fig. 6. Typical neutron spectrum for the G3 geometry measured at 11 m TOF path

5. 1 Neutron Monitor Counts

The BF_3 proportional counter was operated in the count mode as a neutron monitor. The neutron monitor was tested by using a neutron source ^{252}Cf with a mean neutron energy of 2.13 MeV and an activity of 5.4×10^4 n/sec. The pulse shape of the neutron monitor was checked with an oscilloscope and no saturation was observed during the linac pulse duration. The typical behavior of neutron counts during the one period of experiment is shown in Fig. 8. Neutron counts during the experiment were changed due to the unstable modulator system for the electron linac. The background count rates for the BF_3 neutron monitor were less than 0.01 counts per second. The background count rates were measured before and immediately after operating the accelerator. The average count rates for the neutron monitor were about 300 counts per second. The neutron monitor counts were used to normalize the neutron intensity between the runs.

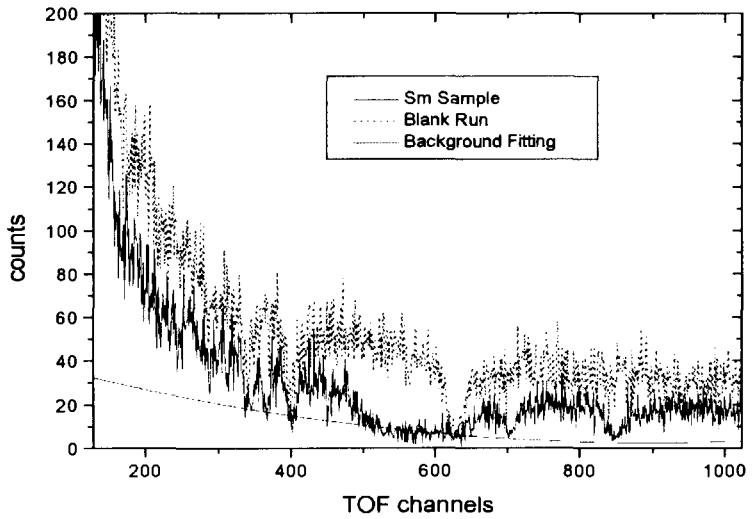

Fig. 7. Typical background level measured at 11 m TOF path length. Solid line and dot line represent the TOF spectrum for Sm sample and without any sample in the beam line, respectively.

5.2 Neutron Energy Spectrum

The measured TOF spectra as a function of channel number were normalized using the neutron counts from the neutron monitor and converted as a function of neutron energy. Each channel I in the time analyzer is converted to the neutron energy E_i via:

$$E_i = \left\{ \frac{72.3 \times L}{(I - I_0) \times \Delta\tau} \right\}^2 \quad (1)$$

Where, L is the neutron flight path in meter, $\Delta\tau$ is the channel width in μs and set to 0.5 μs, and I_0 is the number of channel at the time of flight equals to zero when the neutron burst was produced. The relation between a channel number of the neutron TOF spectrum and its energy was calibrated with resonance energies of Ta, Sm, and other samples with a black resonance. Good linearity was found between the neutron TOF and the channel number. We found the flight path length L equal to 10.81±0.02 m.

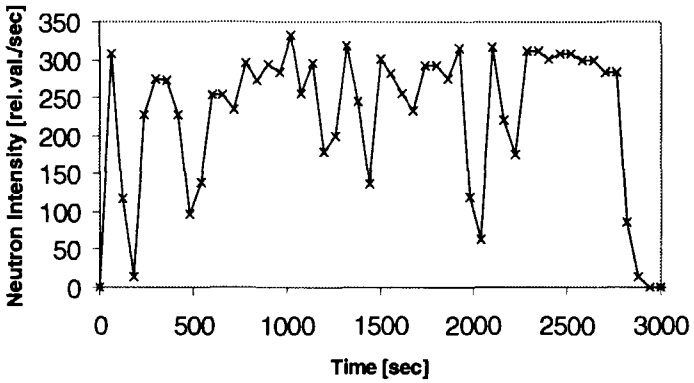

Fig. 8. Typical neutron intensity measured by a BF_3 monitor for an hour operation.

The measured neutron flux was corrected for the detector efficiency, $\varepsilon(E_i)$ which is energy dependent and is given by:

$$\varepsilon(E_i) = 1 - \exp\left(-\frac{t}{C\sqrt{E_i}} \right) \quad (2)$$

where t is the thickness of scintillator in centimeters and C is constant for each scintillator and is given by the manufacturer [7]. In this experiment we used 1.5 cm thick BC702 ^{6}Li-ZnS(Ag) scintillator and for this C= 12.5 cm/eV$^{0.5}$.

Fig. 9 shows the neutron flux (number of neutrons per energy group) in the energy range of 0.01 to 1 eV for different water levels. The neutron flux in each channel was summed up over every 0.23 lethargy width. The G3 geometry with a water level of 5 cm gives more thermal neutrons compared to other geometry. Too high water level in the moderator decreases thermal neutrons due to the absorption of thermal neutrons.

5.3 Compare with the MCNP calculation

The continuous energy Monte Carlo code MCNP version 4B [8] has been used to calculate the neutron spectra for various geometries. The MCNP code has its own nuclear data library generated from the evaluated nuclear data files of ENDF/B-VI [9]. Using the MCNP statistical sampling technique, the neutron distributions of moderated neutrons were calculated as a function of time and energy. The purpose of this calculation is to compare with measurements for the thermal neutron flux leaving the water moderator and to optimize the photoneutron target system.

The neutron source term for the tantalum plates in the target was chosen to be an "evaporation" energy spectrum [10, 11] given by:

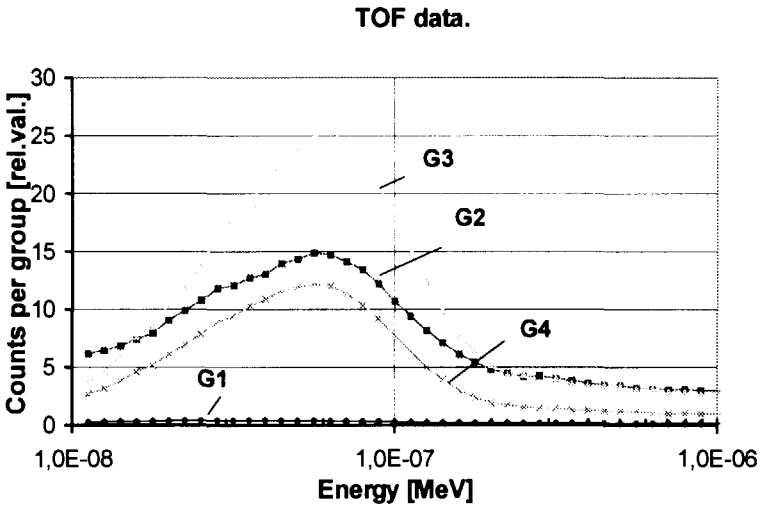

Fig. 9. Measured neutron flux for different geometry in the neutron energy from 0.01 to 1 eV.

$$\phi(E) = cE\exp(-E/T) \quad (3)$$

where E is the neutron energy in MeV, T is the effective temperature of the tantalum target in MeV and c=4.7259 is a normalization constant. Using an effective temperature of 0.46 MeV [12], Eq. (3) gives neutron energy about 0.92 MeV in average. The source parameters were chosen such that the neutrons at "birth" are distributed uniformly throughout a homogenized mixture of tantalum and cooling water with isotropic angular distribution [13].

In the calculation, we ignore the effect of aluminum wall of the water moderator because of its small contribution to the total flux of scattered neutrons. The minimum and maximum neutron cutoff energies were 0.0001 eV and 10 MeV, respectively. The neutron time cutoff was 10^7 Shakes (1 Shake = 10^{-8} sec).

We considered the neutron energy regions from 0.001 eV to 10 MeV for the calculation. The energy region was divided into 200 groups with an equal lethargy width. The neutron current within 15 degrees

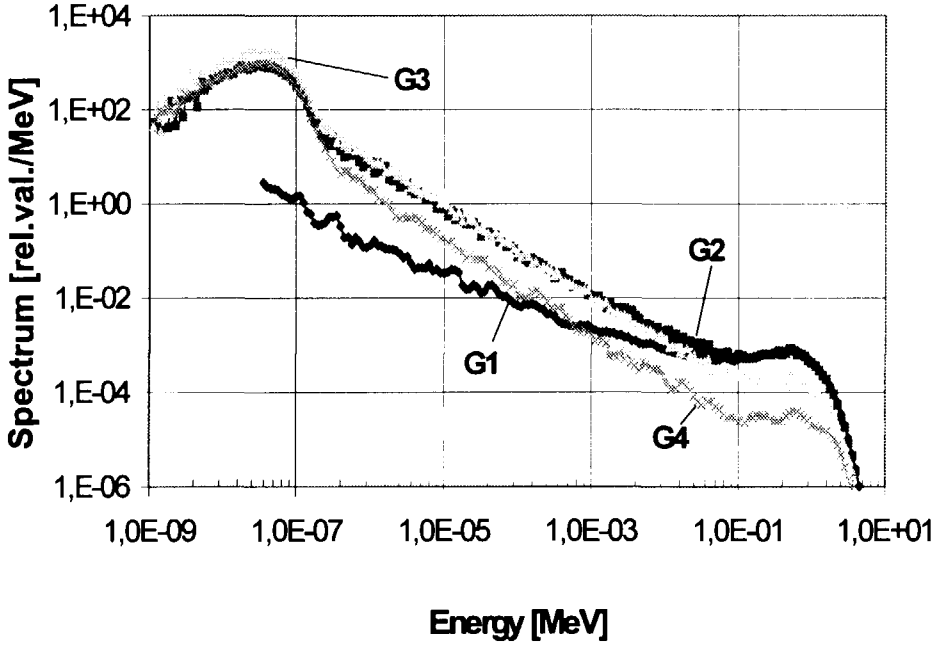

Fig. 10. Neutron energy spectra in the water moderator calculated by the MCNP code for different geometry as shown in Fig. 5.

with respect to the direction of detector from the lead surface was calculated for different water levels inside the moderator. For good statistics in the calculation, the number of particle history calculated for different geometry was more than 50,000,000 counts.

Fig. 10 shows neutron spectra calculated by MCNP code for different geometry described above. For fast neutrons in the energy regions of 0.1 to 10 MeV, the neutron flux for geometry G1 and G2 is almost same and higher than other geometry because there is no water above the target surface. The neutron flux in the energy region from 0.01 eV to 0.1 eV is maximum around at 5 cm of water level, which corresponds to geometry G3, as shown in Fig. 11. The points correspond to MCNP calculation and the line is a polynomial spline interpolation.

The measured differential neutron spectra for three geometries were shown in Fig. 12 compared with those of the MCNP calculations. In this figure, the spectrum for G3 (G4) geometry was multiplied with a factor 10(0.1) for the better visualization. The points (triangles, quadrates, and circles are for G3, G2, and G4 geometry, respectively) represent the result of the MCNP calculation. The measured differential energy spectra were normalized using the neutron monitor counts. The calculated spectra have relative normalization (normalization coefficients are C1= 3540 for G2, C2=35400 for G3, and C3=354 for G4).

The measured neutron spectra were agreed with those of the MCNP calculation within the experimental uncertainty. The statistical uncertainty of MCNP calculation was ranged from 3 to 9 %

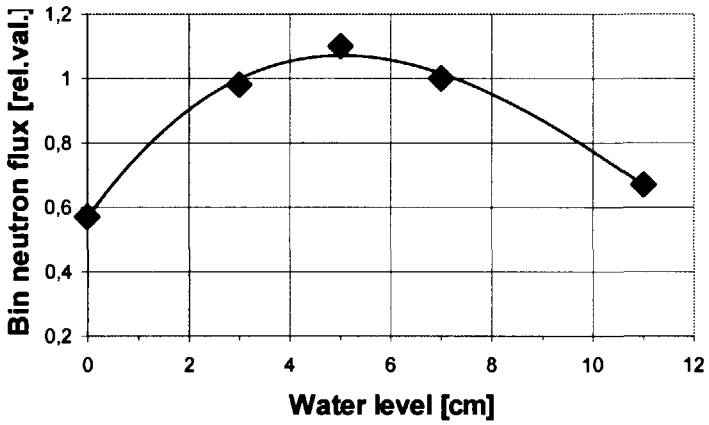

Fig. 11. Calculated neutron flux as a function of the water level in the moderator in the neutron energy from 0.01 eV to 0.1 eV. The measured points are connected by a spline fit.

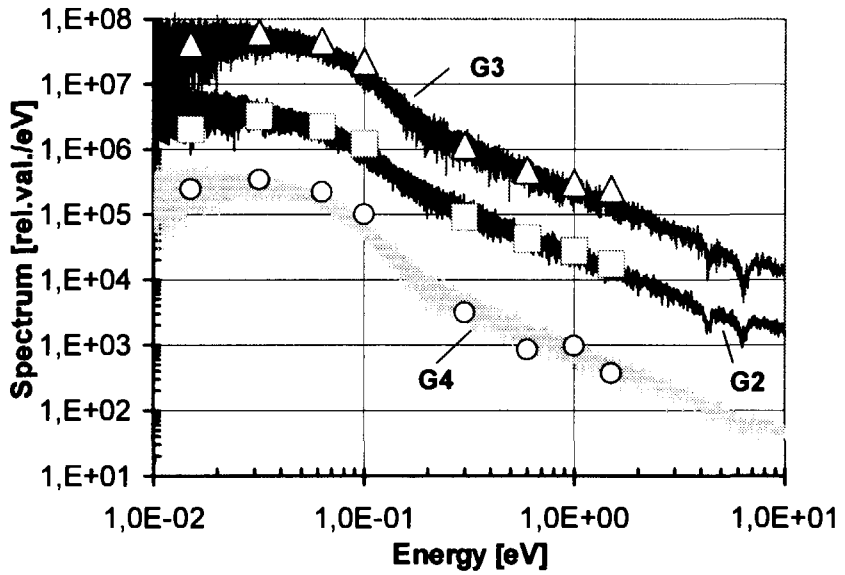

Fig. 12. Measured and calculated differential neutron spectrum for three different geometries. The points correspond to MCNP calculation. The spectrum for G3 (G4) geometry is multiplied by a factor 10 (0.1) for the better view.

depending on the energy bin.

6. Conclusion

The neutron energy spectra produced by the photoneutron target with a water moderator were measured with a ^{6}Li-ZnS(Ag) glass scintillator as a neutron detector with the neutron TOF method at 11 m flight path of Pohang Neutron Facility. As a neutron monitor, a BF_3 proportional counter was used. The neutron TOF spectra were normalized with the neutron monitor counts. We measured the neutron TOF spectra for different water levels inside the moderator and compared with the MCNP calculation in order to maximize the thermal neutron flux.

The measured neutron energy spectra for different water levels in the moderator were verified by the MCNP calculations. The experimental and calculated data were agreed within the experimental uncertainty. According to the results of the measurement and the calculation, the 5 cm water level in the moderator gives the maximal thermal neutron flux for the present geometry of the photoneutron target system.

Acknowledgement

The authors would like to express their sincere thanks to the staff of the Pohang Accelerator Laboratory for the excellent 100 MeV electron linac operation and strong support. This work is supported by the research funds from the Korea Atomic Energy Research Institute.

References

[1] Ministry of Science and Technology of Korea (1997), "1997 Request for Project on Long-Term Nuclear R&D program."

[2] G. N. Kim, *et al.*, "Proposed Neutron Facility using 100-MeV electron linac at Pohang Accelerator Laboratory," in Proceedings International Conference on Nuclear Data for Science and Technology, edited by G. Reffo, A. Ventura and C. Grandi (Trieste, Italy, May 19-24, 1972), p.556.

[3] J. Y. Choi, et al., "Design of 100-MeV electron Linac for Neutron Beam Facility at PAL," in Proceedings of 1997 KAPRA Workshop, edited by Korea Accelerator and Plasma Research Association (Seoul, Korea, June 26-27, 1997), p. 88; H. S. Kang, *et al.*, "Beam Acceleration Result of Test Linac," in Proceedings of First Asian Particle Accelerator Conference, edited by Y. H. Chin *et al.*, (Tsukuba, Japan, Mar. 23-27, 1998), p. 743.

[4] W. Y. Baek, *et al.*, "Design of the Photoneutron Target for Pulsed Neutron Sources at PAL," in Proceedings of Workshop on Nuclear Data Production and Evaluation, edited by J. Chang and G. N. Kim (Pohang, Korea, Aug. 7-8, 1998).

[5] W. P. Swanson, "Radiological Safety Aspects of the Operation of Electron Linear Accelerators," IAEA Technical Reports No. 188 (1979).

[6] B. Wiegel, A. V. Alevra, B. R. L. Siebert, "Calculations of the response functions of Bonner Spheres with He proportional counter using a realistic detector model", PTB Bericht N-21, Physikalisch-Technische Bundesanstalt, Braunschweig, Germany, (1994).

[7] Scintillation detector. BC702. Bicron. Saint-Gobain Norton Industrial Ceramics cooperation. User's Manual. USA (1997).

[8] MCNP, "A General Monte Carlo N-Particle Transport Code System, Version 4B", Los Alamos National Laboratory, LA-12625-M, (1997).

[9] ENDF/B-VI, "Evaluated Nuclear Data Files", Brookhaven National Laboratory, National Nuclear Data Center, On-line data service, (1997).

[10] Y. Danon, "Design and construction of the RPI enhanced thermal neutron target and thermal cross section measurements of rare earth isotopes", Doctoral Thesis, Rensselaer Polytechnic Institute (1993).

[11] Y. Danon, R. C. Block, R. E. Slovacek, "Design and construction of a thermal neutron target for the RPI linac", Nucl. Instr. and Meth. **A352** (1995), 596.

[12] C. R. Stopa, "Measurements of neutron induced fission cross sections of ^{244}Cm, ^{246}Cm and ^{248}Cm by means of lead slowing-down-time spectrometry", Doctoral Thesis, Rensselaer Polytechnic Institute, (1983).

[13] M. E. Overberg, B.Moretti, R.Slovacek, R.Block, "Photoneutron target for the RPI linear accalerator", Nucl. Instr. and Meth. **A438** (1999), 256.

JP0150655

2.11

JENDL-3.2 Performance in Analyses of MISTRAL Critical Experiments for High-Moderation MOX Cores

Naoyuki TAKADA
Fuel Engineering and Development Department, Nuclear Fuel Industries, Ltd.
3135-41, Muramatsu, Tokai-mura, Naka-gun, Ibaraki, 319-1196 Japan
E-mail: takada@nfi.co.jp

Koki HIBI(MHI), Kazuya ISHII(Hitachi), Yoshihira ANDO(Toshiba),
Toru YAMAMOTO, Masao UEJI, Yutaka IWATA(NUPEC)

NUPEC and CEA have launched an extensive experimental program called MISTRAL to study highly moderated MOX cores for the advanced LWRs. The analyses using SRAC system and MVP code with JENDL-3.2 library are in progress on the experiments of the MISTRAL and the former EPICURE programs. Various comparisons have been made between calculation results and measurement values.

1. Introduction

Nuclear Power Engineering Corporation (NUPEC), French Atomic Commission (CEA) and CEA's industrial partners have launched an extensive experimental program called MISTRAL (MOX: Investigation of Systems Technically Relevant of Advanced Light water reactors) [1,2,3,4] in order to obtain basic core physical parameters of highly moderated MOX cores that will be used to improve core analysis methods. NUPEC is conducting this study on behalf of the Japanese Ministry of International Trade and Industry (MITI). This experimental program has been executed in the EOLE facility at Cadarache center. The MISTRAL program consists of 4 core configurations and has been successfully completed by July 2000. As a part of the MISTRAL program, NUPEC also obtained some of the experimental data of the EPICURE program that CEA had conducted for 30% MOX loading in PWRs.

2. EOLE critical facility

Experiments have been performed in the EOLE facility that is a tank type critical

facility. A cylindrical Aluminum vessel (diameter = 2.3 m, height = 3m) is installed with stainless steel over structures. Fuel pins used in the facility are standard PWR types and the active length of the pin is about 80 cm. Four types of enrichment are prepared for MOX pins and one type for UO_2 pin. Grid plates are fixed inside the inner tank and they provide flexibility of the core configurations. The reactivity of the core is controlled mainly with boron (boric acid) concentration in water and core size. During the critical experiments, a water level of the tank is always kept at the height that is on approximately 20 cm above from the top of active length of fuel pins. Small reactivity is compensated using a pilot rod. Core excess reactivity without the pilot rod is determined through the in-hour equation with measuring the doubling time after the withdrawal of the pilot rod. Four pairs of cluster-type safety rods are utilized only for the shutdown.

3. Core configurations and measurements in the MISTRAL program

Figure 1 shows the core configuration of MISTRAL-1. It consisted of about 750 regular enriched UO_2 (3.7% in ^{235}U) fuel pins in a lattice pitch of 1.32 cm and was designed as a reference for the highly moderated MOX cores. Figure 2 shows the core configuration of MISTRAL-2. This is a highly moderated full-MOX core consisting of about 1600 MOX (7% enrichment) fuel pins with the same lattice pitch of MISTRAL-1. Figure 3 shows the core configuration of MISTRAL-3 which is devoted to the physical study of a 100% MOX lattice with higher moderation than MISTRAL-2. This configuration consists of about 1350 MOX 7% fuel pins in the lattice pitch of 1.39 cm. Figure 4 shows the Core configuration of MISTRAL-4 which is a PWR mock-up configuration. A couple of measurement items were selected for each core configuration from following items:

(1) Critical mass and boron concentration
(2) Buckling measurement using reaction rate distribution measurements
(3) Boron worth
(4) Spectrum indices measurement
(5) Modified conversion factor, 238U capture/total fission
(6) Isothermal temperature coefficients
(7) Reactivity worth and associated reaction rate distribution of a single absorber (Natural B_4C, enriched B_4C, Ag-In-Cd alloy, and UO_2-Gd_2O_3) at the center of the core
(8) Reactivity worth and associated reaction rate distribution of the substitution of 9 central fuel pins by water holes

(9) Reactivity worth and associated reaction rate distribution of a cluster absorber
(10) Void coefficient
(11) β eff

4. Experimental methods

The number of fuel pins, core, temperature, the boron concentration and doubling time were measured to determine the core critical mass. Various kinds of experimental methods were applied to obtain physical parameters of the cores in the MISTRAL program as described below. A neutron source multiplication method (a sub-critical method) was utilized for the reactivity measurement. An integral gamma scanning method was applied to determine the fission densities of the fuel pins. Miniature fission chambers of several kinds of isotopes were adopted for the determination of energy dependent neutron flux and also for spectrum index measurements. The effective delayed neutron fraction of a core (β eff) was measured using of the core noise method which had been utilized in the international benchmark of β eff's at the MASURCA and the FCA fast critical facilities.

5. Calculation methods

The analysis has been performed using SRAC system and MVP with JENDL-3.2 library which were developed at Japan Atomic Energy Research Institute (JAERI). SRAC system consists of deterministic codes. A processed nuclear data library with 107-energy group structure is prepared for SRAC. MVP is a continuous energy Monte Carlo code that is utilized to obtain reference calculation results for the SRAC system such as core eigen-values. In SRAC system, the collision probability method is applied for generating the 16-group collapsed and homogenized unit cell cross sections. The neutron energy spectrum affected by the neutron leakage is calculated with the B1 approximation taking into account the measured geometrical buckling. The resonance absorption of Pu isotopes should be precisely evaluated at epi-thermal and thermal ranges for MOX fuels. Therefore, an ultra fine group resonance reaction calculation module, PEACO, is utilized throughout calculation of effective cross section. The thermal cut-off energy was carefully chosen and determined to be 1.855eV through a sensitivity study. After generating 16-group cell cross sections (fast range - 8 groups and thermal range - 8 groups) , core calculations in 1/4 symmetry configuration were performed using CITATION and/or TWOTRAN modules in SRAC system. In two-dimensional calculation model, axial leakage is implicitly taken into account using the measured axial buckling of a core. For a single absorber calculation, a 3×3 cell

model is adopted in the collision probability calculation of the absorber cell at the core center. Also detailed cell models in the collision probability calculation are adopted for the analysis of spectrum indices.

6. Calculation results

Varieties of comparisons between calculations and measurements are in progress for MH1.2 (which is devoted to study on basic characteristics of a MOX core in the EPICURE program), MISTRAL-1, -2 and -3. Table 1 shows the differences of keffs for 4 configurations. The calculated keffs agree well with the experimental values. Table 2 shows the root-mean-square (R.M.S) differences of radial power distribution. The differences are as much as the uncertainty of measurement. Table 3 shows the C/E values of spectrum indices with two calculation methods. The differences of the C/E values obtained by two calculation methods are not large and the C/E tendency are same with two calculation methods.

Acknowledgment

The authors thank Prof. Kanda of the University of Kyoto and other members of the implementation committee of "Study of Advanced LWR Cores for Effective Use of Plutonium," in NUPEC for their technical advices and suggestions.

References

[1] S. Cathalau and J.C. Cabrillat et al: "MISTRAL: an experimental program in the EOLE facility devoted to 100% MOX core physics", International Conference on Physics of Reactors: PHYSOR 96, Vol. 3 (H- 84-92) September 16-20,1996 Mito. Japan

[2] Yamamoto T. et al: "CORE PHYSICS EXPERIMENT OF 100% MOX CORE: MISTRAL" Proc. of Int. Conf. on Future Nuclear Systems, Global '97, Vol.1, pp395 1997.

[3] Kanda K. and Yamamoto T. et al: "MOX fuel core physics experiments and analysis - aiming for Plutonium effective use ", (in Japanese) Journal of the Atomic Energy Society of Japan, No.11, Vol. 40. 1998.

[4] Hibi K. et al: "ANALYSIS OF MISTRAL AND EPICURE EXPERIMENTS WITH SRAC AND MVP CODE SYSTEMS", Proc. of Int. Conf. Physics of Reactor Operation, Design and Computation, PHYSOR 2000.

Table.1 Differences of keff between Calculation and Measurement for each Experimental Core

PROGRAM	EPICURE	MISTRAL	MISTRAL	MISTRAL
CORE NAME	MH1.2	CORE1	CORE2	CORE3
FEATURE	Partial MOX	Uranium CORE	Full MOX	Full MOX
FUEL PIN	3.7%UO2 + 7% MOX	3.7% UO2	7% MOX (Mainly)	7% MOX
H/HM	3.7	5.1	5.1	6.2
CORE DIAMETER	69 cm	41 cm	60 cm	59 cm
MVP	+ 0.27 %Δk ±0.02 % (1σ)	+ 0.48 %Δk ±0.03 % (1σ)	+ 0.70 %Δk ±0.02 % (1σ)	+ 0.77 %Δk ±0.02 % (1σ)
SRAC (Pij + TWOTRAN)	+ 0.13 %Δk	− 0.19 %Δk	+ 0.41 %Δk	+ 0.42 %Δk

Table. 2 R.M.S Differences of Radial Power Distribution between Calculation and Measurement for each Experimental Core

PROGRAM	EPICURE	MISTRAL	MISTRAL	MISTRAL
CORE NAME	MH1.2	CORE1	CORE2	CORE3
FEATURE	Partial MOX	Uranium CORE	Full MOX	Full MOX
MVP	1.2 %	1.7 %	1.7 %	1.4 %
SRAC (Pij + CITATION)	0.9 %	2.0 %	1.1 %	1.3 %

Measurement uncertainty UO2 rod ~1.0 % : MOX rod ~ 1.5 % (1σ)

Table. 3 C/E Values of Spectrum Indices with Two Calculation Methods

CORE NAME		CORE1			CORE2		
Calculation method**		SRAC	MVP	uncertainty*	SRAC	MVP	uncertainty*
SPECTRUM INDICES	238U/235U***	0.67	0.63	(10%)	0.90	0.87	(6.7%)
	239Pu/235U	1.01	1.00	(2.4%)	1.04	1.01	(2.4%)
	238Pu/239Pu	-	-	-	0.94	0.94	(13.7%)
	240Pu/239Pu***	0.95	0.91	(7.5%)	0.83	0.81	(5.9%)
	241Pu/239Pu	0.99	1.00	(2.7%)	0.98	0.99	(2.7%)
	242Pu/239Pu	-	-	-	0.98	0.96	(7.6%)
	237Np/239Pu***	0.76	0.74	(3.2%)	0.90	0.88	(3.2%)

* ( ) measurement uncertainty (1σ)

** Calculation method
SRAC Code: Collision Probability Calculation (107 energy group)
MVP Code: Continuous energy Monte Carlo Calculation

*** These measurement values are now under investigation.

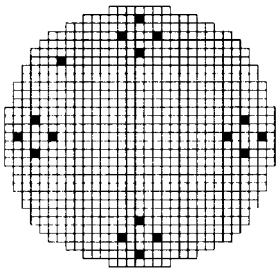

□ MOX(7.0%) fuel rod
■ Guide tube for safty and control rod

Fig.1 Core Configuration of MISTRAL-1

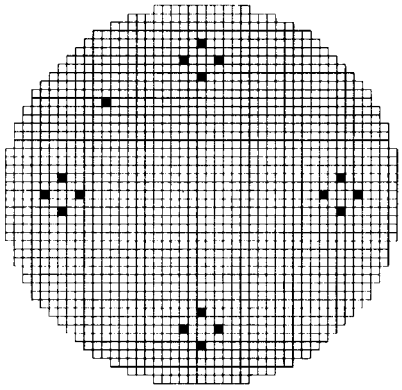

□ MOX(7.0%) fuel rod
□ MOX(8.7%) fuel rod
■ Guide tube for safty and control rod

Fig.2 Core Configuration of MISTRAL-2

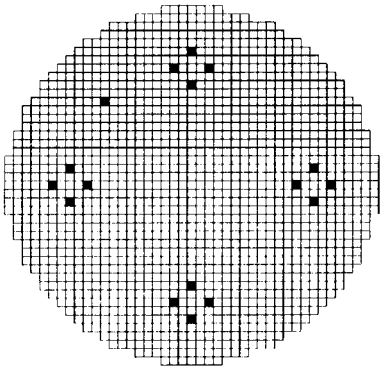

□ MOX(7.0%) fuel rod
■ Guide tube for safty and control rod

Fig.3 Core Configuration of MISTRAL-3

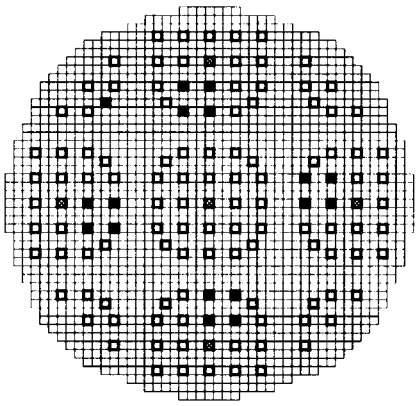

[ ] MOX(7.0%) fuel rod
□ Mock-up thimble tube
⊠ Instrumentation tube
■ Guide tube for safty and control rod

Fig.4 Core Configuration of MISTRAL-4

JP0150656

2.12

Integral Test of JENDL-3.2 Data by Re-analysis of Sample Reactivity Measurements at SEG and STEK Facilities

Klaus DIETZE
Oarai Engineering Center (OEC)
Japan Nuclear Cycle Development Institute (JNC)
Oarai-machi, Ibaraki-ken, 311-1393
e-mail: dietze@oec.jnc.go.jp

Sample reactivity measurements, which have been performed at the fast-thermal coupled facilities RRR/SEG and STEK, have been re-analyzed using the JNC route for reactor calculation JENDL-3.2 // SLAROM / CITATION / PERKY. C/E-values of central reactivity worths (CRW) of FP nuclides, structural materials, and standards are given.

1. Introduction

Integral tests are necessary to check neutron data and codes used in reactor calculations. Such feedback is very important for evaluators and programmers for data corrections and improvements of the codes. The NEA NSC Working Group on International Evaluation Cooperation proposed to use the STEK and SEG experiments, as a joint data base, for the validation and convergence of the last versions of JENDL, JEF and ENDF/B [1].

At Cadarache (CEA France), extensive re-analyses of the SEG and STEK experiments have been recently completed using the competitive European scheme JEF-2.2 / ECCO / ERANOS [2,3]. The STEK experiments also have been analyzed in Japan [4,5,6], but not the SEG experiments. This paper presents results of a re-analysis of the experiments at SEG and STEK using the JNC route, similar to the European scheme. Additionally, a crisscross use of JEF-2.2 with the JNC route was made for SEG to compare data and routes.

2. Sample Reactivity Measurements

The measurements have been performed with FP nuclides, structural materials, and standards for the central position of the fast-thermal coupled facilities RRR/SEG in Rossendorf/Germany and STEK in Petten/Netherlands using the pile-oscillation method, developed to a high perfection. The specific reactivities of the sample materials were measured over a wide mass range. The sample size corrections and extrapolation to the infinitely dilute (zero mass) value CRW were performed using different methods. Data and codes used in calculations of the self-shielding effect were tested in this manner.

In the STEK configurations, the neutron spectra had an increasing softness covering a broad energy range. A great number of FP nuclides have been measured at STEK. The SEG configurations, however, are characterized by especially designed adjoint spectra to check separately capture and scattering data. In the case of an energy-independent adjoint spectrum, the slowing-down effect disappears and the sample reactivity is due only to absorption. On the other hand, the scattering effect is dominant and negative if the adjoint spectrum is monotonously rising with the energy. The neutron and adjoint spectra of two typical SEG facilities and of the 5 STEK configurations are shown in Fig. 1-3. The SEG experiments are considered as "clean" experiments; i.e., the measurements were performed in simple geometry

under clear conditions well suited for calculation. Only a few materials (most of them are standards) were used in the surrounding of the sample and in the inner core region.

3. Calculations

Cell calculations with SLAROM were performed for all zones using the 70 group library JFS-3 of JENDL-3.2. The pellet filling of the inner regions of the core were treated heterogeneously in slab geometry, the outer regions homogeneously. Then, the neutron and adjoint fluxes were calculated with CITATION (R,Z-geometry) for the critical condition. Finally, perturbation theory calculations were carried out with PERKY (mapping version), providing total and partial reactivity contributions for all reaction types and energy groups. The calculated CRW's were then compared with the extrapolated (infinitely dilute) experimental specific reactivity of the sample material by C/E-ratios.

In order to avoid the determination of the normalization integral of the reactor, the C/E-values were normalized to a reference material, preferably a standard. In most cases boron-10 was used for this. In SEG-6 the scattering effect is dominant; therefore, hydrogen (graphite in the European scheme) was preferred as the reference material. C/E-values were determined for more than 85 materials under investigation at SEG and STEK.

4. Results

Five STEK and five SEG configurations have been analyzed. The calculated maps of reactivity contributions in energy groups can be used to find the main contributions to the total reactivity, in order to locate possible sources of discrepancies in C/E-values.

The C/E-values obtained for STEK are compiled in Table 1. A corresponding table of STEK results obtained with the European scheme is given in [3]. A good agreement was found for standards and for most of the strong absorbers. However, for many weak absorbers more discrepancies were found with an obvious tendency towards a systematic underestimation. This trend was also found in former analyses of STEK [6]. This can be explained by compensating effects of the negative capture and scattering contributions (negative and positive!), due to the dependence of the adjoint spectrum on neutron energy. In fact, the scattering effect is calculated larger by the JNC route than with the European scheme, especially the contribution of the inelastic scattering. For important reactor materials , clear discrepancies were found for Mo-98, Mo-100, Tc-99, Ag-109, Cs-133, Sm-151, Pb, and Pu-240 in nearly all STEK configurations. The 22 most important FP nuclides for fast reactor calculation [7], contributing about 85% to the total reactivity effect of all FP nuclides, are given in the comment column in Table 1.

C/E-values for two typical SEG facilities are compiled in Tables 2 and 3. The results of the JNC route are compared with those of the European scheme [2] and a crisscross use of JEF-2.2 also with the JNC route. The C/E-values for SEG-5 show clear discrepancies for the capture data of Mn, Zr, Mo-95, and Ag-109 (for JENDL-3.2), and of Cd, Mo-95, and Sm-149 (for JEF-2.2). The scattering data of JENDL-3.2 should be checked for Cd, Pb, and Be (Table for SEG-6/45). A significant underestimation was found for Mo-100 in SEG-7A. This can be explained only by inaccurate scattering data.

5. Conclusions

The C/E-values show that uncertainties in JENDL-3.2 (and likewise in JEF-2.2) still exist, especially for structural materials and weak absorbers. Of course, the information is integral; precise corrections should be obtained from adjustment studies.

The certainty of integral tests is limited by the experimental error and by the fact that the calculation must be performed in a few steps. When using different input libraries, codes in the routes, self-shielding treatment, and likewise a different energy group structure, it is difficult to locate exactly the source of the differences and deviations in the C/E-values. Concerning data interpretation, an

additional use of group averaged transmissions has proved useful and could complement integral tests to overcome their specific disadvantages [8].

Integral tests using sample reactivity measurements are not recommendable for materials with a very small reactivity or with large compensating effects. The collapsing from 70 to 18 or 7 energy groups is not recommendable for facilities with soft neutron spectra because of the very broad 18^{th} or 7^{th} energy group (from 10^{-5} up to 100.3 eV). Differences were found between the results in 70 and the results in 18 energy groups [9].

The analyses of this work could easily be repeated for the validation of JENDL-3.3.

References

[1] NEA NSC International Evaluation Cooperation, NNDEN/46, March 1993, p.48.
[2] K.Dietze, et al., Int. Conf. Nucl. Data for Sci. and Techn., Gatlinburg, 1994, p.789.
[3] A.Meister, JEF/DOC-746, NEA Paris (1998).
[4] T.Watanabe et al., NEA/NSC/DOC(92) 9, 1992, p.411.
[5] M.Kawai et al., Int. Conf. Nucl. Data for Sci. and Techn., Gatlinburg, 1994, p.727.
[6] T.Watanabe, et al., Final Report of the JNDC FPND Working Group, 1996.
[7] M.Salvatores et al., Proc. Specialist's Meeting on FPND, Tokai, May 25~27, 1992, p.434.
[8] K.Dietze, P.Ribon, P.Siegler, JEF/DOC-777, NEA Paris (1999).
[9] K.Dietze, Report JNC TN9400 99-089, Oarai (1999).
[10] J.J.Veenema, A.J.Janssen, Report ECN-10, Petten (1976).

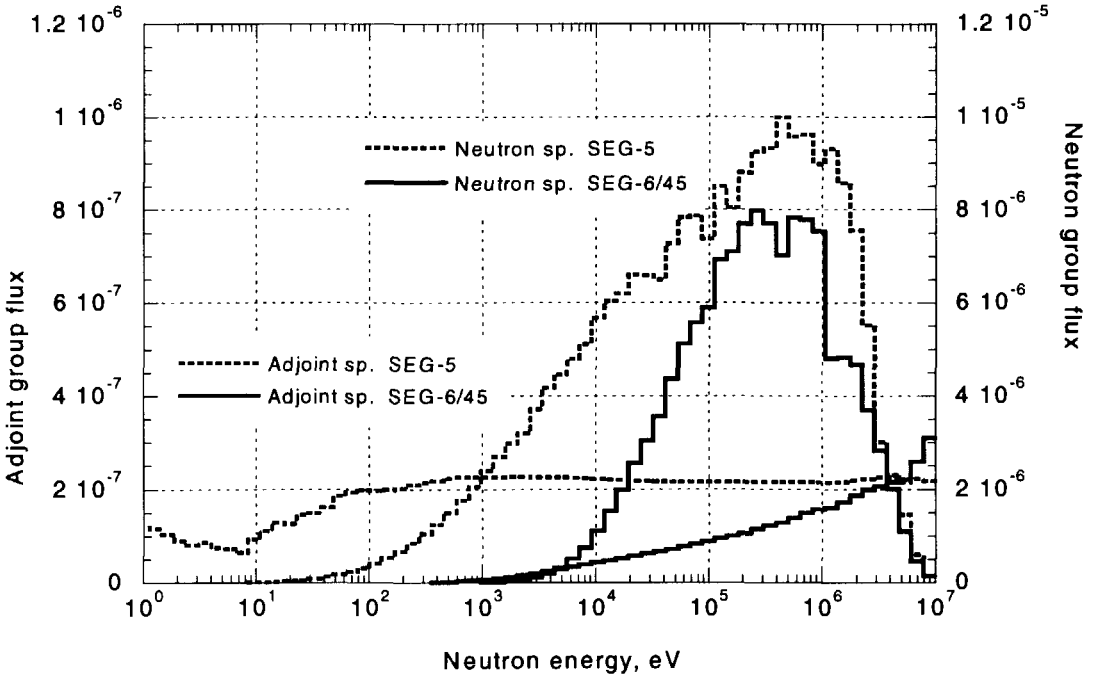

Fig. 1 : Typical neutron and adjoint spectra in SEG facilities

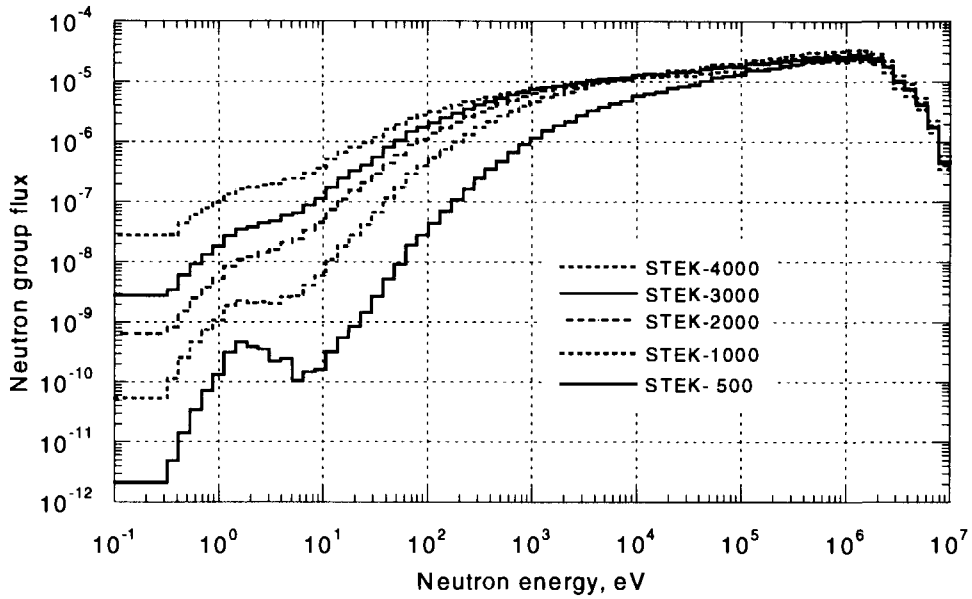

Fig. 2 : Neutron fluxes at the central position of 5 STEK facilities

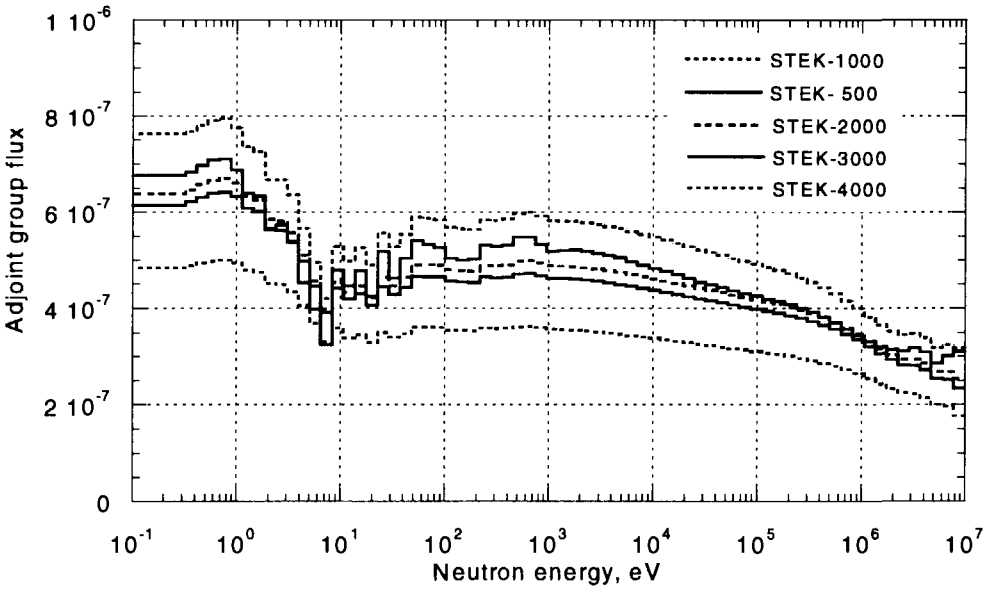

Fig. 3 : Adjoint fluxes at the central position of 5 STEK facilities

Table 1 :

C/E-values of the infinitely dilute sample reactivity of materials under investigation in STEK facilities obtained with the JNC route JENDL-3.2 // SLAROM / CITATION / PERKY. The C/E-values are normalized to the C/E-value of boron-10. The 22 most important FP nuclides for fast reactor calculation are marked. The errors are estimated and based on the experimental (statistical) errors [10] and an additional error due to the normalization.

- no measurement (or CRW) was found in reports.

x measured reactivity or the infinitely dilute values are very small or near zero

! Discrepancies are highlighted (? – questionable)

MAT	STEK-4000	STEK-3000	STEK-2000	STEK-1000	STEK-500	Comment
B-10	1.00 ± 4%	1.00 ± 5%	1.00 ± 4%	1.00 ± 4%	1.00 ± 4%	Normalization
H	1.01 ± 7%	0.96 ± 6%	0.97 ± 6%	1.00 ± 5%	0.98 ± 6%	Standard
C	1.03 ± 5%	0.93 ± 6%	0.94 ± 8%	0.96 ± 6%	0.94 ± 6%	Standard
O	0.91 ±20%	0.96 ± 7%	0.93 ± 6%	0.96 ± 5%	1.01 ± 6%	
Al	1.05 ± 6%	0.97 ± 8%	0.99 ± 8%	1.06 ± 5%	1.07 ± 7%	
Si	**0.87 ± 6%**	**0.77 ±13%**	**0.78 ±12%**	**0.84 ± 6%**	-	**!**
Cl	1.09 ± 9%	1.13 ± 9%	1.32 ±12%	1.53 ±13%	1.11 ±14%	
V	x	**0.54 ± 8%**	**0.59 ± 8%**	**0.73 ± 8%**	-	**Small effect, !**
Cr	x	**0.41 ± 7%**	**0.47 ± 9%**	**0.56 ± 8%**	-	**Small effect, !**
Fe	x	**0.38 ±10%**	**0.50 ± 8%**	**0.70 ± 7%**	**0.86 ± 6%**	**Small effect, !**
Zr-90	**0.58 ±29%**	**0.78 ±28%**	**0.71 ±28%**	**0.75 ±24%**	**0.89 ±21%**	**Small effect, !**
Zr-91	**1.51 ±13%**	**1.37±15%**	**1.43 ±15%**	**1.22 ±22%**	**1.24 ±68%**	**!**
Zr-93	**0.32 ±43%**	**0.40 ±59%**	**0.37 ±54%**	**0.28 ±57%**	**0.35 ±44%**	**!**
Zr-96	2.20 ±28%	x	2.36 ±79%	1.13 ±63%	0.86 ±29%	Small effect
Nb	1.05 ± 8%	1.06 ±10%	1.08± 9%	1.06 ± 7%	1.01 ± 6%	Absorber
Mo	1.02 ± 8%	0.98 ± 9%	1.04 ±12%	0.99 ±10%	0.98 ±11%	Absorber
Mo-92	1.08 ±48%	1.01 ±61%	0.97 ±54%	0.66 ±53%	x	
Mo-94	x	0.66 ±49%	0.85 ±37%	1.62 ±70%	0.37 ±60%	Small effect
Mo-95	0.80 ±12%	0.81 ±14%	0.87 ±14%	0.88 ±13%	0.82 ±16%	Important FP, ?
Mo-96	1.04 ±36%	0.91 ±57%	0.96 ±50%	1.17 ±51%	x	Small effect
Mo-97	0.77 ±16%	0.79 ±15%	0.93 ±12%	0.97 ± 9%	0.99 ±13%	Important FP
Mo-98	**2.33 ±12%**	**1.69 ±20%**	**2.14 ±23%**	x	x	**Important FP, !**
Mo-100	**1.87 ±15%**	**1.75 ±27%**	x	x	x	**Important FP, !**
Tc-99	**0.84 ±11%**	**0.66 ±12%**	**0.69 ±15%**	**0.72 ±17%**	**0.88 ± 8%**	**Important FP, !**
Ru-101	1.16 ±12%	0.99 ±13%	1.03 ±13%	0.98 ±14%	1.04 ±11%	Important FP
Ru-102	0.67 ±27%	1.05 ±20%	1.10 ±19%	1.43 ±23%	1.95 ±61%	Important FP, ?
Ru-104	1.09 ±38%	1.09 ±32%	1.23 ±39%	1.84 ±36%	1.24 ±38%	Important FP
Rh-103	0.95 ± 8%	0.97 ± 9%	0.93 ± 9%	0.92 ± 7%	0.90 ±11%	Important FP
Pd-104	**1.30 ±45%**	**1.46 ±44%**	**1.55 ±47%**	**1.40 ±52%**	**1.58 ±84%**	**?**
Pd-105	0.88 ±10%	0.85 ±12%	0.96 ±10%	1.03 ± 9%	0.99 ± 9%	Important FP
Pd-106	**1.59 ±16%**	**1.47 ±17%**	**1.44 ±15%**	**1.40 ±19%**	**1.43 ±29%**	**!**
Pd-107	0.93 ± 9%	0.92 ±10%	1.07 ±11%	1.11 ±11%	1.04 ± 9%	Important FP
Pd-108	0.97 ±23%	0.81 ±17%	0.95 ±22%	1.39 ±42%	1.17 ±39%	Important FP
Pd-110	1.05 ±36%	x	0.89 ±86%	0.59 ±40%	x	
Ag-109	**0.78 ±11%**	**0.55 ±13%**	**0.84 ±15%**	**0.72 ±19%**	**0.76 ±14%**	**Important FP, !**
Cd-111	0.95 ±24%	1.10 ±25%	1.07 ±22%	0.89 ±21%	0.95 ±22%	
Te-128	x	x	x	x	**0.54 ±28%**	**Small effect, !**
Te-130	x	x	0.79 ±44%	1.02 ±39%	x	Small effect
I-127	**0.73 ±11%**	**0.82 ±17%**	**0.92 ±14%**	**0.87 ±16%**	**0.81 ±20%**	**?**
I-129	0.86 ±28%	0.88 ±29%	0.93 ±28%	1.08 ±21%	1.12 ±26%	Important FP
Cs-133	**0.65 ±10%**	**0.58 ±13%**	**0.70 ± 9%**	**0.80 ± 8%**	**0.71 ±12%**	**Important FP, !**
Cs-135	x	**0.43 ±70%**	**0.61 ±84%**	**0.71 ±85%**	**0.23 ±84%**	**Large err., ?**
La-139	1.17 ± 8%	1.35 ±55%	x	x	0.81 ±53%	Small effect

continued

Ce-140	1.54 ±64%	0.55 ±54%	0.68 ±39%	0.98 ±24%	0.49 ±45%	Small effect
Ce-142	x	**0.44 ±65%**	**0.27 ±25%**	**0.36 ±19%**	**0.33 ±17%**	**!**
Pr-141	0.99 ±19%	1.06 ±25%	0.87 ±21%	1.49 ±29%	0.80 ±38%	Important FP
Nd-142	x	0.76 ±69%	0.98 ±47%	0.73 ±40%	0.93 ±54%	Small effect
Nd-143	0.66 ±18%	0.84 ±25%	0.86 ±25%	0.99 ±14%	0.88 ±24%	Important FP
Nd-144	0.36 ±37%	0.58 ±45%	0.92 ±54%	0.85 ±44%	x	
Nd-145	0.47 ±25%	0.58 ±28%	0.71 ±22%	0.87 ±18%	0.90 ±22%	Important FP
Nd-146	0.82 ±37%	0.87 ±72%	1.58 ±84%	x	x	Small effect
Nd-148	0.76 ±23%	0.79 ±24%	0.92 ±18%	1.13 ±19%	x	
Nd-150	0.75 ±33%	0.92 ±49%	1.30 ±25%	1.69 ±23%	x	
Pm-147	0.78 ±19%	0.65 ±24%	0.76 ±21%	0.86 ±15%	0.89 ±12%	Important FP
Sm-147	0.86 ±15%	0.87 ±24%	1.11 ±24%	0.95 ±12%	0.96 ±14%	
Sm-148	0.49 ±25%	0.59 ±52%	0.90 ±33%	1.23 ±36%	1.54 ±84%	
Sm-149	1.25 ±14%	0.89 ±15%	0.87 ±14%	0.88 ±13%	1.05 ±10%	Important FP
Sm-150	0.86 ±19%	0.75 ±25%	0.77 ±21%	0.81 ±22%	0.89 ±21%	
Sm-151	**0.46 ±60%**	**0.42 ±54%**	**0.44 ±51%**	**0.50 ±53%**	**0.55 ±55%**	**Important FP, !**
Sm-152	0.80 ±25%	0.69 ±39%	0.75 ±27%	0.78 ±26%	0.92 ±37%	
Sm-154	0.77 ±27%	0.85 ±38%	0.99 ±32%	1.00 ±28%	0.84 ±46%	
Eu-151	0.84 ±14%	0.72 ±17%	0.80 ±16%	0.86 ±12%	0.81 ±17%	From Eu-nat
Eu-153	0.92 ±11%	0.94 ±16%	1.02 ±14%	0.99 ±12%	0.98 ±13%	Important FP
Gd-156	1.69 ±18%	1.89 ±28%	1.43 ±25%	0.98 ±27%	1.17 ±63%	?
Gd-157	3.19 ± 8%	1.41 ±11%	1.24 ±12%	0.99 ±14%	1.23 ±21%	?
Tb-159	0.96 ± 6%	0.92 ±13%	1.01 ± 7%	1.08 ± 8%	1.10 ±12%	
Hf	1.27 ±11%	1.00 ±18%	0.99 ±14%	0.98 ±11%	1.02 ±13%	Absorber
W	0.69 ±13%	-	0.90 ±15%	0.87 ±12%	0.80 ±24%	Absorber, ?
Pb	**1.67 ± 7%**	**1.98 ± 9%**	**1.53 ±13%**	**1.55 ± 7%**	**1.72 ± 6%**	**Small effect, !**
Th-232	**1.64 ± 7%**	-	-	**1.32 ±10%**	-	**!**
U-235	1.09 ± 6%	0.98 ± 7%	0.96 ± 6%	1.00 ± 5%	1.01 ± 5%	Standard
U-236	1.27 ±12%	-	-	0.81 ±29%	-	
U-238	0.87 ±15%	0.90 ±20%	1.11 ±22%	1.41 ±24%	x	
Pu-239	1.13 ± 8%	0.94 ± 8%	0.96 ± 7%	1.01 ± 8%	1.03 ± 7%	
Pu-240	**1.62 ±20%**	**1.65 ±45%**	**1.28 ±53%**	x	-	**Large err., ?**

Table 2 :
C/E-values of SEG-5 normalized to the C/E-value of boron-10. The capture effect is dominant. Very discrepant results are highlighted.

Sample Material	**C/E-values JNC route 70g JENDL-3.2/JNC codes**	**C/E-values Cross-wise use 70g JEF-2.2/JNC codes**	**C/E-values European scheme 33g JEF-2.2/ECCO/ERANOS**	**Error (%)**
B-10 ss	1.000	1.000	1.000	2
Ta	0.956	0.933	0.956	7
U-235	1.138	1.124	1.084	10
Mo	1.031	0.984	0.964	10
Mn	**0.658**	0.942	0.952	7
Cd	1.070	**1.214**	**1.215**	9
Nb	1.072	1.048	1.022	9
Cu	1.174	1.214	1.119	14
Zr	**1.302**	1.085	1.032	13
W	0.918	1.019	1.085	8
Fe	**1.342**	**1.232**	1.084	11
Cr	1.037	1.095	1.032	10
Ni	**1.237**	**1.185**	1.073	10
Co	1.032	1.076	0.992	10

continued

B-10 fp	1.000	1.000	1.000	2
Mo-95	**1.185**	**1.194**	**1.133**	10
Mo-97	0.980	0.994	0.954	10
Mo-98	1.035	1.039	1.061	15
Mo-100	0.996	0.923	0.888	16
Rh-103	0.899	0.914	0.901	7
Pd-105	1.117	1.077	1.064	7
Ag-109	**0.886**	0.926	0.929	8
Cs-133	0.909	0.912	0.926	13
Nd-143	0.882	0.897	0.896	9
Nd-145	1.020	1.018	1.066	9
Sm-149	1.023	**1.121**	**1.191**	9
Eu-153	1.059	1.068	1.091	10

Table 3 :
C/E-values of SEG-6/45 normalized to the C/E-value of hydrogen or carbon. The scattering effect is dominant. Very discrepant results are highlighted.

Sample Material	**C/E-values JNC route 70g JENDL-3.2/JNC codes**	**C/E-values Cross-wise 70g JEF-2.2/JNC codes**	**C/E-values European scheme 33g JEF-2.2/ECCO/ERANOS**	**Error (%)**
H	1.000	1.000	1.071	5
C	0.918	0.959	1.000	8
B-10	0.823	0.821	0.896	12
Mo	0.935	0.898	0.913	7
Fe	0.925	0.952	0.916	7
Cr	0.887	0.977	0.915	7
Ni	0.986	1.096	1.133	9
Al	1.109	1.202	1.032	8
Zr	0.918	**0.859**	**0.860**	8
Ti	0.911	0.881	0.921	8
Cd	**0.802**	1.026	1.105	7
Pb	**1.166**	0.883	0.913	12
Bi	0.911	0.986	1.016	12
Mg	1.082	1.014	1.094	13
Be	**1.186**	**1.138**	**1.323**	7
W	0.926	0.912	0.942	9
Cu	1.046	1.063	1.095	8
Au		0.919	0.963	9
Mn	0.896	1.045	1.076	8
Ta	0.874	0.834	0.895	7
V	0.934	1.034	1.016	9
Si	0.893	1.049	**1.207**	11
Nb	0.943	0.900	0.955	8
Co	1.119	**1.184**	**1.241**	8
U-235	0.898	0.907	0.978	7
U-238	0.906	0.881	0.923	12
Th-232	0.858	0.832	0.865	9

JP0150657

2.13

WHAT WE LEARN FROM THE NUCLEAR DATA IN OKLO NATURAL REACTOR

Akira Iwamoto
Dep. Materials Science, Japan Atomic Energy Research Institute
Tokai-mura, Naka-gun, Ibaraki-ken 319-1195
e-mail:iwamoto@hadron01.tokai.jaeri.go.jp

collaborators
Y. Fujii(Nihon Fukushi U.), T. Fukahori(JAERI), T. Ohnuki(JAERI), M. Nakagawa(JAERI), H. Hidaka(Hiroshima U.), Y. Ohura(Tokyo Metropolitan U.), P.Möller(LANL)

We reexamined the constraint for the time variation of the coupling constant of the fundamental interaction by studying the isotropic abundance of Sm observed at Oklo natural reactor. Using the most modern and reliable data, together with the study of the isotropic abundance of Gd, we found that the original finding of Shlyakhter is essentially correct, that is, the Oklo data provides us the most stringent limit for the time variation compared with any other methods.

1 Large Number Hypothesis of Paul Dirac

In 1938, Paul Dirac [1] discussed that gravitational and electromagnetic coupling constants G & α might *not* be constants. He suggested that they might evolve as the evolution of our universe. The underlying idea is the followings: The ratio of the gravitational and electromagnetic forces for a pair of protons are written with the electric charge e and the mass of the proton m,

$$Gm^2/e^2/4\pi\epsilon_0 =\sim 10^{-37}. \tag{1}$$

The discussion of Paul Dirac was that the appearance of such large ratio of fundamental interactions is unnatural, at least at the beginning of our universe where everything should be symmetric. If it was the case, the large ratio observed presently is caused by the change of coupling constant according to the time.

The lifetime of our universe t_0 is about $10^{10} years$, whereas the characteristic time of proton is given by $\tau_0 = \hbar/mc^2 \sim 10^{-24}$s. Thus we get a large ratio of two time scale,

$$t_0/\tau_0 \sim 3 \times 10^{41} \tag{2}$$

We can observe the similarity of factors appearing in Eqs.(1) and (2)!! It means that if the gravitational constant G changes inversely proportional to time as

$$G(t) \sim 1/t, \tag{3}$$

at time $t = \tau_0$, the ratio of gravitational and electromagnetic forces is almost unity if all other constants are real constants.

On the other hand, in modern quantum gravitational theories which unify the fundamental interactions at the Planck energy scale 10^{19} GeV, it is expected G, α and m are

t-dependent. They are related to the dynamics of scalar field, the features of it is not clarified yet.

Several experimental efforts have been done to check the constancy of G and other constants to check the hypothesis. Among them, the upper limit of the change of G obtained from Viking Project [2] is given as

$$|\dot{G}/G| \lesssim (0.2 \pm 0.4) \times 10^{-11} \mathrm{y}^{-1}. \quad (4)$$

For the time change of α, F. Dyson obtained from the ratio of long-life isotope ^{187}Re and its daughter ^{187}Os [3] as

$$|\dot{\alpha}/\alpha| \lesssim 3 \times 10^{-13} \mathrm{y}^{-1}. \quad (5)$$

From Comparison of Atomic Clocks, A. Godone et al. obtained [4]

$$\dot{\alpha}/\alpha| \lesssim 3 \times 10^{-13} \mathrm{y}^{-1}. \quad (6)$$

From the spectra of quasar (QSO), J.K. Webb et al. obtained the following results [5],

$$|\dot{\alpha}/\alpha| \lesssim 5 \times 10^{-15} \mathrm{y}^{-1}. \quad (7)$$

For strong interaction coupling constant $\alpha_s = g^2/\hbar c$, A.I. Shlyakhter used the nuclear data from Oklo natural reactor to give [6]

$$|\dot{\alpha_s}/\alpha_s| \lesssim 5 \times 10^{-19} \mathrm{y}^{-1}, \quad (8)$$

which gives apparently *far more stringent* upper limit than those obtained by other methods for the time-change of the coupling constant.

As we will see later, the change of α_s and α are interchangeable and if we assume that the strong interaction is constant, we can replace α_s in EQ(8) by α .

2 Oklo Natural Reactor

The reason why the natural reactor was possible 2 billion years ago is given by the following data. The essential fact is that the half life of ^{235}U is smaller than that of ^{238}U.

	^{235}U	^{238}U
Nat. Abund. (Present)	0.720%	99.27%
Half Life	7×10^8years	4.5×10^9years
Nat. Abund. (2×10^9 years ago)	3.7%	96.3%

Based on these facts, K. Kuroda first predicted [7] that with the presence of some amount of water, the vein of uranium could undergo a chin reaction spontaneously. In 1972, the uranium slightly depleted in ^{235}U was detected at French uranium-enrichment plant. It was traced and found out that at Oklo in Gabon Republic, uranium with ^{235}U abundance of 0.4% - 0.5% was mined. It is well proved now that in 2 billion years ago, the reactors were operating in Oklo area (Oklo, Oklobondo, Bagombe). In spite of serious efforts to find the natural reactors in other area, no evidence was found up to now.

3 Isotope Ratio of Sm and Gd in Oklo Area and the Change of Strong Interaction Constant

Four years after the discovery of Oklo, A.I.Shlyakhter published a paper [6] in which he obtained the value given in Eq.(8) from the isotope ratio of Sm isotopes in Oklo. This value is at least 3 orders of magnitude more accurate than any other modern experiments!!!

Now we will trace the method with which A.I. Shlyakhter obtained such precise result from the nuclear data of Oklo. The typical data for Sm isotopes is given by the followings:

	^{147}Sm	^{148}Sm	^{149}Sm	^{150}Sm
1st res.(eV)	3.397	140.4	0.0973	
2nd res.(eV)	18.30	288.8	0.872	
3rd res.(eV)	27.1	422.6	4.95	
half-life(yr)	1.06×10^{11}	7×10^{15}	stable	stable

Another data of our interest are

	$^{147}Sm(\%)$	$^{148}Sm(\%)$	$^{149}Sm(\%)$	$^{150}Sm(\%)$
nat. abund.	15.1	11.3	13.9	7.4
^{235}U ther. FP	1.52×10^{-12}	1.96×10^{-10}	1.11×10^{-8}	-
^{235}U cum. FP	2.25	1.13×10^{-8}	1.07	3.57×10^{-5}

The resonance parameters for the lowest resonance for ^{149}Sm + neutron system are

$$\begin{array}{ll} E_0 & 97.3 \text{ meV} \\ \Gamma_n & 0.533 \text{ meV} \\ \Gamma_\gamma & 60.5 \text{ meV} \\ \Gamma_{tot} & 60.8 \text{ meV} \\ s & 1/2\ \hbar \\ I & 7/2\ \hbar \\ J & 4\ \hbar \\ g_0 & 9/16 \end{array} \tag{9}$$

Under the neutron flux of operating Oklo reactor, the ^{149}Sm quickly tuned to ^{150}Sm by capturing neutron, but ^{148}Sm is stable. (^{147}Sm slowly turns to ^{148}Sm.) Isotope ratio of Sm are given by

$$\begin{array}{lll} (^{147}Sm + ^{148}Sm)/^{149}Sm & = (15.1 + 11.3)/13.9 & = 1.889 \quad : \textit{natural abundance} \\ & = (55.34 + 2.79)/0.5546 & = 104.81 \quad : \textit{for Oklo } SF84 - 1469 \\ & = (2.25 + 0.0)/1.07 & = 2.103 \quad : \textit{for } ^{235}U \textit{ cumulative} \\ & & \quad \textit{thermal fission products} \end{array} \tag{10}$$

A value in Oklo reactor core given in the middle line of above equation differs remarkably from the values of the top and bottom lines. This Oklo value is a typical example of the isotope composition in the reactor core. If we know the value of the neutron fluence and its spectra, we can calculate the theoretical value of the ratio given in the middle line of Eq.(10) by using the neutron capture cross section σ_{149} for ^{149}Sm. The theoretical estimation thus depends on the cross section σ_{149}. Conversely, if we use the experimental value of the middle line of Eq.(10) as a given quantity, we can estimate the cross section σ_{149} at two billion years ago. This estimated cross section is directly related to the position of the neutron capture resonance level. If this position differs from the one observed presently, we can estimate the change of the coupling constant between present one and that of two billion years ago by the consideration given in the following sections.

4 Neutron Capture Cross Section

We assume Bright-Wigner one-level formula for ^{149}Sm,

$$\sigma = \frac{g_0 \pi \hbar^2}{2mE} \frac{\Gamma_n \Gamma_\gamma}{(E - E_0)^2 + (\Gamma_n + \Gamma_\gamma)^2/4}, \tag{11}$$

where E_0 is the resonance energy. The statistical weight g_0 is written in terms of spin s of neutron, I of target and J of compound nucleus as

$$g_0 = \frac{2J+1}{(2s+1)(2I+1)}. \tag{12}$$

Γ_n is written as

$$\Gamma_n = \frac{2k}{K} v_l \frac{D}{\pi}, \tag{13}$$

where k is the wave number of neutron in the laboratory frame given by

$$k^2 = \frac{2mE}{\hbar^2}, \tag{14}$$

and K is the wave number inside the target nucleus, v_l represents centrifugal and Coulomb effects for emitted particle and D is the level spacing of the compound level. For $l = 0$ neutron, eq.(13) is reduced as,

$$\Gamma_n = \frac{2k}{K} \frac{D}{\pi}. \tag{15}$$

On the other hand, the normalized flux Φ_N for Maxwell-Boltzmann distribution is given by

$$\Phi_N = \frac{\exp(-E/T)}{T^2} E dE. \tag{16}$$

where integration with respect to E yields unity.

Thermally averaged neutron capture cross section Σ is written as

$$\Sigma \equiv \int_0^\infty dE \sigma \Phi_N, \tag{17}$$

which is expressed from eqs.(11),(15) and (16)as

$$\Sigma = \int_0^\infty dE \frac{g_0 \pi \hbar^2}{2mE} \frac{2k}{K} \frac{D}{\pi} \frac{\Gamma_\gamma}{(E - E_0)^2 + \Gamma_{tot}^2/4} \frac{\exp(-E/T)}{T^2} E, \tag{18}$$

where

$$\Gamma_{tot} = \Gamma_n + \Gamma_\gamma. \tag{19}$$

5 Relation between Isotope Ratio of Oklo and Capture Cross Section

Assuming constant neutron flux ϕ during the operation of Oklo reactor (we can generalize this assumption easily to the time-dependent flux, but for simplicity we use this assumption. The calculated results are independent of this assumption),

$$N_{235} = N_{235}^0 e^{-\sigma_a \phi t}, \tag{20}$$

where N_{235} is the number of Uranium at time t, N^0_{235} is its value at time t=0 (the starting time of the operation of Oklo reactor) and σ_a is the thermally averaged total neutron capture cross section of ^{235}U, somewhat different from the thermally averaged neutron capture fission cross section σ_f. The difference comes from the effect of restitution, that is, some portion of the neutron captured by ^{238}U produces ^{235}U by double beta decay followed by alpha decay. Here we assumed that

$$\sigma_f \phi \gg \lambda_{235}, \tag{21}$$

where λ_{235} is the spontaneous fission decay constant of ^{235}U. We define the number of ^{147}Sm, ^{148}Sm and ^{149}Sm by N_{147}, N_{148} and N_{149}. ^{147}Sm slowly absorbs neutron and turns to ^{148}Sm but ^{148}Sm does not absorb neutron.

The equations for N_{149}, N_{147} and N_{148} are written as

$$\begin{cases} \frac{dN_{149}}{dt} = -\sigma_{149}\phi N_{149} + N^0_{235}\exp(-\sigma_a\phi t)\sigma_f\phi Y_{149} \\ \frac{dN_{147}}{dt} = -\sigma_{147}\phi N_{147} + N^0_{235}\exp(-\sigma_a\phi t)\sigma_f\phi Y_{147} \\ \frac{dN_{148}}{dt} = +\sigma_{147}\phi N_{147} + N^0_{235}\exp(-\sigma_a\phi t)\sigma_f\phi Y_{148} \end{cases} \tag{22}$$

where Y_{149}, Y_{147} and Y_{148} are the fission yield of ^{149}Sm, ^{147}Sm and ^{148}Sm. The quantity σ_{149} stands for the thermally averaged neutron capture cross section of ^{149}Sm, which form is given by Eq.(18) and σ_{147} stands for the thermally averagedneutron capture cross section of ^{147}Sm, which form is completely different from Eq.(18) because this nucleus has no low lying resonance level.

To solve Eq.(22) for N_{149}, N_{147} and N_{148}, we need to know the fluence ϕ, the cross section σ_a and temperature of neutron flux. These quantities are obtained from the Oklo data for each reactor core as explained in [8]. Using these quantities, we can calculate the ratio between ^{149}Sm and (^{147}Sm + ^{148}Sm). By comparing this calculated value with the observed value of each Oklo reactor core, we deduce the value of σ_{149} at two billion years ago. What we need finally is to compare this value with the present data. A possible difference of this cross section at two billion years ago and the one at present tells us a possible change of the resonance position which is located at 97.3meV presently as is shown in Eq(9).

6 Change of Fundamental Constant from Oklo Data

We reexamined the Shlyakhter's effort to constrain the time variability of the coupling constants of the fundamental interaction by studying the anomalous isotope ratio in Oklo natural reactor. What's new in our approach are the use of newly obtained data, which are relatively free from contamination, careful treatment of the temperature effect, use of Gd data to confirm the conclusion, and generalized equations which include the effect of flow-in and others. As target reactor cores, we chose 5 samples from two reactor zones [9]. These are newly obtained data taken from deep underground. This new data are thought to be less contaminated than those obtained previously.

According to the method given in the previous sections, we can calculate the possible shift of the neutron capture resonance level. From the detailed analysis [8], we obtained the following value from the analysis of Sm isotopes,

$$\Delta E_0 = 9 \pm 11 meV, \tag{23}$$

where ΔE_0 stands for the shift of the lowest resonance energy of ^{149}Sm. To obtained this value, we took the most reliable estimate of the neutron temperature of T=200-400 C. We

performed the same kind of analysis for the Gd isotope data for the same samples. In case of Gd, the results are very sensitive to the small contamination which is caused by the flow-in. Detailed analysis, however, tells us that the resonance sift of Eq.(23) is consistent with the Gd data [8].

Next, we need to relate this resonance shift to the possible change of the fundamental constant. For this, we assumed the relation

$$\Delta E_0/M = \Delta\alpha_s/\alpha_s \tag{24}$$

where M stands for the mass scale corresponding to the resonance level. For the choice of this mass scale, Schlyakhter chose [6] the depth of the nuclear one-body potential of about 50 MeV. Damor and Dyson [10] chose it as about 1MeV from the consideration of the isotope shift data. If we choose it as 50MeV, we obtain

$$|\dot{\alpha_s}/\alpha_s| \lesssim 2 \times 10^{-19}\mathrm{y}^{-1}, \tag{25}$$

and if we choose it as 1MeV, we obtain

$$|\dot{\alpha_s}/\alpha_s| \lesssim 1 \times 10^{-17}\mathrm{y}^{-1}. \tag{26}$$

We see that the original conclusion of Shlyakhter [6] is essentially the same as our result Eq.(25). Such a good coincidence shouldn't be taken so seriously because the original Shlyakhter's analysis is much simpler than ours and the original Oklo data he used is cited nowhere, which is definitely not so good as ours. Nevertheless, the essential finding of Shlyakhter that the Oklo data tells us the most stringent upper limit of the time variation of the fundamental interactions was correct. We like to add finally that the time variation of the electromagnetic coupling constant, if we assume that the strong interaction coupling constant is fixed, has the same values as are given by Eq.(25) and Eq.(26).

References

[1] P. Dirac, Proc. Roy. Soc. **A165** (1938) 199.

[2] R.W. Hellings et al., Phys.Rev.Lett. **51** (1983) 1609.

[3] F. Dyson, Phys. Rev. Lett. **19** (1967) 1291.

[4] A. Godone et al., Phys. Rev. Lett. **71** (1993) 2364.

[5] J.K. Webb el al., Phys.Rev.Lett. **82** (1999) 884.

[6] A.I. Shlyakhter, Nature **264** (1976) 340.

[7] K. Kroda, J.Chem.Phys. **25** (1956) 781.

[8] Y. Fujii et al., Nucl.Phys. **B573** (2000) 377.

[9] H. Hidaka and P. Holliger, Geochim.Cosmochim.Acta **62** (1998) 89.

[10] T. Damour and F. Dyson, Nucl.Phys. **B480** (1996) 37.

JP0150658

2.14

Reaction Cross-Sections and Nuclear Radii in the Quantum Molecular Dynamical Approach

Tomoyuki Maruyama
College of Bioresource Sciences, Nihon University

Abstract

We make a new formulation of the QMD approach, which can give correct mean-square radii for initial nuclei. Then the reaction cross-sections are calculated with various energy region. We succeed to reproduce experimental data even below 100 MeV/u nicely.

The measurament of the innteraction cross-section (σ_I) at relativistic energy must be a good tool to to determine radii of anormalous nuclei as well as normal nuclei. By combining this measurament with the Glauber calculation, furthermore, we will get information of density-distribution of anormalous nuclei, such as halo and skin structures. This method is, however, satisfied only for collisions above several hundred MeV/u, where the elementary NN cross-section does not have strong energy-dependence, and the trajectory of a projectile nucleus is well approximate to be straight.

On the other hand we need to make theoretical analysis of experimental results with the beam energy below 100 MeV/u, where a lot of data is available from RIKEN. In this calculation we must consider effects of energy-dependence of the NN cross-section and curved trajectory of initial nuclei in reaction around 50-100 MeV/u energy region.

Recently we developed a framework of QMD [1] plus statistical decay model (SDM) [2], and applied systematically this QMD + SDM to nucleon- (N-) induced reactions. It was shown [2] that this framework could reproduce quite well the measured double-differential cross-sections of (N,xN') type reactions from 100 MeV to 3 GeV incident energies in a systematic way. In the subsequent papers [3, 4], we gave detailed analysis of the pre-equilibrium (p,xp') and (p,xn) reactions in terms of the QMD in the energy region of 100 to 200 MeV. In these analysis, a single set of parameters was used, and no readjustment was attempted.

In this work we make initial nulcei with correct root-mean-square radii while one has not carefully treated them, and examine reaction cross-sections with the QMD approach in several kinds of energy region.

Now we briefly explain our formulation.

In the QMD, each nucleon state is represented by a Gaussian wave-function of width L,

$$\phi_i(\mathbf{r}) = \frac{1}{(2\pi L)^{3/4}} \exp\left[-\frac{(\mathbf{r}-\mathbf{R}_i)^2}{4L} + \frac{i}{\hbar}\mathbf{r}\cdot\mathbf{P}_i\right], \tag{1}$$

where $\mathbf{R}_i$ and $\mathbf{P}_i$ are the centers of position and momentum of i-th nucleon, respectively. The total wave-function is assumed to be a direct product of these wave-functions. Thus the

one-body distribution function is obtained by the Wigner transform of the wave-function,

$$f(\mathbf{r},\mathbf{p}) = \sum_i f_i(\mathbf{r},\mathbf{p}), \tag{2}$$

$$f_i(\mathbf{r},\mathbf{p}) = 8 \cdot \exp\left[-\frac{(\mathbf{r}-\mathbf{R}_i)^2}{2L} - \frac{2L(\mathbf{p}-\mathbf{P}_i)^2}{\hbar^2}\right]. \tag{3}$$

The equation of motion of $\mathbf{R}_i$ and $\mathbf{P}_i$ is given by the Newtonian equation

$$\dot{\mathbf{R}}_i = \frac{\partial H_{QMD}}{\partial \mathbf{P}_i}, \quad \dot{\mathbf{P}}_i = -\frac{\partial H_{QMD}}{\partial \mathbf{R}_i}, \tag{4}$$

and the stochastic N-N collision term. Hamiltonian H consists of the kinetic energy and the energy of the two-body effective interaction.

The Hamiltonian is separated into several parts as follows.

$$H_{QMD} = T + V_{\rm Pauli} + V_{\rm local} + V_{\rm MD} + V_{\rm Coulomb} \tag{5}$$

where T, $V_{\rm Pauli}$, $V_{\rm local}$ and $V_{\rm MD}$ are the kinetic energy, the Pauli potential, the local (momentum-independent) potential and the momentum-dependent potential parts, respectively.

The Pauli potential [5, 6, 7, 8] is introduced for the sake of simulating the Fermionic property in a semiclassical way. This phenomenological potential prohibits nucleons of the same spin σ and isospin τ from coming close to each other in the phase space. Here we employ the Gaussian form of the Pauli potential [6] as

$$V_{\rm Pauli} = \frac{1}{2} C_{\rm P} \left(\frac{\hbar}{q_0 p_0}\right)^3 \sum_{i,j(\neq i)} \exp\left[-\frac{(\mathbf{R}_i-\mathbf{R}_j)^2}{2q_0^2} - \frac{(\mathbf{P}_i-\mathbf{P}_j)^2}{2p_0^2}\right] \delta_{\tau_i\tau_j}\delta_{\sigma_i\sigma_j}\,. \tag{6}$$

For the convenience of the explanation we separate the local potential part into the Coulomb force, the Skyrme type force with the symmetry terms and the Gaussian force.

$$V_{\rm local} \;=\; V_{\rm Sky} + V_{\rm Sym} + V_{\rm G} \tag{7}$$

The $V_{\rm Sky}$ and the $V_{\rm Sym}$ describe the zero range nuclear force whose detailed form is given as

$$\begin{aligned} V_{\rm Sky} &= \frac{\alpha}{2\rho_0}\sum_i <\rho_i> + \frac{\beta}{(1+\tau)\,\rho_0^\tau}\sum_i <\rho_i>^\tau \\ V_{\rm Sym} &= \frac{C_s}{2\rho_0}\sum_{i,j(\neq i)} (1-2|c_i-c_j|)\,\rho_{ij} \end{aligned} \tag{8}$$

with

$$\begin{aligned} <\rho_i> &\equiv \sum_{j\neq i}\rho_{ij} \equiv \sum_{j\neq i}\int d^3r\;\rho_i(\mathbf{r})\,\rho_j(\mathbf{r}) \\ &= \sum_{j\neq i}(4\pi L)^{-3/2}\exp\left[-(\mathbf{R}_i-\mathbf{R}_j)^2/4L\right], \end{aligned} \tag{9}$$

To describe the finie range nuclear interaction the Yukawa force is often used, but it consumes a rather long CPU time. Instead of that we take the Gaussian force $V_{\rm G}$ as

$$V_{\rm G} \;=\; \frac{\alpha_G}{2\rho_0}\sum_i <g_i> \tag{10}$$

Table 1: Effective interaction parameter set

α (MeV)	-1.00
β (MeV)	188.42.
τ	1.33333
α_G (MeV)	-107.52
C_s (MeV)	-258.54
$C_{\rm ex}^{(1)}$ (MeV)	-258.54
$C_{\rm ex}^{(2)}$ (MeV)	375.6
μ_1 (MeV)	2.35
μ_2 (MeV)	0.4
L (fm^2)	1.2
L_g (fm^2)	2.0
q_0 (fm)	2.0
p_0 (MeV)	100.0
C_p (MeV)	53.5

with

$$\begin{aligned} < g_i > &\equiv \sum_{j\neq i} g_{ij} \equiv \sum_{j\neq i} \int d^3r d^3r' \, \rho_i(\mathbf{r}) \, (4\pi\gamma_g)^{-3/2} \exp\left[-(\mathbf{r}-\mathbf{r}')^2/4\gamma_g\right] \rho_j(\mathbf{r}') \\ &= \sum_{j\neq i} (4\pi L_g)^{-3/2} \exp\left[-(\mathbf{R}_i - \mathbf{R}_j)^2/4L_g\right], \end{aligned} \tag{11}$$

where

$$L_g = 2L + \gamma_g \tag{12}$$

The momentum-dependent term is introduced as a Fock term of the Yukawa-type interaction. We divide this interaction into two ranges so as to fit the effective mass and the energy dependence of the real part of the optical potential [11]:

$$\begin{aligned} V_{\rm MD} &= V_{\rm MD}^{(1)} + V_{\rm MD}^{(2)} \\ &= \frac{C_{\rm ex}^{(1)}}{2\rho_0} \sum_{i,j(\neq i)} \frac{1}{1+\left[\frac{\mathbf{P}_i-\mathbf{P}_j}{\mu_1}\right]^2} \rho_{ij} + \frac{C_{\rm ex}^{(2)}}{2\rho_0} \sum_{i,j(\neq i)} \frac{1}{1+\left[\frac{\mathbf{P}_i-\mathbf{P}_j}{\mu_2}\right]^2} \rho_{ij} \, . \end{aligned} \tag{13}$$

In the above expression we have forteen parameters $V_p, q_0, P_0, \alpha, \beta, \tau, \alpha_g, C_s, V_{MD}^{(1)}, V_{MD}^{(2)}, \Lambda_1, \Lambda_2$ and the Gaussian width L and L_g. We parametrzie their values to reproduce properties of the ground state and the energy-dependence of the empirical proton-nucleus optical potential; in Table 1 we give a parameter-set

In our method we do not define the ground state of nuclei as a energy minimum state of the system, while in a usual method they get the initial distribution by searching the energy minimum state with the frictional cooling method [5]. The other parameters are determined to reproduce properties of finite nuclei as follows. To get the initial nuclear distribution we first distribute the particles randomly in phase space and cool down the system according to the damping equation of motion until the energy reaches the experimental value. Then we

examine its stability by evaluating equations of motion for initial nucleons until 500 fm/c. We determine the parameters of the mean-fields to root-mean-square radii of various nuclei, which are calculated by averaging events and several time steps, when the binding energies agree with the experimental value. Here the Pauli potential is determined to give a averaged kinetic energy 25 MeV for ^{40}Ca.

Fig. 1 shows calculation results of time-averaging root-mean-square radii of several nuclei, whose binding energies are given as experimental data.

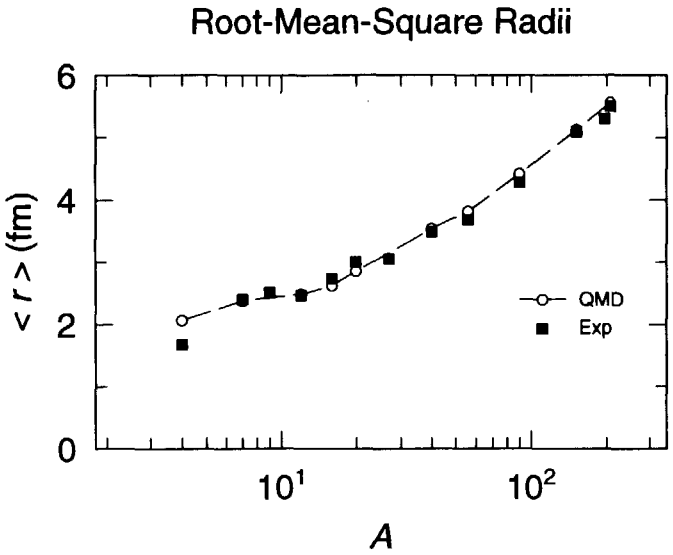

Fig. 1: Time averaging root-mean-square radius of ground state nuclei. Open circles show the results of QMD and the full squares indicate expermental results.

In Fig. 2 we show the time-dependence of the root-mean-square radii in one event. We can see that the fluctuation is not so large in the time evolution.

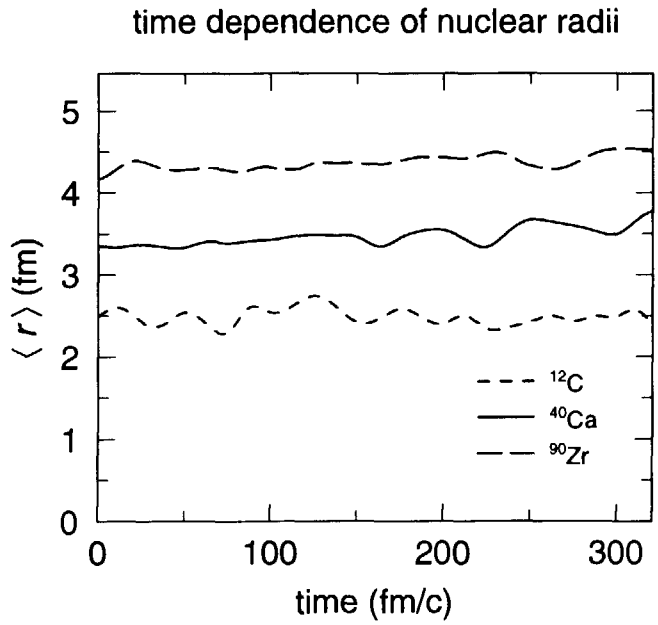

Fig. 2: Time dependence of root-mean-square radii of ^{12}C (dashed line), ^{40}Ca (solid line), ^{92}Zr (solid line).

As a next step we calculate energy-dependence of reaction cross-sections in the QMD approach. We define a reaction event where one NN collision occures, and evaluate the reaction cross-section by summing reaction probabilities for all impact-parameters.

For the collision judgment including the Gaussian width we use the possibility given by the following equation

$$\frac{1}{(2\pi L)^3}\int d^3x d^3y \theta\{b_{coll} - |\mathbf{x}_T - \mathbf{y}_T|\} \exp\left[-\frac{(\mathbf{x}-\mathbf{R}_i)^2 + (\mathbf{y}-\mathbf{R}_j)^2}{2L}\right], \tag{14}$$

where θ is the step function, and b_{coll} is given from the total NN cross-section as

$$\sigma_T = \pi b_{coll}^2 \tag{15}$$

with the NN collision cross-section σ_T experimentally observed.

In Fig. 3 we draw target-mass-number dependence of reaction cross-sections for the carbon beam at 83 MeV/u and 300 MeV/u. We can see that the QMD approach nicely reproduce exerimental results [9] even below 100 MeV/u. Then we can conclude that our approach is effective for the present purpose.

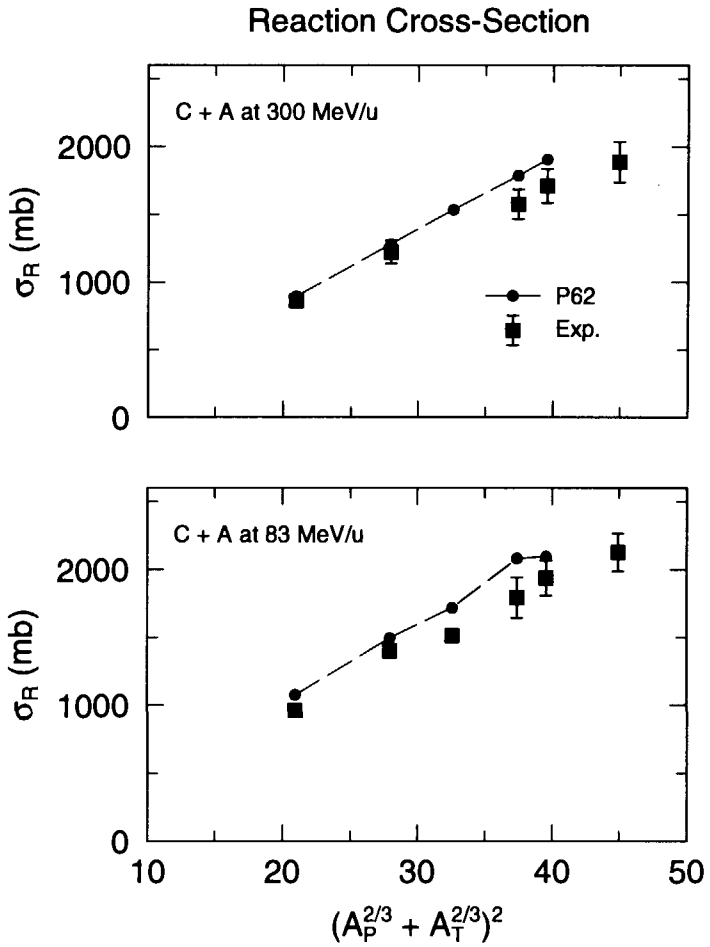

Fig. 3: Target-mass dependence of the reaction cross-sections of collisions with the carbon beam at the incident energies 300 MeV/u (upper column) and 83 MeV/u (lower column). Experimental data (squares) are taken from Ref. [9].

In summary we make a new QMD formulation to give correct root-mean-square radii

for stable nuclei, anc calculate the reaction cross-sections in several energy region. We well succeed to reproduce experimental data up to about 80 MeV. Now we are testing reactions with isotope beams. After that we will extend this approach to control initial distribution and to determine the radii of exotic nuclei.

References

[1] J. Aichelin, Phys. Rep. **202**, 233 (1991), and references therein.

[2] K. Niita, S. Chiba, T. Maruyama, T. Maruyama, H. Takada, T. Fukahori, Y. Nakahara and A. Iwamoto, Phys. Rev. C**52**, 2620 (1995).

[3] M. B. Chadwick, S. Chiba, K. Niita, T. Maruyama and A. Iwamoto, Phys. Rev. C **52**, 2800 (1995); S. Chiba, M. B. Chadwick, K. Niita, T. Maruyama and A. Iwamoto, Phys. Rev. C **53**, 1824 (1996); S. Chiba, O. Iwamoto, T. Fukahori, K. Niita, T. Maruyama, T. Maruyama and A. Iwamoto, Phys. Rev. C **54**, 285 (1996).

[4] S. Chiba, M.B. Chadwick, K.Niita, T. Maruyama, T. Maruyama and A. Iwamoto, Phys. Rev. C **53**, 1824 (1996).

[5] T. Maruyama, K Niita, K. Oyamatsu, T. Maruyama, S. Chiba, A. Iwamoto, Phys. Rev. **C57** 655.

[6] G. Peilert, J. Konopka, H. Stöker, W. Greiner, M. Blann and M. G. Mustafa, Phys. Rev. C **46** (1992) 1457.

[7] D. H. Boal and J. N. Glosli, Phys. Rev. C **38** (1988) 1870.

[8] A. Ohnishi, T. Maruyama and H. Horiuchi, Prog. Theor. Phys. **87** (1992) 417.

[9] S. Kox, et al.: Phys. ReV. C**35**, 1678 (1987).

[10] D. G. Ravenhall, C. J. Pethick and J. R. Wilson, Phys. Rev. Lett. **27** (1983) 2066.

[11] S. Hama, B. C. Clark, E. D. Cooper, H. S. Scherif and R. L. Mercer, Phys. Rev. C **41** (1990) 2737.

JP0150659

2.15

Data for Radiation Protection and Nuclear Data

Yasuhiro YAMAGUCHI, Akira ENDO
and Yukio SAKAMOTO
Department of Health Physics, Japan Atomic Energy Research Institute
Tokai-mura, Naka-gun, Ibaraki-ken 319-1195
e-mail: yasu@frs.tokai.jaeri.go.jp

Various conversion coefficients have been used in external and internal dosimetry in radiation protection practices. Radiation doses in the human body cannot be directly measured in general situation and the conversion coefficient has been used to correlate the human body dose with physical quantities such as radioactivity, particle fluence and other dosimetric quantities to be used to describe the radiation field. Fluence-to-organ dose conversion coefficients have been calculated using Monte Carlo radiation transport codes in conjunction with an anthropomorphic mathematical phantom. Neutron and photon interaction cross-section libraries are indispensable for these calculations. ICRP Publication 74 gives tables of conversion coefficients for estimation of organ doses and effective dose for photons, neutrons and electrons. Based on these results, shielding calculation parameters have been prepared for simple and easy dose estimation in radiation facilities. Dose factors, organ doses and effective dose per unit intake of radionuclide, have been also calculated for internal dosimetry purpose. ICRP Publications 68 and 72 give tables of dose factors for a variety of radionuclides. Revision of radiation data library has been made to reflect updated information on radionuclides to internal dosimetry.

1. Introduction

The Medical Use Group on Atomic, Molecular and Nuclear Data, one of standing groups of the Japanese Nuclear Data Committee, has been studying various data necessary for medical diagnosis and treatment, and radiation protection. The Group's mission is to investigate needs coming from doctors, medical physicists and health physicists, and to convey them to developers and editors of nuclear data. The present paper describes one of the Group's activities focusing on radiation protection aspect of nuclear data.

2. Radiation Exposure and Dose Assessment

The dose assessment is one of the most important practices of radiation protection in reactor, accelerator and radionuclide-handling facilities. Radiation exposures are caused by radiations coming from the outside of the body and radiations originated from radionuclides taken into the body. Since it is practically impossible to measure directly the doses to the human body, the doses should be assessed using measurable quantities such as radioactivity taken into the body and radiation fluence incident on the body. Dose conversion coefficients play a very important role to transform these measurable quantities to a human dose, not measurable quantity. The conversion coefficients are usually estimated by numerical simulation using a radiation transport program and a mathematical human model. In the transport simulation, nuclear data such as interaction cross-section should be provided.

A set of dosimetric quantities used in radiation protection is defined by the International Commission on Radiological Protection (ICRP) in its Publication 60[1]. One of two basic quantities representing the human tissue or organ dose due to radiation R is the equivalent dose H_T, the absorbed dose $D_{T,R}$ multiplied by the radiation weighting factor w_R given by ICRP. The other is the effective dose E, a summation of the equivalent doses in tissues or organs, each multiplied by the relevant tissue weighting factor w_T given by ICRP and it is given by the expression

$$E = \sum_T w_T \cdot H_T = \sum_T w_T \sum_R w_R \cdot D_{T,R}$$

In the case of exposure from in-body radionuclide, the entire dose is not given at the moment of the intake, but the exposure extends over a certain period undergoing decay and removal of the radionuclide. For this case, the committed effective dose $E(\tau)$ is used, which is the effective dose accumulated over a period τ, where 50 and 70 years are recommended for adult and children, respectively. The conversion coefficients are therefore prepared for estimating these quantities.

3. Calculation of Dose Conversion Coefficients

Conversion coefficients correlating the fluence of incident radiation with the equivalent dose or effective dose are generally used in external dose assessment. These coefficients are calculated using a Monte Carlo radiation transport program in conjunction with a mathematical human model. The anthropomorphic mathematical phantom shown in Fig. 1 is widely used in such calculations, which is described with a variety of geometrical formulas. Various codes have been applied to calculate radiation transport from a source to organs or tissues in the body. Well-used codes are MCNP[2] for neutron and photon, and EGS4[3] for electron and photon. Some other codes used in radiation shielding are also applicable to such dose calculation. Nuclear data are indispensable in these calculations: neutron and photon interaction cross-section data and kerma factor or stopping power for charged particles. Since the issue of ICRP 1990 Recommendations[1], dose conversion coefficients for a variety of radiations were calculated by many groups in the world and compiled in ICRP Publication 74[4] and ICRU Report 57[5] for photons, neutrons and electrons of conventional energies. Dose conversion coefficients for these radiations of higher energies and other types of radiation have been calculated and discussed[6] after the issue of above-mentioned reports.

For internal dose assessment, data of dose factors are prepared, which represent the equivalent dose in organ and effective dose per unit intake of radionuclide. When calculation the dose factor, distribution of radionuclides in the body after the intake should be calculated using a biokinetic model for metabolism at the first step of calculation. Then the radiation energy transfer from source organ to target organ is calculated by Monte Carlo radiation transport and mathematical phantom in the same way of external dose calculation. Less penetrating radiations such as α particle and low energy β particle are treated as such they deposit their whole energy at the source organ as an approximation. In this calculation, radiation data file has a quite important role. It describes the type, energy, intensity per disintegration, and other important data. ICRP Publication 38[7] including data for 830 radionuclides has been widely used in the calculation, but it should be updated because it is based on an old database, 1970s ENSDF. For this reason, revising work of this radiation data library has being made by JAERI[8] to adopt new version of ENSDF[9]. ICRP Publications 68[10] and 72[11] give tables of dose factors for a variety of radionuclides. For the practical use, maximum permissible limits are more convenient, which represent activity

concentration giving 50mSv per year in the exhaust or drainage.

4. Current Topics

Regulation laws regarding radiation protection are going to be amended in April 2001 to adopt ICRP 1990 Recommendations, which include revisions of dose limit, dose quantities, etc. Necessary data were prepared prior to the enforcement of the new regulation laws. In radiation shielding calculation for reactor, accelerator and radionuclide-handling facilities, the effective dose in Anterior-posterior (AP) irradiation geometry, instead of the ambient dose equivalent $H^*(10)$, shall be estimated at the boundary of controlled area. Database of effective dose attenuation factors were developed for various RI γ-ray, neutron and β-ray sources and for six different shielding materials[12]. In this work, radiation transmission calculations were performed using JENDL-3.2[13].

A criticality accident happened on September 30,1999 at the uranium fuel processing plant in Tokai, Japan. Three workers were exposed to intense neutrons and γ-rays on the spot and two of the three died. A computer simulation has been performed to estimate detailed dose distribution in the body due to neutrons γ-rays from fission reaction[14]. In this simulation, Monte Carlo transport calculation code MCNP was used together with a special mathematical phantom that enables to simulate any working postures as shown in Fig. 2. Neutron cross-section library JENDL-3.2 was used in this calculation. The result is going to be published elsewhere in the near future.

5. Conclusion

Radiation dose to human body cannot be directly measured. Dose conversion coefficients play a very important role to transform measurable quantities such as particle fluence and radioactivity to the human dose. Various nuclear data have been used in the calculation of these conversion coefficients. In this context, we can say that nuclear data are supporting the radiation safety in the recent society.

References

1) ICRP: ICRP Publication 60 (1991).
2) Briesmeister, J.F.(Ed.): "A General Monte Carlo N-Particle Transport Code, version 4B -Manual", LA-12625-M (1997).
3) Nelson, W.R., Hirayama, H. and Rogers, D.W.O.: "The EGS4 code-system", SLAC-235 (1985).
4) ICRP: ICRP Publication 74 (1996).
5) ICRU: ICRU Report 57 (1998).
6) Yoshizawa, N., Sakamoto, Y., Iwai, S. and Hirayama, H.: "Benchmark Calculation with Simple Phantom for Neutron Dosimetry", Proc. SATIF-5, Paris, July17-21, 2000.
7) ICRP: ICRP Publication 38 (1983)
8) Endo, A. and Yamaguchi, Y.: "Compilation of Nuclear Decay Data Used for Dose Calculation: Revised Data for Radionuclides Listed in ICRP Publication 38", JAERI-Data/Code (to be published).
9) Tuli, J.K.: "Evaluated Nuclear Structure Data File: A Manual for Preparing of Data Sets", BNL-NCS-51655-Rev.87 (1987).
10) ICRP: ICRP Publication 68 (1994).
11) ICRP: ICRP Publication 72 (1996).
12) Sakamoto, Y., Endo, A., Tsuda. S., Takahashi, F. and Yamaguchi, Y.: "Shielding

Calculation Constants for Use in Effective Dose Evaluation for Photons, Neutrons and Bremsstrahlung from Beta-ray", JAERI-Data/Code 2000-044 (2000).
13) Nakagawa, T. et al.: "Japanese Evaluated Nuclear Data Library Version 3 Revision-2: JENDL-3.2", J. Cucl. Sci. Tech, 32[12], 1259-1271 (1995).
14) Endo, A., Yamaguchi, Y., Sato, O. and Ishigure, N.: "Analysis of Dose Distribution of Victims Using Mathematical Phantoms and Computer Simulation Technique", Proc. 28th NIRS Seminar on Environmental Research, Chiba, December 7-8, 2000 (in preparation).

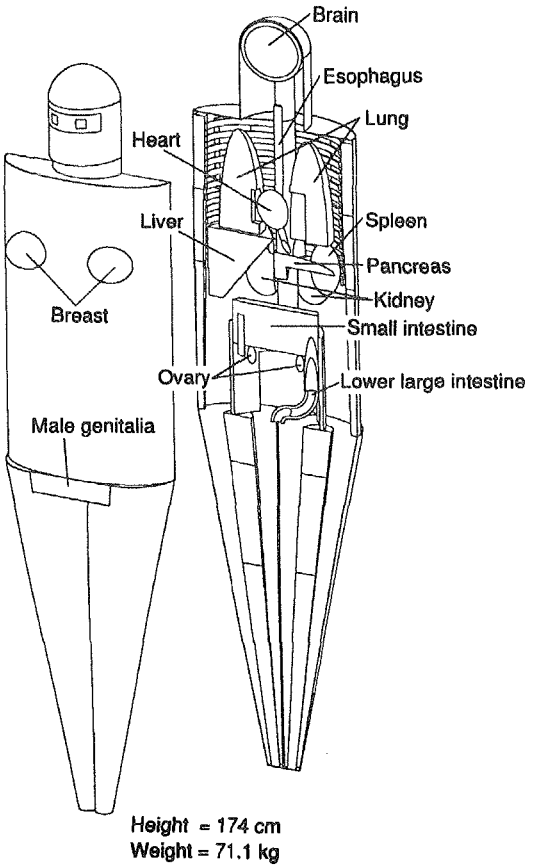

Fig. 1 Anthropomorphic mathematical phantom used in dose calculation

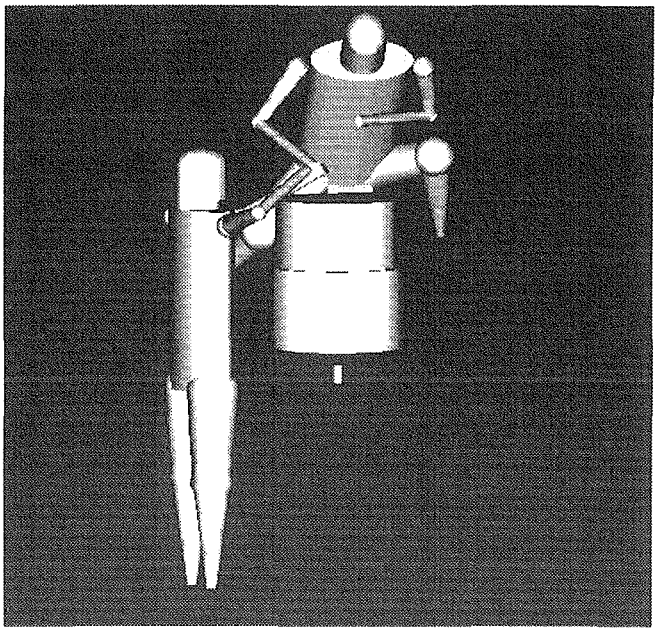

Fig.2 Simulation model to calculate detailed dose to two workers in the criticality accident

JP0150660

2.16
Present Status of JENDL High-Energy File

Yukinobu Watanabe
Department of Advanced Energy Engineering Science, Kyushu University, Kasuga, Fukuoka 816-8580, Japan,
Email: watanabe@aees.kyushu-u.ac.jp
and
JNDC High Energy Nuclear Data Evaluation Working Group

The high energy nuclear data evaluation working group in the Japanese Nuclear Data Committee has a mission to evaluate neutron and proton nuclear data for energies ranging from 20 MeV to 3 GeV, and to compile the evaluated data as JENDL high-energy file. The present status of this activity is reported.

1. Introduction

In recent years, high-energy nuclear data are required for various applications of accelerators, such as accelerator-driven transmutation system and advanced cancer therapy with particle beams, and space development [1]. Proton data as well as neutron data are necessary in these high-energy applications. It should be noted that "high-energy" stands for incident nucleon energies above 20 MeV that corresponds to the upper limit of existing data files for fission and fusion reactors. Major nuclear data required in high-energy files are as follows: cross sections relevant to particle transport calculations, such as total cross sections, elastic scattering cross sections, and double-differential particle production cross sections, isotope production cross sections for dosimetry and activation, and gas production cross sections for material damage evaluation. Nuclear data evaluation is generally carried out on the basis of experimental data and theoretical model calculations. However, the experimental data are sparse for neutron-induced reactions in the high-energy region and systematic measurements are not necessarily enough for proton data. Therefore, theoretical model calculations play a major role in the high-energy nuclear data evaluation.

Under these circumstances, the Japanese Nuclear Data Committee (JNDC) continues some activities concerning neutron and proton nuclear data evaluation for energies ranging from 20 MeV to 3 GeV towards completion of JENDL high-energy file [2]. The present status is reported below.

2. High-energy nuclear reactions

Some features of high-energy nuclear reactions are summarized in Fig. 1. First, dynamical processes, such as preequilibrium process and multi-fragmentation process, become dominant. Particle emission via such processes shows forward-peaked angular distribution in the center of mass system. Second, reaction products over a wide range of mass and atomic numbers are generated via high-energy nuclear reactions with high multiplicity of light charged particles and neutrons as shown in the right panel of Fig.1. Third, the degree of freedom of pions and excited nucleons, such as Δ and N^*, becomes important as the incident energy increases. Therefore, it is also necessary to take into account such hadrons by regarding a nucleus as hadron many-body system beyond a picture of nucleon many-body.

High-energy nuclear data evaluation needs reliable theoretical models that can account for these features well over the wide incident energy range: statistical multistep models for preequilibrium process, simulation methods using molecular dynamics for hadronic reactions followed by multi-fragmentation, and so on.

3. JENDL High-Energy File

3.1 Outline

Nuclides to be evaluated are summarized in Table 1. They are categorized into three parts in accordance with users' priority. The upper limit of incident energy is 3 GeV. The following cross sections are evaluated on the basis of experimental data and theoretical model calculations: total cross sections, elastic scattering cross sections and their angular distributions, particle production cross sections and double-differential cross sections, and isotope production cross sections. These cross section data are stored in the JENDL high-energy file in the ENDF-6 format.

3.2 Evaluation method

A theoretical model calculation system for JENDL high-energy evaluation is illustrated in Fig.2. Different theoretical models are used in accordance with incident energies: (I) intermediate energies ranging from 20 MeV to 250 MeV and (II) high energies above 150 MeV. A major code used in (I) is the GNASH code [3] based on statistical Hauser-Feshbach plus preequilibrium models. The other code, such as EXIFON [4], is partially used for evaluation of light nuclei, such as N and O. The ECIS code [5] or the OPTMAN code[6] is used for optical model calculations. It should be noted that the ECIS plus GNASH code system is basically same as that used in LA150 evaluation [7]. In (II), the code JQMD[8] based on Quantum Molecular Dynamics (QMD) plus statistical decay model is employed. Also, the code TOTELA [9] based on systematics is employed as a tool for evaluation of total, elastic, and proton reaction cross-sections in (II). Both calculation results for (I) and (II) are combined in the overlapping energy region between 150 and 250 MeV. Isotope production cross sections are evaluated using the GMA code[10] based on the generalized least-squares method or empirical fits in cases where there are a lot of available experimental data.

3.3 Results

Some results of evaluations of ^{12}C and $^{63,65}Cu$ are shown below in comparisons with experimental data and the other evaluated high-energy file. Other results for several nuclides have also been reported elsewhere, *e.g.*, ^{27}Al [11], ^{28}Si [12], W-isotopes[13], and ^{56}Fe [14].

Figure 3 presents comparisons of experimental and calculated angular distributions for elastically scattered nucleons from ^{12}C. The calculation was carried out using the OPTMAN code based on the coupled-channels method with the nuclear Hamiltonian parameters determined by the soft-rotator model [15]. Both experimental data for neutron and proton are reproduced well by the CC calculation. Thus, these calculated results were adopted as evaluated values of total cross sections, elastic and inelastic scattering cross sections, and total reaction cross sections up to 150 MeV. Transmission coefficients obtained by the CC calculation were used in GNASH calculations of particle and gamma-ray emission cross sections and isotope production cross sections up to 150 MeV. Two examples of evaluated production cross sections are shown with experimental data and LA150 evaluation[7] in Fig. 4. For energies above 150 MeV, the QMD+SDM calculation was used. Double-differential cross sections calculated with the Kalbach systematics[16] are compared with measured ones for the ^{12}C (p,xp) reaction at 90 MeV, showing overall good agreement with measured data.

For $^{63,65}Cu$, the ECIS code was employed for analyses of total cross sections and elastic scattering cross sections, and spherical optical potential parameters were adjusted for neutron and proton up to 250 MeV. Calculated angular distributions of nucleon elastic scattering from ^{63}Cu are compared with experimental ones in Fig. 5. Evaluated total cross sections are plotted

together with experimental data and JENDL-3.3 evaluation less than 20 MeV in Fig.7. Niita's systematics [17] was used for energies above 250 MeV. The evaluated cross section shows excellent agreement with the experimental data in the energy range between 20 MeV and 3 GeV. Isotope production cross sections were evaluated with the GMA code[10] based on experimental data of each isotope and natural Cu. In the case of sparse measurement, theoretical calculations with GNASH and QMD were mainly adopted. Those results are shown in Figs. 8 to 10.

4. Summary and future plan

The present status of JENDL high-energy file was reported. The evaluations of cross sections for nuclides with the 1st priority have almost been completed and the compilation work is now in progress. For nuclides with the 2nd and 3rd priorities, evaluations and their compilation are intensively in progress. Review and benchmark test should be performed for the data file of the nuclides that have already been evaluated. Results of the related benchmark test for iron are reported elsewhere [14]. Finally, it is planned to release the 1st version of JENDL high-energy file in March 2001.

Acknowledgements

The author is grateful to Dr. N. Yamano for providing several figures related to his evaluation of ^{63,65}Cu.

References

[1] T. Fukahori et al., J. Atomic Energy Soc. Japan, **40**, 3 (1998) in Japanese.
[2] T. Fukahori (Ed.), Proc. the third specialists' meeting on high energy nuclear data; JAERI-Conf 98-016 (1998).
[3] P.G. Young et al., LA-12343-MS, Los Alamos National Laboratory (1992).
[4] H. Kalka et al., Z. Phys. A **341**, 289 (1992).
[5] J. Raynal, "Notes on ECIS94", CEA-N-2772 (1994).
[6] Efrem Sh. Sukhovitskii et al., OPTMAN and SHEMMAN codes, JAERI-Data/Code 98-019 (1988)
[7] M.B. Chadwick et al., Nucl. Sci. Eng. **131**, 293 (1999).
[8] K. Niita et al., Phys. Rev. C, **52**, 2620 (1995); JAERI-Data/Code 99-042 (1999).
[9] T. Fukahori, TOTELA code, private communication (1999).
[10] S. Chiba et al., Proc. 1993 Nuclear Data Symp., JAERI-M 94-019, p.300 (1994).
[11] Y.O. Lee et al., J. Nucl. Sci. and Technol. **36**, 1125 (1999).
[12] Sun Weili et al., presented at this symposium (2000).
[13] H. Kitsuki et al., presented at this symposium (2000).
[14] N. Yoshizawa et al., presented at this symposium (2000).
[15] S. Chiba et al., J. Nucl. Sci. and Technol. **37**, 498 (2000).
[16] C. Kalbach, Phys. Rev. C **37**, 2350 (1988).
[17] K. Niita, Proc. of the 1999 Nuclear Data Symp.; JAERI-Conf 2000-005 (2000), p.98.

Table 1. Nuclides to be stored in JENDL high-energy file

1st priority	^{1}H, ^{12}C, ^{14}N, ^{16}O, ^{23}Na, ^{27}Al, ^{50,52,53,54}Cr, ^{54,56,57,58}Fe, ^{58,60,61,62,64}Ni, ^{63,65}Cu, ^{181}Ta, ^{180,182,183,184,186}W, ^{197}Au, ^{196,198,199,200,201,202,204}Hg, ^{204,206,207,208}Pb, ^{209}Bi, ^{235,238}U
2nd priority	^{9}Be, ^{24,25,26}Mg, ^{28,29,30}Si, ^{39,41}K, ^{40,42,43,44,46,48}Ca, ^{46,47,48,49,50}Ti, ^{51}V, ^{55}Mn, ^{59}Co, ^{90,91,92,94,96}Zr, ^{93}Nb, ^{92,94,95,96,97,98,100}Mo, ^{238,239,240,241,242}Pu
3rd priority	^{2}H, ^{6,7}Li, ^{10,11}B, ^{13}C, ^{19}F, ^{35,37}Cl, ^{35,38,40}Ar, ^{50}V, ^{64,66,67,68,70}Zn, ^{69,71}Ga, ^{70,72,73,74,76}Ge, ^{75}As, ^{89}Y, ^{232}Th, ^{233,234,236}U, ^{237}Np, ^{241,242,242m,243}Am, ^{243,244,245,246}Cm

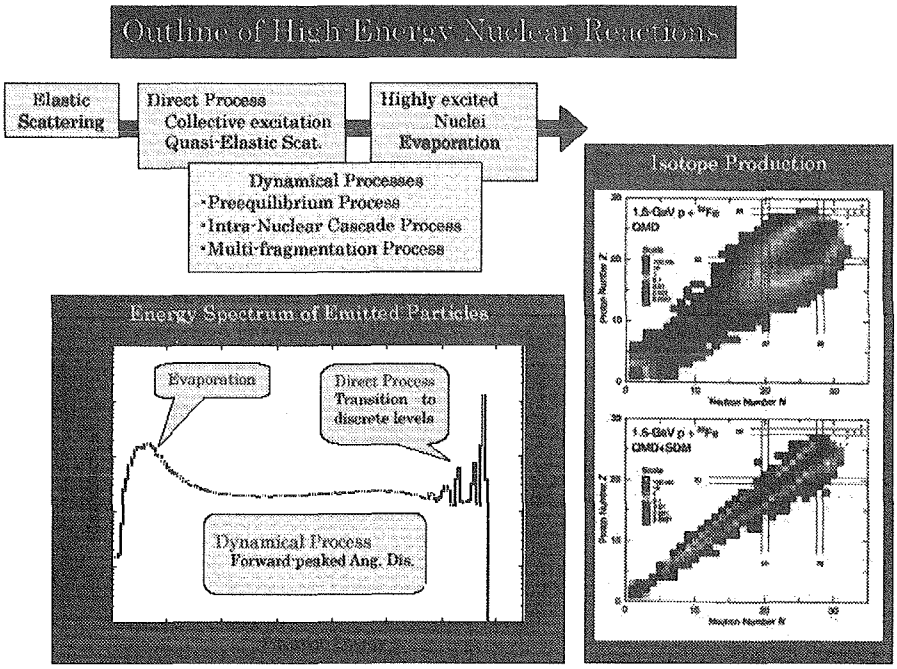

Fig.1 High-energy nuclear reactions

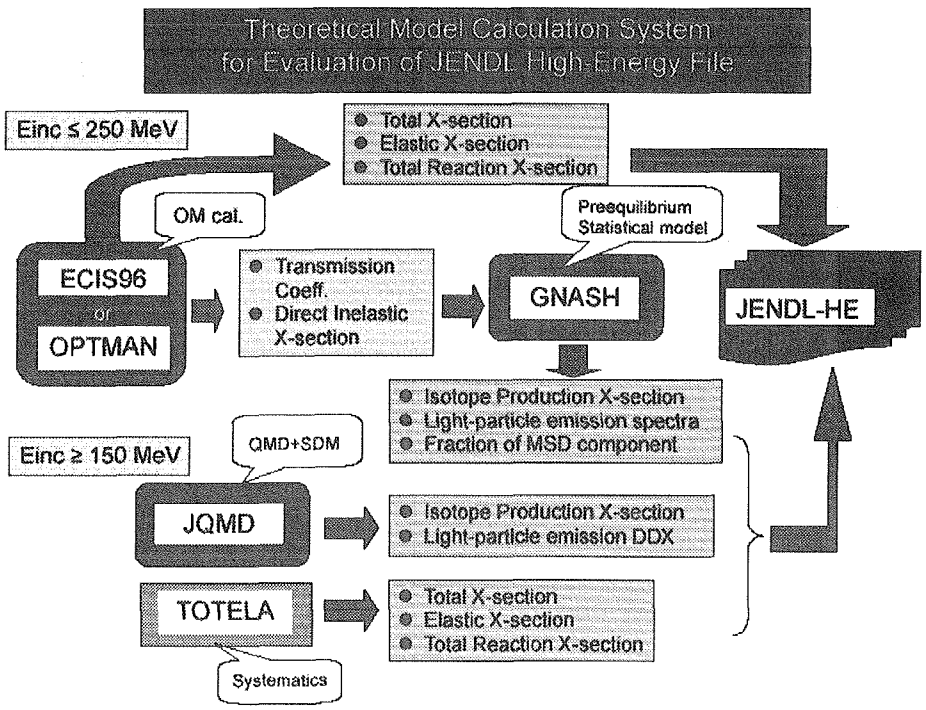

Fig.2 Model calculation code system for JENDL high-energy nuclear data evaluation.

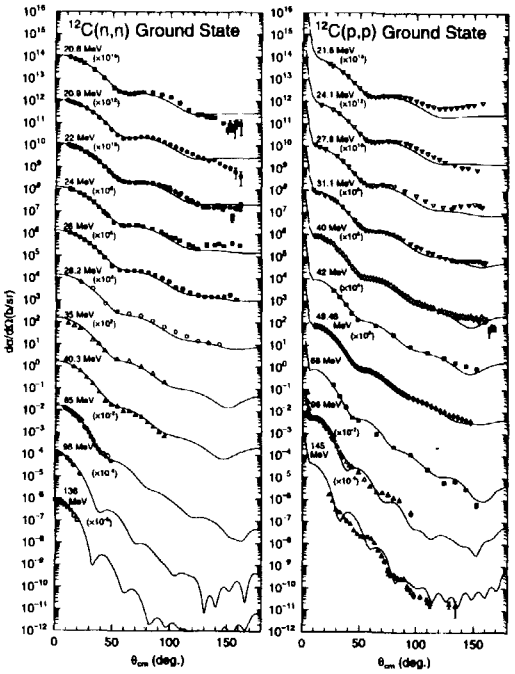

Fig.3 Comparison of measured (symbols) and calculated (solid lines) angular distributions for elastically scattered nucleons from ^{12}C. This figure is taken from Ref.[15].

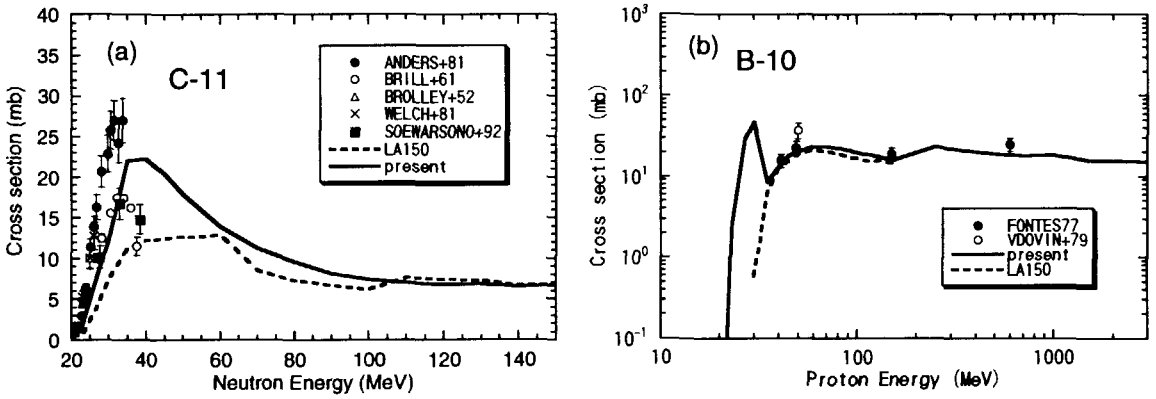

Fig.4 Isotope production cross sections: (a) ^{12}C(n,2n)^{11}C and (b) ^{12}C(p,x)^{10}B.

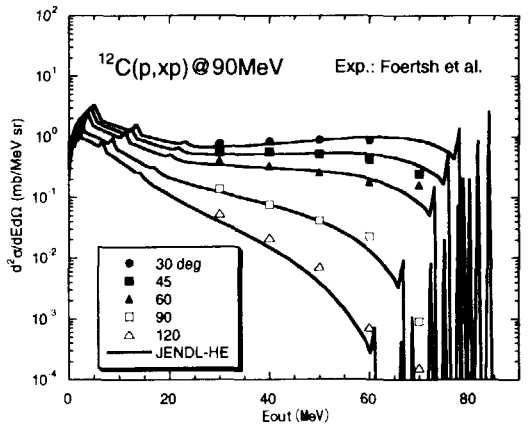

Fig.5 Double-differential cross sections of the (p,xp) reaction on ^{12}C at 90 MeV.

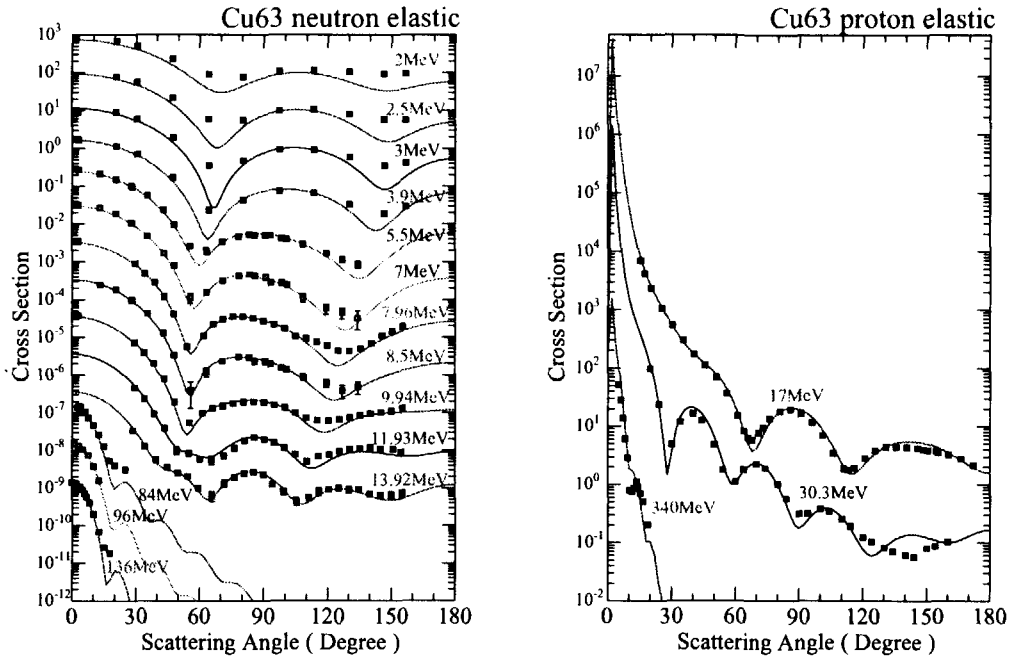

Fig.6 Comparison of calculated and measured angular distributions of nucleon elastic scattering from ^{63}Cu.

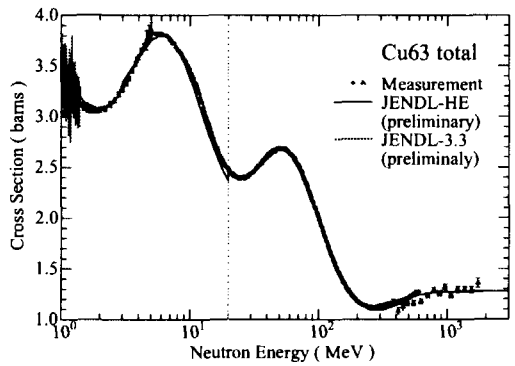

Fig.7 Total cross sections of ^{63}Cu.

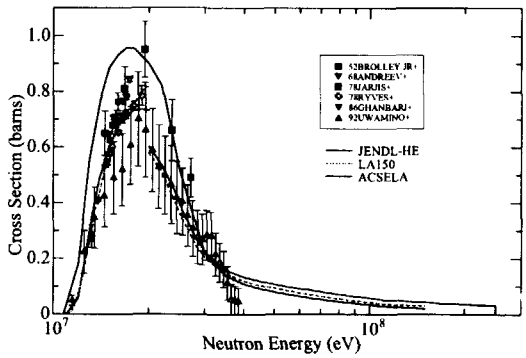

Fig.8 ^{63}Cu(n,2n)^{62}Cu production cross sections.

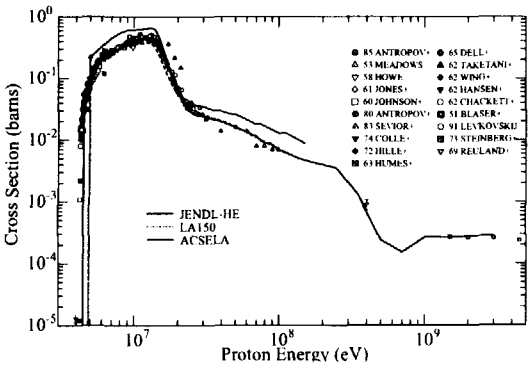

Fig.9 ^{63}Cu(p,n)^{63}Zn production cross sections.

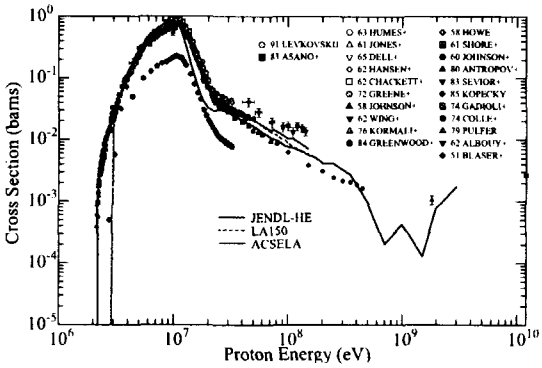

Fig.10 ^{65}Cu(p,n)^{65}Zn production cross sections.

JP0150661

2.17
Integral Test for JENDL High Energy File

Fujio MAEKAWA
Center for Neutron Science, Japan Atomic Energy Research Institute
Tokai-mura, Naka-gun, Ibaraki-ken 319-1195
e-mail: fujio@fnshp.tokai.jaeri.go.jp

As activities of the Intermediate and High Energy Nuclear Data Integral Test Working Group in the Japanese Nuclear Data Committee, integral tests of JENDL High Energy File (JENDL-HE) have started. Processing method of JENDL-HE with the NJOY code has been established. As a result of benchmark tests for the ^{56}Fe data in JENDL-HE with the two neutron incident experiments conducted at TIARA and RCNP, calculations with JENDL-HE agreed excellently with the experimental data. The data were found to be adequate for nuclear design calculations as far as the energy range tested, below 68-MeV, was concerned.

1. Introduction

Evaluation of JENDL High Energy File (JENDL-HE) for the first priority nuclides is going to be completed in the early 2001. The data have been strongly required for many applications for intermediate and high energy fields. The JAERI/KEK project for high-intensity proton accelerator is one of such applications. The data in JENDL-HE are therefore needed to be validated urgently before they are used practically in nuclear design calculations for the accelerator facilities. Under this situation, the Intermediate and High Energy Nuclear Data Integral Test Working Group* has been organized since May 2000 in the Japanese Nuclear Data Committee. This report summarizes a part of results obtained so far by the Working Group.

2. Needs for JENDL-HE

Since no evaluated cross section data for higher energy, i.e., up to 3 GeV, have been available, intranuclear cascade Monte Carlo calculation codes such as NMTC/JAM [1] and MCNPX [2] are used for design calculations for the accelerator facilities. We encountered the following difficulties in the calculations.

(1) Bulk shielding calculations have to deal with attenuation of neutron fluxes by ~ 15 orders of magnitude as shown in Fig. 1. The calculations are very tough for the Monte Carlo codes to obtain results with good statistics although they are feasible. Deterministic calculation codes with a multigroup cross section library are suitable for such the bulk shielding calculations.

---

* Intermediate and High Energy Nuclear Data Integral Test Working Group
Members: N. Yamano (Leader), Y. Ando, K. Kosako, F. Maekawa, H. Nakashima, K. Ueki, N. Yoshizawa
Observers / Collaborators:
T. Fukahori, S. Furihata, H. Handa, C. Konno, S. Meigo, T. Mori

(2) The point estimator in Monte Carlo codes requires total and neutron scattering cross section data. Since no evaluated cross section data beyond 150 MeV are available, use of the point estimator is limited to 150 MeV.
(3) The intranuclear cascade model is adequate for medium- and heavy-mass nuclei, but not for light nuclei such as Be, B, C, N and O. Use of evaluated cross section data will improve calculations for the light nuclei.
(4) At present, no activation cross section library beyond 150 MeV is available.

When the JENDL-HE up to 3 GeV will be available, these difficulties will be solved.

3. Production of Cross Section Data for Transport Calculation Codes

The JENDL-HE files provided by evaluators, i.e., ^{1}H, ^{56}Fe and all the isotopes for Ca, Ti, Cr and Cu, were processed by the NJOY-99.24 code [3] into ACE-type cross section data for the MCNP code [4]. The new ACE-type format that included outgoing particle distributions and a new cumulative angle distributions was adopted. In the processing, several invalid data in JENDL-HE files were found, and most of them were corrected. One problem still remained that energy-angle distributions of secondary particles were represented in the laboratory system below 250 MeV while in the center-of-mass system above 250 MeV. The representation was not allowed in the ENDF-6 format, but not easy to correct. Hence, the problem was avoided temporarily by giving patches for both the NJOY and MCNP codes.

Multi-group cross section data for deterministic transport calculation codes were also produced successfully by NJOY.

4. Benchmark Problems and Analysis

The Working Group has selected benchmark experiments for validation of JENDL-HE as listed in Table 1. This report deals with neutron incident experiments, and the TIARA and RCNP experiments on iron [5, 6] indicated in bold letters in Table 1 are the only experiments for which cross section data are provided for the calculations.

The MCNP-4C code [4] was used for neutron transport calculations. Since the cross section data for iron was given only for the main isotopes of iron, i.e., ^{56}Fe, other three isotopes of iron were replaced by ^{56}Fe. Calculations with the LA-150 library [7] were also performed for comparisons.

5. Results and Discussion

Figure 2 compares calculated neutron spectra for the RCNP experiment with the experimental data. The MORSE calculation [5] with HILO86 library is also plotted for comparisons. Results by

Table 1 Benchmark experiments selected for the benchmark test of JENDL-HE.

Facility / Institute	Material	Energy	Remarks
TIARA / JAERI	**Fe**, PE, Concrete	**43, 68 MeV**	**n-incident [5]**
RCNP / Osaka Univ.	C, **Fe**, Pb	**65 MeV**	**n-incident [6]**
AGS / BNL	Hg/Pb/Fe	1.9, 12, 24 GeV	p-incident
TIARA / JAERI	C, Al, Cu, Pb	68 MeV	p-incident, TTY
WNR / LANL	C, Al, Fe	113, 256 MeV	p-incident, TTY
Proton Synchrotron / KEK	W, Pb	0.5, 1.5 GeV	p-incident
Synchrophasotron / JINR	Pb	2, 2.5 GeV	p-incident

JENDL-HE and LA-150 are close to each other, and they agree well with the experimental data. Although the spectrum by LA-150 is slightly larger than that by JENDL-HE in the energy range below 50 MeV for the 40 cm iron case, it is difficult to judge which calculation is better than the other.

Results for the TIARA experiment with 68-MeV and 43-MeV p-Li neutrons are shown in Figs. 3 and 4, respectively. Although both the JENDL-HE and LA-150 calculations predict adequately the measured neutron flux spectra, results by JENDL-HE are better than those by LA-150 as a general trend. The only significant discrepancy in the shape of neutron spectrum between JENDL-HE and LA-150 is found in the valley of neutron flux at about 5 MeV below the neutron peak. Although the spectrum by JENDL-HE follows adequately the experimental spectrum, that by LA-150 has a tiny peak at the valley. There would be a problem in the energy distributions for secondary neutrons in LA-150.

Figure 5 and 6 shows ratios of calculated to experimental neutron fluxes (C/E values). The left-hand-side figures in Figs. 5 and 6 indicate C/E values of neutron fluxes on the incident neutron beam axis as a function of penetration thickness. The LA-150 calculations tend to overestimate neutron fluxes as penetration thickness increases. This indicats that there are some problems in total or elastic/nonelastic scattering cross sections in LA-150. The JENDL-HE calculations give better agreements with the experimental data. Especially, neutron fluxes for the 68-MeV experiment are predicted excellently, i.e., ± 20 %, up to 130 cm thickness in the iron shield in which neutron fluxes attenuate by approximately 6 orders of magnitude.

The right-hand-side figures in Figs. 5 and 6 show C/E values of neutron fluxes as a function of offset distance from the neutron beam axis, and these results are suitable for testing angular distributions of secondary neutrons. The C/E curves almost flat regardless of the offset distance. This suggests that the angular distributions of secondary neutrons in both JENDL-HE and LA-150 are adequate.

6. Summary

As a result of benchmark tests for the ^{56}Fe data in JENDL-HE with the two neutron incident experiments, calculations with JENDL-HE agreed excellently with the experimental data. The data were found to be adequate for nuclear design calculations as far as the energy range tested, below 68-MeV, was concerned.

From a standpoint of the shielding design for the JAERI/KEK Project, it is expected that data for the three minor isotopes of iron (^{54}Fe, ^{57}Fe and ^{58}Fe) and for elements included in concrete (e.g., O, Al and Si) will be available as soon as possible.

Acknowledgments

The author would like to express his sincere gratitude to all the members, observers and collaborators of the Intermediate and High Energy Nuclear Data Integral Test Working Group for their efforts in the benchmark testes of JENDL-HE.

References

[1] Niita K., Takada H., Meigo S. and Ikeda Y.: "High Energy Particle Transport Code NMTC/JAM", Proc. 15th Meeting of the International Collaboration on Advanced Neutron Sources, ICANS-XV, November 6-9, 2000, Tsukuba, Japan (to be published).

[2] Waters L. S. (Ed.), "MCNPX™ User's Manual", TPO-E83-G-UG-X-00001, Los Alamos National Laboratory (1999).

[3] MacFarlane R. E. and Muir D. W.: "The NJOY Nuclear Data Processing System, Version 91", LA-12740-M, Los Alamos National Laboratory (1994).

[4] Briesmeister J. F., (Ed.): "MCNP - A General Monte Carlo N-Particle Transport Code, Version 4C", LA-13709-M, Los Alamos National Laboratory (2000).
[5] Nakashima H., et al.: *Nucl. Sci. Eng.*, 124, 243 (1996).
[6] Shin K., et al.: *Nucl. Sci. Eng.*, 109, 380 (1991).
[7] Chadwick M. B., et al.: *Nucl. Sci. Eng.*, 131, 293 (1999).

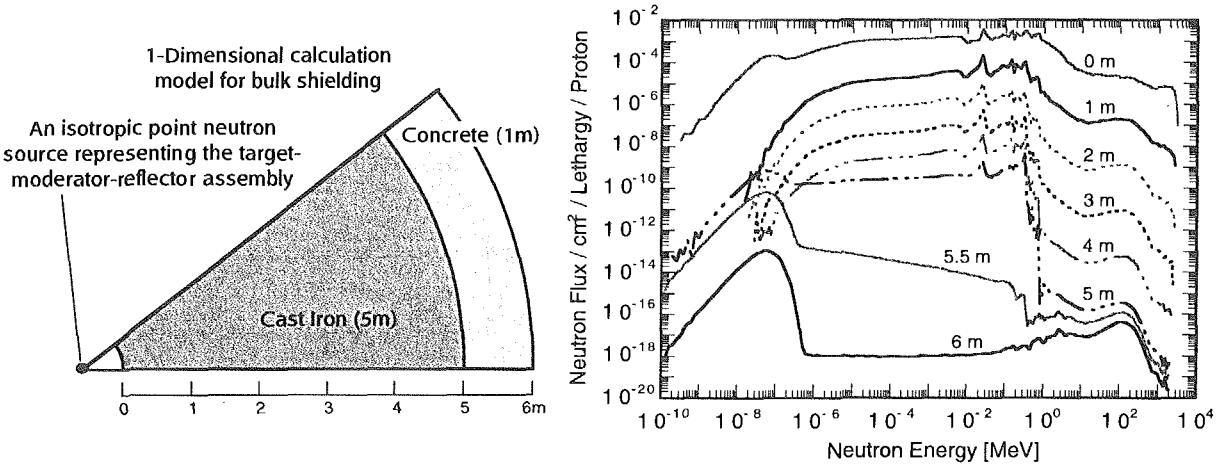

Fig. 1 An example of the bulk shielding calculation for a 3-GeV proton beam driven spallation neutron source by Monte Carlo calculation codes: calculation model (left) and calculated neutron spectra (right).

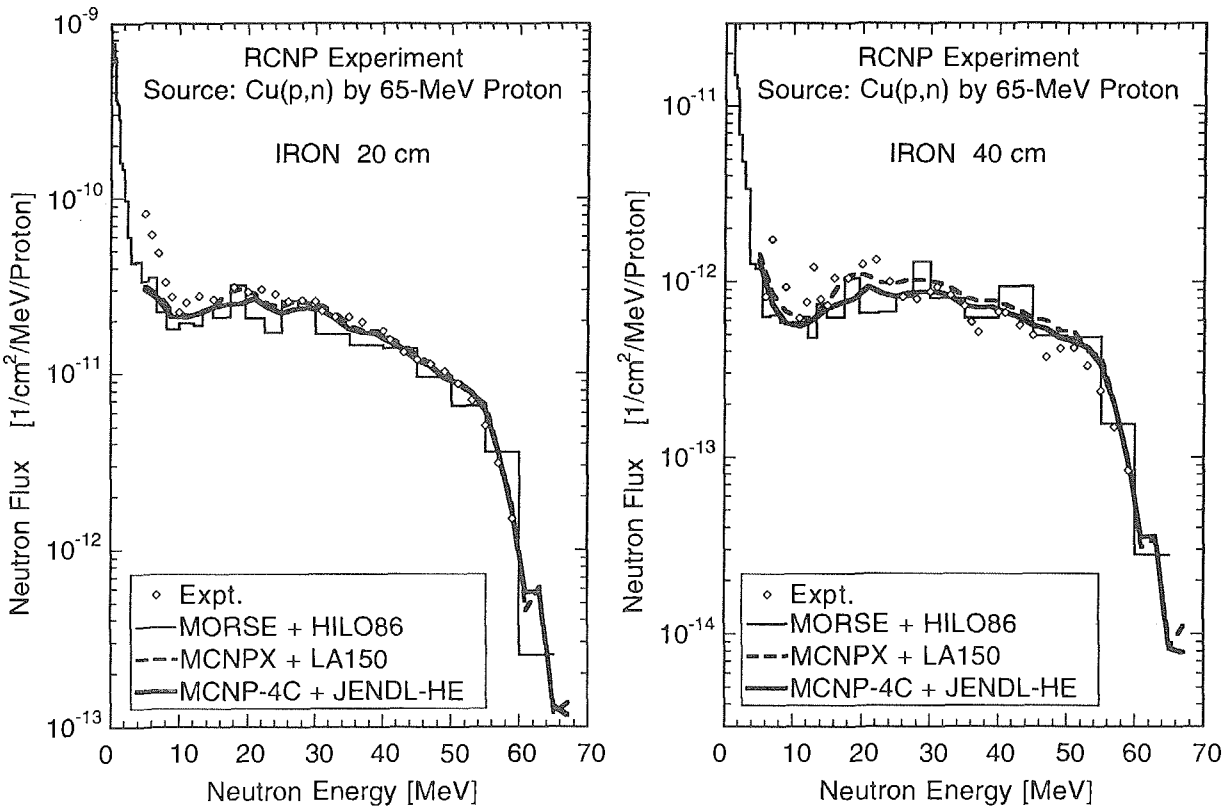

Fig. 2 Neutron flux spectra for the RCNP shielding experiment on iron for 20 cm and 40 cm thicknesses with a white neutron source produced by 65-MeV proton bombardment on a copper target.

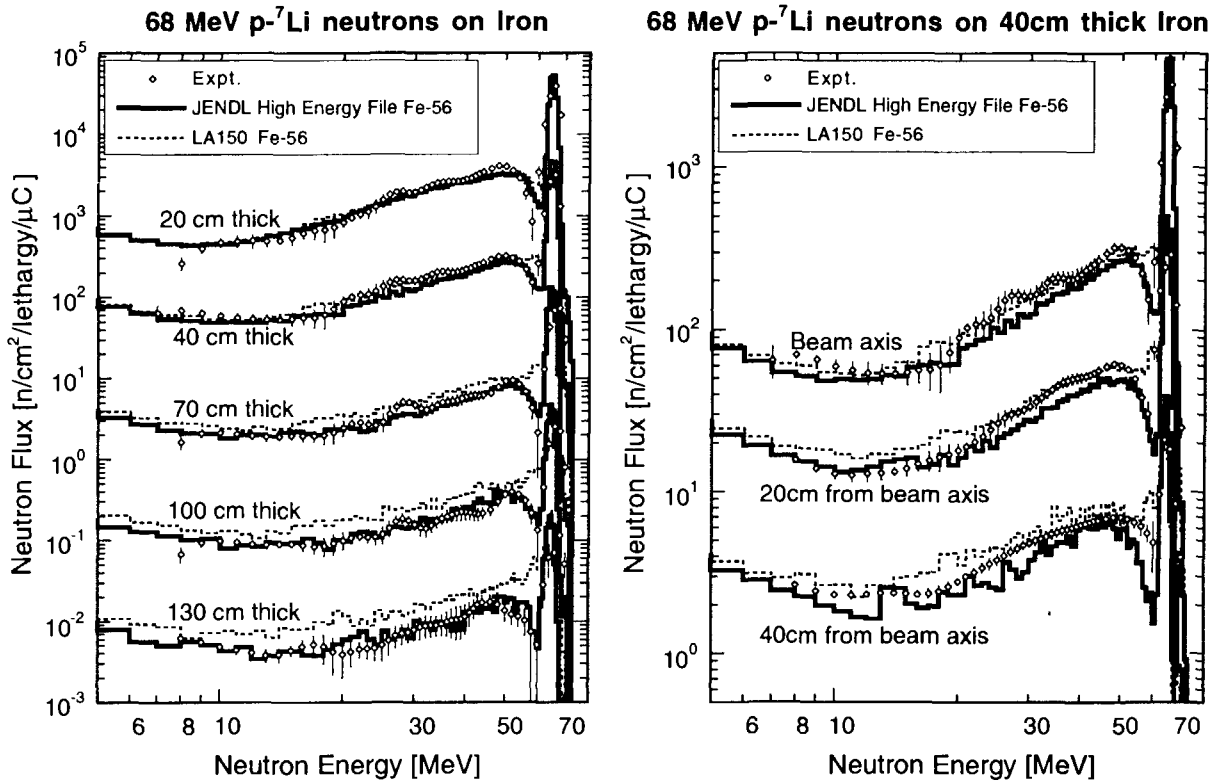

Fig. 3 Neutron flux spectra for the TIARA shielding experiment on iron with 68-MeV p-^{7}Li neutrons as a function of penetration thickness (left) and offset distance (right).

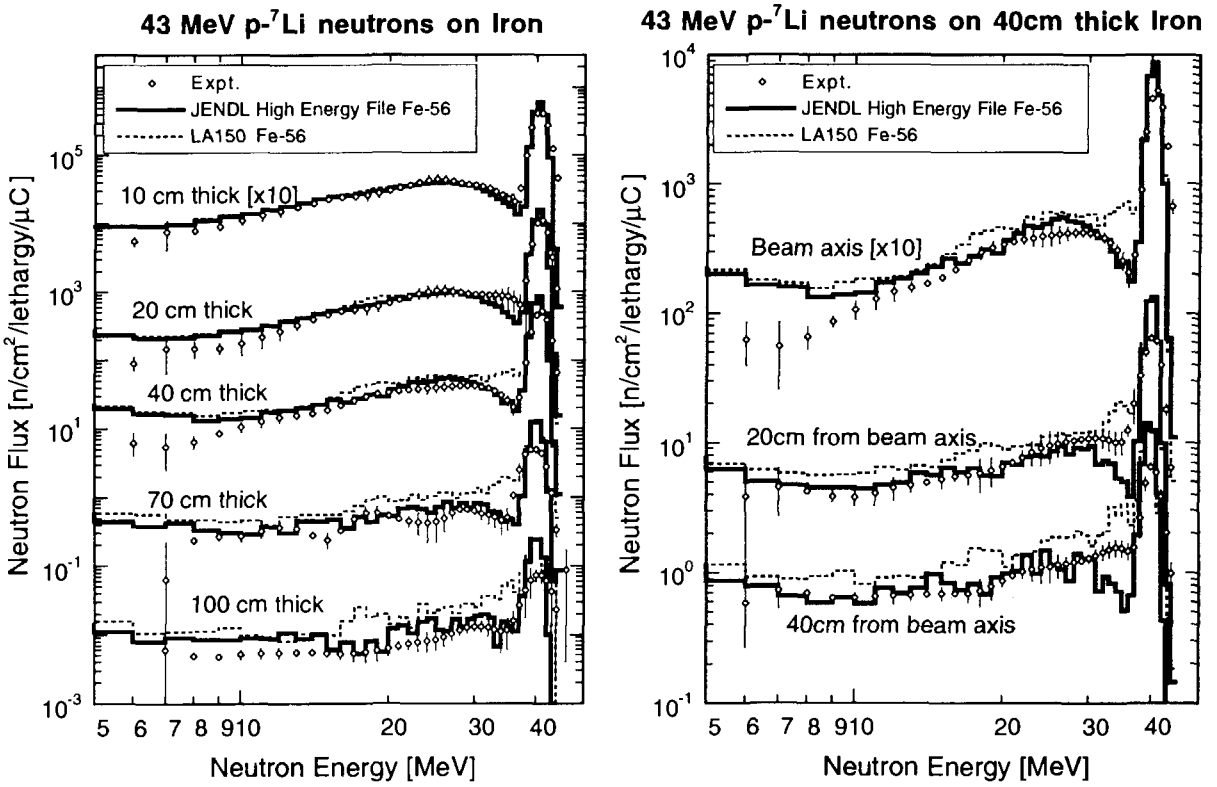

Fig. 4 Neutron flux spectra for the TIARA shielding experiment on iron with 43-MeV p-^{7}Li neutrons as a function of penetration thickness (left) and offset distance (right).

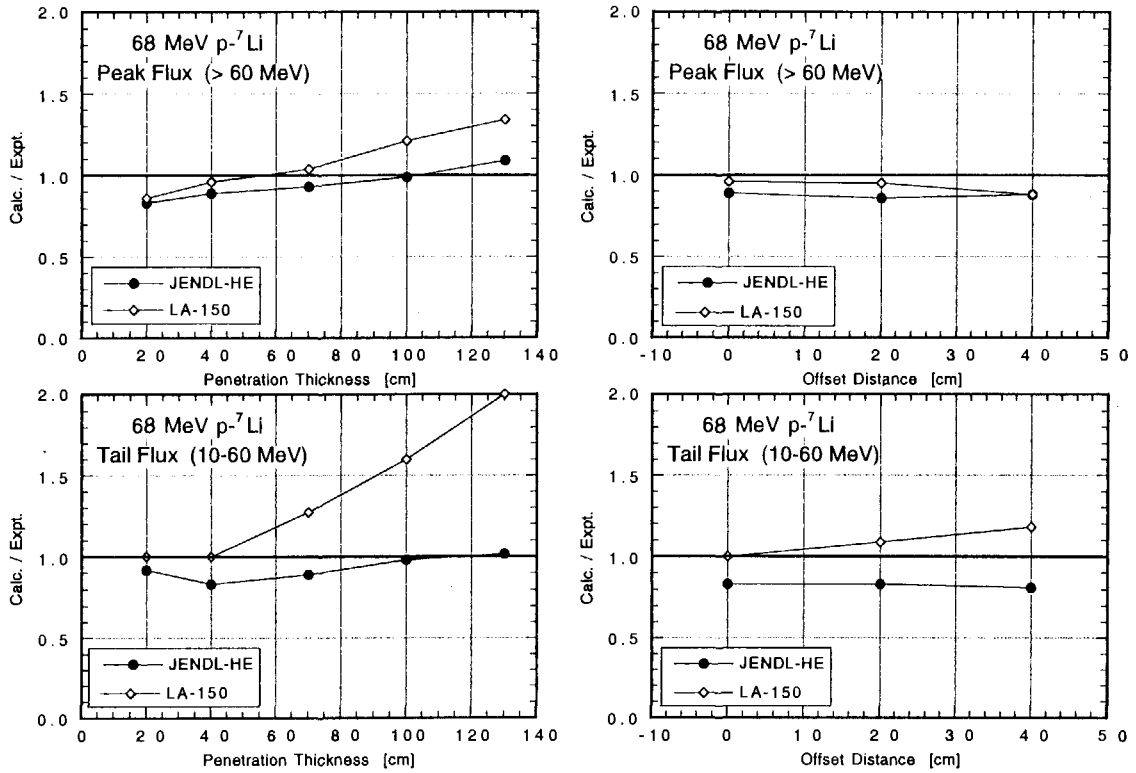

Fig. 5 C/E values for integral neutron fluxes for the TIARA shielding experiment on iron with 68-MeV p-^{7}Li neutrons: penetration thickness dependence (left) and offset distance dependence (right), and peak neutron flux above 60 MeV (top) and tail neutron flux between 10-60 MeV (bottom).

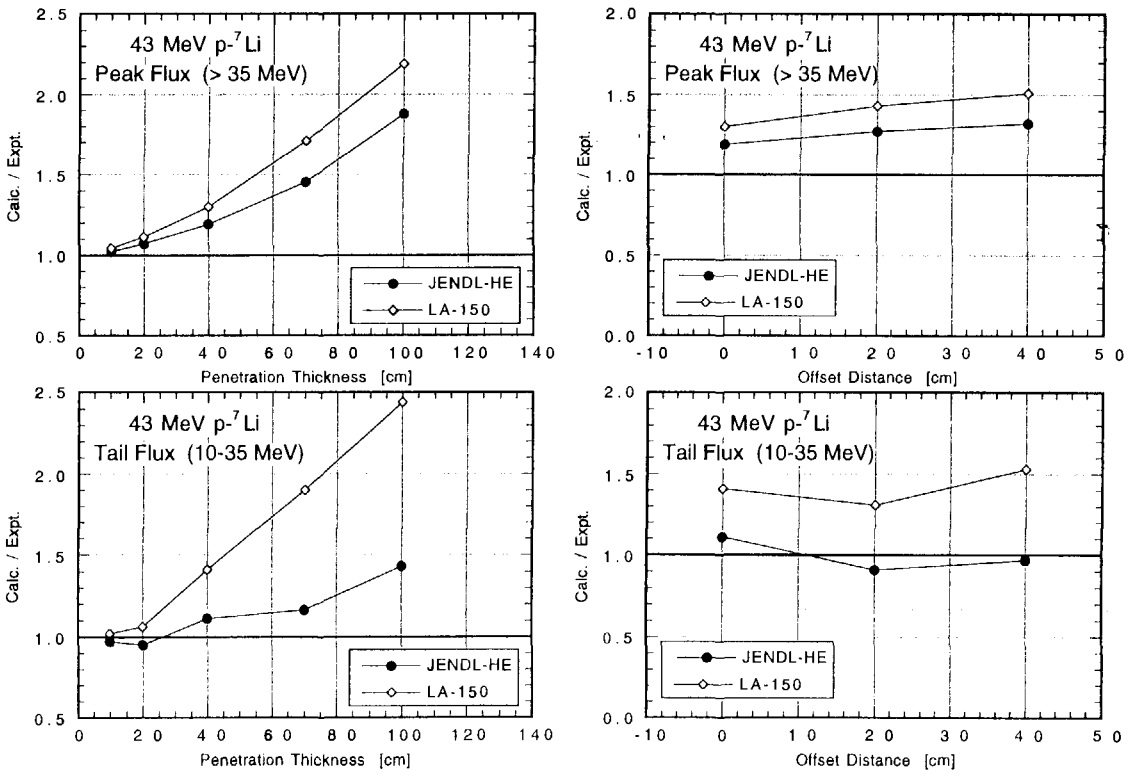

Fig. 6 C/E values for integral neutron fluxes for the TIARA shielding experiment on iron with 43-MeV p-^{7}Li neutrons: penetration thickness dependence (left) and offset distance dependence (right), and peak neutron flux above 35 MeV (top) and tail neutron flux between 10-35 MeV (bottom).

JP0150662

2.18

Evaluation of Cross Sections of ^{56}Fe up to 3 GeV and Integral Benchmark Calculation for Thick Target Yield

Nobuaki YOSHIZAWA*, Shin-ichiro MEIGO**, and Naoki YAMANO***

*Mitsubishi Research Institute, Inc.
2-3-6,Otemachi, Chiyoda-ku,
Tokyo, 100-8141, Japan
**Center for Neutron Science, Japan Atomic Energy Research Institute
Tokai-mura, Naka-gun, Ibaraki-ken 319-1195
***Sumitomo Atomic Energy Industries, Ltd.
2-10-14, Ryogoku, Sumida-ku,
Tokyo 130-0026, Japan
*e-mail: yoshizaw@mri.co.jp

The neutron and proton cross sections of ^{56}Fe were evaluated up to 3 GeV. JENDL High Energy File of ^{56}Fe were developed for use in transport calculation. For neutrons, the high-energy data are merged with JENDL3.3-file. Integral benchmark calculations for thick target neutron yields (TTY) for 113 MeV and 256 MeV proton bombardment of Fe targets were performed using the evaluated libraries. Calculated TTY neutron spectra were compared with experimental data. For 113 MeV, calculated TTY at 7.5 degree underestimated in the emitted neutron energy range above 10 MeV. For 256 MeV, calculated TTY well agree with experimental data except below 10 MeV.

1. Introduction

High-energy evaluated nuclear data are needed for accelerator engineering and radiation protection of air crew and space astronauts. In LA150[1], neutron and proton cross sections up to 150 MeV are included. Above 150 MeV, nuclear data file are also needed. High-energy nuclear data evaluation for more than 40 elements has been started by JNDC High Energy Nuclear Data Evaluation Working Group. For some elements, evaluations were performed. Integral benchmark calculations has also been performed by the JNDC Intermediate and High Energy Nuclear Data Integral Test Working Group. In this study, nuclear data evaluation for ^{56}Fe and Integral benchmark calculations for proton induced thick target neutron yields were reported.

2. Evaluation of ^{56}Fe cross section

2.1 Evaluation code

Several kinds of computation codes were used in this evaluation as shown in **Fig.1**. ECISPLOT [2] and Quick-GNASH [3] code system were used for data evaluation up to 250 MeV. Total, elastic and non-elastic cross sections for neutron and proton in the energy range from 250 MeV to 3GeV were calculated by TOTELA [4] code. Particle production cross sections and angular distributions for non-elastic scattering were evaluated with JQMD code [5]. For neutrons, the high-energy data are merged with JENDL3.3-file [6].

2.2 Results of evaluation

Experimental data [7] are presented from **Fig.2** to **Fig.5** compared with evaluated data. **Figure 2** shows neutron induced total cross section of ^{56}Fe. Neutron elastic scattering cross sections were also presented in **Fig. 3**. As shown in those figures, evaluated cross sections well agree with experimental data. Proton induced reaction and elastic cross sections are shown in **Figures 4 and 5**, respectively. In the same manner for neutron, there are good agreement between evaluated data and experimental data.

In **Fig.6**, evaluated double differential cross sections of (p,xn) reactions are shown compared with experimental data[8,9,10,11]. PLDDX[12] were used to calculate DDX from evaluated nuclear data file. Above 597 MeV, evaluated data well agree with experimental data. At 113 MeV, there is some differences below neutron energy 10 MeV. There are also some differences above 80 MeV at 30 degree. and above 60 MeV at 60 degree.

3. Integral benchmark calculation

3.1 Experimental data

Experimental data of Thick target neutron yield (TTY) were used in this integral benchmark calculation. For Fe target, experimental data from LANL[11,13] were compared with calculation results. For, Cu target, JAERI data[14] were used. Experimental conditions are shown in **Table 1**.

Table 1 Experimental conditions of TTY data

Target	Proton energy (MeV)	Detected angle (degree)	Reference
^{nat}Fe	256	7.5, 30, 60, 150	[13]
	113	30, 60, 120, 150	[11]
^{nat}Cu	68	0, 15, 30, 45, 90, 120	[14]

3.2 Calculation method

TTY spectra were calculated by **Eq(1)** [15], using neutron production cross sections and non-elastic cross sections of evaluated nuclear data.

$$\frac{d^2n}{d\Omega dE_n} = \int_0^{E_p} N \frac{d^2\sigma}{d\Omega dE_n} \left|\frac{dE}{dx}\right|^{-1} \exp\left(-N \int_E^{E_p} \sigma_{non}(E') \left|\frac{dE'}{dx}\right|^{-1} dE' \right) dE , \qquad (1)$$

where $d^2n/d\Omega dE_n$ is the TTY neutron spectra, N the atomic density of the target material, $d^2\sigma/d\Omega dE_n$ the double differential neutron production cross section, dE'/dx the stopping power and $\sigma_{non}(E')$ the non-elastic cross section for proton at the energy E'. PLDDX was used to calculate double differential neutron production cross sections from JENDL high-energy file.

3.3 Results of calculation

(1) Fe

For TTY calculation of ^{nat}Fe, evaluated reaction cross section and DDX of ^{56}Fe were used. **Figures 7 and 8** show comparisons of experimental[11,13] and calculated TTY for 256 MeV and 113 MeV proton incidence, respectively. There are some differences in these comparisons. For 256 MeV, neutron energy below 10 MeV, calculated results overestimated experimental data. This differences are attributed to multiple scattering of neutron in Fe target. In this TTY calculation, multiple scattering is ignored. Above 60 MeV, calculated results also show overestimation. Calculated 113 MeV TTY using LA150 are shown in **Fig.**7. Calculated TTY with present evaluated data overestimate below 10 MeV. There are no overestimation with LA150 in the same energy region. It is necessary to compare between present evaluation and LA150. Above 10MeV, there are no large differences between results from present data and LA150. For 7.5 degree, there are large differences between experimental data and calculation results.

One of the reason is assumed to thickness of experimental target is not enough long. Because, in this calculation, all primary proton is stopped in the target.

To check the reason of the above mentioned differences, bench mark calculation using transport code (ex. MCNPX[16]) is needed. Unfortunately, the latest distributed version of MCNPX, transport calculation with proton nuclear data library can not be performed.

(2) Cu

For TTY calculation of ^{nat}Cu, evaluated reaction cross section and DDX of ^{63}Cu were used. **Figure 9** shows comparisons of experimental and calculated TTY. From 0 to 45 degree. calculated results well agree with experimental data. From 60 to 120 degree., above 15 MeV, calculated results overestimated experimental data.

4. Conclusion

The neutron and proton cross sections of iron (^{56}Fe) were evaluated up to 3 GeV and JENDL High Energy File of iron were developed. Integral benchmark calculations for thick target neutron yields (TTY) for Fe and Cu targets. Several differences were found between experimental data and calculation results. Bench mark calculation using transport code is needed to investigate these differences. The evaluated data are very useful for accelerator engineering related to radiation.

References

[1] Chadwick M.B., et al.: Nucl. Sci. Eng.,131,293(1999).
[2] Lee Y. : NDL-9/99(1999).
[3] Young P.G., et al.: LA-12343-MS(1992).
[4] T.Fukahori T. and Niita K..:"Program TOTELA Calculating Basic Cross Sections in Intermediate Energy Region by Using Systematics," INDC(NDS)-416,"Nuclear Model Parameter Testing for Nuclear Data Evaluation," Summary Report of the Second Research Co-ordination Meeting, Varenna, Italy 12-16 June,2000.
[5] Niita K., et al.: JAERI-Data/Code 99-042(1999).
[6] JNDC private communications.
[7] EXFOR: OECD/NEA Nuclear Data Services (http://www.nea.fr/html/dbdata/).
[8] Ishibashi, et al., J. Nucl. Sci. Technol., 34, 529 (1997).
[9] Amian W.B., et al.: Nucl. Sci. Eng.,112,78(1992).
[10]Amian W.B., et al.: Nucl. Sci. Eng.,115,1(1993).
[11]Meier M.M., et al.: Nucl. Sci. Eng.,102,310(1989).
[12]Fukahori T., et al.: JAERI-M 92-053(1992).
[13]Meier M.M., et al.: Nucl. Sci. Eng.,104,339(1990).
[14]Meigo S., et al., "Measurements of neutron spectra from stopping-length targets irradiated by 68-MeV protons, 100-MeV alpha and 220-MeV carbon particles", Proc. Nucl. Data for Sci and Technol., Trieste 19-24 May 1997.
[15]Meigo S., et al.: J.Nucl.Sci.Tech.,36,250(1999).
[16]Hughes H.G., et al.: XTM-RN(U) 97-012(1997).

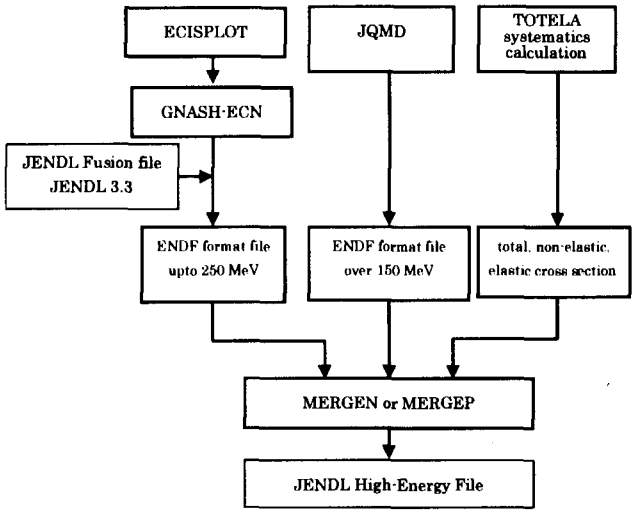

Fig 1 Flow chart of high-energy nuclear data evaluation and file development

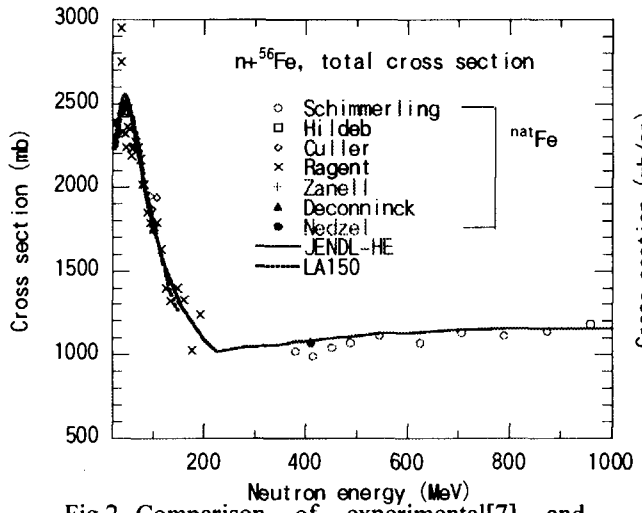

Fig.2 Comparison of experimental[7] and evaluated total cross sections of n + ^{56}Fe

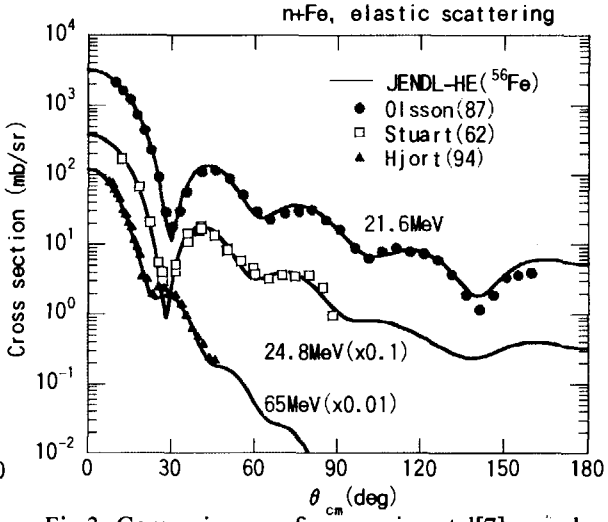

Fig.3 Comparison of experimental[7] and evaluated elastic cross sections of n + ^{56}Fe

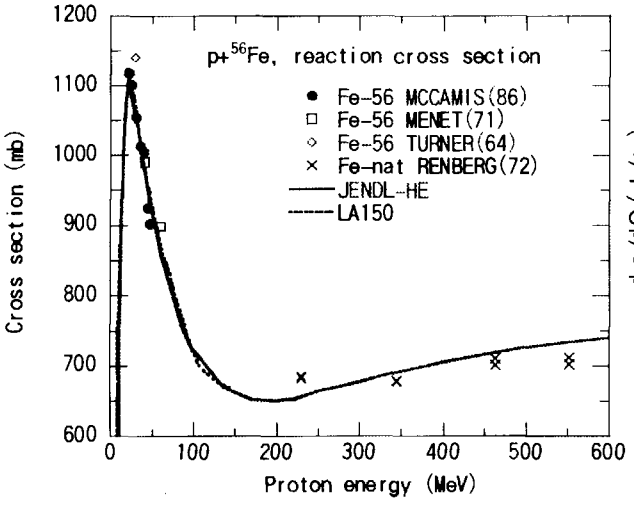

Fig.4 Comparison of experimental[7] and evaluated total cross sections of p + ^{56}Fe

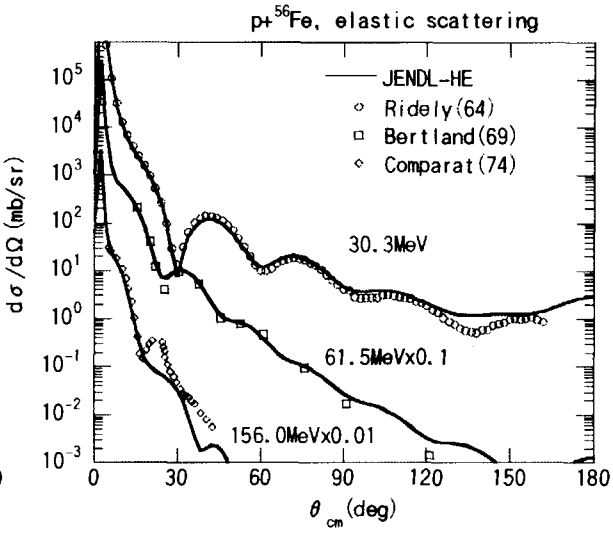

Fig.5 Comparison of experimental[7] and evaluated elastic cross sections of p + ^{56}Fe

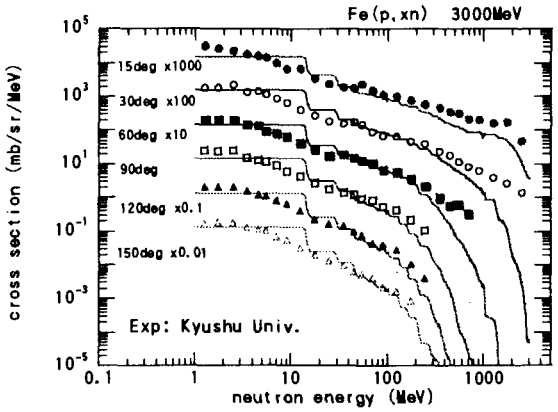

(a)

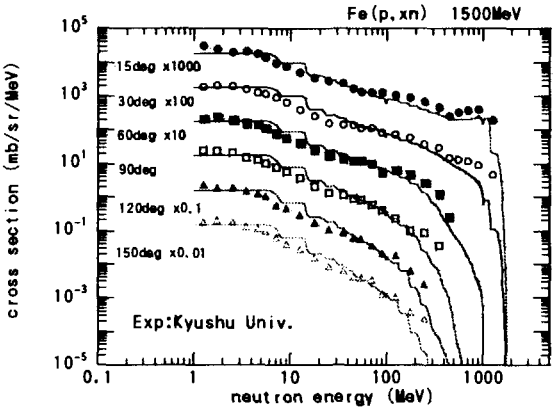

(b)

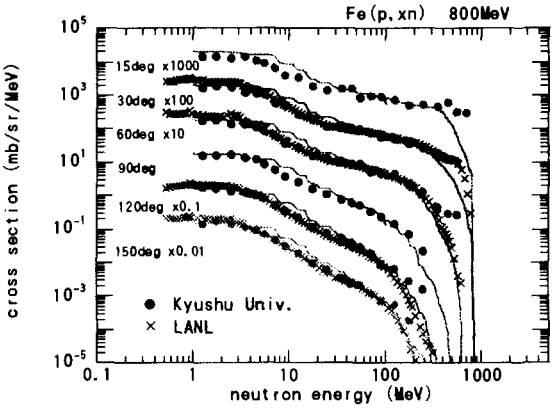

(c)

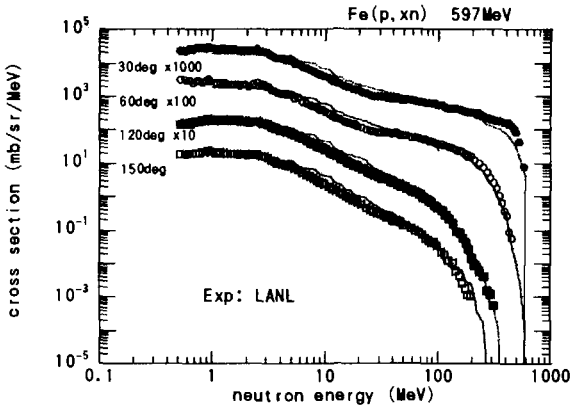

(d)

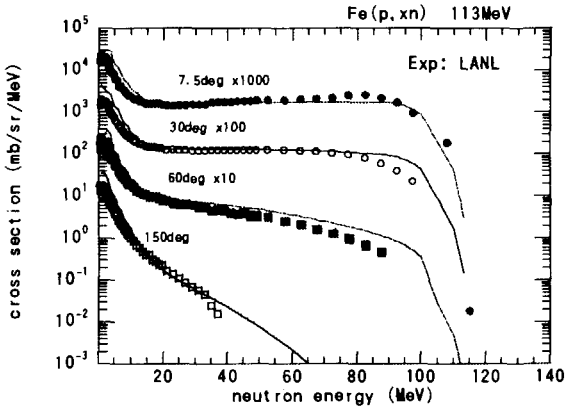

(e)

Fig.6 Comparison of experimental (p,xn) reactions of ^{56}Fe and evaluated DDX (a)3000 MeV[8], (b)1500 MeV [8], (c)800 MeV[8,9], (d)597 MeV[10] and (e)113 MeV[11]

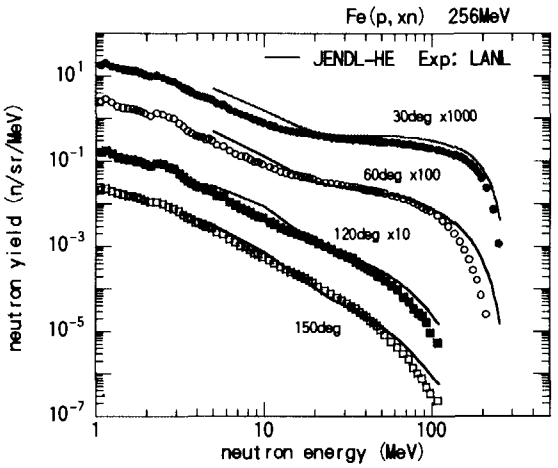

Fig.7 Comparison of experimental[13] and calculated 256 MeV proton TTY from Fe

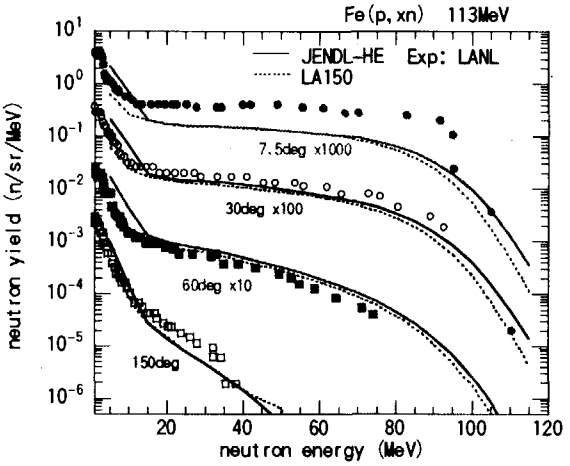

Fig.8 Comparison of experimental[11] and calculated 113 MeV proton TTY from Fe

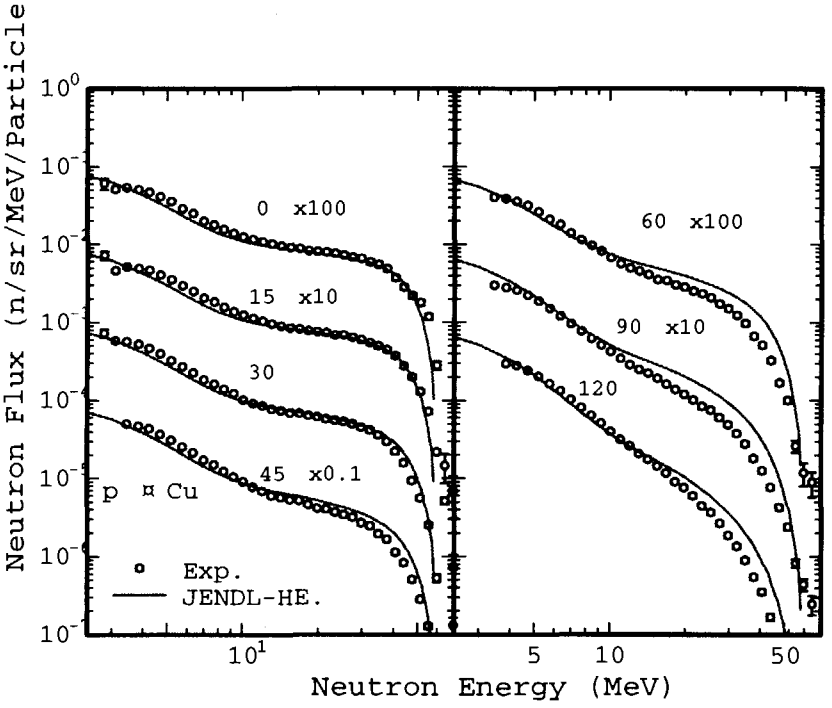

Fig.9 Comparison of experimental[14] and calculated 68 MeV proton TTY from Cu

3. Papers Presented at Poster Sessions

JP0150663

3.1
Decay Heat Measurement of Actinides at YAYOI

Yasushi OHKAWACHI, Akira SHONO

Reactor Physics Research Group,System Engineering Technology Division,OEC,JNC

4002 Narita-cho Oarai-machi 311-1393 JAPAN

E-mail:okawachi@oec.jnc.go.jp

Actinides decay heat were measured for fast neutron fissions using the fast neutron source reactor "YAYOI" of the University of Tokyo. Measured nuclides were U-235 and Np-237, using beta and gamma spectroscopic method. The newest results on gamma-ray decay heat are reviewed in this paper. Measurement results were compared with those measured in 1983 by Dr. Akiyama using the same method, as well as with the summation calculation results using JNDC-V2, ENDF-B/VI, JEF-2.2.

Introduction

The decay heat is important in designing the heat removal system of nuclear reactors and spent fuel handling systems. The decay heat for fast neutron fissions was measured on U-233, U-235, U-238, Pu-239, Th-232 by Dr. Akiyama.[1),2),3),4)] However, equivalent measurement has not been performed for minor actinides. In this study, minor actinide decay heat was measured using the fast neutron source reactor "YAYOI".[5)] Experiment and evaluation procedures are almost same as Akiyama's one. The decay heat of U-235 was measured for cooling times between 19 and 20,000 seconds, and Np-237 was measured for cooling times between 64 and 20,200 seconds.

Experiments

The samples of U-235 consisted of about 1.6mg of the metallic fissile materials electrodeposited on 18mm diameter, 0.1mm thick titanium foils. The diameter of the electrodeposited area was 10mm. The samples of Np-237 consisted of about 0.5mg of the nitride fissile materials electrodeposited on 18mm diameter, 0.1mm thick titanium foils. The diameter of the electrodeposited area was 10mm. The enrichment is 97.652% for U-235, and 99.9% for Np-237. Each sample was covered with thin myler film, and packed in a thin polyethylene sack. The dummy samples were prepared, which were the same configuration as the U-235 and Np-237 sample except that the fissile materials were not electrodeposited on the titanium foils. The dummy sample was used to estimate the activity of the titanium foil.

The samples were irradiated at the center of the grazing hole at YAYOI for time periods of 10 and 100 seconds for U-235, 100 and 500 seconds for Np-237. The cross-sectional view of YAYOI and measurement position is shown in Fig.1. The samples were transported by air pressure to the irradiation position and rapidly returned to a counting room following the irradiation. Gamma-ray energy spectra were measured using a NaI(Tl) scintillation detector located inside the lead box. Conceptual view of decay heat measurement system is shown in Fig.2. The front face of the detector was covered by 30mm thick polyethylene plate in order to prevent beta-rays from being detected. The distance from the sample to the front face of the detector was 100mm. As this detector had been used by Dr. Akiyama, the response function of the detector obtained experimentally by him was used for the data processing.

The number of fission for normalization was evaluated from measured gamma spectra by Ge detector. The decay series to be used for evaluating the number of fission should have a large fission yield, a sufficient gamma-ray intensity, and nuclides with proper gamma-ray energy and half life. Nb-97, Nb-97m, Y-91m, and Xe-135 were used to evaluate the number of fission. These nuclides can be approximated by a simple decay series. For example, in a decay chain of mass number 97, the preceding nuclides of the Zr-97 have rather short half life comparing with that of Zr-97. And the independent fission yields of Nb-97m and Nb-97 are negligible comparing with the cumulative yield of Zr-97. In this case, the decay chain is simplified as follows;

Zr-97 · Nb-97 (Nb-97m) · Mo-97

Experimental Results and Comparisons with AKIYAMA's Data and Calculations

Measured pulse height data were corrected for background data, and unfolded using the FERDO[6] code with the use of the response function of the detector. Each unfolded spectrum was divided by the number of fission per second to obtain the normalized spectra. And, the finite irradiation decay heat data were obtained from the normalized spectra. The finite irradiation decay heat was directly obtained by experiments. But, it can not be compared with experimental results and calculation results obtained under different irradiation conditions. So, it is convenient to convert the finite irradiation decay heat into the fission burst decay heat. If

$$T_W \cdot T_R + T_C \cdot \cdot \cdot \cdot \cdot (1)$$

T_W : waiting time, T_R : irradiation time, T_C : measurement time

is established, the fission burst decay heat is as follows;

$$f(t) = F(t)/T_R \cdot \cdot \cdot \cdot \cdot (2)$$

f(t) : fission burst decay heat, F(t) : finite irradiation decay heat

If the condition of equation (1) is not established, the correction factor is required. The correction factor is as follows;

$$\cdot = f_{cal}(t)/(F_{cal}(t)/T_R) \quad \cdot \cdot \cdot \cdot \cdot \cdot (3)$$

$\cdot$: correction factor,

$f_{cal}(t)$: result of the summation calculation based on a condition of the fission burst decay heat

$F_{cal}(t)$: result of the summation calculation based on a condition of the finite irradiation decay heat

· Results on U-235

The experimental result for U-235 is shown in Fig.3. The present results on U-235 are compared with the data of Akiyama that were measured in 1983 using the same method and summation calculations [7] results using JNDC-V2, ENDF-B/VI, and JEF-2.2. The present results agreed with Akiyama's data within experimental error. This agreement suggests the repeatability of Akiyama's method. And, the present results agree with a summation calculation results using JNDC-V2 and ENDF-B/VI.

· Results on Np-237

The experimental result for Np-237 is shown in Fig.4. The present results on Np-237 are compared with the summation calculations results using JNDC-V2, ENDF-B/VI, and JEF-2.2. The present results on Np-237 agree with a summation calculation results using JNDC-V2 and ENDF-B/VI between 200 to 2,500 seconds. Between 60 to 200 seconds the agreement is not so well. The reason may be a larger correction considered in this time zone. To improve accuracy of decay heat data in shorter time range after fission burst, reduced irradiation experiment may be useful. The accuracy of the present results between 2,500 to 20,000 seconds is bad The reason is gamma-rays released from Np-238, that were generated by neutron capture reaction of Np-237. Fig.5 shows gamma spectrum of irradiated Np-237 measured by Ge detector about 56,000 seconds after irradiation. Four gamma-ray peaks were seen. These peaks were not seen on U-235 irradiation data, titanium foil irradiation data, and background data. Main gamma energy and release rate of Np-238 are 923.98keV(2.86%), 984.45keV(27.8%), 1025.87keV(9.65%), and 1028.54keV(20.385%). Four gamma-ray peaks agree with each energy, respectively. And, the ratio of the peak count rates are consistent with the gamma release rates. It is also confirmed that the transition of these peak counts can be explained by the half life of Np-238, 2.12 day. As for the time zone between 2,500 to 20,000 seconds, the decay heat corrected for four gamma-ray peaks of Np-238 will improve the agreement with a summation calculation result using JNDC-V2.

Summary

The decay heat of U-235 for fast neutron fissions was measured for cooling times between 19 and 20,000 seconds, and that of Np-237 for cooling times between 64 and 20,200 seconds. Experimental method is same as Akiyama's one by which the decay heat of U-235, Pu-239 etc had been measured. The present results on U-235 agreed with Akiyama's data within experimental error. And, the present results agree with a summation calculation results using JNDC-V2 and ENDF-B/VI. The present results on Np-237 agree with a summation calculation results using JNDC-V2 and ENDF-B/VI between 200 to 2,500 seconds. Between 60 to 200 seconds, the agreement is not so well. The reason may be a larger correction considered in this time zone. As for the time zone between 2,500 to 20,000 seconds, the decay heat corrected for four gamma-ray peaks of Np-238 will improve the agreement with a summation calculation result using JNDC-V2.

References:

1) M. AKIYAMA, et al.: Measurements of gamma-ray decay heat of fission products for fast neutron fissions of U-235, Pu-239 and U-233. J. At. Energy Soc. Japan 24(9) 709-722 (1982).

2) M. AKIYAMA, et al.: Measurements of beta-ray decay heat of fission products for fast neutron fissions of U-235, Pu-239 and U-233. J. At. Energy Soc. Japan 24(10) 803-816 (1982).

3) M. AKIYAMA.: Study on decay heat of fission products for fast neutron fissions. Dr. Thesis, University of Tokyo (1983).

4) M. AKIYAMA, et al.: Measurement of decay heat of fast neutron fission products. Progress in Nuclear Energy, Vol 32, No. 1/2, 53-60 (1998).

5) S. AN, et al.: Physics Experiments with YAYOI. Proceedings of the International Symposium on Physics of Fast Reactors, Tokyo,1973.

6) Bert W. Rust, et al.: A User's Manual for The FERDO and FERD Unfolding Codes. ORNL/TM-8720, (1983).

7) K. Oyamatsu. : Easy-to-use Application Programs to Calculate Aggregate Fission-Product Properties on Personal Computers. JAERI-Conf 99-002, (1999).

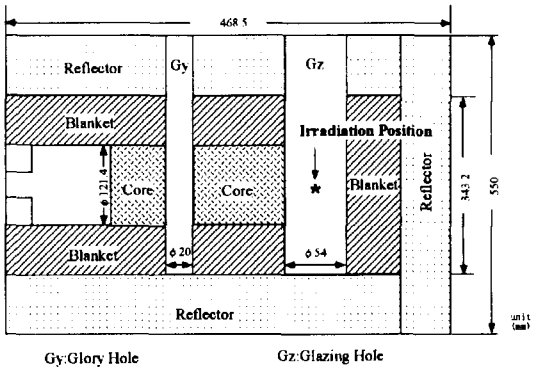

Fig.1 Cross-sectional View of YAYOI and Measurement Position

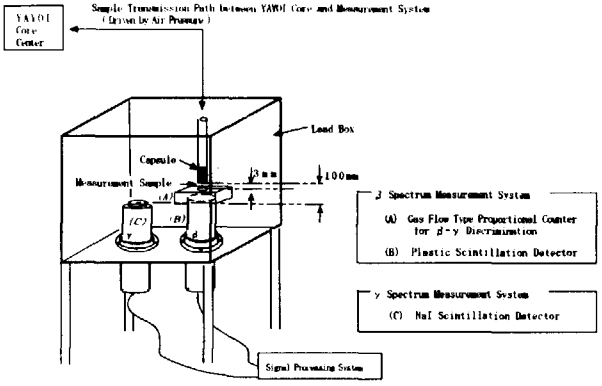

Fig.2 Conceptual View of Decay Heat Measurement System

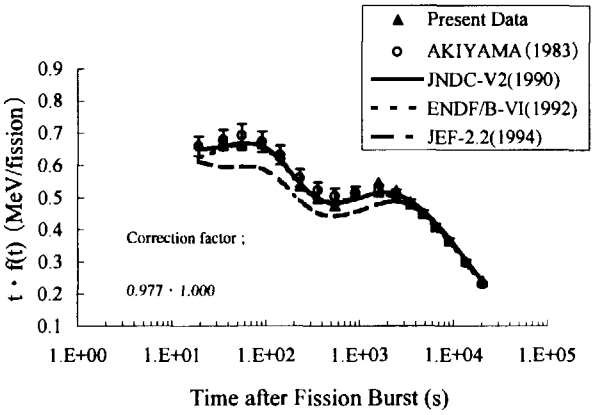

Fig. 3 Gamma Fission Burst Decay Heat for U-235

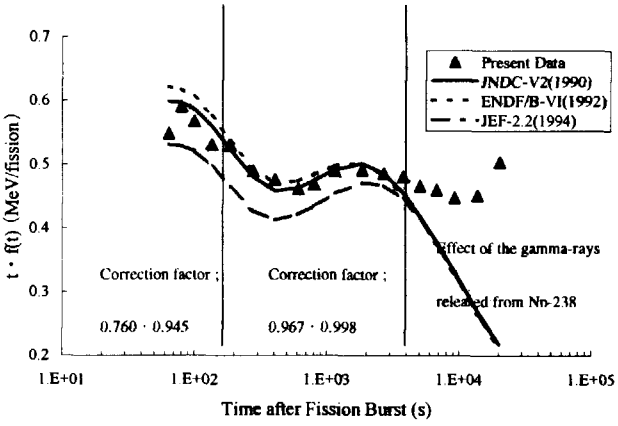

Fig. 4 Gamma Fission Burst Decay Heat for Np-237

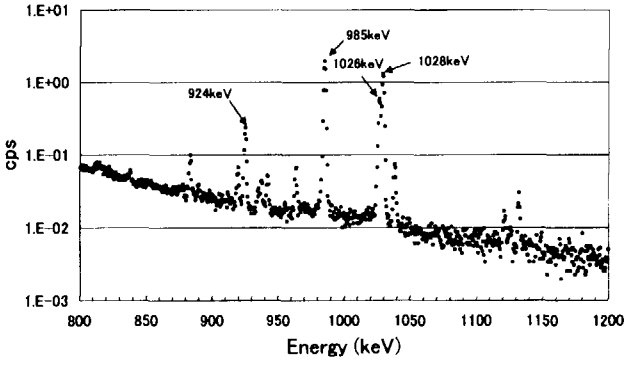

Fig. 5 Gamma spectrum of irradiated Np-237 by Ge detector

(about 56,000 seconds after irradiation)

JP0150664

3.2

Measurement of Resonance Integral of the $^{90}Sr(n, \gamma)^{91}Sr$ Reaction

Shoji NAKAMURA[1], Kazuyoshi FURUTAKA[1], Hiroaki WADA[1†], Toshiyuki FUJII[2], Hajimu YAMANA[2], Toshio KATOH[1,3] and Hideo HARADA[1]

1 Japan Nuclear Cycle Development Institute, Tokai works, Tokai-mura, Naka-gun, 319-1194

2 Research Reactor Institute, Kyoto University, Noda, Kumatori-cho, Sennan-gun, Osaka-fu, 590-0494

3 Gifu College of Medical Technology, Nagamine, Ichihiraga, Seki-shi, Gifu, 501-3892

† Present address: College of Science and Technology, 7-24-1 Narashinodai, Funabashi-shi, Chiba-ken 274-8501

E-mail: rgm@tokai.jnc.go.jp

To obtain fundamental data for research on nuclear transmutation method of radioactive wastes, the resonance integral (I_0) of the $^{90}Sr(n, \gamma)^{91}Sr$ reaction was measured with an activation method.

1. INTRODUCTION

Accurate data of the thermal neutron capture cross section (σ_0) and the resonance integral (I_0) are required for the research on nuclear transmutation of fission product (FP) nuclides with large fission yields and long half-lives, so that the present authors have measured the σ_0 and the I_0 of FP. ^{90}Sr is one of the most important nuclides in the low-level radioactive nuclear wastes, and remains for long period of time because of its long half-life (28.8 yr). However, the cross section data of ^{90}Sr have not been prepared sufficiently. There was only a value of upper limit on I_0 which was measured by Harada *et al.* in 1994 [1]. They measured σ_0 and I_0 of the $^{90}Sr(n, \gamma)^{91}Sr$ reaction by an activation method in the research reactor JRR-4 at JAERI. The upper limit of I_0, however, was only obtained in that experiment The reason for this is as follows: the ratio of the epithermal flux component to total neutron flux was so small (e.g. 0.033 ± 0.007 [1]) at the irradiation position in JRR-4 that the sufficient yields of ^{91}Sr were not obtained in case of the irradiation within a Cd capsule. It was found that it was possible to precisely measure I_0 of ^{90}Sr by using more harder neutron filed in Kyoto University Reactor (KUR) than that in JRR-4, and then the measurement of I_0 for the $^{90}Sr(n, \gamma)^{91}Sr$ reaction was planed once more.

2. EXPERIMENTS

$SrCl_2$ solution containing 3.7×10^5 (Bq) of ^{90}Sr was poured into a high purity quartz tube, which was 8mm in diameter and 100mm in length. $SrCl_2$ solution containing 900 (Bq) of ^{85}Sr was also added into the tube. Strontium-85 was used as a tracer for ^{90}Sr because ^{85}Sr was a γ-ray emitter. After drying of the solution, the tube was shaped into an

ampoule that was 25mm in length.

A target was constructed from the Sr ampoule and flux monitors, i.e. Co/Al and Au/Al alloy wires. Wires of Co/Al alloy (Co: 0.46 wt%, 0.381 mm in diameter) and Au/Al alloy (Au: 0.112 wt%, 0.510 mm in diameter) were used to monitor the neutron flux at the target position. Because ^{59}Co and ^{197}Au have different sensitivities to thermal and epithermal neutrons, these wires are adequate to determine the thermal and the epithermal fractions of neutron flux The amount of Co and Au contained in wires were determined by weight measurement in a microbalance.

The target was put into an Al capsule, and then the Al capsule was housed in an irradiation capsule. In the case of irradiation to measure I_0, the target was housed in a Cd capsule, which was 10mm in diameter, 26mm in length and 0.5mm in thickness. During the neutron irradiation, the Al capsule have two roles: **(a)** Target confinement and **(b)** heat removal of the Cd capsule. This was confirmed by a test irradiation with no target for 1 hour in hydraulic transfer tube of KUR. Irradiations in hydraulic transfer tube of KUR were performed for 10 hours without and within the Cd capsule, respectively. After the cooling for more than 12 hours, targets were pulled out from the irradiation capsules.

The chemical separations were accordingly performed to eliminate ^{24}Na nuclide from the Sr samples. The irradiated Sr targets was washed with 2.5 mol/l $(NH_4)_2SO_4$ solution, and then Sr nuclides were precipitated as a form of Sr_2SO_4. The Na nuclides were retained in the solvent solution, so that they were removed from the Sr precipitates with a filter, which was 25mm in diameter and 0.1μm in thickness. The filter was wrapped with a vinyl tape, and then used as a measurement sample.

A high purity Ge detector was employed to measure the γ rays from the irradiated targets and monitor wires. Its performance was characterized by a relative efficiency of 90 % to a 7.6 cm×7.6 cmϕ NaI(Tl) detector and an energy resolution of 2.1 keV full width at half-maximum(FWHM) at the 1.33 MeV peak of ^{60}Co. The peak detection efficiencies were calibrated with γ-ray sources, i.e. ^{152}Eu, ^{137}Cs and ^{22}Na, whose activities were well determined. Signals from the detector were fed to a fast data acquisition system, and γ-ray spectra data were recorded on a hard disk of a personal computer. Details of the data taking system were described elsewhere **[2]**. The measurement samples were mounted on the surface of the Ge detector. An example of γ-ray spectrum after the chemical processing was shown in **Fig. 1**. As seen in Fig.1, two γ rays revealed themselves around the energy points of 750 keV and 1024 keV. The γ-ray measurements were performed for about 12hours in the case of the irradiated Sr sample within the Cd capsule and for about 15hours in the case of that without the Cd capsule. Spectra data were saved every 3 hours to confirm whether observed γ rays were originated in ^{91}Sr or not. **Fig. 2** shows the decay curves for the counts from the 1024 keV γ-ray peak. The half-life was found to be 9±1(h), which was in agreement with the evaluated half-life value of ^{91}Sr (9.63 h **[3]**) within the limit of errors. Therefore, it was confirmed that the 1024 keV γ ray has originated from ^{91}Sr.

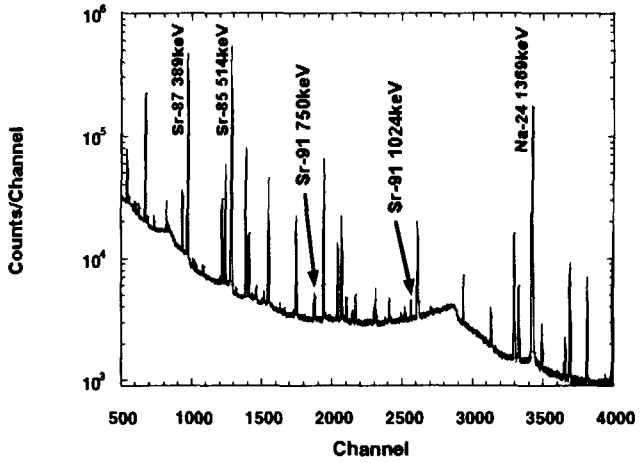

Fig.1 Gamma-ray spectrum of Sr after chemical procedure

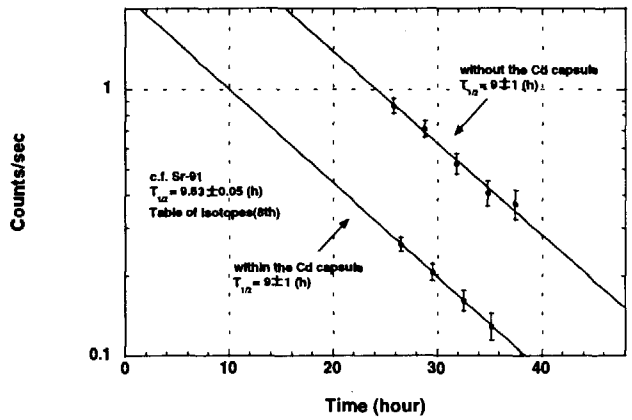

Fig. 2 Decay curves of 1024keV γ-ray emitted form ^{91}Sr

3. ANALYSIS

Since the details of the method that we used to determine the thermal cross section and resonance integral were described elsewhere, here a brief outline of the analysis is only presented.

Westcott's convention **[4]** can be rewritten by using simplified flux notation as follows:

$$R/\sigma_0 = \phi_1 G_{th} + \phi_2 s_0 G_{epi}, \quad (1)$$

for irradiation without a Cd shield capsule,

$$R'/\sigma_0 = \phi_1' G_{th} + \phi_2' s_0 G_{epi}, \quad (2)$$

for irradiation with a Cd shield capsule. Here, the R (or R') is the reaction rate and σ_0 the thermal neutron (2,200m/s neutron) capture cross section; ϕ_1 and ϕ_1' are neutron flux components in the thermal energy region, and ϕ_2 and ϕ_2' are those in the epithermal energy region. The neutron flux components were obtained with flux monitors. The results of the neutron fluxes were listed in **Table 1**.

Table 1 Neutron flux measured in Hydraulic Transfer tube at KUR

	ϕ_1 or ϕ_1' (10^{14} n/cm^2 · sec)	ϕ_2 or ϕ_2' (10^{13} n/cm^2 · sec)
without the Cd	ϕ_1=1.063 ±0.007	ϕ_2=0.243±0.004
within the Cd	ϕ_1' =0.033±0.001	ϕ_2' =0.404±0.001

The G_{th} and G_{epi} are self-shielding factors to thermal and epi-thermal neutrons, respectively. The G_{th} and G_{epi} are unity in the following analysis in current target conditions. The s_0 is the parameter defined by

$$s_0 = \frac{2}{\sqrt{\pi}} \frac{I_0'}{\sigma_0}, \tag{3}$$

where I_0' is the reduced resonance integral, i.e. the resonance integral after subtracting the 1/υ components. The resonance integral I_0 is calculated as follows:

$$I_0 = I_0' + 0.45\sigma_0, \tag{4}$$

where $0.45\sigma_0$ is the 1/υ contribution given by assuming the Cd cut-off energy to be 0.5eV.

Eqs.(1) and (2) give the relation,

$$s_0 = -\frac{\phi_1 - \phi_1'(R/R')}{\phi_2 - \phi_2'(R/R')}, \tag{5}$$

so that the value of s_0 is obtained from R/R' value of each irradiated target. The σ_0 is derived by substituting the s_0 into Eq.(1), and then the values of I_0' and I_0 are calculated from Eqs.(3) and (4).

4. PRELIMINARY RESULTS AND DISCUSSION

Reaction rates were obtained from the 1024 keV γ-ray count data, and listed in **Table 2.**

Table 2 Preliminary results of reaction rates and cross sections of ^{90}Sr(n,γ)^{91}Sr reaction

Irradiation Type	Chemical yield	^{90}Sr(n,γ)^{91}Sr reaction			
		Reaction rates (1/s)	σ_0 (mb)	s_0	I_0 (mb)
Without the Cd capsule	0.836±0.110	1.559±0.215 ×10^{-12}	**11.7±1.7**	**11.2±2.3**	**121±29**
Within the capsule Cd	0.770±0.025	5.678±0.310 ×10^{-13}			
References:					
[1] Harada *et al.*			15.3± $^{1.3}_{4.2}$	≤11	≤160
[5]Zeisel			800±50		
[6]McVey *et al.*			14.0±2.4		
[7]Lone et al.			9.7±0.7		

With the experimental results of the reaction rates and neutron flux, quantity s_0 was derived from Eq.(5), and then the resonance integral was obtained by s_0, and Eq.(3) and (4). The present result for the resonance integral of ^{90}Sr was

found to be 121±29 (mb). By substituting s_0 into Eq.(1), the thermal neutron capture cross section was obtained as 11.7±1.7 (mb). The present results were summarized in Table 2 together with the evaluated data.

The present result for I_0 was found to be 121±29 (mb), and it was within the upper limit reported in Ref.[3]. The neutron capture cross section was also reported in Ref.[3] as 15.3±1.3 (mb) assuming the quantity s_0 was zero. The σ_0 can be estimated from this value and the present result for s_0, the σ_0 was obtained as 11.2±1.3 (mb). This value was in good agreement with the present result, σ_0 = 11.7±1.7 (mb), within the limit of errors. It was found that the present results were consistent with those in Ref. [3].

5. CONCLUSION

To obtain fundamental data for research on nuclear transmutation method of radioactive wastes, the resonance integral of the $^{90}Sr(n, \gamma)^{91}Sr$ reaction was measured with an activation method. However, there is still a problem which is to perform the chemical procedure more precisely, therefore it should be note that these results were only preliminary ones.

ACKNOWLEDGMENTS

The authors would like to appreciate S. Nishikawa and K. Miyata of the Research Reactor Institute, Kyoto University for their cooperation. The authors wish to Prof. H. Moriyama of Kyoto University for their interest and encouragement during this work

This work has been carried out in part under the Visiting Researcher's Program of the Research Reactor Institute, Kyoto University.

REFERENCES

[1] Harada, H., Sekine, T., Hatsukawa, Y., Shigeta, N., Kobayashi, K., Ohtsuki, T., Katoh, T.: *J. Nucl. Sci. Technol.*, 31, 173 (1994).

[2] Harada, H., Nakamura, S., Katoh, T., Ogata, Y.: *J. Nucl. Sci. Technol.*, **32**, 395 (1995).

[3] Firestone, R. B., Shirley, V. S.(ed.): "*Table of Isotopes*" ,8th ed., John Wiley & Sons, New York, (1996).

[4] Westcott, C. H., Walker, W. H., Alexander,T. K.: "*Proc. 2nd Int. Conf. Peaceful Use of Atomic Energy, Geneva*", United Nations, New York, vol. **16**, 70 (1958).

[5]Zeisel, G.: *Acta. Ohys. Austr.*, **23**, 5223 (1996).

[6]McVEY, L.A., Brodzinski, R.L. and Tanner, T.M.: *J. Radioanal. Chem.*, **76**, 131 (1983).

[7]Lone, L.A., Edwards, W.J. and Collins, R: *Nucl. Instr. Meth.*, **A332**, 232 (1993).

JP0150665

3.3

Measurement of the Thermal Neutron Capture Cross Section andthe Resonance Integral of the $^{109}Ag(n,\gamma)^{110m}Ag$ Reaction

S. NAKAMURA[1], H.Wada[1†], K.Furutaka[1], H. HARADA[1] and T. KATOH[1,2]

1 Japan Nuclear Cycle Development Institute, Tokai Works, Tokai-mura, Naka-gun, 319-1194

2 Visiting staff at Gifu College of Medical Technology, Ichihiraga, Seki, 501-3892

† Present address: College of Science and Technology, Nihon University, Narashinodai, Funabashi-shi, Chiba

E-mail: rgm@tokai.jnc.go.jp

The thermal neutron capture cross section (σ_0) and the resonance integral (I_0) of the $^{109}Ag(n,\gamma)$ reaction were measured by the activation and γ-ray spectroscopic methods to develop a neutron flux monitor for the long irradiation.

1. Introduction

To know neutron fluxes by multi neutron flux monitors, the cross section data of monitors are needed to be precisely measured. The nuclides, ^{197}Au and ^{59}Co, are popularly used as monitors because their cross sections are well known. However, the daughter nuclide ^{198}Au after neutron irradiations have short half-live as 2.69 days, therefore it is not adequate to use ^{197}Au as the flux monitor in the long neutron irradiation. If there are some nuclides which have longer half-lives than that of ^{198}Au and have the same sensitivities to epi-thermal neutrons as that of ^{198}Au, they can be used as flux monitors. Then, ^{109}Ag was one of candidates for flux monitors instead of ^{197}Au. Its daughter nucleus ^{110m}Ag has relatively long half-life as 249.9 day, and also the intensities of γ-rays emitted from ^{110m}Ag are precisely obtained. The reported data of ^{109}Ag cross section are σ_0=4.7$\pm$0.2 (b) and I_0=72.3$\pm$4.0 (b), of which errors are large. To develop the neutron flux monitors for the long irradiation, the σ_0 and I_0 of ^{109}Ag were measured precisely.

2. Brief Outline of Analysis

Since the details of Westcott's convention [1] that we used to determine the cross sections and neutron fluxes were described elsewhere [2], here we present only a brief outline of the analysis. Equations based on Westcott's convention can be rewritten by using simplified flux notation [2] as follows:

$$R/\sigma_0 = \phi_1 G_{th} + \phi_2 s_0 G_{epi}, \quad (1)$$

for irradiation without a Cd shield capsule,

$$R'/\sigma_0 = \phi_1' G_{th} + \phi_2' s_0 G_{epi}, \quad (2)$$

for irradiation with a Cd shield capsule. Here, the R (or R') is the reaction rate and σ_0 the thermal neutron (2,200m/s neutron) capture cross section; ϕ_1 and ϕ_1' are neutron flux components in the thermal energy region, and ϕ_2 and ϕ_2' are those in the epithermal energy region. The neutron flux components were obtained with flux monitors. The G_{th} and G_{epi} are self-shielding factors to thermal and epi-thermal neutrons, respectively. The G_{th} and G_{epi} were estimated as 0.9985 and 0.9236, respectively. In this analysis, the parameters for 0K were used to calculate the factors G_{th} and G_{epi}. The s_0 is the parameter defined by

$$s_0 = \frac{2}{\sqrt{\pi}} \frac{I_0'}{\sigma_0}, \quad (3)$$

where I_0' is the reduced resonance integral, i.e. the resonance integral after subtracting the 1/υ components. The resonance integral I_0 is calculated as follows:

$$I_0 = I_0' + 0.45\sigma_0, \tag{4}$$

where $0.45\sigma_0$ is the 1/υ contribution given by assuming the Cd cut-off energy to be 0.5eV.

Eqs.(1) and (2) give the relation,

$$s_0 = -\frac{\phi_1 - \phi_1'(R/R')}{\phi_2 - \phi_2'(R/R')} \cdot \frac{G_{th}}{G_{epi}}, \tag{5}$$

so that the value of s_0 is obtained from R/R' value of each irradiated target. The σ_0 is derived by substituting the s_0 into Eq.(1), and then the values of I_0' and I_0 are calculated from Eqs.(3) and (4).

3. Experiment

The cross section measurements were performed by the activation and γ-ray spectroscopic methods.

Targets were high purity(99.97%) Ag foils which were 0.001mm in thickness to reduce effects of impurities and self-shielding. The target amount was 1mg. The neutron irradiation was performed at rotary specimen rack(RSR) in Rikkyo Univesity Reactor. The irradiation of the Ag foil was performed for 1 hour, and for 5hours within a Cd capsule. The Cd capsule was 20mm in diameter, 26mm in length and 1mm in thickness. The wires of 0.112wt% Au/Al alloy (0.510mm in diameter) and 0.46wt% Co/Al alloy (0.381mm in diameter) were irradiated together with the Ag targets to monitor the neutron flux at the target position. The method of measuring the neutron flux was the same as that for the cross section measurements. Using the well-known data of both the cross sections σ_0 and the parameter s_0 for cobalt and gold, the values of the flux terms, i.e. $\phi_{1,2}$ and $\phi'_{1,2}$, were determined by solving the simultaneous equations for cobalt and gold from Eqs. (1) and (2) in Sec.2. For example, **Table 1** summarizes the experimental results of the neutron fluxes in the case of Rikkyo Reactor together with the R and R' values of the flux monitors.

Table 1 Neutron fluxes at RSR in Rikkyo University reactor

	ϕ_1 of ϕ_1'	ϕ_2 of ϕ_2'
	(10^{11} n/cm^{2}sec)	
Without Cd	5.19±0.09	0.175±0.004
Within Cd	0.149±0.005	0.196±0.004

The yields of γ-rays emitted from the irradiated targets were measured by a high purity Ge detector with a 90% relative efficiency to a 7.6cm×7.6cmφ(NaI) detector and an energy resolution of 2.1keV FWHM at 1.33MeV of ^{60}Co. The details of the data taking system were described elsewhere [2]. An example of the gamma-ray spectrum is shown in **Figure 1**.

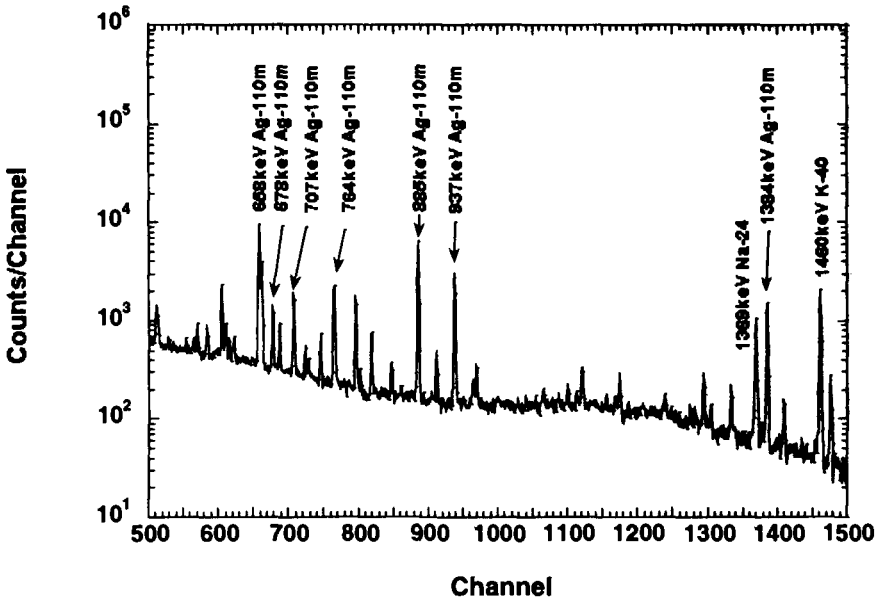

Fig. 1 Gamma-ray spectrum of Ag target irradiated without the Cd capsule

As can be seen in Fig.1, the 7 γ-rays originated from ^{110m}Ag, 658, 678, 707, 764, 885, 937 and 1384 keV γ-rays, were clearly measured These g-ray yields were used to calculated the reaction rates of the ^{109}Ag(n,γ)^{110m}Ag reaction.

4. Results and Discussion

The cross sections of ^{109}Ag were derived from the measured γ-ray yields based the Westcott's convention. The results obtained in this work are summarized in **Table 2** together with the previously reported data[3-9].

The σ_0 was 14% smaller than evaluated one, but the I_0 was in agreement with the evaluated one within the limits of error. The data of σ_0 were reported as 3~6 (b) for the period of 1960 - 70. The present adapted one(4.7±0.2(b)) might be evaluated from these data. F. D. Corte et al.[4] re-measured the cross sections of ^{109}Ag, and obtained 3.90 (b) for σ_0. Their result was in agreement with our result within the limit of error.

Table 2 Results of σ_0 and I_0 and the previously reported data

Authors	σ_0 (b)	s_0	I_0 (b)	$Q=I_0/\sigma_0$	Ref.
Present result	4.13±0.08	18.4±0.7	69.2±3.0	16.8±0.9	
HOLDEN('81)	4.7 ±0.2		72.3±4.0		[3]
CORTE('89)	3.90±0.08		69	17.5	[4]
RAO('78)	4.5 ±0.7				[5]
RYVES('71)	4.72±0.21				[6]
SIMS('68)	4.98±0.47				[7]
KEISH('63)	3.20±0.50				[8]
LYON('60)	5.78±0.58				[9]

5. Conclusions

To develop the flux monitor for the long irradiation, the cross section of ^{109}Ag were measured with the activation method. The σ_0 and I_0 for the $^{109}Ag(n,\gamma)^{110m}Ag$ reaction were obtained as 4.13±0.08(b) and 69.2±3.0(b), respectively. The sensitivities to the epi-thermal neutrons was estimated to be s_0=18.4, which was closed to 17.22 of ^{197}Au. It conclude that the ^{109}Ag is applicable to the flux monitor for the long irradiation instead of ^{197}Au monitor. However, it should be note that the problems remained is to evaluate the self-shielding factors more precisely.

Acknowledgments

The authors wish to acknowledge their indebtedness to the crew of both the Rikkyo Research Reactor for their cooperation.

This work was supported by JNC and Inter-University Program for the Joint Use of Rikkyo University Reactor, and by the Grant-in-Aid for Scientific Research of the Ministry of Education, Science and Culture.

References

[1] Westcott C.H., Walker W.H., Alexander T.K.: *Prc. 2nd Int. Conf. Peasuful Uses of Atomic Energy, Geneva*, Vol.**16**, 70 (1958).

[2] Harada H., Nakamura S., Katoh T. and Ogata Y.: Journal of Nuclear Science and Technology, Vol.**32**, 395 (1995).

[3] Mughabghab S.F., Divadeenam M., Holden, N.E.: "*Neutron Cross Sections*", Vol.**1**, (1981), Academic Press, New York.

[4] Corte F.DE and Simonits A.: Journal of Radioanalytical and Nuclear Chemistry, Articles, Vol.**133**, 43 (1989).

[5] Rao D.V., Govelitz G., Mallams J.: International Journal of Applied Radiation and Isotopes, Vol. **29**, 405 (1978).

[6] Ryves T.B.: Journal of Nuclear Energy, Vol.**25**, 129 (1971).

[7] Sims G.H and Juhnke D.G.: J. inorg. Chem., Vol.**30**, 349 (1968).

[8] Keish B.: Physical Review, Vol **129**, 769 (1963).

[9] Lyon W.S.: Nuclear Science and Engineering, Vol.**8**, 378 (1960).

JP0150666

3.4

Evaluation of Neutron Cross Sections for Er Isotopes

A.K.M. HARUN-AR-RASHID, K. SHIBATA[1] and M. IGASHIRA[2]

Department of Physics, University of Chittagong, Chittagong 4331, Bangladesh.

[1]Nuclear Data Centre (NDC), Japan Atomic Energy Research Institute (JAERI), Tokai-mura, Naka-gun, Ibaraki-ken, Japan.

[2]Research Laboratory for Nuclear Reactors, Tokyo Institute of Technology O-okayama, Meguro-ku, Tokyo, Japan.

Abstract:

The neutron reaction cross sections of ^{166,167,168,170}Er from 10^{-5} eV to 20 MeV were studied. The cross sections were calculated with a variety of nuclear-reaction models by different codes. The calculations were mainly based on the statistical and optical modes. In the calculation, the Optical Model Parameters (OMP) for ^{nat}Er were determined. The calculated capture cross sections are in good agreement with the very recent measurements. The calculated total cross sections of ^{166,168,170}Er are also in good agreement with the experimental results at 14 MeV. The direct inelastic scattering cross sections for the first excited state of the above nuclei were calculated by Distorted-Wave Born-Approximation (DWBA). The direct and semi-direct (DSD) capture cross sections were also calculated. The pre-equilibrium correction was done. The parameters for the electric-dipole pygmy resonance and the depression factor were extracted from a comparison between the calculated and very recent observed capture gamma-ray spectra. The other cross sections, such as (n,n'), (n,2n) and (n,p) reactions and, the emitted-particle (n,p,d, etc.) spectra from these reactions were also calculated. In the thermal and resonance region, the total, elastic scattering and capture cross sections were derived from the resonance parameters.

1. Introduction:

The study of neutron reaction cross sections is important in many fields, especially neutron capture cross section is important in nuclear engineering, nuclear physics and nuclear astrophysics. The neutron capture cross sections are necessary for the studies on neutron capture reaction mechanism and nuclear modes of excitation. However, Er is proposed as one of the burnable poisons in the thermal nuclear reactors, but there is a scarcity of neutron cross section data. JENDL 3.2 has no evaluated data for Er isotopes, however, ENDF/B-VI has data for ^{166,167}Er only, but the evaluation was done many years ago [Wri+90]. Other reaction cross sections data are necessary for many researches. Therefore, the aim of the present study is to supply new evaluated data.

2. Evaluation of Neutron Cross Sections from Resonance Parameters

2.1. Evaluation Method

The Multi-level Breit-Wigner (MLBW) formula was adopted to calculate the cross sections in the resolved resonance region. In this energy region, only elastic scattering and radiative capture are possible for Er isotopes. Therefore, the total cross section must be equal to their sum. In order to calculate the total, elastic and radiative capture cross sections in the resolved resonance region, the computer program RECENT [Cul 96] was used. RECENT can calculate neutron energy dependant cross sections from the resonance parameters. In the thermal region, the same method as in the resolved resonance region was adopted. Therefore, negative-energy resonances were assumed for ^{166,168,170}Er isotopes so as to reproduce the experimental cross sections at thermal energy. The cross sections in the thermal and resolved resonance regions were calculated from the resonance parameters taken from the recent compilation of Landolt-Bornstein New Series I/16B [Suk+98]. As for the scattering radii, the recommended values of Mughabghab [Mug 84] were employed, but a small modification within the given error was made so as to reproduce the experimental thermal neutron scattering cross sections.

In the unresolved resonance region, the Single-Level Breit-Wigner (SLBW) formula with the average resonance parameters was used to calculate infinitely dilute average cross sections.

3. Statistical Model Calculation

3.1 Optical Potential

In any optical model calculations, the optical model parameters (OMPs) are important. However, no study has been performed on the OMPs of Er isotopes. Therefore, assuming the same OMPs for the individual Er isotopes, a new set of OMPs for ^{nat}Er was searched by using the total cross section data of ^{nat}Er. Figure 1 shows the total cross sections of ^{nat}Er calculated by CASTHY [Iga 75] with the newly searched set of OMPs, together with the experimental data. The calculated results with the global OMP sets of Moldauer [Mol 63] and Modified Walter-Guss [Yam 90, Wal+86] are also shown in the figure. It is clearly seen from Fig. 1 that the calculations with the present OMP set are in good agreement with the experiments in the region of 10 keV to 20 MeV. The new set of OMP is shown in Table 1.

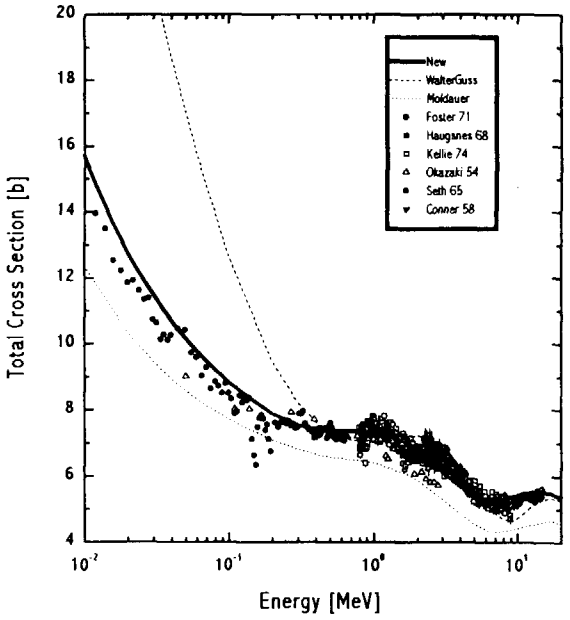

Fig 1. Calculated and experimental total cross sections of ^{nat}Er.

Table 1 Present Optical Model Parameters

$$V_0 = 48.2 - 0.25E - 16.0\frac{N-Z}{A} \qquad W_s = 7.84 + 0.51E$$

$$V_{so} = 6.0 \qquad a_R = a_s = a_{so} = 0.63$$

$$r_R = 1.18 \qquad r_s = 1.29 \qquad r_{so} = 1.26$$

Table 2. Reaction Processes, Reaction Models, and Computer Programs used in the present calculation.

Reactions	Processes	Models[†1]	ComputerPrograms
Total	-	-	CASTHY
Elastic	Shape	-	CASTHY
	Compound	Statistical	CASTHY
Capture	Compound	Statistical	CASTHY
	Direct & Semi-direct	Exciton Decay	GNASH
Inelastic	Compound	Statistical	GNASH
	Pre-equilibrium	Exciton Decay	GNASH
	Direct	DWBA	DWUCKY
Other Reactions	Compound	Statistical	GNASH
	Pre-equilibrium	Exciton Decay	GNASH

[†1] Models other than the optical model.

3.2 Calculational Method

The calculations of neutron reaction cross sections of ^{166,167,168,170}Er were performed above the resonance region with a variety of nuclear-reaction models. Table 2 shows the nuclear-reaction models and the computer codes employed in the present calculations. The statistical model is adopted in both CASTHY and GNASH [You+92]. GNASH implements Hauser-Feshbach theory in an open ended sequence of reaction chain.

The pre-equilibrium process is important for the emission of relatively high-energy particle. Therefore, in the calculation of the inelastic scattering cross section, the pre-equilibrium process was taken into account in addition to the statistical process. Those processes were simultaneously treated with GNASH using an exciton model [Kal 74, Kal 85]. Above several MeV, the direct and semi-direct capture mechanism becomes dominant in the capture reaction. In the calculations the direct and semi-direct capture model as well as the statistical model were taken into account. GNASH was used to estimate the direct and semi-direct capture cross section. GNASH adopts the pre-equilibrium photon decay model, which gives a simple estimate of the direct and semi-direct capture cross section.

In the present study, the cross section of the direct inelastic scattering to the first excited state of each Er isotope was calculated with the computer program DWUCKY [Yam+88, Kun+92].

4 Results and Discussion

Figures 2-5 show the presently evaluated results for the neutron cross sections of ^{166,167,168,170}Er, respectively. In the figures, the (a) total, (b) elastic scattering, and (c) capture cross sections are shown. The previous experimental results, the recommended values at thermal energy, and the ENDF/B-VI evaluations are also shown in the figures. The present evaluations for the elastic scattering and capture cross sections of each isotope well reproduce the recommended values at thermal energy as shown in Figs. 2-5. As for the total cross sections at thermal energy, the experimental results contain the paramagnetic scattering [Mug 84] component (about 20 b), and those of ^{166,168,170}Er are much larger than the evaluated results. The experimental results for ^{167}Er also contain the component, but the difference between the evaluation and experiments is not seen in Fig. 3(a) because of the large total cross section.

Vertebnyj *et al.* [Ver+65] measured the total and elastic scattering cross sections at the average energy of 2 keV for the Er isotopes. However, it is difficult to compare the present evaluations with their results for ^{166,168,170}Er, because the resolved resonance regions continue up to several keV. As for ^{167}Er, the unresolved resonance region starts around 0.6 keV, and the present evaluation reproduces their results, as shown in Fig . 3.

A significant difference is seen in the region of 100 to 300 eV for ^{166}Er between the present and ENDF/B-VI evaluations as shown in Fig. 2(a). It is caused by new resonances around 200 eV adopted in the present evaluation. A small difference is also seen in the unresolved resonance region for the total and elastic scattering cross sections of ^{167}Er.

The evaluation with the average resonance parameters was performed only for ^{167}Er whose upper boundary of the resolved resonance region is around 600 eV. It is seen in the figure that the present results give better agreement with the measurement of Vartebnyj *et al.* at 2 keV than the ENDF/B-VI evaluation. For the other isotopes whose upper boundaries are around several keV, the results from the nuclear-reaction model calculations were directly adopted even in the unresolved resonance region.

In the calculations with CASTHY, the E1 γ-ray strength functions were adjusted so as to reproduce the very recent experimental capture cross sections [Har+00] at 31 keV: 0.717 b for ^{166}Er, 1.50 b for ^{167}Er, 0.239 b for ^{168}Er. As for ^{170}Er, the capture cross section measured by Stupegia *et al.* [Stu+68] was adopted for the normalization: 0.275 b at 30.08 keV.

The calculated capture cross sections for ^{166,167,168}Er are in good agreement with the very recent experimental results [Har+00] in the region of 10 to 90 keV because of normalization. The calculation by CASTHY also well reproduces the same measurements at 550 keV for ^{166,167,168}Er. As for ^{170}Er, the calculated capture cross sections seem to rapidly decrease from about 1.5 MeV compared to the experimental data, although experimental data largely scatter above 0.8 MeV. It is worth noting that all experiments for ^{170}Er except for that of Kononov *et al.* [Kon+77] were performed with activation methods. The calculated cross sections suddenly decrease around 80 keV in Figs. 2-5. It is due to the inelastic neutron scattering to the first excited states of the target Er nuclei. It is seen from Figs. 2-5 that the direct and semi-direct capture component becomes dominant above a few MeV.

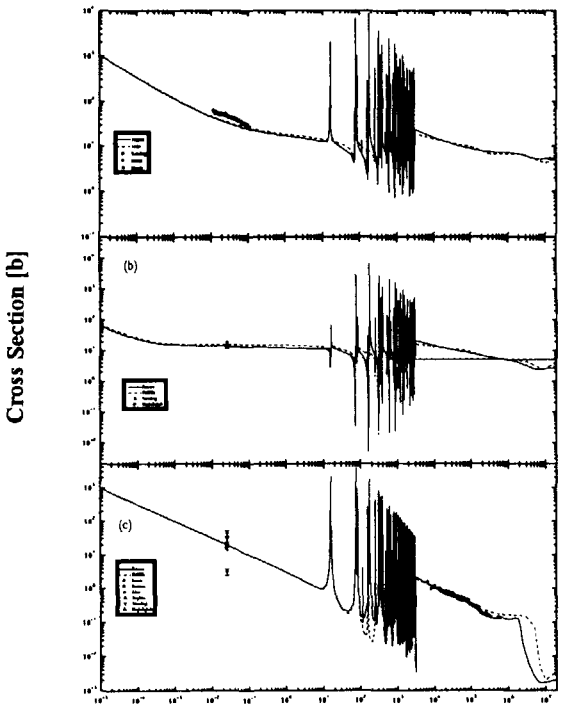

Fig. 2 Cross sections of ^{166}Er in the thermal and resonance regions: (a) Total, (b) Elastic and (c) Capture. The solid and dotted lines represent the present and ENDF/B-VI evaluations, respectively.

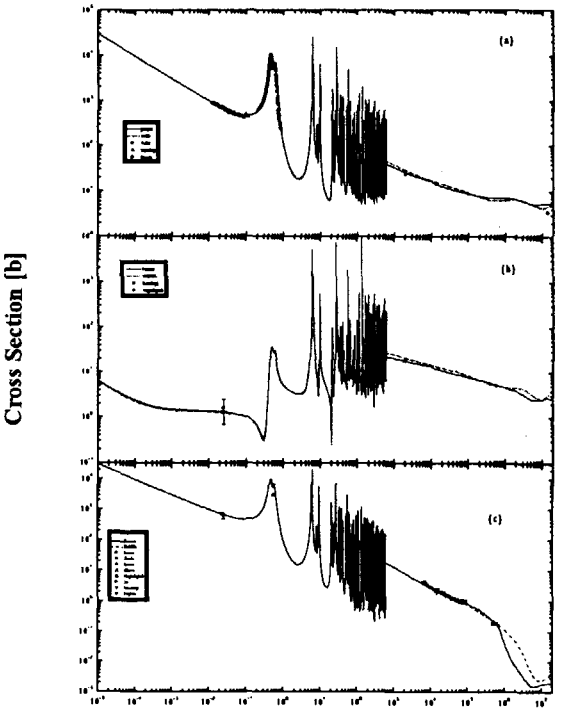

Fig. 3 Cross sections of ^{167}Er in the thermal and resonance regions: (a) Total, (b) Elastic and (c) Capture. The solid and dotted lines represent the present and ENDF/B-VI evaluations, respectively.

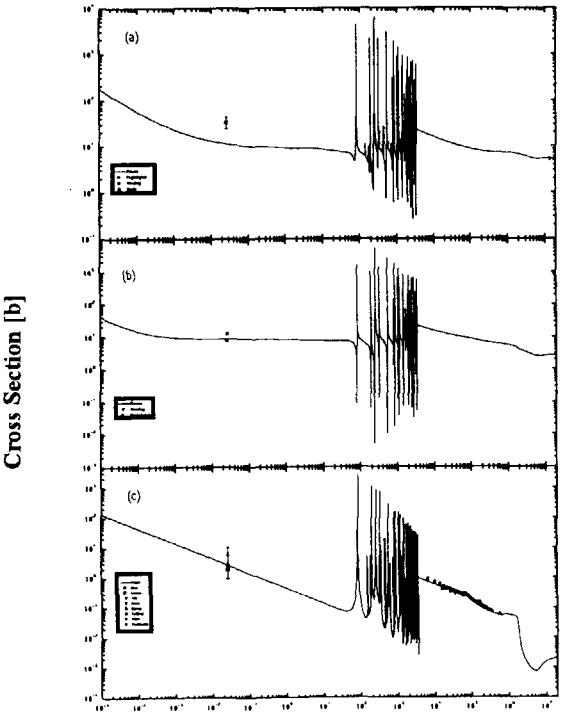

Fig. 4 Cross sections of ^{168}Er in the thermal and resonance regions: (a) Total, (b) Elastic and (c) Capture. The solid and dotted lines represent the present and ENDF/B-VI evaluations, respectively.

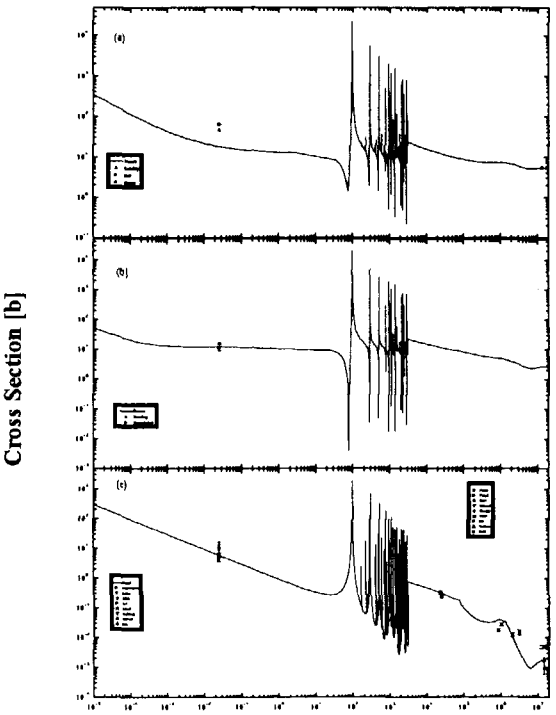

Fig. 5 Cross sections of ^{170}Er in the thermal and resonance regions: (a) Total, (b) Elastic and (c) Capture. The solid and dotted lines represent the present and ENDF/B-VI evaluations, respectively

The ENDF/B-VI evaluation for ^{166}Er is similar to the present calculations below 1.5 MeV, but is much larger than the present calculation above 2 MeV. As for ^{167}Er, the ENDF/B-VI evaluation is similar to the present calculation below 0.7 MeV, but is much larger above 1 MeV.

The experimental total cross sections results of Djumin *et al.* [Dju+77] at 14.2 MeV are in good agreement with the present calculations for ^{166,168,170}Er. As for ^{167}Er, the experimental value is about 35 % smaller than the present calculation. There is no reason why the total cross section of ^{167}Er is so small compared to the other isotopes. The ENDF/B-VI evaluations are based on the optical model calculation with a global OMP set, and are considerably different from the present calculations with the newly determined OMP set.

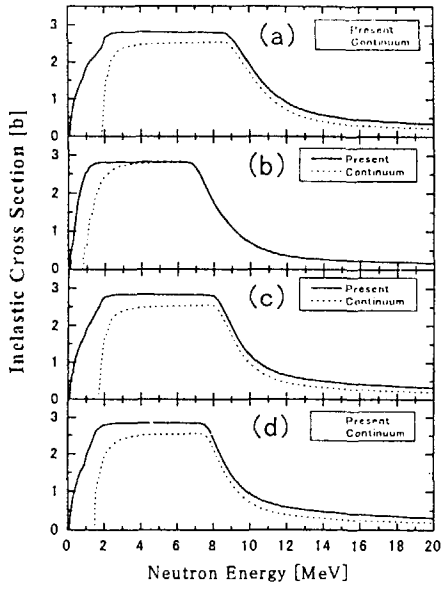

Fig. 6 Calculated inelastic scattering cross sections (solid lines of (a) ^{166}Er, (b) ^{167}Er, (c) ^{168}Er and (d) ^{170}Er. The dotted lines show the contributions of continuum levels.

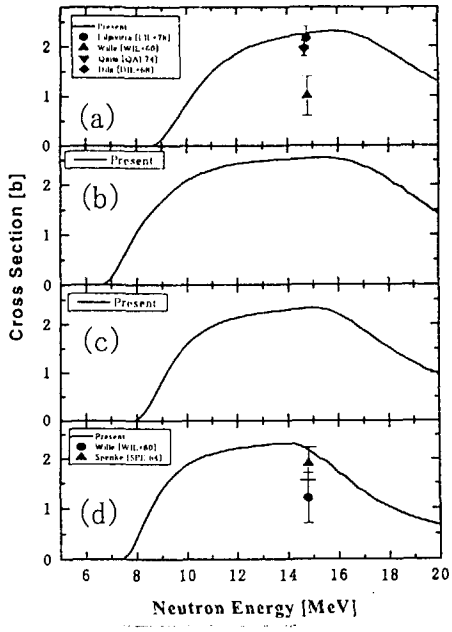

Fig. 7 Calculated (n,2n) reaction cross sections (a) ^{166}Er, (b) ^{167}Er, (c) ^{168}Er and (d) ^{170}Er. The experimental data are also shown.

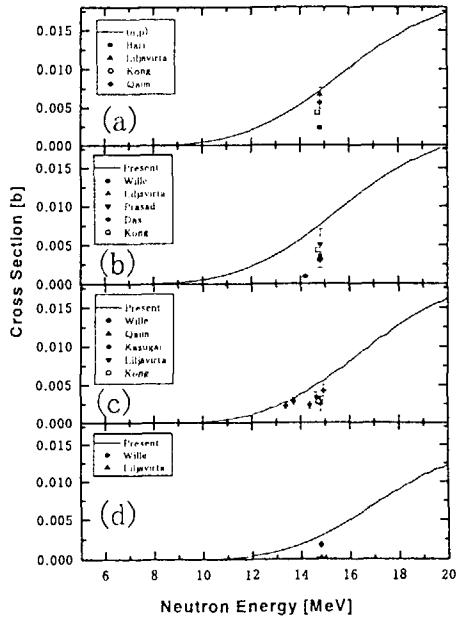

Fig. 8 Calculated (n,p) reaction cross sections (a) ^{166}Er, (b) ^{167}Er, (c) ^{168}Er and (d) ^{170}Er. The experimental data are also shown.

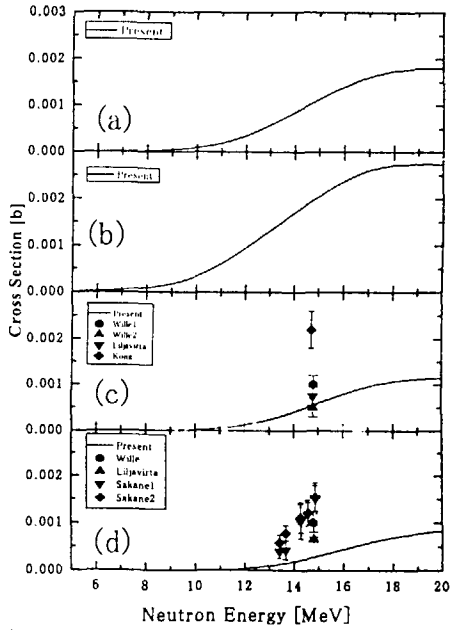

Fig. 9 Calculated (n,α) reaction cross sections (a) ^{166}Er, (b) ^{167}Er, (c) ^{168}Er and (d) ^{170}Er. The experimental data are also shown.

There are no experimental data for the elastic scattering cross sections of Er isotopes in the MeV region. Figure 6 shows the inelastic scattering cross sections (solid lines) of ^{166,167,168,170}Er, together with the contributions (dotted lines) of continuum levels. The inelastic scattering cross section rapidly increases from the threshold energy, and reaches a constant value around a few MeV. Then, it decreases above the threshold energy of the (n,2n) reaction.

The calculated (n,2n) cross sections of ^{166,167,168,170}Er are shown in Fig. 7 and compared with a few experimental results. The experimental result of Liljavirta *et al.* [Lil+78] for ^{166}Er is in good agreement with the present calculation, and that of Spenke [Spe 64] for ^{170}Er is in agreement with the present calculation within the experimental error. The (n,2n) cross section rapidly increases from the threshold energy, reaches the maximum value around 2.5 b and then decreases.

The calculated (n,p) reaction cross sections are shown in Fig. 8 and compared with experimental results around 15 MeV. The calculated results are somewhat larger than the experimental results.

In Fig. 9 the calculated (n,α) reaction cross sections are compared with experimental results around 15 MeV. The calculated results are somewhat smaller than the experimental results.
It is seen from Figs. 6-9 that the cross sections of charged particle emission reactions are much smaller compared to those of neutron emission reactions such as (n,n') and (n,2n) reactions.

5 Conclusion

The neutron reaction cross sections of the major Er isotopes, ^{166,167,168,170}Er, were studied in the incident neutron energy region of 10^{-5} eV to 20 MeV.

The following conclusions are made:

(1) the optical model parameters for ^{nat}Er were firstly determined so as to reproduce the total cross sections of ^{nat}Er,
(2) the calculated total cross sections of all major Er isotopes except for ^{167}Er were in agreement with the experimental results at 14 MeV,
(3) the calculated capture cross sections of ^{166,167,168}Er in the keV region were in good agreement with the very recent measurements,

In the thermal and resonance regions, the evaluations of the cross sections of ^{166,167,168,170}Er were also performed. A negative-energy resonance was introduced for each of ^{166,168,170}Er to reproduce the experimental values at thermal energy.

In conclusion, the present results are thought to be very useful for many research fields. Therefore, the present results should be contained in the next version of Japanese Nuclear Data Library, JENDL-3.3, in order to provide the numerical data for worldwide researchers in many fields.

References

Cul 96: Cullen, D. E.: *"The 1996 ENDF Pre-processing Codes",IAEA-NDS-39, Rev. 9,* 1996.
Dju+77: Djumin, A.N. *et al.; Proc. 4th All Uni. Conf. On Neutron Physics, Kiev. USSR 18-22 April,* 1977.
Har+00: Harun-ar-Rashid, A.K.M. *et al. J. Nucl. Sci. Tech.*, **37**, 421, 2000.
Iga 75: Igarasi, M. *et al. Nucl. Phys.* **A457**, 301, 1986.
Kal 85: Kalbach, C. *Phys. Rev.* **C32**, 1157, 1985.
Kon+77: kononov, V. N. *et al. Yad. Fiz.* , **26**, 947 1977.
Kun 92: Kunz, P. D. *Computational Nuclear Physics 2: Published by Springer-Verlag,* 1992.
Lil+68: Liljavirta, H. *et al. J. Physica Scripta* **18,** 75, 1978. EXFOR 20860
Mol 63: Moldadauer, P.A. *Nucl. Phys.*, **47**, 65, 1963
Mug 84: Mughabghab, S.F. *et al. Phys. Rev.* **162**, 1130, 1967.
Spe 64: Spenke, H. *Nucl. Phys.*, **51**, 329, 1964. EXFOR 20058
Stu+68: Stupegia, D.C. *et al. J. Nucl. Energy.*, **22**, 267, 1968.
Suk+98: Sukhoruchkin, S. I. *et al. Landolt-Bornstein New Series,* **Vol. 16,** 1998.
Ver+65: vertenbnyj, V.P. *et al. J. Ukrinskij Fizichij Zhuranal (UFZ)* **8**, 947, 1965. EXFOR 40061.
Wal 86: Walter, R. L. *et al. Proc. Int. Conf. On Nucl. Data. for Basic and Applied Sciences, Santa Fe, N.M. May 13-17,* 1985 [*Gordon and Issledovanij (YFI)*-**1**, 25, 1965.
Wri+90: Wright, R.Q. *et al. ENDF/B-VI evaluated data file for ^{166}Er and ^{167}Er,* 1988.
Yam 90: Yamamuro, N. *SINCROS-II, Rep. JAERI-M 90-006,* 1990.
You 92: Young, P.G. *et al. Report LA-12343-MS/UC-413/LA,NM, USA,* 1992.

JP0150667

3.5

Neutron Capture Cross Section Measurement of Np-237 below 10 keV by Linac Time-of-Flight Method

Samyol Lee[1], Shuji Yamamoto[1], Hyun-Je Cho[1*], Takaaki Yoshimoto[1],
Katsuhei Kobayashi[1], Yoshiaki Fujita[1], and Yasushi Ohkawachi[2]

[1] Research Reactor Institute, Kyoto University, Kumatori-cho, Sennan-gun, Osaka 590-0494, Japan

[2] O-arai Engineering Center, Japan Nuclear Cycle Development Institute,
4002, O-arai-machi, Higashi-ibaraki-gun, Ibaraki 311-1393, Japan

[*] Present address: Korea Atomic Energy Research Institute, P.O. Box 105, Taejeon 305-600, Korea

The neutron capture cross section of ^{237}Np has been measured in the energy region from 0.01 eV to 10 keV by using the neutron time-of-flight (TOF) method with a 46 MeV electron linear accelerator (linac) at the Research Reactor Institute, Kyoto University (KURRI). A pair of C_6D_6 scintillation detectors, which was placed at a distance of 12.0±0.02 m from the pulsed neutron source, was employed for the prompt capture gamma-ray measurement from the ^{237}Np sample. The measured result has been normalized to the reference value of the ^{237}Np(n,γ)^{238}Np reaction in ENDF/B-VI at 0.0253 eV.

The existing experimental and the evaluated capture cross sections in ENDF/B-VI and JENDL-3.2 have been compared with the present measurement. For the neutron capture cross section of ^{237}Np, the data by Weston et al. and the evaluated data are in good agreement with the present measurement. However, the data by Hoffman et al. are obviously lower in the relevant energy region.

The data, which were measured before using a lead slowing-down spectrometer at KURRI, have been in good agreement with the data obtained by energy-broadening the present TOF measurement.

1. Introduction

The ^{237}Np, which is one of the minor actinides with a long half-life, is abundantly produced in light water reactors. The nuclear data are of great importance for investigating the generation and the burn-up characteristics of ^{237}Np in the reactor. Neutron capture by ^{237}Np produces an intense alpha-emitter of ^{238}Pu through the beta-decay of ^{238}Np. In order to decrease an undesirable inheritance or a risk of these high level radioactive materials, in recent years, a great interest has been taken in the nuclear transmutation using conventional or advanced reactors and accelerator-driven subcritical reactors [1, 2, 3]. Accurate determinations of the fission and the capture cross sections for ^{237}Np are indispensable to research and development of the nuclear transmutation technology.

Although several measurements for the capture cross section of ^{237}Np have been reported at higher energies and thermal energy, the cross section has rarely been measured in the low/resonance energy region [4]. Weston et al. measured the capture cross section between about 0.01 eV and 0.2 MeV by the neutron

TOF method using an Oak Ridge Electron Linear Accelerator [5]. Hoffman et al. measured the neutron capture cross section of ^{237}Np by the neutron time-of-flight (TOF) method using a Moxon-Rae detector [6].

In the present work, the neutron capture cross section of ^{237}Np has been measured in the energy region from 0.01 eV to 10 keV by using the neutron TOF method with a 46 MeV electron linear accelerator (linac) of the Research Reactor Institute, Kyoto University (KURRI). The present result is compared with the previous experimental[7] and the evaluated data in ENDF/B-VI [8] and JENDL-3.2 [9].

The capture cross section was measured before using the lead slowing-down spectrometer (KULS) at KURRI. The result obtained by the KULS is compared with the present TOF measurement, which is energy-broadened by the resolution function of the KULS.

2. Experimental Procedure

2.1. Capture Samples

Neptunium oxide (NpO_2) powder of 1.13 g was purchased from Amersham, which was packed in an aluminum disk container of 20 mm in inner-diameter and 1.4 mm in thickness (outer-diameter: 30 mm and thickness: 2.2mm). The purity of the sample is 99.6% by weight and the major impurities are about 4μg in total weight of Ga, K, P, Rb, and S. The gamma-rays of 86.5 keV from ^{237}Np and 300, 312, 341 keV from ^{233}Pa which was produced through the α-decay of ^{237}Np, were measured with a high-purity germanium detector (HPGe). No peak from the impurities except for ^{233}Pa was found in the pulse height distribution data.

The enriched ^{10}B powder of 90.4% was put into a thin Al (0.2 mm in thickness) plug of 1.8×1.8 cm^2 and 8mm in thickness, and the sample thickness was 1.102 g/cm^2.

2.2. Experimental Arrangement

The neutron capture measurement was performed in the neutron energy region of 0.01 eV to 10 keV using the 46 MeV electron linac at KURRI. The experimental arrangement is shown in **Fig. 1**. Pulsed fast neutrons were produced from a water-cooled Ta target. The flight path, which is 12.0 ± 0.02 m from the neutron source to the sample, is located at an angle of 135° with respect to the linac electron beam direction. The target is consists of twelve sheets of Ta plates of 5 cm in diameter and 2.9 cm long in effective thickness [10]. The target was set at the center of the cylindrical water tank, which was 30 cm in diameter and 1 cm in tank wall thickness, to moderate fast neutrons. A shadow bar made of Pb block (size: 5×5 cm^3 $\times 10$ long) was placed in the neutron flight path in front of the Ta target to reduce the γ-flash generated by the electron burst in the target.

The linac was operated with a pulse width of 3μs, a repetition rate of 30 Hz, electron peak current of 400 *mA* and the electron energy of 22 MeV for the measurement in the lower energy region, and with a pulse width of 33 ns, a repetition rate of 100 Hz, electron peak current of 3 *μA* and the electron energy of 20 MeV in the higher energy region, respectively.

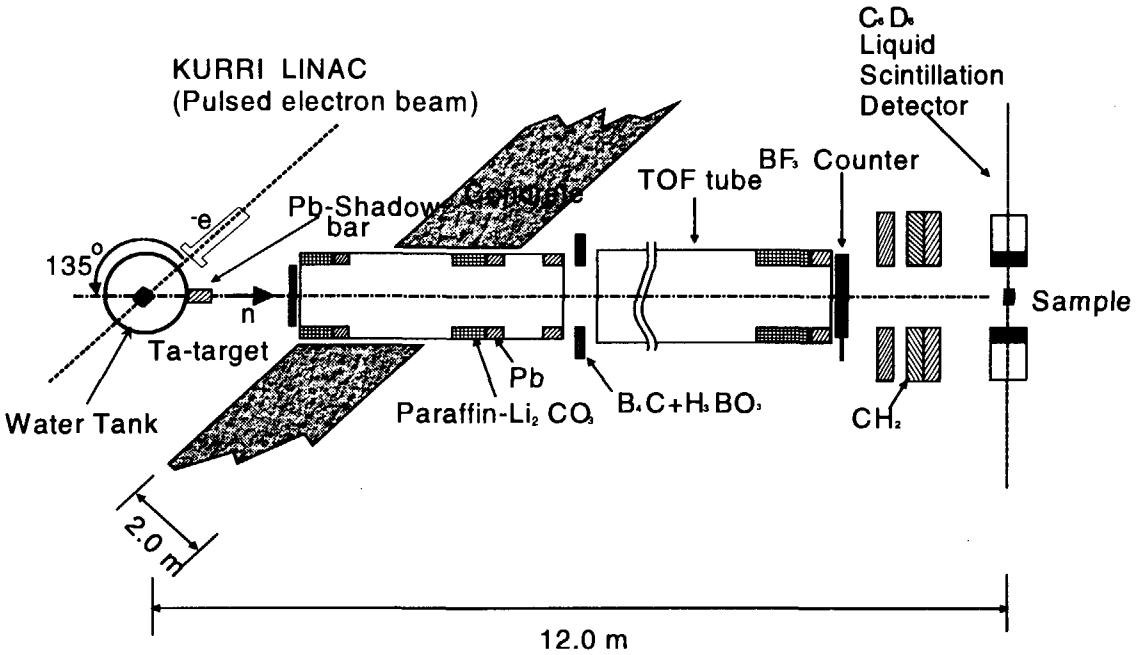

Fig. 1. Experimental arrangement for the capture cross section measurement.

2.3. Detectors and Data Taking

A pair of C_6D_6 liquid scintillation detectors was used for detection of γ-rays from the sample. The ^{237}Np sample was inserted into the neutron TOF beam between the detectors, each 11cm in diameter and 5cm thick. The detectors are adequate to the capture γ-rays measurement because of less sensitive to scattered neutrons. For the measurement of the incident neutron flux/spectrum on the sample, a ^{10}B plug (1.102 g/cm^2) was inserted into the TOF beam instead of the ^{237}Np sample. A background run was carried out with an aluminum disk container without the ^{237}Np sample. In the background measurement, a thick ^{10}B plug (4.54 g/cm^2) was placed in front of the collimator before the C_6D_6 detectors to black-out the neutron beam. The background level was also confirmed by those measured with a 0.5 mm thick Cd sheet and notch-filters of Ag, Co and Mn. The neutron beam intensity during the experiment was monitored with a BF_3 counter, as shown in **Fig. 1**. In order to monitor the neutron intensities during the experimental runs, the BF_3 counter was placed in the neutron beam. Through the amplifiers and the discriminators, signals from a pair of C_6D_6 liquid scintillation detectors or the BF_3 counter for the neutron flux/spectrum monitor were fed into the time digitizer, which was initiated by the linac electron burst. The multi-channel data were stored as two sets of 4096-channel data with a channel width of 4μs.

3. Data Analysis

3.1. Neutron Capture Cross Section

The relative neutron capture yield of the $^{237}Np(n,\gamma)$ reaction is given by the following relation:

$$Y_{Np}(E) = \frac{C_{Np}(E)}{C_B(E)} Y_B(E), \qquad (1)$$

$$Y_{Np}(E) = (1 - \exp(-N\sigma_t(E)t))\frac{\sigma_c(E)}{\sigma_t(E)} f_c, \quad (2)$$

where $C_{Np}(E)$ is capture counts of ^{237}Np at energy E, $C_B(E)$ is capture counts of ^{10}B at energy E, N is atomic density of the ^{237}Np sample, f_c is the correction factor for the neutron scattering in the sample, $\sigma_c(E)$ is the neutron capture cross section, $\sigma_t(E)$ is the total cross section, t is thickness of the ^{237}Np sample, and $Y_B(E)$ is the capture yield of ^{10}B. Since the cross section of the ^{10}B(n,α) reaction is a well-known reference one, it has been used to determine the neutron flux/spectrum in the present measurement. When t is thin enough, Eq. (2) can be written as follows:

$$\sigma_c(E) = \frac{Y_{Np}(E)}{Ntf_c} \quad (3)$$

3.2. Self-shielding Correction

The self-shielding effect of neutrons has to be taken into account in the capture cross section measurements, especially near the large resonance region. We have assumed that the sample is irradiated by the neutron TOF beam. The self-shielding correction in the ^{237}Np sample has been calculated by the Monte Carlo code MCNP [11]. The correction factor has been obtained from the ratio of the effective capture cross section for the ^{237}Np sample to that for the infinite diluted one that is obtained by multiplying the atomic density by 10^{-6}. The result has been applied to the neutron scattering and self-shielding correction for the present cross section measurement of the ^{237}Np(n, γ)^{238}Np reaction.

4. Results and Discussion

The neutron capture cross sections have been measured relative to that of the ^{10}B(n,α) reaction at the energy region from 0.01 eV and 10 keV. The result obtained has been normalized to the reference value of the thermal neutron cross section of 181 *b* of ENDF/B-VI at 0.0253 eV. The experimental uncertainties are in the range of 0.05% to 44%, and the major uncertainties are due to the statistical error and that in the reference cross section for the ^{10}B(n,α) reaction. Since the ^{237}Np sample was almost free from impurities, no correction was made for the impurity effect.

The capture cross sections measured by Weston et al. [5] are in good agreement with the present measurement as seen in **Fig. 2**, but the data measured by Hoffman et at.[6] are remarkably lower than the present values [6]. The evaluated data in ENDF/B-VI [8] and JENDL-3.2 [9] are also in good agreement with the present measurement in the relevant energy region, as shown in **Fig. 3**.

We measured the capture cross section before using the lead slowing-down spectrometer (KULS) at KURRI. The measured data are in good agreement with the data that the present TOF measurement is broadened by the resolution function of the spectrometer, as shown in **Fig.4**.

5. Conclusion

The neutron capture cross section of ^{237}Np has been measured in the energy region from 0.01 eV and

10 keV by using the neutron TOF method and the C_6D_6 liquid scintillation detectors. The data by Weston et al. and the evaluated data in ENDF/B-VI and JENDL-3.2 are in good agreement with the present measurement in the relevant energy region. However, the data by Hoffman et al. are lower obviously. The data measured with the lead slowing-down spectrometer have been in good agreement with the data which were obtained by energy-broadening the present TOF measurement.

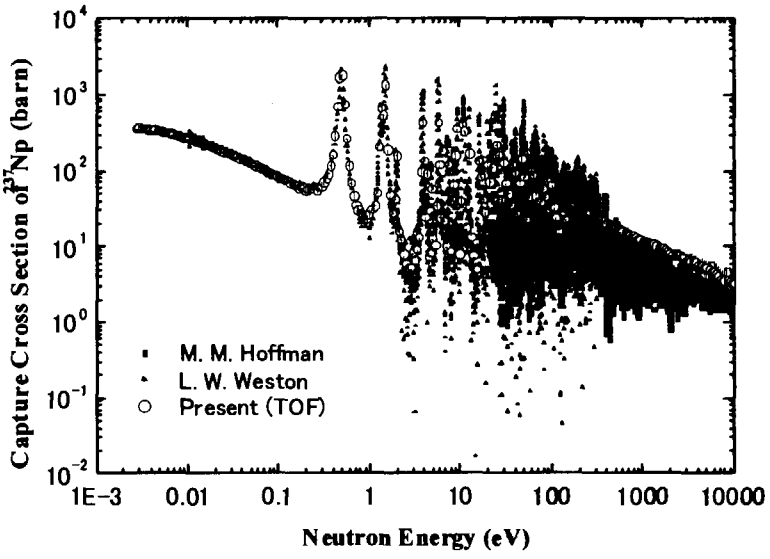

Fig. 2. Comparison of the experimental capture cross sections of ^{237}Np and the present measurement obtained by the linac TOF method.

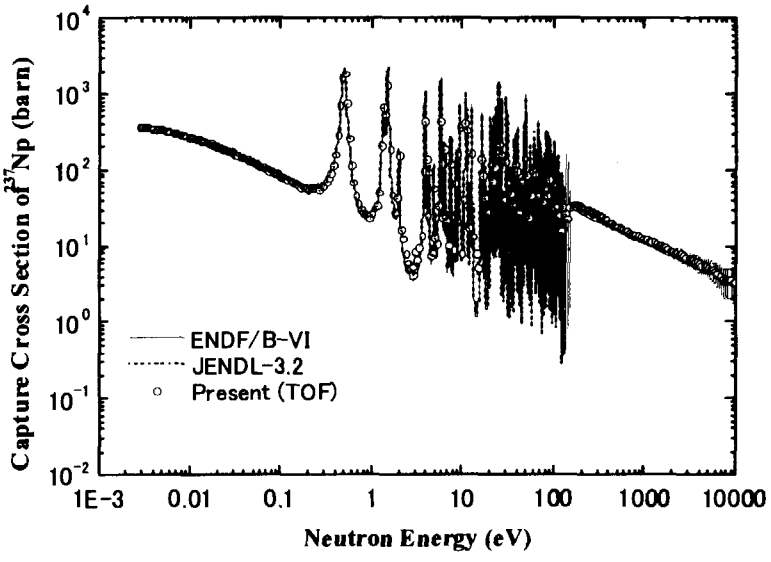

Fig. 3. Comparison of the evaluated capture cross sections of ^{237}Np and the present measurement obtained by the linac TOF method.

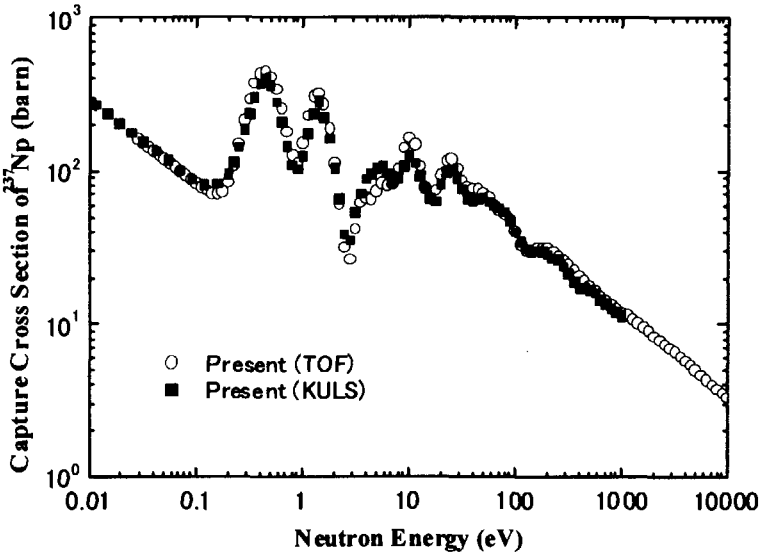

Fig. 4. Comparison of the measurement obtained with the KULS and the linac TOF data broadened by the KULS resolution.

Reference

[1] T. Mukaiyama, et al., "*Conceptual Study of Academic Burner Reactors*", Proc. of the 1988 Int. Reactor Phys. Conf., Jackson Hale, Vol. IV, 369 (1988).

[2] D. H. Berwald and J. J. Duderstadt, *Nucl. Technol.*, Vol. **42**, 34 (1979).

[3] H. Takano, et al., "*Concept of Actinide Transmutation with Intense Proton Accelerator*", 6th Int. Conf. On Emerging Nuclear Energy System, Monterey, USA (1991).

[4] K. Kobayashi et al., *J. Nucl. Sci. Technol.*, **31**, 1239 (1994).

[5] L. W. Weston & J. H. Todd, *Nucl. Sci. Eng.*, **79**, 184 (1981).

[6] M. M. Hoffman et al., *Bull. Am. Phys. Soc.*, **21**, 655 (1976).

[7] K. Kobayashi et al., *JAERI-Conf 2000-005*, p. 119 (1999).

[8] P. F. Rose (Ed.), "*ENDF-201, ENDF/B-VI Summary Documentation,*" BNL-NCS-17541, 4th Ed. (ENDF /B-VI) (1991), and "*ENDF/B-VI MOD2 Evaluation,*" by P. G. Young (1996).

[9] T. Nakagawa et al., "*Japanese Evaluated Nuclear Data Library Version 3 Revision 2: JENDL-3.2", J. Nucl. Sci. Technol.*, 32, 1259 (1995), and K. Shibata and T. Narita, "*Descriptive Data of JENDL-3.2*", JAERI-Data/Code 98-006 (1998).

[10] K. Kobayashi, G. Jin, S. Yamamoto, K. Takami, Y. Kimura, T. Kozuka and Y.Fujita: *Annu. Rep. Res. Reactor Inst., Kyoto Univ.*, **22**, 142 (1987).

[11] "*MCNP-A General Monte Carlo Code for Neutron and Photon Transport, Version 3A*", LA-7396-M, Rev. 2, Los Alamos National Laboratory (1986).

JP0150668

3.6 Projectile Dependency of Radioactivities of Spallation Products Induced in Copper

Hiroshi Yashima
Department of Quantum Science and Energy Engineering, Tohoku University,
Aoba01, Aramaki, Aobaku, Sendai 980-8578,Japan
e-mail:yashima@cyric.tohoku.ac.jp
Hiroshi Sugita, Takashi Nakamura, Tomoyuki Shiomi
Department of Quantum Science and Energy Engineering, Tohoku University,
Aoba, Aramaki, Aobaku, Sendai 980-8578,Japan
Yoshitomo Uwamino, Sachiko Ito
Institute of Physical and Chemical Research, Hirosawa, Wako, Saitama 351-01, Japan
Akifumi Fukumura
National Institute of Radiological Sciences, 4-9-1, Anagawa, Inage-ku
Chiba-shi, Chiba, 263-8555, Japan

The reaction cross sections of spallation products in a Cu target by 230MeV/nucleon Ne,C,He,p and 100MeV/nucleon Ne,C ions were obtained. Irradiation experiments were performed at HIMAC (Heavy Ion Medical Accelerator in Chiba), National Institute of Radiological Sciences. Gamma-ray spectra from activation samples were measured with a HPGe detector. From the gamma-ray spectra, we obtained the variation of reaction cross sections of Cl-38, Cr-49, Mn-55, Cu-60, Cu-61 and Co-62m in Cu sample with Cu target thickness and mass-yield distribution of nuclides in Cu sample on the surface of Cu target. The results showed that the dependence of the cross sections to the projectile mass varies with the mass number difference between Cu and produced nuclide

1. Introduction

Recently the high-energy and high-intensity accelerators have increasingly been used for nuclear physics, solid-state physics, radiotherapy, material damage study, and so on. Safety design consideration for the accelerator facilities requires reaction cross

section data for high-energy ions to estimate the radioactivities induced in the accelerator components and in the shielding materials. We therefore irradiated 230MeV/nucleon Ne,C,He,p and 100MeV/nucleon Ne,C ions onto a Cu target, and investigated the projectile dependency of induced radioactivities of spallation products.

2. Experiment and Analysis

Irradiation experiments were performed at HIMAC (Heavy Ion Medical Accelerator in Chiba), National Institute of Radiological Sciences. A schematic view of the experimental set-up is shown in Fig.1. The Cu target was composed of a stack of 100mm×100mm×5mm Cu plates, and C, Al, Cr, Fe, Ni, Cu, Pb samples were inserted between the Cu plates. The thickness of Cu target is longer than the flight path of the projectile beam. Table1 shows the flight path of the projectile beam calculated by the SPAR code [1]. After irradiation, we measured the gamma-ray spectra from samples with a HPGe detector. Fig.2 shows a schematic view of the gamma-ray detection system. The reaction rates of radionuclides produced in samples which were identified from the gamma-ray spectra and the decay curves were estimated after being corrected for the peak efficiency of the HPGe detector and the coincidence-summing effect.

3. Results and Discussions

From the reaction rates, we obtained the reaction cross sections of Cl-38, Cr-49, Mn-56 Cu-60, Cu-61 and Co-62m in a Cu target by 230 MeV/nucleon Ne,C,He,p and 100MeV/nucleon Ne,C ions and mass-yield distribution of nuclides in Cu sample at surface of Cu target.

Fig.3 shows the variation of reaction cross sections of Cl-38 produced in the Cu sample with Cu target thickness. Target thickness is expressed as the unit of the flight path. In Fig.3, the reaction cross sections of Cl-38 are almost constant down to the beam flight path and rapidly decrease beyond it in the case of C and Ne ion (230,100MeV/nucleon) irradiations, while it gradually decreases with target thickness in the case of 230MeV/nucleon He ion. Since the mass number difference between Cu and Cl-38 is large, Cl-38 is produced dominantly by a primary projectile beam.

Fig.4 shows the variation of reaction cross sections of Cr-49 produced in the Cu sample with Cu target thickness. In Fig.4, the reaction cross sections of Cr-49 increase down to the beam flight path and decrease beyond it in the case of C and Ne ion (230,100MeV/nucleon) irradiations while it is almost constant down to the beam flight path and rapidly decrease beyond it in the case of 230MeV/nucleon He ion and it monotonously decreases with target thickness in the case of 230MeV/nucleon p ion. Since the mass number of Cr-49 becomes closer to Cu than that of Cl-38, the fraction of Cr-49

produced by secondary particles increases.

Figs.5 to 8 show the variation of reaction cross sections of Mn-56,Cu-60,Cu-61,Co-62m produced in the Cu sample with Cu target thickness, respectively. In these figures, the reaction cross sections of these nuclides show the similar tendency as that of Cr-49 although the cross section increase with the target thickness is much higher for spallation products of lighter mass.

Fig.9 shows the mass-yield distribution of nuclides in Cu sample on the surface of Cu target. The cross section is normalized to the cross section for 230MeV/u Ne ions. Table2 shows the cross section ratio of nuclides normalized to the cross section for 230MeV/u p ions. In Fig.9 and Table2, the projectile dependency of the cross section is small in the nuclide of which the mass number is closer to Cu while it becomes larger with the lower mass nuclides.

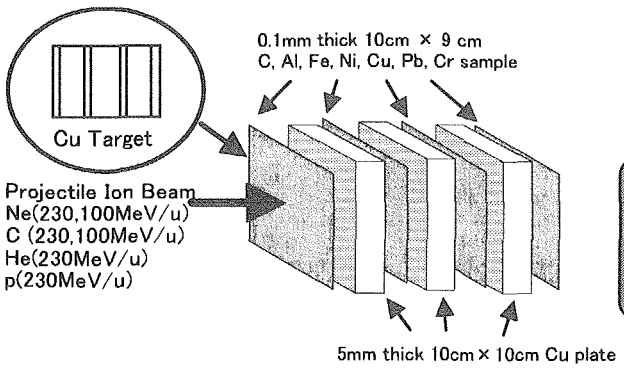

Fig.1 Schematic view of the experimental geometry.

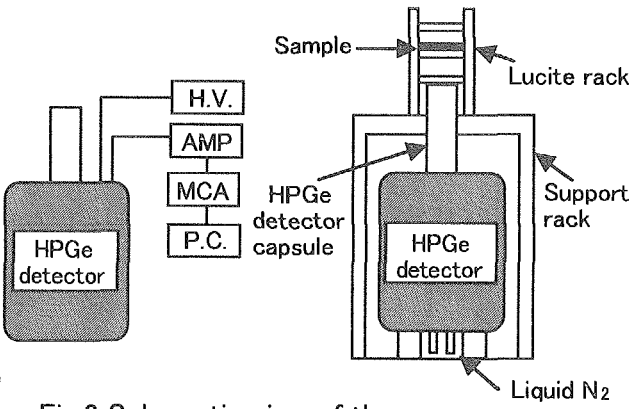

Fig.2 Schematic view of the gamma-ray detection system

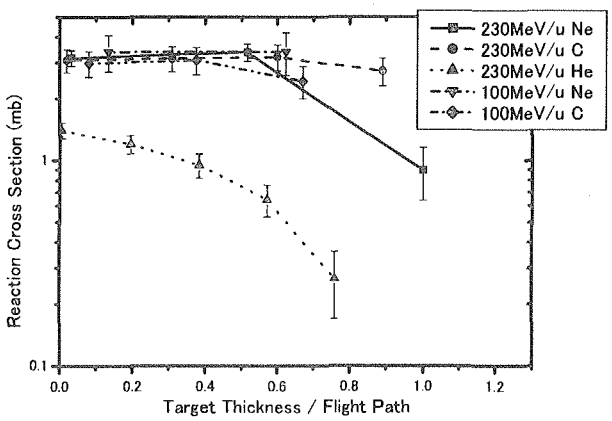

Fig.3 Reaction cross section of Cl-38 in Copper

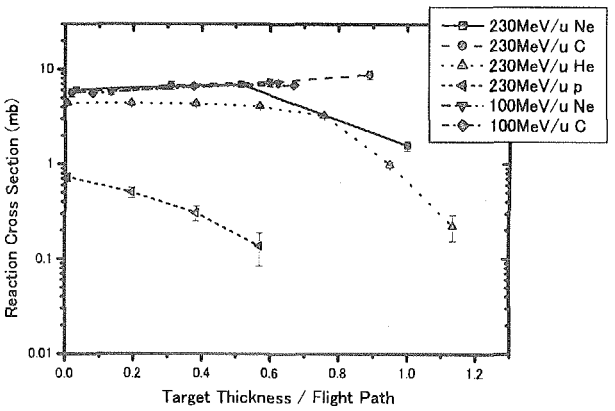

Fig.4 Reaction cross section of Cr-49 in Copper

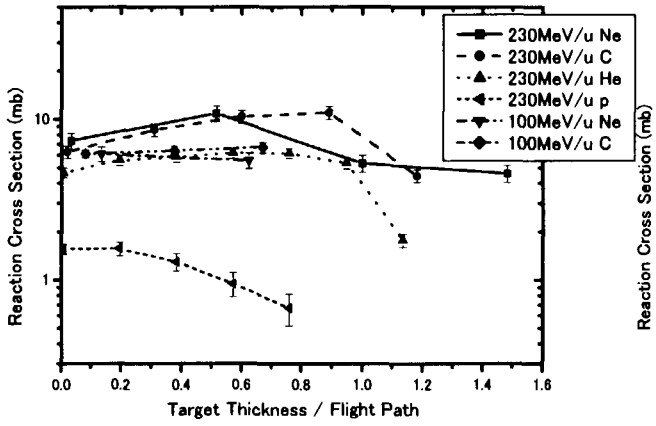

Fig.5 Reaction cross section of Mn-56 in Copper

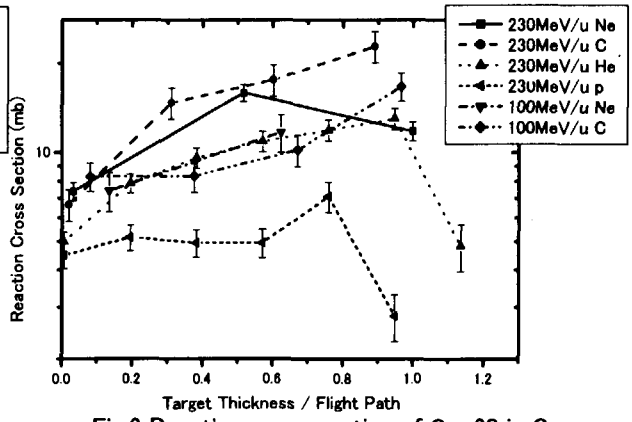

Fig.6 Reaction cross section of Cu-60 in Copper

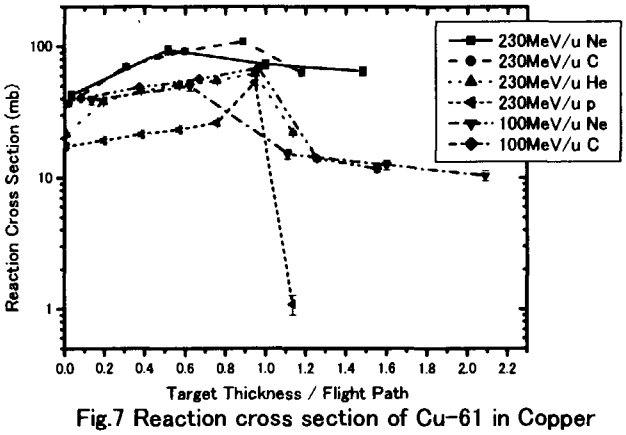

Fig.7 Reaction cross section of Cu-61 in Copper

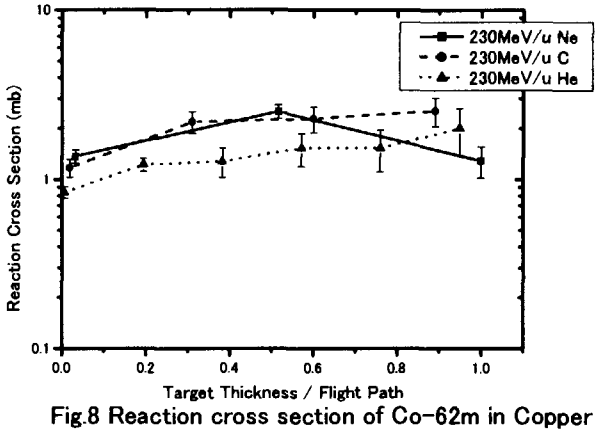

Fig.8 Reaction cross section of Co-62m in Copper

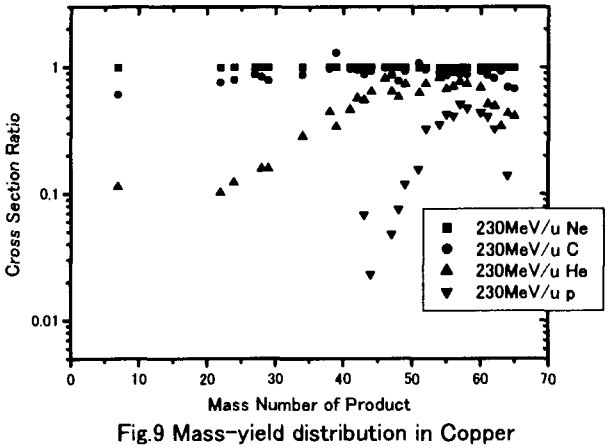

Fig.9 Mass-yield distribution in Copper

Table1 The flight path of the projectile beam

Projectile Ion	Flight Path[mm]
230MeV/u Ne	11.0
230MeV/u C	18.2
230MeV/u He	54.7
230MeV/u p	54.7
100MeV/u Ne	2.7
100MeV/u C	4.4

Table2 Cross Section Ratio in Copper
(projectile energy 230MeV/u)

Product	Ne	C	He	p
Sc-43	7.0	6.1	3.8	1
Sc-44	36.5	54.7	26.1	1
Sc-44m	50.1	44.0	29.2	1
Sc-47	20.9	18.1	13.4	1
Cr-48	13.3	10.3	7.7	1
Cr-49	8.3	7.7	6.1	1
Cr-51	6.4	6.9	4.0	1
Mn-52m	3.1	3.0	2.3	1
Fe-52	3.0	2.8	2.0	1
Mn-54	2.8	2.6	2.3	1
Co-55	2.3	2.0	1.6	1
Mn-56	4.7	4.0	3.0	1
Co-56	1.8	1.7	1.4	1
Co-57	1.9	1.7	1.5	1
Ni-57	2.0	1.7	1.3	1
Co-58	2.1	1.8	1.5	1
Co-60	2.7	2.5	1.9	1
Cu-60	1.6	1.5	1.1	1
Cu-61	2.4	2.1	1.2	1
Zn-62	1.9	1.5	0.8	1
Cu-64	7.2	5.0	3.1	1

4.Conclusion

We performed the irradiation experiments by 230MeV/nucleon Ne,C,He,p and 100MeV/nucleon ions, and obtained the variation of reaction cross sections of nuclides produced in Cu sample with Cu target thickness and mass-yield distribution of nuclides in Cu sample on the surface of Cu target. It was found that these cross sections have two tendencies. When the mass number difference between Cu and produced nuclide is small, the fraction of nuclides produced by secondary particle is large. The reaction cross section is almost equal for Ne and C ions but smaller for He and p ions. The more the projectile mass number of ion and energy increases, the more the reaction cross section increases toward the inner part of Cu target. When the mass number difference between Cu and produced nuclide is large, where the threshold energy is high, and nuclide is almost produced by a primary projectile beam. The cross section difference between Ne,C and He,p becomes larger in the lower mass nuclides. We are now analyzing the induced radioactivities produced in other samples.

References

[1] T. Nakane, Nucl. Phys., A491, 130 (1989).

JP0150669

3.7 Measurement of Neutron Production Cross Sections by High Energy Heavy Ions

Hisaki Sato, T.Kurosawa, H.Iwase, T.Nakamura, N.Nakao, Y.Uwamino

The double-differential cross section (DDX) of neutron production from thin C, Al, Cu, and Pb targets bombarded by 135MeV/nucleon He, C, and Ne ions and by 95MeV/nucleon Ar ion were measured using the RIKEN Ring Cyclotron of the Institute of Physical and Chemical Research, Japan. The neutron energy spectra were obtained by using the time-of-flight method. The NE213 liquid scintillator was used for neutron detector (E counter), and the ΔE counter of the NE102A plastic scintillator was used to discriminate charged particles from noncharged particles, neutrons and photons. The experimental spectra were compared with the calculation using the HIC and the QMD codes.

1. INTRODUCTION

Recently, the use of high-energy heavy ions have been increasing in various fields. To design the accelerator facility, it is important to protect workers from radiation, particularly penetrating neutrons produced by high-energy heavy ions. There exist a few published data on the double-differential cross sections (DDX) of neutron production for 337MeV/nucleon Ne ions on C, Al, Cu, and U targets [1] and 790MeV/nucleon Ne ion on Pb target[2], but still very poor. In this work we present the double-differential cross sections (DDX) of neutron production from thin C, Al, Cu, and Pb targets bombarded by 135MeV/nucleon He, C, and Ne ions and by 95MeV/nucleon Ar ion. These results will be useful as a benchmark experimental data to investigate the accuracy of high-energy particle transport calculation code. Here, the measured spectra are compared with the calculation using the two heavy-ion Monte Carlo codes of the internuclear-cascade and evaporation model (HIC) and the quantum molecular dynamics model (QMD).

2. EXPERIMENT

The measurements were carried out at the RIKEN Ring Cyclotron, the Institute of Physical and Chemical Research. A schematic view of the experimental set-up is shown in Fig.1. The NE213 liquid scintillator (12.7cm diameter by 12.7cm thick), which was designed to expand the dynamic range of output pulses for high energy neutron measurements, was used as the E counter, and the NE102A plastic scintillator (15cm by 15cm square and 0.5cm thick) as the ΔE counter was placed in front of the E counter to discriminate charged particles from noncharged particles, neutrons and photons. The target thicknesses are 1mm of C, 0.6mm of Al, 0.3mm of Cu, 0.3mm of Pb. The direction

of incident beam was rotated around the target from 0 to 110 degrees using the beam swinger, in order to measure the energy-angle distribution of neutrons produced from the target by the time-of-flight (TOF) method having the flight path of 847cm. In order to shield the spurious scattered neutrons, the neutrons from the target were introduced to the detector through the iron-concrete collimator of 120cm thickness. The measurements were carried out at 0° ,15° ,30° ,50° ,80° and 110° .

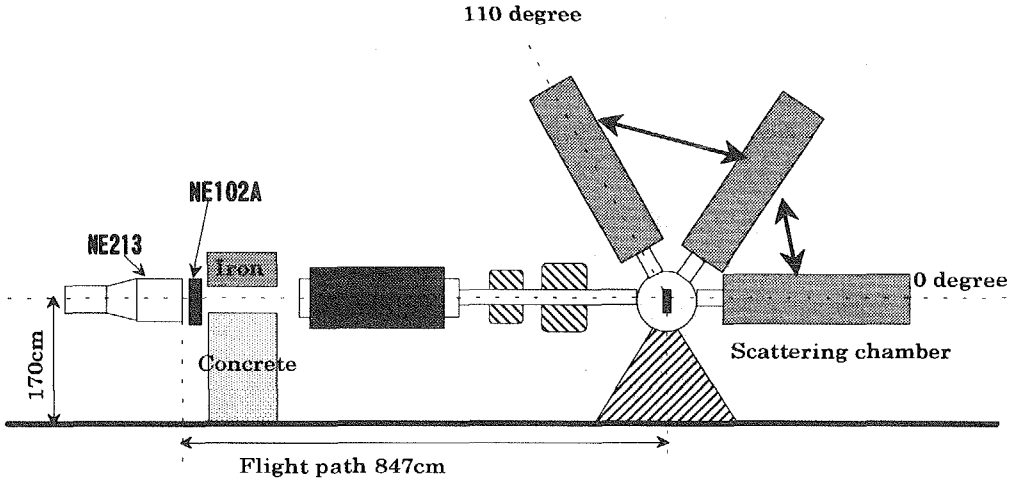

Fig.1 Schematic view of the experimental set-up

3. RESULTS AND DISCUSSIONS

We obtained neutron energy spectra for C,Al,Cu, and Pb targets bombarded by 135 MeV/nucleon He, C, and Ne ions and by 95MeV/nucleon Ar ion. These experimental results were compared with the calculation using the HIC [3] and the QMD [4] codes. Figs.2-5 show the experimental and calculated double-differential cross sections of neutron production by He, C, Ne and Ar ion, respectively. The neutron energy spectra measured in the forward direction have a peak near the projectile energy per nucleon. This peak is due to a knock-on process in which a neutron is knocked out by the direct collision between the target nucleon and the projectile nucleon. This peak becomes more prominent in the forward direction and for a lighter target, since the momentum transfer from projectile to target nuclei is higher for lighter nucleus than for heavier nucleus [5]. The high energy end of neutrons in the forward direction reaches about 2.5 - 3 times of incident particles energy per nucleon. The neutron spectra have another two components based on cascade-preequilibrium emission process and evaporation-equilibrium emission process. At small angles, knock-on process is dominant, and at large angles, evaporation process is dominant. Two calculations using HIC and QMD show a tendency to underestimate the high-energy neutron components beyond the peak at all angles. The HIC overestimates the peak, while the QMD underestimates the peak. At large angles, the calculated spectra are in good agreement with the measured spectra. In general, the QMD gives better agreement with the experimental results, especially for a heavy target, than the HIC.

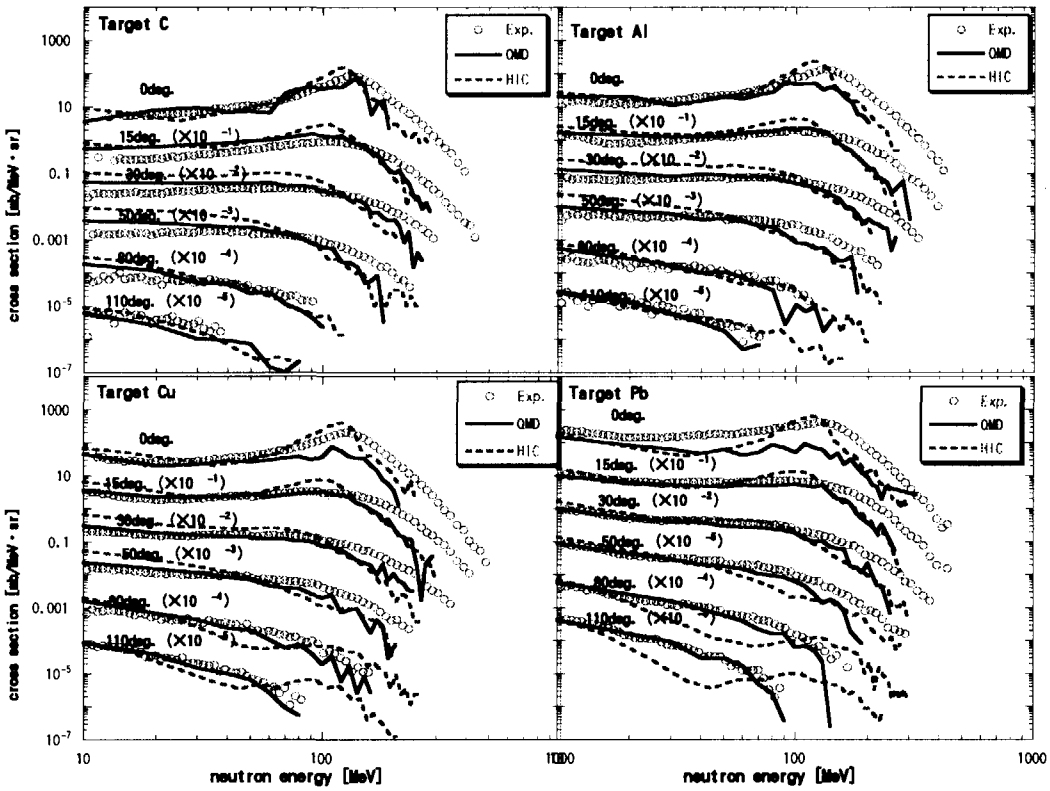

Fig. 2 Neutron energy spectra by 135MeV/nucleon C ion

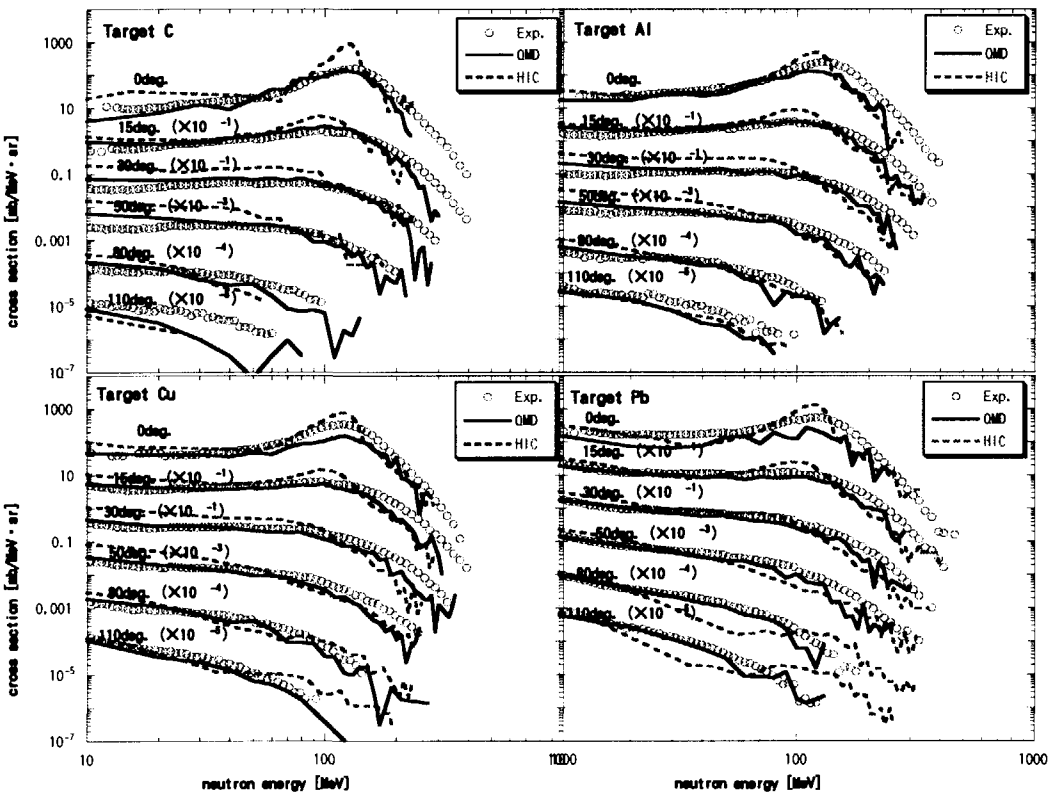

Fig. 3 Neutron energy spectra by 135MeV/nucleon Ne ion

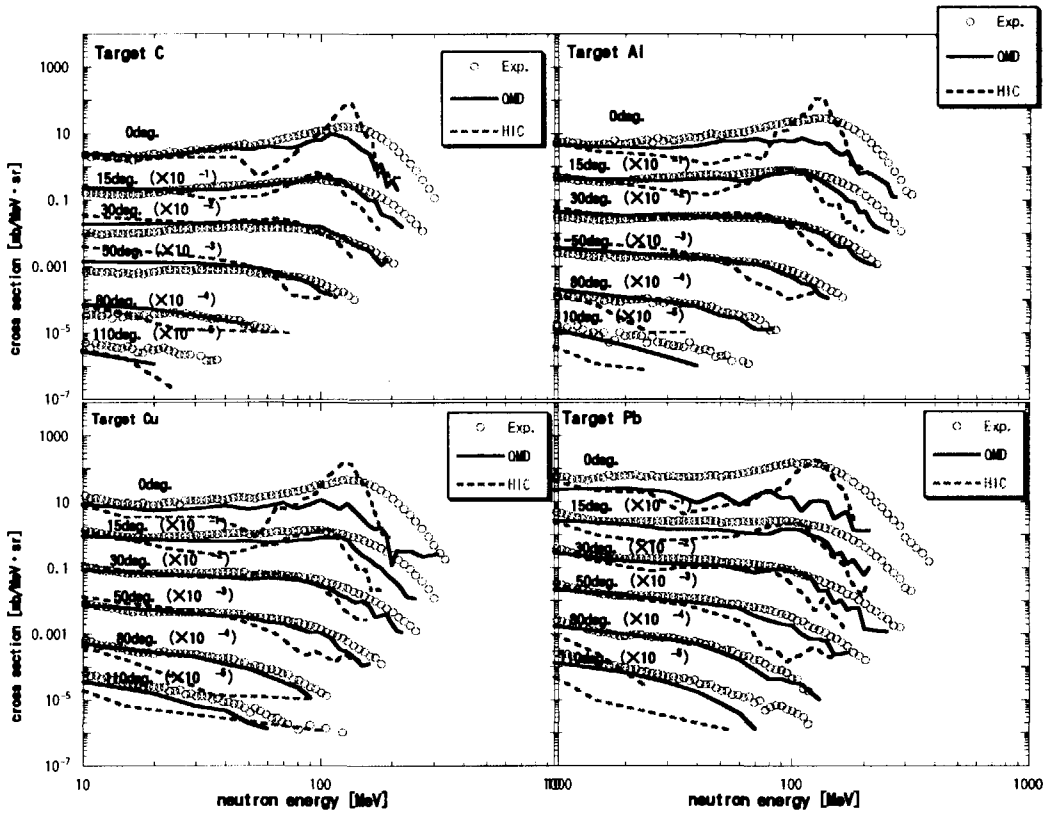

Fig. 4 Neutron spectra by 135MeV/nucleon He ion

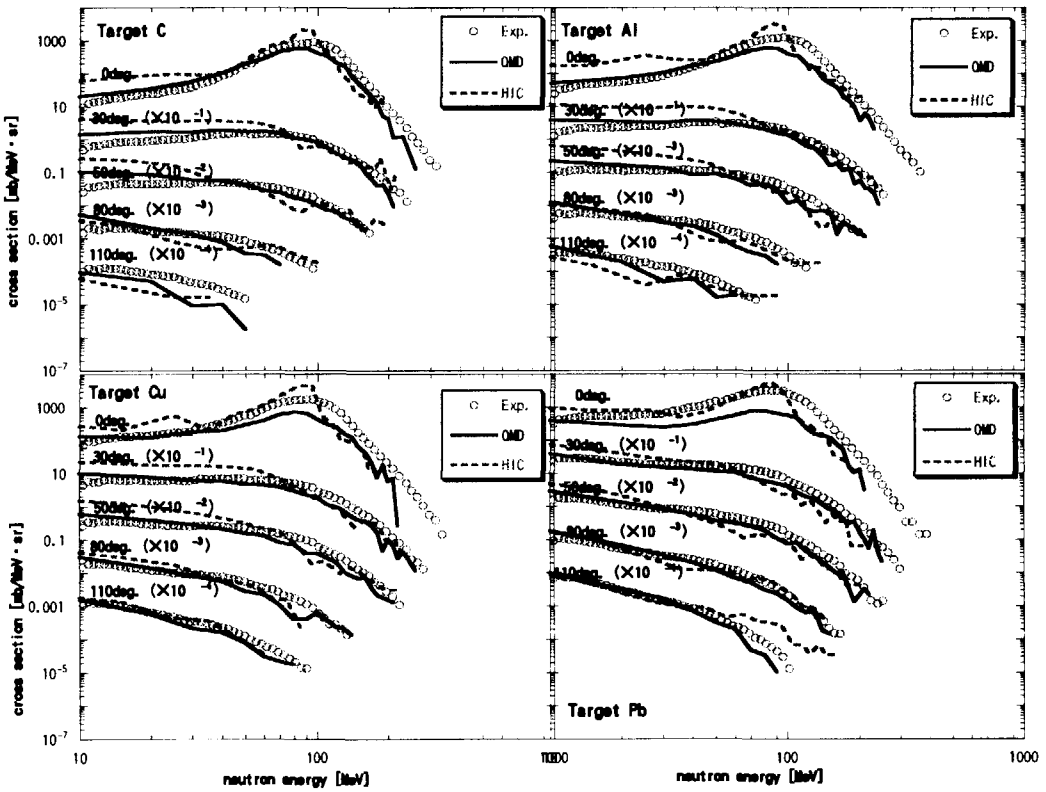

Fig.5 Neutron spectra by 95MeV/nucleon Ar ion

4. CONCULUSIONS

We measured double-differential cross sections of neutron production from thin C, Al, Cu, and Pb targets bombarded by 135MeV/u He, C, and Ne ions and by 95MeV/nucleon Ar ion. The experimental spectra were compared with the calculation using the HIC and the QMD codes. The calculated spectra tend to underestimate the high-energy neutron region. At large angles, the calculated spectra, particularly the QMD, are in rather good agreement with the measured spectra. These experimental results will be useful as the benchmark data for investigating the accuracy of the calculation code.

References

[1] Cecil, R. A. *et al.* : Inclusive neutron production by 337 MeV/nucleon neon ions on carbon, aluminum, copper, and uranium, *Phys. Rev. C*24, 2013 (1981)

[2] A. R. Baldwin *et al.,* : Inclusive neutron cross sections from Ne-Pb collisions at 790MeV/nucleon, *Phys. Rev. C*46, 258(1992)

[3] Bertini, W. H. : HIC-1 : First Approach the Calculation of Heavy-ion Reactions at Energy>50MeV/nucleon., ORNL-TM-4134.

[4] K. Niita *et al.*, : Analysis of the (N,*x*N') reactions by quantum molecular dynamics plus statistical decay model, *Phys. Rev. C*52, 2620(1995)

[5] Kurosawa T. and Nakamura S. ,*et al.* : Spectral measurements of neutrons, protons, deuterons and tritons produced by 100 MeV/nucleon He bombardment., *Nucl. Instrum. Methods. A*430, 440(1999)

JP0150670

3.8

New Evaluation of Prompt Neutron Spectra of U-235 and Pu-239 for JENDL-3.3

Takaaki Ohsawa

Depatment of Nuclear Engineering, Faculty of Science and Technology

Kinki University, 6-3-1 Kowakae, Higashi-osaka, Osaka

e-mail: ohsawa@mvg.biglobe.ne.jp

New evaluation of prompt neutron spectra for ^{235}U and ^{239}Pu was made on the basis of Madland-Nix model combined with multimodal random-neck rupture model of the fission process. The resulting spectrum for $^{235}U(n_{th}, f)$ was harder than the previous evaluation in JENDL-3.2 but a bit softer than the ENDF/B-VI evaluation.

1. Introduction

One of the central problems in calculating the prompt neutron spectra is *how to deal with a variety of fission fragments with a variety of excitation energies.* In order to give an approximate solution to this problem, the present author [1, 2] proposed to introduce the idea of multimodal random-neck rupture fission model [3] into the Madland-Nix model [4] of prompt neutron emission. The energy partition between the fragments is different for different fission modes, and this is fairly well described by the multimodal model. Thus we divided the the entire fission fragments into a few groups, each represented by modal average masses and total kinetic energies (TKEs), and calculated the prompt neutron spectrum for each mode independently using available empirical data. The total spectrum was obtained by synthesizing the modal spectra. Application of this methodology to prompt neutron spectra for $^{237}Np(n,f)$ [1] was found to give improved account of the the spectra.

This report describes results of calculation of the prompt neutron spectra for ^{235}U and ^{239}Pu performed on the basis of the method of multimodal analysis for JENDL-3.3.

2. Method

The average masses of pre-neutron-emission light and heavy fragments (LF, HF) and TKEs for each fission mode, such as Standard 1 (S1), Standard 2 (S2), Superlong (SL), were taken from multimodal analyses of experiments. The fission Q-values for each mode were calculated with TUYY mass formula [5]. The inverse cross section for fission fragments were calculated using Becchetti-Greenlees optical model potential [6].

Some modifications were made in the Madland-Nix model; *(a)* the level density parameters were calculated with the Ignatyuk model [7] taking into account the shell effects, and *(b)* difference in the number of neutrons emitted from LF and HF are allowed. The average number of neutrons $\nu_{iL(H)}$ emitted from LF and HF for each mode i were calculated from the prescission shapes for each mode.

The prompt-neutron spectra for each mode (modal spectra) χ_i were synthesized with respective weighting of the modal nu-values $\nu_{iL(H)}$.

$$\chi_i(En) = [\nu_{iL}\chi_{iL}(En) + \nu_{iH}\chi_{iH}(En)] / (\nu_{iL} + \nu_{iH}) \quad (1)$$

The total neutron spectrum was calciulated by averaging the modal spectra with respective weighting w_i and ν_I

$$\chi_{tot}(En) = [\sum_i w_i \nu_i \chi_i(En)] / (\sum_i w_i \nu_i) \quad (2)$$

where w_i is the mode branching ratio and ν_I the average number of neutrons emitted in a fission of type i. The shape parameters of the prescission nuclear shapes taken from Fan *et al.* [8] were used to calculate the neutron multiplicity $\nu_I(A)$ as a function of fragment mass A for mode i.

3. Results

3.1 U-235

Three fission modes, *i.e.*, Standard 1 (S1), Standard 2 (S2), Superlong (SL), as pointed out by Knitter *et al.* [9] , together with relevant fragment kinetic energies, were adopted in the calculation for (n_{th},f) . The modal spectra for the three modes and the synthesized total spectrum are shown in **Fig.1**. The S1-spectrum is the softest, because the total excitation energy (TXE) is the lowest for this mode. In contrast, the SL-spectrum is the hardest, as expected from the fact that total deformation energy, which in turn converts into fragment excitation energy after scission, is largest for this mode. The S2-spectrum comes in between. The total spectrum lies close to the S2-spectrum, because the branching ratio to the S2-mode accounts for 82% of the total process. **Figure 2** plots the ratio of the present and the ENDF/B-VI evaluations relative to the JENDL-3.2 evaluation. As can be seen, the present spectrum is *harder* than the previous one stored in JENDL-3.2. The calculation was then extended up to 5 MeV using the incident-energy dependence of the mode branching ratios [10].

3.2 Pu-239

Multimodal analysis of experiments by Schillebeeckx *et al.* [11] was adopted as the basis of calculation for ^{239}Pu(n_{th},f). For this nuclide, another mode, called Standard-3 (S3), was

confirmed in addition to S1 and S2 modes; on the other hand, the SL-mode component was not separated due to poor statistics of the measurement. These differences however do not bring about any important consequences, because their contributions are quite small. **Figure 3** shows the modal and total spectra; main features of the spectra are similar to ^{235}U. Relative ratios of the present and ENDF/B-VI evaluations to JENDL-3.2 evaluations are shown in **Fig.4**. The result is that the ratio to JENDL-3.2 evaluation is greater than unity except the region 0.9 - 4 MeV. Thus it is difficult to summarize the features of the new spectrum in a simple word. Considering that the peak of the absolute spectrum lies around 0.8 MeV and the neutron spectrum within the FBR core lies around several hundred keV, we may say that the relative increase of 5% in the region E_n<1 MeV impresses like 'softening' of the spectrum. However, in the case of high leakage system like critical safety research facility, the increase of high energy component (E_n>5 MeV) will enhance leakage of fast neutrons from the core.

For higher incident energies, calculations were made using the mode branching ratios from a study on the systematics in the ratios for many nuclides [10].

References

[1] T. Ohsawa, T. Horiguchi and H. Hayashi, Nucl. Phys. **A653**, 17 (1999);

[2] T. Ohsawa, T. Horiguchi and M. Mitsuhashi, Nucl. Phys. **A665**, 3 (2000);

[3] U. Brosa, S. Grossmasnn and A. Müller, Phys. Reports **197**, No.4, 167 (1990).

[4] D. G. Madland and J. R.Nix, Nucl. Sci. Eng. **81,** 213 (1982).

[5] T. Tachibana, M. Uno, M. Yamada and S. Yamada, Atomic Data and Nuclear Data Tables, **39,** 251 (1988).

[6] F. D. Becchetti, Jr., and G. W. Greenlees, Phys. Rev. **182,** 1190 (1969).

[7] A. V. Ignatyuk, Sov. J. Nucl. Phys. **29**, 450 (1979).

[8] T.-S. Fan, J.-M. Hu and S.-L. Bao, Nucl. Phys. **A591**, 161 (1995).

[9] H.-H. Knitter, F.-J. Hambsch, C. Butz-Jørgensen, Z. Naturforsch. **42a**, 786 (1987).

[10] U. Brosa, H.-H. Knitter, T.-S. Fan, J.-M. Hu and S.-L. Bao, Phys. Rev. **C59**, 767 (1999).

[11] P. Schillebeeckx, C. Wagemans, A. J. Derutter and R. Barthelemy, Nucl. Phys. **A545,** 623 (1992).

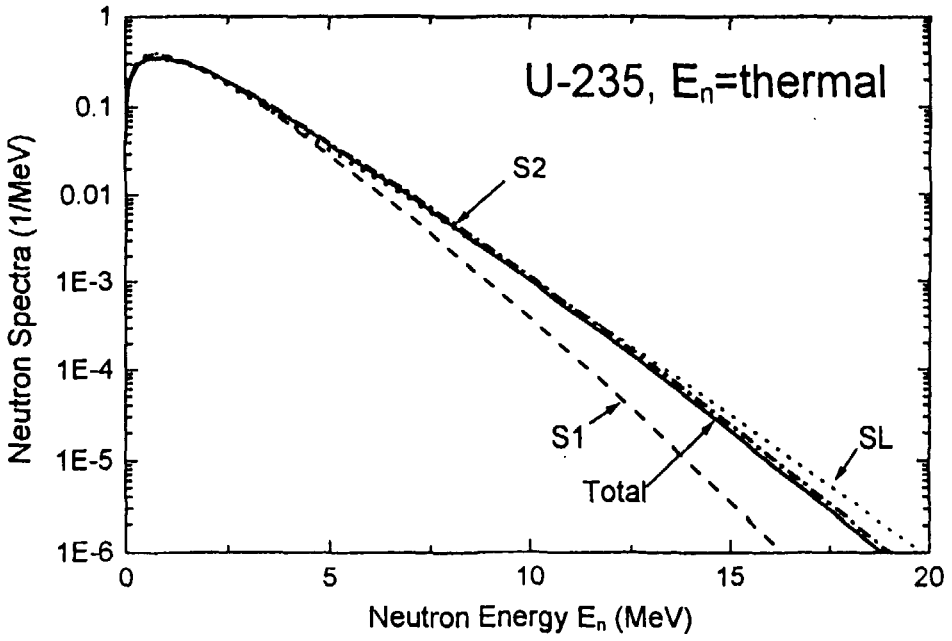

Fig.1 Modal and total prompt neutron spectra for $^{235}U(n_{th},f)$.

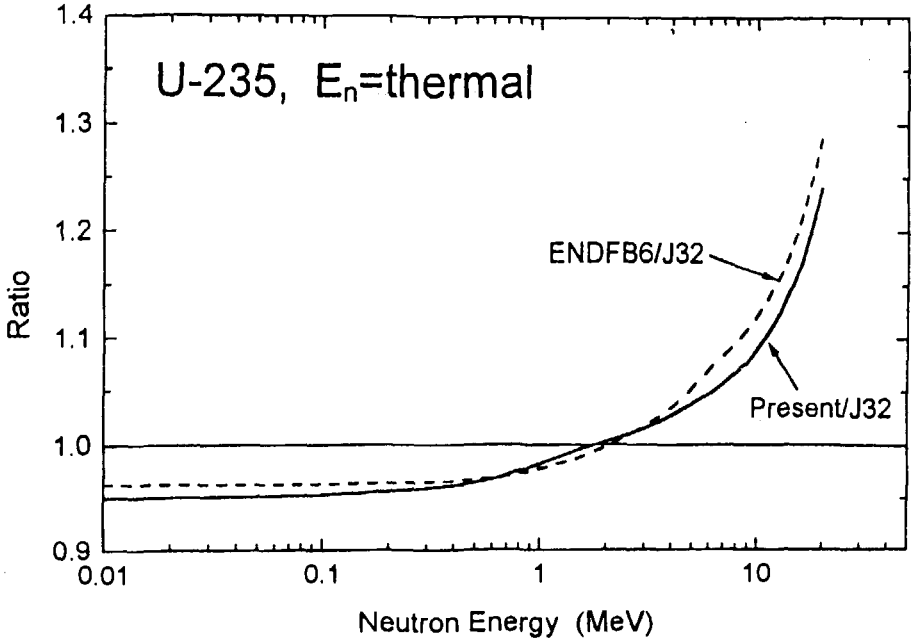

Fig.2 Ratio of the present and ENDF/B-VI evaluations relative to JENDL-3.2 for $^{235}U(n_{th},f)$.

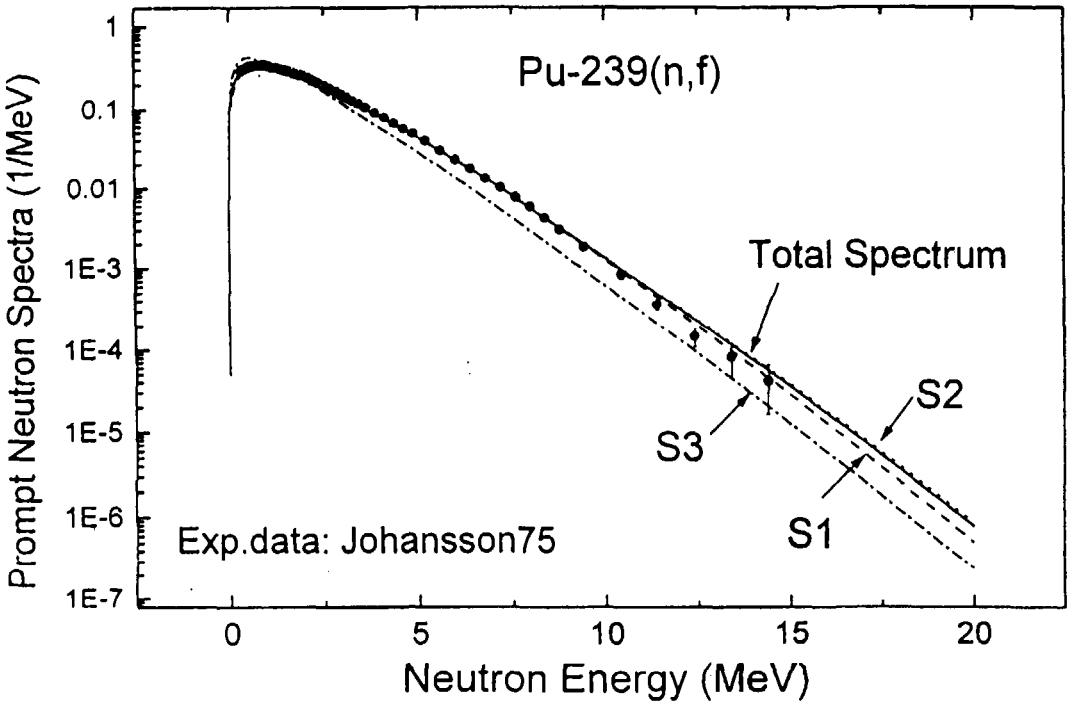

Fig.3 Modal and total prompt neutron spectra for ^{239}Pu(n_{th},f).

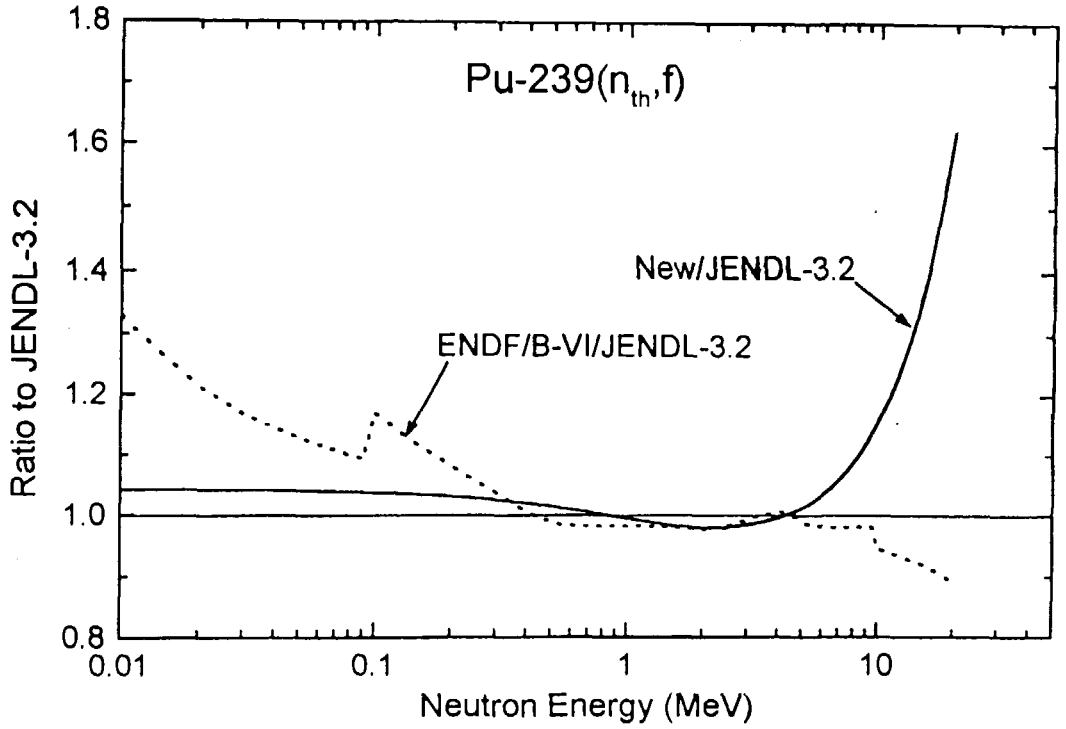

Fig.4 Ratio of the present and ENDF/B-VI evaluations relative to JENDL-3.2 for ^{239}Pu(n_{th},f).

JP0150671

3.9

Reactor Kinetics Calculated in the Summation Method and Key Delayed-neutron Data

Kazuhiro OYAMATSU

Department of Media Production and Theories, Aichi Shukutoku University
9 Katahira, Nagakute, Nagakute-cho, Aichi-gun, Aichi, 480-1197, Japan
e-mail : oyak@asu.aasa.ac.jp

The point-reactor kinetics after a step reactivity insertion to a critical condition is solved directly form fission-product (FP) data (fission yields and decay data) for the first time. Numerical calculations are performed with the FP data in ENDF/B-VI. The inhour equation obtained directly from the FP data shows a different behavior at long periods from the one obtained from Tuttle's six-group parameter sets. The behavior is quite similar to the one obtained from the six-group parameter sets in ENDF/B-VI, that were obtained from FP data in a preliminary version of ENDF/B-VI. To identify the erroneous FP data, we examine the asymptotic form of the inhour equation at an infinitely long period. It is found that the most important precursors for long reactor periods are found ^{137}I, ^{88}Br and ^{87}Br. They cover more than 60 % of the reactivity. It is remarkable that ^{137}I alone covers 30-50 % depending on the fissioning system. In addition to the three precursors, ^{136}Te is found a candidate precursor for the peculiarity from the time dependence of the delayed neutron activity. It is recommended that the precision of their Pn values should be improved experimentally. For ^{137}I, ^{88}Br, and ^{87}Br, the relative uncertainty, dPn/Pn, should be decreased down to 2 % and for ^{136}Te to 5%.

1. Introduction

It was pointed out that the reactor kinetics obtained from the ENDF/B-VI delayed-neutron (DN) data shows a peculiar behavior [1]. For analyses of the reactor kinetics, not only the number of the total delayed neutrons but also its time dependence is needed. In principle, these quantities can be calculated from decay and buildup of fission-product (FP) nuclei. From this viewpoint, the DN data in ENDF/B-VI were obtained from the summation calculation with FP data in a preliminary version of ENDF/B-VI.

This paper demonstrates the reactor kinetics calculation directly from the FP decay and buildup for the first time. For simplicity, the calculation is performed for a step insertion after a critical condition. The FP data are taken from ENDF/B-VI so as to identify the source of the peculiarity of the DN data in ENDF/B-VI.

The following notations are use in this paper.

ν : average number of total neutrons emitted after a pulse fission

$\overline{\nu}_d$: average number of delayed neutrons emitted after a pulse fission

$\beta = \overline{\nu}_d / \nu$

$n_d(t)$: delayed neutron activity after a pulse fission

k : neutron multiplication = (neutron production)/ (neutron loss)

$\rho = (k - 1) / k$: reactivity

$\Lambda = 1 / k$: mean neutron generation time

2. Kinetics of a point reactor

The kinetics of a point reactor is obtained from an integro-differential equation for the reactor power $p(t)$ in the inverse method with a simple modification.

$$\frac{dp}{dt} = \frac{\rho(t) - \beta}{\Lambda} p(t) + \int_{-\infty}^{t} du \frac{p(u)}{\Lambda} \frac{n_d(t-u)}{\nu} \tag{2.1}$$

The essential point is to replace the DN kernel by the DN activity after a pulse fission, $n_d(t)$. The DN activity is calculated from the fission yields and decay data in the summation method. Equation (2.1) can be solved formally using Laplace transform.

From Eq. (2.1), we can obtain the inhour equation that relates the reactivity ρ with the asymptotic reactor period T.

$$\rho = \frac{\int_0^{\infty} dt \exp(-t/T) m_d(t)}{\nu T} . \tag{2.2}$$

Here, $m_d(t)$ is the DN activity after the infinite irradiation at a constant fission rate 1 fission/s. It is given by

$$m_d(t) = \int_{-\infty}^{0} du \exp n_d(t-u) . \tag{2.3}$$

It is interesting that the inhour equation (2.2) is written simply with $m_d(t)$. This reflects the fact that the system was critical at $t < 0$.

It is useful to consider an asymptotic formula of Eq. (2.2) for a long $T\left(T \to \infty\right)$. It is given by

$$\rho = \frac{N}{\nu} \frac{1}{T} \tag{2.4}$$

with $$N = \int_0^{\infty} dt\, m_d(t) \tag{2.5}$$

being the number of total delayed neutrons emitted after the infinite irradiation.

3. Delayed neutron data in ENDF/B-VI and their summation calculation

In ENDF/B-VI, the time dependence of DN emission is given in terms of parameter values for the following conventional fitting formula

$$n_d(t) = \overline{\nu}_d \sum_{i=j}^{6} \alpha_j \lambda_j \exp\left(-\lambda_j t\right) . \tag{3.1}$$

with $$\sum_{j=1}^{6} \alpha_j = 1 \tag{3.2}$$

Here, α_j and λ_j are the fractional DN yield and the decay constant of group j, respectively.

The DN data, $\overline{\nu}_d$, α_j and λ_j , are conventionally evaluated from direct measurements of $\overline{\nu}_d$ and $n_d(t)$. However, ENDF/B-VI obtained these values from summation calculations of $\overline{\nu}_d$ and $n_d(t)$.

The summation calculation simulates decay and buildup of FP's using the FP fission-yield and decay data.

$$\overline{\nu}_d = \sum_{i}^{all\ FP} Y_i P_{ni} . \tag{3.3}$$

Here, Y_i and Pn_i are the cumulative fission yield and the DN emission probability of FP i. The time dependence is given by

$$n_d(t) = \sum_{i}^{all\ FP} Y_i P_{ni} \lambda_i \exp\left(-\lambda_i t\right) + \left(decay\ chain\ effect\right) , \tag{3.4}$$

where λ_i is the decay constant of FP i. The decay chain effect in Eq. (3.4) reflects the fact that DN precursors can be created in part from decays of their parent FP's. This term is not very large but gives an appreciable contribution to $n_d(t)$.

The summation calculation requires fission yield and decay data of many short lived FP's. However their data were not known precisely enough. This is the reason why the DN data have been evaluated from the direct measurements except for ENDF/B-VI.

Including the decay chain effect, $n_d(t)$ are calculated with an FP decay code in the summation method [2] in the following. The FP fission yield and decay data are taken from ENDF/B-VI.

4. Key precursors for kinetics of a point reactor

The inhour equation (2.2) is calculated with $n_d(t)$ obtained in the summation method. In Fig. 1, it is compared with the conventional calculation obtained from the six-group parameter set evaluated by Tuttle. This figure clearly shows a peculiar behavior at long periods, which is similar to the one obtained from the ENDF/B-VI six-group parameter set [1]. Furthermore, it is seen that the value at the infinitely large period is a good measure of the difference.

DN precursors which contribute much to the reactivity at the infinitely long period can be examined from Eqs. (2.4) and (2.5). They are the ones that give large contributions to N, which is the number of the delayed neutrons emitted after the infinite irradiation. Figure 2 shows the contribution from each DN precursor. ^{137}I, ^{88}Br and ^{87}Br cover more than 60 % of the reactivity. It is interesting that the most important precursor is ^{137}I although it has been believed that the longest lived ^{87}Br is the most important at a large period.

To identify DN precursors which cause the peculiar behavior in Fig. 1, the time dependence of $m_d(t)$ is analyzed in the following way because the reactivity ρ is proportional to the Laplace transform of $m_d(t)$ in Eq.(2.2). Specifically, the summation calculation of $m_d(t)$ is compared with the one obtained from Tuttle's six-group parameter set. For simplicity, the difference between the summation calculation and Tuttle's,

$$\Delta m_d(t) = m_d^{\text{Tuttle}}(t) - m_d^{\text{SUM}}(t) \ , \qquad (4.1)$$

is assumed to be caused by an erroneous FP data of a DN precursor with half life λ. Then, we have $\Delta m_d(t) = c \exp(-\lambda t)$. The graph of $t \times \Delta m_d(t)$ has a peak at t=1/λ as a function of t. The lifetime 1/λ corresponds with half life (ln2)/λ. Hence, from the peak time, we can identify a DN precursor whose FP data is questionable.

This prescription is applied to fast fissioning systems of ^{235}U, ^{238}U because the ENDF/B-VI six-group parameters were obtained from the summation calculations for the fast systems. For the fast fission of ^{239}Pu, the summation calculation agrees well with Tuttle's. For ^{235}U(f) in Fig. 3, $t \times \Delta m_d(t)$ has a peak at 36.7 s corresponding to half life 25.4 s. Hence, this difference can be attributed to ^{137}I whose half life is 24.5 s. For ^{238}U, the obtained half life is 20.5 s. So the ^{88}Br (half life 16.5 s) and ^{136}Te (17.5 s) as well as ^{137}I can also be candidates to explain the difference.

5. Precision of fission yields and decay data

To identify key DN data for the peculiar results of the summation calculations, we examine fission yields and decay data of ^{137}I, ^{88}Br, ^{87}Br and ^{136}Te. Here, we include ^{87}Br because it is one of the most important precursors, too. For their half lives, the precision is quite good. It is about 1% or better. Hence, it is expected that the argument in the previous section works well.

Required precision of $n_d(t)$ is evaluated to be 5 % [3]. For simplicity, let us neglect the decay chain effect in Eq. (3.4) and assume all FP half lives are known well. Then, we may consider the following simple relation for the precision.

$$(\text{dPn/Pn})^2 + (\text{dY/Y})^2 = (5\%)^2. \qquad (5.1)$$

If we notice that the fission yields are more difficult to evaluate precisely, we may put

$$\text{dPn/Pn} = 3\%, \qquad \text{dY/Y} = 4\%. \qquad (5.2)$$

As for Pn values in ENDF/B-VI, however, the relative precision, dPn/Pn, is still large. It is 6 % even for the most important ^{137}I. Uncertainties of fission yields are much larger in ENDF/B-VI.

It is recommended to improve the precision of Pn values of ^{137}I, ^{88}Br, ^{87}Br, and ^{136}Te firstly because precise Pn measurements can now be performed at some laboratories. For the most important precursors ^{137}I, ^{88}Br and ^{87}Br, the precision should be better than 3%, and as

good as 2 % to eliminate uncertainties from the Pn values. For ^{136}Te, the precision should be as good as 5 % because this precursor has a relatively smaller contribution than the others.

Once we obtain the precise Pn values, it is much easier to identify remaining erroneous data. It also helps to improve the precision of fission yield values because Pn values are branching ratios of decay chains. Hence, the precise Pn measurement is the first step to make the summation calculation practical for the reactor kinetics calculation.

6. Conclusion

We calculate the reactor kinetics directly from FP fission yields and decay data for the first time. The obtained inhour equation shows peculiar underestimate of reactivity at long periods. It is similar to the one obtained from the DN data in ENDF/B-VI. ^{137}I, ^{88}Br and ^{87}Br are found to cover 60-80% of the reactivity at the infinitely long period. Among them, ^{137}I is the most important. From an additional analysis on the time dependence of the DN activity, we conclude that ^{137}I, ^{88}Br and ^{136}Te could cause the peculiarity of the inhour equation. In order to improve the summation calculation of the reactor kinetics, it is recommended that the precision of the Pn value should be improved to 2 % for the most important ^{137}I, ^{88}Br and ^{87}Br, and to 5 % for ^{136}Te.

[1] D.G.Spriggs, Nucl. Sci. Eng. 114, pp. 342-351, 1993.
[2] K. Oyamatsu, Proc. 1998 Symp. on Nucl. Data, JAERI-Conf 99-002, pp. 234-239, 1999.
[3] private communication with J. Rowlands.

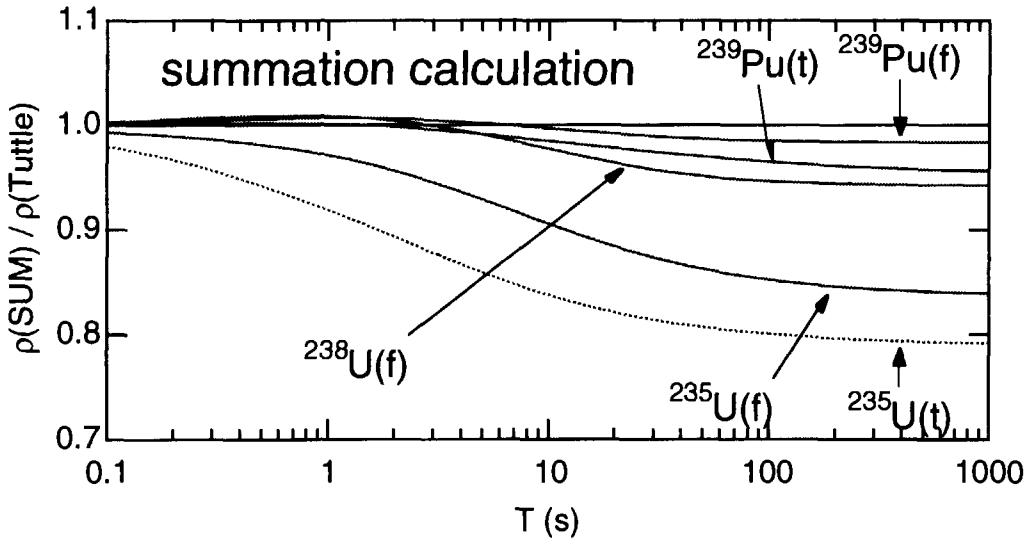

Fig. 1. Comparison of reactivity ρ in dollar between the summation method and the six-group approximation with Tuttle's parameter set.

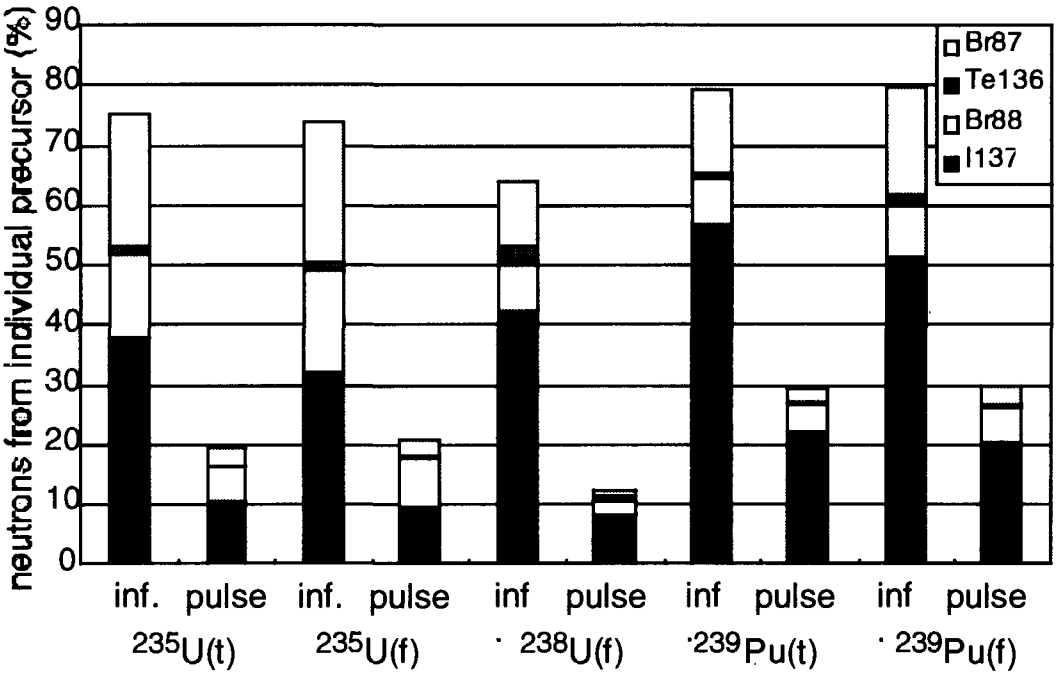

Fig. 2. Delayed neutrons from individual precursors after the infinite irradiation and after a pulse fission. The corresponding precursors in a bar are ^{137}I, ^{88}Br, ^{136}Te and ^{87}Br from the bottom.

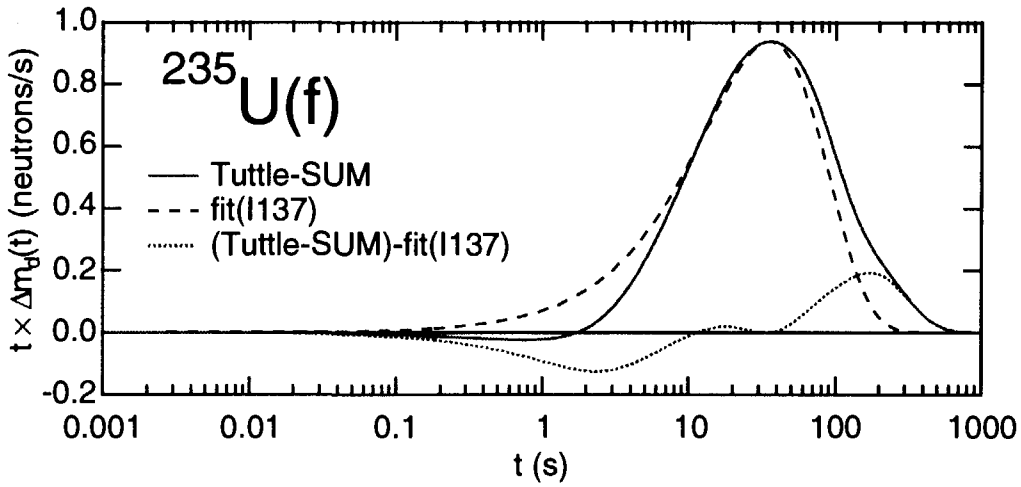

Fig. 3. The difference between summation calculation and Tuttle's. Shown are $t \times \Delta m_d(t)$ and its fitting (adjustment) with ^{137}I.

JP0150672

3.10
Measurement of γ-ray Emission Probabilities of ^{100}Tc

Kazuyoshi FURUTAKA, Shoji NAKAMURA, Hideo HARADA and Toshio KATOH

Japan Nuclear Cycle Development Institute, Tokai works,
Tokai-mura, Naka-gun, Ibaraki-ken 319-1194
email : furutaka@tokai.jnc.go.jp

Toshiyuki FUJII and Hajimu YAMANA

Research Reactor Institute, Kyoto University,
Kumatori-cho, Sennan-gun, Osaka 590-0494

Abstract

In order to precisely determine thermal neutron capture cross section of ^{99}Tc nuclide, γ-ray emission probabilities of ^{100}Tc were measured using a newly developed β-γ coincidence system, which utilizes a plastic scintillator as a β-ray detector.

About 5 kBq of ^{99}Tc samples were irradiated for 15 seconds, and then β and γ rays were measured for three minutes. The measurements were repeated 99 times.

From the obtained data, ratios of coincidence counting rates to β singles counting rates, n_c/n_β, was determined for 540 keV γ ray. To determine γ-ray emission probabilities, a method has been developed which uses a Monte Carlo simulation and takes into account β feedings to excited levels and detection threshold of β rays.

1 Introduction

The ^{99}Tc is a long-lived ($T_{1/2} \doteq 2.1 \times 10^5$ y) fission product nuclide with a large fission yield. Therefore, it is suggested as a candidate for neutron transmutation, and many experimental works have been done in order to determine the thermal neutron capture cross sections of ^{99}Tc, in particular by using an activation method[1].

In order to precisely determine the cross section in the activation method, precise values of γ-ray emission probabilities of the reaction product, ^{100}Tc, are required. These values are, however, determined with large errors (7.0 ± 1.2 % for 540 keV γ ray [2]) mainly because of its short half-life ($T_{1/2} = 15.5$ s).

To determine γ-ray emission probabilities of the ^{100}Tc nuclide, a β-γ coincidence measurement has been done by using a newly developed β-γ coincidence system which utilizes a plastic scintillator as a β-ray detector[3].

2 The experiment and data analysis

The experiment has been carried out at the Research Reactor Institute of Kyoto University. About 10 μl of ammonium hydroxide solution which contained 5 kBq of ^{99}Tc as ammonium pertechnetate, was dried on an acrylic plate and irradiated by neutrons for 15 seconds using a pneumatic tube Pn-3 at the institute, and then β- and γ-rays emitted from the sample were measured.

Beta rays were measured using a plastic scintillation detector placed at 10 cm distance from the sample, whose thickness was 4 mm and which has a trapezoidal shape with an area of 33 cm^2. For γ-ray detection, a HPGe detector was used, whose relative efficiency is 90 % of that of 3"×3" NaI detector. The distance between the irradiated sample and the Ge detector was 3 cm. To follow the decay of the ^{100}Tc nuclei, the obtained data were partitioned every 5 seconds. The irradiations and the measurements were repeated 99 times to improve the statistical accuracy. A total of 2×10^6 counts were obtained for a peak area of the 540 keV γ-ray, which is emitted after β decay of the ^{100}Tc nuclei.

In **figure 1**, an energy spectrum of γ rays observed by the Ge detector is shown, which is obtained by summing singles (projection) spectra over all runs. From the spectrum, γ rays emitted following the decay of ^{100}Tc, namely 540, 591 and 1512 keV, are clearly identified. The figure also shows a

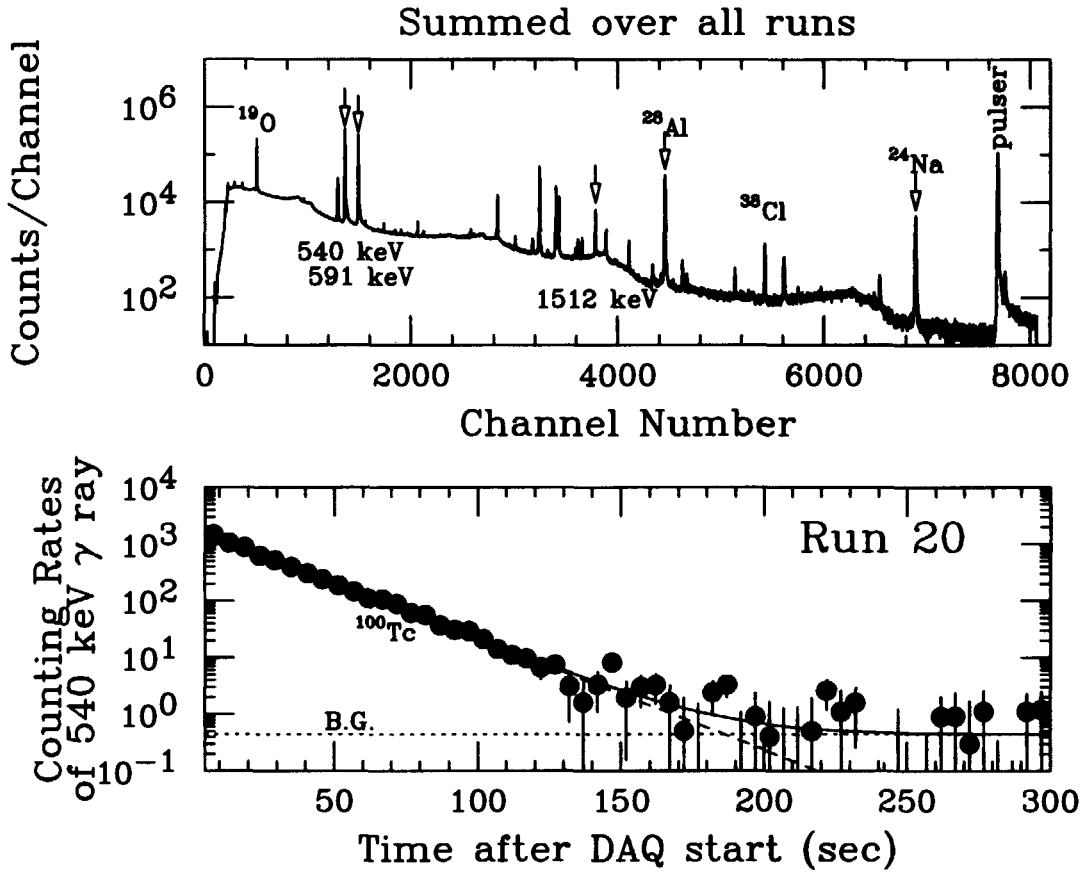

Figure 1: (upper) Singles spectrum of γ rays summed over all runs. (lower) Decay curve of 540 keV peak yields. The dashed line represents contribution from ^{100}Tc, while dotted lines are that from backgrounds.

decay curve of peak-areal counts of the 540 keV γ ray in a typical run. The decay data for each run were fitted by a function with the following form:

$$Y(t) = a \exp\left(-\frac{\ln(2)}{\tau} t\right) + C, \tag{1}$$

where τ, a and C were varied as free parameters. The τ corresponds to the half-life of ^{100}Tc. By averaging the obtained values for τ over all runs, τ for ^{100}Tc was determined to be 15.27 ± 0.02 (s), thus the 540 keV γ rays were confirmed to be emitted following the decay of ^{100}Tc.

Shown in **figure 2** is a β-ray energy spectrum summed over all runs. A bump around 50 channel bin was caused by noises, and therefore counts above 90 channel (inclusive) are summed as a β counts. **Figure 3** shows a decay curve for the β-ray counting rate in a typical run. To extract a contribution from ^{100}Tc to the singles β counts, the decay curves were fitted by a function with the following form:

$$Y'(t) = \sum_{i=1}^{3} a_i \exp\left(-\frac{\ln(2)}{\tau_i} t\right) + C', \tag{2}$$

In the fit, a_is and C' were varied as free parameters while τ_is were fixed to half-lives of ^{100}Tc (15.27 s), ^{19}O (26.91 s [2]) and ^{27}Al (2.248 min. [3]). The solid line in the figure shows a result of a fit, while contribution from the decay of ^{100}Tc was shown by the dashed line. Coincidence counting rates of the β rays were determined in the same manner.

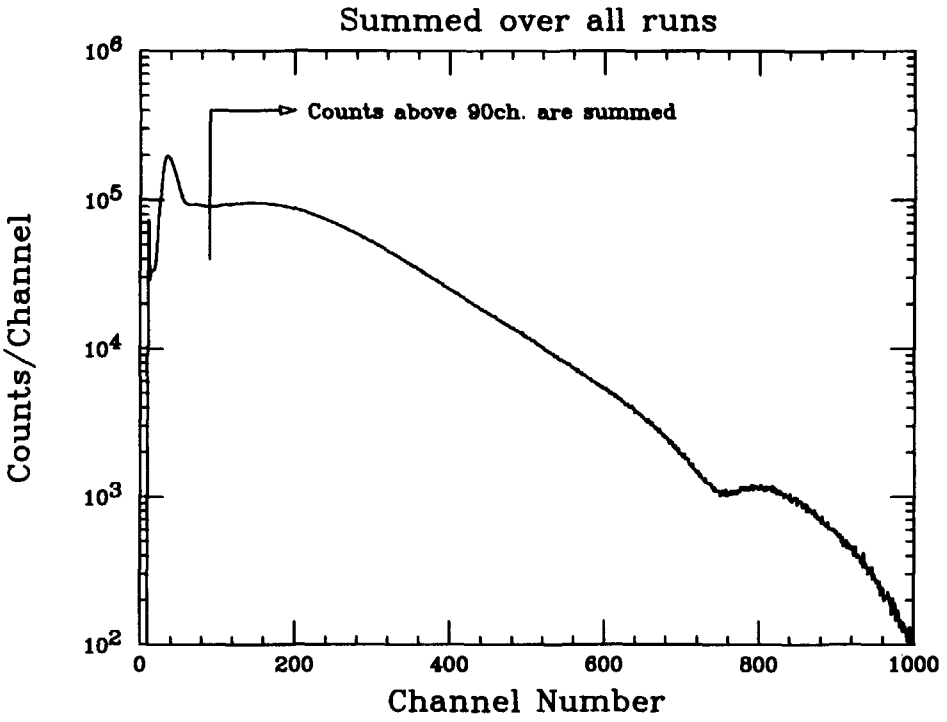

Figure 2: Singles spectrum of β rays summed over all runs.

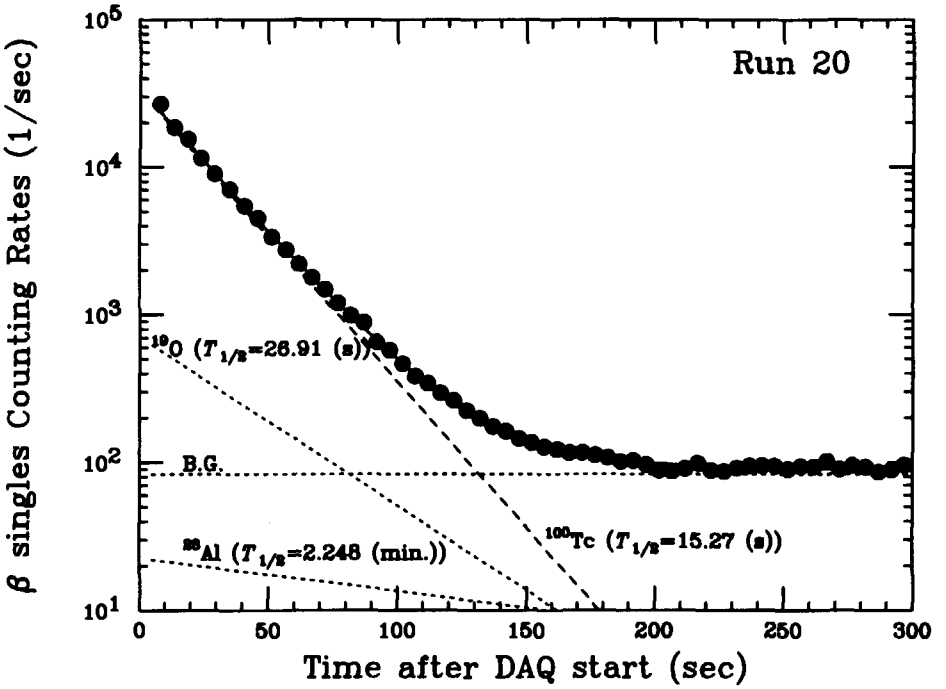

Figure 3: Decay curves of singles β ray counts above 90 ch. The solid line represents the result of the fit and dashed line contribution from ^{100}Tc. The dotted lines express contributions from ^{19}O, ^{28}Al and backgrounds.

From the result of the above mentioned fits, ratios of coincidence counting rates to β singles counting rates, n_c/n_β, were calculated for each time bin in each run. The final values of n_c/n_β were obtained after averaging over all time bins and all runs. For 540 keV γ ray, $n_c(540\ keV)/n_\beta$ was determined to be 0.00168 ± 0.00001.

To deduce γ-ray emission probabilities from the obtained n_c/n_β values, a method has been developed using the Monte Carlo simulation code EGS4[4]. It simulates the decay of the ^{100}Tc nuclei and the interaction between the detectors and the emitted particles (β and γ rays), and calculates n_c/n_β values as a function of β branching ratio to the ground state of ^{100}Ru. Four excited states of ^{100}Ru with large β branching ratios were taken into account in the simulation, namely the ground state, 540, 1131, 1362 and 2052 keV levels. With the five levels, more than 99.8 % of β decay feedings are exhausted[2]. Ratios between the feeding probabilities to the excited states were determined from the obtained singles γ-ray spectrum, after sum-coincidence corrections. By varying the β feeding probability to the ground state and searching for the value which reproduce the observed n_c/n_β values, the γ-ray emission probabilities can be determined. The analysis is now under way.

This work has been carried out in part under the Visiting Researcher's Program of the Research Reactor Institute, Kyoto University.

References

[1] Harada, H., Nakamura, S., Katoh, T., Ogata, Y.: *J. Nucl. Sci. Tech.*, **32**, 395 (1995)
[2] Firestone, R. B.: "*Table of Isotopes*", 8th ed., John Wiley & Sons, Inc., New York (1996)
[3] Furutaka, K., Nakamura, S., Harada, H., Katoh, T.: *J. Nucl. Sci. Tech.*, **37**, 832 (2000)
[4] Nelson, W. R., Hirayama, H., Rogers, D. W. O.: *SLAC*-265, (1985)

JP0150673

3.11

Measurement of Secondary Gamma-ray Spectra from Structural and Blanket Materials bombarded by D-T Fusion Neutrons

Takashi Nishio[1], Isao Murata[1], Akito Takahashi[1], Fujio Maekawa[2] and Hiroshi Takeuchi[2]

1) Department of Nuclear Engineering, Osaka University
Yamada-oka, 2-1, Suita, 565-0871, Japan
e-mail: nishio@newjapan.nucl.eng.osaka-u.ac.jp
2) Japan Atomic Energy Research Institute
Tokai-mura, Ibaraki 319-1195, Japan

Benchmark experiments have been carried out to validate the nuclear data files of JENDL-3.2, JENDL fusion file, ENDF/B-VI, FENDL/E-1.0 and FENDL/E-2.0 for blanket materials of $LiAlO_2$, Li_2TiO_3 and Li_2ZrO_3 and structural materials, i.e., C, V, Fe, SUS-316, Cu, Pb and W at Fusion Neutronics Source (FNS) of JAERI, Japan. Some discrepancies between measured and calculated spectra were observed. However, the C/E values for the energy multiplied integral spectrum show that all the nuclear data files were fairly reliable.

1.Introduction

In a fusion reactor design, neutron reaction cross section data are required and usually the evaluated values in nuclear data files are used for the neutronics calculation. So it is very important to carry out the benchmark experiments for candidate blanket and structural materials and to analyze their results in order to validate the nuclear data. In this study, benchmark experiments have been carried out to validate the nuclear data files of JENDL-3.2, JENDL fusion file, ENDF/B-VI, FENDL/E-1.0 and FENDL/E-2.0 for blanket materials of $LiAlO_2$, Li_2TiO_3 and Li_2ZrO_3 and structural materials, i.e., C, V, Fe, SS316, Cu, Pb and W, at Fusion Neutronics Source (FNS) of JAERI, Japan. The former three are regarded as an advanced solid breeder material because of their inherent advantages such as chemical stability at high temperature, good tritium recovery characteristics and so on, however the experimental data of these blanket materials have not been obtained so far. The latters are well-known important structural materials to be used in a fusion reactor.

2.Experiment

The experiments have been carried out at FNS. Secondary gamma ray spectra from the slab assemblies have been measured using an NaI (Tl) (3"-diam by 3"-long) scintillation detector for three emission angles of 0, 24.9 and 50.0 deg. by using the time-of-flight (TOF) method. The dimensions of the assemblies were 654～2088cm^2 in the front surface (square or circle) and 5.0～40.6cm in thickness as shown in Table 1. Figure 1 shows the experimental arrangement. The detector was positioned at about 7.5m from the slab assembly to realize good energy resolution by the TOF method. The detector was heavily shielded to reduce background gamma rays from other materials except for the sample assembly.

Table 1 Experimental assemblies.

Sample	Shape	Dimensions (cm)
C	Slab	35.6 x 35.6 x '10.2, '25.4, '40.6
V	Slab	25.4 x 25.4 x '10.2, '25.4
Cu	Slab	45.7 x 45.7 x '10.2, '25.4
Pb	Slab	40.0 x 40.0 x '5.0
W	Slab	35.6 x 35.6 x '5.1, '10.2
Fe	Slab	30.0 x 40.0 x '10.0
SS316	Slab	35.6 x 35.6 x '10.2, '20.3
$LiAlO_2$	Slab	25.4 x 25.4 x '10.2, '25.4
Li_2TiO_3	Slab	25.4 x 25.4 x '10.2, '25.4
Li_2ZrO_3	Pseudo-cylinder	23.8 ϕ x '10.2, '25.4

3.Data analysis

The response matrix of the NaI(Tl) scintillation detector was made from the results of the Monte Carlo code MCNP-4B calculation. It was confirmed that the calculated response function agrees well with the measured pulse height spectrum using the standard gamma-ray sources within 10%. The unfolding code HEPRO was used to convert measured pulse height spectrum into energy spectrum. The experimental energy spectra were compared with the calculated results obtained by using the Monte Carlo code MCNP-4B to discuss the validity of the evaluated nuclear data files of JENDL-3.2, JENDL fusion file, FENDL/E-1.0, FENDL/E-2.0 and ENDF/B-VI. Original nuclear data quoted in each nuclear data library for each element are listed in Table 2. The assemblies as well as the detector collimator were modeled precisely for the MCNP calculation. The neutron and gamma-ray source spectrum made and used in FNS was used.

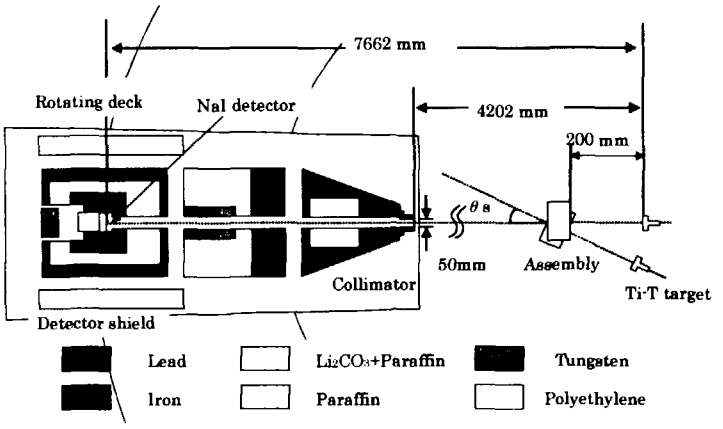

Fig.1 Experimental arrangement.

Table 2 Libraries used in the calculation.

Library name used in the calculation	Nuclear data quoted*1										
	Li	O	Al	Ti	Zr	C	V	Fe	Cu	Pb	W
JENDL-3.2	J32	J32	J32	J32	J32	J32	J32	J32	J32	J32	J32
JENDL-FF	J32	J32	JFF	JFF	JFF	J32	JFF	JFF	JFF	JFF	JFF
ENDF/B-VI	B-VI	B-VI	B-VI	B-VI	B-VI	B-VI	B-VI	B-VI	B-VI	B-VI	BVI
FENDL/E-1.0	B-VI	B-VI	J31	J31	B2	B-VI	B-VI	B-VI	B-VI	B-VI	B-VI
FENDL/E-2.0	B-VI	J32	EF3	J31	JFF	JFF+ B-VI	JFF	B-VI+ EF3	B-VI	B-VI	JFF

*1 J32, JFF, B-VI, J31, EF3 and B2 are abbreviations of JENDL-3.2, JENDL fusion file, ENDF/B-VI, JENDL-3.1, EFF-3 and BROND-2, respectively

4.Results

i) Carbon

Figure 2 shows the comparison of measured and calculated gamma-ray spectra for carbon of 10.16 cm in thickness and scattering angle of 50.0 degree. The calculated spectra are in almost good agreement with all the experimental data for all the nuclear data files.

ii) Vanadium

Figure 3 shows the comparison of measured and calculated gamma-ray spectra for vanadium of 10.16 cm in thickness and scattering angle of 24.9 degree. All the calculated spectra show underestimation leading to the conclusion that the evaluated secondary gamma ray production cross sections may be small. The peaks around 1.5 and 3 MeV are not reproduced in all the nuclear data files.

iii) Iron

Figures 4 and 5 show the comparison of measured and calculated gamma-ray spectra for iron of 10.16 cm in thickness and scattering angle of 50.0 degree and the evaluated gamma ray emission energy differential cross section (EDX) of ^{nat}Fe, respectively. JENDL fusion file is in fairly good agreement with the experimental data as shown in Fig. 4. Overestimation of the secondary gamma ray production cross section in JENDL-3.2 is reconfirmed [1]. The cross section of ^{56}Fe in ENDF/B-VI is adopted in FENDL/E-1.0, also that of ^{56}Fe in EFF-3 is adopted in FENDL/E-2.0 as shown in Table 2. As a result, the peak of 1238 keV from ^{56}Fe has not been reproduced in FENDL/E-2.0 as one can see it from the EDX spectrum of ^{56}Fe,though the reproduction is fairly good in FENDL/E-1.0.

iv) SS316

Figure 6 shows the comparison of measured and calculated gamma-ray spectra for SS316 of 10.16 cm in thickness and scattering angle of 50.0 degree. The result shows the same tendency as the case of iron because SS316 is mainly composed of iron. The influences of other elements such as Ni and Mn were not observed.

v) Copper

Figure 7 shows the comparison of measured and calculated gamma-ray spectra for copper of 10.16 cm in thickness and scattering angle of 50.0 degree. Large discrepancy is not observed and five nuclear data files reproduce the measured spectrum very well. Five nuclear data files are therefore confirmed to be fairly reliable with respect to the prediction of gamma ray spectrum.

vi) Lead

Figures 8 and 9 show the comparison of measured and calculated gamma-ray spectra for lead of 5.00 cm in thickness and scattering angle of 50.0 degree and the evaluated gamma ray emission EDX of ^{nat}Pb, respectively. ENDF/B-VI calculation gives the best agreement with the experimental data among five nuclear data files. In JENDL-3.2 and JENDL fusion file, the peaks of 1770 keV and 2615 keV from ^{nat}Pb are not observed because there is no structure around 2-3 MeV in the EDX spectrum of ^{nat}Pb as shown in Fig. 9.

vii) Tungsten

Figure 10 shows the comparison of measured and calculated gamma-ray spectra for tungsten of 5.08 cm in thickness and scattering angle of 24.9 degree. Because there is no complicated structure including discrete peaks, large discrepancy is not observed, however a slight discrepancy is found around 2 MeV.

viii) $LiAlO_2$

Figures 11 and 12 show the comparison of measured and calculated gamma-ray spectra for $LiAlO_2$ of 25.4 cm in thickness and scattering angle of 24.9 degree and the evaluated gamma ray emission EDX of ^{nat}O, respectively. A significant discrepancy between the experimental and calculated spectra is observed around 6 MeV in JENDL-3.2 and JENDL fusion file as shown in Fig. 11, that is due to the fact that the intensity of the 6130 keV gamma ray from the second excited level of ^{16}O is not evaluated in JENDL-3.2 and JENDL fusion file as shown in the EDX spectrum of Fig. 12. All the nuclear data files properly reproduce discrete gamma ray peaks from ^{27}Al.

ix) Li_2TiO_3

Figures 13 and 14 show the comparison of measured and calculated gamma-ray spectra for Li_2TiO_3 of 10.16 cm in thickness and scattering angle of 50.0 degree and the evaluated gamma ray emission EDX of ^{nat}Ti, respectively. The same tendency as $LiAlO_2$ is observed for ^{16}O. The calculated spectra in JENDL-3.2 and JENDL fusion file agree well with the experimental data below 3 MeV as shown in Fig.13. The ENDF/B-VI calculation seems to underestimate expcept for peaks over 5 MeV as is understood from the EDX spectrum of ^{nat}Ti in Fig.14.

x) Li_2ZrO_3

Figures 15 and 16 show the comparison of measured spectra and calculated gamma-ray spectra for Li_2ZrO_3 of 10.16 cm in thickness and scattering angle of 24.9 degree and the measured gamma ray spectrum of ^{nat}Zr with Hp-Ge detector by Kondo et. al.[2], respectively. A large underestimation is observed for ENDF/B-VI as shown in Fig.15 because there is no evaluated secondary gamma ray production cross section for Zr. The FENDL/E-1.0 calculation is in excellent agreement with the experimental data among all the nuclear data files. This means that the secondary gamma ray production cross section of ^{nat}Zr in BROND-2 is very reliable. The gamma ray peak around 2 MeV from ^{nat}Zr is not reproduced in all the nuclear data files, though this peak was observed in the measured gamma ray spectrum as shown in Fig.16.

xi) The ratio of C/E in energy integral

The ratio of calculated to measured gamma ray spectrum multiplied by the gamma ray energy (C/E) is described for all the samples in Fig.17. The C/E values deviate within $\pm$ 20% from 1.0 except for ^{nat}V and ^{nat}Fe. All the nuclear data files are thus confirmed to be reliable in general with respect to the prediction of gamma ray transport.

5.Conclusion

Secondary gamma ray benchmark experiments for advanced blankets and structural materials have been conducted. The nuclear data files of JENDL-3.2, JENDL fusion file, ENDF/B-VI, FENDL/E-1.0 and FENDL/E-2.0 were validated by means of comparing measured with calculated secondary gamma ray spectra. It was found from the comparison that there were some discrepancies between experiment and calculation and it was pointed out that several nuclear data files should be improved. However, for the energy integral, all the C/E values deviate within 20% except for ^{nat}V and ^{nat}Fe in all the nuclear data files.

Acknowledgments

The authors wish to acknowledge the operating staff of FNS, JEARI. for their excellent operation of FNS.

Reference

[1] Maekawa F., Oyama Y., Konno C., Wada M. and Ikeda Y.: Nucl. Sci. Eng., 126, 187 (1997).
[2] Kondo T. Private Communication, Osaka University (1999).

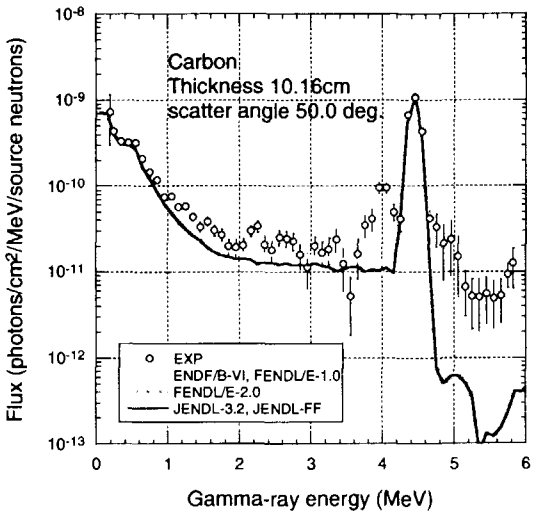

Fig.2 Gamma-ray flux for Carbon of 10.16 cm in thickness at 50.0 degree

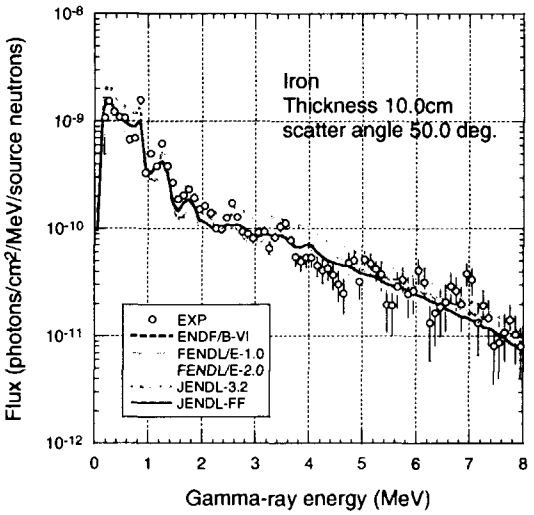

Fig.4 Gamma-ray flux for Iron of 10.16 cm in thickness at 50.0 degree

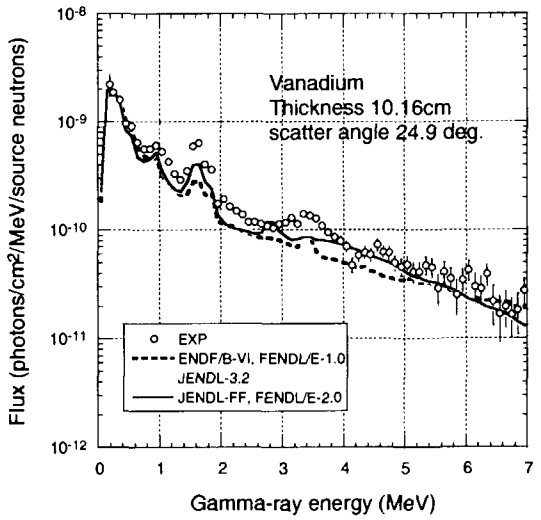

Fig.3 Gamma-ray flux for Vanadium of 10.16 cm in thickness at 24.9 degree

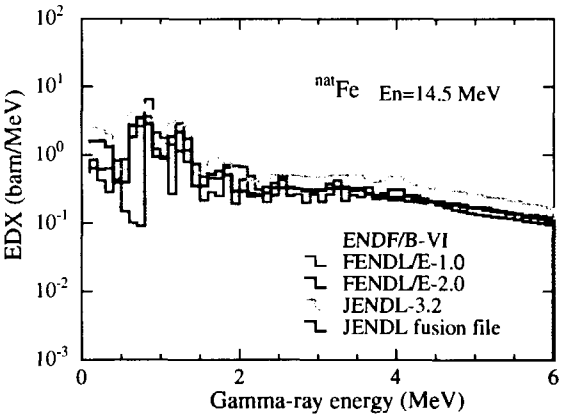

Fig.5 Evaluated gamma ray emission EDX of ^{nat}Fe

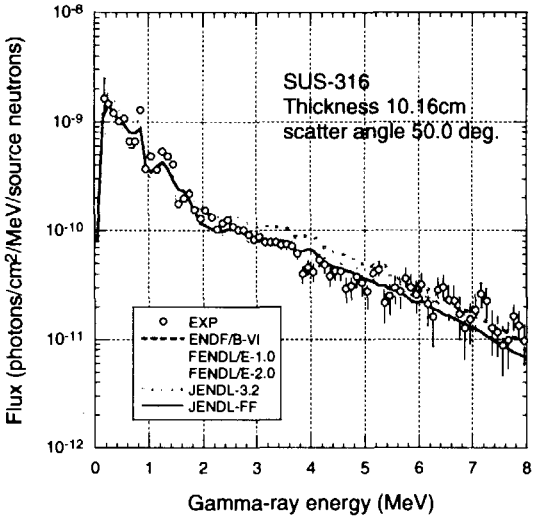

Fig.6 Gamma-ray flux for SUS-316 of 10.16 cm in thickness at 50.0 degree

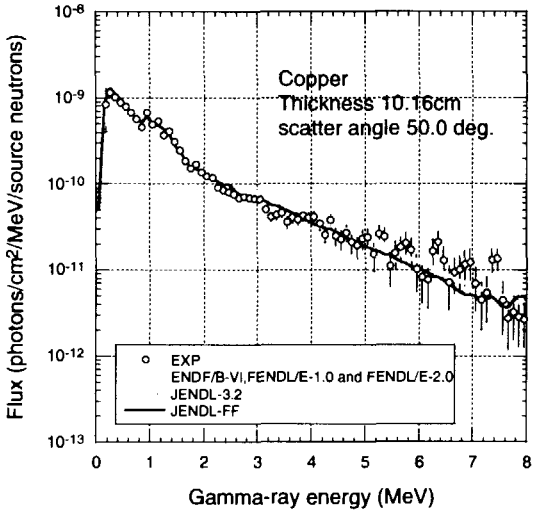

Fig.7 Gamma-ray flux for Copper of 10.16 cm in thickness at 50.0 degree

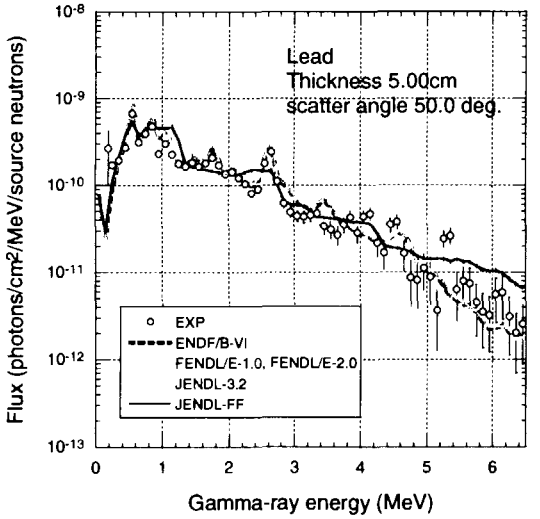

Fig.8 Gamma-ray flux for Lead of 5.00 cm in thickness at 50.0 degree

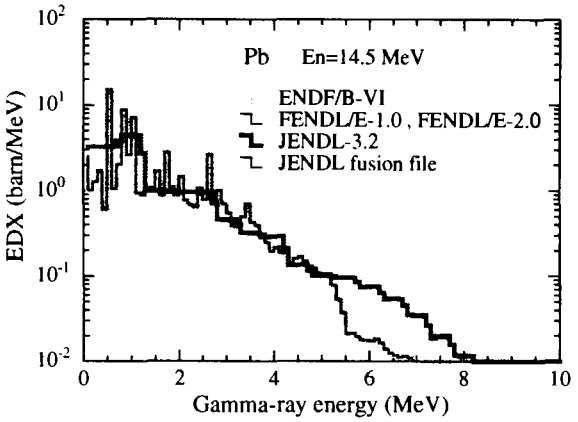

Fig.9 Evaluated gamma ray emission EDX of ^{nat}Pb

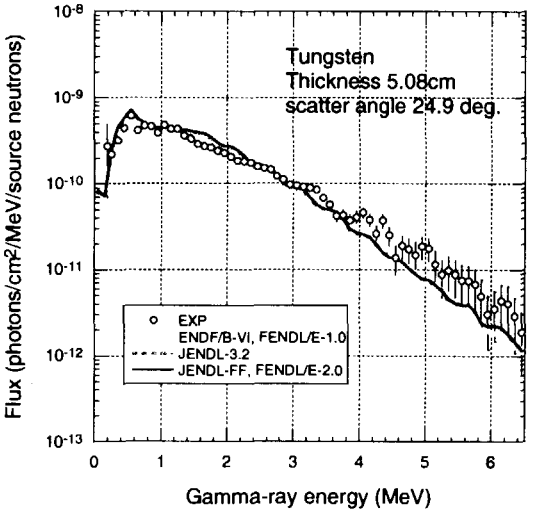

Fig.10 Gamma-ray flux for Tungsten of 5.08 cm in thickness at 24.9 degree

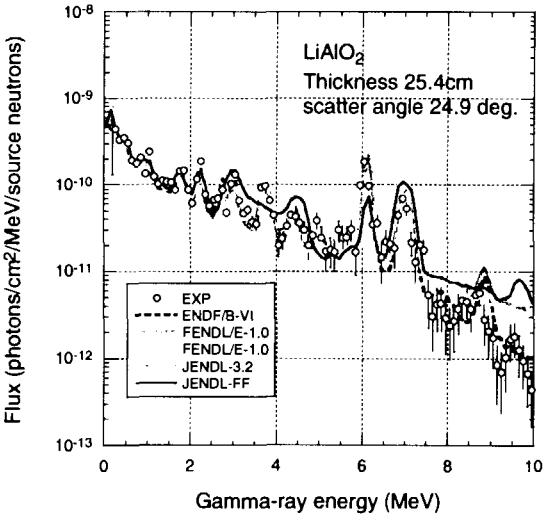

Fig.11 Gamma-ray flux for $LiAlO_2$ of 25.4 cm in thickness at 24.9 degree

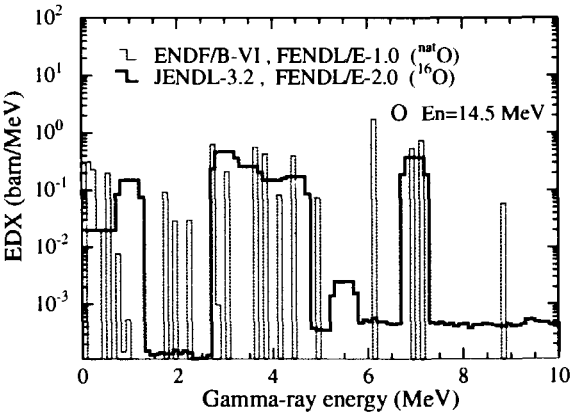

Fig.12 Evaluated gamma ray emission EDX of ^{nat}O

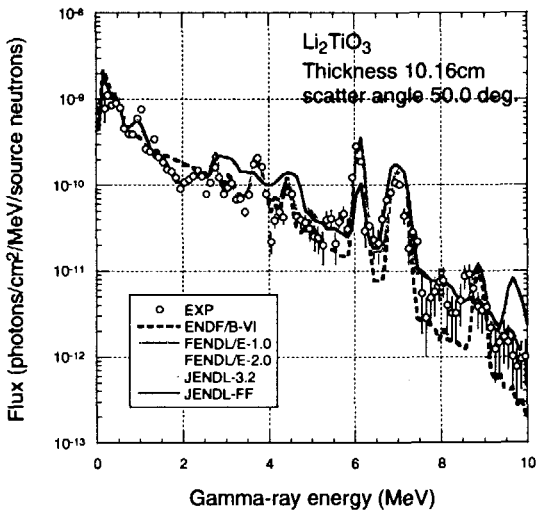

Fig.13 Gamma-ray flux for Li_2TiO_3 of 10.16 cm in thickness at 50.0 degree

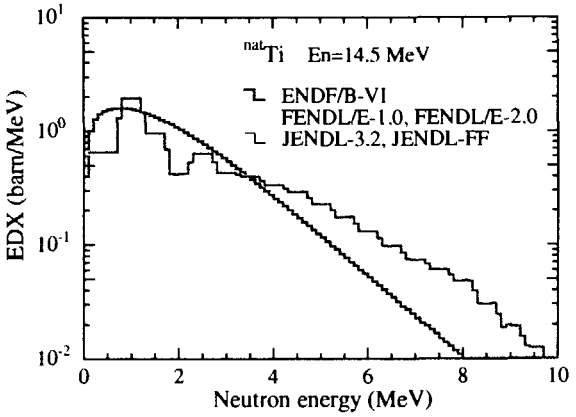

Fig.14 Evaluated gamma ray emission EDX of ^{nat}Ti

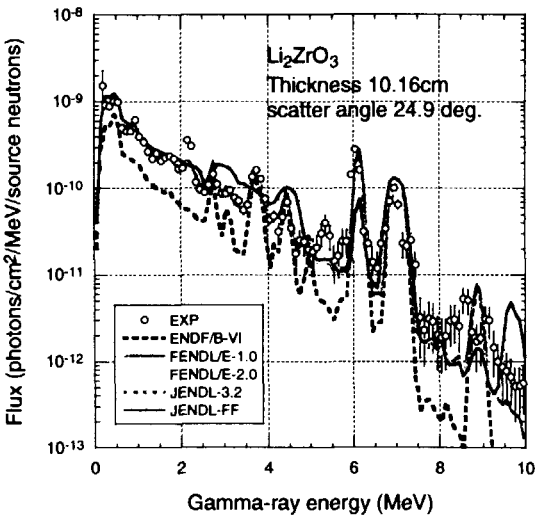

Fig.15 Gamma-ray flux for Li_2ZrO_3 of 10.16 cm

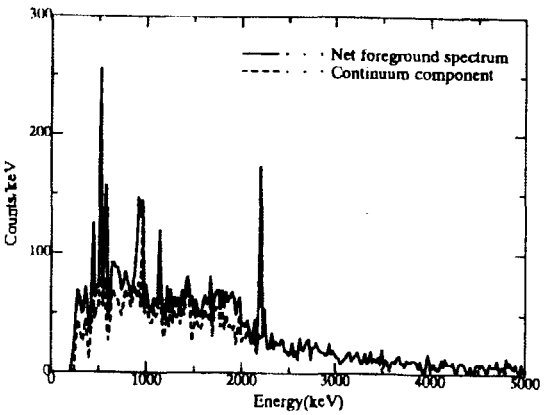

Fig.16 The gamma ray spectra of Zr with Ge detector by Kondo et. al.

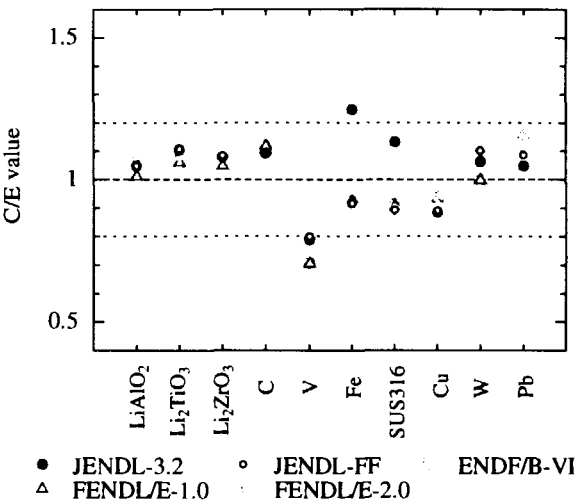

Fig.17 The ratio of calculation to experiment

JP0150674

3.12

Measurement of Double Differential Cross Section for Proton Emission Reactions of Silicon and Fluorine by Incident DT Neutrons

Yasuaki. Terada, Hiroyuki Takagi, Isao Murata, Akito Takahashi
Department of Nuclear Engineering, Osaka University
Yamadaoka 2-1, Suita, Osaka, 565-0871, Japan
e-mail: terada@newjapan.nucl.eng.osaka-u.ac.jp

In OKTAVIAN, the Intense 14MeV Neutron Source Facility of Osaka University, the double differential cross sections (DDXs) of (n,xp) reaction for ^{nat}Si, ^{19}F induced by incident DT neutrons have been measured by using by two-dimensional analysis of the E-TOF spectrum, combined with the pulse-shape discrimination technique. From the result of comparison with JENDL fusion file, JENDL fusion file fairly reproduced the shape of the spectra, however, a slight underestimation was observed.

1. Introduction

In fusion power reactor development, it is indispensable to understand behavior of charged particles, because the DDX of charged particles emission reactions (DDXc) induced by 14 MeV incident neutrons is of primary importance for evaluation of nuclear heating and material damages in the elements and components of DT fusion devices. However, until now only a few data have been measured worldwide because of experimental difficulties such as high background and low net-count rate due to small cross section and thin sample.

In the previous experiments, we could use relatively thin samples because they were mostly medium-heavy metals. However, in light elements, a thin sample cannot be prepared easily and the thickness of their compounds available becomes more than a few hundred micrometers. In the last few years, the new unfolding method (spectrum type Bayes estimation method [1]) was therefore introduced to realize measurements with a thick sample [2]. The purpose of this study is to measure the DDXs of proton emission reaction from ^{nat}Si(320 μ m) and ^{19}F(500 μ m) by using the spectrum type Bayes estimation method and

Table.1 Description of the measured samples

Sample nucleus	Measured particle	Sample material	Measured angle (deg)	ϕ (mm)	Thickness (μ m)	Abundance (%)
^{19}F	Proton	Teflon	45, 60, 70, 90, 110	60.0	500	^{19}F 100.0
^{nat}Si	Proton	Si wafer	45, 60, 70, 90, 110	28.0	320	^{28}Si 92.23 ^{29}Si 4.67 ^{30}Si 3.10

E-TOF method combined with the pulse-shape discrimination technique [3]. Silicon is a very important semiconductor material and can be used as a plasma facing material (SiC), blanket material (Li_2SiO_3), and so on. Fluorine is well known as is contained in FLIBE (Li_2BeF_4), which is one of the famous liquid blanket materials. The details of the samples are shown in Table 1.

2. Experimental procedure

The charged-particle spectrometer, the schematic view of which is shown in Fig.1, was arranged in a cylindrical vacuum chamber of 1 m in diameter and 1 m in length. The chamber was kept at a pressure of ~1.3 Pa. The background counts in charged-particle detection ware reduced by the pulse-shape discrimination technique and shielding set made of iron, lead and polyethylene. The detector was placed inside the lead shield. The particle-emission angle can be changed by adjusting the sample position as shown in Fig.2. The flight path of emitted particle varies from 42 cm to 59 cm according to the emission angle. The measurements of the DDXc were carried out at five angles of 45, 60, 70, 90 and 110 deg.

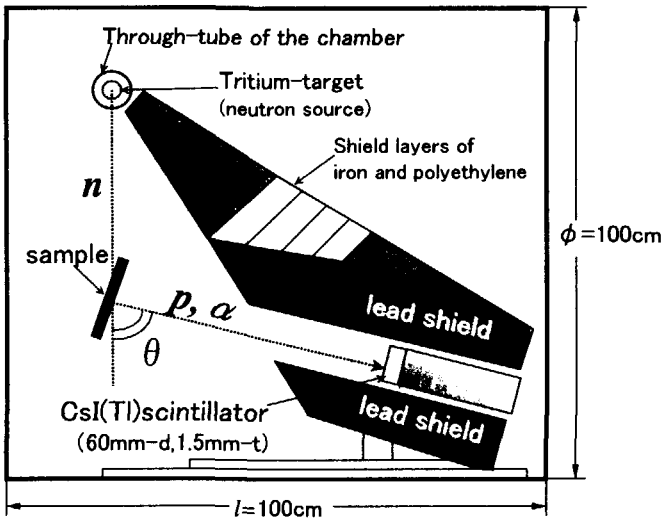

Fig.1 Schematic arrangement of the charged particle spectrometer

As neutron source, pulsed D-T neutrons at OKTAVIAN of Osaka University were used. The OKTAVIAN generates 5×10^8 neutrons/s by bombarding a 370 GBq TiT target using pulsed deuteron beams with ~3 ns pulse width and 2 MHz repetition frequency. The TiT target was positioned in a stainless steel through-tube and out of the vacuum chamber.

A CsI(Tl) scintillator (1.5 mm in thickness and 50 mm in diameter) was used as charged-particle detector because of its good performance in pulse-shape discrimination.

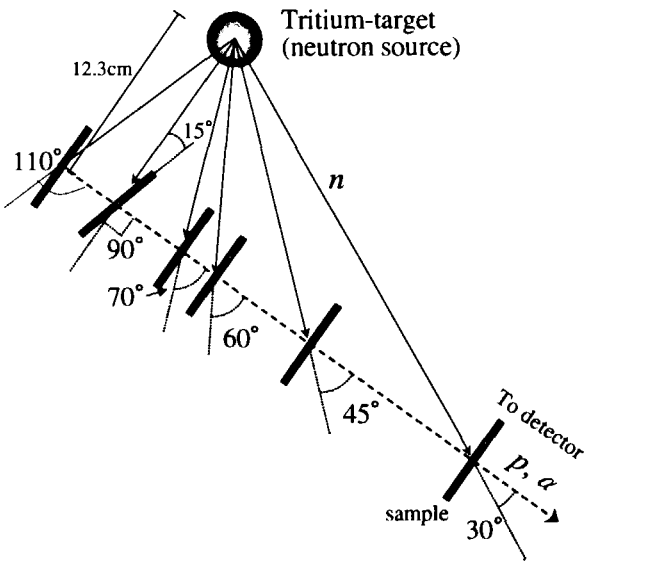

Fig.2 The sample position for various emission angle

Figure 3 shows the electronic circuit for the present measurement. The two-dimensional data acquisition has been done by using the pulse height of the dynode signal corresponding to energy and the TOF signal. The latter was created by the time-to-pulse-height converter using the fast signals of the anode as the start signal and the stop signal (with delay) from the trigger pulse of the deuteron beam. The logic signal created by the pulse-shape discrimination circuit has been fed as the gate signal to extract the charged particle of interest.

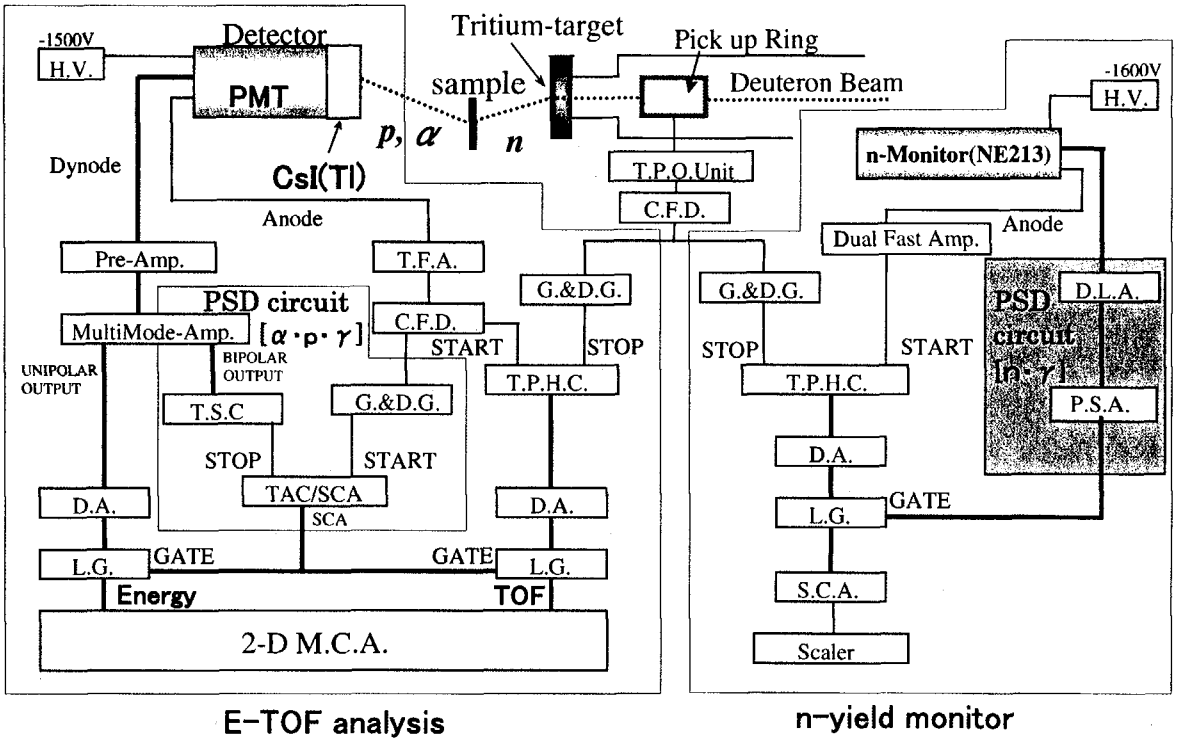

Fig.3 Block diagram of the measuring system

An example of two-dimensional energy and rise time distribution acquired by the CsI(Tl) scintillator is shown in Fig.4. The contours of each particle signals are separated with each other. Thus, we can eliminate the obstructive background and choose a contour of either alpha particles or protons signals by this technique. In addition, since background can be also eliminated with the selected contour zone for either alpha particle or proton in an E-TOF spectrum as shown in Fig.5, satisfactory charged-particle measurement with low background was realized. The principle of two-dimensional E-TOF analysis for charged particles is understood by the following equation,

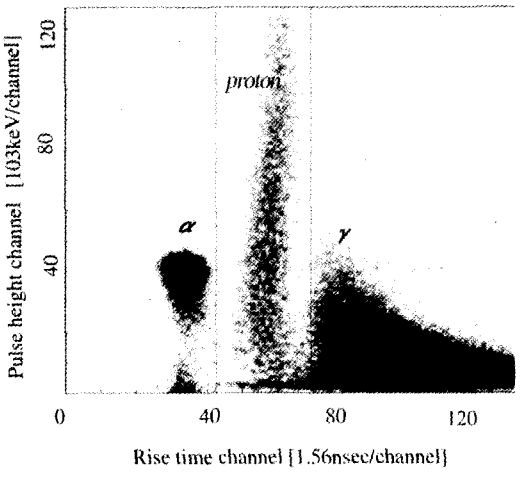

Fig.4 Two-dimensional distribution of rise time and pulse height spectrum

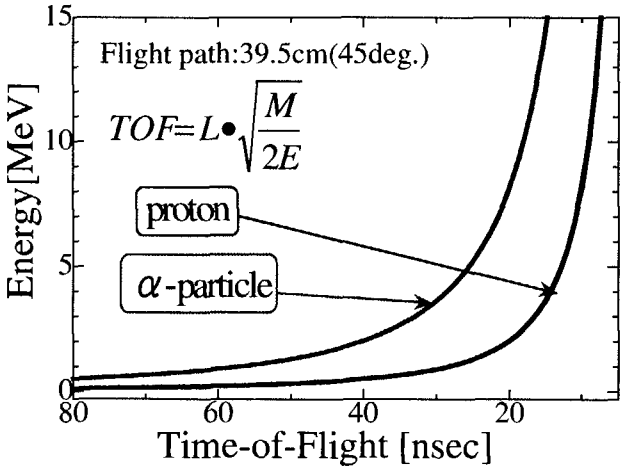

Fig.5 Ideal E-TOF spectra

$$TOF = L \bullet \sqrt{\frac{M}{2E}} \qquad (1)$$

where, TOF is the time-of-flight, L the flight path length, E and M the energy and mass of the particle, respectively.

3. Data analysis

Figure 6 shows an example of the E-TOF spectrum of proton from ^{19}F(n,xp) reaction at the emission angle of 45 degree. The spectrum in the background run has been already subtracted from that of the foreground run. Background run was undertaken by removing the sample. Since thick samples were used in this work, background proton produced in the scintillation crystal (CsI) induced by scattered neutrons of source neutrons in the sample was removed. The net energy spectra have been obtained by properly choosing the region of interest around the corresponding ideal curve [Eq.(1)] in the E-TOF spectrum. To deduce DDXs, σ ($E_n \rightarrow E, \theta$) [barn/sr/MeV], the net energy spectrum was normalized by comparing the evaluated angular differential cross section (ADX) of H(n,xp) with the measured cross section obtained using a polyethylene sample. In proton measurements, the result with the polyethylene sample was also utilized for calibration of the detected proton energy. Finally, the DDX is expressed as the following equation,

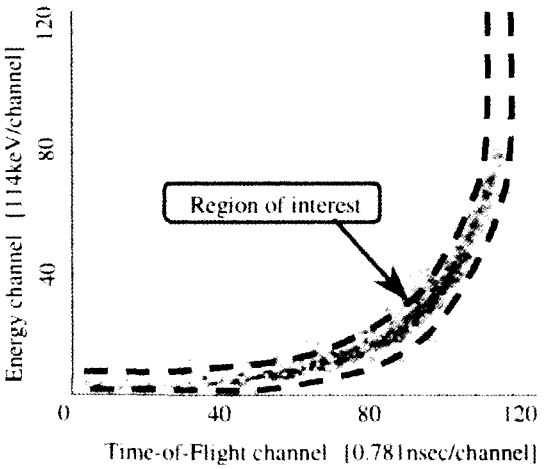

Fig.6 Measured E-TOF spectrum for ^{19}F(n,xp) reaction at 45 deg

$$\sigma(E_n \rightarrow E,\theta) = \frac{r^2 F_p^2}{r'^2 F_p'^2} \times \frac{N'}{N} \times \frac{R(E_n \rightarrow E,\theta)}{\int R'(E_n \rightarrow E,\theta)dE} \times \int \sigma'(E_n \rightarrow E,\theta)dE \qquad (2)$$

where, r is the distance between the neutron source and the center of the sample, N the number density of the sample atom, $R(E_n \rightarrow E, \theta)$ the net count rate per unit energy of the charged particle emitted from the sample, $\int R'(E_n \rightarrow E, \theta)dE$ the total net count of the charged particle for the reference cross section measurement, $\int \sigma'(E_n \rightarrow E, \theta)dE$ the reference angular differential cross section of the H(n,p) reaction. r', F_p' and N' the parameters of the reference polyethylene sample.

The raw DDX data had to be corrected because the broadening functions of angular resolution and the energy loss of the charged particles in the sample were not negligible. In the present work, the spectrum type Bayes estimation method was applied to our charged particle unfolding problem to realize thick sample measurement. This estimation method was recently developed by extending the Bayes theorem [1]. The unfolding procedure is expressed by the following equation,

$$est_j^{(l+1)} = \sum_{i=1}^{m}\left(d_i \times \frac{est_j^{l} \times r_{ij}}{\sum_j^n est_j^{(l)} \times r_{ij}} \right) \quad ,(j=1,n) \qquad (3)$$

where, r_{ij} is the response of detection system which provides the probability of a detection event giving pulse height h_i for charged particle event E_j, d_i the detected pulse height spectrum, $est_j^{(l)}$ the estimated spectrum in the *l*-th estimation calculation. This formula was repeatedly used for the uncorrected spectrum d_i in this work. The revised $est_j^{(l)}$ is used as prior information for the next revise calculation.

4. Results and discussion

The energy differential cross sections (EDXs), angular differential cross sections (ADXs) and total cross sections (TOXs) were deduced by using the measured DDX data. The measured data were compared with the evaluated nuclear data of JENDL fusion file. The experimental results and discussion are described in the following in detail. The comparisons of the total cross sections among the measured data and JENDL-FF are shown in Figs.9 and 12. The TOX value for JENDL-FF used for the comparison was corrected by removing the low energy contribution in the spectra because the charged-particle spectrometer could not measure DDX data for low-energy regions (< 3MeV). In the experimental results, the error bar only includes statistical error.

4.1 Silicon (^{nat}Si)

The comparison of the measured DDX data of ^{nat}Si(n,xp) for the emission angles of 45, 60, 70, 90 and 110 deg and the measured EDX and ADX with JENDL-FF is shown in Figs.7, 8 and 9, respectively. The ADX data were fitted with the legendre polynomials. From the comparison of the measured DDX spectra with JENDL-FF, JENDL-FF fairly reproduced the shape of the spectra for forward angles. However, an underestimation was observed in the higher energy region for the EDX spectrum. In the ADX data, JENDL-FF showed a slight underestimation, but the tendency is the same as the experimental result.

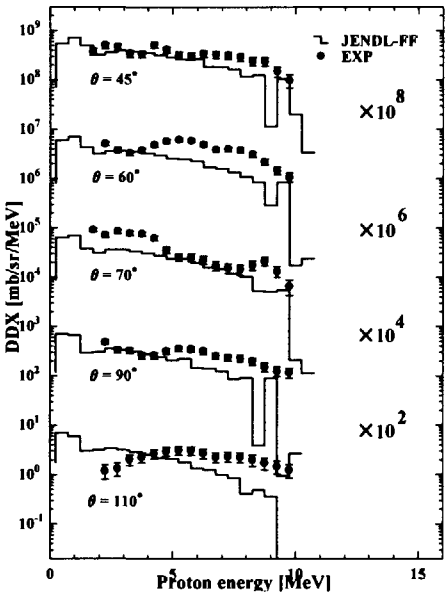

Fig.7 The DDX Data of silicon for the proton emission reaction

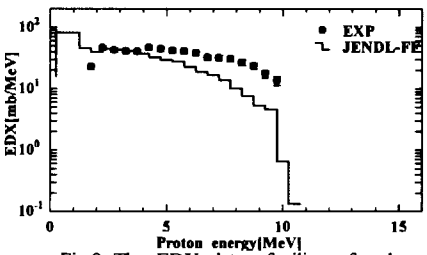

Fig.8 The EDX data of silicon for the proton emission reaction

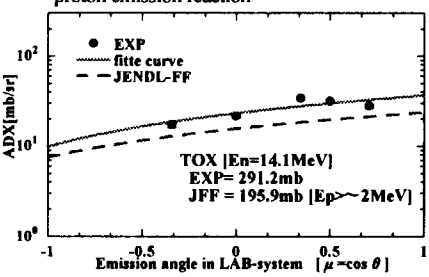

Fig.9 The ADX data of silicon for the proton emission reaction

4.2 Fluorine (^{19}F)

The comparison of the measured DDX data of ^{19}F(n,xp) for the emission angles of 45, 60, 70, 90 and 110 deg and the measured EDX and ADX data with JENDL fusion file are shown in Figs.10, 11 and 12, respectively. From the comparison of the measured DDX and EDX spectra with JENDL fusion file, JENDL fusion file fairly reproduced the shape of the spectra, however, an underestimation was observed. In the ADX data, JENDL fusion file showed an underestimation. Also a stronger forward oriented distribution was observed in the experimental ADX compared with the evaluation. In the EDX data, it is presumed that one of the causes of the discrepancy above 3.5MeV is that the F(n,np) reaction is underestimated in JENDL fusion file because of deficiency of the experimental data.

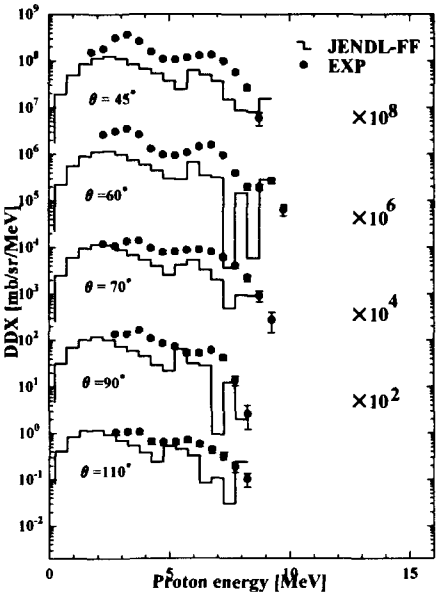

Fig.10 The DDX Data of fluorine for the proton emission reaction

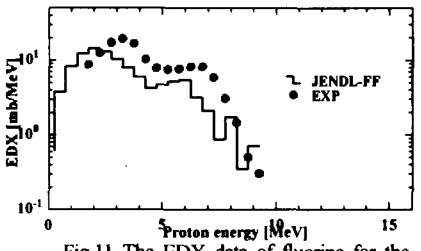

Fig.11 The EDX data of fluorine for the proton emission reaction

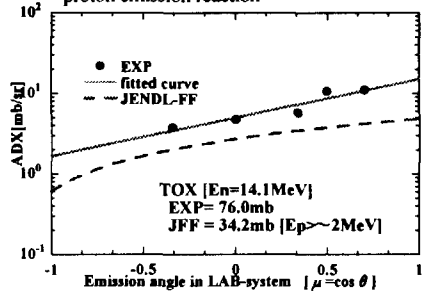

Fig.12 The ADX data of fluorine for the proton emission reaction

5. Conclusion

In present study, the measurement of the DDX for proton emission reaction of silicon and fluorine by incident DT neutrons has been carried out at emission angles from 45 to 110 deg. The measured data were compared with evaluated nuclear data of JENDL-FF.

From the comparison of the measured DDX and EDX spectra of ^{nat}Si(n,xp) reaction with JENDL-FF, An underestimation was observed in the higher energy region especially for the EDX spectrum. In the ADX data, JENDL-FF showed a slight underestimation, but the tendency was the same as the experimental result. For the DDX and EDX spectra of ^{19}F(n,xp) reaction, JENDL fusion file fairly reproduced the shape of the spectra, however, an underestimation was observed. In the ADX data, JENDL-FF showed an underestimation. Also a stronger forward oriented distribution was observed in the experimental ADX compared with the evaluation.

Reference

[1] Iwasaki, S.,: "A New Approach for Unfolding Problems Based Only on the Bayes' Theorem", 9th International Symposium on Reactor Dosimetry, Prague, Chezk, Sep. 2-6, (1996).

[2]Takahashi, A., et al.: "A Time-of-Flight Spectrometer with Pulse-Shape Discrimination for Measurement of Double Differential Charged-Particle Emission Cross Section", Nucl. Instr. Meth., A401, 93 (1997).

[3]Takagi, H., et al.: "Measurement of Double Differential Cross Sections of Charged Particle Emission Reactions by Incident DT Neutrons –Correction for Energy Loss of Charged Particle in Sample Materials- ", Proc.1998 Symp. Nul. Data, JAERI-Conf2000-005, 178 (2000).

JP0150675

3.13

(n,2n) Reaction Cross Section Measurement with A Beam DT Neutron Source

-Measurement Method-

Isao Murata[1)], Takashi Nishio[1)], Yasuaki Terada[1)], Takao Hayashi[1)], Motoyuki Mitsuda[1)], Akito Takahashi[1)] ,Kentaro Ochiai[2)], Fujio Maekawa[2)] and Hiroshi Takeuchi[2)]
[1)]Department of Nuclear Engineering, Osaka University
Yamada-oka 2-1, Suita, Osaka 565-0871, Japan
E-mail: murata@nucl.eng.osaka-u.ac.jp
[2)]Japan Atomic Energy Research Institute
Tokai-mura, Ibaraki 319-1195, Japan

The method has been established to measure (n,2n) reaction cross section with the coincidence detection technique using a newly developed beam-type DT neutron source at FNS, JAERI. A cylindrical manganese, the (n,2n) cross section of which was measured precisely with the foil activation method, was used to check the experimental method. It was confirmed from the experimental results that the present new method was basically functioning to measure only two neutrons emitted through (n,2n) reaction. Also, for manganese not so strong angular dependence was observed though the statistical accuracy was not sufficient. Consequently, it is expected that complete measurement for stable-isotope producing element by (n,2n) reaction would become possible by several measurements.

1. Introduction

The (n,2n) reaction plays a very important role in the design of fusion reactor, because it is a neutron multiplication reaction and has a large cross section value over 1 barn except for light and heavy nuclides in the energy range of several to 14 MeV. In the previous experiments, the (n,2n) reaction cross sections were measured mainly by the foil activation method. Thus, the measurement became difficult unless appropriate radioisotopes were produced by the reaction. Even now, there are many natural elements left the experimental values of which are not obtained[1]. Also, especially for light elements measurements of the neutron energy spectrum and the angular distribution for the (n,2n) reaction are important, however, they were not carried out so far.

In the present study, using a newly developed beam-type DT neutron source at fusion neutronics source (FNS), JAERI, the method is established to measure (n,2n) reaction cross section and its energy and angular distribution of simultaneously emitted two neutrons with the coincidence detection technique for elements having no experimental data.

2. Experimental

Measurement of (n,2n) reaction cross section is possible in principle with the coincidence detection technique for two neutrons emitted simultaneously. However, an acceptable signal to noise (S/N) ratio could

not be obtained because isotropically produced source neutrons, the great majority of which does not bombard the sample, act as a large amount of background signals in the measurement. The newly developed beam-type (2 cm ϕ -collimated) DT neutron source at FNS can realize the measurement by using the coincidence detection technique. The beam DT neutron source was developed by making a narrow (2cm ϕ) hole (collimator) through the very thick shield ($\sim$2m) between the target room and the measurement room. The intensity of neutrons is $\sim 1\times10^{6}$ n/sec/cm^2 at the exit of the collimator. The neutron flux rapidly decreases outside the beam region, therefore detectors can be arranged near the beam line. For this reason, differential cross sections which were difficult to be measured can be measured.

The schematic experimental arrangement is shown in Fig. 1. A small sample was positioned on the beam line at $\sim$60 cm from the collimator, that means the sample was placed at $\sim$350 cm from the neutron source. The dimensions of the sample are 1.5 cm ϕ $\times$3 cm long. The neutron flux intensity at the sample, determined by Al foil, was 1×10^{6}. Two NE213 (4cm ϕ spherical) detectors were arranged at several positions (20 cm from the sample).

The measurement was carried out with the coincidence detection technique and n/γ pulse shape discrimination technique. The former is a technique to measure selectively two neutrons emitted simultaneously from (n,2n) reaction by coincidence detection. The (n,3n) reaction can be detected by this method, but it can be neglected because the threshold energy is mostly larger than 14 MeV. The latter technique was employed to exclude coincident signals of nγ pairs through (n,n'γ), (n,2nγ) and so on by discriminating the rise time spectrum of dynode signals. Two delay line amplifiers with different gains were used to extend the dynamic range of the detector from 100 keV to 10 MeV. The electronic circuit used in the present experiment is shown in Fig. 2. Foreground (FG) and background (BG) indicated in the figure correspond to coincident and time-independent signals as shown later in Fig. 3, respectively. As for the neutron angular distribution, it is known that a slightly forward oriented distribution can be obtained if simultaneously emitted two neutrons are not distinguished. However, in the present measurement, the angular correlation of the two neutrons should be taken into account to yield the cross section because the two neutrons are measured separately with two detectors. Thus several measurements were carried out for one sample considering the symmetrical arrangement of the detectors. As the sample, a cylindrical manganese (1.5 cm ϕ $\times$3 cm long), the (n,2n) cross section of which was measured precisely with the foil activation method, was used to check the experimental method. Also, sample-out measurements were carried out to remove time-dependent background.

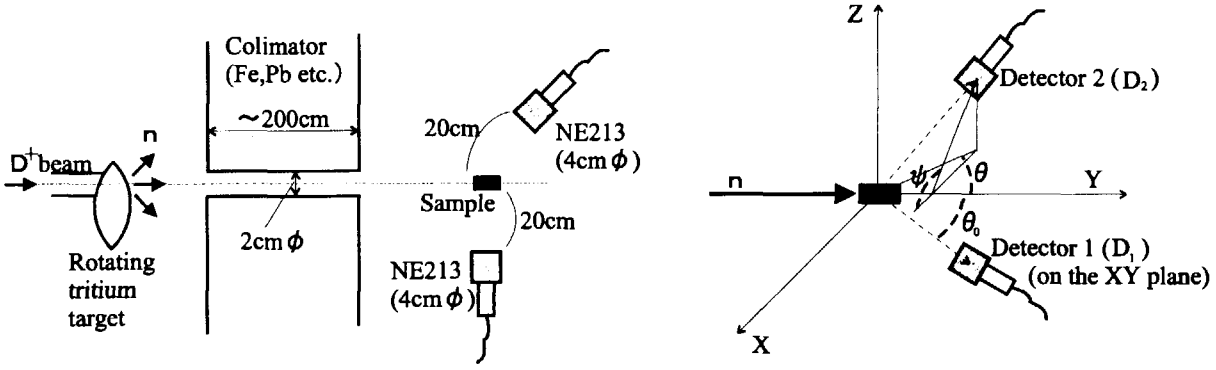

(a) Schematic arrangement of the detectors.

(b) Details of the detector arrangement.

Fig. 1 Experimental arrangement.

3. Data processing and correction

The net raw neutron spectrum is deduced by the following equation:

$$y=(y_{in,FG}-\alpha\cdot y_{in,BG})-\beta(y_{out,FG}-\alpha\cdot y_{out,BG}), \quad (1)$$

where, y is the net raw FG spectrum, $y_{in,FG}$ and $y_{in,BG}$ the raw FG and BG spectra in sample-in measurement, $y_{out,FG}$ and $y_{out,BG}$ the raw FG and BG spectra in sample-out measurement, α the ratio of the gated width in the time difference spectrum of two anodes signals of the detectors, and β the normalization factor between the sample-in and -out measurements, respectively. This equation can be used for spectra obtained by both detectors. Then the cross section can be obtained by the next equations:

$$N\sigma\phi\eta(d\Omega_1/4\pi)(d\Omega_2/4\pi)f_1 f_2' R_1 = y_1, \text{ for detector 1,} \quad (2)$$

$$N\sigma\phi\eta(d\Omega_1/4\pi)(d\Omega_2/4\pi)f_2 f_1' R_2 = y_2, \text{ for detector 2,} \quad (3)$$

where, N is the number of manganese atoms, σ the (n,2n) cross section, ϕ the neutron flux at the sample, η the neutron multiplicity of (n,2n) reaction, = 2, $d\Omega_1$ and $d\Omega_2$ the solid angles of the detectors (1 and 2), f_1 and f_2 the efficiencies of the detectors, f_1' and f_2' the conditional efficiencies of the detectors, R_1 and R_2 the response functions of the detectors, y_1 and y_2 the pulse height spectra of the detector (identical to y in Eq.(1)), respectively. Also, f_1' and f_2' are calculated by the equations,

$$f_1'(E_2) = \Sigma_1 \xi_{2\to1}(E_2,E_1) f_1(E_1) \quad (4)$$

$$f_2'(E_1) = \Sigma_2 \xi_{1\to2}(E_1,E_2) f_2(E_2) \quad (5)$$

where, $\xi_{2\to1}$ is a normalized spectrum of correlated neutrons to be detected at detector 1 when a neutron with the energy of E_2 is detected at detector 2. $\xi_{1\to2}$ has a similar meaning as $\xi_{2\to1}$. Σ_1 and Σ_2 mean summations over E_1 and E_2, respectively. In the present study, a simple condition was assumed that there was no angle dependence in energy spectrum, and the EDX spectrum data in the nuclear data file were used to deduce the conditional efficiencies, f_1' and f_2'. The terms, $y_1R_1^{-1}$ and $y_2R_2^{-1}$, in eqs. (2) and (3) were calculated by the FORIST[2] unfolding code with the detector response matrix evaluated by the SCINFUL[3] code.

The obtained cross section should be corrected for the following problems. One is neutron multiple-scattering in the sample. Multiple-scattering due to incident neutrons as well as emitted neutrons through (n,2n) reaction should be taken into consideration. And the other is inter-detector scattering of neutrons produced in the sample. This means that sequential detections of a neutron in the two detectors can be recognized as coincidence signal. Neutrons coming from materials other than the sample can be also scattered at two detectors sequentially, however their contribution can be removed by using the sample-out measurement. These correction calculations were carried out with the Monte Carlo code MCNP-4B[4] and

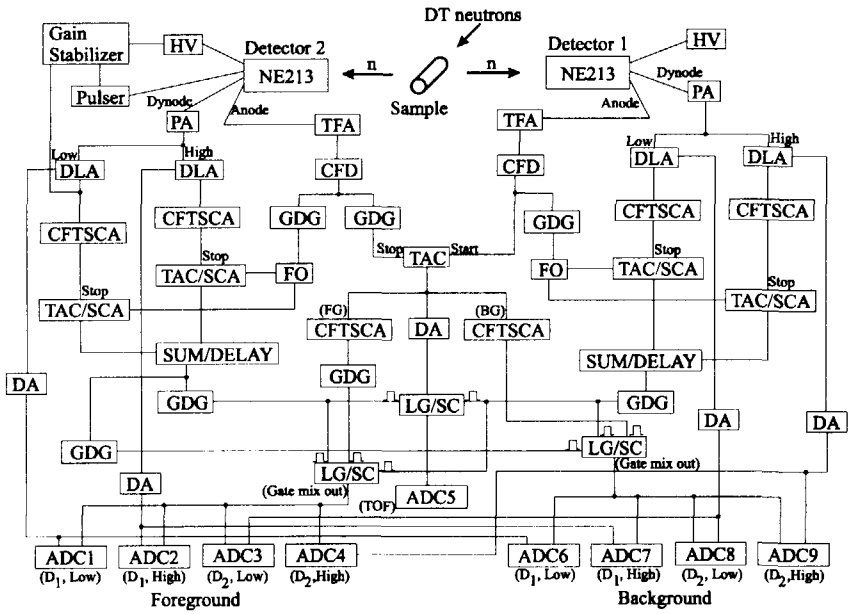

Fig. 2 Electronic circuit of the measurement.

the correction factor was estimated to be about 10%.

4. Results and discussion

Figure 3 shows time difference spectrum between anode signals of the two NE213 detectors. A large peak corresponding to the FG signals is found at around 200 ns in the sample-in spectrum. Since correlated signals are detected almost simultaneously, a 200 ns delay is artificially added to one anode signal. In the sample-out spectrum, a very small peak around the same position as the FG peak is seen. This corresponds to detection of two coincident neutrons due to (n,2n) reaction induced at materials surrounding the sample and detectors or inter-detector scattering of neutron between the two detectors. Also the BG counts are successfully suppressed and a good S/N ratio is therefore achieved.

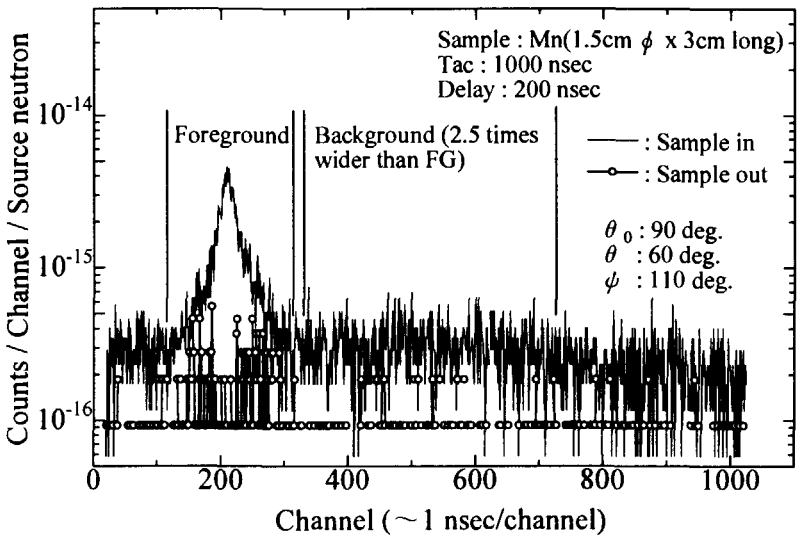

Fig. 3 Time spectrum between anode signals of two NE213 detectors.

Figure 4 shows raw neutron pulse height spectra in FG and BG measurements. It is confirmed that the FG spectrum is sufficiently larger than that of BG. Also, two spectra for high- and low-gain modes smoothly overlapped each other around 1~2 MeV. This means that the two-gain method is successfully functioning.

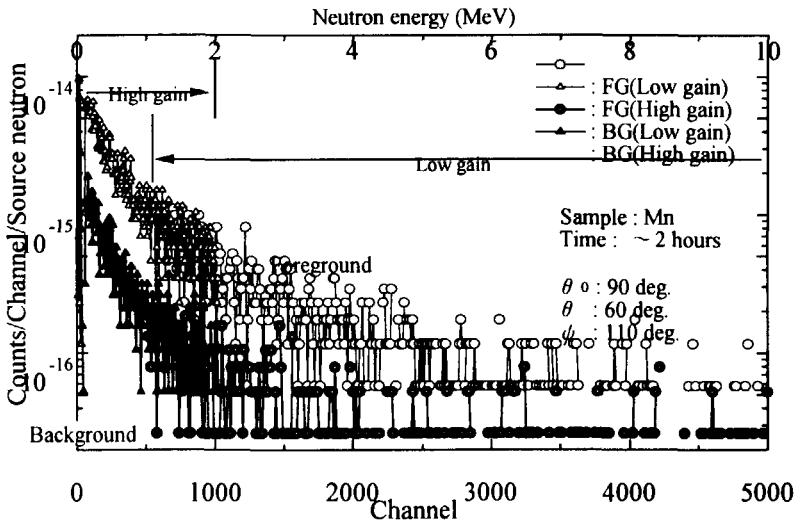

Fig. 4 Raw neutron pulse height spectra in FG and BG measurements.

Figure 5 shows neutron spectrum obtained by unfolding the pulse height spectrum with FORIST. In the figure, the error bars are not specified because the error value is so large that the spectra become not legible if specified. The values are around several tens percentages. A slight fluctuation is observed in each spectrum. However, a fairly good agreement between experiment and JENDL fusion file is seen except for low energy region. Large discrepancies in the low energy region are thought to be caused by the detector response matrix, which is to be re-evaluated.

Figure 6 shows angular distribution for axial direction compared with the nuclear data of JENDL fusion file. It seems that one can see a slightly forward oriented distribution. However, the accuracy is not so good as to conclude it. Nevertheless, the integral value, that is (n,2n) reaction cross section, is acceptable even if considering the discrepancy observed below 1 MeV in Fig. 5. This indicates that the present new measurement method is significantly successful. Figure 7 shows angular distribution for circumferential direction. It seems that there is no angular dependence. However, this cannot be concluded because the accuracy is not so good. From the results, it was confirmed that the angular dependence was, if any, very weak. Thus, it is expected that one complete measurement for a medium-heavy element would become possible by several measurements.

5. Conclusion

Using a newly developed beam-type DT neutron source at FNS, JAERI, the method was established to measure (n,2n) reaction cross section and its energy and angular distributions of simultaneously emitted two neutrons with the coincidence detection technique. In the present measurement, a cylindrical manganese, the (n,2n) cross section of which was measured precisely with the foil activation method, was

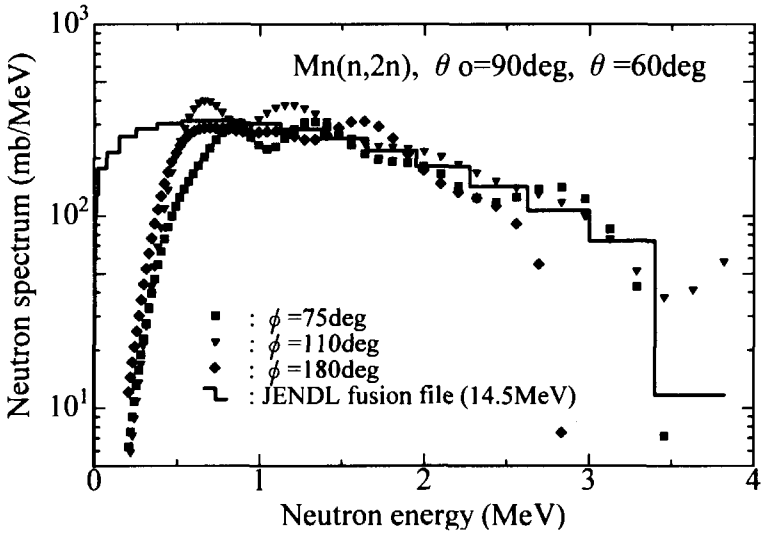

Fig. 5 Neutron spectrum obtained by unfolding the pulse height spectrum.

used to check the experimental method. From the results, it was confirmed that the present new method was basically functioning to measure only two neutrons emitted through (n,2n) reaction, however one problem was still left that the statistical accuracy was not sufficient. Some improvement of experimental and data processing procedure are necessary to solve it. Also, it was found that for Mn not so strong angular dependence was observed. Consequently, it is expected that complete measurement for a medium-heavy

element and for stable-isotope producing element by (n,2n) reaction would become possible by several measurements.

Acknowledgments

The authors wish to acknowledge the FNS staff for their excellent operation of FNS.

References

[1] for example, see compiled data in EXFOR.

[2] Johnson R. H. and Wehring B. W.: "The FORIST Unfolding Code," ORNL/RSIC-40 (1976).

[3] Dickens, J. K.: "SCINFUL: A Monte Carlo Based Computer Program to Determine a Scintillator Full Energy Response to Neutron Detection for E_n between 0.1 and 80 MeV," ORNL-6462 (1988).

[4] Briesmeister, J. F. (Ed.),: "MCNP- A General Monte Carlo N-Particle Transport Code, Version 4B," LA-12625-M (1997).

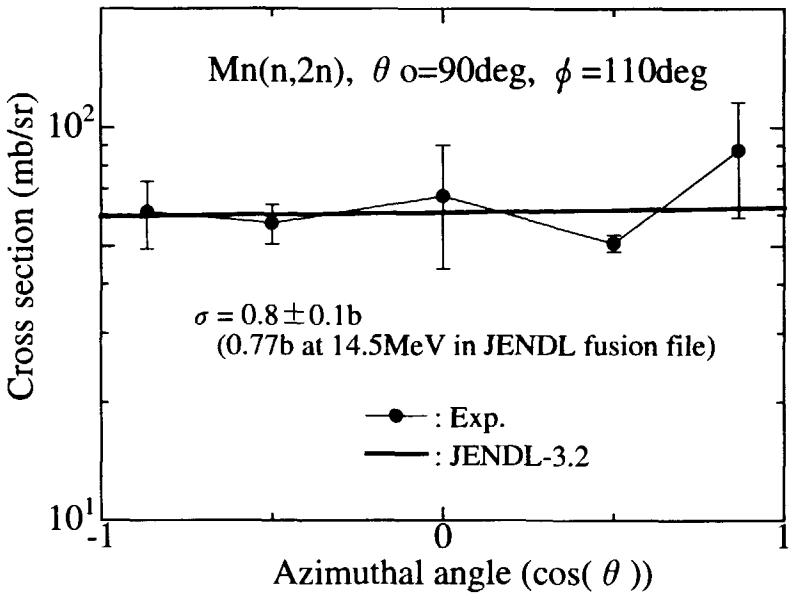

Fig. 6 Angular distribution for axial direction.

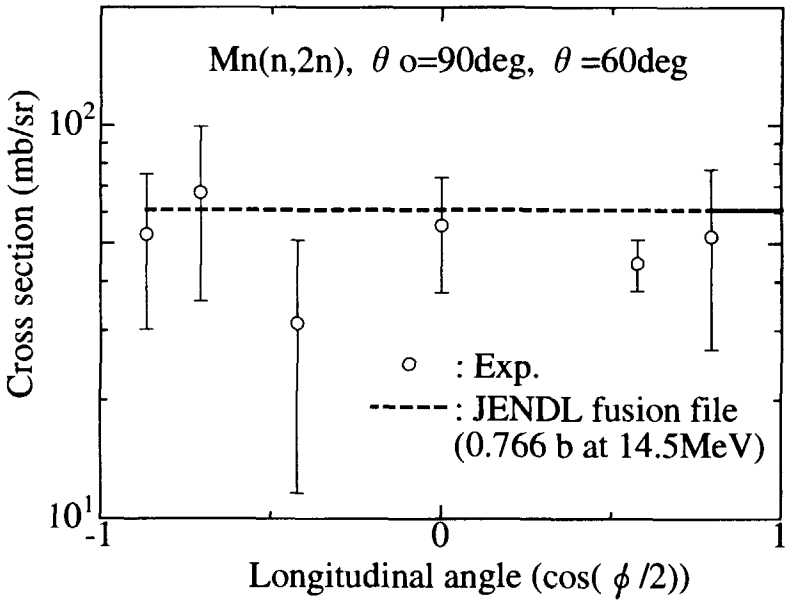

Fig. 7 Angular distribution for circumferential direction.

JP0150676

3.14

Measurement of (n, p) Reaction Cross Sections for Short-lived products ($T_{1/2}$=0.6~13.8 s) by 14 MeV Neutrons

Yoshimi Kasugai*[1], Yujiro Ikeda[1] and Hiroshi Takeuchi[2]
[1] *Center for Neutron Science, Japan Atomic Energy Research Institute*
Tokai-mura, Naka-gun, Ibaraki-ken 319-1195, Japan
[2] *Department of Fusion Engineering, Japan Atomic Energy Research Institute*
Tokai-mura, Naka-gun, Ibaraki-ken 319-1195, Japan
e-mail: kasugai@fnshp.tokai.jaeri.go.jp

Activation cross sections of the (n, p) reactions at 14 MeV for short-lived products were measured by using the D-T neutron source, FNS (Fusion Neutronics Source) at JAERI. Measured reactions were $^{11}B(n, p)^{11}Be$ ($T_{1/2}$=13.8 s), $^{18}O(n, p)^{18}N$ (0.63 S), $^{26}Mg(n, p)^{26}Na$ (1.07 s), $^{30}Si(n, p)^{30}Al$(3.60 s) and $^{34}S(n, p)^{34}S$ (12.4 s). Using the present results, systematic trend of the (n, p) reaction cross sections for light-mass-targets was discussed.

1. Introduction

The cross sections for 14 MeV neutrons were fundamental data for fusion reactor design. Especially for light-mass-targets (A<40), reactions with charged particle emission, including (n, p), (n, α), etc. are relatively important in the viewpoint of activation, because the cross sections of charger particle emission reactions are much larger than those of the (n, 2n) reactions. However, accuracy of some experimental data for the light-mass-target has been insufficient because it is difficult to measure short-lived activities associated with the reactions.

Therefore we measured cross sections of five (n, p) reactions for the target nuclei with A=11~34. The half-lives of the products are ranged from 0.63 s to 12.4 s. The measured reactions and decay data of the products are listed in Table 1. In this report, the experimental procedure and measurement results are presented. Applicability of a systematic trend of the (n, p) reaction cross sections [1] for the light-mass-target is also discussed.

2. Experiment

D-T neutrons were produced via the $^{3}T(d,n)^{4}He$ reaction by bombarding a tritium-target with d^+ beams using the FNS facility. The d^+ beam current and energy were 2 mA and 350 keV, respectively. A semi-automatic sample transfer system, which rapidly transports a sample from the neutron field to a measurement position in front of the gamma-ray detector by compressed nitrogen air, were used for the measurement. Gamma-rays from the samples were measured with a Ge detector. The acquisition of a gamma-ray spectrum started when the sample reached a measurement position in front of the Ge detector. A schematic drawing of the sample transfer system is shown in Fig. 1. The procedure of the sample-transfer, irradiation, transfer and gamma-ray measurement were repeated 20~160 times for each sample.

The neutron energy, which are determined on the basis of the neutron spectra calculated by a Monte Carlo, were validated by measuring the ratio between $^{92}Nb(n, 2n)^{92m}Nb$ and $^{90}Zr(n, 2n)^{89m}Zr$ reaction rates. The uncertainty in the reaction energy determination was estimated to be less than 0.1 MeV.

The cross sections were derived by dividing reaction rates by neutron fluxes. The reaction rates were derived from the gamma-ray spectrum obtained by summing all the acquired spectra. The summed gamma-ray spectrum of a silicon sample is shown in Fig. 2. The neutron flux for each irradiation was obtained with the associated-α-particle counts monitored using the Multi-Channel Scaling (MCS) method.

The dwell time of the MCS was 1 s. In order to convert the α-particle counts to the neutron fluxes, the conversion factor was measured using the $^{27}Al(n,p)^{27}Mg$ reaction cross section.

The sources of errors were attributed to the neutron flux determination and the activation rate determination. The errors of the neutron flux determination came from the neutron yield determination using the associated-α-particle counting method and the conversion factor from the neutron yield to the neutron flux. The error of the standard cross section of the $^{27}Al(n,p)^{27}Mg$ reaction gave a main contribution to the error of the conversion factor. The errors of the reaction rate determination included the followings: gamma-ray counting statistics, a gamma-ray detection efficiency, half-lives and intensities of the products, sample weight. The final uncertainty was derived by adding the uncertainties of all the experimental parameters in a quadrate.

3. Results and Discussion

The measured cross sections are shown in Figs. 3.1 to 3.5, along with corresponding values from the literature and results from the comprehensive evaluation: JENDL-3 and ENDF/B-VI. Numerical values for the measured cross sections are given in Table 2 along with the experimental data.

For the $^{11}B(n, p)^{11}Be$ reaction, the JENDL-3 evaluation is more consistent with the present data than the ENDF/B-VI evaluation. The cross section for the $^{18}O(n, p)^{18}N$ reactions has not been measured previously. This work provided the first experimental data for the reaction. The JENDL-3 evaluation of $^{26}Mg(n, p)^{26}Na$ is higher by 10-20% than the present data. For the $^{30}Si(n, p)^{30}Al$ reactions, the ENDF/B-VI evaluation is consistent with the present data within the uncertainty. The JENDL-3 evaluation is lower by 50% than the present data. The cross section of the $^{34}S(n, p)^{34}P$ reaction were measured at the neutron energies between 13.4 and 14.9 MeV. The present data show the increasing trend of the excitation function around 14 MeV. The JENDL-3 evaluation is consistent with the present data.

Previously, using the cross section data measured at FNS [2, 3], the systematic trends of (n, p) reaction cross section were proposed [1]. In Fig. 4, the (n, p) cross sections divided by N-Z+1 are plotted as a function of (N-Z+1)/A, where N, Z and A are the mass, neutron and proton number of target nuclei, respectively. It has already been shown that the empirical rule shown in the figure is applicable for the target with A=19~188. In order to confirm the applicability of the empirical rule for the light mass target, the present data were plotted in the figure. The cross section data for $^{16}O(n, p)^{16}N$, $^{17}O(n, p)^{17}N$ reactions, which are previously measured [4], were also plotted in the figure. Except the $^{11}B(n, p)^{11}Be$ reactions, the present data also follow the empirical rule. This means that the empirical rule is applicable for the target with A≥16.

4. Conclusion

Activation cross sections for $^{11}B(n, p)^{11}Be$, $^{18}O(n, p)^{18}N$, $^{26}Mg(n, p)^{26}Na$, $^{30}Si(n, p)^{30}Al$ and $^{34}S(n, p)^{34}S$ reactions at 14 MeV were measured. The cross sections for the $^{18}O(n, p)^{18}N$ reactions were measured for the first time. Using the present results, it was shown that the simple empirical rule of the (n, p) reaction cross section at 14.9 MeV is applicable for the target with A≥16.

Acknowledgements

We would like to thank to FNS accelerator operation team, C. Kutukake, S. Tanaka, Y. Abe, Y. Seki and Y. Oginuma for their operation of FNS.

Reference

[1] Y. Kasugai et al., "Systematics for (n, p) Excitation Functions in the Neutron Energy between 13.3 and 15.0 MeV", Ann. Nucl. Energy, 23, 1429 (1996).

[2] Y. Ikeda et al., "Activation Cross Section Measurements for Fusion Structural Materials at Neutron

Energy from 13.3 to 15.0 MeV Using FNS Facility", JAERI-1312, (1988).

[3] C. Konno et al., "Activation Cross Section Measurements for at Neutron Energy from 13.3 to 15.0 MeV Using the FNS Facility", JAERI-1329, (1993).

[4] Y. Kasugai et al., "Cross-section Measurement for the $^{17}O(n, p)^{17}N$ Reaction by 14-MeV Neutrons", Nucl. Sci. Eng., 136, 258 (2000).

Table 1 Measured reaction and decay data [a]

Reaction	$T_{1/2}$ [b]	Eγ[keV] [c]	Iγ[%] [d]
$^{11}B(n, p)^{11}Be$	13.8 s	2124.5	35.5±1.8
$^{18}O(n, p)^{18}N$	0.63 s	821	44.5±1.8
$^{26}Mg(n, p)^{26}Na$	1.07 s	1808.6	99.0± 0.4
$^{30}Si(n, p)^{30}Al$	3.60 s	2235.2	65±1
$^{34}S(n, p)^{34}P$	12.4 s	2127.5	15± 2

[a] *Table of Isotopes*, 8th edition, R. B. Firestone and V.S. Shirley, editors, John Wiley & Sons, Inc. (1996).
[b] Half-life of the product.
[c] Energy of a gamma-ray with decay of a product.
[d] Gamma-ray intensity per decay.

Table 2 Numerical values of measured cross sections

Reaction	E_n[MeV] [a]	σ[mb] [b]
$^{11}B(n, p)^{11}Be$	14.94	5.2± 0.4
$^{18}O(n, p)^{18}N$	14.94	1.15±17
$^{26}Mg(n, p)^{26}Na$	14.94	31±4
$^{30}Si(n, p)^{30}Al$	14.94	34±5

[a] Neutron energy.
[b] Measured cross section value.

Reaction	E_n[MeV]	σ[mb]
$^{34}S(n, p)^{34}P$	14.94	100±22
	14.68	88±19
	14.37	88±20
	14.02	90±20
	13.68	82±20
	13.36	88±22

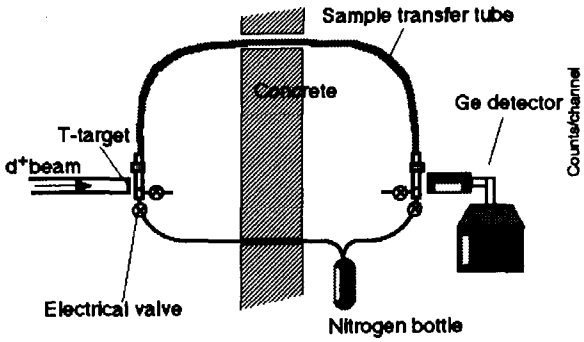

Fig. 1 Schematic drawing of the sample transfer system

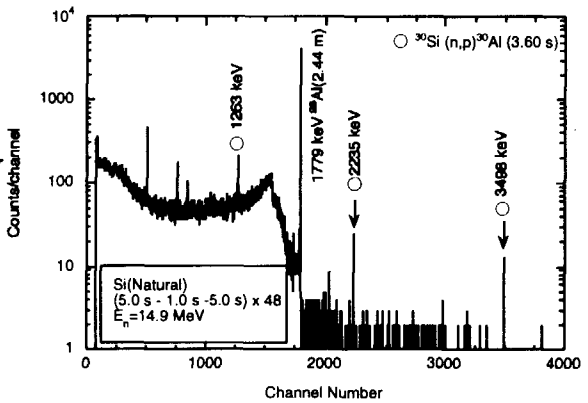

Fig.2 Gamma-ray spectrum of the silicon sample.

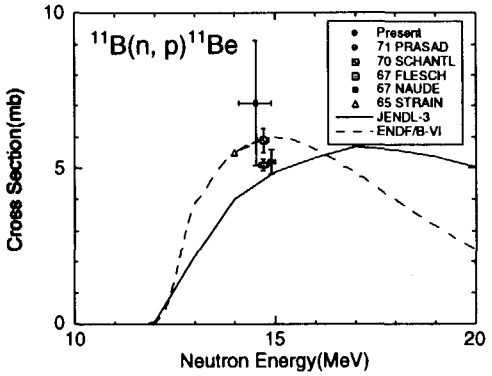

Fig. 3.1 Cross section of the ^{11}B(n, p)^{11}Be reaction

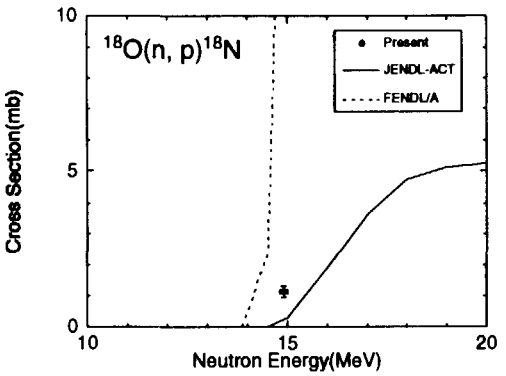

Fig. 3.2 Cross section of the ^{18}O(n, p)^{18}N reaction.

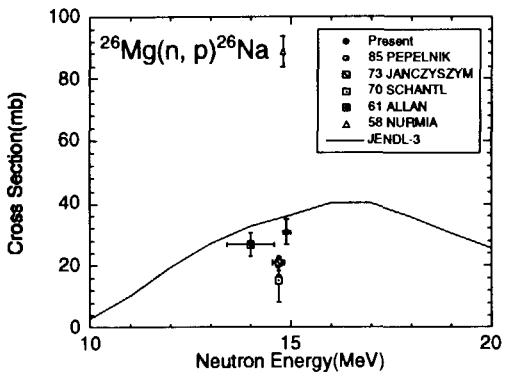

Fig. 3.3 Cross section of the ^{26}Mg(n, p)^{26}Na reaction

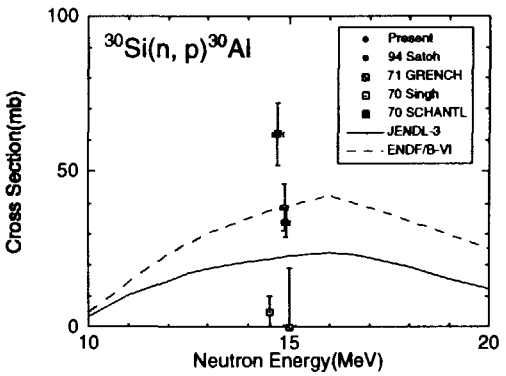

Fig. 3.4 Cross section of the ^{30}Si(n, p)^{30}Al reaction

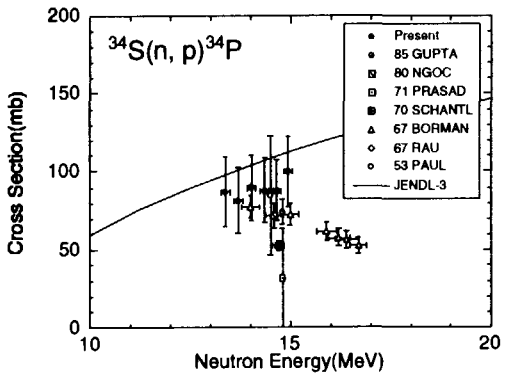

Fig. 3.5 Cross section of the ^{34}S(n, p)^{34}P reaction

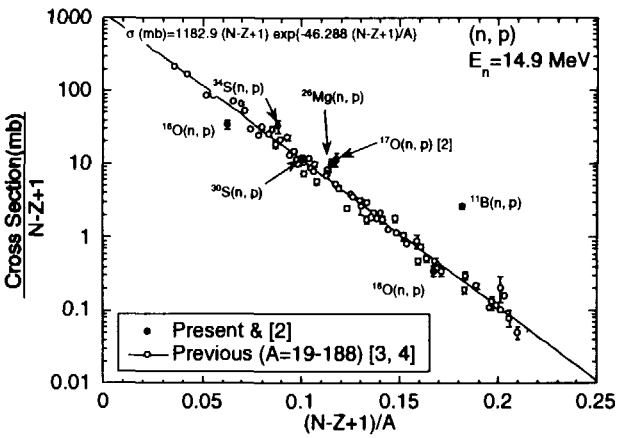

Fig. 4 Systematics of the (n, p) reaction cross sections

JP0150677

3.15

Measurement of activation cross sections with d-D neutrons in the energy range of 2.0-3.2 MeV

Toshiaki Shimizu[1], Shinya Furuichi[1], Hitoshi Sakane[2], Michihiro Shibata[2], Kiyoshi Kawade[2], Yoshimi Kasugai[3], and Hiroshi Takeuchi[3]

[1]*Department of Nuclear Engineering, Nagoya University.*

[2]*Department of Energy Engineering and Science, Nagoya University.*

[3]*Japan Atomic Energy Research Institute*

e-mail: toshiaki_s@lycos.ne.jp

Activation cross sections for six (n,p) reactions were measured in the neutron energy range between 2.0 and 3.2 MeV. The measured target isotopes were ^{27}Al, ^{51}V, ^{61}Ni, ^{65}Cu, ^{69}Ga, and ^{92}Mo. The cross sections for ^{61}Ni, ^{69}Ga and ^{92}Mo were obtained at the first time. The cross sections are overestimated for ^{51}V, ^{69}Ga and ^{92}Mo in JENDL-3.2.

1 Introduction

Database of activation cross section for neutron energy up to 15 MeV was required for a design of fusion reactors. The cross section data are world-widely serviced as the evaluated libraries such as JENDL-3.2[1)] etc.. To evaluate the excitation function of cross section with accuracy, the experimental cross section data which covered with the neutron energy up to 15 MeV, are needed. Available cross section data in the neutron energy range between 13 and 15 MeV were reported. However, in the energy range between 2 and 13 MeV, the experimental data were rather scarce owing to the lack of available intense neutron source.

Using a KN3750 Van de Grraff accelerator at Nagoya University and a Fusion Neutronics Source (FNS) at Japan Atomic Energy Institute, we have measured (n,n'),(n,p) and (n,α) reaction cross sections in the energy range between 2.0 and 6.8 MeV [2),3)]. In previous works at FNS, the distance between the D-target and irradiation positions was chosen to be 10 cm, a typical neutron fluence rate at irradiation positions was 5×10^{6} n/cm^{2}·s. It is necessary for the measurement of much smaller cross section to irradiate the sample at more intense neutron field.

In the present work, the six (n,p) reaction cross sections have been measured in the energy range between 2.0 and 3.2 MeV by using an improved pneumatic transport system, which can obtain more than one order of magnitude larger than previous one.

2 Experiment

2.1 Irradiation and flux determination

The neutrons were generated by bombarding a deuterated titanium target on a copper backing with a d^+ beam of 1.5 mA and 350 keV using the Fusion Neutronics Source (FNS) at Japan Atomic Energy Research Institute. As shown in Fig.1, a pneumatic sample transport system is used to transport samples from the irradiation position to the measurement position rapidly. The system is composed six acrylic tubes of 0.1 mm in thickness. The angles of the irradiation positions with respect to the incident d^+ beam are between 0° and 155°, which covered the neutron energies ranging from 3.2 to 2.0 MeV.

In previous works, the samples were irradiated at the distance of 10 cm from the d-target. In the present arrangement, the samples were irradiated at 2 –6 cm. As shown in Fig. 2, the neutron fluence rate at irradiation positions were 5×10^6-10^8 n/cm^2/s, which was 20 times larger than a previous system. The neutron fluence rate were measured with use of the standard reaction $^{115}In(n,n')^{115m}In$ ($T_{1/2}$=4.486h), whose cross section data from JENDL Dosimetry File 99. The samples were sandwiched by two Indium foils of 10mm×10mm×0.2mm thick.

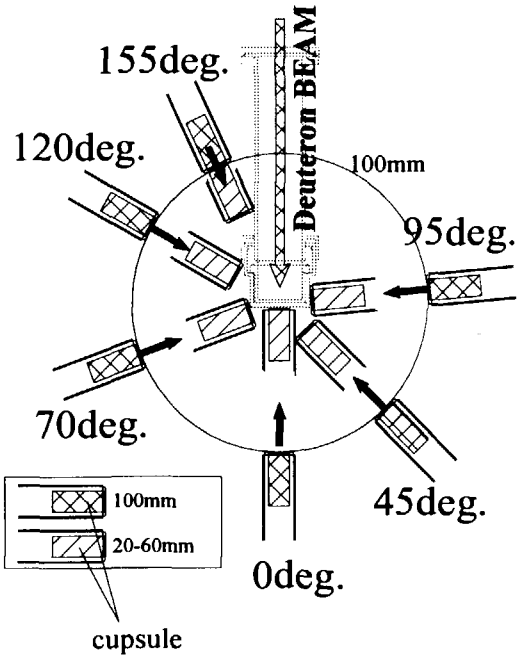

Fig.1: Schematic view of pneumatic transport system.

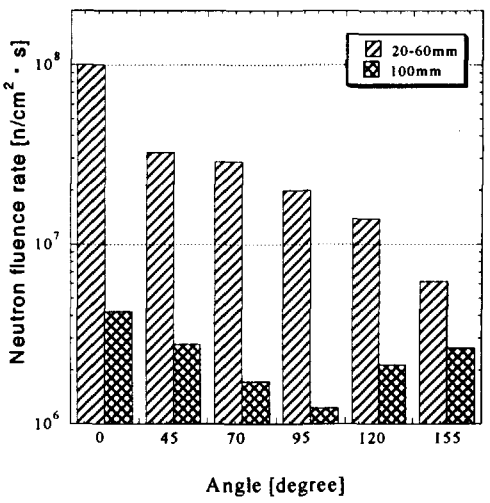

Fig.2: Typical neutron flux.

The energy spectrum of incident neutrons was determined by TOF measurement and the calculation from deuteron distribution in titanium target and neutron angular distribution as shown in Fig. 3. The effective neutron energies shift owing to angular distribution. As shown in Fig. 4, the effective energy of incident neutrons at each irradiation position was determined by the reaction-rate ratio of the $^{115}In(n,n')^{115m}In$ reaction to the $^{64}Zn(n,p)^{64}Cu$ reaction(JENDL-Dosimetry File). The measured effective neutron energies were well reproduced with the calculation value. The irradiation position is chosen to be 20 mm.

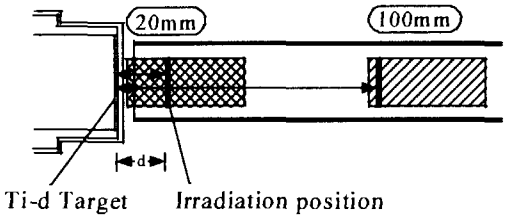

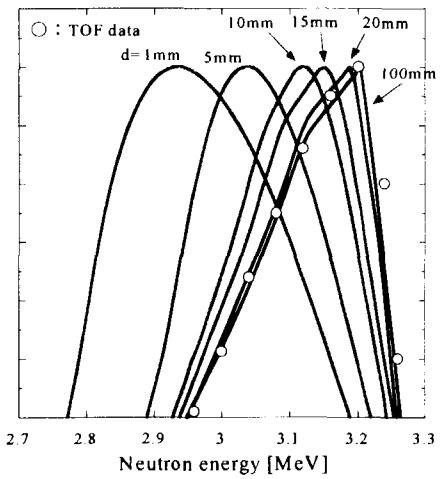

Fig.3 Neutron spectrum by TOF measurement and calculation at each irradiation position.

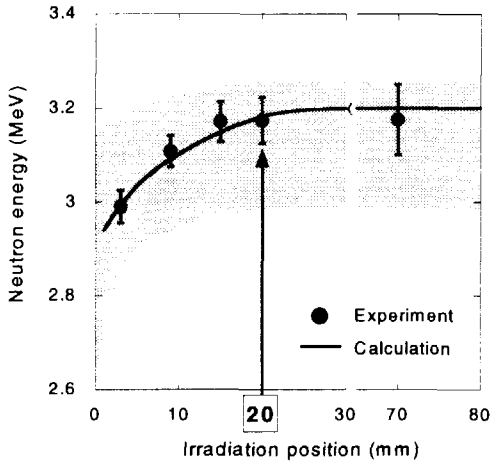

Fig.4 Neutron energy spread and effective energy at the distance between d-target and irradiation position.

Usually the target assembly at FNS 80° beam line was used as d-T and d-D neutron sources. Therefore, 14 MeV neutron was a little produced via $T(d,n)^4He$ reaction owing to tritium contaminated in the extended tube. Since most cross sections at 14 MeV are 10^2-10^3 times larger than that at 3 MeV, contribution of it was not ignored. We measured the d-T neutron fluence rate with use of the $^{93}Nb(n,2n)^{92m}Nb$ ($T_{1/2}$=10.15d, Q=-8.97MeV) reaction. The neutron fluence rate at each irradiation position was about 10^{-3} to d-D neutron.

2.2 Activity measurement

Gamma-ray emitted from the irradiated samples were measured with a well-type and a 30% closed end-type HPGe detectors. The efficiencies in the bottom of the well-type detector were 6-7 times larger than those at the close position of closed end-type detector. The closed end-type detector covered with a 5mm thick acrylic absorber in order to reduce beta rays, and the acrylic spacer with length at 4.5cm were also put on the detector. We call it standard position. The error in the efficiency at standard position is estimated to be 3%. The efficiency at the bottom of the well-type HPGe and at the surface of the end-cap of the coaxial-type HPGe were obtained by efficiency calibration method. To measure efficiently for weak induced activities, the irradiated samples were put on the surface of the acrylic plate at the distance of 5 mm from the end-cap of the HPGe detectors. The counts obtained at 5 mm were converted to those at 5 cm, using experimentally determined ratio of the efficiency at 5 mm to that of at 5 cm. This procedure improved the detection efficiency by a factor of about 7 in comparison with the measurements at 5 cm, and brought an additional error of only 1% to the results. The details of the procedure are described elsewhere (Sakane et al., 1999).

2.3 Decay data

In Table 1, measured reactions of associated decay data of the half-life, the gamma ray energy and the absolute intensity are listed together with Q-values.

Table 1: Measured reactions and decay parameters.

Reaction	Half life	Eγ (keV)	Iγ (%)	Q-value (keV)
$^{27}Al(n,p)^{27}Mg$	9.458min	843.74	71.8(8)	-1827.99
$^{51}V(n,p)^{51}Ti$	5.76min	320.0842	93.1(4)	-1688.30
$^{61}Ni(n,p)^{61}Co$	1.65h	67.412	84.7(4)	-539.38
$^{65}Cu(n,p)^{65}Ni$	2.52h	1481.84	23.59(14)	-1354.79
$^{69}Ga(n,p)^{69m}Zn$	13.76h	438.63	94.8(2)	-123.64
$^{92}Mo(n,p)^{92m}Nb$	10.15d	934.46	99.07(4)	425.84

2.4 Corrections

The following principal corrections were made for deduction of the cross sections. The details of procedures are described elsewhere (Kawade et al., submitted to Nucl. Instr. Meth.). Corrections were made for time fluctuation of neutron flux, thickness of samples, self absorption of γ-ray, summing effect of γ-ray and contribution of low energy neutron and d-T neutrons.

3 Results and discussion

The numerical values of the cross sections measured in the present study are given in Table 2. The present cross section data are shown in Fig. 5 together with the previous data[4)-6)] and the evaluated data in JENDL-3.2, -Activation File and -Dosimetry File.

The cross section data of six (n,p) reactions were obtained in the energy range between 2.0 and 3.2 MeV. The cross sections for ^{61}Ni, ^{69}Ga and ^{92}Mo were obtained at the first time. The cross sections are overestimated for ^{51}V, ^{69}Ga and ^{92}Mo in JENDL-3.2.

4 Conclusion

We have measured the cross sections down to about 10 micro barn for short-lived nuclei using the improved pneumatic sample transport system and a high efficient well-Type HPGe detector.

References

(1) T.Nakagawa, et al., Japanese Evaluated Nuclear Data Library Varsion 3 Revision-2: JENDL-3.2. Nucl. Sci. Technol., 32, 1259 (1995).
(2) T. Furuta et al., JAERI-Conf 99-002, 186 (1999).
(3) T. Senga et al., JAERI-Conf 2000-005, 208 (2000).
(4) Hussain et al., App. Radiat. Isotopes, 34, (4), 731 (1983).
(5) Smith et al., Ann. Nucl. Energy, 11, 623 (1984).
(6) D.C.Santry et al., Can. Jour. Phys., 44, 1183 (1965).

Table 2: Measured cross section data.

Reaction	Abundance (%)	En (MeV)			
		3.2	3.0	2.7	2.5
^{27}Al(n,p)^{27}Mg	100 (natural)	1.58(8)	0.58(6)	0.08(4)	-
^{51}V(n,p)^{51}Ti	99.75 (natural)	0.029(7)	0.014(8)	-	-
^{61}Ni(n,p)^{61}Co	88.84 (enriched)	1.3(1)	0.65(11)	-	0.20(8)
^{65}Cu(n,p)^{65}Ni	99.61 (enriched)	0.09(2)	0.04(2)	-	-
^{69}Ga(n,p)^{69m}Zn	60.108 (natural)	0.59(7)	0.33(6)	0.20(3)	0.13(3)
^{92}Mo(n,p)^{92m}Nb	97.37 (enriched)	3.1(2)	2.0(2)	1.6(3)	1.0(3)

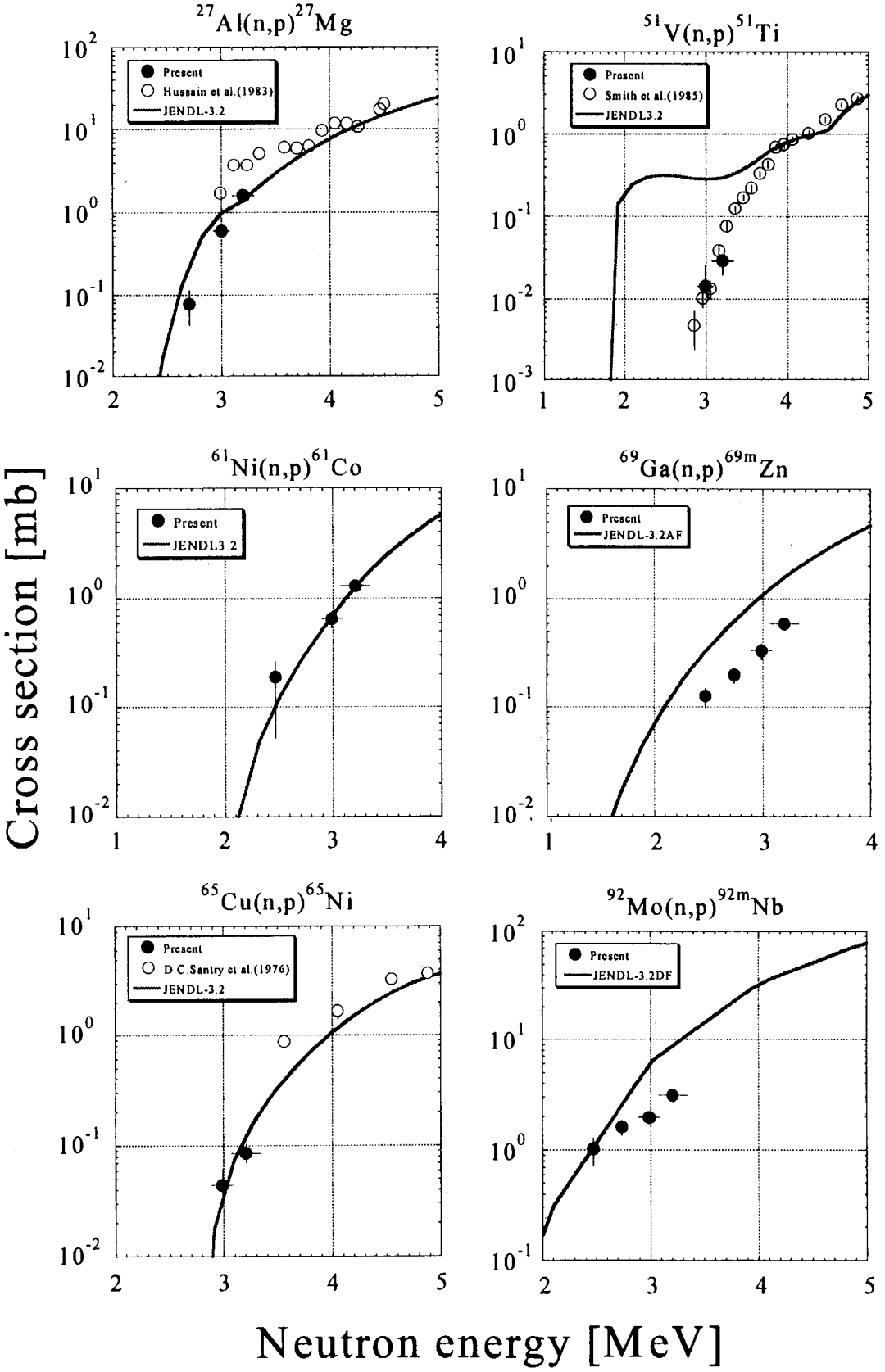

Fig. 5 Cross section data for the (n,p) reactions.

JP0150678

3.16

Measurement of nuclear reaction cross sections of Li-d and Be-d at low energy

Kentaro Ochiai

Fusion Engineering Research Naka Fusion Research Establishment, JAERI

Tokai-mura, Naka-gun, Ibaraki-ken 319-11

e-mail: ochiai@fnshp.tokai.jaeri.go.jp

To estimate basic dose-rate data (PKA and KERMA) and material damage, it is important to measure nuclear cross sections of prospective candidates for blanket materials and deuteron at low energy (about 10 ~ 300 keV). And then, the nuclear reactions at low energy are also useful for Nuclear Reaction Analysis (NRA). However, we have few nuclear data of such reactions. According to we have measured nuclear-cross sections of ^{nat}Li(d,x) and 9Be(d,x) and obtained S-factors of these reactions.

1. Introduction

Lithium and beryllium metal and these compound materials are prospective candidates for fusion plasma facing material and blanket materials. Since these materials are exposed with D-T nuclear reaction particle (3.5-MeV α and 14-MeV neutron) and plasma particles (low energy deuteron and triton) in fusion reactor, the light element of fusion-reactor materials are produced proton, deuteron, triton and helium in the material and are caused tritium activation and embitterment. Therefore, the spectroscopy analysis needs to search the material properties and especially, NRA method with low-energy deuteron beam is useful for lithium and beryllium materials. However, the spectroscopy method and these cross sections data (^{nat}Li(d,x) and 9Be(d,x)) are not enough to established such a NRA. Therefore, we have established Li-d nuclear reaction spectroscopy and obtained the cross section (and/or S-factors) of ^{nat}Li(d,x) and 9Be(d,x),

2. Experimental procedure

The experiment was carried out using the Cockcroft-Walton type accelerator, Osaka-University, Japan and tandem-Pelletron type accelerator and Kobe University of Mercantile Marine (Fig1). Thick oxide lithium layer on backing metal (Ti) plate with LiOD-electrolysis was used as lithium sample and Beryllium sample was sheets of beryllium (10 ~ 100 μm). Two Si-SBDs with aluminum-screening foil were set up inside the vacuum chamber and the charged particles emitted from ^{6}Li(d,x), ^{7}Li(d,x) and ^{9}Be(d,x) reactions have been measured with the detectors (Fig.2). Since ^{nat}Li-d nuclear reactions have many kind blanches, it was predicted that charged-particle spectrum emitted from Li-d reaction was piled up, therefore to separate the charged-particle spectra emitted from ^{7}Li-d and ^{6}Li-d reaction, we have used a pair of ΔE and E Si-SBD for the measurement of charged particles.

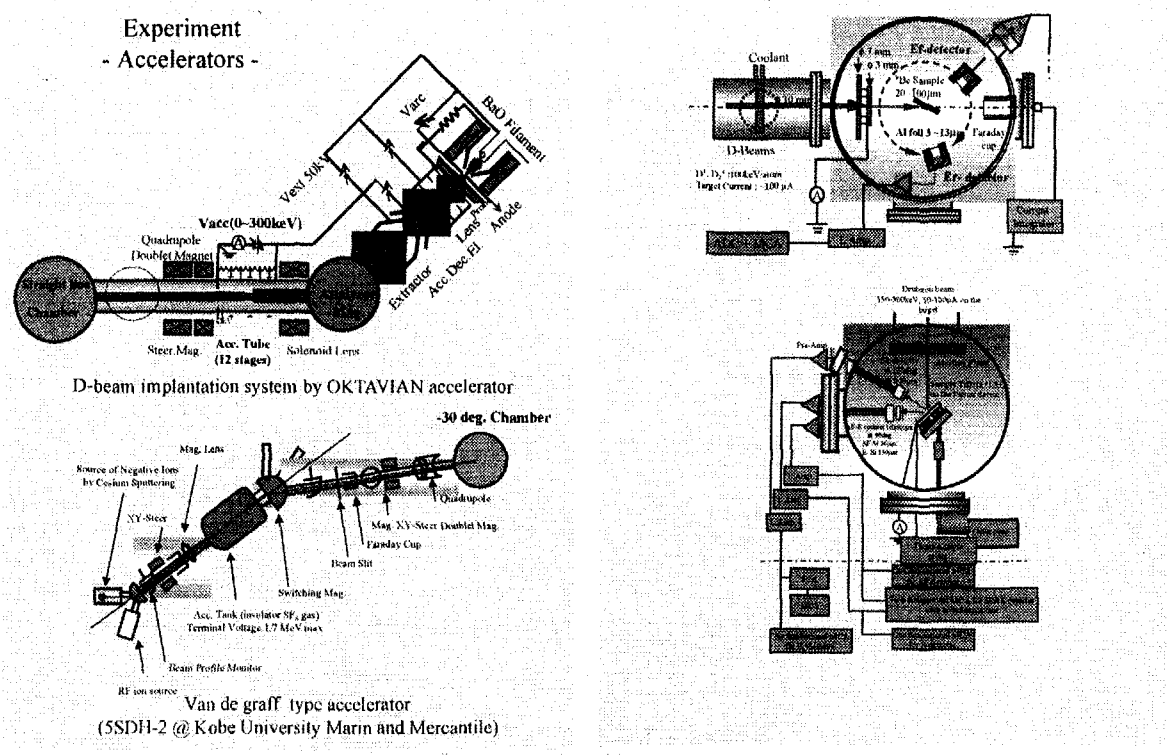

Figure 1 Apparatuses of the Cockcroft-Walton type accelerator, Osaka-University, Japan and tandem-Pelletron type accelerator and Kobe University of Mercantile Marine (left)
Figure 2 Measurement systems for the charged-particles spectroscopy of Li-d and Be-d nuclear reactions (Right)

3. Spectroscopy

Figure 3 and 4 are shown that the charged-particle spectrum emitted from Li and Be samples implanted 300-keV D^+ beam. Figure 3 is shown that 2-dimensional data of the charged-particle spectrum emitted from lithium sample implanted 300-keV D^+ beam. In case of the spectrum of ^{nat}Li-d reaction, measured with the ΔE and E counter method, we could have separate the charged-particle spectrum of Li-d from the charged-particle spectrum of impurity reactions (^{12}C-d and D-D) have obtained clear spectrum of ^{6}Li(d,α), ^{7}Li (d,p_0) and ^{7}Li (d,p_1). Figure 4 is the typical the charged-particle spectrum of ^{9}Be-d nuclear reaction. From this spectrum of detected charged particles, we have recognized the branches of ^{9}Be-d nuclear reaction. The branches which were recognized are as follow, ^{9}Be(d,p), ^{9}Be(d,t_0), ^{9}Be(d,t_1),^{9}Be(d,α_0), ^{9}Be(d,α_1) and ^{9}Be(d,α_2). Also the broad spectrum at ~2 MeV is due to ^{7}Li as residual particle from ^{9}Be(d,α_0) and ^{9}Be(d,α_1).

After we have distinguished the branches from the charged-particles spectrum, we have done the experiment to obtain the angular distributions and energy dependences of the cross sections for ^{9}Be-d nuclear reaction (at detected angle 30 ~ 150 deg and d-beam energy 90 ~300 keV).

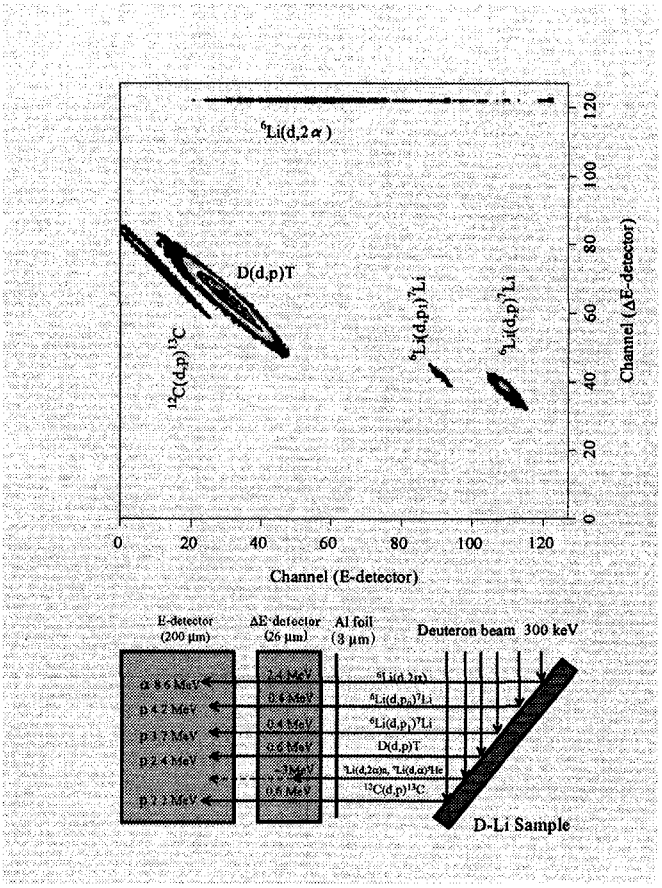

Figure 3 Contour map of the charged-particles spectrum from lithium sample using ΔE&E SSBD counter telescope

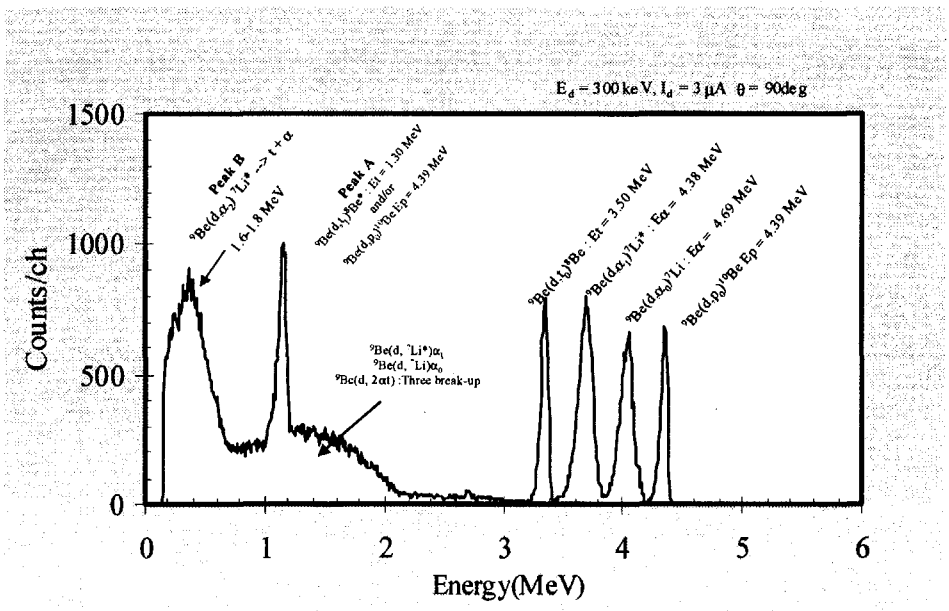

Figure 4 The typical charged spectrum from beryllium sample with 300 keV-d beam

4. Cross sections and S-factors

Figure 5 and 6 are shown that the angular distributions for ^{9}Be(d,p) and ^{9}Be(d,t_0). at E= 280 keV and 180 keV. The angular distributions of both cross sections tend to be backward-peaking. The differential cross sections at backward-angles for E = 280 keV increase about ten times at maximum larger than the value at forward-angles. The curve of the differential cross sections of ^{9}Be(d,t)^{8}Be at E = 280 keV reaches a maximum value at about θ_{cm} = 110 degree and the differential cross section of ^{9}Be(d,t) at θ_{cm} =110 degree is larger by two and a half times than the differential cross section at θ_{cm} = 20 degree. Figure 7 shows the angular distributions of differential cross sections of ^{9}Be(d,α_0)^{7}Li and ^{9}Be(d,α_1)^{7}Li* at E = 280 keV. Though in Figure 7 the differential cross sections of ^{9}Be(d,α_0) ^{7}Li increases at backward angles, the one of ^{9}Be(d,α_1) ^{7}Li* show opposite tendency (forward high).

The angular distributions of all differential cross sections show asymmetric around 90 degree (both for forward- or backward- peaking). The Oppenheimer-Phillips process (charge polarization) may be considered to explain the asymmetry. However up to now, we can not full-theoretically explain the mechanism of the asymmetry of angular distributions at low energy. To clarify this phenomena, theoretical approaches using on the theory of Distorted Wave Born Approximation (DWBA) processes, Coupled Channel (CC) considering α-cluster model[7], or R-Matrix theory for the stripping, α-emission, and/or pick-up processes seems to be required.

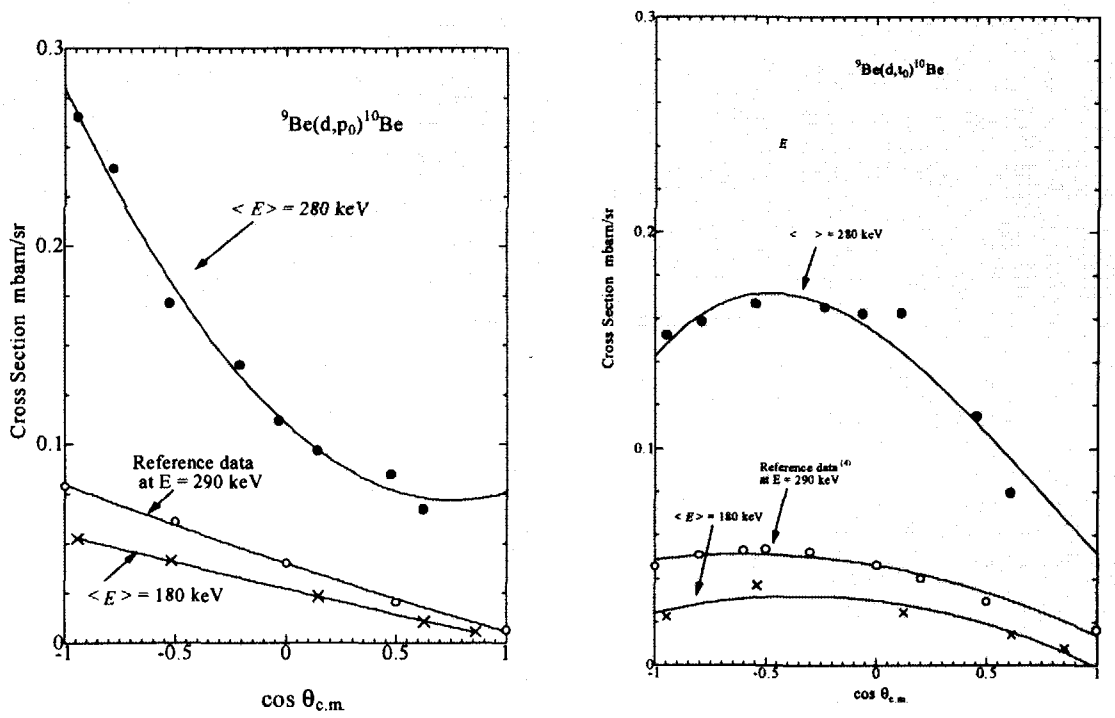

Figure 5 and 6 The angular distributions for ^{9}Be(d,p) and ^{9}Be(d,t_0). at E= 280 keV and 180 keV

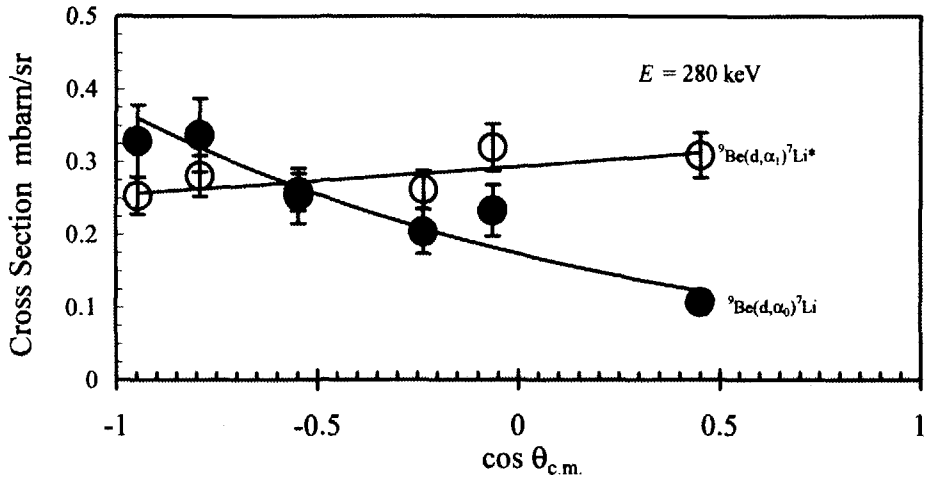

Figure 7 The angular distributions of differential cross sections of $^{9}Be(d,\alpha_0)^{7}Li$ and $^{9}Be(d,\alpha_1)^{7}Li^*$ at E = 280 keV

The energy dependencies of the cross section for $^{9}Be(d,p_0)^{10}Be$ nuclear reaction, as the representative data, are shown in Fig. 8. All of the measured cross section is the order of μbarns at $E \sim 100$ keV and then cross sections of ^{9}Be-d increase to the order of mbarns at $E \sim 300$ keV. Also, all cross section shows to keep the order of 10 mbarns above $E \sim 0.8$ MeV. Closed triangles in Fig. 8 shows the cross sections obtained from one point experiment (e.g. $4\pi\sigma_{(\theta r = 90deg.)}$ at $E_{lab.}$ = 90-280 keV).

Nuclear reaction cross sections ($\sigma_{(E)}$) which drop steeply according to energies E at low energy are given as

$$\sigma_{(E)} = f_{(E)} \cdot S_{(E)} E^{-1} \exp(-2\pi\eta) \qquad (6)$$

$$f_{(E)} = \sigma_{s(E)} / \sigma_{b(E)} \approx \exp(\pi\eta U_e / E) \qquad (7)$$

where $2\pi\eta = 31.29 Z_1 Z_2 (m/E)^{1/2}$ is the Sommerfeld parameter (Z_1 and Z_2 = charge numbers of interacting nuclei, m = reduced mass in amu, E = c.m. effective incident energy in keV). Also $f_{(E)} = \sigma_{s(E)} / \sigma_{b(E)}$ is the enhancement ratio of the bare cross section ($\sigma_{b(E)}$) and the cross section $\sigma_{s(E)}$ with an electron screening effect in solid target, where U_e is the electron screening potential energy (e.g. $U_e \sim Z_1 Z_2 e^2 / r_a$ approximation, with r_a an atomic radius (about 2~3 x 10^{-8} cm))[8-9].

Table 1 shows astrophysical $S_{(E)}$-factors obtained from the measured cross sections of $^{9}Be(d,p)$, $^{9}Be(d,t_0)$, $^{9}Be(d,\alpha_0)$ and $^{9}Be(d,\alpha_1)$ at $E_{lab.}$ = 90-280 keV, respectively. Measured S-factors slightly decrease according as E decreases. However, all of the S-factors at E = 90 keV enhanced about twice larger than the one at E = 140 keV. For this phenomenon, we assumed that it is not due to the ^{9}Be-d resonance reaction

because exited levels of $^{11}B^*$ which make S-factor of ^{9}Be-d reactions enhanced have not found.

We rather suggest that S-factors increase due to an effect of effective electron screening potential (e.g. U_e of formula (7)). The U_e is usually regarded as negligible small value (the order of eV). Therefore, such an enhancement of S-factor appeared hardly at the several hundred keV energy region. However, a recent review paper has reported that the experimental value of the U_e makes the enhancement of S-factors appeared at near E = 100 keV[12]. The U_e which was estimated from our S-factors corresponds to the order of 100 eV.

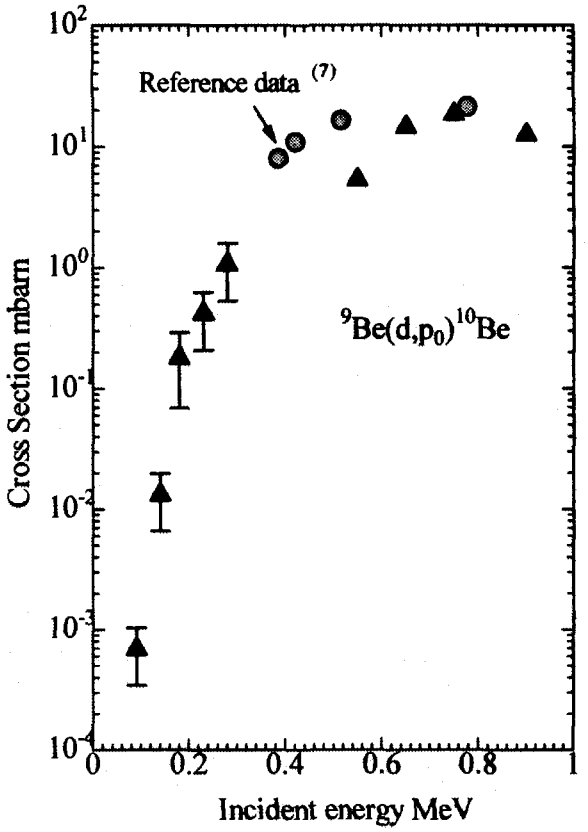

Figure 8 The energy dependencies of the cross section for $^{9}Be(d,p_0)^{10}Be$ nuclear reactions

Table 1 Astrophysical $S_{(E)}$-factors obtained from the measured cross sections of $^{9}Be(d,p)$, $^{9}Be(d,t_0)$, $^{9}Be(d,\alpha_0)$ and $^{9}Be(d,\alpha_1)$

$<E>_{lab}$	S-factor			
keV	MeV barn			
	$^{9}Be(d,\alpha_0)^{7}Li$	$^{9}Be(d,\alpha_1)^{7}Li^*$	$^{9}Be(d,p_0)^{10}Be$	$^{9}Be(d,t)^{8}Be$
90	3.5±0.7	5.7±1.2	2.0±0.4	0.9±0.2
140	1.9±0.4	3.1±1.1	1.4±0.3	0.4±0.1
190	2.7±0.6	4.2±0.8	1.7±0.4	0.5±0.1
240	4.3±0.9	6.5±1.3	2.6±0.5	0.9±0.2
290	5.7±1.2	7.6±1.5	2.8±0.6	1.0±0.2

JP0150679

3.17
Precise Determination of Gamma-ray Emission Probabilities and Beta-ray Intensities for Nuclides with Relatively Short Half-lives

Nada Marnada, Hiroshi Miyahara*, Gatot Wurdiyanto
Keiichi Ikeda, Nobuo Hayashi, and Yoshichika Katoh
Department of Nuclear Engineering, Graduate School of Engineering
Nagoya University, Furo-cho, Chikusa-ku, Nagoya 464-8603
e-mail: nada@avocet.nucl.nagoya-u.ac.jp
*Department of Radiological Technology, School of Health Sciences
Nagoya University, 1-1-20 Daiko-Minami, Higashi-ku, Nagoya 461-8673

The ability of a 4πβ-γ coincidence apparatus to measure shortly and precisely disintegration rates has resulted in precise emission probabilities of principal γ-rays for nuclides of ^{76}As, ^{139}Ba, ^{159}Gd, ^{183}W and ^{193}Os of which the half-lives are relatively short. The precise emission probabilities gave β-ray intensities for transitions to excited states and the ground states of the daughter nuclides with precise values.

1. Introduction

Gamma-ray emission probability is an important factor in some research fields of nuclear radiation products and radioisotope applications such as fission product decay-heat, isotopic monitoring, neutron activation analysis, and nuclear medicine. Precise data of emission probabilities are therefore desired in order to get precise results. Many nuclides have been investigated or evaluated by previous authors to provide the data of γ-ray emission probabilities. However, the results are still incorrect due to inappropriate method used.

Emission probabilities can be determined directly using disintegration rate, and disintegration rate can be precisely measured by the 4πβ-γ coincidence apparatus [1]. To satisfy the need for precise γ-ray emission probabilities of nuclides with relatively short half-lives, i.e. ^{76}As, ^{138}Ba, ^{159}Gd, ^{183}W and ^{193}Os, the apparatus was used in the present work. The nuclides were selected, as their evaluated emission probabilities show large uncertainties.

2. Experimental Details and Data Analysis

Sample sources with activities between 15 and 40 kBq were produced at KURRI by thermal neutron activation and measurements were carried out at KURRI and Nagoya University. The coincidence apparatus [1] consisted of 4πβ-counter, γ-detector, electronics for coincidence, and two-dimensional data-acquisition system. One atmospheric 4πβ proportional counter and vertical-type coaxial HPGe γ-detector were used at KURRI, and high-pressure 4πβ proportional counter and horizontal-type HPGe γ-detector were used at Nagoya University. Absolute disintegration rates and absolute γ-ray intensities were obtained from the coincidence apparatus. Measurements were also carried out by γ-ray spectrometer for obtaining relative γ-ray intensities. Sample sources with stronger activities than those used in the coincidence apparatus were prepared for the spectrometry. The results were used to establish β-ray intensities of the nuclides under study. Six standard sources of ^{46}Sc, ^{56}Co, ^{57}Co, ^{60}Co, ^{133}Ba and ^{152}Eu were also measured in every series with the same manner for determination of γ-ray detection efficiency curve.

Data obtained from the coincidence apparatus were analyzed by computer discrimination method [2] to deduce coincidence efficiency function [3]. Extrapolation of the function to β-ray detection efficiency of 100% resulted in absolute disintegration rate. The γ-ray detection efficiencies of the standard sources were fitted using a method described by Brandt [4] to obtain detection efficiency curves. Detection efficiencies of designated energies for the sample sources were derived from the efficiency curves.

3. Results and Discussions

Emission probabilities (P_γ) are calculated from $P_\gamma = N_\gamma/(N_0 \cdot \varepsilon_\gamma)$, where N_γ is absolute γ-ray intensity, N_0 is absolute disintegration rate and ε_γ is detection efficiency. The uncertainty of emission probability consists of statistical uncertainty coming from those three parameters and systematical uncertainty of about 0.7%. The results are shown in Tables 1 to 5 for emission probabilities of principal γ-rays and strong β-ray intensities. The means of the present results are also given for comparison with the evaluated values or the previously reported ones. Uncertainties are indicated by numbers in respective parentheses.

The present emission probabilities of principal γ-rays for ^{76}As shown in Table 1 agree with each other within standard deviations for respective energies. The uncertainties of about 1% are obtained for the means of emission probabilities of 559.1, 657.1 and 1228.5 keV γ-rays, and those are much smaller

than the uncertainties of emission probabilities evaluated in the Nuclear Data Sheets [5]. The uncertainties for the other energies are more than 1% due to peak pileup. Present γ-ray emission probabilities which are smaller by about 10% brought to smaller β-ray intensities of the excited states and larger β-ray intensity of the ground state by about 10% than the evaluated values.

Table 2 shows the present and previous emission probabilities of 165.9 and 1420.5 keV γ-rays for ^{139}Ba. The present emission probability of 165.9 keV γ-rays is smaller by about 3% than those of refs. [6] and [7] and the uncertainty is much smaller. Burrows [6] evaluated the emission probability using relative γ-ray intensity and a normalizing factor. He adopted the emission probability for 1420.5 keV reported in ref. [7] for deducing the normalizing factor. Gehrke [7] used nickel foils to obtain various β-ray efficiencies for determination of disintegration rate. The method resulted in relatively not precise disintegration rate and the emission probabilities with large uncertainties. The emission probabilities of 1420.5 keV γ-rays were deduced using relative intensities of 1420.5 keV γ-rays and emission probabilities of 165.9 keV γ-rays by us and Gehrke. However, the present result is more precise because it was calculated using more precise emission probability. The present precise emission probabilities provided precise β-ray intensities for excited states and the ground state of ^{139}La. The results are also shown in Table 2.

Agreeable γ-ray emission probabilities within standard deviations for ^{159}Gd are exhibited in Table 3 for the present results. Uncertainty of the mean of the present strongest γ-rays is less than 0.5%, whereas that of evaluated one [8] is more than 25%. The evaluated value was derived using the relative γ-ray intensity and a normalizing factor, and the uncertainties of those two parameters were 5 and 23.7%, respectively. As the precise γ-ray emission probabilities were used in the calculation, the present β-ray intensities shown in Table 3 for excited states and the ground state are more precise than those reported by Helmer [8].

The present emission probabilities of principal γ-rays for ^{187}W shown in Table 4 are the mean values of twelve measurement results. Therefore, much small uncertainties are provided for the γ-ray emission probabilities. Uncertainty of the strongest emission probability of 685.8 keV γ-rays is less than 0.3% which is much smaller than the uncertainty of that evaluated in ref. [9] or reported by Herman et al. [10]. Larger absolute values of the means by about 20% than those in both references brought to larger β-ray intensities of excited states by about 20% and smaller β-ray intensities of the ground state of ^{187}Re by about 40%.

Table 1 γ-ray emission probabilities and β-ray intensities for ^{76}As

γ-ray emission probabilities (%)								β-ray intensities (%)		
Energy (keV)	Present work						Singh and Viggars [5]	Energy (keV)	Present work	Singh and Viggars [5]
	a	*b*	*c*	*d*	*e*	Mean				
559.1	40.70 (66)	41.37 (75)	40.29 (68)	40.55 (56)	40.45 (59)	40.67 (29)	45 (2)	306.7	0.96 (1)	1.03 (6)
563.2	1.106 (97)	1.125 (114)	1.105 (103)	1.103 (78)	1.100 (81)	1.108 (43)	1.20 (8)	532.9	1.52 (7)	1.69 (12)
657.1	5.454 (72)	5.590 (86)	5.520 (50)	5.601 (60)	5.583 (72)	5.550 (31)	6.17 (42)	1174.4	1.58 (1)	1.77 (13)
1212.9	1.310 (165)	1.301 (181)	1.324 (163)	1.264 (97)	1.280 (101)	1.296 (65)	1.44 (11)	1745.9	6.72 (11)	7.5 (5)
1216.1	3.055 (227)	3.032 (247)	3.040 (218)	2.947 (133)	2.984 (139)	3.012 (88)	3.42 (24)	2402.9	31.9 (3)	35.2 (16)
1228.5	1.037 (32)	1.029 (41)	1.035 (15)	1.034 (24)	1.037 (31)	1.034 (13)	1.22 (10)	*2962.0*	*56.0 (3)*	*51 (2)*

Table 2 γ-ray emission probabilities and β-ray intensities for ^{139}Ba

γ-ray emission probabilities (%)								
Energy (keV)	Present work						Burrows [6]	Gehrke [7]
	a	*b*	*c*	*d*	*e*	Mean		
165.9	23.06 (18)	22.95 (15)	23.12 (15)	22.91 (15)	22.93 (15)	22.99 (7)	23.7 (34)	23.76 (25)
1420.5						*0.259 (2)*	0.261 (37)	*0.261 (5)*

β-ray intensities (%)			
Energy (keV)	Present work	Burrows [6]	Gehrke [7]
833.6	0.0175 (10)	0.0175 (20)	
889.5	0.292 (2)	0.287 (7)	
2144.1	28.70 (7)	29.68 (31)	29.65 (32)
2310.0	*70.95 (7)*	*69.98 (31)*	

Table 3 γ-ray emission probabilities and β-ray intensities for ^{159}Gd

γ-ray emission probabilities (%)								β-ray intensities (%)		
Energy (keV)	Present work						Helmer [8]	Energy (keV)	Present work	Helmer [8]
	a	*b*	*c*	*d*	*e*	Mean				
58.0	2.350 (94)	2.371 (97)	2.550 (89)	2.539 (82)	2.410 (55)	2.44 (4)	2.3 (6)	607.1	12.19 (5)	12 (3)
226.0	0.215 (8)	0.215 (11)	0.221 (9)	0.218 (5)	0.216 (6)	0.217 (4)	0.21 (5)	622.4	0.310 (3)	0.31
348.2	0.254 (8)	0.255 (11)	0.241 (7)	0.237 (5)	0.258 (5)	0.249 (3)	0.22 (6)	912.6	29.01 (44)	26 (7)
363.5	11.61 (11)	11.65 (11)	11.98 (13)	11.85 (10)	11.83 (10)	11.78 (5)	10.8 (28)	*970.6*	*58.38 (45)*	*62 (9)*

Table 4 γ-ray emission probabilities and β-ray intensities for ^{187}W

γ-ray emission probabilities (%)				β-ray intensities (%)			
Energy (keV)	Present work	Firestone [9]	Herman *et al.* [10]	Energy (keV)	Present work	Firestone [9]	Herman *et al.* [10]
134.2	10.219 (28)	8.85 (28)	8.77	538.3	5.09 (2)	4.23 (9)	4.2 (4)
551.5	6.134 (21)	5.08 (17)	5.0 (5)	625.4	66.09 (79)	54.9 (8)	53.1 (16)
618.4	7.613 (25)	6.28 (21)	8.0 (8)	685.7	4.09 (53)	3.3 (4)	5.2 (5)
625.5	1.333 (10)	1.09 (4)	1.58 (15)	692.8	5.82 (53)	4.7 (5)	5.2 (5)
685.8	32.868 (85)	27.3 (9)	26.9 (11)	1177.0	1.27 (62)	0.7 (3)	0.7 (3)
772.9	4.953 (19)	4.12 (13)	4.1 (4)	*1311.2*	*16.1 (13)*	*29.8 (10)*	*25.1 (24)*

Table 5 γ-ray emission probabilities and β-ray intensities for ^{193}Os

γ-ray emission probabilities (%)							β-ray intensities (%)		
Energy (keV)	Present work					A-Cohen [11]	Energy (keV)	Present work	A-Cohen [11]
	a	*b*	*c*	*d*	Mean				
138.9	3.66 (12)	3.63 (17)	3.80 (18)	3.70 (17)	3.69 (8)	4.27 (26)	583.3	2.33 (13)	2.4 (2)
280.4	1.21 (1)	1.19 (1)	1.27 (1)	1.26 (1)	1.22 (1)	1.24 (8)	680.1	7.69 (6)	7.9 (4)
321.6	1.21 (1)	1.21 (1)	1.29 (1)	1.27 (1)	1.24 (1)	1.28 (8)	1001.7	10.2 (2)	12.4 (9)
387.5	1.21 (1)	1.20 (1)	1.26 (1)	1.27 (1)	1.23 (1)	1.26 (8)	1067. 6	17.6 (29)	18 (4)
460.5	3.81 (4)	3.78 (3)	3.97 (4)	3.95 (4)	3.86 (2)	3.95 (25)	*1140.6*	*58.0 (29)*	*55 (4)*

The emission probabilities of principal γ-rays for ^{193}Os obtained from present measurements are shown in Table 5. The uncertainties of less than 1% are obtained for the means of respective energies except for that of 138.9 keV. The 138.9 keV γ-rays make peak-pileup on 142.1 keV γ-rays; therefore, the uncertainty of emission probability is about 2.2%. But this uncertainty is still smaller than 6% given for the evaluated value [11]. Excluding the emission probability of 138.9 keV γ-rays, the present results are smaller on the average by about 2.5% than those evaluated in ref. [11]. Table 5 also shows the β-ray intensities obtained from the present work and the evaluation [11]. The present β-ray intensities of excited state calculated using present γ-ray emission probabilities and relative γ-ray intensities are smaller than the evaluated values.

The smaller values resulted in larger present β-ray intensities of the ground state of ^{193}Ir by about 5%. The uncertainty is large because the relative intensity of 73 keV γ-rays reported in ref. [11] was used for calculation of β-ray intensities of first excited state with energy level of 73 keV.

4. Conclusions

Emission probabilities of principal γ-rays for short half-life nuclides of ^{76}As, ^{139}Ba, ^{159}Gd, ^{187}W and ^{193}Os have been established in the present work. The results are more precise than the previously evaluated or reported ones. The precise results are obtained due to the ability of the 4πβ-γ coincidence apparatus to provide precise parameters of disintegration rate, absolute γ-ray intensities, and detection efficiency. Present precise γ-ray emission probabilities and measured relative γ-ray intensities brought to more precise β-ray intensities than those previously evaluated or reported.

Acknowledgments

Most of the experiments were carried out at Kyoto University Research Reactor Institute (KURRI). The authors would like to appreciate Drs. S. Yamada and A. Taniguchi of KURRI for supporting the experiments.

References

[1] Miyahara, H., Matumoto, H., Wurdiyanto, G., Yanagida, K., Takenaka, Y., Yoshida, A. and Mori, C.: Nucl. Instr. Meth., A353, 229 (1994).
[2] Smith, D.: Metrologia 11, 73 (1975).
[3] Baerg, A. P.: Nucl. Instr. Meth., 112, 143 (1973).
[4] Brandt, S.: "Statistical and Computation Methods in Data Analysis," North-Holland, Amsterdam (1976).
[5] Singh, B. and Viggars, D. A.: Nucl. Data Sheets, 42, 233 (1984).
[6] Burrows, T. W.: Nucl. Data Sheets, 57, 337 (1989).
[7] Gehrke, R. J.: Int. J. Appl. Radiat. Isot., 31, 37 (1980).
[8] Helmer, R. G.: Nucl. Data Sheets, 72, 83 (1994).
[9] Firestone, R. B.: Nucl. Data Sheets, 62, 159 (1991).
[10] Herman, A. W., Heighway, E. A. and MacArthur, J. D.: Can. J. Phys., 48, 1040 (1970).
[11] Agda Artna-Cohen: Nucl. Data Sheets, 83, 921 (1998).

JP0150680

3.18

Short Comments to ^{56}Fe of FENDL/MG-2.0

Chikara KONNO
Center for Neutron Science, Japan Atomic Energy Research Institute
Tokai-mura, Naka-gun, Ibaraki-ken 319-1195 JAPAN
e-mail: konno@fnshp.tokai.jaeri.go.jp

Ulrich FISCHER
Institut für Reaktorsicherheit, Forschungszentrum Karlsruhe
P.O. Box 3640, D-76021 Karlsruhe, Germany

Dr. Kodeli pointed out a large discrepancy between neutron spectra below 1.5 keV calculated by MCNP and ANISN with the FENDL-2 library for an iron sphere benchmark, which consisted of an iron sphere of 10 cm in radius with 14 MeV neutron source in the center. Reasons of the discrepancy were investigated in detail. The benchmark calculations with FENDL-1, FENDL-2 and EFF-3.1 by ANISN and MCNP suggested that FENDL/MG-2.0 ^{56}Fe data have some problems. It was identified that reasons of the discrepancy are the LIST data of the first neutron energy of the FILE6 in FENDL/E-2.0 ^{56}Fe, through the detail check of the original libraries of ^{56}Fe of FENDL-1, FENDL-2 and EFF-3.1. The FENDL/MG-2.0 ^{27}Al data also have the same problem, though the influence is small.

1. Introduction

At the EFF meeting in April and November, 1999, Dr. Kodeli pointed out that there was a large discrepancy between neutron spectra below 1.5 keV calculated by MCNP and ANISN with the FENDL-2 [1] library for an iron sphere benchmark, which consisted of an iron sphere of 10 cm in radius with 14 MeV neutron source in the center. [2,3] We investigated reasons of that discrepancy in detail.

2. Iron Sphere Benchmark Calculation

At first we carried out an iron benchmark calculation similar with one which Dr. Kodeli did in order to confirm the large discrepancy between neutron spectra below 1.5 keV calculated by MCNP and ANISN. The iron assembly was a natural iron sphere of 10 cm in radius (atomic density : 0.083 /barn/cm) and a point neutron source with uniform distribution in energy interval 13.84 – 14.19 MeV covering group 8 of the VIATMIN-J [4] group structure was set in the center of the iron sphere as shown in Fig. 1. A neutron spectra at the distance of 15 cm from the center of the iron sphere was compared.

We used the MCNP-4A [5] and ANISN (included in the DOORS 3.2 package [6]) codes. The iron sphere was modeled in 1D spherical geometry. The nuclear data library for MCNP was

FENDL/MC-2.0 [7], while the P_5 multigroup library for ANISN with self-shielding correction was generated from FENDL/MG-2.0 [7] by the TRANSX2.15 [8] code. Calculations with the FENDL-1 [9] nuclear data library were also performed for comparison. The inputs were the same as those for FENDL-2 except for the nuclear data library part.

The calculated neutron spectra are shown in Figs. 2 and 3. As Dr. Kodeli pointed out, there is a large discrepancy between neutron spectra below 1.5 keV calculated by MCNP and ANISN in the case of FENDL-2, while there is no large discrepancy in the case of FENDL-1. Since the neutron spectra have no rapid change around 1.5 keV in the MCNP and ANISN calculations of FENDL-1 and the MCNP calculation of FENDL-2, it is considered that the iron data of FENDL/MG-2.0 have some problems. The ^{56}Fe data of FENDL-2 is that of EFF-3.0, while the data of other iron isotopes are those of FENDL-1. It is concluded that the ^{56}Fe data of FENDL/MG-2.0 cause the discrepancy. The ^{56}Fe data of FENDL/MG-2.0 was generated with NJOY94.105, which is an older version of the NJOY code [10]. We reprocessed FENDL/E-2.0 ^{56}Fe with the newer version NJOY97.95 and recalculated a neutron spectrum by ANISN with this newly processed library. The result was, however, the same as the previous calculation.

Recently a new evaluation EFF-3.1 ^{56}Fe [11], which was re-evaluated based on EFF-3.0 ^{56}Fe, was released only for EFF members. In order to examine whether the same phenomena as EFF-3.0 ^{56}Fe appears in EFF-3.1 ^{56}Fe, we performed the benchmark calculation by ANISN and MCNP with EFF-3.1 ^{56}Fe and other iron isotopes of FENDL-2. We used the official ace file of EFF-3.1 ^{56}Fe in EFF members for MCNP, which Dr. Trkov processed [12] with NJOY. A matxs file of EFF-3.1 ^{56}Fe was newly generated with NJOY97.95 for the multigroup library for ANISN. The rapid change of neutron spectrum around 1.5 keV does not appear in this ANISN calculation.

3. Double Differential Cross section Data Reconstructed from Multigroup Libraries

In order to specify problems included in FENDL/MG-2.0 ^{56}Fe, we reconstructed double differential cross section (DDX) data from 175 group multigroup libraries generated from the ^{56}Fe matxs files of FENDL-1, -2 and EFF-3.1 and compared each other. As the result, we found out that the only DDX data of FENDL-2 ^{56}Fe have huge sharp peaks around 1.5, 2.5 and 3.5 keV in the incident neutron energies of groups 28-33 (4.4933 - 6.0653 MeV), 11-12 (12.214 - 12.84 MeV) and 13-14 (11.052 - 12.214 MeV), respectively, as shown in Fig. 4. Particularly the peak around 1.5 keV in the incident neutron energy of group 32 is very large. This peak energy, 1.5 keV, is the same as the energy, below which the neutron spectra calculated by MCNP and ANISN with FENDL-2 were different. The reason of the discrepancy is considered to be this huge peak in the DDX.

4. Comparison of ^{56}Fe among FENDL/E-1.1, FENDL/E-2.0 and EFF-3.1

Next we checked the original libraries of ^{56}Fe in FENDL/E-1.1, FENDL/E-2.0 and EFF-3.1 in detail. The FILE2, FILE3 and FILE4 data seemed to have no problem. But we detected two different points for the FILE6. One point is the reference system of secondary energy and angle; the laboratory (LAB) coordinates are used in FENDL/E-1.1, while the center-of mass (CM) coordinates are used in FENDL/E-2.0 and EFF-3.1, though all the libraries use Legendre

coefficients for the angular presentation of the FILE6. The other point is the LIST data of the first incident neutron energy. Figure 5 shows the LIST data of the first incident neutron energy in FILE6, MT91. The highest secondary energy is 1 x 10^{-5} eV in FENDL-1 and EFF-3.1, while it is 1 eV in FENDL-2 (the difference of the b_0 data is due to normalization and interpolation scheme). From these two points, we suspected that the GROUPR module of NJOY could not deal with the LIST data of the first incident neutron energy of the FILE6 in FENDL-2 ^{56}Fe correctly since the CM to LAB conversion in the GROUPR module of NJOY seemed to have no problem in EFF-3.1 ^{56}Fe. Then we modified the highest energy and b_0 data of the LIST data of the first incident neutron energy of all the MTs (MT16, MT22, MT28 and MT91) in FENDL/E-2.0 ^{56}Fe to those in EFF-3.1 ^{56}Fe, made a new matxs file of FENDL-2 ^{56}Fe with NJOY97.95 and executed the ANISN calculation with the multigroup library generated from the new matxs file. The calculated neutron spectrum is shown in Fig. 6 with the previous MCNP result. The discrepancy between the ANISN and MCNP calculations disappears. Figure 7 plots the DDX data reconstructed from 175 group multigroup libraries generated from the original and modified ^{56}Fe matxs files of FENDL-2. The huge peak around 1.5 keV disappears in the modified FENDL-2 ^{56}Fe. It is concluded that the GROUPR module of NJOY can not deal with the LIST data of the first incident neutron energy of the FILE6 in FENDL/E-2.0 ^{56}Fe correctly. On the contrary, the ACER module of NJOY can process the LIST data of the first incident neutron energy of the FILE6 in FENDL/E-2.0 ^{56}Fe without problem, since the MCNP calculation shows no strange results.

5. FENDL/MG-2.0 ^{27}Al

The ^{27}Al data of FENDL/E-2.0 are also from EFF3.0. Since the highest energy and b_0 data in the LIST data for the first incident neutron energy of the FILE6 of FENDL/E-2.0 ^{27}Al have the same as those of FENDL/E-2.0 ^{56}Fe, the same trouble may appear in calculations with FENDL/MG-2.0 ^{27}Al. Figure 8 shows calculated leakage neutron spectra (at the distance of 15 cm from the center of an aluminum sphere) for an aluminum sphere of 10 cm in radius with 14 MeV neutron source in the center by ANISN and MCNP with FENDL-2. The large discrepancy between ANISN and MCNP calculations does not appear in ^{27}Al seemingly. The FENDL/MG-2.0 ^{27}Al data, however, have the same huge sharp peak as FENDL/MG-2.0 ^{56}Fe as shown in Fig. 9. Probably the reason why the discrepancy does not appear is because the sharp peak in FENDL/MG-2.0 ^{27}Al is smaller by one order than that in FENDL/MG-2.0 ^{56}Fe.

6. Conclusion

We investigated reasons of a large discrepancy between neutron spectra below 1.5 keV calculated by MCNP and ANISN with the FENDL-2 library for an iron sphere benchmark, which consisted of an iron sphere of 10 cm in radius with 14 MeV neutron source in the center. The benchmark calculations with FENDL-1, FENDL-2 and EFF-3.1 by ANISN and MCNP suggested that FENDL/MG-2.0 ^{56}Fe causes the discrepancy. Through the detail check of the original and multigroup libraries of ^{56}Fe of FENDL-1, FENDL-2 and EFF-3.1, it is identified that reasons of the discrepancy are the LIST data of the first incident neutron energy of the FILE6 in FENDL/E-2.0 ^{56}Fe. We recommend revising the FENDL/MG-2.0 ^{56}Fe data. The FENDL/

MG-2.0 ^{27}Al data have the same problem, though the influence is small. We also recommend revising FENDL/MG-2.0 ^{27}Al.

References

[1] Pashchenko A.B. and Wienke H. : IAEA-NDS-175 Rev. 3 (1998).
[2] Kodeli I. : EFF-DOC-684 (1999).
[3] Kodeli I. : EFF-DOC-698 (1999).
[4] Vontobel P. and Pelloni S. : EIR-Bericht Nr. 636 (1987).
[5] Briesmeister J.F. (edited) : LA-12625-M (1993).
[6] DOORS3.2 : One, Two- and Three-Dimensional Discrete Ordinates Neutron/Photon Transport Code System, RSICC CODE PACKAGE CCC-650 (1998).
[7] Wienke H. and Herman M. : IAEA-NDS-176 Rev. 1 (1998).
[8] MacFarlane R.E. : LA-12312-MS (1993).
[9] Ganesan S. and McLaughlin P.K. : IAEA(NDS)-128, Rev. 1 (1995).
[10] MacFarlaneR.E. and Muir D.W. : LA-12740-M (1994).
[11] Trkov A. : EFF-DOC-657 (1998).
[12] Trkov A. : private communication (1998).

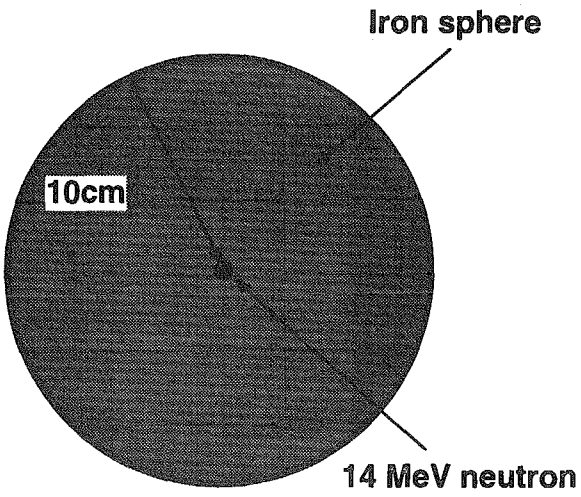

Fig.1 Calculation model.

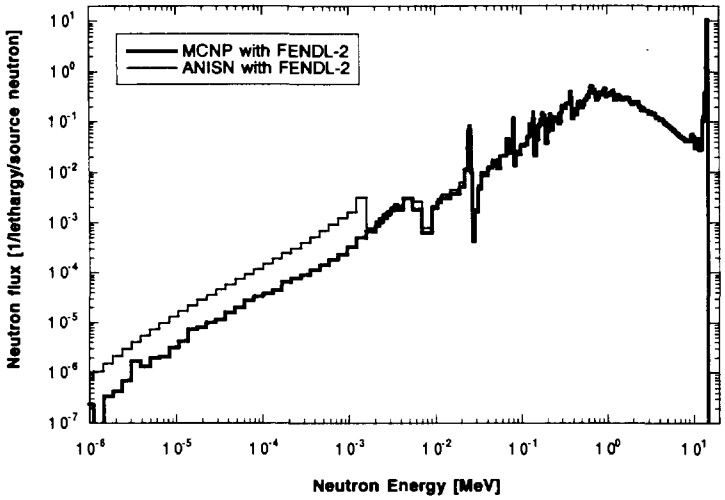

Fig. 2 Calculated neutron spectra at the distance of 15 cm from the center of the iron sphere (FENDL-2).

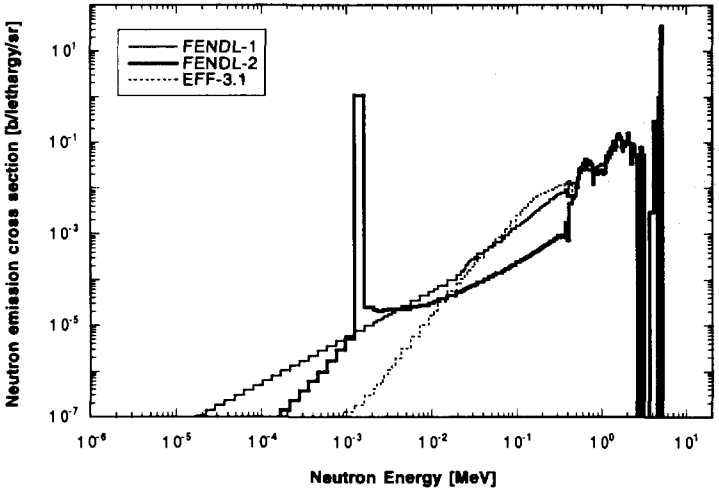

Fig. 4 ^{56}Fe DDX reconstructed from 175 group multigroup libraries in the incident neutron energy of group 31 (4.9659 – 5.2205 MeV) and the emission angle of 0 degree.

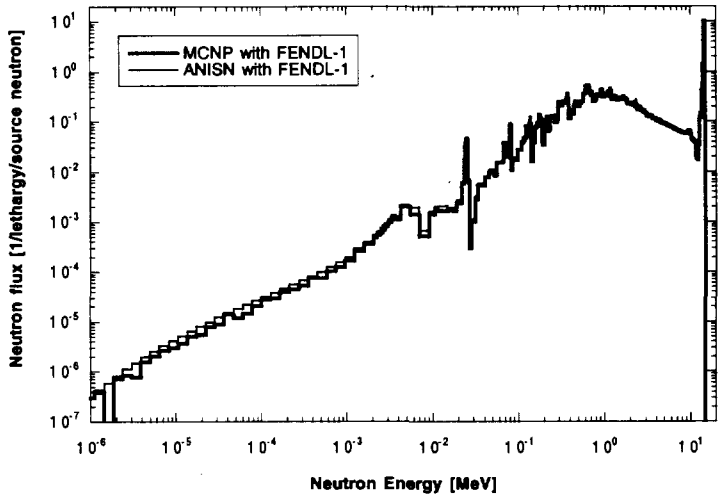

Fig. 3 Calculated neutron spectra at the distance of 15 cm from the center of the iron sphere (FENDL-2).

```
0.000000+0 4.620600+6          0          0      4   22631 6 91 8331
0.000000+0 1.000000+5 1.000000-5 0.000000+0          2631 6 91 8332
```

(a) FENDL-1 (interpolation scheme is histogram)

```
.00000+ 0  4.61780+ 6          0          0      4   22631 6 9111120
.00000+ 0  2.00000+ 0 1.00000+ 0  .00000+ 0          2631 6 9111121
```

(b) FENDL-2 (interpolation scheme is linear-linear)

```
0.000000+0 4.617800+6          0          0      4   22631 6 91     7
0.000000+0 2.000000+5 1.000000-5 0.000000+0          2631 6 91     8
```

(c) EFF-3.1 (interpolation scheme is linear-linear)

Fig. 5 LIST data of FILE6, MT91 in ^{56}Fe of FENDL-1, FENDL-2 and EFF-3.1.

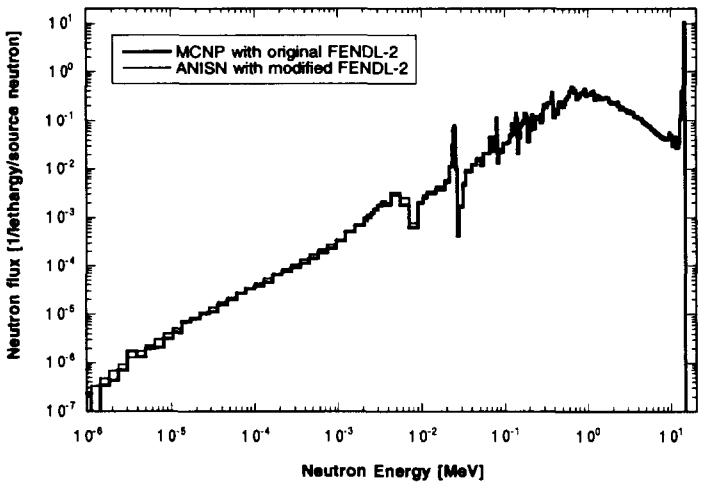

Fig. 6 Calculated neutron spectra at the distance of 15 cm from the center of the iron sphere (MCNP with original FENDL-2, ANISN with modified FENDL-2).

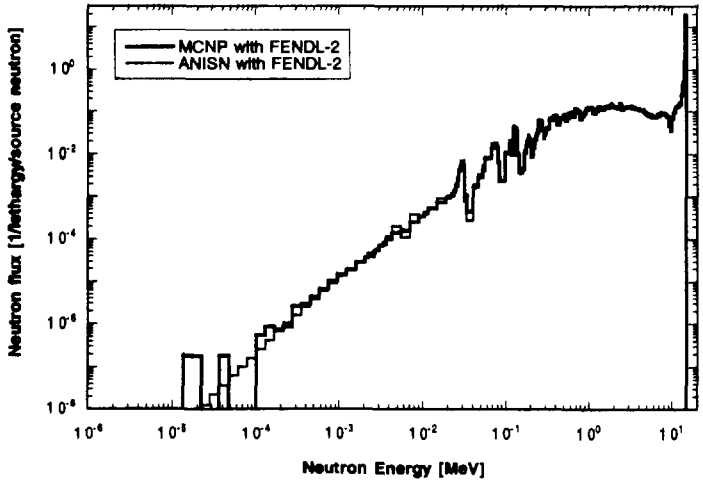

Fig. 8 Calculated neutron spectra at the distance of 15 cm from the center of the iron sphere (FENDL-2).

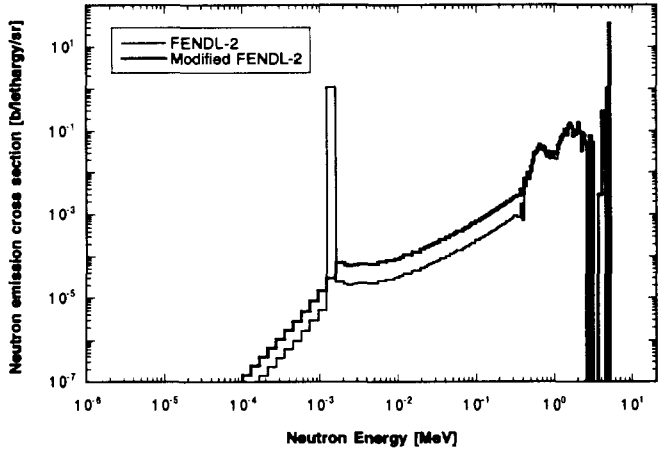

Fig. 7 ^{56}Fe DDX reconstructed from 175 group multigroup libraries of the original and modified FENDL-2 in the incident neutron energy of group 31 (4.9659 – 5.2205 MeV) and the emission angle of 0 degree.

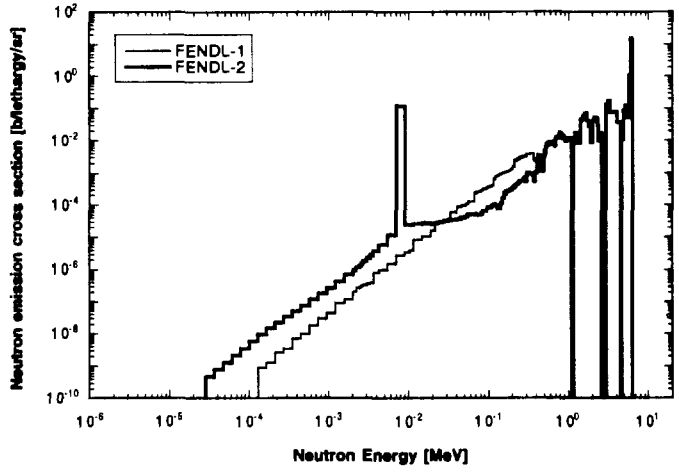

Fig. 9 ^{27}Al DDX reconstructed from 175 group multigroup libraries in the incident neutron energy of group 27 (6.0653 – 6.3763 MeV) and the emission angle of 0 degree.

JP0150681

3.19

DORT Analysis of Iron and Concrete Shielding Experiments at JAERI/TIARA with P_7 and P_9 Approximated LA150 Multigroup Libraries

Chikara KONNO, Yujiro IKEDA
Center for Neutron Science, Japan Atomic Energy Research Institute
Tokai-mura, Naka-gun, Ibaraki-ken 319-1195 JAPAN
e-mail: konno@fnshp.tokai.jaeri.go.jp

Kazuaki KOSAKO
Sumitomo Atomic Energy Industries, Ltd.
2-10-4, Ryogoku, Sumida-ku, Tokyo 130-0026 JAPAN

The accuracy of DORT calculations with P_7 and P_9 approximated LA150 multigroup libraries for tens MeV neutrons was investigated through the analysis of the shielding experiments on iron and concrete for 43 and 68 MeV p-^{7}Li quasi-monoenergetic neutrons at JAERI/TIARA.

1. Introduction

In the 1998 Symposium on Nuclear Data we presented [1] analyses of the shielding experiments [2,3] on iron and concrete for 43 and 68 MeV p-^{7}Li quasi-monoenergetic neutrons performed at JAERI/TIARA with the two-dimensional Sn Code DORT and P_5 approximated LA150 [4] multigroup library. It was noted that these DORT calculations were very different from the MCNP calculations [5] with LA150. This discrepancy was considered to be due to the P_5 approximation in the multigroup library since the P_5 Legendre expansion can not present forward-peak angular distributions of higher energy neutrons precisely. This time we modified the NJOY97 and TRANSX codes so as to produce higher order Legendre expanded multigroup libraries than the fifth order, generated P_7 and P_9 approximated LA150 multigroup libraries and investigated the effects of P_7 and P_9 approximated LA150 multigroup libraries through analyses of the shielding experiments at JAERI/TIARA.

2. Overview of Shielding Experiments on Iron and Concrete at JAERI/TIARA

The shielding experiments were performed with collimated 43 and 68 MeV p-^{7}Li neutron source at Takasaki Ion Accelerator for Advanced Radiation Application (TIARA), at JAERI. Figure 1 shows the experimental arrangement. The test shield of iron and concrete from 10 cm up to 200 cm in thickness was located at the end of the collimator with or without an additional iron shield. Neutron spectra were measured with a BC501A scintillator and Bonner Ball detectors on the beam axis and at 20 and 40 cm off the beam axis behind the test shield.

3. Calculation Procedure

The Sn code DORT3.2 [6] was used in the analysis. Only the collimated source neutrons and experimental assembly, which was modeled as a cylinder instead of a rectangular parallelepiped, were adopted in the analysis according to Ref. 2. The first collision source was calculated from collimated source neutrons with the GRTUNCL code [7]. P_5, P_7 and P_9 approximated multigroup libraries were generated from LA150 with NJOY97.95 [8] and TRANSX2.15 [9] modified for higher order P_L expansion. Its group structure was 100 groups of 1 MeV interval from 0.5 MeV to 100.5 MeV. As well as the previous paper [1], we used the multigroup libraries with and without the extended transport approximation (TA) [9], which was devised mainly for fast breeding reactors in order to mitigate the effects of truncating the Legendre expansion at finite order. MCNP-4B calculations [5] with the continuous energy library processed from LA150 were adopted as a reference.

4. Results and Discussion

The comparison between the calculations and measurements for neutron spectra above 10 MeV on the beam axis is carried out in this paper. The ratios of the calculated values to the experimental ones (C/E) of integrated neutron flux at peak and continuum regions are plotted in Figs. 2 - 9. These C/E figures indicate the followings;

1) The discrepancy between the MCNP and DORT calculations generally becomes smaller with the Legendre order of multigroup libraries used in the DORT calculations.
2) Effect of extended transport approximation is smaller in the P_7 and P_9 approximated DORT calculations, but the DORT calculation with extended transport approximation is more similar with the MCNP calculation.

Figure 10 shows angular distributions of elastic scattering in the original library and MCNP

library of LA150 and in-group scattering in P_5, P_7 and P_9 approximated LA150 multigroup libraries for ^{56}Fe at 60 MeV. The angular distribution of in-group scattering in the P_5 approximated LA150 multigroup library is very different from that of elastic scattering in the original LA150 library, while angular distribution of in-group scattering in the P_9 approximated LA150 multigroup library is similar with that of elastic scattering in the original LA150 library. It is considered that the P_9 approximation is enough for transport calculations for tens MeV neutrons.

5. Concluding Remarks

We analyzed the shielding experiments on iron and concrete for 43 and 68 MeV p-^{7}Li quasi-monoenergetic neutrons at JAERI/TIARA with the DORT code and P_5, P_7 and P_9 approximated LA150 multigroup libraries which were generated by using modified NJOY and TRANSX codes. The discrepancy between the MCNP and DORT calculations in the case of P_5 approximated LA150 multigroup library became much smaller in P_7 and P_9 approximated DORT calculations. Effect of extended transport approximation is smaller in P_7 and P_9 approximated DORT calculations, but the DORT calculation with extended transport approximation is more similar with MCNP calculation. It is concluded that P_5 approximation is not adequate in multigroup library and P_7 or P_9 approximated multigroup library is required in transport calculations of neutrons of more than a few tens MeV with Sn codes.

References

[1] Konno C., et al. : Proc. of 1998 Symposium on Nuclear Data, JAERI-Conf 99-002 (1999), p.164.

[2] Nakao N., et al. : Nucl. Sci. Eng., 124,228 (1996).

[3] Nakashima H., et al. : Nucl. Sci. Eng., 124,243 (1996)

[4] Chadwick M.B. et al. : Nucl. Sci. Eng., 131, 293 (1999).

[5] Wada M. et al. : Proc. of 1998 Symposium on Nuclear Data, JAERI-Conf 99-002 (1999), p.158.

[6] DOORS3.2 : One, Two- and Three-Dimensional Discrete Ordinates Neutron/Photon Transport Code System, RSICC CODE PACKAGE CCC-650 (1998).

[7] Johnson J.O. (Ed.): ORNL/TM-11778 (1992).

[8] MacFarlane R.E. and Muir D.W.: LA-12740-M (1994).

[9] MacFarlane R.E. : LA-12312-MS (1992).

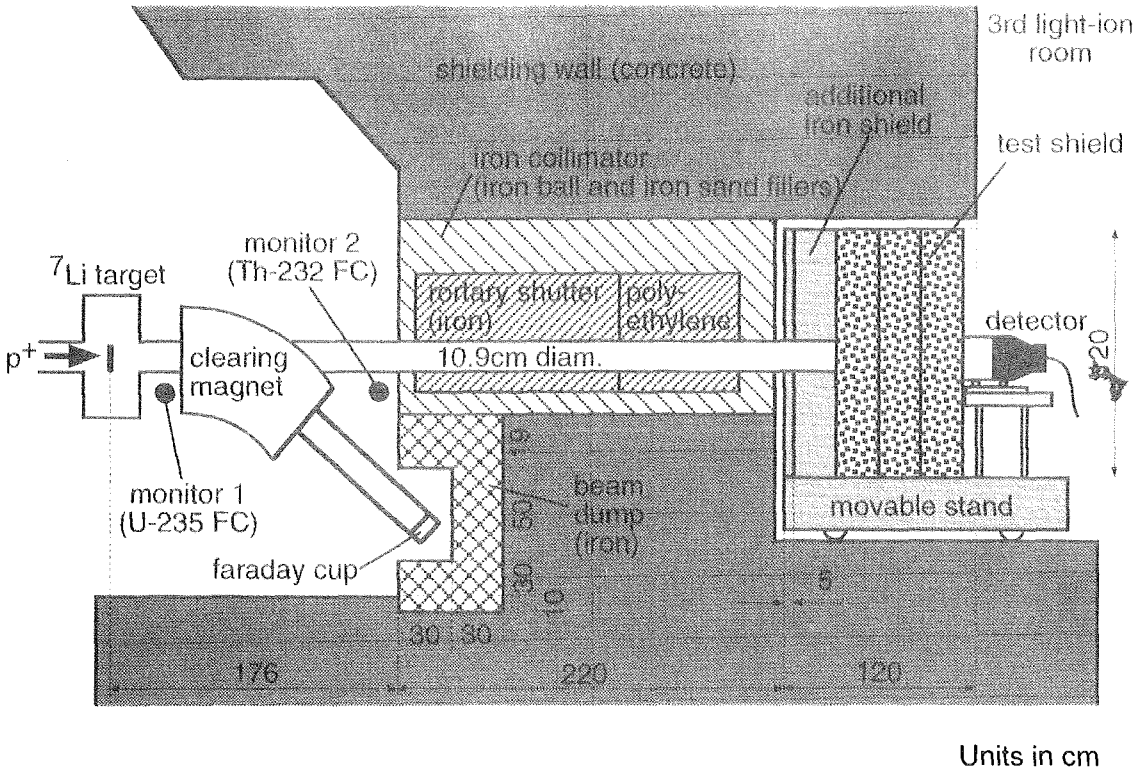

Fig. 1 Experimental arrangement of shielding experiments at JAERI/TIARA.

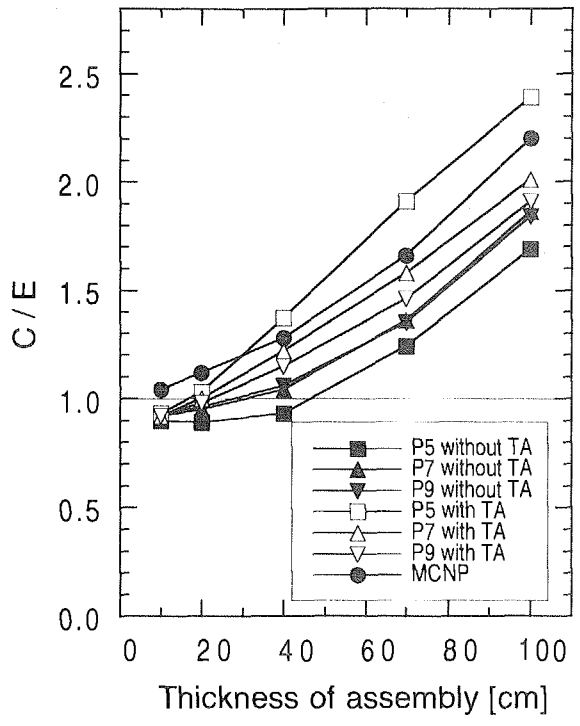

Fig. 2 C/E of peak neutron flux (35 - 45 MeV) of the iron experiment for 40 MeV neutrons.

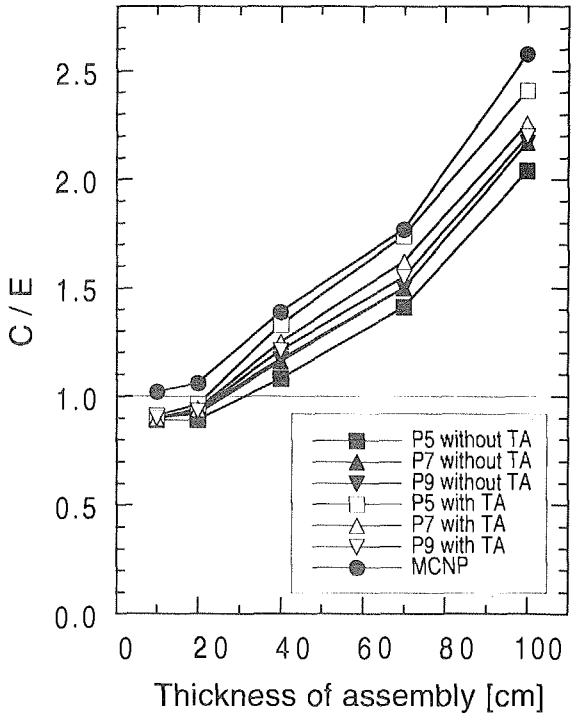

Fig. 3 C/E of continuum neutron flux (10 - 35 MeV) of the iron experiment for 40 MeV neutrons.

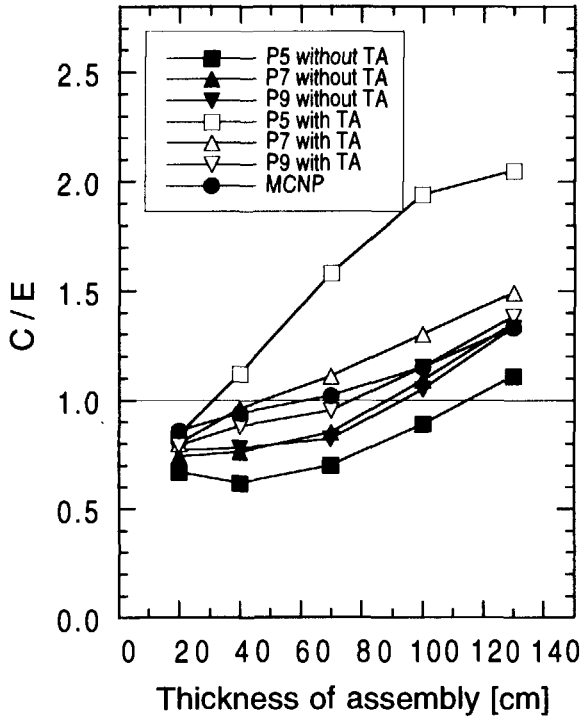

Fig. 4 C/E of peak neutron flux (60 - 70MeV) of the iron experiment for 65 MeV neutrons.

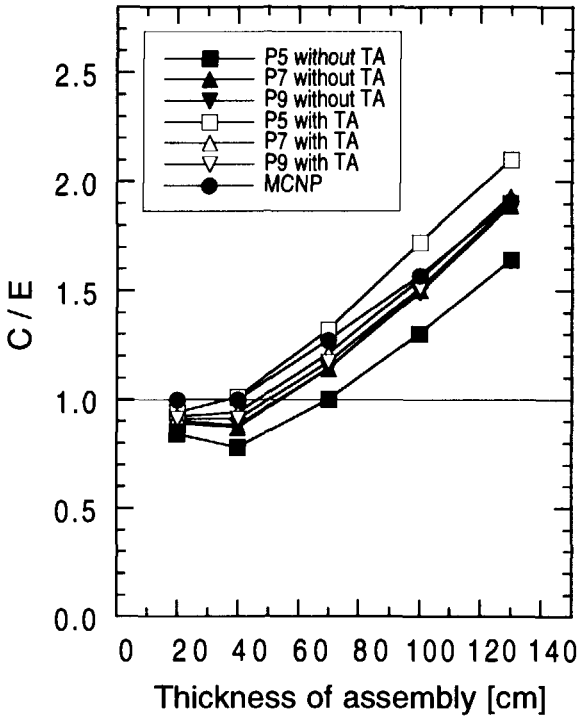

Fig.5 C/E of continuum neutron flux (10 - 60 MeV) of the iron experiment for 65 MeV neutrons.

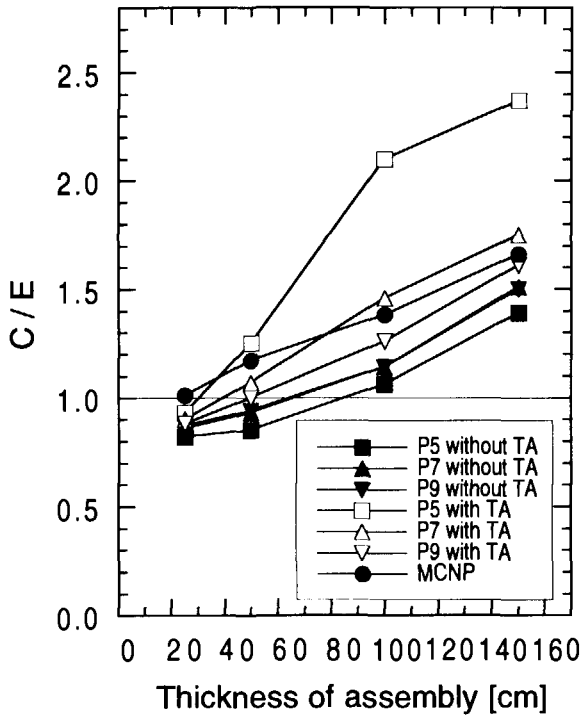

Fig. 6 C/E of peak neutron flux (35 - 45 MeV) of the concrete experiment for 40 MeV neutrons.

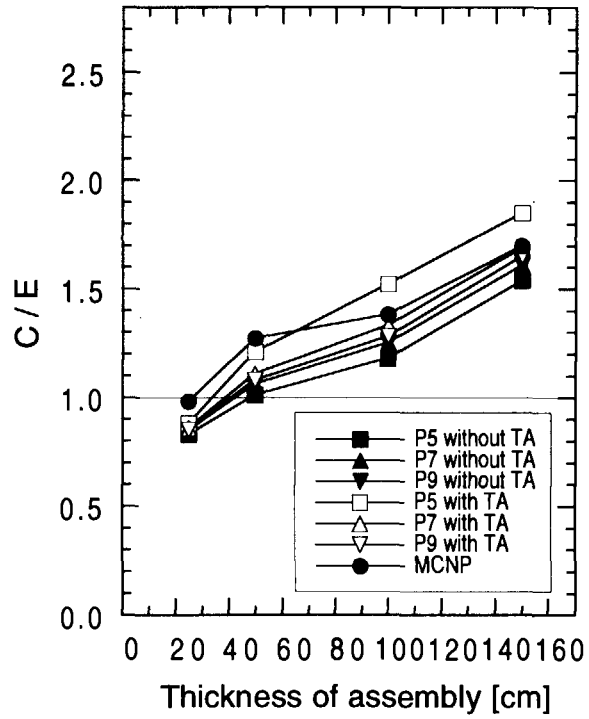

Fig. 7 C/E of continuum neutron flux (10 - 35 MeV) of the concrete experiment for 40 MeV neutrons.

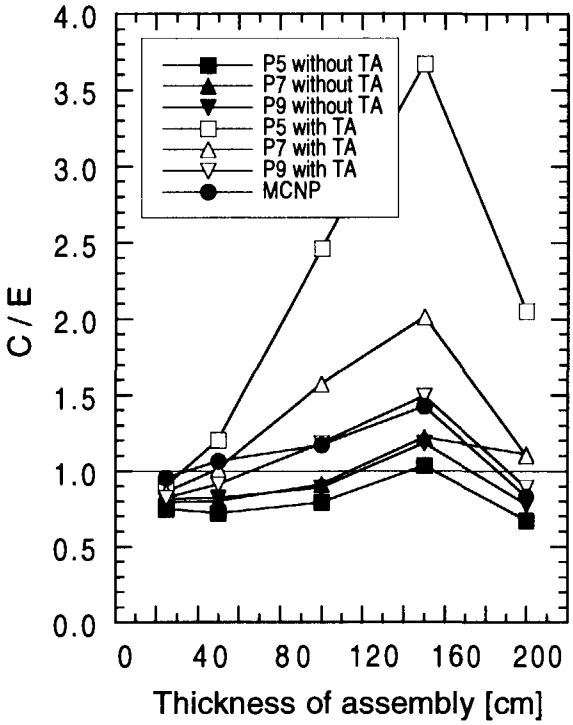

Fig. 8 C/E of peak neutron flux (60 - 70 MeV) of the concrete experiment for 65 MeV neutrons.

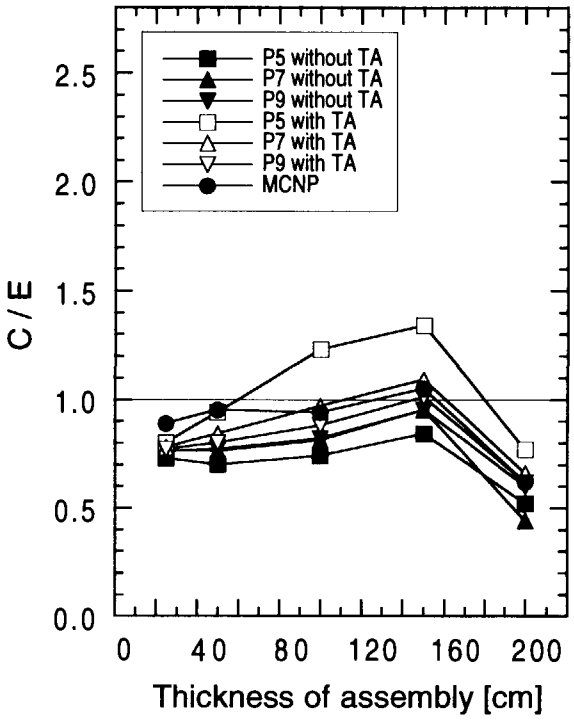

Fig. 9 C/E of continuum neutron flux (10 - 60 MeV) of the concrete experiment for 65 MeV neutrons.

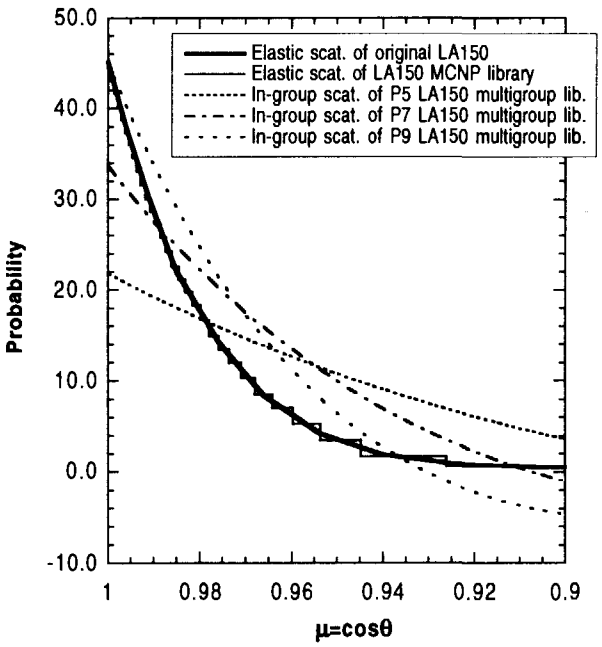

(a) 0 - 25.8 degree

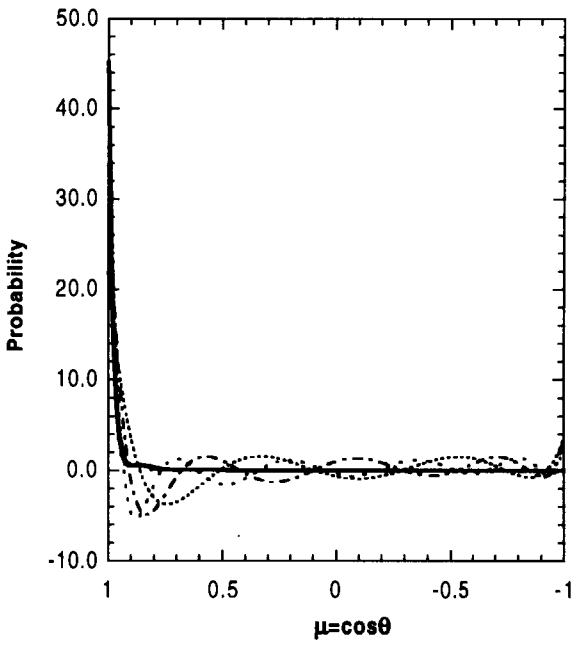

(b) 0 - 180 degree

Fig. 10 Angular distribution of elastic and in-group scattering for ^{56}Fe at 60 MeV.

JP0150682

3.20

Measurements of Neutron Spectra Produced from a Thick Iron Target Bombarded with 1.5 GeV Protons

Shin-ichiro Meigo*,†, Hiroshi Takada*, Nobuhiro Shigyo**, Kiminori Iga**, Yousuke Iwamoto**, Hirohiko Kitsuki**, Kenji Ishibashi**, Keisuke Maehata**, Hidehiko Arima**, Tatsushi Nakamoto*** and Masaharu Numajiri***

*Center for Neutron Science, Japan Atomic Energy Research Institute
Tokai-mura, Naka-gun, Ibaraki-ken 319-1195

**Department of Applied Quantum Physics and Nuclear Engineering, Kyushu University
Hakozaki, Higashi-ku, Fukuoka 812-8581

***High Energy Accelerator Research Organization (KEK)
Oho, Tsukuba, Ibaraki 305-0801 Japan

e-mail: †meigo@linac.tokai.jaeri.go.jp

For validation of calculation codes which are employed in the design of accelerator facilities, spectra of neutrons produced from a thick iron target bombarded with 1.5-GeV protons were measured. The calculated results with NMTC/JAM was compared with the present experimental results. It is found the NMTC/JAM generally shows in good agreement with experiment. Furthermore, the calculation gives good agreement with the experiment for the energy region 20 $\sim$ 80 MeV, whereas the NMTC/JAM gives 50 % of the experimental data for the heavy nuclide target such as lead and tungsten target.

1. Introduction

Applications of high energy particle accelerators are rapidly growing in many fields such as spallation neutron source and accelerator driven system. For the design of the target and shielding of the accelerator facilities, it is necessary to estimate the reaction rate and the neutron production in a thick medium in the energy region up to several GeV.

Nucleon-Meson Transport codes such as NMTC/JAM[1] NMTC/JAERI[2, 3], and LAHET[4] have been widely employed for the neutronics calculation. It is generally known that the codes can describe the particle productions and the transport in a thick medium. The accuracy of the codes, however, has not been completely satisfactory yet. In order to comprehend and improve the accuracy of the code, studies[5, 6] have been performed from both the theoretical and the experimental points of view. A series of the measurements of neutron production double differential cross sections were carried out at LANL and High Energy Accelerator Organization (KEK)[7]. For the spectrum of the thick target, the spectrum of neutrons produced from a thick lead[8] and tungsten targets[9] were measured. The experiment data of the spectrum are, however, very scarce for incident energies higher than 256 MeV.

For the validation of the calculation code employed in the design of the accelerator facilities, it is required the spectrum of neutrons produced from a thick target which is longer than the mean free path of the outgoing particles. In the accelerator facilities, iron takes important roles, because the yoke of magnet was made of iron steel. By the interaction between protons and irons, the neutron are produced in the beam line and accelerator, which is a source of the neutrons for the shielding of accelerator. For the shielding for the accelerator facilities, it should be confirmed the spectrum of neutrons produced from a iron target between the

calculation and experiment. However, these experimental data were scarce for the projectiles above 0.8 GeV. In this study, the spectrum produced from the iron target bombarded with 1.5-GeV protons, which was the same energy of the previous experiment, was measured. These experimental data were compared with the calculation of NMTC/JAM.

2. Experimental procedure

2.1 Incident particles and target

The experiment was carried out at the $\pi 2$ beam line of the 12-GeV Proton Synchrotron. Schematic view of the experimental arrangement is shown in Fig. 1. The incident particles were supplied as the secondary particle generated by an internal target which was placed in the primary 12-GeV proton beam. After passing the bending magnet, the secondary beam having a unique momentum was introduced to the thick target. The interval between and duration of the primary proton pulses were 4 and 2.5 s, respectively. The intensity of the incident particles was so weak ($\leq 10^5$ particles/pulse) that incident particles were counted one by one with beam scintillators. As incident projectiles, 2.3 GeV/c protons were employed, whose energies are 1.5- GeV for protons. The incident particles were identified 1.5-GeV protons from other particles by the time-of-flight (TOF) technique with a pair of scintillators (Pilot U) located at a separation distance of 4 m. The size of the incident beams was 2.0 and 1.6 cm in FWHM on the perpendicular and horizontal plains, respectively. Each Pilot U scintillator was connected with two photo-multipliers on opposite sides to obtain good time resolution. In order to subtract the neutrons produced from the beam scintillator, background measurements were performed without target.

A iron target was bombarded with the proton beams. The target was a rectangular parallelepiped $15 \times 15 \times 20$ cm^3, which was the same size as the target used in the previous experiments[8, 9]. In the iron target, protons caused the partially energy loss which is 0.23 GeV in the average. A beam dump consisted of a carbon block pile of 0.5×0.5 m^2 in the area and 1 m in thickness was located at a 8.5 m distance from the target. The carbon was surrounded by sufficiently thick iron blocks except on the beam-incident surface.

2.2 Neutron detector

As neutron detectors, NE213 scintillators(12.7 cm in diam. and 12.7 cm in thick.) were used. The detectors were placed at angles between 30° and 90° to the beam axis and at a common distance of 1.5 m from the center of the target. At the angle 15°, the distance was chosen 2.0 m so that the higher energy resolution was achieved. In order to reject the detection of the charged particles (i.e. π, p, d), NE102A scintillators of $17 \times 17 \times 1$ cm^3 were used as veto counters. They were placed at a distance of 2 cm from the surface of the NE213 scintillators. The pulse height of the neutron detectors was calibrated using gamma-rays from ^{137}Cs, ^{60}Co and ^{241}Am-Be.

As the neutron detection efficiency, the calculation results of SCINFUL-R[10] were used. Hence, the results of SCINFUL-R were utilized for detection efficiencies below 80 MeV. Above 80 MeV, the calculated efficiency of CECIL[11] adjusted to connect smoothly with that of SCINFUL-R at 80 MeV was employed. The detection efficiencies for ^{60}Co and ^{137}Cs biases were employed for the analysis of the neutron spectrum above and below 20 MeV, respectively.

2.3 Electronic Circuit

The diagram of the electronic circuit is shown in Fig. 2. A personal computer (PC-AT) was

utilized for controlling CAMAC ADCs and TDCs. The events arising from μ^+ projectiles were eliminated by the unti-coincidence of all beam scintillators. The number of incident particles was accumulated by the scaler. A good discrimination for the incident proton against the π^+ was achieved so that the uncertainty of the incident proton counts could be less than 1 %.

Anode signals of the photomultipliers coupled with NE213 scintillators were branched out to three pulses. One pulse was put into a CFD to produce the start signal of TOF measurement. Other two pulses were put into three ADCs (Fast, Total) which collected the charge of pulse during each gate signal duration. In order to eliminate gamma-ray counting, the two-gate integration method After the elimination of the photons, the TOF spectrum of the neutrons was obtained.

3. Calculation

The neutron spectrum calculation was carried out with NMTC/JAM[1] and MCNP-4A[12]. NMTC/JAM calculated the nuclear reactions and the particle transport above 20 MeV. MCNP-4A calculated the neutron transport below 20 MeV using a continuous energy cross section library FSXLIB-J3R2[13] processed from the nuclear data file JENDL-3.2[14]. In NMTC/JAM, the Niita's systematics[1] was implemented to estimate total, elastic and non-elastic nucleon-nucleus cross sections in the transport calculation part. The level density parameter derived by Ignatyuk[15] was also employed in the statistical decay calculation in NMTC/JAM.

Furthermore, additional calculations were performed by substituting the in-medium nucleon-nucleon cross sections (NNCS) for the free NNCS in the nuclear reaction calculation part of NMTC/JAM. The in-medium NNCS parameterized[16] similarly to those of Cugnon[17] were employed in this calculation.

In order to compare the experimental results, the calculation results should be smeared with the energy resolution. The calculated result with and without smearing of the resolution are shown in Fig 3. By the comparison of both results with and without smearing, it is found that the effect of the energy resolution on the spectra is smaller than 25 % for the energy lower than 150 MeV.

4. Results and Discussion

4.1 Neutron spectra produced from the iron target

The calculated results with the NMTC/JAM-MCNP-4A code system are compared with the present experimental results shown in Fig. 4. It is observed that the calculations using both free(shown by solid lines in the figure) and in-medium(shown by dot lines in the figure) NNCS give good agreement with the experiment within 50 %. For the angle at 90 °, the calculation with the in-medium NNCS shows better agreement with the experiment than calculation with free NNCS.

4.2 Dependence on the target nuclei

In order to comprehend the dependence of the target nuclei, the comparisons between calculation and experiment [8, 9] for the heavy metal target are shown in Figs 5 and 6. It is found that the difference of calculation results between Free and in-medium NNCS for iron target is much smaller than those for heavy metal targets. For the heavy metal target, the calculation with the in-medium NNCS gives much better agreement with the experiment in the

energy region above 20 MeV. By using in-medium NNCS in NMTC/JAM, *n-p* cross sections becomes smaller than free NNCS. This improvement is ascribed to the fact that the high energy nucleon emission is enhanced in the calculation because the mean free path of nucleon in a target nucleus is estimated longer by in-medium NNCS than the free one. Iron nuclei has almost same neutron and proton numbers. Therefore, difference is relatively smaller than difference for heavy metals. On the other hand, lead and tungsten are neutron rich nuclei. As a result, the dependence of NNCS on the neutron spectrum is stronger than the iron case.

5. Conclusion

For the validation of the nucleon meson transport code, the neutron spectra from a thick iron target bombarded with 1.5 GeV protons were measured at 4 angles between 15° and 90°. The accurate neutron spectra were obtained in the energy region between 4 and 1-GeV by the time-of-flight technique.

The calculation results with the NMTC/JAM-MCNP-4A code system are compared with the present experiment data. The calculation was made by using free and in-medium nucleon-nucleon cross sections (NNCS). It is found that calculation with both free and in-medium NNCS show good agreement with the experiment within 50 %. Even the calculation with free NNCS gives good agreement in the energy range between 20 and 80 MeV, whereas calculation gave about 50 % lower neutron flux for heavy metal target. For the result at 90 °, the calculation with in-medium NNCS shows better agreement than the calculation with free NNCS. It can be concluded that NMTC/JAM code system can be predicted the neutron spectrum from iron magnet and collimator with 50 % uncertainties.

By the comparison of heavy metal target, it is recognized the NNCS dependence on iron target is not stronger than heavy metal cases. It can be thought this dependence will become an clue to improve the calculation for the heavy metal targets.

References

[1] Niita K., et al. : "High Energy Nuclear Reaction Code JAM", *Proc. 1999 Sympo. Nucl. Data, Nov. 18-19, 1999, Tokai, JAERI, JAERI*-Conf 2000-5, pp98-103 (2000).

[2] Nakahara Y. and Tsutui T.: JAERI-M 82-198 (1982).

[3] Takada H. et al.: JAERI-Data/Code 98-005 (1998).

[4] Prael R. E. and Lichtenstein H.: LA-UR 89-3014 (1989).

[5] Intermediate Energy Nuclear Data: Models and Code, Proc. of OECD/NEA Mtg., Paris (1994).

[6] Yoshizawa N., et al.: *J. Nucl. Sci. Technol.*, **32** 601 (1995).

[7] Ishibashi K., et al.: *J. Nucl. Sci. Technol.*, **34** 529 (1997).

[8] Meigo S. et al.,: *Nucl. Instr. and Meth. A* **431** 521 (1999).

[9] Meigo S., et al: "Measurements of Neutron Spectra Produced from a Thick Tungsten Target Bombarded with 1.1 and 2.3 GeV/c Protons and π^+", *Proc. 1999 Sympo. Nucl. Data, Nov. 18-19, 1999, Tokai, JAERI, JAERI*-Conf 2000-5, pp249-254 (2000).

[10] Meigo S.: it Nucl. Instrum. Meth., **A401**, 365 (1997).

[11] Cecil R. A., et al.: *Nucl. Instrum. Meth.* **161** 439 (1979).

[12] Briesmeister J. F. (Ed.): *MCNP A General Monte Carlo N-Particle Transport Code Version 4A*, LA-12625 (1993).

[13] Kosako K., et al.: *A Continuous Energy Cross Section Library for MCNP Based on JENDL-3.2*, JAERI-Data/Code 94-020 (1994).

[14] Shibata K., et al.: *Japanese Evaluated Nuclear Data Library, Version-3 -JENDL-3-*, JAERI-1319 (1990).

[15] Ignatyuk A. V., Smirenkin G. N. and Tishin A. S.: *Sov. J. Nucl. Phys.*, **21** 256 (1975).

[16] Takada H. : *J. Nucl. Sci Technol.*, **33**, 275 (1996).

[17] Cugnon J., Mizutani T. and Vandermeulen J.: *ibid.*, **A352**, 505 (1981).

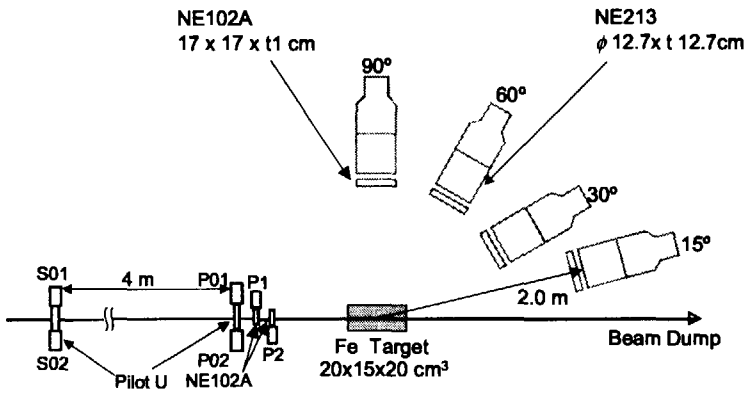

Fig. 1: Illustration of the experimental arrangement.

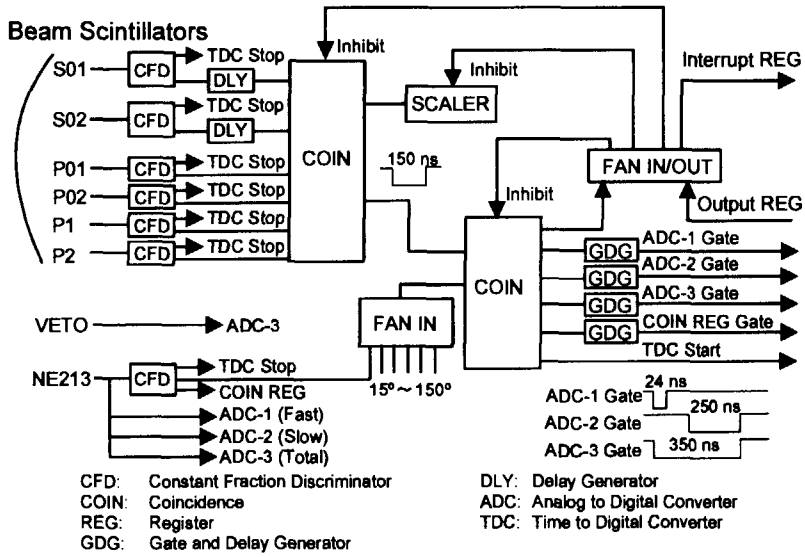

Fig. 2: Diagram of the electronic circuit used in the present experiment.

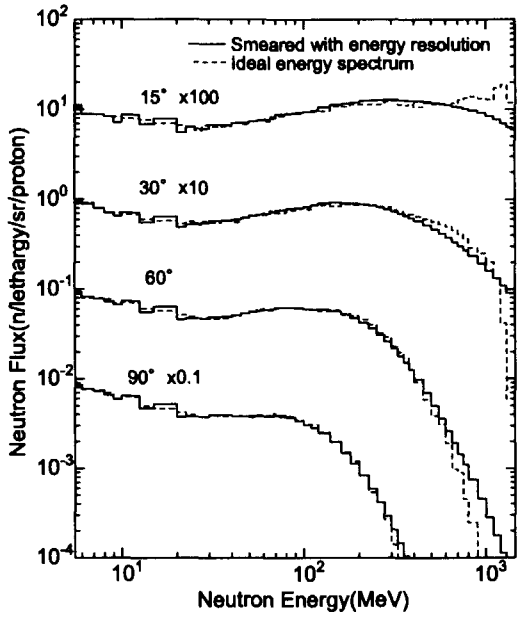

Fig. 3: Comparison of neutron spectrum between with and without energy resolution.

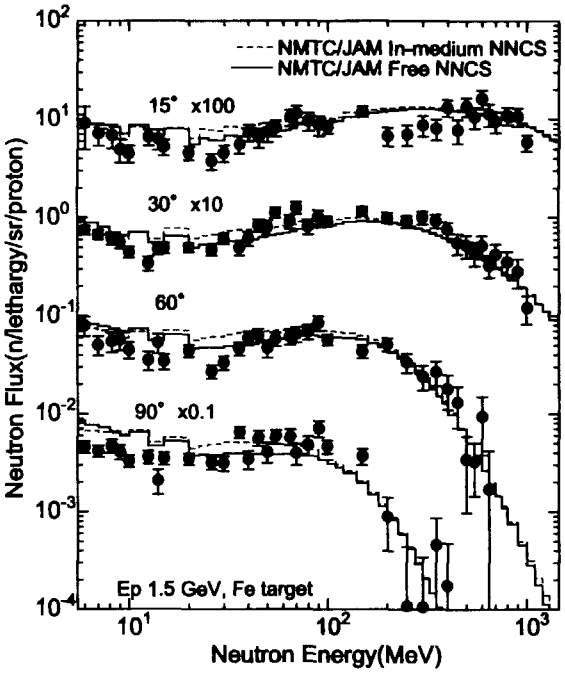

Fig. 4: Comparison of neutron spectra for 1.5-GeV protons between NMTC/JAM and present experiment.

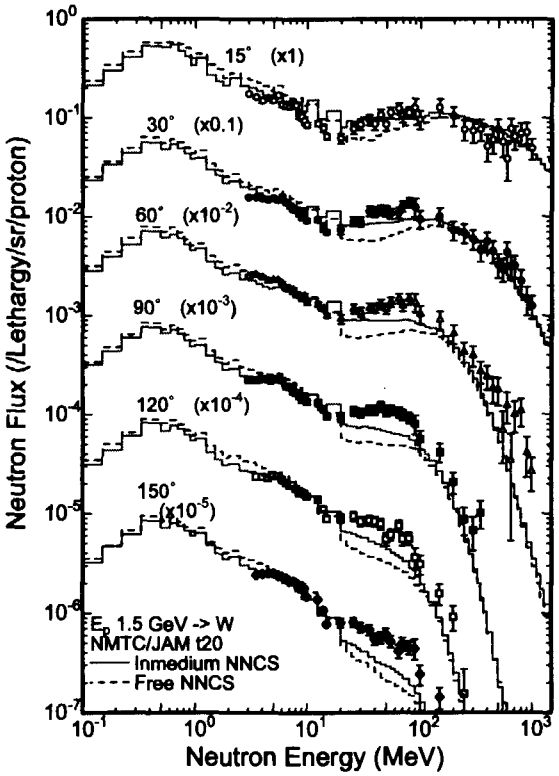

Fig. 5: Comparison of neutron spectra between NMTC/JAM and experiment data for 1.5-GeV protons bombarded with tungsten target.

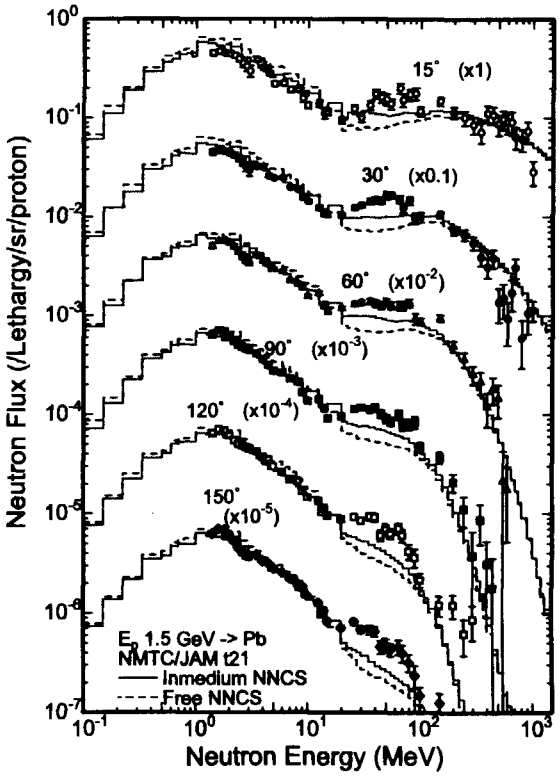

Fig. 6: Comparison of neutron spectra between NMTC/JAM and experiment data for 1.5-GeV protons bombarded with lead target.

JP0150683

3.21

Recoil Properties of Radionuclides Formed in Photospallation Reactions on Complex Nuclei at Intermediate Energies

Hiromitsu Haba[1], Koh Sakamoto[2], Hiroshi Matsumura[2], Yasuji Oura[3], Seiichi Shibata[4], Michiaki Furukawa[5], and Ichiro Fujiwara[6]

[1]Research Group for Nuclear Chemistry of Heavy Elements,
Advanced Science Research center, Japan Atomic Energy Research Institute,
Tokai, Naka-gun, Ibaraki 319-1195, Japan
e-mail: haba@popsvr.tokai.jaeri.go.jp
[2]Department of Chemistry, Faculty of Science, Kanazawa University,
Kanazawa-shi, Ishikawa 920-1192, Japan
[3]Department of Chemistry, Graduate School of Science, Tokyo Metropolitan University,
Hachioji-shi, Tokyo 192-0397, Japan
[4]Research Reactor Institute, Kyoto University, Sennan-gun, Osaka 590-0494, Japan
[5]Faculty of Environmental and Information Sciences, Yokkaichi University,
Yokkaichi-shi, Mie 512-8512, Japan
[6]Department of Economics, Faculty of Economics, Otemon-Gakuin University,
Ibaraki-shi, Osaka 567-8502, Japan

A short review is given on our studies of recoil properties of radionuclides formed in photospallation reactions induced by bremsstrahlung of end-point energies (E_0) from 600 to 1100 MeV, in which the thick-target thick-catcher method was employed. The measurements have been successful on 14, 24, 26, 31, 21 and 20 nuclides from ^{nat}V, ^{nat}Cu, ^{93}Nb, ^{nat}Ag, ^{nat}Ta, and ^{197}Au, respectively. Reflecting the resonance character in a photonuclear reaction, the mean ranges *FW* and *BW* in the forward and backward directions, respectively, are E_0-independent at the studied energies and classified into two groups accounting for the (γ,xn) ($x \geq 1$) and (γ,xnyp) (x, $y \geq 1$) processes. The forward-to-backward ratios (*F*/*B*) are independent of the mass difference (ΔA) between a product (A_p) and a target (A_t) and also of A_t. The kinematic properties of the product nuclei were analyzed by the two-step vector velocity model. The forward velocity v after the first step of photon-reaction is quite different from that of proton-reaction at proton energies of $E_p \leq 3$ GeV, though the difference disappears at higher energies. On the other hand, the mean kinetic energy T of the residual nucleus in the second step is almost equal to that of proton-reaction irrespective of E_p. A comparison with T values calculated by the PICA (Photon-Induced Intranuclear Cascade Analysis) code at $E_0 = 400$ MeV was also performed. It was found that although the code well reproduces the experimental results of ^{nat}V and ^{nat}Cu, the same calculation for heavier targets gives T values lower than the experimental results, indicating some nuclear-structure effect, such as a medium effect notably at $A_t \geq 100$. An average kinetic energy carried off by the emitted particles $\varepsilon_s = T/(\Delta A/A_t)$ of both photon- and proton-reactions seem to increase with an increase of A_t up to around $A_t = 100$, and become almost constant at larger A_t, implying some change in the nuclear structure effect in this heavy target region, as also found in our recent yield measurements of photospallation and photopion reactions. The ε_s values of photon-reaction appear to be slightly lower than those of proton-reactions for ^{nat}Ag, ^{nat}Ta, and ^{197}Au. This difference may indicate the lower excitation energy left after the first step in photon-reactions than in proton-reactions.

1. Introduction

The photonuclear reactions at low and intermediate energies are initiated by three types of resonance processes: giant resonance, quasi-deuteron resonance, and (3,3) resonance. These initial

interactions of photons with nuclei are purely electromagnetic and are quite different from that of hadron-induced reactions, which are initiated by the strong interaction between the projectile and a nucleon in the target nucleus. It seems interesting to pursue whether there exist similarities or dissimilarities between the final steps of these two nuclear reactions.

In our group nuclear recoil experiments using the thick-target thick-catcher method were applied to photonuclear reactions in order to examine the effect due to a difference in the initial interactions between photon-induced reaction and hadron-induced one dynamically [1–3]. The possibility of this technique was first successfully examined with photospallation reactions on ^{nat}Cu at bremsstrahlung end-point energies (E_0) of 250–1000 MeV [1], because the reaction yields were previously well investigated at E_0 = 100–1000 MeV by Shibata *et al.* [4]. The observed recoil properties of the photospallation products from ^{nat}Cu were found to be E_0-independent at $E_0 \geq 600$ MeV and classified into two groups accounting for the (γ,xn) and (γ,$xnyp$) processes. Also, the PICA (Photon-induced Intranuclear Cascade Analysis) code [5, 6] at E_0 = 400 MeV was shown to reproduce well the kinetic energies (T) of the product nuclei, except for the (γ,xn) products. Furthermore an extended work of the recoil technique to the photospallation products from ^{nat}Ag, ^{nat}Ta, and ^{197}Au at the same energy region [2] showed the similar trends as found in ^{nat}Cu, though they were preliminary in terms of the replicated experiments and the detailed data analyses. Recently, the kinematic properties of ^{24}Na from the ^{27}Al(γ,2pn)^{24}Na reaction at E_0 = 60–1100 MeV were analyzed by the two-step vector model [7] and compared with those from the ^{27}Al(p,3pn) reactions [3]. The recoil velocity v after the first step of the photon-reaction was found to be quite different from those of the proton-induced reaction, reflecting the difference in the reaction mechanism at the initial step. On the other hand, the mean kinetic energies T of ^{24}Na in the second step at $E_0 \geq 600$ MeV appeared to be equal to those at 0.18–300 GeV-protons.

More recently we reported a result of an extensive recoil study of the photospallation reactions on ^{nat}V, ^{nat}Cu, ^{93}Nb, ^{nat}Ag, ^{nat}Ta, and ^{197}Au at $E_0 \geq 600$ MeV [8]. We have accumulated the additional data for ^{nat}Cu, ^{nat}Ag, ^{nat}Ta, and ^{197}Au, and added ^{nat}V and ^{93}Nb as new targets since the previous works [1–3]. The kinematic parameters such as v and T obtained from an analysis based on the two-step vector model [7] were then discussed systematically with respect to E_0 and A_t, by referring to the proton results as well as to the PICA calculations at E_0 = 400 MeV. The following is a short review of these studies.

2. Experimental

Irradiations by bremsstrahlung beams with end-point energies of E_0 = 600–1100 MeV were carried out using the 1.3-GeV electron synchrotron of the High Energy Accelerator Research Organization (KEK) at Tanashi. The targets consisted of a stack of 20–50 sets of a high-purity target metal foil of 25 x 25 mm^2 in size. The target thicknesses were 14 mg/cm^2 for ^{nat}V, 22 mg/cm^2 for ^{nat}Cu, 24 mg/cm^2 for ^{93}Nb, 32 mg/cm^2 for ^{nat}Ag, 32 mg/cm^2 for ^{nat}Ta, and 90 mg/cm^2 for ^{197}Au. Each metal foil was sandwiched by one pair of 3.5–7.0 mg/cm^2 thick Mylar foils of the same size, which collected the recoil nuclei in the forward or backward directions with respect to the beam. The photon intensities evaluated from the monitor reaction of ^{27}Al(γ,2pn)^{24}Na were 10^9–10^{10} equivalent quanta per second (eq.q./s). The typical irradiation times were 3 h for ^{nat}V, ^{nat}Cu, and ^{93}Nb, 4 h for ^{nat}Ag and ^{nat}Ta, and 5 h for ^{197}Au. After irradiation, some selected target foils and all of the forward and backward catcher foils from one target pile were collected separately, and assayed for radioactivities nondestructively with high-purity Ge detectors.

3. Results and Discussion

Radioactivities of 14, 24, 26, 31, 21 and 20 nuclides produced from ^{nat}V, ^{nat}Cu, ^{93}Nb, ^{nat}Ag, ^{nat}Ta, and ^{197}Au, respectively, have been identified both in the target and catcher foils [8]. From the fractions of each nuclide measured in the forward and backward catcher foils, expressed as $F = N_F/(N_F + N_B + N_{target})$ and $B = N_B/(N_F + N_B + N_{target})$, N being the number of atoms, respectively, the effective mean ranges, FW and BW, in the targets were obtained by multiplying the target thickness W in units of μg/cm^2. As found previously [1–3], the FW and BW values observed in the present work are

independent of E_0 above 600 MeV. This E_0-independece of *FW* and *BW* is consistent with that of the slope parameter (*P*) in the CDMD formula [4, 9], and indicates that the photons responsible for the production of these nuclides are mostly of energies lower than 600 MeV, and that there is no appreciable change in the reaction mechanism at $E_0 \geq 600$ MeV. Therefore, the following discussion proceeds on the basis of the average quantities at $E_0 \geq 600$ MeV. The *FW* values are higher than the corresponding *BW*, and both increase in parallel with an increase of the mass difference (ΔA) between a product (A_p) and a target (A_t). This increasing trend of *FW* and *BW* with ΔA can be divided into two components: one is a steep increase for the (γ,*x*n) ($x \geq 1$) products mainly produced by the giant resonance absorption; the other is a gentle increase for the (γ,*x*n*y*p) ($x, y \geq 1$) products mainly produced by the quasi-deuteron mechanism and/or the (3,3) resonance absorption. It is interesting to note that the forward-to-backward ratios (*F*/*B*) at $E_0 \geq 600$ MeV are independent of ΔA and also A_t (*F*/*B* = 2–3).

The measured recoil data were used to derive some recoil parameters by means of the vector velocity model embodying the two-step mechanism commonly invoked in high-energy proton reactions. In the present series of work, the two-step vector model developed by Winsberg [7] was employed for this purpose. The analytical details were described in our previous papers [1, 3]. The forward velocity *v* is a good parameter to estimate the momentum transferred to an intermediate nucleus in the first cascade step, and is related to the deposited excitation energy. On the other hand, the average recoil energy *T* imparted to a residual recoiling nucleus is a convenient parameter to investigate the second evaporation step of the reaction.

As an example, the variations of *v* and *T* at $E_0 \geq 600$ MeV are shown as a function of ΔA by large open circles for ^{nat}Cu in Figs. 1a and 1b, respectively. The cascade velocity *v* in the photoreaction increases linearly with an increase of ΔA, indicating that the higher excitation energy is deposited on an intermediate nucleus to form a residual nucleus with a larger ΔA. The kinetic energy *T* also increases almost linearly with an increase of ΔA, as explained by a random-walk theory [10]. Proton results on ^{nat}Cu [11–16] are available at various proton energies (E_p), as indicated in the inset of Fig. 1b. The *v* values at $E_p \leq 3$ GeV (open symbols) are apparently higher than those of the photon-reactions and decrease with an increase of E_p up to 3 GeV. The values at $E_p > 3$ GeV, indicated by closed symbols, are almost the same as those of the photon-reactions. On the other hand, all of the *T* values of the proton-reactions are about the same as those of the photon-reactions, irrespective of E_p.

Based on a comparison with the available proton results for other targets of ^{27}Al, ^{nat}V, ^{93}Nb, ^{nat}Ag, ^{nat}Ta, and ^{197}Au [3, 8], it was found that for typical spallation the *v* values of proton-reactions at $E_p \leq 3$ GeV are higher than those of photon-reactions at $E_0 \geq 600$ MeV, and decrease steeply with an increase of E_p up to around $E_p = 3$ GeV, and become constant at $E_p \geq 3$ GeV. This distinct difference of the *v* values in the two types of nuclear reaction at the lower-energy region may be attributed to the lower momentum transferred in the initial electromagnetic resonance interaction in photon-reactions. The steep decrease of *v* in proton-reactions at $E_p \leq 3$ GeV is due to the increasing nuclear transparency to the incoming proton; the difference disappears at proton energies above 3 GeV, where the momentum transfer in proton-reactions is almost the same as that in photon-reactions. It seems interesting to note that the *v* values for photon-reactions at $E_0 \geq 600$ MeV are almost equal to those for proton-reactions in the limiting region above $E_p = 3$ GeV, though the initial interactions should be quite different from each other. On the other hand, *T* in proton-reactions seems to be independent of E_p in the energy region cited above, and agrees well with those of photon-reactions at $E_0 \geq 600$ MeV. This consistency of the *T* values suggests that the mechanism of the second deexcitation step is very similar in both photon- and proton-reactions, and the memory of the difference in the initial interaction seems not to remain in the second step.

The reproducibility of the kinetic energies *T* of residual nuclei of photospallation by the PICA code [5, 6] at $E_0 = 400$ MeV was examined. The calculated *T* values are indicated by crosses for the nuclides corresponding to the measured ones in Fig. 1b. The calculated *T* values increase with an increase of ΔA in a similar way as the experimental results. The *T* values of the (γ,*x*n) ($x \geq 1$) products are overestimated due to the absence of giant resonance in the PICA code. The PICA

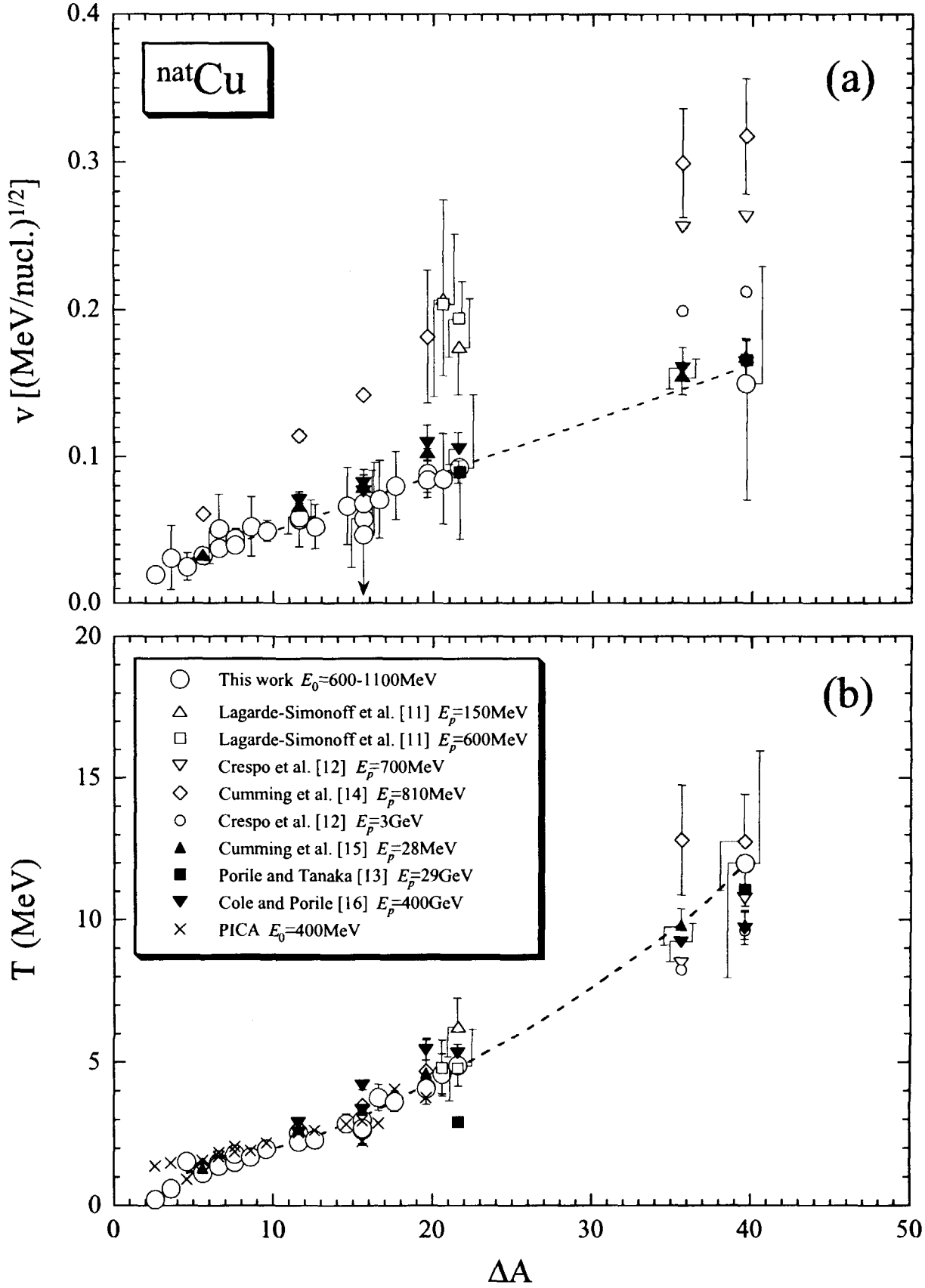

Fig. 1. (a) Forward velocity, v, in the first step and (b) kinetic energy, T, in the second step as a function of ΔA for ^{nat}Cu.

calculation reproduces the experimental results of the (γ,$xnyp$) products well for ^{nat}V and ^{nat}Cu, but the code underestimates the experiments for the heavier targets of ^{93}Nb, ^{nat}Ag, ^{nat}Ta, and ^{197}Au, especially at larger ΔA. This trend of the agreement and the disagreement is consistent with the findings from the systematic yield measurements of photospallation by Sarkar *et al.* [9, 17, 18]. The PICA code can reproduce the spallation yields of the medium-mass targets from ^{nat}V to ^{89}Y at E_0 = 400 MeV, but the code gives the yields higher than the observed ones, and results in asymmetric isotopic yield distributions for targets heavier than A_t = 100. The underestimation of the mean kinetic energies and the overestimation of the reaction yields by the PICA code in the heavy target region may imply that the separation energies of nucleons are higher than those assumed in the code.

Winsberg [10] suggested that $\varepsilon_s = T/(\Delta A/A_t)$, which represents the average energy carried off by an evaporated nucleon, is a good parameter to systematize the second step, and found that ε_s is independent of $\Delta A/A_t$ for typical spallation reactions induced by protons. In the present work, the ε_s values were obtained for the (γ,$xnyp$) products in the limiting region at $E_0 \geq$ 600 MeV, and they were found to be independent of $\Delta A/A_t$, as in proton reactions. The average ε_s values for each target are plotted as a function of A_t by open circles in Fig. 2, together with those of the proton-reactions by closed squares based on our compilation [8]. The ε_s values of both the photon- and proton-reactions seem to increase slightly with an increase of A_t up to around A_t = 100 and become almost constant at heavier targets. This A_t-dependent feature of ε_s has not been reported previously as far as we are aware. The suppression of the increasing trend above A_t = 100 may reflect a decrease of the separation energy per nucleon with an increase of A_t from about 8.2 MeV for ^{nat}Ag to 7.0 MeV for ^{197}Au.

It was reported [4, 9] that there are linear relationships between the neutron-to-proton ratios of the most probable product, $(N/Z)_p$, and those of targets, $(N/Z)_t$, both in the photon- and proton- (and α-) spallation of ^{nat}V–^{197}Au. The slope for the photospallation is steeper than that for proton- (and α-) spallation, and the $(N/Z)_p$ of photospallation is shifted to the more neutron rich side for the targets of $(N/Z)_t > 1.2$ with respect to that of proton- (and α-) spallation. This suggests that the average excitation energy of cascade residues in photospallation is lower than in hadron-spallation. The ε_s values of the photon-reactions obtained in the present work are almost equal to those of the proton-reactions for ^{27}Al of $(N/Z)_t$ = 1.08 and ^{nat}Cu of $(N/Z)_t$ = 1.19, but systematically lower for the targets of $(N/Z)_t > 1.2$, such as ^{nat}Ag of $(N/Z)_t$ = 1.30, ^{nat}Ta of $(N/Z)_t$ = 1.48, and ^{197}Au of $(N/Z)_t$ = 1.49. This variation of ε_s shown in Fig. 2 seems to be consistent with the above-mentioned findings of A_t-dependent features of T and also of the photospallation [9] and photopion reaction [19] yields, though fairly large errors are accompanied with the ε_s values.

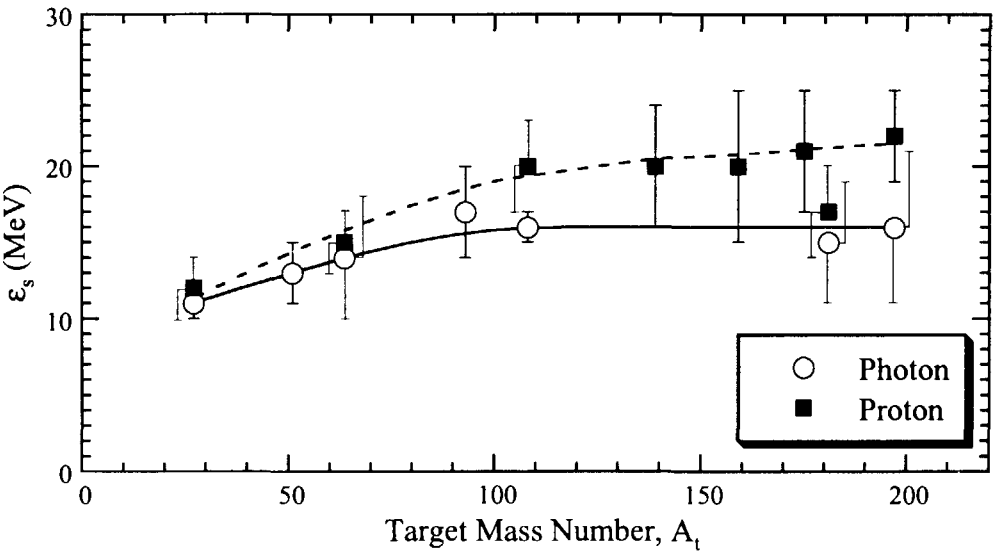

Fig. 2. Parameter ε_s as a function of target mass A_t for photon-reaction (open circles connected by a solid line) and proton-reaction (closed squares connected by a dashed line).

Acknowledgement

The authors would like to express their gratitude to Drs. H. Okuno and K. Masumoto, and the ES crew members of the High Energy Accelerator Research Organization at Tanashi, for their invaluable cooperations in the course of experiments. This work was supported in part by the Grant-in-Aid for Scientific Research (07304077) of the Ministry of Education, Science and Culture of Japan.

References

[1] Haba, H., Matsumura, H., Miyamoto, Y., Sakamoto, K., Oura, Y., Shibata, S., Furukawa, M., and Fujiwara, I.: J. Radioanal. Nucl. Chem. **239**, 133 (1999).
[2] Fujiwara, I., Haba, H., Matsumura, H., Miyamoto, Y., Sakamoto, K., Oura, Y., Shibata, S., and Furukawa, M.: Czech. J. Phys. **49**, 831 (1999).
[3] Haba, H., Matsumura, H., Sakamoto, K., Oura, Y., Shibata, S., Furukawa, M., and Fujiwara, I.: Radiochim. Acta **85**, 1 (1999).
[4] Shibata, S., Imamura, M., Miyachi, T., Mutou, M., Sakamoto, K., Hamajima, Y., Soto, M., Kubota, Y., Yoshida, M., and Fujiwara, I.: Phys. Rev. C **35**, 254 (1987).
[5] Gabriel, T. A. and Alsmiller, Jr., R. G.: Phys. Rev. **182**, 1035 (1969).
[6] Gabriel, T. A., Guthrie, M. P., and Hermann, O. W.: Oak Ridge National Laboratory Report No. ORNL-4687 (1971).
[7] Winsberg, L.: Nucl. Instr. Meth. **150**, 465 (1978).
[8] Haba, H., Matsumura, H., Sakamoto, K., Oura, Y., Shibata, S., Furukawa, M., and Fujiwara, I.: Radiochim. Acta **88**, 375 (2000).
[9] Sarkar, S. R., Kubota, Y., Fukasawa, T., Kawaguchi, K., Sakamoto, K., Shibata, S. and Fujiwara, I.: Radiochim. Acta **55**, 139 (1991).
[10] Winsberg, L.: Phys. Rev. C **22**, 2116 (1980) and C **22**, 2123 (1980).
[11] Lagarde-Simonoff, M., Regnier, S., Sauvageon, H., and Simonoff, G. N.: Nucl. Phys. **A260**, 369 (1976).
[12] Crespo, V. P., Alexander, J. M., and Hyde, E. K.: Phys. Rev. **131**, 1765 (1963).
[13] Porile, N. T. and Tanaka, S.: Phys. Rev. **135**, B122 (1964).
[14] Cumming, J. C., Haustein, P. E., and Hseuh, H. -C.: Phys. Rev. C **18**, 1372 (1978).
[15] Cumming, J. B., Haustein, P. E., and Hseuh, H. -C.: Phys. Rev. C **24**, 2162 (1981).
[16] Cole, G. D. and Porile, N. T.: Phys. Rev. C **25**, 244 (1982).
[17] Sarkar, S. R., Soto, M., Kubota, Y., Yoshida, M., Fukasawa, T., Matsumoto, K., Kawaguchi, K., Sakamoto, K., Shibata, S., Furukawa, M., and Fujiwara, I.: Radiochim. Acta **55**, 113 (1991).
[18] Sarkar, S. R., Oura, Y., Kawaguchi, K., Yazawa, A., Sakamoto, K., Shibata, S. and Fujiwara, I.: Radiochim. Acta **62**, 7 (1993).
[19] Sakamoto, K., Sarkar, S. R., Oura, Y., Haba, H., Matsumura, H., Miyamoto, Y., Shibata, S., Furukawa, M., and Fujiwara, I.: Phys. Rev. C **59**, 1497 (1999).

JP0150684

3.22

Analysis of activation yields by INC/GEM

Shiori FURIHATA[1] and Hiroshi NAKASHIMA[2]

[1] *Mitsubishi Research Institute, INC., 2-3-6 Otemachi, Chiyoda-ku, Tokyo 100-8141*
e-mail: furihata@mri.co.jp
[2] *Japan Atomic Energy Research Institute, Tokai-mura, Naka-gun, Ibaraki-ken, 319-1195*

Excitation functions of the nuclides produced from the reaction on nitrogen and oxygen target irradiated by nucleons are analyzed using INC/GEM. It is shown that INC/GEM reproduces most of the cross sections within a factor of two to three.

1 Introduction

It is very important issue to estimate activation yields in water and air for radiological safety in the shielding design of a high intensity proton accelerator facility. In order to investigate scenarios of drainage of activated cooling water and of ventilation of activated air, it is required to calculate precise activation cross sections of oxygen and nitrogen.

The combination of the Bertini intranuclear cascade model and the generalized evaporation model has been succeeded to predict the cross sections of light particle produced from proton induced on O to Nb target reactions [1]. In this study, we apply this calculation procedure to nucleon induced light target reactions, and investigate its prediction power of nuclide productions from the reactions on light targets. Excitation functions of nuclides produced from the reactions are calculated using the combination of the Bertini intranuclear cascade model (INC) implemented in LAHET [2] and the GEM code [3] which is based on the generalized evaporation model proposed by Furihata [1] (We call this calculation procedure "INC/GEM"). MASS A_i, charge Z_i, excitation energy E, recoil energy, and the direction of motion are extracted from the INC calculation done by LAHET. Then GEM simulates the rest of a nuclear reaction, i.e, de-excitation of an excited nucleus, which is mostly described by the Fermi break-up model in LAHET. The results are compared with those estimated by LAHET as well as experimental data.

2 Generalized Evaporation Model

The generalized evaporation model proposed by Furihata [1] is based on the Weisskopf-Ewing model [4]. According to the model, the total emission width Γ_j of a particle j from the nucleus i with excitation energy E is expressed as

$$\Gamma_j = \frac{g_j}{\rho_i(E)} \int_V^{E-Q} \epsilon \sigma_{inv}(\epsilon) \rho_d(E - Q - \epsilon) d\epsilon, \tag{1}$$

where Q is the Q-value, V is the Coulomb barrier, and $g_j = (2S_j + 1)m_j/\pi^2\hbar^2$ with the spin S_j and the mass m_j of the emitted particle j. The Q-value is calculated by using the Audi-Wapstra mass table [5]. The cross section for an inverse reaction is expressed in the general form as $\sigma_{inv}(\epsilon) = \sigma_g \alpha(1 + \beta/\epsilon)$, where σ_g is the geometric cross section, and $\beta = -V$ for charged particles. We use the parameters in σ_{inv} (i.e. α, β and parameters for V) determined

by Dostrovsky *et al.* [6] for n, p, d, t, ^{3}He, and α emissions. For other ejectiles, the parameters determined by Matuse *et al* [7] are used. Based on the Fermi-gas model, the level density function ρ is expressed as [8]

$$\rho(E) = \begin{cases} \dfrac{\pi}{12}\dfrac{e^{2\sqrt{a(E-\delta)}}}{a^{1/4}(E-\delta)^{5/4}} & \text{for} \quad E \geq E_x \\ \dfrac{1}{T}e^{(E-E_0)/T} & \text{for} \quad E < E_x \end{cases}, \tag{2}$$

where a is the level density parameter, δ is the pairing energy, and E_x is determined by Gilbert and Cameron [8] as $E_x = U_x + \delta$ where $U_x = 150/A_d + 2.5$ and A_d is the mass of a daughter nucleus. Nuclear temperature T is also given as $1/T = \sqrt{a/U_x} - 1.5/U_x$, and E_0 is defined as $E_0 = E_x - T(\log T - 0.25\log a - 1.25\log U_x + 2\sqrt{aU_x})$. In the GEM code, the Gilbert-Cameron-Cook-Ignatyuk (GCCI) level density parameter a [2], and the pairing energy δ tabulated by Cook [9], Gilbert and Cameron [8] are used.

By substituting Eq. (2) into Eq. (1), the following expression can be obtained.

$$\Gamma_j = \frac{\pi g_j \sigma_g \alpha}{12\rho_i(E)} \times \begin{cases} \{I_1(t,t) + (\beta+V)I_0(t)\} & \text{for } E-Q-V < E_x, \\ [I_1(t,t_x) + I_3(s,s_x)e^s + (\beta+V) & \{I_0(t_x) + I_2(s,s_x)e^s\}] \\ & \text{for } E-Q-V \geq E_x. \end{cases} \tag{3}$$

$I_0(t)$, $I_1(t,t_x)$, $I_2(s,s_x)$, and $I_3(s,s_x)$ are expressed as:

$$\begin{aligned} I_0(t) &= e^{-E_0/T}(e^t - 1), \\ I_1(t,t_x) &= e^{-E_0/T}T\{(t-t_x+1)e^{t_x} - t - 1)\}, \\ I_2(s,s_x) &= 2\sqrt{2}\left\{s^{-3/2} + 1.5s^{-5/2} + 3.75s^{-7/2} - (s_x^{-3/2} + 1.5s_x^{-5/2} + 3.75s_x^{-7/2})e^{s_x - s}\right\}, \\ I_3(s,s_x) &= (\sqrt{2}a)^{-1}\left[2s^{-1/2} + 4s^{-3/2} + 13.5s^{-5/2} + 60.0s^{-7/2} + 325.125s^{-9/2}\right. \\ &- \{\,(s^2 - s_x^2\,)s_x^{-3/2} + (1.5s^2 + 0.5s_x^2)s_x^{-5/2} + (3.75s^2 + 0.25s_x^2)s_x^{-7/2} + (12.875s^2 \\ &+ 0.625\ s_x^2\,)s_x^{-9/2} + (59.0625s^2 + 0.9375s_x^2)s_x^{-11/2} + (324.8s^2 + 3.28s_x^2)s_x^{-13/2}\Big\}\left. e^{s_x - s}\right], \end{aligned}$$

where $t = (E-Q-V)/T$, $t_x = E_x/T$, $s = 2\sqrt{a(E-Q-V-\delta)}$, and $s_x = 2\sqrt{a(E_x-\delta)}$.

Beside nucleons and helium nuclei, the nuclides up to ^{28}Mg, not only in their ground states but also in their excited states, are taken into account in GEM. The excited state is assumed to survive if its lifetime $T_{1/2}$ [sec] is longer than a decay time, i.e., $T_{1/2}/\ln 2 > \hbar/\Gamma_j^*$, where Γ_j^* is the emission width of the resonance calculated in the same manner as for ground state particle emission. The total emission width of an ejectile j is summed over its ground state and all its excited states which satisfy the above condition.

In the GEM code, ejectile j is selected according to the probability distribution calculated as $p_j = \Gamma_j / \sum_j \Gamma_j$, where Γ_j is given by Eqs. (3). The total kinetic energy ϵ of the emitted particle j and the daughter nucleus is chosen according to the probability distribution given by Eq. (1). The angular distribution of the motion is randomly selected from an isotropic distribution in the center-of-mass system.

3 Results

We calculated the excitation functions of nuclides produced from bombardment of nitrogen and oxygen irradiated by nucleons. The excitation functions are shown in Fig. 1 $\sim$ Fig. 6. All the

experimental data in the figures are extracted from and refs. [10, 11] and the EXFOR database maintained by National Nuclear Data Center [12]. Both the results of INC/GEM and LAHET agree with most of experimental data within a factor of 2 to 3.

Figure 1 shows the excitation functions of tritium productions from the reactions on N and O target irradiated by protons. The experimental data and the INC/GEM results are in good agreement above 1 GeV, while the LAHET results agree with the measurements better than INC/GEM below 1GeV.

The excitation functions of ^{14}N(p,X)^{11}C and ^{16}O(p,X)^{13}N reactions are shown in Fig. 2. The threshold reactions of these nuclide production are (p,α) reaction. The threshold energies estimated by INC/GEM are slightly higher than those by LAHET. Neither INC/GEM nor LAHET reproduces the complicated shape of resonances shown by the experimental data below a few tens of MeV.

Figure 3 shows the cross sections of beryllium productions. INC/GEM reproduces these excitation functions successfully, except for the threshold energy of ^{16}O(p,X)^{7}Be reaction. As shown in Fig. 2, INC/GEM overestimates threshold energy of α particle emissions The overestimate is also observed in the threshold energy of ^{16}O(p, 2α)^{7}Be reaction.

Figure 4 shows the excitation functions of (n,2n) reactions. The estimates calculated using INC/GEM are larger than those using LAHET, particularly at low incident energy.

Figure 5 shows the excitation functions of (p,np) reactions. Both INC/GEM and LAHET produce almost the same results for O target, whereas for N target, the results of INC/GEM is larger than those of LAHET by a factor of two.

The excitation function of (p,n) and (n,p) reactions are shown in Fig. 6. Above 10 MeV, INC/GEM produces more cross sections of (p,n) than LAHET. while LAHET produces more for (n,p) reactions than INC/GEM.

4 Conclusion

We analyze the activation yields from the reactions on light targets by INC/GEM. The combination of INC and GEM reproduces most of the excitation functions within a factor of 2 to 3, as well as LAHET. It has been said that the implementation of the Fermi break-up model is necessary to accurately describe de-excitation process of a light excited nucleus. The results show that the generalized evaporation model has comparable prediction power to the Fermi break-up model.

INC/GEM overestimates the threshold energy of α emission reactions, however. It also underestimates proton emissions as shown in the figure of (n,p) reaction. The reevaluation of the parameters of the Coulomb potential V and the cross sections for inverse reaction (i.e., α and β) used in GEM might improve the suppression of charged particle emission.

Acknowledgements

The authors would appreciate to Dr. R. E. Prael for the LAHET code.

References

[1] S. Furihata, Nucl. Inst. Meth. in Phys. Res. B **171** (2000) 251–258.

[2] R. E. Prael and H. Lichtenstein, LA-UR-89-3014, "User Guide to LCS: The LAHET Code System" (1989).

[3] S. Furihata, *"The GEM code - The Generalized Evaporation Model and the fission model"*, Proceedings of International Conference on Advanced Monte Carlo for Radiation Physics, Particle Transport Simulation and Application, Lisbon, Portugal (2000),to be published by Springer-Verlag.

[4] V. F. Weisskopf and P. H. Ewing, Phys. Rev. **57** (1940) 472.

[5] G. Audi and A. H. Wapstra, Nucl. Phys. A **595** (1995) 409–480.

[6] I. Dostrovsky, Z. Fraenkel, and G. Friedlander, Phys. Rev. **116** (1959) 683–702.

[7] T. Matsuse, A. Arima, and S. M. Lee, Phys. Rev. C **26** (1982) 2338–2341.

[8] A. Gilbert and A. G. W. Cameron, Can. J. Phys. **43** (1965) 1446–1496.

[9] J. L. Cook, H. Ferguson, and A. R. DEL. Musgrove, Aust. J. Phys. **20** (1967) 477.

[10] H. Schopper (ed.), "LANDOLT-BÖRNSTEIN: Numerical Data and Functional Relationship in Science and Technology, Group I: Production of Radionuclides at Intermediate Energies, subvolme a, b, c, d : Interactions of Protons with Nuclei",Springer-Verlag, Berlin Heidelberg (1994).

[11] R. Michel and P. Nagel, NSC/DOC(97)-1, "International Codes and Model Intercomparison for Intermediate Energy Activation Yields" (1997).

[12] The National Nuclear Data Center On-Line Data Service, http://www.nndc.bnl.gov/.

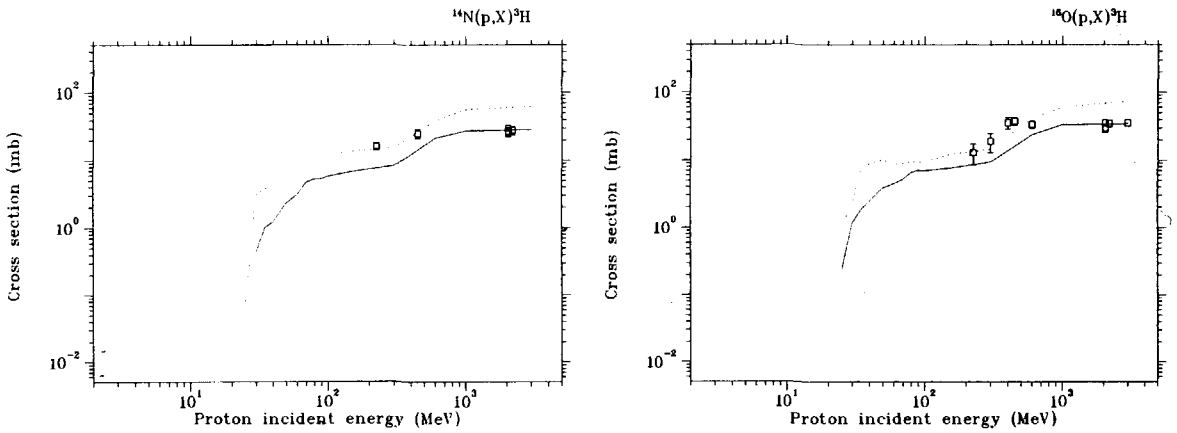

Figure 1: The excitation functions of tritium productions. Left figure shows the reaction on N target, and right figure shows the one on O target. The solid lines show the estimates calculated using INC/GEM, the dotted lines represent the LAHET results, and open squares show experimental data.

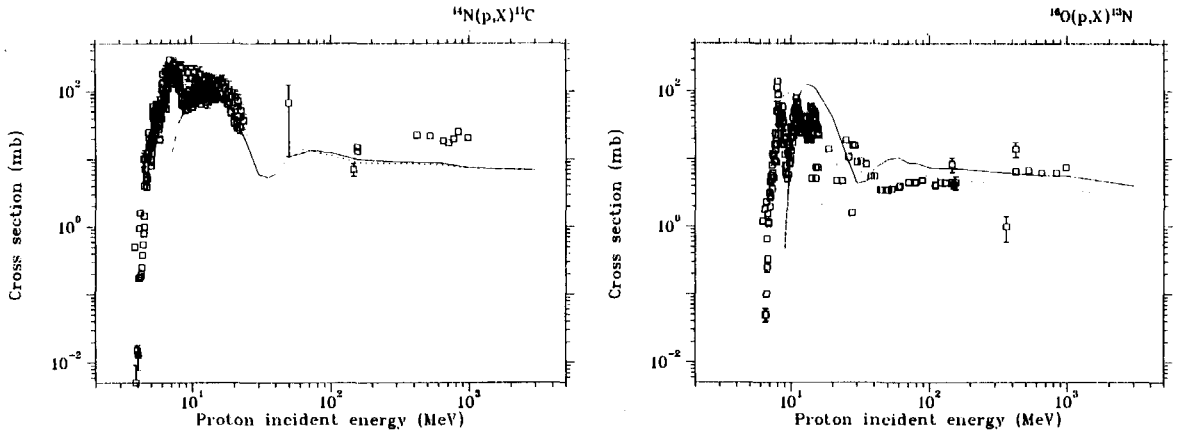

Figure 2: The excitation functions of ^{14}N(p,X)^{11}C (left) and ^{16}O(p,X)^{13}N reaction (right). The threshold reactions of these nuclide production are (p,α) reaction. The notations are the same as in Fig. 1.

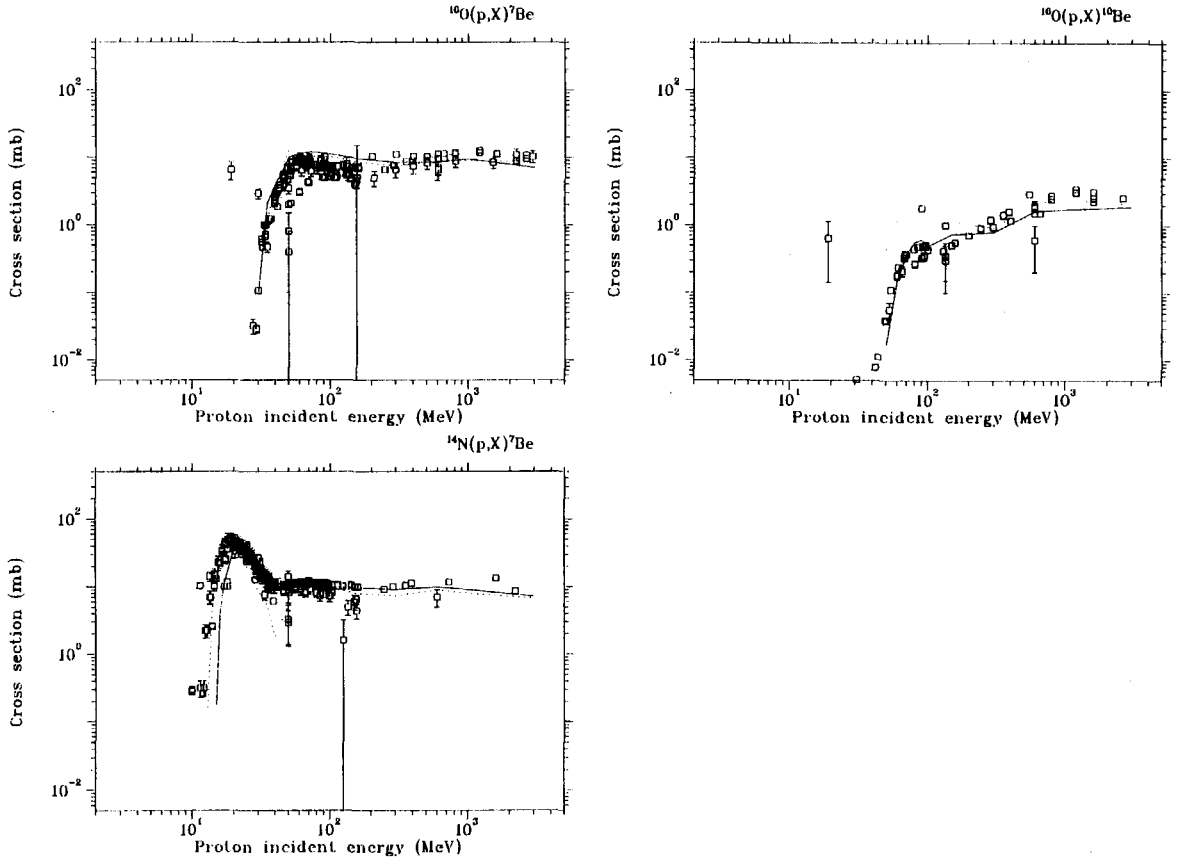

Figure 3: The excitation functions of beryllium productions. Upper left figure shows ^{7}Be produced from O target, upper right one shows ^{10}Be productions, and lower left one shows ^{7}Be productions from N target. The notations are the same as in Fig. 1.

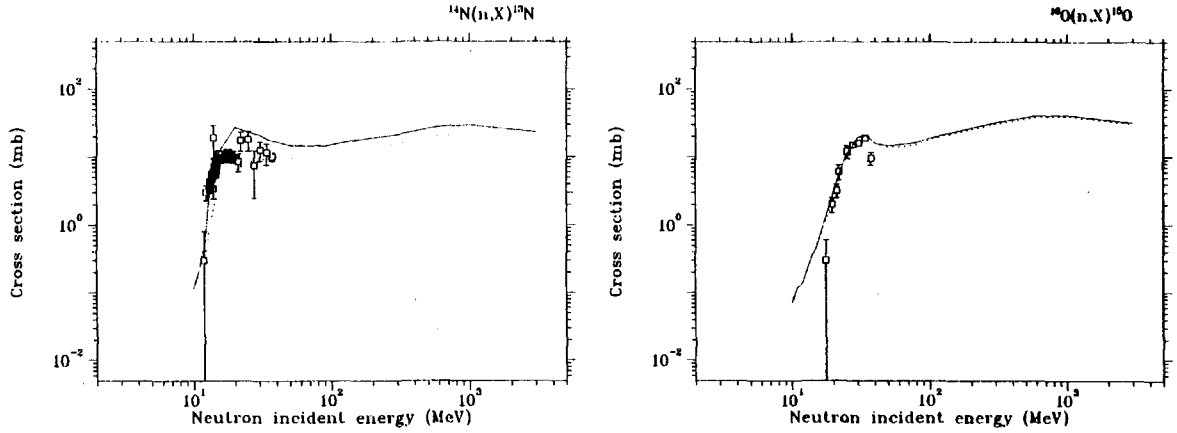

Figure 4: The excitation functions of (n,2n) reaction. Left figure shows the reaction on N target, and right figure shows the one on O target. The notations are the same as in Fig. 1.

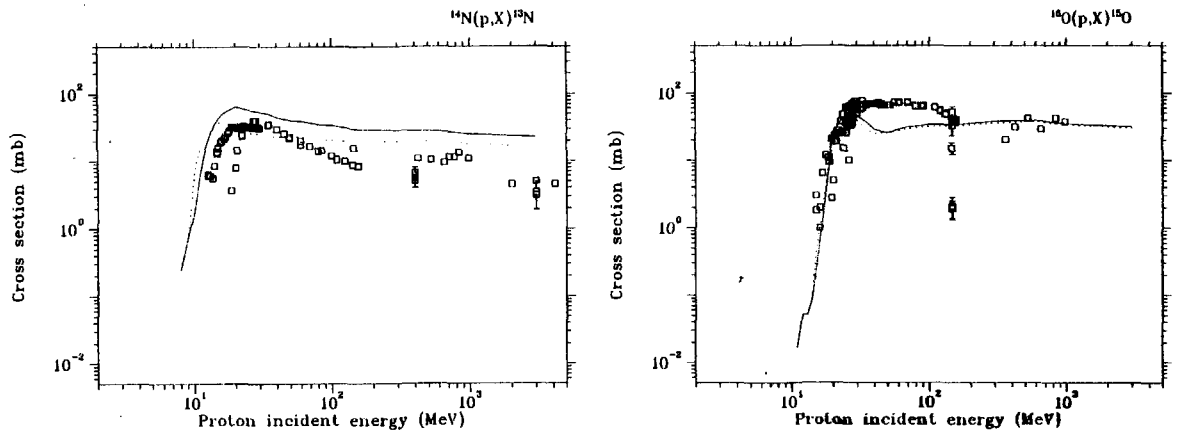

Figure 5: The excitation functions of (p,np) reaction. Left figure shows the reaction on N target, and right figure shows the one on O target. The notations are the same as in Fig. 1.

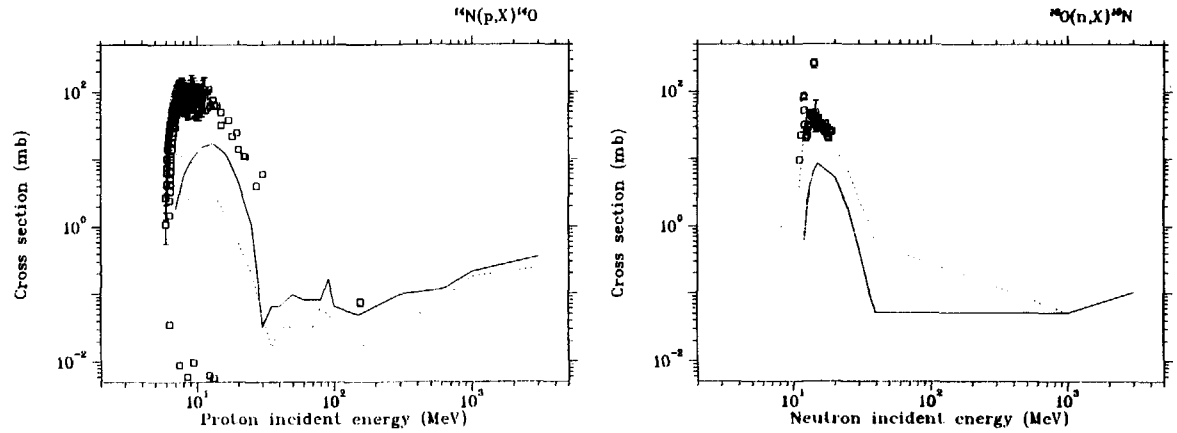

Figure 6: The excitation functions of (p,n) and (n,p) reaction. Left figure shows (p,n) reaction, and right one shows (n,p) reaction. The notations are the same as in Fig. 1.

JP0150685

3.23

Production of Charged Particles by Proton-induced Reaction at Intermediate Energy

Fuminobu SAIHO[1,†], Junji TANAKA[1], Bin CAO[1], Shozo AOKI[1]
Yusuke UOZUMI[1], Genichiro WAKABAYASHI[1], Masaru MATOBA[1]
Takashi MAKI[2], Masahiro NAKANO[2], Norihiko KOORI[3]
[1] *Department of Applied Quantum Physics and Nuclear Engineering, Kyushu University Hakozaki, Higashi-ku, Fukuoka 812-8185*
[2] *University of Occupational and Environmental Health, Kitakyushu 807-8555*
[3] *Faculty of integrated Arts and Sciences, University of Tokushima, Tokushima 770-8502*
e-mail: †saiho@nucl.kyushu-u.ac.jp

We measured the differential cross section of (p,p'x) and (p,dx) reactions by 300- and 392-MeV proton-induced reactions. The measurements were made for targets, ^{12}C, ^{27}Al, ^{93}Nb and ^{197}Au. We compared the mesurements with the Quantum Molecular Dynamics (QMD) model calculations. It is shown that QMD model calculations underestimate the differential cross section of (p,dx).

1.Introduntion

Nuclear data in the intermediate energy are required from various fields of basic physics and nuclear technologies. Differential cross sections and Double-differential cross sections are needed for calculations of particle transport in matter. There are currently some available proton data of proton-induced reactions, but few systematic measurements above 200 MeV of incident energy. There are few deuteron data in this range. The deuteron data are details important to comprehend production of fragment, since deuteron are coupled proton and neutron with small binding energy. In this energy range, the characteristics of highly excited nucleus and the behavior of Δ inside the nucleus will be investigated through systematic measurements.

The purpose of this work is to measure differential cross sections of protons and deuterons in the incident proton energy at 300 MeV and 392 MeV, and to compare the measurements with the Quantum Molecular Dynamics (QMD) model calculations.

2.Experimental and Data Analysis

The beam experiment was performed at the Research Center for Nuclear Physics (RCNP), Osaka University. A sketch of the experimental setup is shown in Figure 1. Protons accelerated up to 300 MeV and 392 MeV by the ring cyclotron were bombarded onto targets set at the center of a vacuum chamber. The measurements were made for targets, ^{12}C, ^{27}Al, ^{93}Nb and ^{197}Au. We measured energy spectra from 19.7° to 104.1° in laboratory frame.

The stacked GSO(Ce) scintillator spectrometer was used in the measurements. Stopping detectors, such as scintillator detectors are useful for measurements of proton spectra over a wide energy range. Especially stacked spectrometers are suitable for these measurements in the intermediate energy region. The cerium doped gadolinium orthosilicate, $Gd_2SiO_5(Ce)$ - GSO(Ce), has several advantages such as

a relatively high density and a high radiation hardness, and is suitable for experiments in this energy region. A stacked GSO(Ce) spectrometer was designed to measure continuum spectra from proton-induced reactions at incident energy of 200 - 400 MeV. It consisted of 10 mm, 2 mm (or 1 mm) and 5 mm thick plastic scintillators and two cubic and one cylindric GSO(Ce) scintillators. Coincidence among the signals from the plastic plates produced trigger signals for analog-to-digital converters. The 10 mm thick plastic scintillator had an aperture of 15 mm diameter and played as an active slit to determine the solid angle of the spectrometer. The size of GSO(Ce) scintillators used were $43 \times 43 \times 43$ mm^3 for cube and 62 mm in diameter and 120 mm long for cylinder.

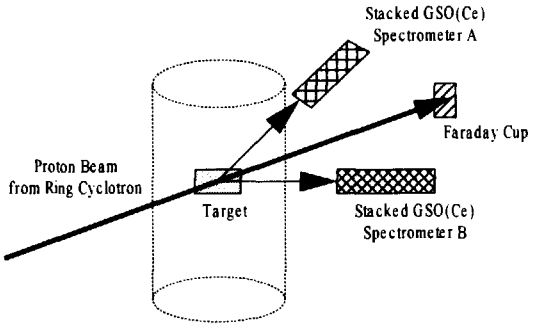

Figure 1: Layout of ES course

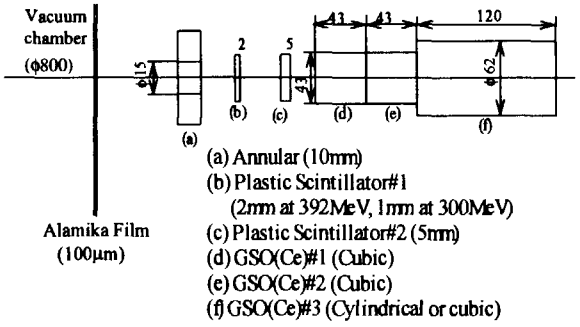

Figure 2: Stacked spectrometer with GSO(Ce) and plastic scintillators

The ΔE-E techniques were used in order to separate deuterons from protons. Protons and deuterons concentrate on a well-defined locus like Figure 3. To obtain total number of several charged particles, first we divided them into several areas. Then the events corresponding to protons and deuterons were counted up respectively.

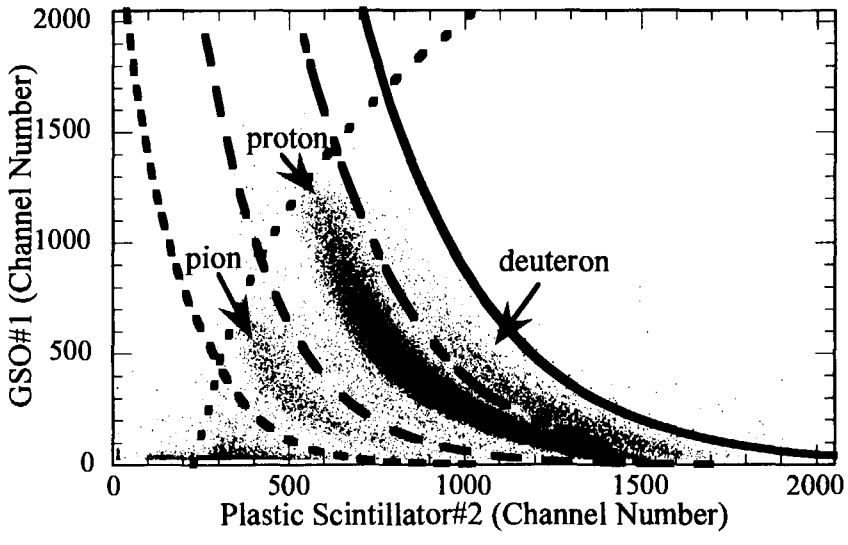

Figure 3: Particle-identification spectra of ΔE vs E

3.Results and Discussion

A. Target mass dependence

Differential cross sections obtained from the experiment via 300 MeV proton-induced reactions are shown in Figure 4 and Figure 5 for p and d, respectively. The abscissa shows the scattering angle. Every dot shows the results by measurement. First, we analyzed the the data of Gold. We assumed the angular distributions are well described by liner relations. Next, other nuclei were analysed by using the same relation but the strength is proportional to $A^{2/3}$ with respect to Gold data. The lines in Figure 4 and Figure 5 show the results of analysis.

In the same way, the results obtained via 392 MeV proton-induced reactions are shown in Figure 6 and Figure 7. Both differential cross sections of p and d are found to depend on $A^{2/3}$ approximately. Differential cross section for ^{27}Al, however, show different behavior from other targets.

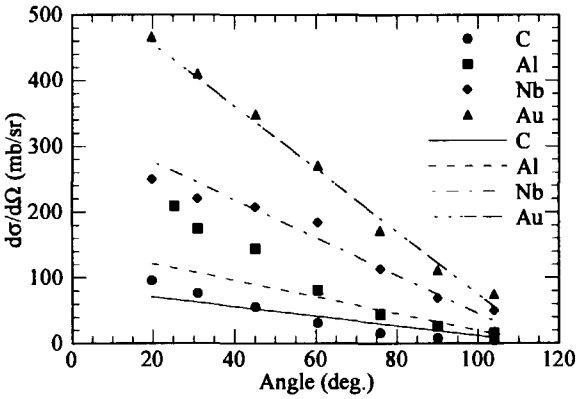

Figure 4: Angular distributions of proton production from 300 MeV proton-induced reactions

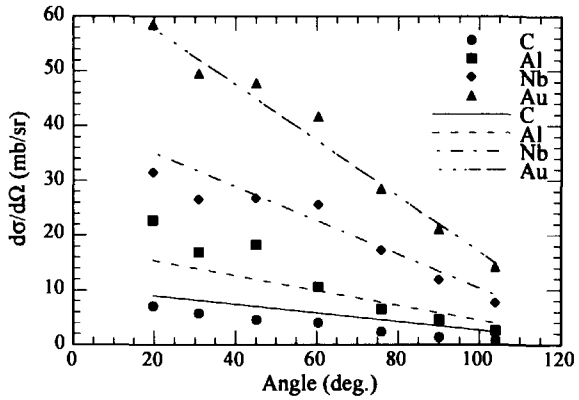

Figure 5: Angular distributions of deuteron production from 300 MeV proton-induced reactions

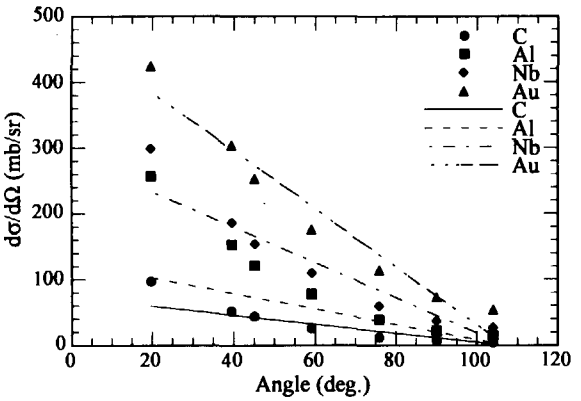

Figure 6: Angular distributions of proton production from 392 MeV proton-induced reactions

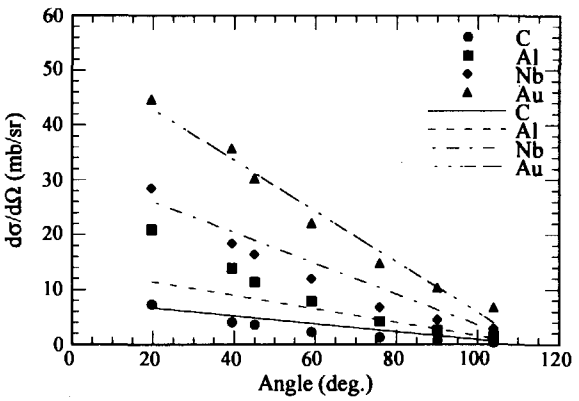

Figure 7: Angular distributions of deuteron production from 392 MeV proton-induced reactions

B. Comparison between mesurements and QMD model calculations

We compared the measurements with the QMD model calculation. Differential cross sections obtained from the QMD model calculation via 300 MeV proton- induced reactions are shown in Figure 8 and Figure 9 for p and d,respectively. Every dot shows the results by measurement. The lines in Figure8 and Figure9 show the results of the QMD model calculation.

In the same way, the results obtained via 392 MeV proton-induced reactions are shown in Figure10 and Figure11. Differential cross sections of protons obtained from QMD model calculation agree with the measurements. (Figure 8, Figire 10) But, differential cross sections of deuterons obtained from QMD model calculation are much smaller than the measurements. (Figure 9, Figure 11)

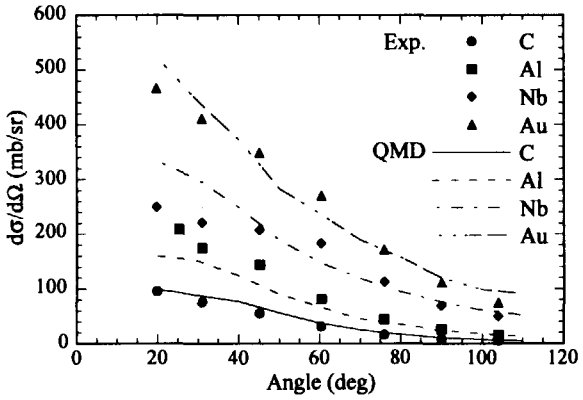

Figure 8: Comparison between the proton mesurements and QMD model calculations at incident proton energy of 300 MeV

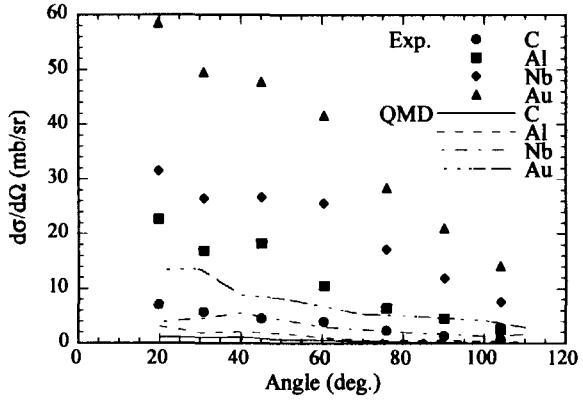

Figure 9: Comparison between the deuteron mesurements and QMD model calculations at incident proton energy of 300 MeV

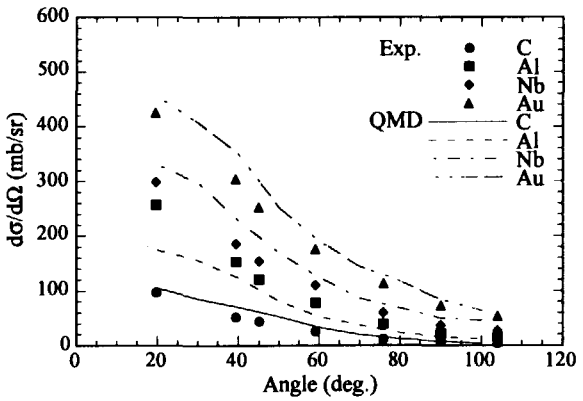

Figure 10: Comparison between the proton mesurements and QMD model calculations at incident proton energy of 392 MeV

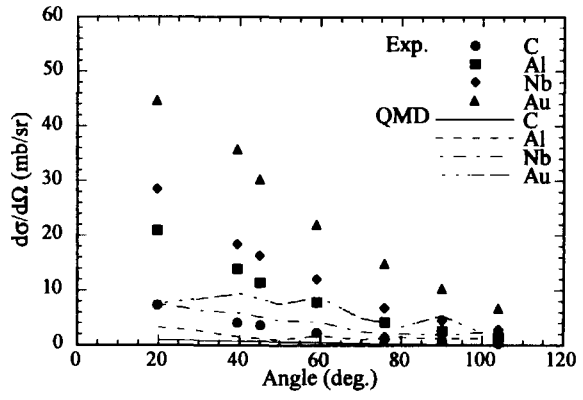

Figure 11: Comparison between the deuteron mesurements and QMD model calculations at incident proton energy of 392 MeV

4.Conclusion

Differential cross section of proton and deuteron productions were measured for proton-inducet reactions at 300- and 392-MeV. It is found that the production of p and d depend on $A^{2/3}$ approximately. A different behavior from other target nuclei are shown in ^{27}Al.

Differential cross sections of proton production reactions are consistent between QMD model calculations and the measurements. But, large discrepancies are seen in deuteron production reactions.

Reference

[1] K. Anami, et al. : Nucl, Inst. Meth. A404, 327 (1998).
[2] H.Yosida, et al. : Nucl. Inst. Meth. A411, 46 (1998).
[3] R. E. Segel, et al. : Phys. Rev. C26, 2424 (1982).
[4] A. A. Cowley, et al. : Phys. Rev. C45, 1745 (1992).
[5] Niita, K, et al. : Phys. Rev. C52, 2620 (1995).

JP0150686

3.24

Evaluation of Neutron and Proton Nuclear Data of ^{28}Si for Energies up to 200 MeV

Sun Weili[1], Y. Watanabe[2], E. Sh. Sukhovitskiĭ [3], O. Iwamoto[4], and S. Chiba[4]
[1]*Department of Applied Quantum Physics and Nuclear Engineering, Kyushu University, Fukuoka 812-8581, Japan*
[2]*Department of Advanced Energy Engineering Science, Kyushu University, Kasuga, Fukuoka 816-8580, Japan*
[3]*Radiation Physics and Chemistry Problems Institute, 220109, Minsk-Sosny, Belarus*
[4]*Japan Atomic Energy Research Institute, Tokai-mura, Naka-gun,Ibaraki-ken,319-1195, Japan*
e-mail: sun@aees.kyushu-u.ac.jp

The neutron and proton nuclear data of ^{28}Si up to 200 MeV are evaluated for various nuclear engineering applications. The soft rotator model and the coupled-channel method are used to perform a consistent analysis of the collective band structure of ^{28}Si and nucleon scattering from ^{28}Si. The GNASH nuclear model code is used for compound and preequlibrium particle emission calculations, where the emission of ^{3}He is also included. Comparisons show overall good agreement with various experimental data.

1. Introduction

Recently, neutron and proton nuclear data in the intermediate energy range are required in various fields related to advanced sciences and technologies, such as accelerator-driven transmutation of nuclear waste, cancer therapy and soft-error evaluation in computer memories. From the viewpoint of applications, nucleon-induced nuclear data of silicon are of importance since silicon is a major component of shielding materials and memory chips in computers. To meet these needs, the neutron and proton nuclear data of ^{28}Si are evaluated up to 200 MeV, based on the measured data as well as nuclear model predictions.

Since ^{28}Si is considered to be as a deformed nucleus with a rotational structure, the coupled-channel (CC) method with a coupling based on the wave functions of soft rotator model, developed by Minsk group[1], is used to perform a consistent analysis of the collective band structure and nucleon scattering. A very interesting characteristic of this model is that the nuclear Hamiltonian parameters for nuclear wave functions are adjusted first to reproduce the experimentally observed low-lying collective structure, and then these functions will be used to construct the coupling scheme for CC calculations. With the applications to a light nucleus, ^{12}C [2], an intermediate heavy nucleus ^{58}Ni [3], and heavy (actinide) nuclei[4], this model shows its success and high accuracy in describing nuclear structure, nucleon scattering and spectroscopic data in a uniform approach. It is, therefore, expected that such a consistent analysis will create a reliable and high accurate evaluation for ^{28}Si.

2. Coupled-Channel Calculations

This work has used the soft rotator model including nonaxial quadrupole, octupole, and hexadecapole deformation, and the β_2, β_3, and γ vibration, where the symbols and definitions are same as those in Refs. [2, 3].

By giving suitably an initial assignment of quantum numbers to low-lying levels, the SHEMMAN code[5] is used to adjust the nuclear Hamiltonian parameters to describe ten experimental

levels. The final parameters and the predicted level scheme are given in Table 1 and Fig. 1, respectively. Note that only six predicted levels with spins and parities as 0_1^+, 2_1^+, 4_1^+, 0_2^+, 2_2^+, and 3_1^- are plotted. These levels are coupled most strongly, and are used in CC calculations as described below. It is seen that these levels are predicted well within 10-15 % accuracy.

The wave functions with those adjusted Hamiltonian parameters are used to construct the coupling scheme among the six levels, as shown in Fig. 2, in the CC calculations using OPTMAN code[5]. The present calculation, as did in the previous works [2, 3], has considered that the each level is coupled not only with all other levels, but also with itself. The Coulomb interaction enhances the coupling in all the pairs of the levels except between 0^+ (g.s) and 0_2^+ (4.9798 MeV). These two levels are coupled only by nuclear potential, due to the account of nuclear charge conservation which leads to the truncation of Coulomb potential zero multipoles.

The optical model parameters are searched by minimizing the quantity χ^2 to fit best to the experimental data. To describe the scattering data at higher energies, the simple exponential energy dependence of spin-orbit potential suggested by dispersion relationship is taken into account. The best fitted parameters are given in Table 2. Fig.3-6 show that the total and proton reaction cross sections as well as nucleon scattering data are predicted well by the present model parameters in a consistent way. One can see that the predictions for the proton elastic scattering data over 100 MeV, as shown in right panel of Fig. 5, show some oscillating patterns at backward angles. The reason might be due to the use of simple energy dependence of potential, which make the adjustment of parameters over a wide range of incident energies very difficult. On the the hand, the calculation underestimates the neutron inelastic scattering on 2^+ at 14.2 MeV. This may be because the compound inelastic scattering processes are not included in the calculations.

3. Particle Emission Calculations

The GNASH[6] nuclear reaction model code is used for calculations of compound and preequilibrium particle and γ-ray emissions. Six light particles, n, p, d, t, ^{3}He and α, are taken into account. The transmission coefficients are required in these calculations. A method of connecting the CC method and Hauser Feshbach theory in terms of generalized transmission coefficients was proposed by Ohsawa[7]. In the present work, $T_\ell^{(cc)}(\varepsilon)$ obtained from the above-mentioned CC calculations are used for the entrance channel. Note that this results in use of a compound formation cross section without the contributions from direct inelastic cross sections. For the exit channels of neutron and proton, renormalized transmission coefficients, $T_\ell(\varepsilon) \approx \sigma_r(\varepsilon)/[\sigma_r(\varepsilon) - \sigma_{dir}(\varepsilon)]T_\ell^{(cc)}(\varepsilon)$, are used, where $\sigma_r(\varepsilon)$ is the total reaction cross section, and $\sigma_{dir}(\varepsilon)$ the sum of all direct inelastic cross sections. This renormalization leads to approximate use of spherical optical model transmission coefficients.

The Wilmore-Hodgson [8] and Becchetti-Greenlees [9] potentials are used for lower neutron and proton energies (<20 MeV), respectively. They give an approximate continuity in reaction cross sections to those by the potentials in Table.2. The Daehnick potential [10] is used for deutron, Becchetti-Greenlees potential for triton and ^{3}He, and Avrigeanu potential[11] for alpha particle. The level densities of Ignatyuke et al.[12] are used for all residual nuclei, except the level density parameters of ^{28}Si (a=3.35 MeV^{-1}, $\triangle$=3.89 MeV), ^{28}Al (a=3.55, $\triangle$=0), and ^{25}Mg (a=4.325, $\triangle$=1.75), which are taken as those of Bateman [13].

Figures 7-9 show comparisons of energy spectra, double differential cross sections (DDXs), and isotope production cross sections with experimental data and those from the evaluated data library "LA150"[14]. It is obvious that all spectra and DDXs have an evaporation peak from compound processes at lower emission energy, and a smooth high energy tail from preequlibrium processes. The present results describe overall good agreement with the experimental data.

Figure 9 shows such an example where the QMD calculations at higher energies (200 MeV-

Table 1: The Hamiltonian parameters used to reproduce the experimental level scheme.

$\hbar\omega_0 = 4.218$	$\mu_{\beta_{20}} = 0.6299$	$\mu_{\gamma_0} = 0.727$	$\gamma_0 = 0.3706$	$a_{32} = 0.0$	$a_{42} = 0.01997$
$\delta_4 = 0.6858$	$\gamma_4 = 0.03269$	$\mu_\epsilon = 0.1274$	$\eta = 0.1346$	$\delta_n = 4.092$	

Table 2: The optical potential parameters allowing the best fit of the experimental data. Strength and incident energy E in MeV; radii and diffusenesses in fm.

V_R=54.21-0.288E+0.0004E^2			
W_D = 0.46+0.225E	E$\leq$ 19.85 MeV		
=4.926-0.0507(E-19.85)	E>19.85 MeV		
W_V = 0.1046+0.152E	E$\leq$ 19.85 MeV		
=3.122+0.0954(E-19.85)	E>19.85 MeV		
V_{SO}=4.43$e^{0.005E}$	W^0_{SO}=0.69	W^1_{SO}=-0.00211	
r_R=1.1207	a_R=0.644+0.00003E		
r_D=1.2897	a_D=0.37+0.0052E	E$\leq$19.85 MeV	
	=0.4732	E>19.85 MeV	C_{Coul}=0.662
r_V=1.0719	a_V=0.49+0.0018E		β_{20}=0.414
r_{SO}=1.0987	a_{SO}=0.618		$\beta_{30} = \beta_{20}\epsilon_0$=0.215
r_C=1.1298	a_C=0.872		β_4=0.0622

3 GeV) are given and has a good continuity at 200 MeV to those results by the GNASH code. Note that the experimental data are those for natural silicon. The present results include only the data for ^{28}Si, while those of LA150 and QMD include both data for ^{28}Si and natural silicon.

In conclusions, the present consistent analysis of collective structure and nucleon scattering data, based on the soft rotator model, describe the experimental levels and nucleon scattering data well. The present evaluations show the overall agreement with experimental energy spectra, DDX and production cross sections, and as well as LA150.

Our next step is planned to include the calculations of double differential recoil spectra of heavy reaction products.

References

[1] Y. V. Porodzinskiĭ and E. Sh. Sukhovitskiĭ, Sov. J. Nucl. Phys. **53**, 41 (1991); Sov. J. Nucl. Phys. **54**, 941 (1991).

[2] S. Chiba et al., Nucl. Phys. **A624**, 305 (1997).

[3] E. Sh. Sukhovitskiĭ et al., Phys. Rev. C**62**, 044605 (2000).

[4] Y. V. Porodzinskiĭ and E. Sh. Sukhovitskiĭ, Phys. At. Nucl. **59**, 244 (1996).

[5] E. Sh. Sukhovitskiĭ et al., Report No. JAERI-Data/Code 98-019, JAERI, 1998.

[6] P. G. Young et al., Proc. IAEA Workshop Nucl. Reaction Data and Nucl. reactor -Physics, Design, and Safety, Triest, Itaty, April 15- May 17, 1996, p.227

[7] T. Ohsawa et al., Proc. Int. Conf. Nucl. Data for Basic and Appl. Sci., Santa Fe, May 1985, p. 1193.

[8] D. Wilmore and P. E. Hodgson, Nucl. Phys. **55**, 673 (1964).

[9] F. D. Becchetti and G. W. Greenlees, Proc. Conf. Polarization Phenomena in Nuclear Reactions, p. 682 (1971).

[10] B. Daehnick et al., Phys. Rev. C**21**, 2253 (1980).

[11] V. Avrigeanu et al., Phys. Rev. C**49**, 2136 (1994).

[12] A. V. Ignatyuke et al., Sov. J. Nucl. Phys. **21**, 255 (1975).

[13] F. B. Bateman et al., Phys. Rev. C**60**, 064609 (1999).

[14] M. B. Chadwick et al., Nucl. Sci. Eng. **131**, 293 (1999).

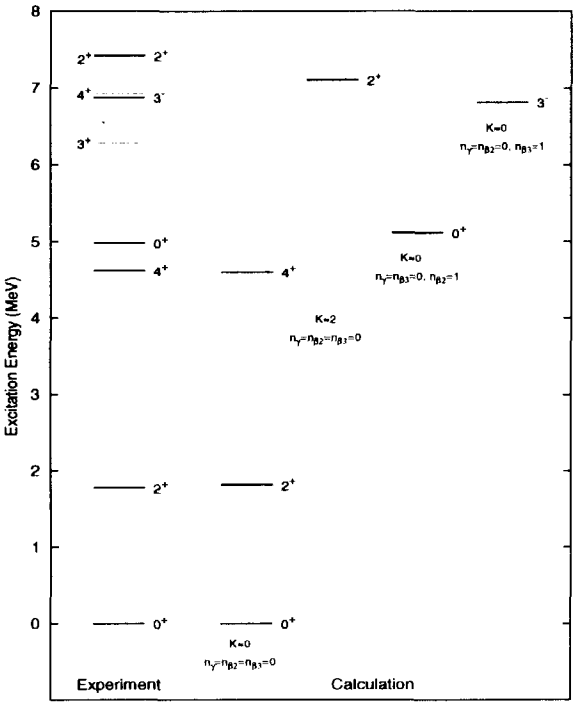

Figure 1. Comparison of the experimental and calculated level schemes. Thick lines show experimental levels described by the soft rotator model.

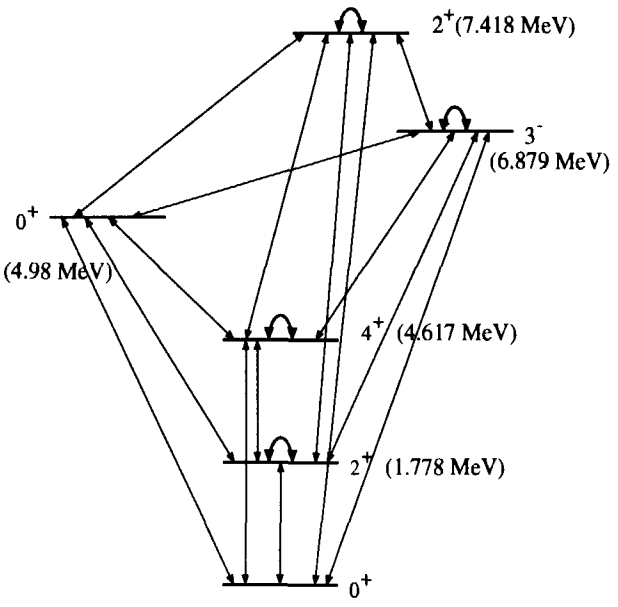

Figure 2. Coupled scheme employed in the present calculations. Arrows show the coupling used in the parameter search procedure.

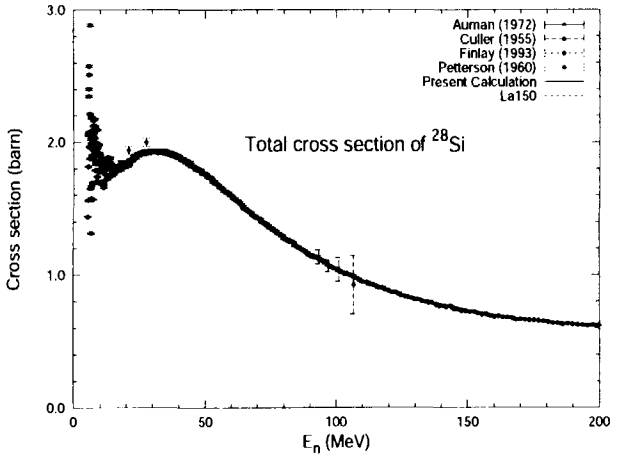

Figure 3. Comparison of the calculated total cross sections with experimental data and evaluated data from LA150.

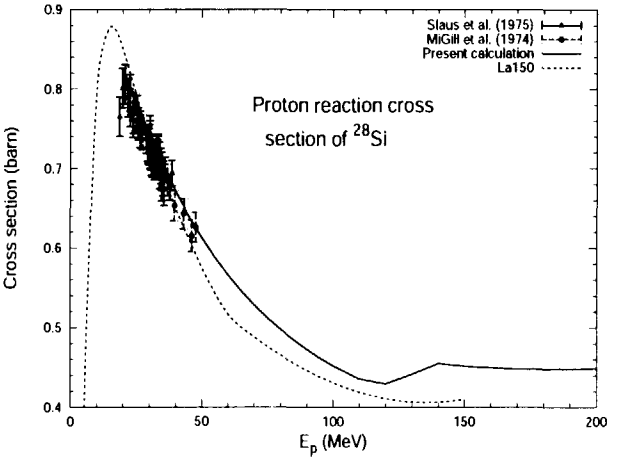

Figure 4. Comparison of the calculated proton reaction cross sections with experimental data and LA150. The present calculations do not give the cross sections for lower energies (< 20 MeV).

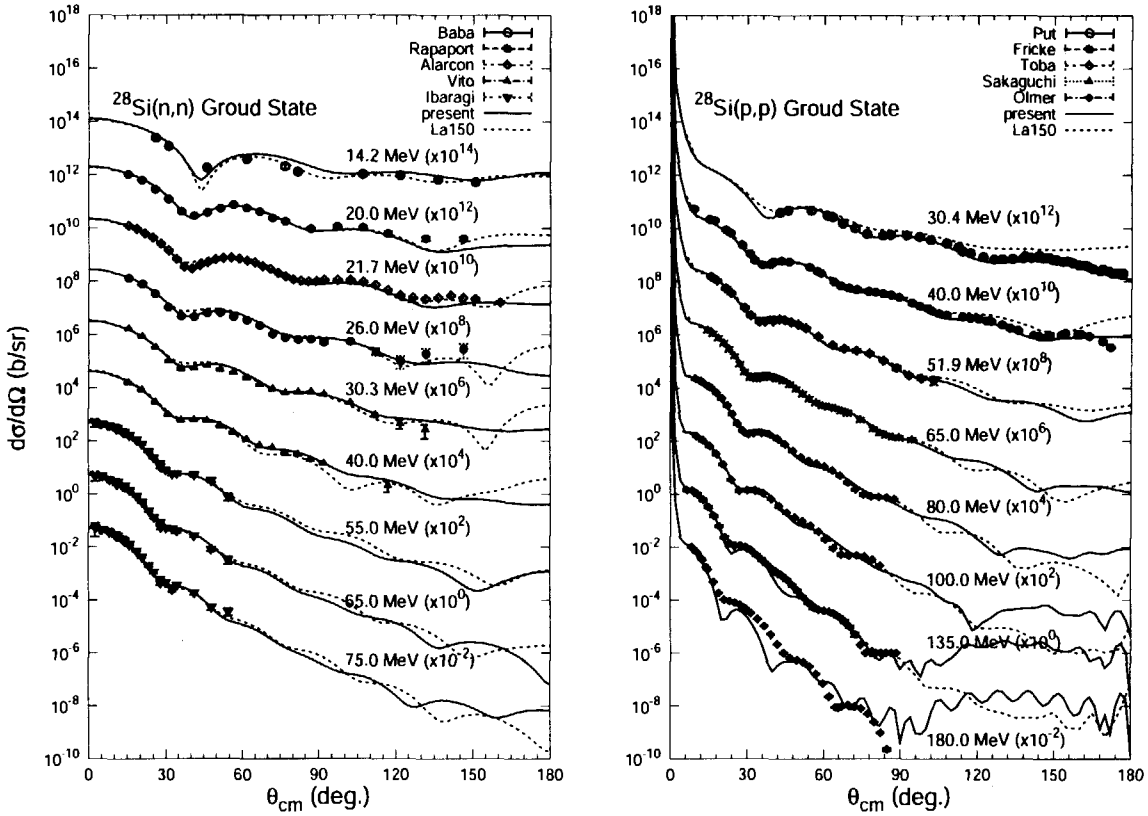

Figure 5. Comparison of the elastic scattering angular distribution with experimental data and LA150.

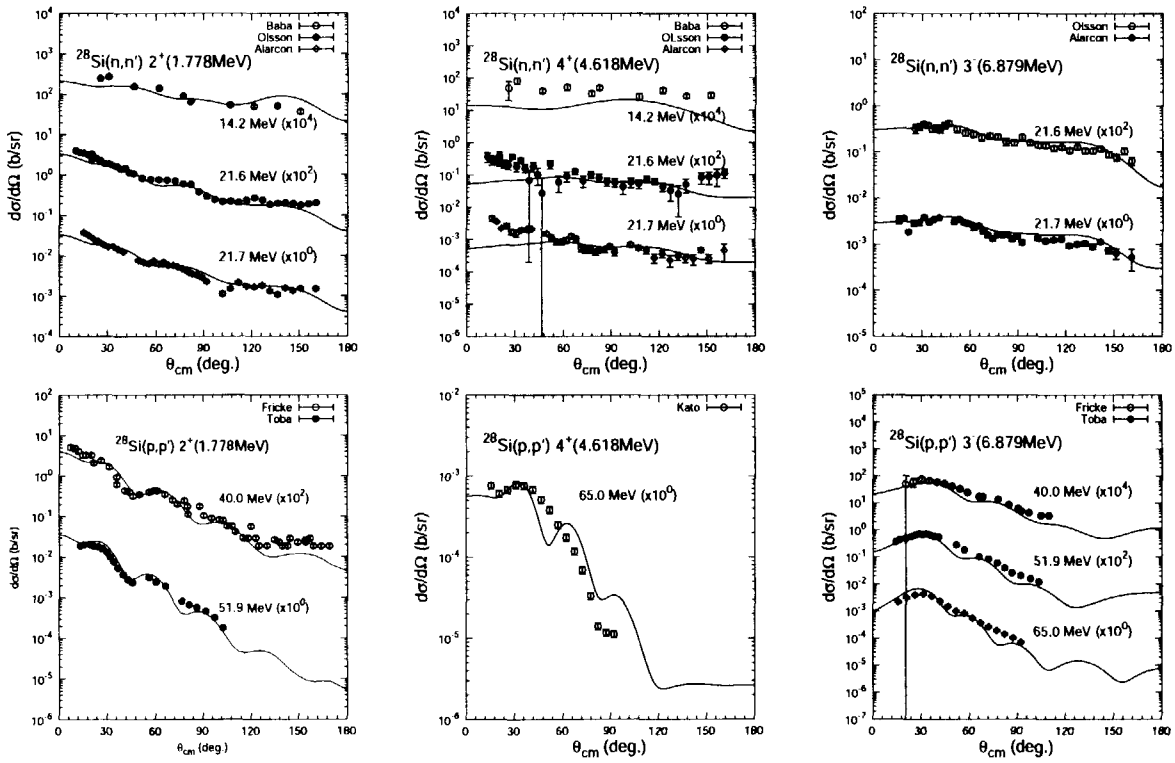

Figure 6. Comparison of the inelastic scattering angular distributions with experimental data.

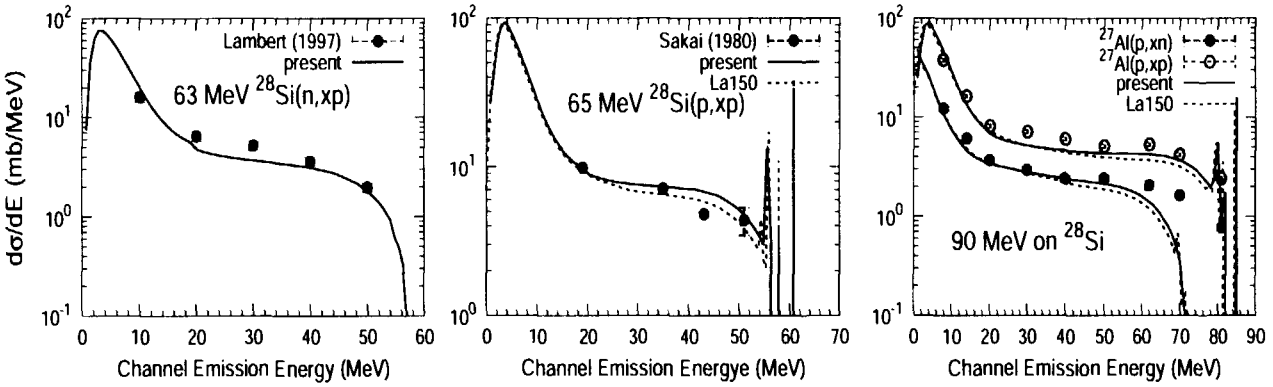

Figure 7. The emitted particle energy spectra of (n, xp), (p, xn) and (p, xp) reactions, compared with experimental data and LA150. The (p, xn) and (p, xp) data at 90 MeV are taken from p+^{27}Al reaction scaled by $A^{2/3}$.

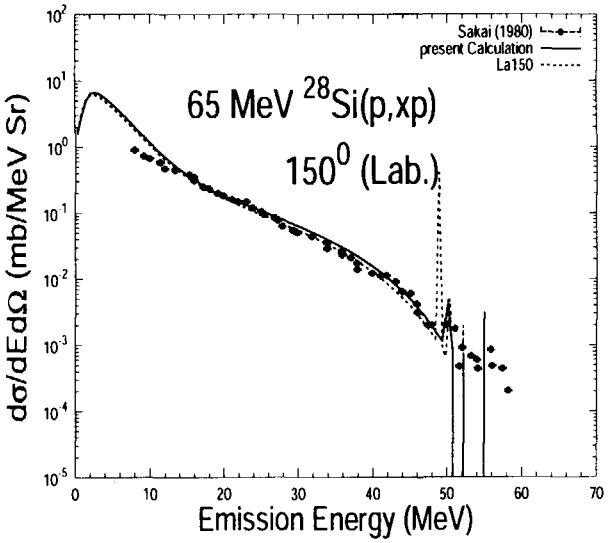

Figure 8. The double differential cross sections at 150^0 for ^{28}Si(p, xp) reaction, compared with experimental data and LA150.

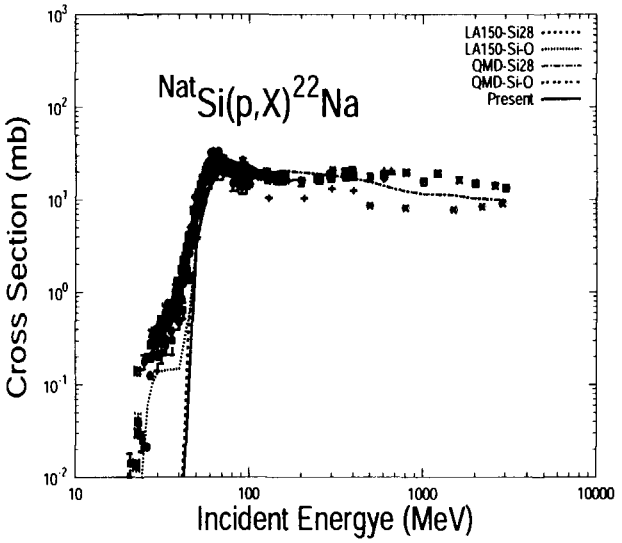

Figure 9. The production cross sections for ^{22}Na, compared with experimental and LA150. The experimental data are those for natural silicon. The present calculations give only the results for ^{28}Si, while the LA150 gives the results for ^{28}Si and natural silicon. The QMD calculations are also presented to show the continuity at 200 MeV to the results of GNASH calculations. All symbols are experimental data taken from EXFOR.

JP0150687

3.25
Calculations of Neutron and Proton Induced Cross Sections on Tungsten up to 3 GeV

Hirohiko KITSUKI, Satoshi Kunieda, Nobuhiro SHIGYO, Kenji ISHIBASHI
Department of Applied Quantum Physics and Nuclear Engineering, Kyushu University
Hakozaki, Higashi-ku, Fukuoka 812-8185
e-mail:kituki@meteor.nucl.kyushu-u.ac.jp

Neutron and proton-induced cross section on tungsten were calculated in the energy region from 20 MeV up to 3 GeV for nuclear data evaluation. Reparameterizaion of optical model potential for tungsten target is made by modification of reported global parameter set. Nucleon emission spectra from (p, xn), (n, xn), (p, xp) and (n, xp) reaction are evaluated by use of moving source model.

1 Introduction

Nuclear data covering incident energies up to several GeV are required for applications such as radiation transport simulations in the high-intensity neutron source and the accelerator-driven transmutation of nuclear wastes. For the design of target of spallation neutron source, especially, it is necessary to know the reaction rate and particle production of tungsten in the energy region up to several GeV accurately. In this study, neutron and proton induced cross sections of tungsten were calculated up to 3 GeV for nuclear data evaluation. Optical model parameters were determined for incident proton and neutron up to 250 MeV. New parameterization of optical model was obtained by adjusting the global optical potential parameter sets to the measured data for tungsten target. Activation yields for incident proton and neutron below 150 MeV at the energies below 150 MeV were calculated by GNASH code[1] with transmission coefficients derived from this optical model analysis. Ones at the energies below 3 GeV were computed by QMD+SDM (Quantum Molecular Dynamics + Statistical Decay Code) code[2]. The MS model[4] based on the Maxwell-like distribution was employed to analyze the nucleon emission double cross section in the incident proton energy region up to 3 GeV. In the forward direction of neutron emission, the Gaussian term was introduced into the MS model with momentum transfer-based parameterization[4]. The present work takes the experimental data on W target. Results of the QMD+SDM code are also used to give the cross sections in the neutron region where no measured data are available.

2 Description of calculation model

2.1 Optical model analysis

Global potential parameters for incident neutrons from 10 to 80 MeV are obtained by Walter and Guss[6]. In incident energy region from 50 to 400 MeV, proton and neutron global optical potentials are parameterized by Madland[7]. In this work, these optical potential was reparameterized to reproduce neutron and proton cross sections accurately.

The general potential form factor having Woods-Saxon form for V_r and W_v and Thomas-Fermi form for spin-orbit are used as

$$\begin{aligned} U(r) = & - V_r f_v(r) - iW_v f_w(r) + 4ia_{wd}W_d \frac{df_{wd}(r)}{dr} \\ & - \frac{1}{r}\left(\frac{\hbar}{m_\pi c}\right)^2 \left(V_{so}\frac{d}{dr}f_{vso}(r) + iW_{so}\frac{d}{dr}f_{wso}(r)\right) \boldsymbol{l}\cdot\boldsymbol{s}, \end{aligned} \quad (1)$$

where m_π is the mass of pion, and the form factors f standard Woods-Saxon shape. Incident energy dependency of parameters by Madland and by Walter and Guss are adjusted to the experimental data for W target. Potential parameters V_r and W_v are shown in Fig. 1 for neutron and proton incidence. Dashed lines and dotted lines stand for parameters by Madland and by Walter and Guss, respectively. The quantities reparameterized in this analysis are indicated by solid lines. Since experimental data for polarized particle incidence are poorly measured for W target in the incident energy region, parameters set of spin-orbit terms obtained by Walter and Guss and ones by Madland were applied for following calculations of cross sections.

2.2 Emission cross section

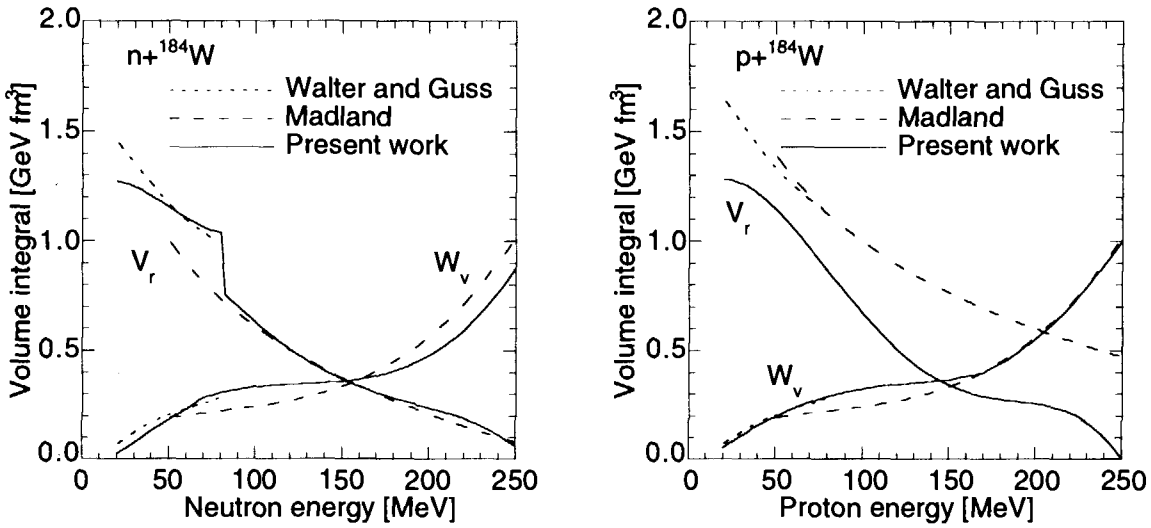

Figure 1: Volume integrals of V_r and W_v

Calculation of the light particle emission cross sections up to 200 MeV was performed by use of GNASH[1] based on the exciton model of Kalbach and Hauser-Feshbach statistical theory. Quick-GNASH code system[3] originating from GNASH was employed in this calculation. The transmission coefficients for neutron and protons calculated from the optical model analysis are utilized to GNASH calculation

The excitation of the giant isoscalar broad resonances(GR) was accounted for the calculation of neutron inelastic scattering, which is dominant for low-excited scattering induced by several-tens MeV nucleon[5]. In this analysis, deformation parameters effectively were determined by searching for the experimental angle integrated inelastic cross section[13] with utilization of PREGNASH code. Lorentzian shaped function was used to evaluate the contribution of giant resonance. The equation is written as

$$\left(\frac{d\sigma}{dE}\right)_{GR} = \sigma_{GR}\Gamma^2 / \left((E - E_{GR})^2 - \frac{\Gamma^2}{4}\right), \tag{2}$$

where σ_{GR} and E_{GR} are adjustable parameters, and are fitted to the results calculated by use of effective deformation parameter. The distribution width $\Gamma = 5$ MeV broadened by the fragmentation of the giant resonances in deformed nuclei was used[5].

For computing cross sections above 100 MeV, QMD+SDM code was used. In QMD+SDM code, dynamical process is calculated by QMD and the contribution derived from the statistical process is obtained by the SDM. The QMD codes takes a semiclassical simulation method in which each nucleon state is represented by a Gaussian wave function. The SDM code considers n, p, d, t, ^{3}He and α evaporation.

2.3 Nucleon production double differential cross sections

Calculations of nucleon production double differential cross sections were performed by the use of moving source(MS) model. In this model, nucleons are assumed to be emitted isotropically with an exponential-type energy distribution at a temperature T (MeV) in the moving frame. For the spallation reaction induced by nucleons about above a hundred MeV, the nucleon emission double differential cross section in the laboratory frame is expressed by a form of summation of three exponential-components as the cascade, the preequilibrium and the evaporation. In the forward emission direction below 30°, the quasi-elastic and -inelastic scattering processes are dominant in this region, and the neutron emission spectrum is strongly forward-peaked. In this work, simple Gausssian shaped term for evaluation of forward-peaked emission spectra is combined with three components of the MS model. Nucleon emission spectra is analyzed by the equation[4] as,

$$\left(\frac{d^2\sigma}{d\Omega dE_{kin}}\right)_{MS+G} = \sum_{i=1}^{3} pA_i \exp\left\{-\left(\frac{E_{kin} + m - p\beta_i \cos\theta}{(1-\beta_i^2)^{\frac{1}{2}}} - m\right)/T_i\right\}$$

$$+ \quad A_G \exp\left\{-\frac{(E_{kin}-E_G)^2}{\sigma_G^2}\right\}, \tag{3}$$

Three components of $i = 1$ to 3 of the first term in the right side of Eq. 3 correspond to individual processes of the cascade, the preequilibrium and the evaporation, respectively. In this term, E_{kin} and p is the kinetic energy (MeV) and the momentum (MeV/c) of an emitted neutron in the laboratory frame, respectively and m the neutron mass (MeV). Quantities A_i, β_i and T_i are called amplitude, velocity and temperature parameters, respectively. A_G, E_G and σ_G are quantities with dependency of incident particle momentum-transfer, and represents emission spectra originated from the quasi-elastic and quasi-inelastic-like scattering. The parameters are adjusted to the experimental nucleon emission spectra and the calculated data results by QMD+SDM. For the spallation reaction at incident nucleon energies up to 3 GeV, the fitting by Eq. 3 well reproduces the experimental data for wide target mass range of C to Pb[4].

3 Results and comparison

3.1 Total, elastic and reaction cross section

Total and Reaction cross section and elastic angular distribution were calculated by use of optical potential parameters obtained by this analysis. Figures 2, 3 and 4 show neutron total cross section, proton reaction cross section and neutron angular distribution of ^{184}W, respectively. The results by use of new optical parameters are represented by solid curves. For comparison, LA150 evaluations are indicated by dashed curves. Our optical parameters give good agreement with the experimental data[8][9][11][10][12] over wide incident energy range.

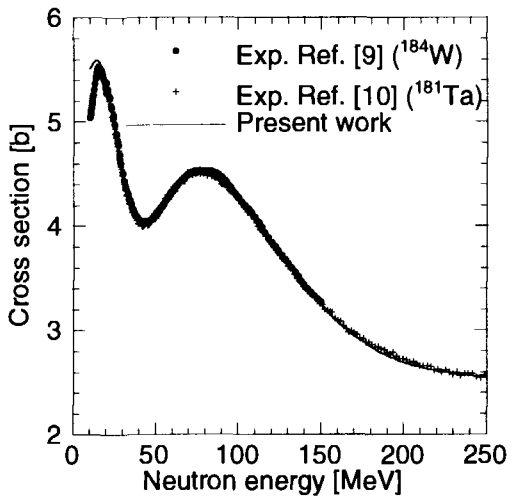

Figure 2: Neutron total cross section of ^{184}W

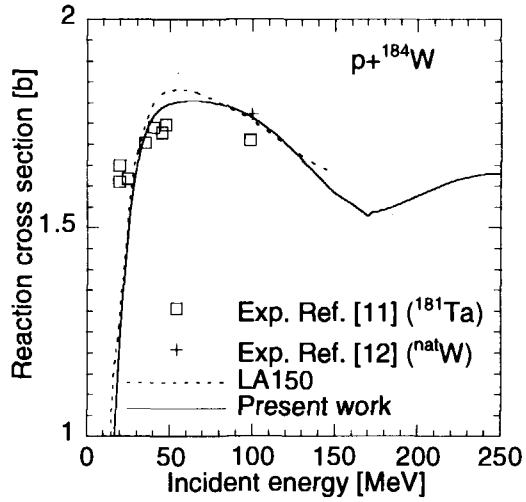

Figure 3: Proton reaction cross section of ^{184}W

3.2 Light particle emission

The (n,n') reaction cross sections for 26.5 MeV neutron incidence are shown in Fig. 5. Dashed curve indicates GNASH calculation, dotted one evaluation of giant resonance component by Eq. 2 with searching effective deformation parameters. Solid line stands for the sum of GNASH calculation and the component of giant resonance. The Lorentzian function adjusted for effective deformation parameters reproduce inelastic neutron emission about above 17 MeV well.

n, p, d, t, ^{3}He and α emission cross sections are shown in Fig. 6. Solid lines with marks stand for the results calculated by QMD+SDM, solid ones with no marks the results by GNASH, and dashed ones LA150 evaluations. Calculation of GNASH and QMD+SDM result to almost similar productions of n, d, and ^{3}He at the incident energy about 150 MeV. For p, t, α emission, however, serious disagreement between the calculations appear about with a factor of 3.

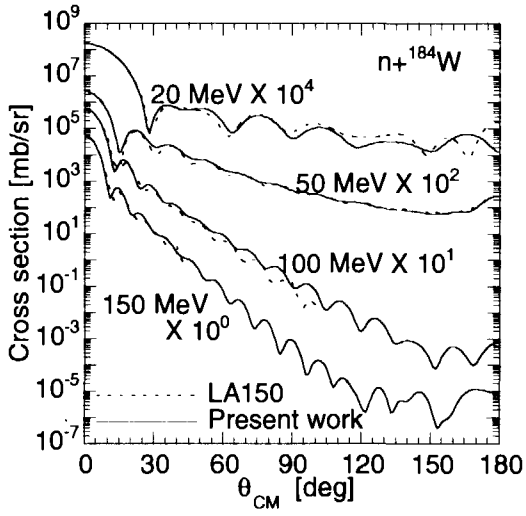

Figure 4: Elastic angular distribution of ^{184}W

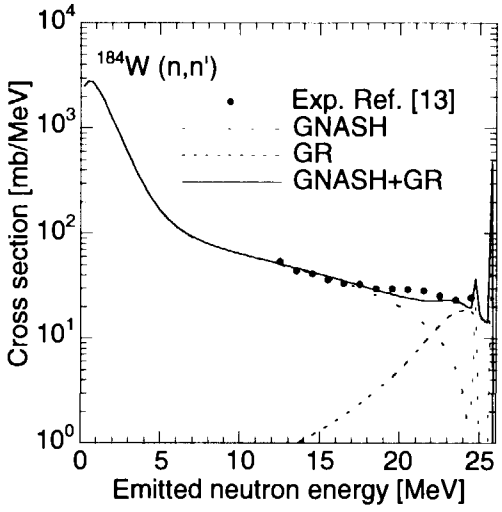

Figure 5: 26MeV neutron-induced neutron production cross section

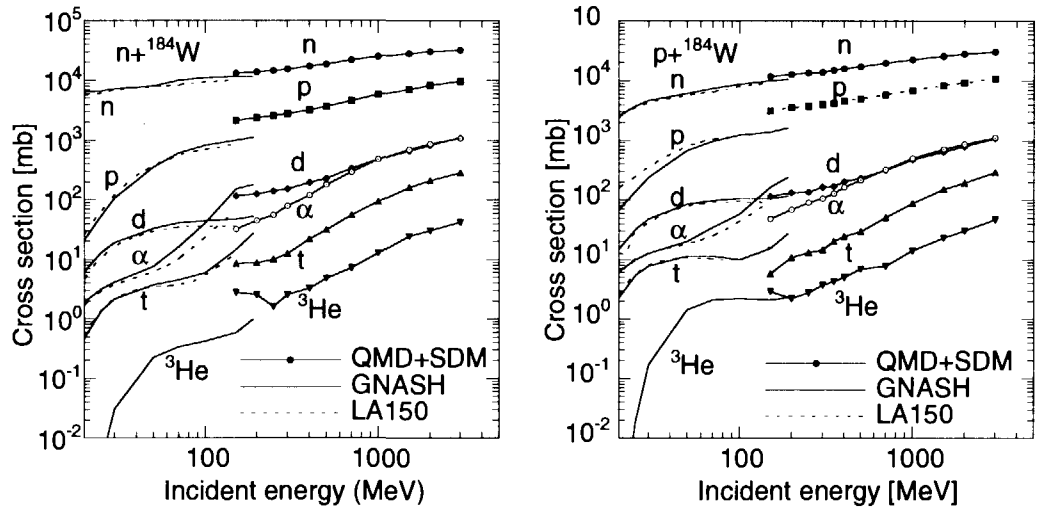

Figure 6: Particle production cross section induced by protons and neutrons up to 3 GeV

3.3 Nucleon emission double differential spectra

Proton incident neutron production double differential cross sections from ^{184}W target are shown in Fig 7. Marks stand for the experimental data[14][15], dashed curves the neutron data computed by QMD+SDM, and solid curves the results analyzed by use of the MS model utilizing the Gaussian-term. The MS model with Gaussian-term reproduced the experimental and calculated neutron data in the whole emission angle region well. Figure 8 shows neutron emission spectra induced by 1 GeV protons and neutrons. Dotted and dashed-dotted curves represent QMD+SDM calculation for (p, xn) and (n, xn) reaction, respectively. Difference of cross section derived from incident nucleon locally appears for emission neutron energies corresponding to the component of cascade process in the MS model. In this study, the common quantities are evaluated for the parameters of the preequilibrium and the evaporation processes to reduce number of MS model parameters.

In Fig. 9, amplitude parameters A_i of the MS model are shown for (p, xn), (n, xn), (p, xp) and (n, xp) reactions on ^{184}W target. Marks are the quantities by fitting to individual target mass number and incident nucleon energy. The solid lines are systematics of MS model parameters.

4 Concluding remarks

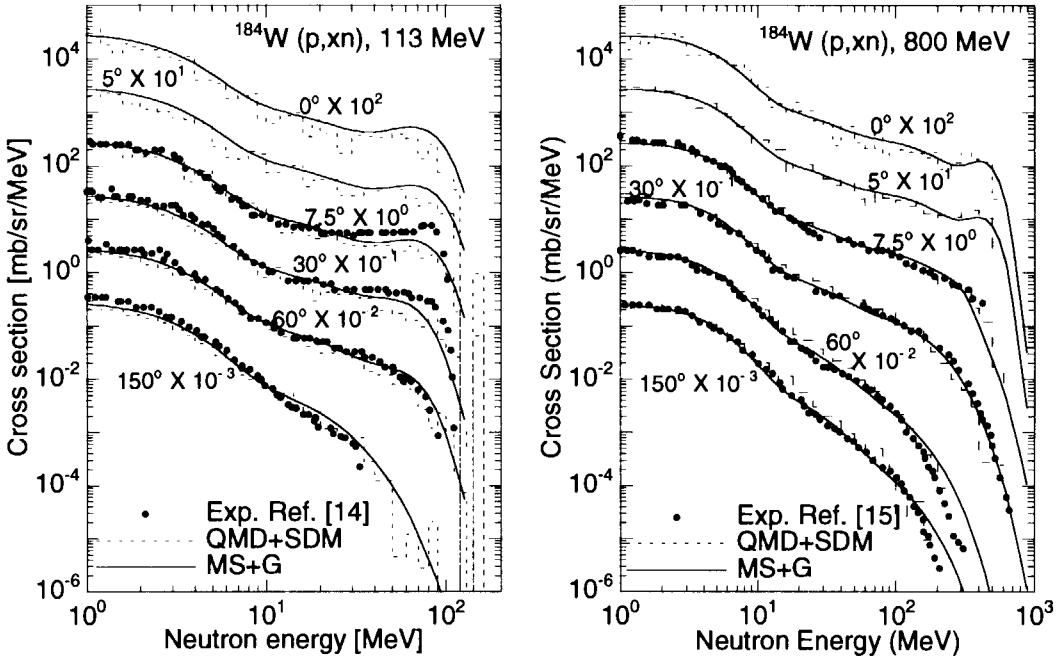

Figure 7: 113 MeV and 800 MeV proton induced neutron production double differential cross section of ^{184}W

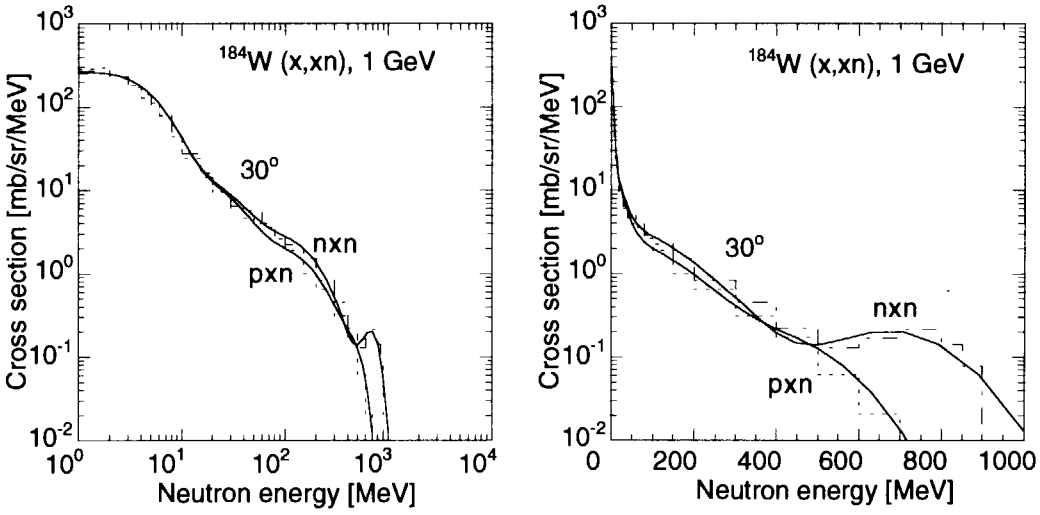

Figure 8: Neutron production double differential cross section of ^{184}W induced by 1 GeV protons and neutrons

New optical potential parameters made by modification of ones by Walter and Guss and by Madland reproduced neutron and proton cross section up to 250 MeV. For light particle production cross sections in the incident energy region about at 170 MeV, large difference of cross sections between calculations of GNASH and QMD+SDM are found. It is seemed that some adjustments of the cross sections in the energy region are required for nuclear data evaluation. Nucleon production double differential cross sections for (p, xn), (n, xn), (p, xp) and (n, xp) reactions were evaluated by use of the MS model combining Gaussian term.

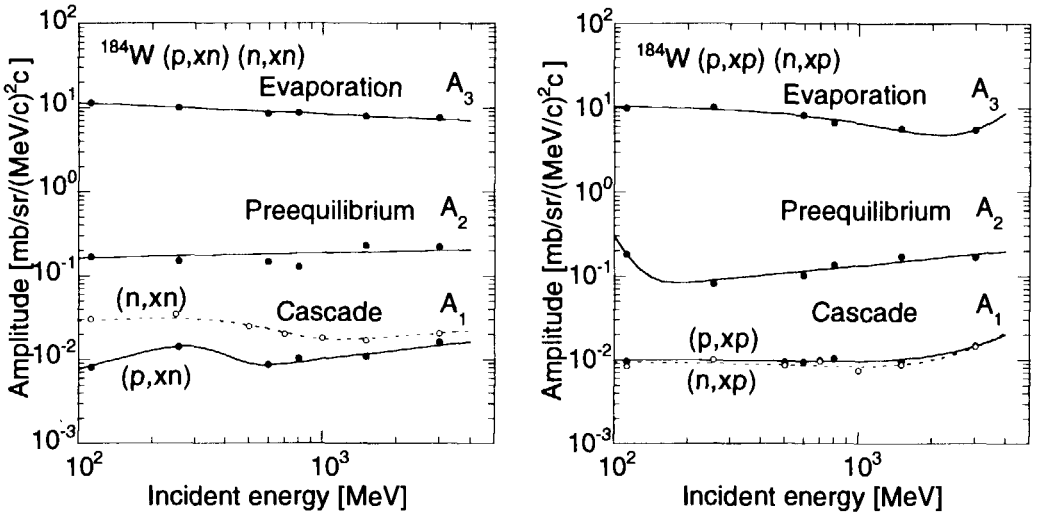

Figure 9: The Amplitude parameter A_i of the MS model

References

[1] Young, P.G., *et al.* : *Comprehensive Nuclear Model Calculations : Introduction to the Theory and Use of the GNASH Code ,"* LA-22343-MS (1992).

[2] Niita, K., *et al.* : *Phys. Rev.*, **C52**, 2620 (1995).

[3] Yamano, T. : *private communication.*

[4] Kitsuki, H. *et al.* : *J. Nucl. Eng. Soc,* to be published.

[5] Marcinkowski, A., Demetriou, P., Hodgson, P.E. : *J. Phys. G.*, **22**, 1219 (1996).

[6] Walter, R.L., Guss, P.P. : *Rad. Eff.*, **95**, 73 (1986).

[7] Young, P.G., Madland, D.G. : IAEA INDC(NDS)-335, 109 (1995).

[8] Dietrich, T.S., et al. : *Proc.Int. Conf. Nuclear Data for Science and Technology*, Trieste, Italy, May 19-24, 1997, 402 (1997).

[9] Hildebrand, R.H., Leith, C.E. : *Phys. Rev.*, **80**, 842 (1950).

[10] Finlay, R.W., *et al.* : *Phys. Rev.*, **C47**, 237 (1993).

[11] Kirkby, P., Link, W.T. : *Can. J. Phys.*, **44**, 1847 (1966).

[12] Abegg, R, *et al* : *Nucl. Phys.*, **A324**, 109 (1979).

[13] Marcinkowski, A., *et. al.* : *Nucl. Phys.*, **A501**, 1 (1989).

[14] Amian, W.B. *et. al.* : *Nucl. Sci. Eng.*, **102**, 310 (1989).

[15] Amian, W.B. *et. al.* : *Nucl. Sci. Eng.*, **112**, 78 (1992).

JP0150688

3.26

Optical Model Parameter Search with Simulated Annealing and Marquardt-Levenberg Method

Young-Ouk LEE, Choong-sup GIL, and Jonghwa CHANG
Korea Atomic Energy Research Institute,
Tokio FUKAHORI
Japan Atomic Energy Research Institute
e-mail: yolee@lui.kaeri.re.kr

1. Introduction

The search for the best set of optical model parameters having energy dependent terms is a non-linear multi-dimensional minimization problem with a given set of reference measurements and physical constraints. Deterministic approaches, such as the gradient or non-linear least square methods, often lead a resulting χ^2 to local minima for their fast convergence. On the other hand, grid search approach such as the simulated annealing (SA) method [1] is known to give a pseudo-global minimum of χ^2 [2, 3]. But the SA method has two major shortcomings; the convergence speed and the absence of a covariance matrix. The convergence of the SA method becomes extremely slow as χ^2 approaches the minimum. Furthermore, the SA method does not provide a covariance matrix, which the deterministic method does, and this is useful for a parametric study of the optical model analysis. In the present work, the grid search and deterministic approaches were sequentially applied to take advantage of both methods.

2. Simulated Annealing Method

Simulated annealing method tries to find coefficients of the global optimum parameters, giving minimum χ^2 with respect to the reference measured data.

The actual procedure of SA operation in the present work is :

- Start with initial coefficients within their upper and lower bounds provided by the user and set initial sampling range VM_j as half of the bounds. Estimate χ^2 with starting set of coefficients.

$$\begin{aligned} \alpha_j &\in [\mathrm{LB}_j, \mathrm{UB}_j] \\ \mathrm{VM}_j &= \frac{1}{2}(\mathrm{UB}_j - \mathrm{LB}_j) \\ (\chi^2)^0 &= \chi^2\,(\alpha_j^0) \end{aligned} \tag{1}$$

- For next step, it randomly chooses a trial point within the step length of VM_j and χ^2 is evaluated at this point with random variable y_j

$$\begin{aligned} \alpha_j^{k+1} &= \alpha_j^k + y_j \cdot r_j, \quad y_j \in [-1, 1] \\ (\chi^2)^{k+1} &= \chi^2(\alpha_j^{k+1}) \end{aligned} \tag{2}$$

- This χ^2 is compared to its previous one. All downhill moves are accepted and the algorithm continues from that trial point. i.e.

$$\text{accepted if} \quad (\chi^2)^{k+1} < (\chi^2)^k \tag{3}$$

- Uphill moves may be accepted; the decision is made by the Metropolis criteria with random variable z

$$\text{also accepted if} \quad \exp\left(\frac{(\chi^2)^k - (\chi^2)^{k+1}}{T}\right) > z, \qquad z \in [0, 1] \tag{4}$$

It uses T(temperature) and the size of the uphill move in a probabilistic manner. The smaller T and the size of the uphill move are, the more likely that move will be accepted.

- If the trial is accepted, the algorithm moves on from that point. If it is rejected, another point is chosen instead of a trial evaluation.
- Each element of VM_j is periodically adjusted so that half of all function evaluations in that direction are accepted.

$$\beta_j = \frac{\text{number of accepted}}{\text{number of trial}} \tag{5}$$

$$\begin{aligned} \mathrm{VM}_j &= \mathrm{VM}_j\ (1.0 + c\ (\beta_j - 0.6)/0.6) \quad \text{if } \beta_j > 0.6 \\ \mathrm{VM}_j &= \mathrm{VM}_j\ (1.0 + c\ (0.4 - \beta_j)/0.4) \quad \text{if } \beta_j < 0.4 \end{aligned} \tag{6}$$

- A fall in T is imposed upon the system with the RT variable by

$$\mathrm{T}_{n+1} = \mathrm{RT} \cdot \mathrm{T}_n \tag{7}$$

where n is the nth iteration with the same T. Thus, as T declines, uphill moves are less likely to be accepted and the percentage of rejections rise. Given the scheme for the adjusting VM, VM falls. Thus, as T declines, VM falls and SA focuses upon the most promising area for optimization.

- The termination criteria for the search is set if the last four χ^2's from the last four different T's differ from the current χ^2 by less than the user-defined tolerance(EPS) and the current χ^2 at the current T differs from the current optimal χ^2 by less than EPS.

The parameter T is crucial in using SA successfully. It influences VM, the step length over which the algorithm searches for optima. For a small initial T, the step length may be too small; thus the search may fail to find the global optima. The user should carefully examine to make sure that VM is appropriate. The relationship between the initial temperature and the resulting step length is function-dependent.

3. Nonlinear model and Marquardt-Levenberg Method

Let us briefly review the nonlinear fitting using excerpts of ref. [4]. With nonlinear dependences, the minimization must proceed iteratively for a nonlinear model with the set of M unknown parameters $a_k, k = 1, 2, \ldots, M$.

We expect the χ^2 function to be well approximated by a quadratic form, written as

$$\chi^2(\mathbf{a}) \approx \gamma - \mathbf{d} \cdot \mathbf{a} + \frac{1}{2}\mathbf{a} \cdot \mathbf{D} \cdot \mathbf{a} \tag{8}$$

where $\mathbf{d}$ is an M-vector and $\mathbf{D}$ is an $M \times M$ matrix. Let us examine how to calculate the gradient and Hessian of χ^2 merit function. The model to be fitted is

$$y = y(x; \mathbf{a}) \tag{9}$$

and the χ^2 merit function is

$$\chi^2(\mathbf{a}) = \sum_{i=1}^{N} \left[\frac{y_i - y(x_i; \mathbf{a})}{\sigma_i} \right]^2 \tag{10}$$

The gradient of χ^2 with respect to the parameters a, which will be zero at the χ^2 minimum, has components

$$\frac{\partial \chi^2}{\partial a_k} = -2 \sum_{i=1}^{N} \frac{[y_i - y(x_i; \mathbf{a})]}{\sigma_i^2} \frac{\partial y(x_i; \mathbf{a})}{\partial a_k} \qquad K = 1, 2, \ldots, M \tag{11}$$

Taking an additional partial derivative gives

$$\frac{\partial^2 \chi^2}{\partial a_k \partial a_l} = 2 \sum_{i=1}^{N} \frac{1}{\sigma_i^2} \left[\frac{\partial y(x_i; \mathbf{a})}{\partial a_k} \frac{\partial y(x_i; \mathbf{a})}{\partial a_l} - [y_i - y(x_i; \mathbf{a})] \frac{\partial^2 y_i(x_i; \mathbf{a})}{\partial a_l \partial a_k} \right] \tag{12}$$

It is conventional to remove the factors of 2 by defining

$$\beta_k \equiv -\frac{1}{2}\frac{\partial \chi^2}{\partial a_k} \qquad \alpha_{kl} \equiv \frac{1}{2}\frac{\partial^2 \chi^2}{\partial a_k \partial a_l} \tag{13}$$

making $[\alpha] = \frac{1}{2}\mathbf{D}$ in equation (8), and rewriting the equation as a set of linear equations

$$\sum_{l=1}^{M} a_{kl}\delta a_l = \beta_k \tag{14}$$

This set is solved for the increments δ_l that, added to the current approximation, give the next approximation. In the context of least-squares, the matrix $[\alpha]$, equal to one-half times the Hessian matrix, is usually called the curvature matrix. iNote that the components α_{kl} of the Hessian matrix (12) depend both on the first derivatives and on the second derivatives of the basis functions with respect to their parameters. Second derivative term can be dismissed when it is zero (as in the linear case), or small enough to be negligible when compared to the term involving the first derivative. As the definition of the α_{kl}, we will use the formula

$$\alpha_{kl} = \sum_{i=1}^{N} \frac{1}{\sigma_i^2}\left[\frac{\partial y(x_i;\mathbf{a})}{\partial a_k}\frac{\partial y(x_i;\mathbf{a})}{\partial a_l}\right] \tag{15}$$

Marquardt has put forth a method, related to an earlier suggestion of Levenberg, for varying smoothly between the extremes of the inverse-Hessian method and the steepest descent method. The latter method is used far from the minimum, switching continuously to the former as the minimum is approached. This Marquardt-Levenberg method works well in practice and has become the standard of nonlinear least-squares routines. The method is based on two elementary insights. Marquardt's first insight is that the components of the Hessian matrix, even if they are not usable in any precise fashion, give some information about the order-of-magnitude scale of the problem. The quantity χ^2 is non-dimensional, i.e. is a pure number; this is evident from its definition(10).

On the other hand, β_k has the dimensions of $1/a_k$, which may well be dimensional, i.e. have units like cm^{-1}, or kilowatt-hours, or whatever. The constant of proportionality between β_k and δa_k must therefore have the dimensions of a_k^2. Scan the components of $[\alpha]$ and you see that there is only one obvious quantity with these dimensions, and that is $1/\alpha_{kk}$, the reciprocal of the diagonal element. So that must set the constant by some (non-dimensional) fudge factor λ, with the possibility of setting $\lambda \gg 1$ to cut down the step, In other words, replace equation (??) by

$$\delta a_l = \frac{1}{\lambda a_{ll}}\beta_l \quad \text{or} \quad \lambda a_{ll}\delta a_l = \beta_l \tag{16}$$

It is necessary that a_{ll} be positive, but this is guaranteed by definition (15).

Marquardt's second insight is that equations (16) and (14) can be combined if we define a new matrix α' by the following prescription

$$\begin{aligned} \alpha'_{jj} &\equiv \alpha_{jj}(1+\lambda) \\ \alpha'_{jk} &\equiv \alpha_{jk}(j \neq k) \end{aligned} \tag{17}$$

and then replace both (16) and (14) by

$$\sum_{l=1}^{M} \alpha'_{kl}\delta a_l = \beta_k \tag{18}$$

When λ is very large, the matrix α' is forced into being diagonally dominant, so equation goes over to be identical to (16). On the other hand, as λ approaches zero, equation (18) goes over to (14).

Given an initial guess for the set of parameters $\mathbf{a}$, the present work performs the following procedure [5] :

- Compute $\chi^2(\mathbf{a})$.
- Pick a modest value for λ.
- (†) Solve the linear equations (18) for $\delta\mathbf{a}$ and evaluate $\chi^2(a + \delta\mathbf{a})$.
- If $\chi^2(\mathbf{a} + \delta\mathbf{a}) \geq \chi^2(\mathbf{a})$, increase λ by a factor of 10 and go back to (†).
- If $\chi^2(\mathbf{a} + \delta\mathbf{a}) < \chi^2(\mathbf{a})$, decrease λ by a factor of 10, update the trial solution $\mathbf{a} \leftarrow \mathbf{a} + \delta\mathbf{a}$, and go back to (†).

Once the acceptable minimum has been found, one wants to set $\lambda = 0$ and compute the matrix

$$[C] \equiv [\alpha]^{-1} \tag{19}$$

which is the estimated covariance matrix of the standard errors in the fitted parameters $\mathbf{a}$.

4. Application and Results

A reference measurements set was constructed based on the analyses of raw experimental data and/or other sources of evaluations. The search procedure starts with the SA algorithm with the reference data set and physical constraints imposed on the functional forms of optical model parameters. The importance of the reference points were dynamically shifted in the course of the SA search, varying their corresponding errors, based on the physical constraints and eye guidance. Appropriate conditions were studied on whether the SA reaches the vicinity of the global minimum of the χ^2. Then the procedure is switched into a deterministic way using the Marquardt-Levenberg Method to accelerate the convergence to the global minimum, as well as to produce a covariance matrix. Figure 1 shows the characteristics of minimum χ^2's achievable from three cases, namely the simulated annealing alone, the Marguardt-Levenberg alone, and combination of the two methods, in the domain of adjustable parameters. In fig. 2, the change of χ^2 is plotted as the iteration proceeds for three cases. As shown, a global minimum is obtained by combining the Marquardt-Levenberg (ML) Algorithm and the simulated annealing (SA) methods. It is also noted that the SA method alone stops at the vicinity of the real minimum and the M-L method traps in the local minimum.

References

[1] Lee, Y.: *ECISPLOT: An interactive optical model parameter searcher with simulated annealing algorithm.* Tech. Rep. NDL-9/99, KAERI (1999).

[2] Lee, Y., *et al.*: *J. of Nucl. Sci. and Tech.*, **36**(12), 1125 (1999).

[3] Lee, Y., *et al.*: In *Proc. of PHYSOR 2000: ANS International Topical Meeting on Advances in Reactor Physics and Mathmatics and Computation into the Next Millenium.* Pittsburgh, Pennsylvania, U.S.A, May 7-12, 2000 (2000).

[4] Press, W. H., *et al.*: *Numerical Recipes.* Cambridge Univ. Press, The Pitt Building, Trumpington Street, Cambridge CB2 IRP (1986).

[5] Lee, Y.: *MLFIT : A portable fitting tool using the nonlinear least-squares (NLLS) marquardt-levenberg algorithm.* Tech. Rep. NDL-13/00, KAERI (2000).

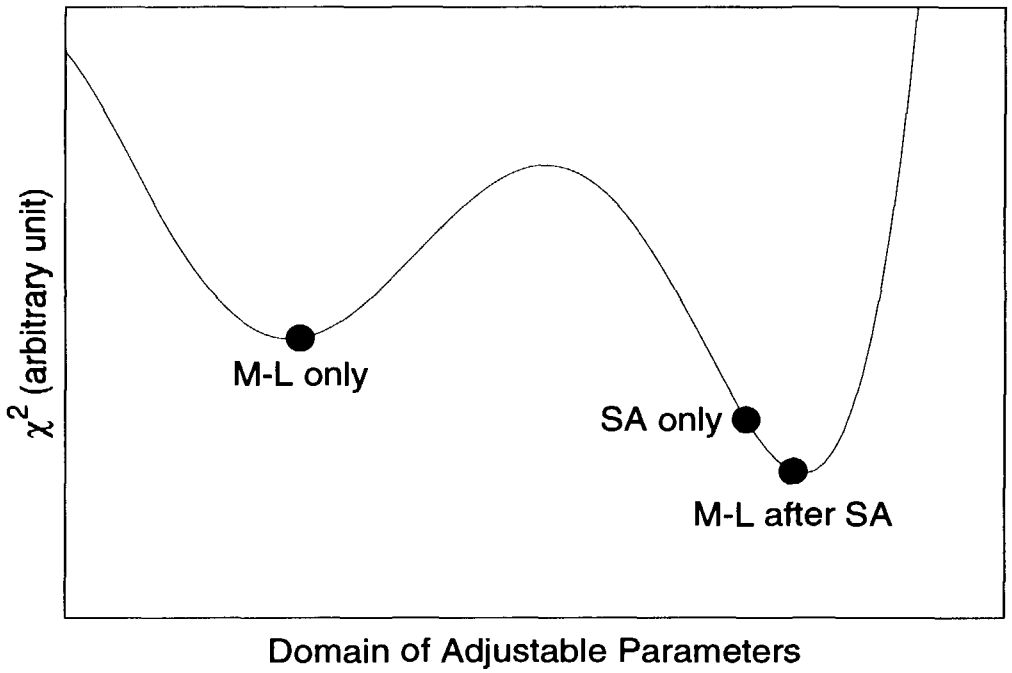

Figure 1: Characteristics of χ^2 for 3 cases: the simulated annealing (SA) alone, the Marguardt-Levenberg(ML) alone, and combination of the two methods

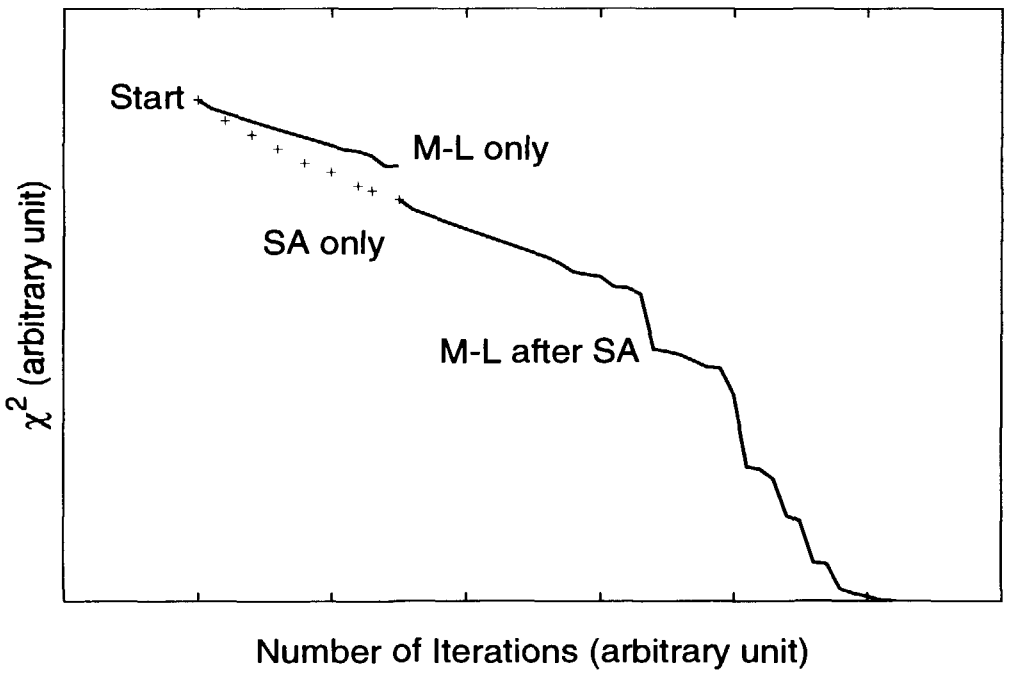

Figure 2: χ^2 changes as a function of iterations as the iteration proceeds for three cases

JP0150689

3.27

Development of Heavy Ion Transport Monte Carlo Code

Hiroshi Iwase
Department of Quantum Science and Energy Engineering, Tohoku University
Aoba, Aramaki, Aoba-ku, Sendai
e-mail:gan@cyric.tohoku.ac.jp

We developed a heavy ion transport Monte Carlo code HETC-CYRIC which can treat the fragments produced by heavy ion reactions. The HETC-CYRIC code is made by incorporating a heavy ion reaction calculation routine, which consists of the HIC, the SPAR, and the Shen's formula, into the hadron transport Monte Carlo code HETC-3STEP. The results calculated with the HETC-CYRIC were compared with the experimental data, and the HETC-CYRIC gave rather good agreement with the experiment.

1 Introduction

Recently, high-energy heavy ions have been used in various fields of nuclear physics, material physics and medical application, especially cancer therapy, and several heavy ion accelerator facilities are now operating or planned for construction. The high-energy heavy ions are also important constituents of cosmic radiation for space utilization, such as the international space station project including the JEM (Japanese Experimental Module). In this circumference, the interaction and transport of heavy ions in a medium including human body are indispensable basic informations to estimate the absorbed dose of the patients during the cancer treatment, to design the shielding of the accelerator facility and to estimate the exposure of the astronauts and the space scientists in space. There exists however only one heavy-ion transport code, HZTRAN[1], developed by NASA in the world, but this code is one-dimensional discrete ordinates calculation code. It is therefore needed to develop the three dimensional heavy-ion transport code. Here in this study, we tried to develop the three-dimensional Monte Carlo code for heavy ion transport calculation.

2 Basic Method of the Code Development

We developed a heavy ion transport Monte Carlo code by incorporating a newly-developed heavy ion routine (HIR) into the HETC-3STEP[2].

The heavy ion transport routine HIR can treat the transport and reaction of incident heavy ion and fragments produced by a chain of heavy ion reactions. For this heavy ion reaction calculation, we used the two existing Monte Carlo code, HIC[3] and ISABEL[4]. First, we compared these two codes with the experimental data in order to investigate the calculational accuracy and to decide which is suitable for the heavy ion routine. The

comparisons were made for double-differential neutron production cross sections (DDX) in angle and energy by heavy ions, as shown in Fig. 1.

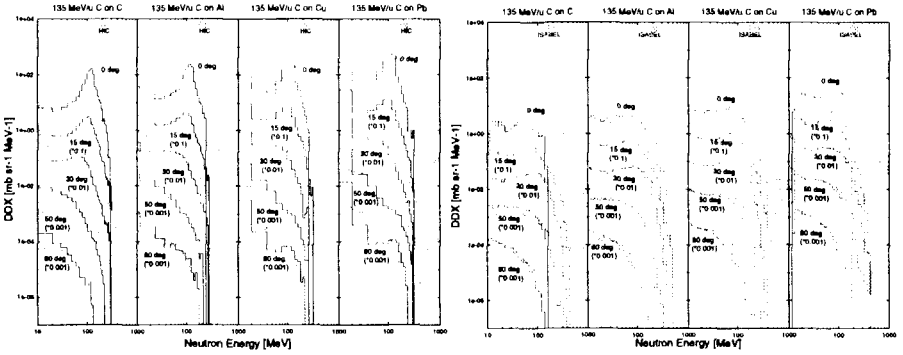

Figure 1: Comparison of HIC and ISABEL calculation; [Left] Neutron DDX calculated by HIC compared with our experimental data of 135MeV/nucleon C ion on C, Al, Cu, and Pb targets[5]. [Right]The same results between ISABEL and the experiment.

The HIC code is the Heavy Ion Code which can treat the heavy ion reaction of energy higher than 50 MeV/nucleon which is based on the intranuclear cascade model and the evaporation model. The ISABEL code includes only intranulear cascade model but this model treats a nucleus by diving into 16 segments which is more precise than 3 segments in the HIC code, and the ISABEL code also considers the reflection at a boundary of a nucleus, which can be the same effect as considering the preequilibrium process. As the results of comparisons shown in Fig. 1, the ISABEL code showed good agreement with the experimental data at angles of larger than 30 degrees, while on the other hand, the ISABEL underestimated the experimental data terribly from 0 degree to 15 degrees. The HIC results rather well with the experimental data at all angles. So, we decided to use the HIC code in heavy ion reaction calculation for the heavy ion transport routine.

We then developed the heavy ion transport routine HIR by combing the HIC code, SPAR[6] code, and Shen's formula[7]. The SPAR code can calculate the heavy ion stopping powers and ranges, and the Shen's formula can calculate the heavy ion total reaction cross sections.

The HETC-3STEP is a high energy hadron transport Monte Carlo code developed by Yoshizawa et al. This code is revised from the original HETC code[8] which includes the intranuclear-cascade evaporation process (2-step model) based on a Fermi free gas model, by adding the pre-equilibrium emission based on the exiton model (3-step model). The HETC-3STEP can also treat the heavy ion (atomic mass less than 20) transport and reaction, but the treatment is restricted to incident particles and the accuracy of heavy ion calculation is poor.

3 Procedure of the Code Development

The heavy ion transport calculation code is composed of the following steps,

1. A distance D in which a heavy ion projectile collides with a target nucleus in a medium

is decided as follows,

$$D = -\frac{ln(r)}{\Sigma_t},$$

where Σ_t is a total reaction cross section of a projectile in a medium calculated by the Shen's formula and r is a uniform random number.

2. A range R of a projectile in a medium can be calculated by the SPAR code.

3. It is decided whether a projectile collides or stops. If $D < R$, a projectile collides with a target nucleus after flying straight-forward to a distance of D and losing its energy. This energy loss can also be calculated by the SPAR code. If $D > R$, a projectile loses its energy completely without collision in a medium, and the transport of this projectile does not follow any more.

4. The heavy ion reaction calculation is performed using the HIC code. The HIC code gives the output results of many heavy ions and hadrons as fragment products. These heavy ion outputs are stored and used as an incident heavy ion for continuing the extranuclear cascade reactions. The hadron outputs on their particle types (neutron, proton and pion), energies, positions, directions and weights are stored in a file during the heavy ion calculations. This file is used as hadron sources produced by heavy ions for the hadron transport calculation using the HETC-3STEP code.

Figure 2 shows the thus-obtained HETC-CYRIC code structure.

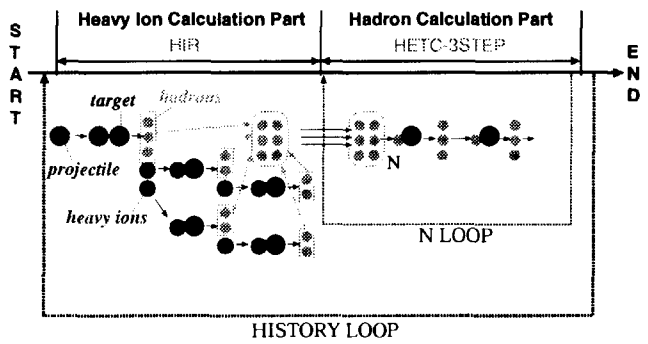

Figure 2: Structure of HETC-CYRIC

4 Comparison of HETC-CYRIC and Experimental Data

In order to investigate the accuracy of the HETC-CYRIC code, we compared the results calculated by the HETC-CYRIC with the data measured by Kurosawa et al[9]. Figures 3 and 4 show the comparison of the HETC-CYRIC results with the measured neutron spectra for 400 MeV/nucleon carbon and iron ions on stopping-length carbon and lead targets.

In Fig. 3 of C ion, the HETC-CYRIC gives good agreement with the experiment from 7.5 to 30 degrees, but gives underestimation at 0 degree and gives overestimation from

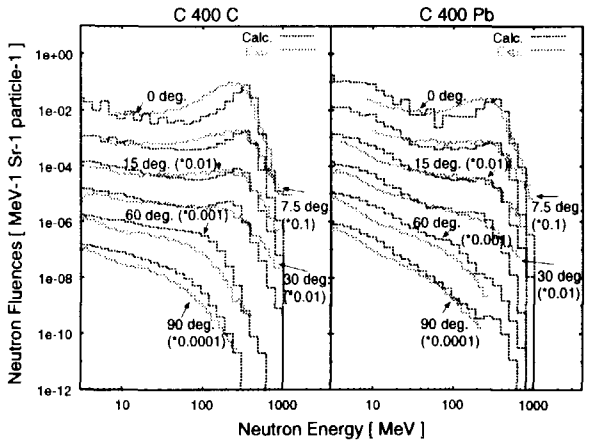

Figure 3: Comparison of the neutron spectra calculated with the HETC-CYRIC and the measured data for 400 MeV/nucleon C ion on C and Pb targets[9]

60 to 90 degrees comparing with the experiment for carbon target. In the case of lead target, the HETC-CYRIC gives good agreement as a whole excluding an overestimation in the low energy region at all angles.

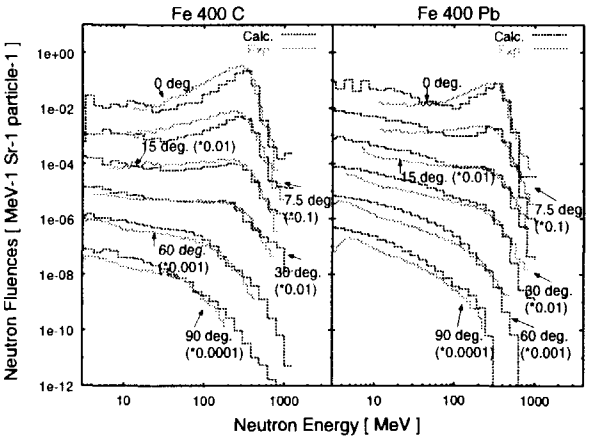

Figure 4: Comparison of the neutron spectra calculated with the HETC-CYRIC and the measured data for 400 MeV/nucleon Fe ion on C and Pb targets[9]

In Fig. 4 of Fe ion, the HETC-3STEP gives good agreement as a whole, excluding an underestimation in the forward direction comparing with the experiment for carbon target, and an overestimation in the low energy region for lead target as well as in the case of carbon ion.

This underestimation in the forward direction and overestimation at large angle and in the low energy region for heavier target material in the HETC-CYRIC code may come from the inaccurate heavy ion model of the HIC code.

We are now investigating the way to improve the present code more accurately by revising the HIC code or using the different heavy ion reaction calculation code such as the QMD code[10] based on the quantum modecular dynamics model.

5 Conclusion

We developed a heavy ion transport Monte Carlo code, HETC-CYRIC by combining the newly-developed heavy ion transport routine HIR including the HIC code and the hadron transport Monte Carlo code HETC-3STEP. The HETC-CYRIC can treat the heavy ion and hadron transport calculations. This code is still under developing and the first general-purpose heavy ion transport Monte Carlo code in the world.

References

[1] W. John. Wilson et al.: *NASA Tech. Paper*, 3146, (1991)

[2] N. Yoshizawa et al.: *J. Nucl. Sci. Tech.*, 32, 601 (1995)

[3] H. W. Bertini: *ORNL-TM-4134*, (1996).

[4] Y. Yariv et al.: *Phy. Rev.*, 188, 1711 (1969)

[5] H. Sato et al.: *JAERI-Conf*, 261, 5 (2000)

[6] T. W. Armstrong et al.: *ORNL-4869*, (1973)

[7] Shen Wen-quinf et al.: *Nucl. Phys.*, A491, 130 (1989)

[8] P. Cloth et al.: *KFA-IRE-E*, AN/12/88 (1988)

[9] T. Kurosawa et al.: *Nucl. Sci. and Engin.*, 132, 30 (1999)

[10] J. Aichelin. et al.: *Phys. Rep.*, 202, 233 (1991)

JP0150690

3.28

Experimental Study of Synthesis of Heavy Nuclei at JAERI

K. Nishio[1], H. Ikezoe[1], S. Mitsuoka[1], J. Lu[2], K. Satou[1]

1. Advanced Science Research Center, Japan Atomic Energy Research Institute
Tokai-mura, Ibaraki 319-1195, Japan
2. Instiute of Modern Physics, Chinese Academy of Sciences, 730000 Lanzhou, China

Abstract

Evaporation residue (ER) cross sections for ^{82}Se+^{nat}Ce and ^{76}Ge+^{150}Nd were measured in the vicinity of the Coulomb barrier, and the fusion probability was obtained with the aid of calculated survival probability. The former system represents fusion of two spherical nuclei, the latter fusion involving the prolately deformed target ^{150}Nd. The collision of ^{76}Ge with the side of ^{150}Nd is more compact in configuration at touching. The system ^{82}Se+^{nat}Ce showed fusion hindrance in form of extra-extra-push energy of 27±5 MeV, whereas the system ^{76}Ge+^{150}Nd does not show fusion hindrance at and above the Coulomb barrier energy, suggesting that the reaction starting from the compact touching point results in a higher fusion probability.

1. Introduction

Heavy ion fusion reactions between massive nuclei near the Coulomb barrier have been investigated experimentally and theoretically so far. This is partly because there is a possibility of synthesizing a super-heavy element as an evaporation residue by complete fusion under a proper choice of colliding particles and the bombarding energy. The production of evaporation residues comprises of two separate processes, the fusion process between two interacting nuclei (entrance channel) and the survival process against fission in the course of the deexcitation process (exit channel). The former process is successfully understood by a coupled channel model [1] in the limit of light projectile-target combination of $Z_1Z_2 \leq 1800$. Fusion enhancement relative to the one-dimensional barrier penetration model was observed below the Coulomb barrier region [2]. This could be explained by replacing the one-dimensional barriers by a distribution of barriers [3][4][5]. On the other hand, in heavy systems ($Z_1Z_2 > 1800$), the formation of a compound nucleus is not warranted even if the system overcomes the fusion barrier. This is because at the contact point the distance between the centers of projectile and target is larger than the distance of the centers of the nascent fission fragments at the fission saddle point. The kinetic energy of the interacting nuclei decreases in the course of the fusion process, with the energy being dissipated into the intrinsic excitation energy, and the system fails to surmount the fission saddle point for the bombarding energy corresponding to the Coulomb barrier. To drive the system into the compound nucleus, an additional energy called extra-extra-push energy (E_{XX}) is needed.

Collisions that fail to form a compound nucleus may break as quasifission after a significant amount of nucleon transfer and kinetic energy loss. Fission fragments from quasifission are difficult to distinguish experimentally from fission fragments of complete fusion, making the fusion cross section ambiguous when only the fission fragments are measured. Therefore detecting the evaporation residues is essential to identify the fusion reaction and obtain the fusion probability.

There are several investigations on the fusion hindrance of massive system based on the measurement of evaporation residues [5]-[8]. These investigations show that E_{XX} increases with Z_1Z_2 above $Z_1Z_2 \sim 1800$.

We expected that there would be a distinct difference in fusion probability between two types of heavy ion fusions ($Z_1Z_2 > 1800$), one is the fusion of two spherical nculei and the other is the fusion involing largely deformed target, from the consideration that the latter type of fusion has a compact configuration at touching with certain probability.

So, we have measured the ER cross sections of ^{82}Se+^{nat}Ce (Z_1Z_2=1972) [10] and ^{76}Ge+^{150}Nd (Z_1Z_2=1920) [9] in order to investigate the effects of nuclear deformation on the entrance channel. ^{nat}Ce is spherical in shape, whereas ^{150}Nd is largely deformed. From the experimental data, we determied the fusion probability with the help of the survival probability calculated by the statistical model code HIVAP. The parameters describing the deexcitation process in this code was determined so as to reproduce the ER cross section following the fusion of ^{28}Si+^{198}Pt (Z_1Z_2=1092) [9][11].

2. Experiment

Measurement of evaporation residue cross sections following the fusion of ^{82}Se+^{nat}Ce and ^{76}Ge+^{150}Nd was made by using ^{82}Se and ^{76}Ge beam supplied by the JAERI-tandem booster accelerator. The targets were made by sputtering the enriched isotopes (Nd_2O_3) or metal (^{nat}Ce−metal) on a 1.5 or 0.8 μm thick aluminum foil. Typical target thickness was 400 μg/cm^2. The target was set to a rotating target frame in the target chamber.

Since the evaporation residues produced in the present reaction are α decaying nuclei, the evaporation channels could be identified by observing α-decay energies and life-times. The experimental details are described in elsewhere [11][9], and thus only the essence is written here. The evaporation residues emitted in beam direction were separated in flight from the primary beam by the JAERI recoil mass separater (JAERI-RMS)[12]. The separated recoils were implanted into a double sided position-sensitive strip detector (DPSD). Two large area timing detectors, one positioned in front of the DPSD and the other 30 cm upstream the DPSD, were used to obtain the time-of-flight (TOF) signal of incoming particles. The presence of the TOF signal was used to distinguish ER implantation events from the subsequent α-decays, which generate no TOF signals. A two-dimensional spectrum of the energy versus TOF gave a rough estimate of a mass number of the incoming particle, allowing the distinction of ERs from background particles. Alpha-decay events later than 5 μs after the implantation of ER were recorded. Typical energy resolution of the DPSD was 70 keV(FWHM). A silicon surface barrier detector to monitor the beams was set at 45° direction in the target chamber to determine the absolute values of the ER cross sections.

3. Data analysis and experimental results

The identification for a specific channel was made by counting the ER-α_1-α_2 chains, where ER stands for the events produced when the incoming evaporation residue hits the DPSD. The α_1 and α_2 are the first and the second correlated α-decay event. Figure 1 shows the two-dimensional spectrum of α particle energy and the time interval between the ER implantation and the α decay in the reaction of ^{82}Se+^{nat}Ce. All the events shown in Fig.1 satisfy the condition that the position agreement between ER and α event is achieved within (ΔX,ΔY)=(1.0, 1.0) mm. We searched the correlated decay chain, ER-α_1-α_2, to identify the specific evaporation channels with help of the known α decay energy and half-life. The events forming ER-α_1-α_2 chains are shown in Fig.1, where each channel is distinguished by different symbols.

To obtain absolute ER cross sections the efficiency of the ER to be transported to the focal plane detectors through the JAERI-RMS has to be known, which was estimated by

the method described in Ref.[9][13]. The estimated transport efficiency for a specific charge state of ER was multiplied by the charge fraction calculated by the Shima formula [14].

The probability of detecting the α decay of evaporation residues implanted in the DPSD was taken into account in the analysis. This is the function of ER kinetic energy (thus the implantation depth) and the α decay energy.

Evaporation residue cross section for ^{76}Ge+^{150}Nd and ^{82}Se+^{nat}Ce are shown in Fig.2 and Fig.3 as a function of c.m. energy by solid circles with error bars. The error includes both statistical contributions and the estimated uncertainty of 50% coming from the transport efficiency of ERs through the JAERI-RMS. The ER cross sections for ^{28}Si+^{198}Pt is shown in Fig.4. In this figure we also show the fission cross section (open circle) taken from Ref.[9]. Since the compound nucleus ^{226}U formed by this reaction (^{226}U) is very fissile, the fission cross section is well approximated to the fusion cross section.

4. Discussions

We have calculated the ER cross sections of ^{28}Si+^{198}Pt by using the HIVAP code [15] in order to find the parameters describing the deexcitation process of highly excited neutron deficient uranium isotopes. Details of the parameteris we used in this code can be found in elsewhere [11][9]. The partial wave cross section in the fusion ^{28}Si+^{198}Pt was calculated by the CCDEF code [16]. In this fusion calculation, effects of static deformation of projectile and target in addition to the couplings of inelastic excitations of the projectile and target to the fusion process were taken into account. The calculated fusion cross section shown in Fig.4 nicely reproduces the measured data. The partial wave cross section determined by the CCDEF code was inputted to the HIVAP code as an initial spin distribution and the ER cross section was calculated, which can represent the measured data quite well. For the present heavy systems, ^{76}Ge+^{150}Nd and ^{82}Se+^{nat}Ce, the initial spin distribution was again determined by the CCDEF code, and the similar calculaton was made. The results are shown by thick dashed curve (Fig.2;^{76}Ge+^{150}Nd, Fig.3;^{82}Se+^{nat}Ce). For ^{76}Ge+^{150}Nd, the calculation predicts the ^{225,224}U channels in $E_{c.m.}$ =185−195 MeV. This is not consistent with the experimental data, where we observed no evaporation residues in this energy region. Above the Coulomb barrer (V_B =209MeV), however, the calculation agrees well with the measured data. For the fuiosn ^{82}Se+^{nat}Ce, the measred data lies below the calculated cross sections below $E_{c.m.}$ <230 MeV, indicating that there is a fusion hindrance up to $E_{c.m.}$ =1.07V_B (V_B =215.3 MeV for ^{82}Se+^{140}Ce).

The experimental ER cross section $\sigma_{er,c}$ for the observed channel c was used to obtain the fusion probability weighted by the angular momentum l by

$$P_{fus}(E_{c.m.}) = \frac{\sum_c \sigma_{er,c}(E_{c.m.})}{\pi \lambda^2 \sum_l (2l+1) \sum_c w_{er,c}(E_{c.m.}+Q, l)}. \quad (1)$$

The survival probability $w_{er,c}$ against fission for the specific evaporation channel c is a function of the excitation energy $E_{ex} = E_{c.m.} + Q$ (reaction Q-value) and the angular momentum l. This was calculated by the HIVAP code [15] using present parameters. To check if the present statistical model calculation reasonably provides the survival probability, we have determined the P_{fus} for the fusion reaction ^{28}Si+^{198}Pt, which is the light fusion system with Z_1Z_2=1092 and is expected to have no fusion hindrance. The result is shown in Fig.5 as a function of $E_{c.m.}/V_B$, where V_B=125.5 MeV is the spherical Coulomb barrier for this reaction. Above this barrier P_{fus} is almost constant with 1, indicating that the present HIVAP calculation reasonably reproduces the survival probability.

When fission is the dominant deexcitation channel like in the present case, the evaporation residue cross section does not contain information on the fusion of high partial waves, because they will lead to fission. The surviving l range is limited to $l <\sim 25\hbar$, corresponding to an impact parameter less than 1 fm, and hence $P_{\rm fus}$ is reasonably approximated to that of central collision.

The obtained fusion probability for ^{82}Se+$^{\rm nat}$Ce is shown in Fig.5 as a function of $E_{\rm c.m.}/V_{\rm B}$, where $V_{\rm B}$ is taken as 215.3 MeV of ^{82}Se+^{140}Ce. The error in $P_{\rm fus}$ includes only statistical error. Below $E_{\rm c.m.}/V_{\rm B} = 1.15$, $P_{\rm fus}$ for ^{82}Se+$^{\rm nat}$Ce decreases considerably with lowering the bombarding energy, exhibiting the curve similar to the massive system having fusion hindrance [5][7][8]. By finding the $E_{\rm c.m.}$ at which $P_{\rm fus}$ of ^{82}Se+$^{\rm nat}$Ce crosses the $P_{\rm fus}$=0.5 level, we obtained the extra-extra-push energy $E_{\rm XX}$=27±5 MeV for this reaction.

The fusion probability $P_{\rm fus}$ for ^{76}Ge+^{150}Nd is shown in Fig.5 by the solid circles with statistical error bars. $P_{\rm fus}$-values of ^{76}Ge+^{150}Nd is nearly flat with ~1.0 down to $E_{\rm c.m.} \sim V_{\rm B}$. ($V_{\rm B}$=209.0 MeV). This trend is similar to the fusion of ^{28}Si+^{198}Pt which exhibits no fusion hindrance, and the spectrum shows marked contrast to that of ^{82}Se+$^{\rm nat}$Ce. It is apparent that the reaction ^{76}Ge+^{150}Nd has no fusion hindrance above the spherical Coulomb barrier. We did not observe any event in $E_{\rm c.m.} < V_{\rm B}$ and thus the upper limit is shown by the solid reversed-triangle in Fig.5.

Fusion probability can be represented by assuming the fusion barrier distribution to have Gaussian in shape [7][8]. By adjusting the center of the barrier and the standard deviation, we could represent the $P_{\rm fus}$ for ^{82}Se+$^{\rm nat}$Ce as shown in Fig.5 (solid curve). The corresponding partial wave cross section was calculated and inputted to the HIVAP code as an initial spin distribution, and the ER cross section was calculated. This is shown in Fig.3 (solid curve), which reproduces the experimetal ER cross sections quite well.

We tried to reproduce the ER cross section for ^{76}Ge+^{150}Nd by assuming the extra-extra-push energy ($E_{\rm XX}$) to depend on the colliding angle $\theta_{\rm coll}$ of ^{76}Ge on the central axis of ^{150}Nd,

$$E_{\rm XX}(r) = E_{\rm XX0}\frac{r - R_{\rm side}}{R_{\rm tip} - R_{\rm side}}, \qquad (2)$$

and the Coulomb barrier height was raised to an amount, $E_{\rm XX}$, from the original barrier of the CCDEF code. Here, the Coulomb barrier distance r is a function of $\theta_{\rm coll}$. $R_{\rm side}$ (=11.7 fm) and $R_{\rm tip}$ (=14.6 fm) are the distance of side collision and that of tip collision, respectively, for ^{76}Ge+^{150}Nd. When $E_{\rm XX0}$ is taken to be 13 MeV, the ^{224,225}U cross sections are suppressed (solid curve in Fig.2), which becomes consistent with the experimental data. It is noted that we assume no fusion hindrance for the side collision in Eq.(2), meaning that the side collision exhibits larger fusion probability than the fusion starting from the distant touching point.

5. Conclusions

Evaporation residue cross sections for ^{76}Ge+^{150}Nd and ^{82}Se+$^{\rm nat}$Ce were measured in the vicinity of the Coulomb barrier. The fusion of ^{82}Se+$^{\rm nat}$Ce is a rection characterized by the spherical and massive colliding partners with Z_1Z_2 =1972, and fusion hindrance was observed in the form of the extra-extra-push energy of 27±5 MeV. For the reaction ^{76}Ge+^{150}Nd, which has a Z_1Z_2 value of 1920 close to ^{82}Se+$^{\rm nat}$Ce, the obtained fusion probability formed striking contrasts to the fusion of ^{82}Se+$^{\rm nat}$Ce and does not exhibit fusion hindrance at all above the spherical Coulomb barrier. The ER cross section was reproduced when the extra-extra-push energy is assumed only on the tip collision in ^{76}Ge+^{150}Nd. The

enhanced fusion probability at the Coulomb barrier for the ^{76}Ge+^{150}Nd reaction compared to the ^{82}Se+^{nat}Ce, as well as the no fusion hindrance for the side collidion in ^{76}Ge+^{150}Nd suggests that the reaction starting from the compact touching point results in higher fusion probability than the fusion from the distant touching point.

References

[1] A.B. Balantekin and N. Takigawa, Rev. Mod. Phys. **70**, 77 (1998).

[2] M. Dasgupta, D.J. Hinde, N. Rowley, and A.M. Stefanini, Annu. Rev. Nucl. Part. Sci. **48**, 401 (1998).

[3] N. Rowley, G.R. Satchler, and P.H. Stelson, Phys. Lett. B **254**, 25 (1991).

[4] W. Reisdorf, F.P. Hessberger, K. D. Hildenbrand, S. Hofmann, G. Münzenberg, K.-H. Schmidt, J.H.R. Schneider, W.F.W. Schneider, K. Sümmerer, G. Wirth, J.V. Kratz, and K. Schlitt, Phys. Rev. Lett. **49**, 1811 (1982).

[5] J.G. Keller, K.-H. Schmidt, F.P. Hessberger, G. Münzenberg, W. Reisdorf, H.-G. Clerc, and C.-C. Sahm, Nucl. Phys. **A452**, 173 (1986).

[6] C.-C. Sahm, H.-G. Clerc, K.-H. Schmidt, W. Reisdorf, P. Armbruster, F.P. Hessberger, J.G. Keller, G. Münzenberg, and D. Vermeulen, Z. Phys. A, **319**, 113 (1984).

[7] C.-C. Sahm, H.-G. Clerc, K.-H. Schmidt, W. Reisdorf, P. Armbruster, F.P. Hessberger, J.G. Keller, G. Münzenberg, and D. Vermeulen, Nucl. Phys. **A441**, 316 (1985).

[8] A.B. Quint, W. Reisdorf, K.-H. Schmidt, P. Armbruster, F.P. Hessberger, S. Hofmann, J. Keller, G. Münzenberg, H. Stelzer, H.-G. Clerc, W. Morawek, C.-C. Sahm, Z. Phys. A **346**, 119 (1993).

[9] K. Nishio, H.Ikezoe, S. Mitsuoka, and J. Lu, Phys. Rev. C, **62**, 014602 (2000).

[10] K. Nishio, H.Ikezoe, S. Mitsuoka, and K. Satou, S.C. Jeong Phys. Rev. C, submitted.

[11] S. Mitsuoka, H. Ikezoe, K. Nishio and J. Lu, Phys. Rev. C, **62** 054603 (2000).

[12] H. Ikezoe, Y. Nagame, T. Ikuta, S. Hamada, I. Nishinaka and T. Ohtsuki, Nucl. Instrum. Meth. A **376**, 420 (1996)

[13] T. Kuzumaki, H. Ikezoe, S. Mitsuoka, T. Ikuta, S. Hamada, Y. Nagame, I. Nishinaka, O. Hashimoto, Nucl. Instrum. Meth. A, **437**, 107 (1999)

[14] K. Shima, T. Ishihara and T. Mikuno, Nucl. Instrum. Meth. **200**, 605 (1982)

[15] W. Reisdorf and M. Schädel, Z. Phys. A **343**, 47 (1992).

[16] J.O. Fernández Niello, C.H. Dasso and S. Landowne, Comput. Phys. Commun. **54**, 409 (1989).

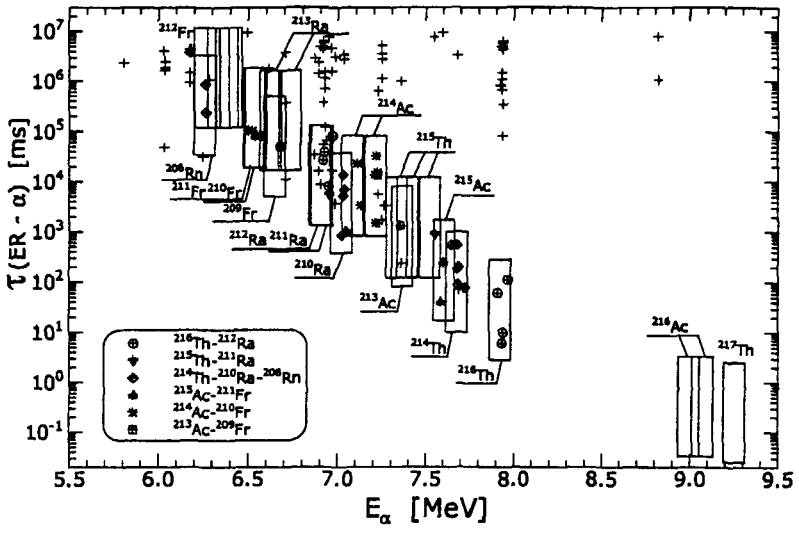

Fig.1 Events of ER-α correlation plotted on the plane of α energy (E_α) and time interval (τ) for ^{82}Se+$^{\mathrm{nat}}$Ce ($E_{\mathrm{c.m.}}$ = 245.0 MeV). Each box represents α decay character having ±60 keV energy width around the known α line and time interval of $\frac{1}{10}T_{\frac{1}{2}} < \tau < 10T_{\frac{1}{2}}$. Correlated chain ER-α_1-α_2 is shown depending on the channel.

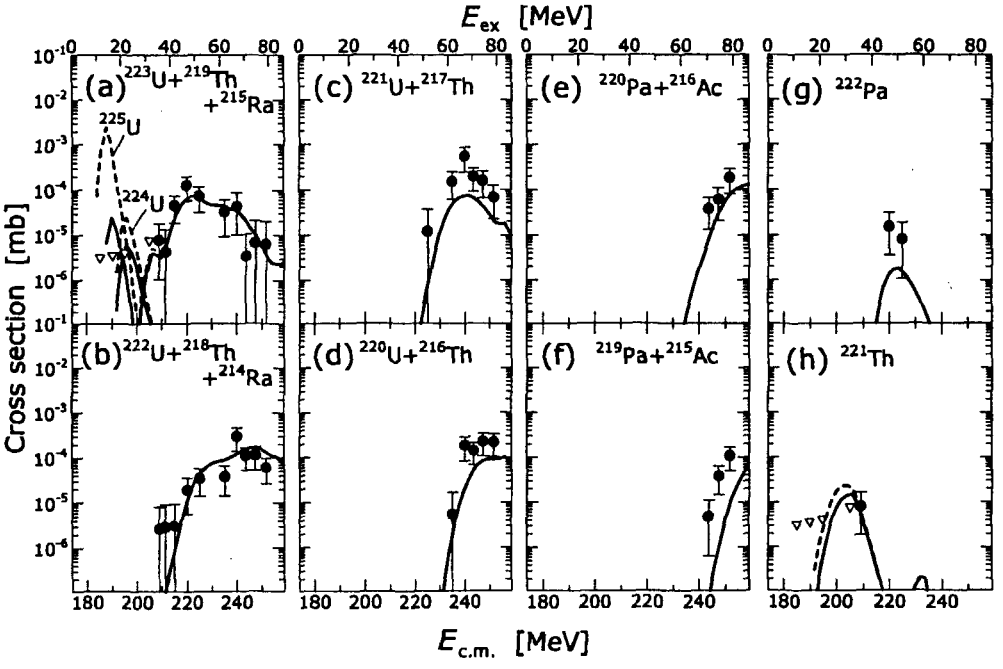

Fig.2 Evaporation residue cross sections for ^{76}Ge+^{150}Nd as a function of c.m. energy. Excitation energy of the compound nucleus, E_{ex}, is also indicated. In (a) and (h), the upper limit of the ER cross section is indicated (reverseed triangle). Dashed curve is the results of the statistical model calculation (HIVAP code) coupled with the CCDEF code. We obtain the solid curves when extra-extra-push energy of eq.(2) is considered in the fusion barrier height.

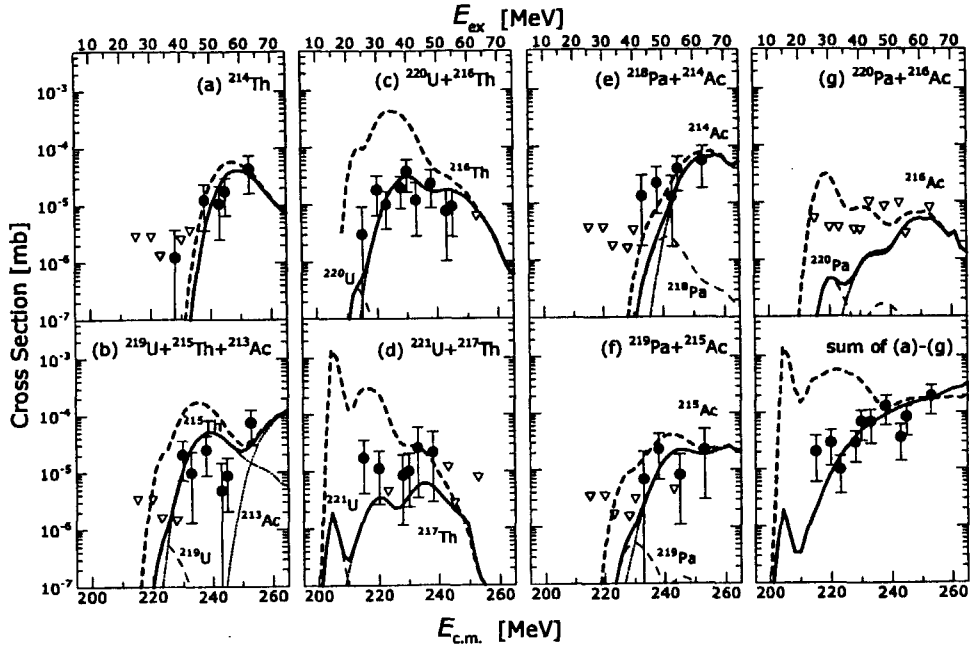

Fig.3 ER cross sections for ^{82}Se+^{nat}Ce. The lower right section is the sum of the cross sections over the channels (a)-(g). Reversed triangle is the upper limit. Dashed curve is the HIVAP calculation with the partial wave cross section determined by the coupled channel calculation. When the Gaussian shape fusion barrier distribution with E_{XX} =27 MeV is adopted in the fusion process, one obtains the solid curve.

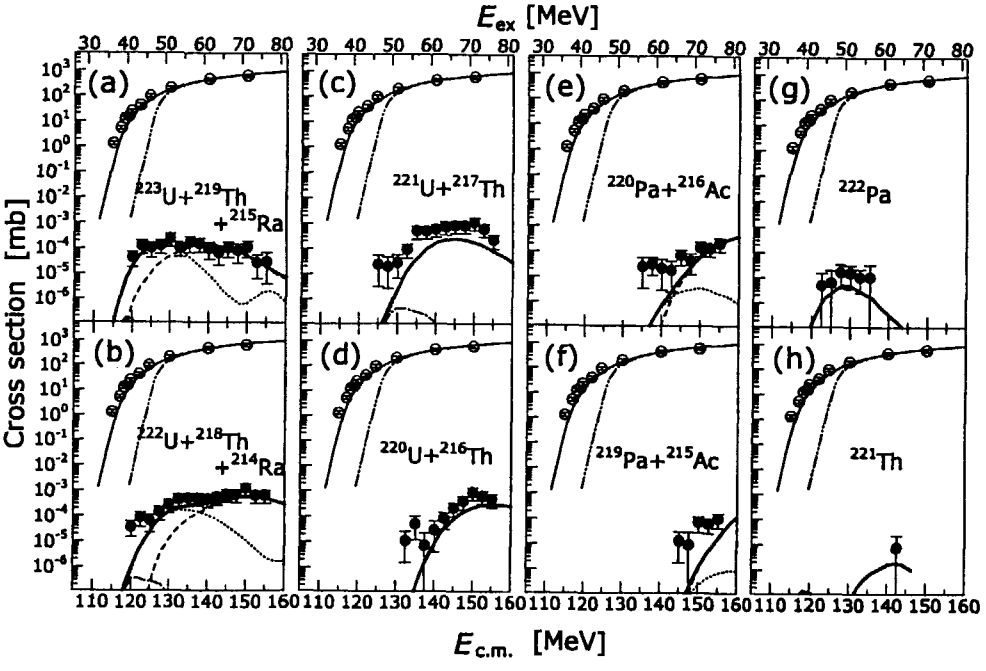

Fig.4 Fusion (open) and evaporation residue (solid) cross sections for ^{28}Si+^{198}Pt. Thick solid curve is the results of the statistical model calculation (HIVAP code) coupled with the CCDEF code. For (a) ~ (f), the cross section includes the components noted in each portion of the figure, and the calculated cross sections of the constituent are show by the dash-dotted (uranium), dotted (thorium or protactinium) and dashed (radium or actinium) curves. The fusion cross section based on the coupled channels calculation is shown by thin solid curve, and the one-dimensional barrier penetration model gives thin dash-dot-dotted curve.

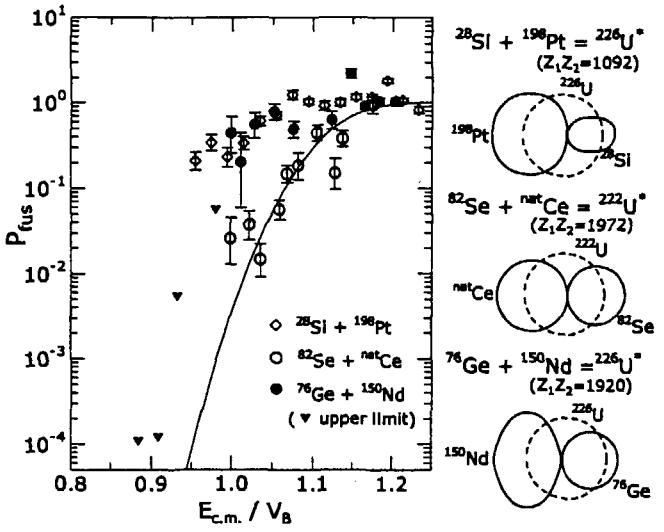

Fig.5 Fusion probability determined from the experimental ER cross sections.

JP0150691

3.29

Nucleon-induced Fission Cross-sections at Transitive Energy Region 20 - 200 MeV

S.Yavshits, O.Grudzevich*, G.Boykov, V.Ippolitov
V.G.Khlopin Radium Institute, St.-Peterburg, Russia
* Institute of Nuclear Power Engineering, Obninsk, Russia
E-mail:yav@mail.rcom.ru

The new approach to the calculation of nucleon induced fission cross sections at energies 20-200 MeV is presented. The cross sections of multiconfiguration fission is calculated as a sum of fission cross-sections for nuclei formed in process of fast (direct) and precompound stage of fission reaction. The intranuclear cascade model is used for description of direct stage and precompound-statistical model for calculation of fission and de-excitation cross sections. Calculated with new optical model parameters sets fission cross sections are compared with experimental data for neutron-induced fission of ^{237}Np, ^{239}Pu, ^{235,238}U and proton-induced fission of ^{235,238}U. Brief information about new code system is also presented.

1. Introduction

Investigation of the properties of nuclear reactions on heavy nuclei induced by nucleons with energies more than 20 MeV is a one of actual problems of modern nuclear physics. The commission of new powerful neutron sources with energies up to 200-250 MeV (such as n_TOF facility in CERN) and need in nuclear data for the development of accelerator-driven hybrid systems lead to the growth of both experimental and theoretical efforts at this energy region.

The energy region 20-200 MeV is a transition region between well-investigated low energy nucleon-induced reactions to reactions where the reaction mechanism is defined by sequential collisions with intranuclear nucleons and as a rule described by the intranuclear cascade model. The enlargement of direct process contribution to the total reaction cross-section leads also to the broadening of spectra of fissionning nuclei in different quantum states and to the appearance of additional fission chances. These facts let us possibility to say on the development of the multiconfiguration fission (MCF) for higher beam energies.

The existing models for the description of nuclear reaction characteristics at the transitive energies can be divided at two main groups. The first one includes pre-equlibrium+statistical approaches to reaction mechanism and the second one is based on the different versions of intranuclear cascade models. The application of statistical codes for higher energies meets with significant difficulties caused mainly by the underestimation of the role of entrance reaction channel and as a consequence by the overestimation of compound nucleus formation cross-section without any account of nuclear configurations populated at the direct stage of the reaction. The second group of models working fairly well for highest energies is in turn can't be directly used for the description of nuclear reactions at transition energies where the effects of nuclear structure have to be taken into account in details.

In the present work the new approach to description of the nucleon-induced reactions at transitive energies is proposed where the detailed statistical code is added by accurate pre-equilibrium and direct reaction stage calculations. The significant reduction of the number of

fitting parameters allows to arise the predicting ability of the approach and to obtain rather reliable nuclear data sets for neutron- and proton-induced reactions on heavy nuclei (fission cross-sections at present as the first step).

2. The model approach and MCFx code system

The fission cross-section for MCF reaction can be presented in the following form [1-3]:

$$\sigma_f(A_i,Z_i,E_i)=\sigma_R(A_i,Z_i,E_i)\cdot\sum_j\int dU_j Y(A_j,Z_j,U_j;p_j,h_j)\cdot\sum_{A_f,Z_f}\int dU_f Y_f(A_j,Z_j;A_f,Z_f;U_j,U_f)\sum_n \sigma_f^n(A_f^n,Z_f^n,U_f^n) \quad (1)$$

The physical sense of this expression is as follows:

- The probability to penetrate of the incoming nucleon to target volume is defined by *the reaction cross-section* σ_R;
- Due to a number of inelastic collisions inside target volume some fast particles escape the volume forming the distribution Y of residual nuclei (configurations) with *mass and charge numbers* A_j,Z_j, *excitation energies* U_j *and particle-hole state* p_j,h_j;
- Each of these nuclei are in the pre-equilibrium state and after emission of a number of pre-equilibrium particles the new distribution Y_f of equilibrated nuclear configurations (A_f,Z_f,U_f) is formed;
- Nuclei in the equilibrium state may undergo fission or particle evaporation forming *fission chances* with *cross-sections of fission chances* σ^n_f.

The code system **MCFx** has been developed for the description of MCF reaction and fission cross-section calculations. The following codes and models are used in **MCFx**:

- The reaction (absorption) cross-section is calculated in the framework of coupled channel method (code ECIS[4]) with modified optical potentials;
- The cascade stage is calculated on the base of adopted Dubna version of intranuclear cascade model [5];
- The pre-equilibrium stage is calculated within HMS version of hybrid exciton model with Monte-Carlo simulation [6];
- The fission/evaporation stage is calculated with modified version of STAPRE code [7,8];

Some results of our calculations are presented in Fig.1-5. The comparison of the calculated reaction cross-sections with experimental data for proton-induced reaction on ^{238}U is shown in the Fig.1 where calculations have been done with real part of optical potential developed by ours recently [3]. The example of intranuclear cascade model calculations are presented in the Fig.2 where the yields of residual nuclei formed due to direct cascade interaction of incoming proton with ^{232}Th are presented. It can be seen form the Figure that for the lowest energies presented the yield of compound nucleus ^{233}Pa is dominate and strongly decreases as energy increases. Such a behaviour indicates on the importance of the accurate account of direct processes for beam energies E ≥ 60-70 MeV in the actinide region. Starting from ~ 100 MeV the formation probability of compound nucleus is close to other one and it is necessary to take into account the fission of mixture of daughter nuclei formed in different quantum particle-hole states with different excitation energies. The pre-compound particle emission also leads to the broadening of spectra (A,Z,E^*) of fissionning nuclei (multiconfiguration fission).

The comparison of fission cross-sections calculated in the MCF approach with experimental ones is shown in the Fig. 3-5 as for neutron-induced and proton-induced fission of actinides. It is seen that our approach is able to reproduce the experimental data with rather

high degree of reliability without any parameter fitting (only standard sets of level density parameters, fission barriers, binding energies and so on [1] have been used in the calculations).

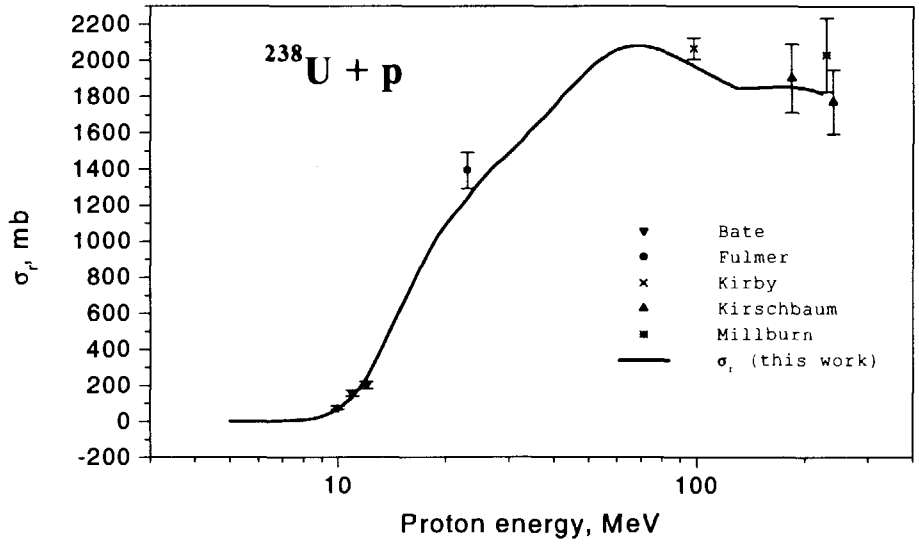

Fig. 1. Experimental and calculated reaction cross-sections for p+^{238}U reaction.

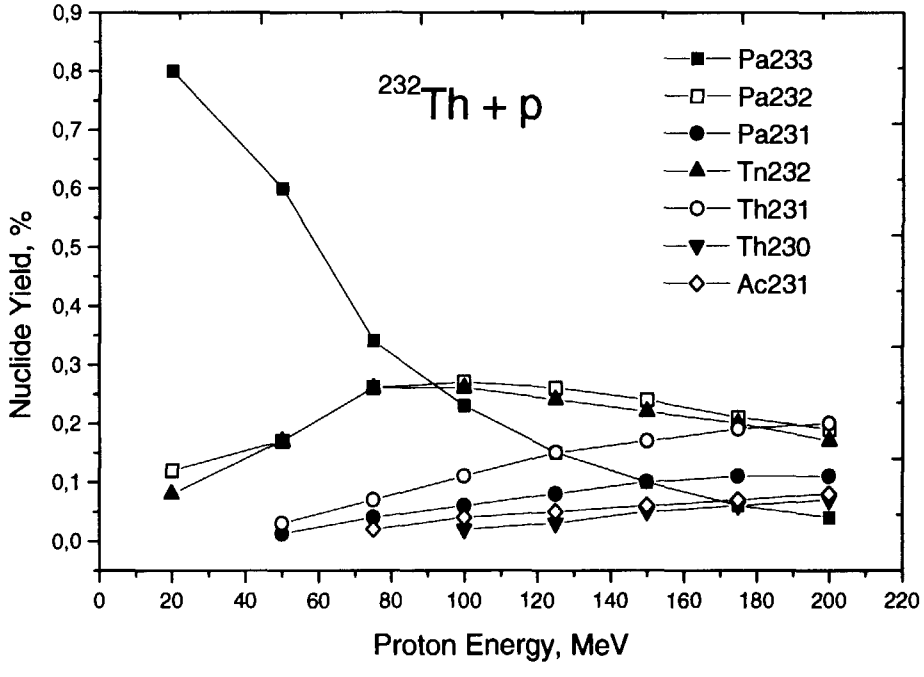

Fig.2. The yield of residual nuclei after cascade stage for proton-induced reaction on ^{232}Th.

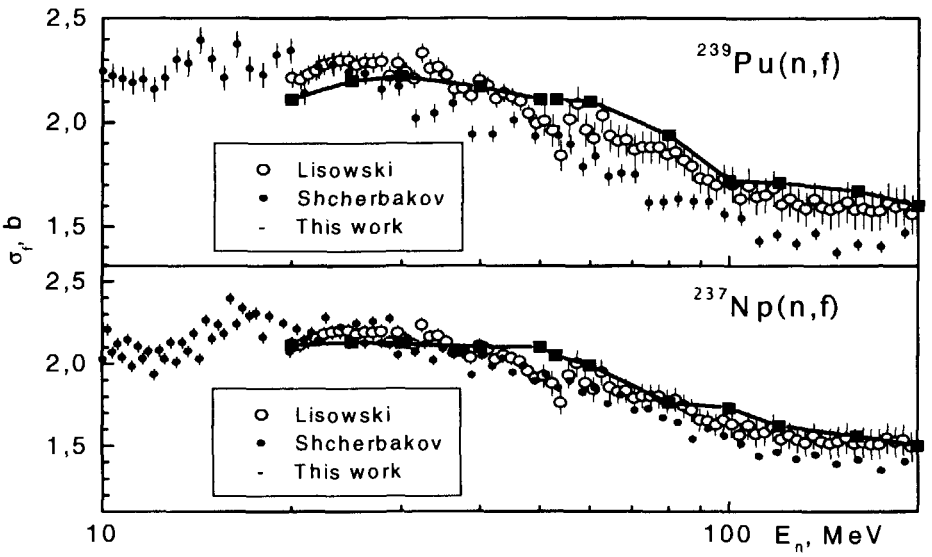

Fig. 3. Fission cross-sections for neutron-induced fission of ^{237}Np and ^{239}Pu.

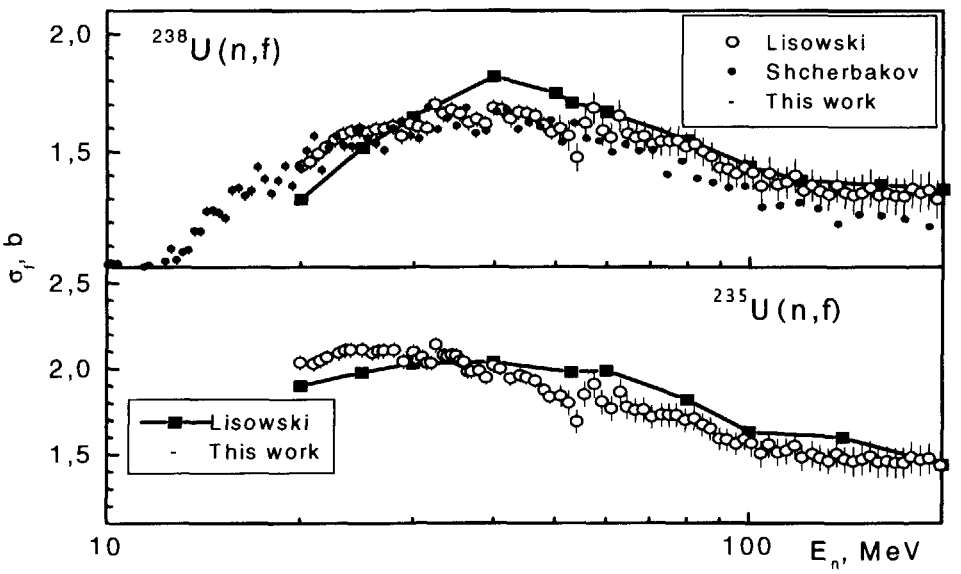

Fig. 4. Fission cross-sections for neutron-induced fission of ^{238,235}U.

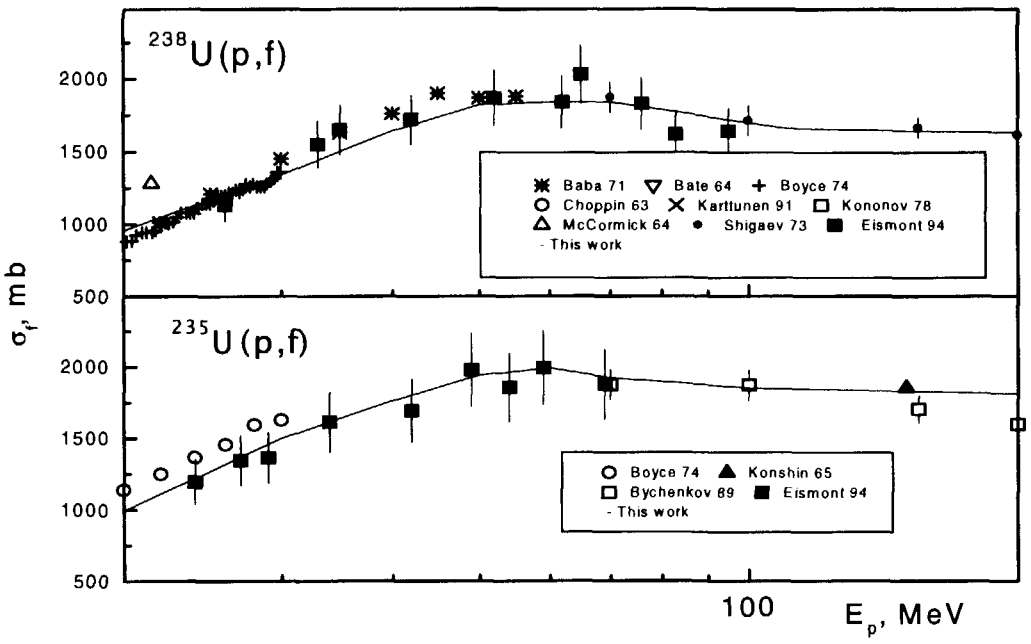

Fig. 5. Fission cross-sections for proton-induced fission of $^{238,235}U$.

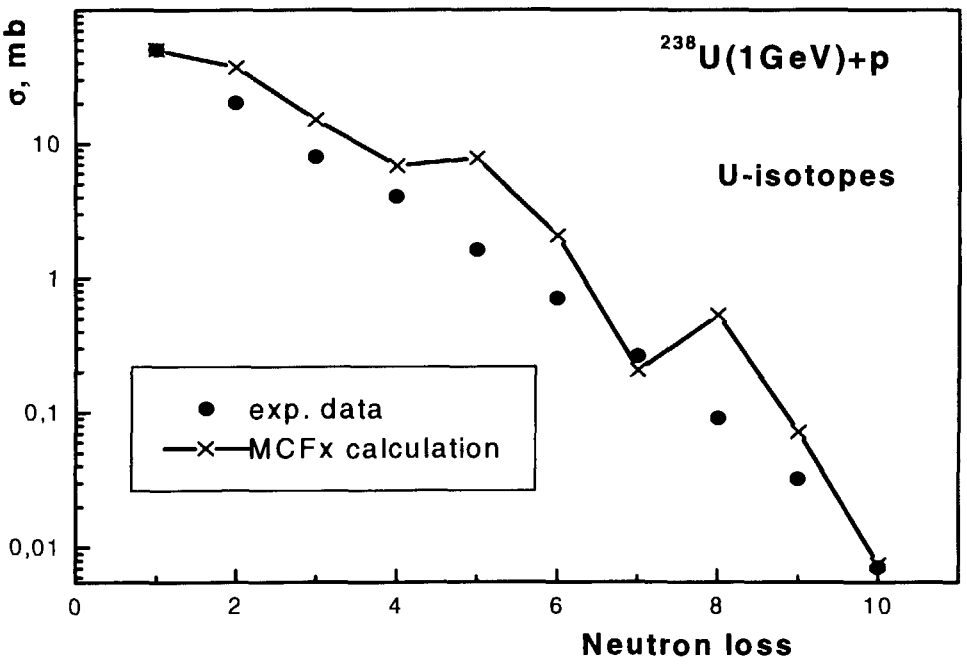

Fig. 6. Neutron loss in ^{238}U+p reaction.

3. Conclusions

- The new approach for nucleon-induced fission cross-section calculations at transition energies has been developed on the base of detailed description of *all* reaction stages (entrance channel, direct, pre-equilibrium and statistical fission/ evaporation stages);
- The importance of account of large number of nuclear configurations is shown; multiconfiguration fission takes place at higher energies;
- The results of MCF cross-sections calculations are in a rather well accordance with experimental data *with standard set of parameters.*

4. Perspectives

Other important point of nuclear data evaluation for nucleon-induced reactions on heavy nuclei is the evaluation of reaction total and elastic cross-sections and yields of reaction products (particles and residual nuclei including fission fragment). The preliminary calculations of residual nuclei yields for ^{238}U (1 GeV) + p shown (Fig. 6) that the results obtained in the framework of approach developed agree satisfactorily with experimental data too. The detailed description of fission chances with inclusion of the statistical model for fission fragment production at each chance let us possibility to compute both fission fragment production and spectra of fission neutrons and to obtain the rather complete set of nuclear data for this kind of reaction.

The work is carried out under ISTC funding as ISTC project #964.

References

[1] Yavshits S., Boykov G., Ippolitov V. et al: Questions of Atomic Science and Technology (Voprosy Atomnoy Nauki i Tekhniki), ser. Nucl.Const., 2000, v.1, p.62
Yavshits S. , Boykov G., Ippolitov V. et al: *ibid*, p.55
[2] Yavshits S., Grudzevich O., Boykov. G. Et al: Proc. of 8th Int. Seminar on interactions of neutrons with nuclei, 2000, Dubna, Russia (to be published).
[3] Yavshits S., Ippolitov V., Boykov G. et al: Proc. of 9th Int. Conf. on Nucl. Reaction Mechanism, 2000, Varenna, Italy, p.219 .
[4] Raynal J. Proc. of a Specialists Meeting, 1996, Bruye'res-le–Chatel, France, p.159.
[5] Gudima K.K., Mashnik S.G., Toneev V.D., Nucl.Phys. A401 (1983) 329.
[6] Blann M., Phys. Rev., 1996, C54 (3), p.1341.
[7] Uhl M. and Strohmaier B., Report IRK 76/01. Vienna. 1976; Addena, Sept. 1976.
[8] Grudzevich O.T., Ignatyuk A.V., Plyaskin V.I.. - Proc. of Int. Conf. On Nuclear Data For Science and Technology, 1988, Mito, Japan. p.1221.

JP0150692

3.30
Validation of neutron data libraries by differential and integral cross sections

B. KIRÁLY , J. CSIKAI and R. DÓCZI
Institute of Experimental Physics, University of Debrecen, 4001 Debrecen, Pf. 105, Hungary
e-mail: csikai@falcon.phys.klte.hu

Some new activation cross sections were measured in the discrepant regions of the excitation functions of the following reactions: Hg-198(n,2n)Hg-197m, Hf-176(n,2n)Hf-175, Tl-203(n,2n)Tl-202, Nb-93(n,2n)Nb-92m, Zr-90(n,2n)Zr-89, Re-185(n,2n)Re-184g, Re-185(n,2n)Re-184m. Results obtained for these reactions could contribute to the improvement of the IAEA Reference Neurtron Activation Library and through it to the quality of neutron data.

The relative values of reflection $R_\beta = \sigma_{\beta,X}/\sigma_{\beta,H}$ and elastic scattering $R_{EL} = \sigma_{EL,X}/\sigma_{EL,H}$ cross sections of thermal neutrons normalized to hydrogen render possible the validation of different neutron data libraries taking the σ_{EL} data from the JEF Report 14. From the R_β/R_{EL} values the recommended libraries for the σ_{EL} elastic scattering cross sections of elements could be deduced.

1. Introduction

The IAEA Nuclear Data Section established in 1994 a Coordinated Research Project for the improvement of the quality of neutron data used in science and technology and to produce a library of neutron activation cross sections. The library produced under the CRP contains cross sections for 256 neutron induced reactions relevant to a wide range of applications [1]. According to the proposed programme goals of this IAEA CRP we have measured, evaluated and calculated a number of new cross sections [2-6] in an international collaboration especially in the discrepant regions of the excitation functions from threshold to 16 MeV. A recent analysis of the excitation functions of (n,2n) reactions has indicated that the precision of the data below 14 MeV should be improved. Therefore, some new and more precise data were determined for the reactions summarized in the abstract of this paper.

The reflection cross section of thermal neutrons as a microscopic parameter for the characterization of the reflection property of substances introduced by Csikai and Buczkó [7] has been determined for 26 elements from H to Pb and for 38 organic and inorganic compounds in addition to the different mixtures of elements. A strong correlation was found between the reflection cross section $\sigma_{\beta,Z}$ and the Maxwellian spectrum averaged elastic scattering cross section $\sigma_{EL,Z}$ of the elements Z. For the cross section ratio $R = \sigma_\beta/\sigma_{EL}$ a value of 0.60 ± 0.02 was obtained in the given source-detector-sample geometry. It seems to be worthwhile to use this method for validation of neutron data libraries of elastic scattering cross sections.

2. Experimental procedure

The activation method and high resolution gamma spectrometry were used for the measurements of (n,2n) cross sections. Neutrons were produced via the $^2H(d,n)^3He$ and $^3H(d,n)^4He$ reactions using D_2 gas and TiT solid targets in the MGC-20 cyclotron (ATOMKI) and

the 200kV intense neutron generator (IEP), respectively. Details of the irradiation arrangements have been described elsewhere [5]. Neutron flux density spectra and mean energies were determined by the multiple foil activation technique combined with the unfolding code SULSA [8] and a pulse height response spectrometer. The mean energy of neutrons has been controlled by using the NEUT code [9]. The variation of the neutron flux in time was monitored by a BF_3 long-counter.

The reflection method based on a point like Pu-Be neutron source and a small BF_3 counter being placed onto the surface of a moderator together with the reflector substance as shown in Fig. 1 is suitable for the determination of the reflection cross section of thermal neutrons. The relative excess count rate $\eta = (I-I_0)/I_0$ measured with (I) and without (I_0) a reflector is proportional to the product of the surface density of atoms N (atoms/cm^2) and the reflection cross section, i.e. $\eta = CN\sigma_\beta$ and so, $\sigma_\beta = \eta/CN$. If $C = 10^{-24}$ cm^2 the value of σ_β is obtained in barn. The sensitive length of the detector is comparable with the 102 mm diameter of the sample, therefore, the reflection cross section is averaged over the ~1cm thick sample. If the target consists of molecules then $\sigma_{\beta mol} = \Sigma_i n_i\sigma_{\beta i} = \eta/CN_{mol}$ where N_{mol} is the number of molecules/cm^2 in the reflector material and n_i is the number of atoms of type i with cross section $\sigma_{\beta i}$ in the molecule. The same expression holds for the mixture of elements, compounds and alloys.

3. Results and conclusions

The (n,2n) cross sections determined by the well known activation expression are summarized in Table 1. Data for Hg-198(n,2n)Hg-197m have been measured for the first time. Cross sections for Hf-176(n,2n)Hf-175 and Tl-203(n,2n)Tl-202 reactions given in ENDF/B-VI and JENDL-3 libraries are in disagreement with the measured trends except of JENDL-3 at 11.2 MeV for Hf. As shown in Fig. 2 the data given in JENDL-3 are lower especially beyond 15 MeV as compared to the ENDF/B-VI. No data are available in the IAEA-NDS library [12] for the above three reactions. The cross section ratios of the Zr-90(n,2n)Zr-89 and Nb-93(n,2n)Nb-92m reactions are used as energy standards around 14 MeV neutron energy. The data given in the three libraries consistent with the measured shape and magnitude of the excitation function for the Zr-90(n,2n)Zr-89 reaction, however, only our data is available at 11.3 MeV, i.e. just at the threshold energy. In the case of Nb-93(n,2n)Nb-92m reaction the measured cross section at 14.1 MeV are in good agreement with the data given in the IAEA-NDS, ENDF/B-VI and JENDL-3 libraries. Considering the strong energy dependence of the reaction cross section near to the threshold further precise measurements are recommended. For Re-185(n,2n)Re-184g and Re-185(n,2n)Re-184m reactions the data are scanty and discrepant. Our measured cross sections support the IAEA-NDS evalutaions, however, the data must be completed and improved both for the isomeric and ground states especially close to the threshold. In Table 2 the evaluated data are given for the same energies as the measured values by interpolation.

The σ_β values were found to be constant up to about 1 cm thick powder, liquid and solid reflectors except for Zn, Fe, Ni and Cu as well as highly absorbing elements (Cl, Co, Ag, Hg) and their compounds. The neutron flux depression caused by such type of samples could be taken into account by a combination of the reflector substances with thin polyethylene foils [10], i.e. the well known reflection cross section (37.6 ± 1.0 b) of CH_2 can be used as a reference (see Fig. 1).

Studies on the cross correlation between the σ_β values deduced from the $\sigma_{\beta mol}$ data have proved that the reflection cross sections are additive. Therefore, the summing expression is valid for different mixtures of elements and compounds and so, the determination of the reflection cross sections is possible even for complex matrices.

The relative values of reflection $R_\beta = \sigma_{\beta,X}/\sigma_{\beta,H}$ and elastic scattering $R_{EL} = \sigma_{EL,X}/\sigma_{EL,H}$ cross sections normalized to hydrogen render possible the validation of different neutron data libraries taking the σ_{EL} data from the JEF Report 14 [11]. The ratio R_β/R_{EL} gives the unity if the measured and accepted data are correct. The recommended libraries for σ_{EL} of different elements are summarized in Table 2. The σ_{EL} data for Hg can be deduced from the measured σ_β value.

Acknowledgements

This work was supported in part by the Hungarian Research Fund (OTKA, T025024) and the International Atomic Energy Agency, Vienna (Contract No. 7687/RO, 9645/R2 and 10886/RO).

References

[1] Reference Neutron Activation Library, (1999), (http://www-nds.iaea.or.at/).

[2] Buczkó Cs. M., Csikai J., Sudár S., Grallert Á., Jonah S. A., Jimba B. W., Chimoye T. and Wagner M. : Phys. Rev., C52, 1940 (1995).

[3] Qaim S. M., Cserpák F. and Csikai J. : Appl. Radiat. Isot., 47, 569 (1996).

[4] Csikai J., Semkova V., Dóczi R., Majdeddin A. D., Várnagy M., Buczkó Cs. M. and Fenyvesi A. : Fusion Eng. Design, 37, 65 (1997).

[5] Dóczi R., Semkova V., Fenyvesi A., Yamamuro N., Buczkó Cs. M. and Csikai J. :Nucl. Sci. Eng., 129, 164 (1998).

[6] Dóczi R., Sudár S., Csikai J. and Qaim S. M. : Phys. Rev., C58, 2577 (1998).

[7] Csikai J. and Buczkó Cs. M. : Appl. Radiat. Isot., 50, 487 (1999).

[8] Sudár S. : INDC(HUN)-026/L, IAEA, Vienna (1989).

[9] Birn I.-G. : Internal Report KFA-INC-IB-1/92, Forschungszentrum Jülich GmbH (1992).

[10] Csikai J., Király B. and Buczkó Cs. M. :20th World Conference of the INTDS, October 2-6, 2000 Antwerp, Belgium.

[11] JEF Report 14, Table of simple integral neutron cross section data from JEF-2.2, ENDF/B-VI, JENDL-3.2, BROND-2 and CENDL-2, NEA OECD, France (1994).

[12] http://iaeand.iaea.or.at/ndspub/rnal/www/rnal.html#top (22 Sept. 2000).

Table 1.
Some measured and evaluated (n,2n) cross sections

Reaction	E_n (MeV)	Measured σ (mb)	IAEA-NDS σ (mb)	ENDF/B-VI σ (mb)	JENDL-3 σ (mb)
$^{198}Hg(n,2n)^{197m}Hg$	11.2 ± 0.20	702 ± 35	—	—	—
	12.5 ± 0.25	910 ± 45	—	—	—
$^{198}Hg(n,2n)^{197g}Hg$	14.7 ± 0.30	1030 ± 60	—	—	—
$^{198}Hg(n,2n)^{197m+g}Hg$	14.7 ± 0.30	1950 ± 70	—	—	—
$^{176}Hf(n,2n)^{175}Hf$	11.2 ± 0.20	1694 ± 85	—	1970	1698
	14.3 ± 0.15	1990 ± 100	—	2043	1890
	14.7 ± 0.30	2050 ±100	—	2045	1895
$^{203}Tl(n,2n)^{202}Tl$	11.2 ± 0.20	1340 ± 70	—	—	2147
	12.5 ± 0.25	1454 ± 80	—	—	2350
	14.7 ± 0.30	1970 ± 110	—	—	2513
$^{93}Nb(n,2n)^{92m}Nb$	11.3 ± 0.20	265 ± 25	323	—	323
	14.1 ± 0.15	460 ± 5	473	—	463
$^{90}Zr(n,2n)^{89}Zr$	11.3 ± 0.20	6.4 ± 1.0	—	—	—
	14.1 ± 0.15	626 ± 6	627	622	634
$^{185}Re(n,2n)^{184g}Re$	11.2 ± 0.20	1530 ± 100	1507	—	—
	14.3 ± 0.15	1670 ± 95	1773	—	—
	14.7 ± 0.15	1780 ± 120	1787	—	—
$^{185}Re(n,2n)^{184m}Re$	11.2 ± 0.20	322 ± 50	368	—	—
	14.3 ± 0.15	380 ± 50	434	—	—
	14.7 ± 0.15	390 ± 70	436	—	—
$^{185}Re(n,2n)^{184m+g}Re$	11.2 ± 0.20	1852 ± 115	1875	1876	1588
	14.3 ± 0.15	2050 ± 110	2207	2205	2029
	14.7 ± 0.15	2170 ± 130	2223	2224	2044

Table 2.

Relative values of reflection and elastic scattering cross sections of thermal neutrons

Element	R_β in %	R_{EL} in %	R_β/R_{EL}	Accepted library
H	$\sigma_{\beta,H}$ = 17.3 b	$\sigma_{EL,H}$ = 29.026 b	1.000	<JEF Rep.>
C	17.34	17.01	1.019	JEF-2.2
N	35.84	35.69	1.004	JENDL-3.2
O	14.45	13.87	1.042	ENDF/B-VI
F	13.87	14.14	0.981	JEF-2.2
Na	10.66	10.65	1.001	JEF-2.2
Mg	13.00	12.42	1.047	JENDL-3.2
Al	4.97	4.99	0.996	JEF-2.2
Si	7.69	7.62	1.009	JENDL-3.2
S	3.58	3.58	1.000	JENDL-3.2
Cl	57.80	57.74	1.001	ENDF/B-VI
K	7.51	7.59	0.989	JEF-2.2
Ca	9.83	10.08	0.975	CENDL-2
Ti	14.45	14.23	1.015	JENDL-3.2
Mn	7.69	7.55	1.019	ENDF/B-VI
Fe	38.15	39.20	0.973	CENDL-2
Co	20.81	20.91	0.995	JENDL-3.2
Ni	61.85	61.70	1.002	BROND-2
Cu	27.17	27.02	1.006	CENDL-2
Zn	14.45	14.57	0.992	BROND-2
Sr	18.38	18.48	0.995	JENDL-3.2
Zr	24.28	22.37	1.085	JEF-2.2
Nb	21.96	21.89	1.003	JENDL-3.2
Sn	17.92	16.97	1.056	BROND-2
Sb	12.72	12.87	0.988	JENDL-3.2
Hg	27.63	no data	—	—
Pb	38.73	38.69	1.001	JEF-2.2

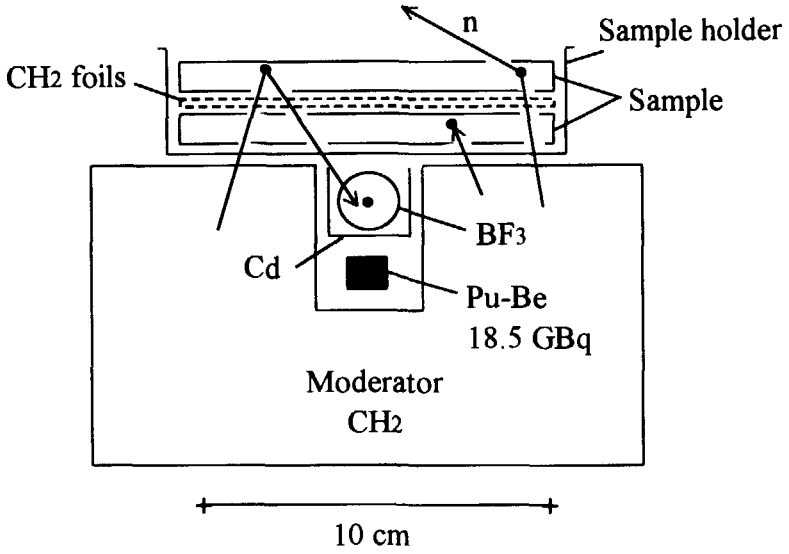

Fig. 1. Geometrical setup for reflection cross section measurements (CH_2 layer for absorbing samples)

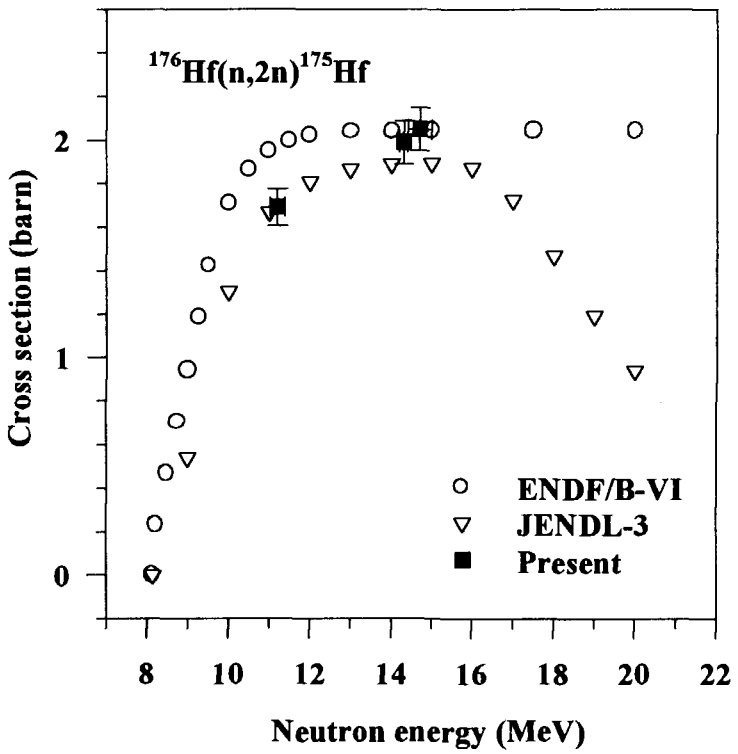

Fig. 2. A comparison of the measured and evaluated data for Hf-176(n,2n)Hf-175 reaction

JP0150693

3.31

Determination of Level Density Parameters for Light Nuclei

Toru Murata
AITEL Corporation
1-5-9 Shiba,Minato-ku,Tokyo
E-mail: murata@aitel.toshiba.co.jp

Level density parameters of light nuclei (Li to Ne, A=6-20, 36 nuclides) were determined for the sake of cross section evaluation of light nuclei. Nuclear temperature **T** of the constant temperature type level density formula, Fermi gas type parameter **a** and connecting energy point of both formulae Ec have been determined following the formalism made by Gilbert and Cameron, who did not give level density parameters for these light nuclei.

1. Introduction

JNDC is now evaluating the high energy cross sections for various nuclides, including light nuclei and also evaluating the (α ,n) reaction cross sections. For these cross section evaluation, statistical nuclear cross section calculation codes are utilized and level density parameters are required. Level density parameters for nuclides which atomic number Z larger than 10 have been prepared by Gilbert and Cameron/1/, and somewhat modified to reproduce experimental data by many researchers. However, for light nuclides, which mass number below 20, systematically determined level density parameters were not available presently.

2. Determination Method

The following formulae of level density defined in the paper of Gilbert and Cameron were adopted.

Fermi Gas Model ($E >= E_C$)

$$\rho_G(E,J) = \frac{\exp[2\sqrt{a(E-\Delta)}]}{C_0(E-\Delta)^2} S(J,E) \quad ,$$

where

$C_0 = 12\sqrt{2}(0.146)^{3/2} aA$, and

$\Delta = 0$ for odd-odd nucleus, $\Delta = 11/\sqrt{A}$ for odd-even or even-odd nucleus and $\Delta = 22/\sqrt{A}$ for even-even nucleus in unit of Mev .

Constant Temperature Model ($E < E_C$)

$$\rho_T(E,J) = \rho_G(E_C,J)\exp[(E-E_C)/T]S(J,E)$$

Spin dependent term S(J,E) is common to the Fermi-gas model and the constant temperature model and given by

$$S(J,E) = (2J+1)\exp[-(J+1/2)^2/(2\sigma(E)^2)],$$

where spin cutoff parameter is given by

$$\sigma(E)^2 = 0.146[a(E-\Delta)]^{1/2}A^{2/3}$$

The nuclear temperature T in the constant temperature model was determined to reproduce the stair-case plot of the level scheme /2/ of the nucleus with the least squares fit method. Then Fermi-gas model level density parameter **a** was determined by connecting the high excitation region level density to the low energy region constant temperature type level density at Ec with the following relation ;

$$a = (\frac{1}{T} + \frac{2}{Ec-\Delta})^2(Ec-\Delta)$$

The connection energy Ec was determined by changing it by rough energy step, say 5 MeV, and to give the best fit.

Examples of the staircase plot and fitted curve are shown in Fig.1.

3. Result and Discussion

Obtained level density parameters are summarized in Table 1. For some small mass number nucleus, number of levels is small up to several tens MeV, and can not reproduce the staircase plot well. Mass number dependence of nuclear temperature **T** and Fermi gas type parameter **a** are shown in Fig.2 and Fig.3, respectively. There will be some effects of the shell model , pairing energy and isospin of each nuclide. These effects will be studied in the future works.

The spin cutoff parameter is studied for ^{17}O, of which spin-parity of many levels are known, by plotting the number of given spin levels and comparing with the spin dependent term S(J,E). Figure 4 shows the spin distribution of ^{17}O. The error bar in the figure represents the square root of the level number. The fitted spin cutoff parameter is somewhat smaller than the value calculated with the above formula.

References

/1/ Gilbert,A,Cameron,A.G.W.: Can.J.Phys.43,1446(1965)

/2/ Evaluated Nuclear Structure Data File compiled in NuDat,BNL

Table 1. Summary of the present level density parameters

Nuclide	T(MeV)	a(1/MeV)	Ec(MeV)	Δ(MeV)	Remarks
Li-6	300	0.09	50.0	0	
Li-7	34.0	0.39	20.0	4.16	
Li-8	11.6	0.69	20.0	0	
Be-6	500	0.02	500	8.98	not reproduced well:5 levels
Be-7	29.2	0.41	20.0	4.16	
Be-8	30.0	0.70	15.0	7.78	not reproduced well
Be-9	10.8	0.75	20.0	3.67	
Be-10	4.4	1.89	20.0	6.96	
B-9	13.2	0.64	20.0	3.67	
B-10	6.7	1.24	20.0	0	
B-11	6.4	1.27	20.0	3.32	
B-12	6.0	1.42	20.0	0	
C-10	4.4	1.89	20.0	6.96	5 levels
C-11	6.2	1.32	20.0	3.32	
C-12	6.3	1.32	15.0	6.35	
C-13	5.1	1.58	15.0	3.05	
C-14	3.2	2.58	15.0	5.88	
N-12	4.9	1.71	15.0	0	
N-13	6.1	1.35	20.0	3.05	
N-14	4.4	1.97	5.0	0	
N-15	6.0	2.58	5.0	2.84	
N-16	3.1	2.73	10.0	0	
O-14	5.9	1.37	20.0	5.88	
O-15	3.4	2.36	10.0	2.84	
O-16	3.6	2.27	15.0	5.50	
O-17	3.1	2.90	15.0	2.67	
O-18	2.9	3.41	20.0	5.19	
O-19	2.5	3.92	15.0	2.52	
O-20	2.9	3.44	20.0	4.92	
F-17	2.2	3.88	10.0	2.67	
F-18	3.3	2.86	15.0	0	
F-19	2.5	3.92	15.0	2.52	
F-20	2.2	4.28	10.0	0	
Ne-18	2.8	3.59	20.0	5.19	
Ne-19	3.3	3.05	20.0	2.52	
Ne-20	2.5	3.59	15.0	4.92	

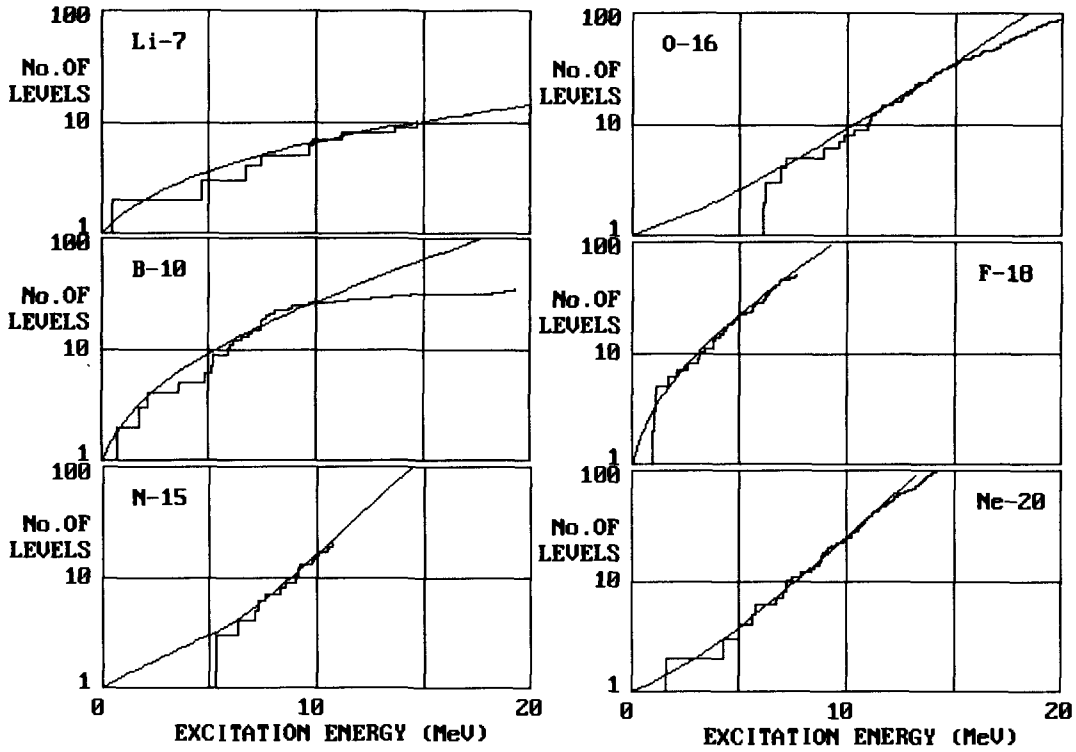

Fig.1 Examples of the stair-case plot of level schemes and fitted curves (solid line).

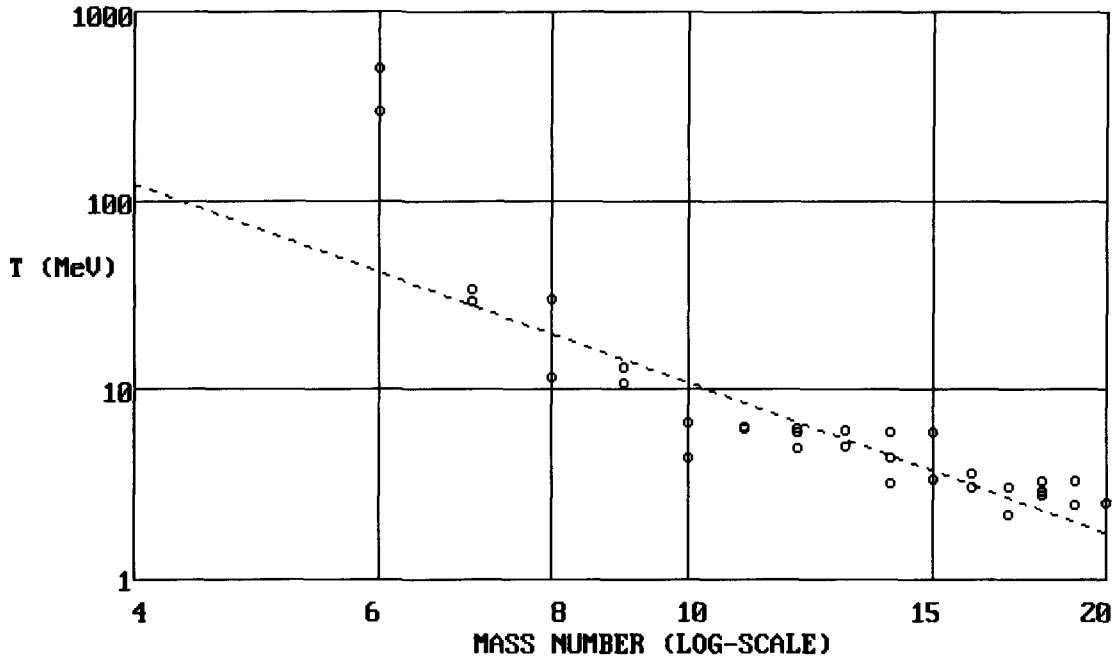

Fig.2 Mass number dependence of nuclear temperature (the dashed line represents log-log linear least squares fit: $T=4.74\times10^{3}A^{-2.63}$)

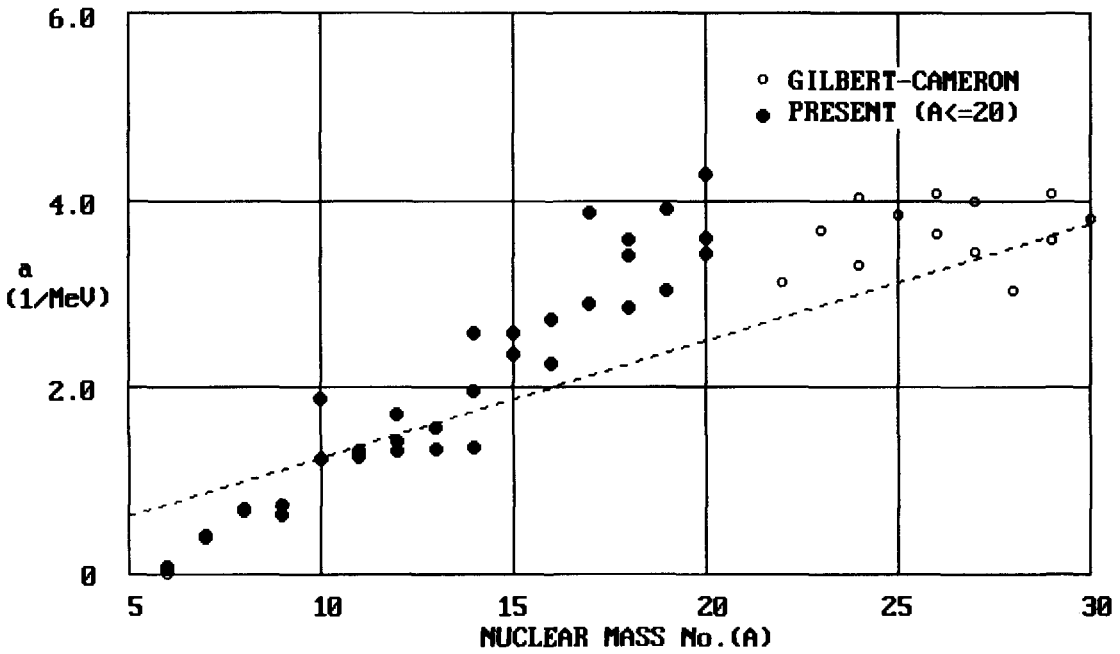

Fig.3 Mass number dependence of Fermi gas type **a** parameters. The parameters in A>20 region were determined by Gilbert and Cameron/1/ (the dashed line represents the line **a**=A/8)

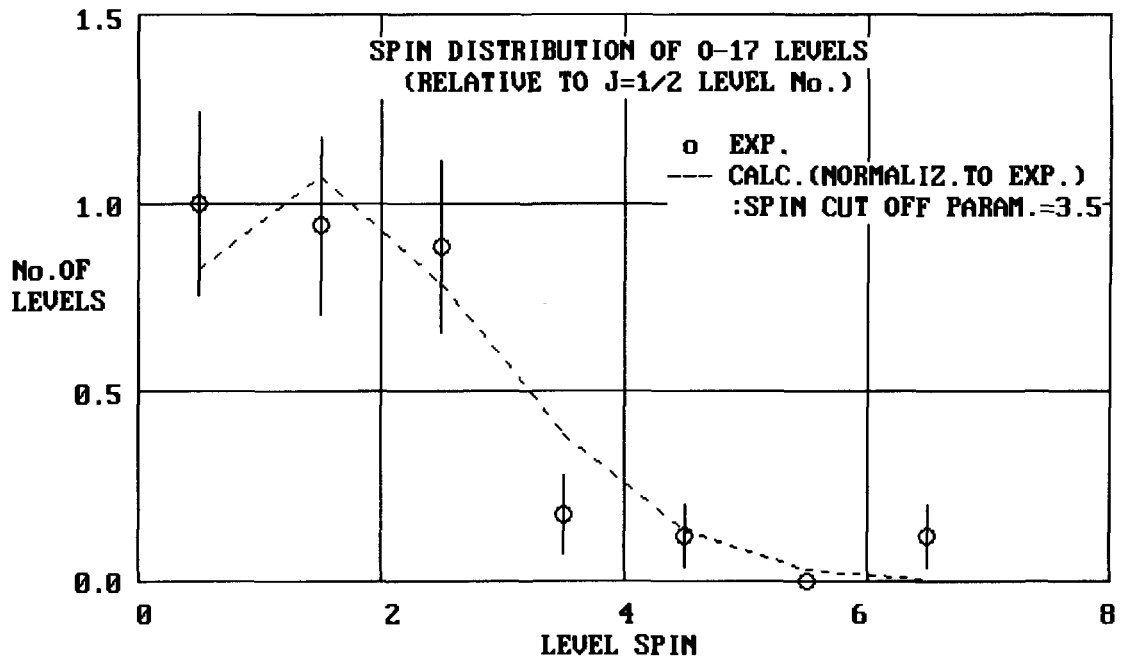

Fig.4 Spin distribution of ^{17}O levels to determine the spin cutoff parameter.(Error bars represent the square root of level number)

JP0150694

3.32

Unified Model of Nuclear Mass & Level Density Formulas

Hisashi Nakamura
8-5-15 Nishituruma,Yamato-City, Kanagawa-ken 242-0005
e-mail:kyu-san@kc4.so-net.ne.jp

The objective of present work is to obtain a unified description of nuclear shell, pairing and deformation effects for both ground state masses and level densities, and to find a new set of parameter systematics for both the mass and the level density formulas on the basis of a model for new single-particle state densities. In this model, an analytical expression is adopted for the anisotropic harmonic oscillator spectra, but the shell-pairing correlation are introduced in a new way.

1. Introduction

In recent years most statistical theory calculations of nuclear reactions have been carried out by using the semiempirical level density formula proposed by Gilbert and Cameron [1] in 1965 , which is based essentially on the Fermi-gas (FG) model and seems to be enough to predict the level densities at a narrow range of excitations. However, it has been in fact well established [2] that the extrapolation of this formula to a wide range of excitation energies is subject to large errors, and that washing out of shell effects should be considered. On the other hand, the energy dependent pairing corrections with the shell-pairing correlation seems to be only correctly considered by means of the microscopic Fermi-gas model or of the Extended Thomas-Fermi plus Strutinsky Integral (ETFSI) model [3], which are based on the numerical shell-model calculations and also on the BCS formalism. The systematics of nuclear level density depends strongly on the shell, pairing and deformation effects. The nuclear mass formula has been used to determine the "empirical" shell, pairing and deformation energies at the ground state, which are defined as the corrections on the liquid-drop part in the mass formula. The most often used correction energies are those of Myers and Swiatecki (M & S) [4], but the discrepancy in absolute values of shell corrections may amount up to 2 MeV.

The main aim of the present work is to find a new set of parameter systematics for both the mass formula and the level density formula on the basis of the new single-particle state density model. In this model, an analytical expression is adopted for single-particle spectra, but the shell-pairing correlation terms are introduced in a new way [5]. In the next sections typical contents and results of the present model are shown, those are physical meanings of unified model, systematics of parameters for the ground state (mass formula) and for the excited state (level density formula).

2. Basic parameters in unified model

Pysical contents of a unified model are shown as follows :

Pysics of model and parameters

Macroscopic model

Finite range droplet model (FRDM : Berkeley Group, 1995) [6]

Quadrupole deformation : vibration and rotation

Microscopic corrections

Anisotropic harmonic oscillator potential

Single-particle spectrum (analytical expression) :

Shell & Pairing Correlation (***SPC***)

Moments of inertia with pairing-rotation correlation

Systematics of parameters

Asymptotic level density parameter	$[a = \alpha A]$	A = mass number
Average frequency of oscillator	$[\omega = \omega_0 A^{1/3}]$	
	$(\alpha,\ \omega_0)$ = fitting constants	

Single-particle spectrum :

$$g(\varepsilon)=\Sigma_X g_X\{1+\tfrac{1}{3}f_X\Sigma_i\cos\omega_i(\varepsilon-\varepsilon_0)\}\{1-\cos\omega_{PX}(\varepsilon-\lambda_X)\} \quad (1)$$

where $\omega_1=\omega_2=\omega_\perp \approx \omega(1+\frac{1}{3}\delta)$, $\omega_3=\omega_\parallel \approx \omega(1-\frac{2}{3}\delta)$, δ = quadrupole deformation parameter, ω = average frequency $= 2\pi/\hbar\omega_{sh}$, ($\hbar\omega_{sh} = 41A^{-1/3}$), g_X = single-particle level density (2-fold degenerate), f_X = amplitude of shell-structure, ε_0 = main-shell energy, λ_X = Fermi level, (x ≡ p or n), ω_{PX} = quasi-particle frequency ($= 2/\Delta_{0X}$), $\frac{1}{2}\, g_X\Delta_{0X}^2 = 2\, g_X/\omega_{PX}^2$, Δ_{0X} = energy-gap at the ground state (from even-odd effects of mass formula). In Fig.1 shell,pairing and deformation corrections to the droplet terms (FRDM,1995) [7] are shown, which are obtain by means of shell-wise average procedures and of polynomial fitting teckniques. A new mass formula consists from those corrections terms shown in Fig.1. Proton and neutron shells are defined in Table 1 and there shown are theoretical (fitting) errors of the new formula and of the previous formulas. Among of formulas Present S & P means the case of direct use of simulated data for shell,pairing and deformation corrections from existent experimental mass data. Temperature dependence of thermodynamic quantities are shown in Fig.2 to present the assumed behavior of quasi-particle spectrum of a new single-particle spectrum Eq.(2).

3. Systematics of parameters

Values of main parameters, quadrupole deformation parameter δ, α and ω_0 are shown in Figs.3 and 4, the later shows effects of collective enhancements for deformed nuclei.

4. Conclusion

The above mentioned results related to systematics of parameters α and ω_0 will give important effects on calculated evaporation spectra. Confirmation of this facts is an objective in future.

Autuor would like to thank menbers of the Working Group on parameters for theoretical calculations in the JNDC for their valuable comments on this work.

References

[1] Gilbert A. and Cameron A.W.G.:Can.J.Phys.43,1446(1965).
[2] Vonach H. *et al.*:Phys.Rev.C 38,2541(1988).
[3] Goriely S. :Nucl.Phys.A605,28(1996).
[4] Myers W.D. and Swiatecki W.J.:Ark.Fys.36,343(1967).
[5] Nakamura H.:IAEA report, INDC(JPN)-172/U(1994).
[6] Moller P.,Nix J.R.,Myer W.D. and Swiatecki W.J.:Atom.Data Nucl.Data Tbl.59,185(1995).
[7] IAEA-TECDOC-1034 (1998).
[8] Migdal A.B.:Nucl.Phys.13,655(1959).

Shell-group		No. of nuclei	[σ th (MeV)]			
Z-	N-		M&S(1967)	M&N(1995)	Present S-P	New formula
20	20	24	6.625	1.477	0.191	0.270
	28	33	9.201	1.363	0.107	0.232
28	28	54	6.528	1.146	0.391	0.415
	50	53	3.969	0.377	0.114	0.250
50	50	192	2.368	0.617	0.329	0.416
	82	267	1.330	0.709	0.318	0.452
82	82	179	1.114	0.479	0.477	0.599
	126	418	0.969	0.484	0.452	0.615
126	126	62	1.118	0.374	0.228	0.719
	184	232	1.302	0.393	0.448	0.534
Total		***1514***	***2.521***	***0.621***	***0.393***	***0.445***

Table 1 Classification into shell-wise groups of nuclei in RIPLE2(1998) experimental mass data and comparison of theoretical fitting error of new mass formulas with those of other previous ones. Present S-P means the results of shell-wise average for shell & pairing corrections by using the FRDM terms by M&N(1995)[6]. Theoretical error σ_{th} is a measure of overall quality representing a precison and is defined by,

$$\sigma_{th}^2 = \frac{1}{\sum w_i} \sum w_i \left[(M^i_{exp} - M^i_{th})^2 - \sigma^{i2}_{exp} \right], \qquad (4)$$

$$w_i = \frac{1}{(\sigma^{i2}_{exp} + \sigma_{th}^2)^2}$$

and is easily obtained in a few iterations.

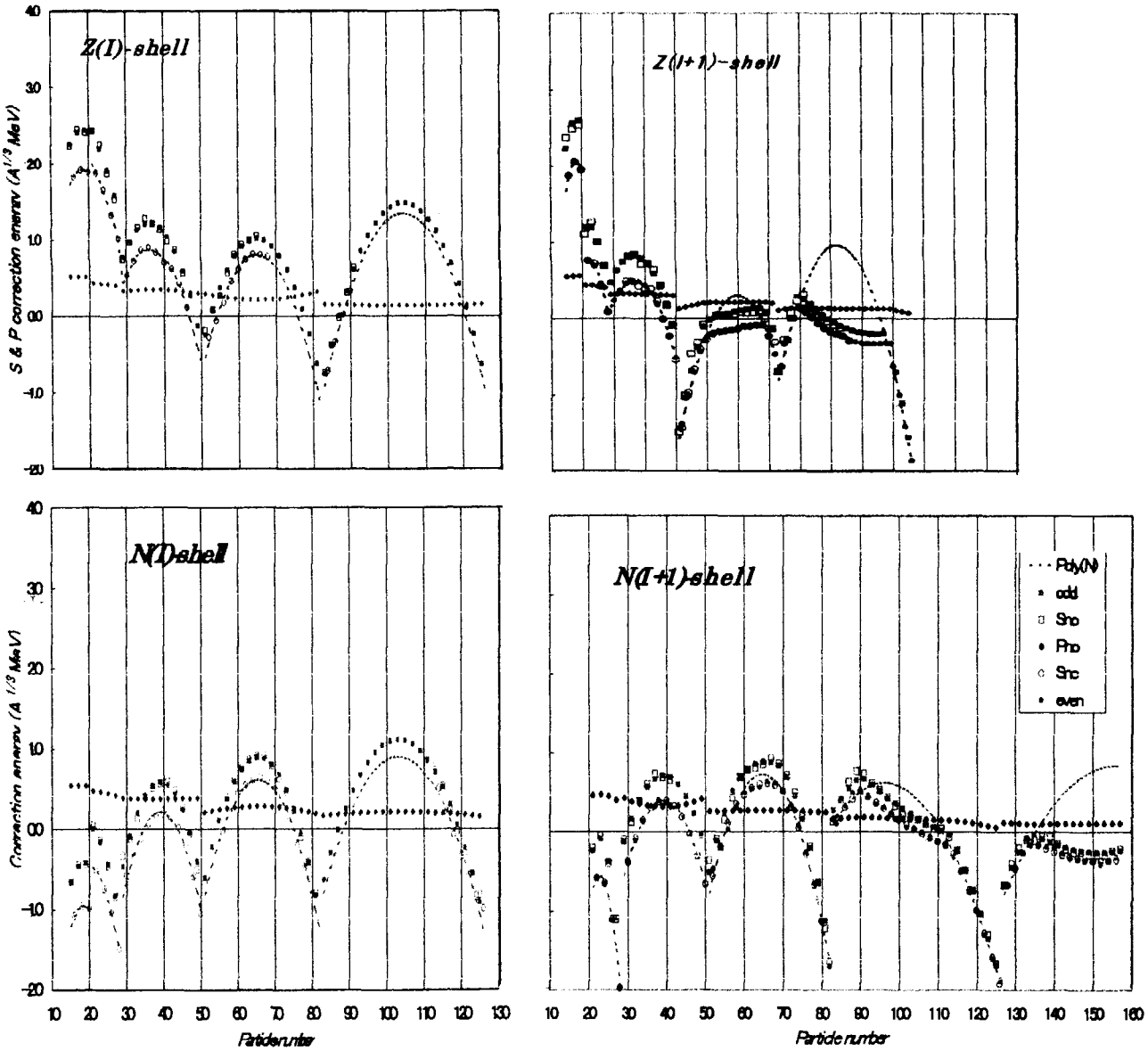

Fig.1 Shell & pairing correction energies of a new mass-formula. Poly (----) is the polynomial expressions of shell corrections without deformation effects for even-even nuclei. Symbols (□,○) represent the shell-wise averaged shell & pairing corrections simulated on the basis of RIPL2 [7] experimental mass-excess data (1995). Symbol (◆) is pairing energies fitted by using shell-pairing correlation term of Eq.(1) for odd-particle numbers. Values of mass-formula are presented by solid symbols, ■ and ●, for odd- and even-particle number, respectively.

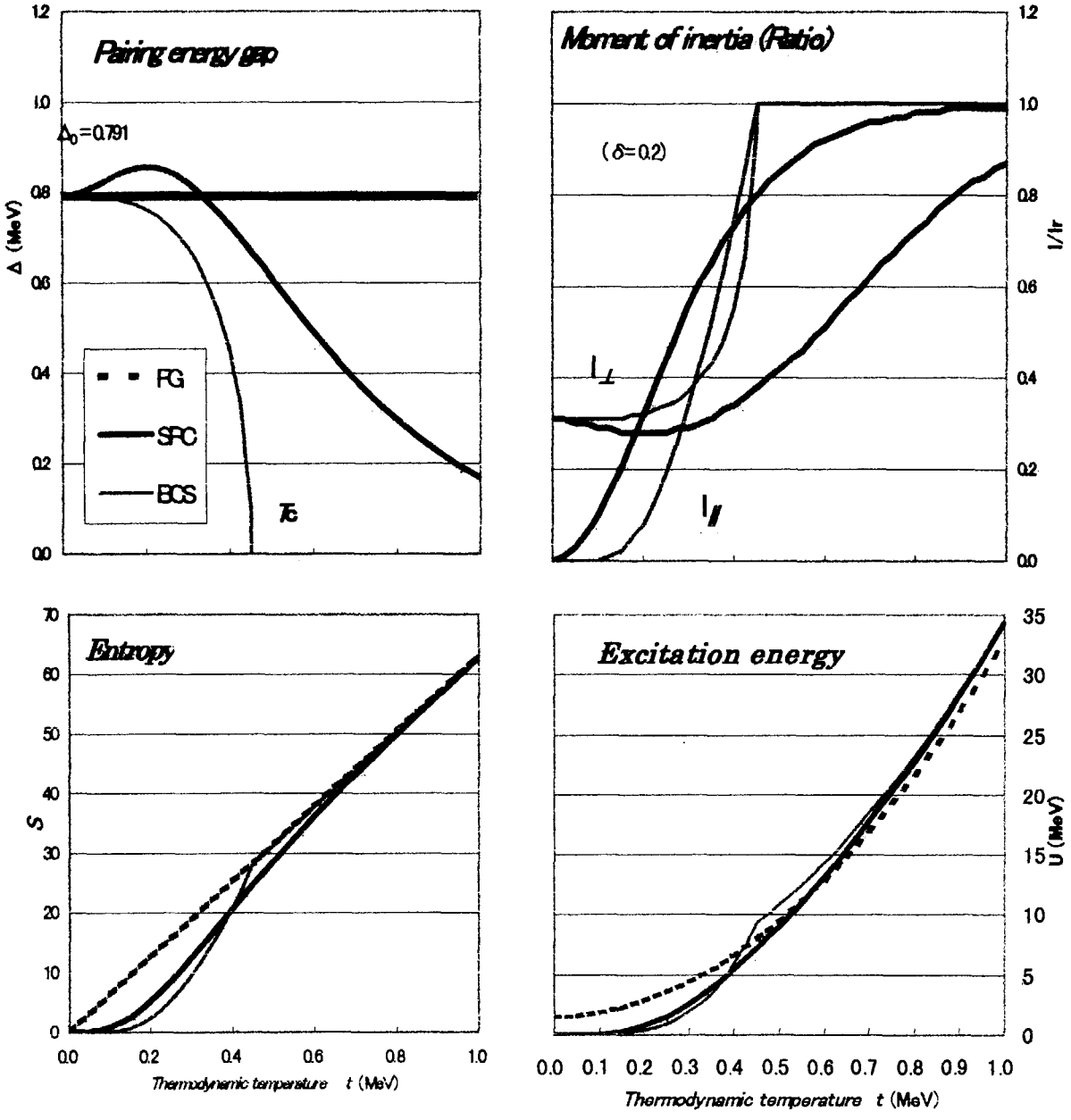

Fig.2 Temperature dependence of pairing correlations in nucleus. Comparisons of 4 kinds of thermodynamic quantities between three models, FG , BCS and BCS (present model). Those of BCS are based on analytical approximations,and the existence of a sharp phase transition point (Tc) is a special feature. For both BCS and SPC moments of inertia for two different directions, parallel and perpendicular to rotational symmetry axis are presented, the later ones do not tend to zero at the ground stste due to the existence of pairing-rotation correlations (Migdal A.B.,1959)[8]. Values of present model are based on the following Eq.(2) for a case of fx = 0 in Eq.(1) in the text and on the method of statistical thermodynamics :

$$g(\varepsilon) = g_0\{1-\cos\omega_P(\varepsilon-\lambda)\} \qquad (2)$$

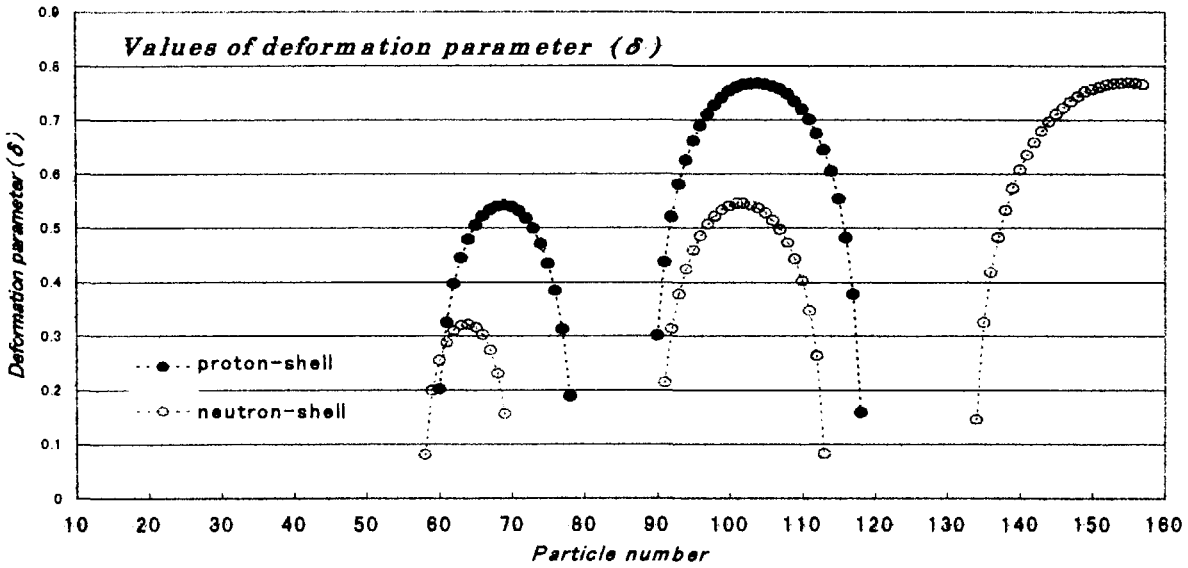

Fig.3 Values of quadrupole deformation parameter (δ).for [Z(I)−N(I+1)]-shells. Equation for determining values of δ is from Eq.(1)

$$Exd(\delta,\chi) = 2g_0 \times \omega^{-2} f_\chi \{ \cos 2\pi d_i(\chi - 1/2) - \frac{1}{3} \Sigma d_i^{-2} \cos 2\pi d_i(\chi - 1/2) \} \quad (3)$$

$$d_1 = d_2 = (1 + \frac{1}{3}\delta), \qquad d_3 = (1 - \frac{2}{3}\delta)$$

where Exd(δ , χ) is deformation energy derived from the mass formula shown in Fig.1, χ the occupation fraction of particle (p or n) in the shell.

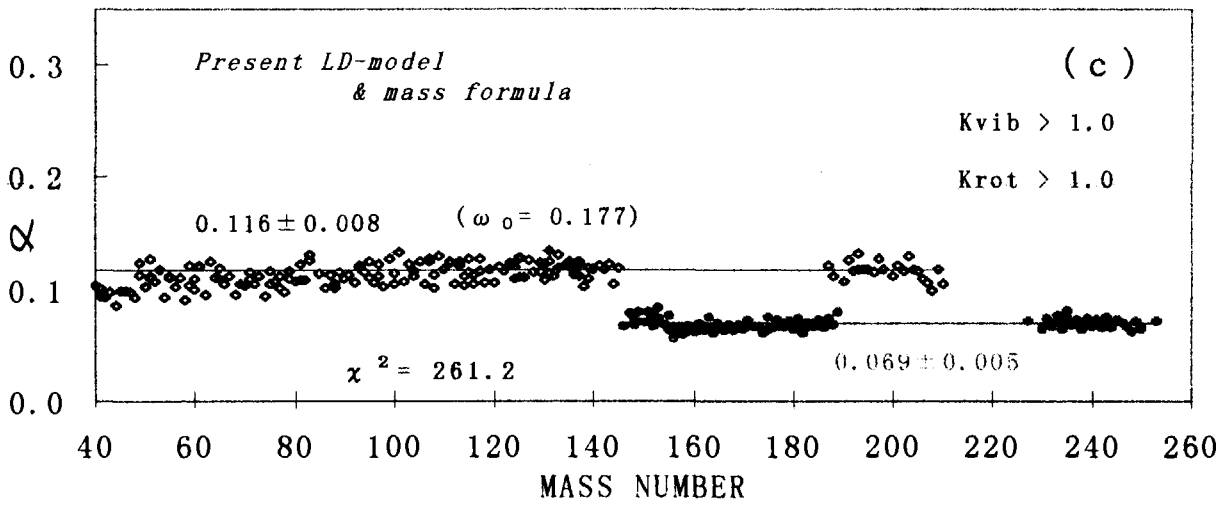

Fig.4 Systematics of asymptotic level density parameter $\alpha = a_0/A$. In the range of deformed nuclei, values of α are lowered due to the collective enhancement factors of Kvib (vibration) and mainly Krot (rotation).

JP0150695

3.33

Quantum recurrence in neutron resonances and a time unit in nuclei

Makio OHKUBO
SOHONRR, 1663-39,Senba-cyo, Mito-shi, Ibaraki-ken 310-0851 Japan

Abstract

Non-statistical properties of the neutron resonance level dispositions are investigated considering time behaviors of the compound nucleus. A resonance which is a quasi-stable state can be decomposed into a set of normal modes. From the requirement of the time periodic recurrence of the resonance state, frequencies of these normal mode must be commensulable (integer ratios) with each other. Therefore the excitation energy of a resonance is described as a sum of inverse integers. We tentatively adopt an expression E_x = C $\sum \frac{1}{n}$, where n=integer and C=34.5MeV. Time unit in recurrence is 1.20×10^{-22}s. Possible sets of inverse integers are deduced for the resonances of light e-e nuclei.

1. Introduction

Non-statistical descriptions of the fine-structure resonances will be a developing field of the nuclear physics. For a long time more than 3-decades, non-statistical distributions of neutron resonance levels are reported by several authors[1-8]. The methods of analyses are Dij distributions (spacings between arbitrary two levels), Fourier analysis, and the compilation of levels or spacings of many levels, etc. By these analyses, dominant level spacings are found which appear more frequently than the statistical predictions. For the neutron resonance levels of light e-e target nuclei up to several hundred keV, many of the dominant spacings D_0^* can be expressed as D_{ij} =C /mn, where C=34.5 MeV and m,n are integers[8].

These features of level distributions are diametrically different from the predictions of the statistical model, which is based on the random hypothese on the highly excited states of the compound nucleus.

In order to interprete these regularities in real resonances, we have developed the "Recurrence model" of the compound nucleus[9], where time periodic behaviors of the resonance reactions are explicitely discussed.

In this article, are described the recurrence relation for normal mode ensemble, and the expansion of nuclear excitation levels into sum of inverse integers. Sets of integers for resonances of ^{32}S+n etc. are deduced.

2. Time periodicity of resonance reactions

Neutron plane wave have a form $\exp i(kx - \omega t)$, where k is wave number vector, ω angular frequency, x and t are space and time coordinates. Wave packet length or coherent length of neutron is $\sim 10^{-8}$ m, measured by the neutron interferometry, or by neutron resonance width, which is suffieciently longer than the nuclear radius. Scattering of the incident plane wave by a spacially peridic scatterer induce "Bragg reflection", where kx term plays essencial role, and the diffraction patterns is the Fourier transform of the periodic lattice structures.

Similarly, scattering by time periodic scatterer induce resonances where ωt term plays essential role. At a resonance, time period of incident neutron wave $2\pi/\omega$ will be in an integer ratio to the time period τ of the compound nuclear system $(A+1)$. Neutron wave incident on target nucleus is divided into passing component and penetrating component. The passing component passes by the target nucleus without interaction, and the penetrating one excites many degrees of freedom on the compound nucleus, and comes out with much information on the compound nucleus. The observed cross section is the resultant of these two components. At a resonance, time structures of the coming out component must be time periodic, coherent with the passing component, and constructive interference occurs in succeeding wave train. At off resonance, destructive interference occurs and make no effect except potential scattering. In a word, resonance phenomena

in energy domain inevitably relate to the recurence phenomena in time domain.

3. Recurrence relation

Eigen functions of stable descrete states are time peridic functions. This will be true for the descrete levels of nuclei with many degrees of freedom. We assume that the states of descrete levels of the compound nucleus can be approximately expanded into a set of M normal modes (M≤10), which are independent with each other and oscillating with angular frequencies $\omega_j, (j = 1, 2, .., M)$. Total Hamiltonian is a sum of ones for these normal modes.

$$H = H_1 + H_2 + ... + H_M, \qquad .....(1)$$

The compound nuclear states $\psi(x,t)$ can be described as a direct products of these normal modes,

$$\psi(x,t) = \psi_1(x_1,t) \otimes \psi_2(x_2,t) \otimes ...\psi_M(x_M,t). \qquad .....(2)$$

Though the detailed structures of $\psi_j(x_j,t)$ are not known, following recurrence theorem for many oscillators system will be valid.
As j-th normal mode oscillates with a fixed frequency ω_j, the initial phase reappears every time period of $\tau_j = 2\pi/\omega_j$. Influence of the tolerable phae error of 1 rad.[9] is negligibly small in the frequency ratios. Total compound nuclear system recurs with a time period τ which is the least common multiple (LCM) of time period τ_j of each normal mode. Therefore, the time periods of these normal modes must be commensulable(integer ratios) with each other, with a time unit τ_0. Then, the total energy of the compound nucleus E_x, sum of $\hbar\omega_j$, must be written as a sum of inverse integers,

$$E_x = \hbar(\sum_{j=1}^{M}\omega_j) = 2\pi\hbar\sum_{j=1}^{M}\frac{1}{\tau_j} = (\frac{2\pi\hbar}{\tau_0})\sum_{j=1}^{M}\frac{1}{n_j}, \qquad .....(3)$$

where n_j are integers and τ_0 is time unit for this resonance. This expression will be valid for energies E_x of the bound and unbound descrete levels.

4. Excitation levels and Time unit

In a previous report[8], we have shown that there are special spacings (dominant spacing) which appear frequently between two arbitrary resonances. For the resonances of 15 light e-e target nuclei up to several hundred keV, 30 dominant spacings D_0(recoil effect corrected) are found. Among these D_0, integer ratios and the least common energy(LCE) (similar to the least common multiple for two integers) are found. LCE distributions are shown in Fig.1, where peaks appear at 1406, 2027, 2655,...,9100keV. Energy ratios among these peaks indicates that they are from few common values, divided by integers. Then we tried second LCE process(LCE-2). Distributions of LCE-2 are shown in Fig.2, where peaks appear at 34.5, 39.9, 48.6, 57.6MeV, where 34.5MeV is the predominant peak. If we use peaks with circles in Fig.1, distributions of LCE-2 are shown in Fig.3, where the 34.5MeV peak remains. Though some umbiguity exists, we got a result that many of D_0 are written as D_0 = C/mn, where C=34.5MeV and m,n = integers.
Therefore, in Eq.(3), we tentatively adopt excitation energies and τ_0 expressed as

$$E_x = C\sum\frac{1}{n} \quad (n : integer), \quad C = 34.5MeV, \qquad .....(4)$$

and the time unit

$$\tau_0 = (\frac{2\pi\hbar}{C}) = 1.20 \times 10^{-22}s. \qquad .....(5)$$

This time unit is neary equal to the reaction time measured by other experiments.

5. Expansion in sum of inverse integers

Roughly speaking, the normal modes here correspond to the excitons [10], of which number are estimated as $n_x \sim (g_0 E_x)^{1/2}$ where E_x is excitation energy in MeV, $g_0 = A/13$ the single particle level density at the Fermi energy for mass number A. For nuclei of A~30, average $n_x is \sim 3$ at $E_x \sim 5$MeV.

To prove the validity of Eq.(4), we tried to expand E_x in sum of C/n_j less than three terms for levels of light nuclei using a computer, where $n_j \leq 100$, with relative accuracy less than 1x 10^{-3}. Resonance parameters are taken from a book of recent eddition[11].

For example, in ^{32}S+n, the 1st 1/2+ resonance is at E_n =102.7 keV. Excitation energy is $E_x = S_n + E_n^*$= 8741.2keV, where S_n=8641.6keV is neutron separation energy and E_n^*=$E_n(A/(A+1)$ is recoil corrected neutron energy. A possible expansion for the above resonance is E_x = C[1/5 +1/30 +1/50] = 34500(38/150) =8740keV. A number set (5,30,50) is considered as a possible index of this resonance. For ten 1/2+ resonances of ^{32}S+n up to 1.66 MeV, E_n, E_n^*, E_x, possible index, LCM, E_{rec}, and δ etc. are shown in Table 1. A shematic energy levels of C/n are shown in Fig.4.

It is interesting that for considerable number of resonances of light nuclei, E_x can be written by two terms of inverse integers, E_x=C(1/m + 1/n), where m is small numbers. Moreover, a few single term levels E_x=C(1/m) are seen. For 57 resonances of ^{32}S+n below 1.66MeV, E_x of 22 resonance are C(1/4 + 1/n), and 3 resonances are C(1/5 + 1/n). Other resonances are of three terms. For 24 resonances of ^{34}S+n below 1.47MeV, E_x of 12 resonance are C(1/5 + 1/n), and 3 resonances C(1/6 + 1/n), and no resonance with C(1/4 +1/n).

6. Level spacings

From Eq.(4), level spacings D_{ij} are written as

$$D_{ij} = E_j - E_i = C(\sum_b \frac{1}{n_b} - \sum_a \frac{1}{n_a}) = C \sum \frac{n_c}{n_a n_b}. \quad \ldots.(6)$$

This include, as a simple case, the dominant level spacings D_0= C/mn [8].

Among 10 s-wave resonances of ^{32}S+n below 1.66MeV, D_0=575keV appears three times. These spacings coincide within error of 1 keV; D_{13}=575.4keV, D_{37}=575.9keV, and D_{510}= 575.5keV,respectively. By the indexes in Table 1, these spacings are equal to C(1/20-1/30) =C(1/10-1/12) = C/60= 575 keV. Another spacing D_0=358keV appears two times; D_{37}= 358.6keV,and D_{710}= 358.2keV=C/96. The ratio 358keV/575keV is equal to 5/8. We denote the spacings 575keV as "a", 358keV as "b". Dispositions of the above resonances are described as /a/b/a-b/b/, where "/" means a real resonance. Amang these resonances, spacing /a+b/=934keV appears two times. In these level dispositions, symmetric patterns /a/b/a/ are seen with a spacing ratio 8:5:8, and /b/a-b/b/ with a ratio 5:3:5. Symmtric patterns similar to the above can be found frequently for the nuclei of wide mass region.

7. Recurrence energies

For the 1st resonance of ^{32}S+n at 102.7 keV, a possible index 5,30,50 are propotional to the time periods of the normal modes excited for this resonance. Therefore, the recurrence time period of the compound nucleus is $150\tau_0$ as the LCM of the indecis. We define the "Recurrence energy E_{rec} " as

$$E_{rec} = C/(LCM), \quad \ldots\ldots\ldots\ldots\ldots\ldots(7)$$

where C=34.5MeV. For this resonance, E_{rec}=C/150=230 keV.

There might be simple integer ratio between time period of incident neutron wave and the compound nucleus; ie. between E_{rec} and E_n^*. We tried to calculate R and δ defined below,

$$\delta = E_{rec} \times R - E_n^* \quad \ldots\ldots\ldots\ldots (8)$$

where R is simple integer(or half integer) which minimize $|\delta|$. For this resonance, E_{rec}= 230 keV, E_n^* = 99.6 keV, and if we take R=1/2, $\delta = 230 \times (1/2) - 99.6 = 15.4keV$. For ten

1/2+ resonances of ^{32}S+n up to $E_n \leq$ 1.66MeV, parameters are shown in Table 1. It is interseting that δ are 10~25keV and δ distribute around S_n - C/4 = 16.6 keV. Similar results are obtained for 47 resonances of $1/2^-$,$3/2^-$,$3/2^+$,$5/2^+$ states of ^{32}S+n.
For the resonances of ^{34}S+n, many of E_x are expressed as E_x=C(1/5+1/n), and δ distribute around S_n - C/5 = 85.8keV.

8. Discussions

From the observes neutron resonance data in light nuclei, we have reduced a common factors C on the resonance energies and τ_0 for the reaction time. Another common factors may exist in different mass region.
In order to back up the reality of C/n expansion, we searched for the case where E_x is simple terms of C/n, and have some speciality.
a) Among 43 resonances of ^{33}S+n below 548keV, Γ_n and Γ_α are extraordinaly large for 84.88keV resonance, where E_x =11499keV =C/3.
b) First excited state of ^{48}Ca is at 3832keV =C/9.
c) Neutron resonances with considerably large Γ_n have E_x with simple integer ratios to C. For example, resonance energies (recoil corrected) of first seven resonances of ^{16}O+n are (17/240)(C/6), (1/4)(C/7), (5/13)(C/7), (9/13)(C/7), (9/11)(C/7), (15/14)(C/7) and (13/10)(C/7).

Sukhoruchkin reported Δ=4.6MeV as a dominant spacing among excited states of many light nuclei, which is equal to the mass difference between $\pi^\pm$ and π^0. Also $\Delta = 9m_e$, where m_e is electron mass 0.511MeV.[12]. The Δ is in simple integer ratio to C. that is Δ = (2/15)C = (1/3-1/5)C.
These facts support possibility of the non-statistical description of the highly excited states of nucleus, where oscillator (exciton) energies are preseved, and simple algebra in eigen energies are valid.
Further investigations are needed to find out more clear images of the resonance compound nucleus.

References

1. S.Sukhoruchkin: Proc.Conf.Nucl.Data for Reactors, Paris,1966,Vol 1, p159, Vienna,1967 ; S.Sukhoruchkin: Proc.Int.Conf. on Statistical Properties of Nuclei (Plenum, New York 1972) p.215
2. K.Ideno, M.Ohkubo: J.Phys.Soc.Jap. 30,620(1971); K.Ideno: ibid.37,581(1974)
3. C.Coceva, F.C.Corvi,P.Giacobbe, and M.Stefanon; Proc.Int.Conf. on Statistical Properties of Nuclei(Plenum, New York 1972) p.447
4.F.N.Belyaev,S.P.Borovlev: Yad.Fiz.27.289(1978)
5.S.Sukhoruchkin: ISINN-4,Dubna 1996,ISINN-5,Dubna 1997, ISINN-6,Dubna 1998
6. G.Rohr: Low Energy Nuclear Dynamics,(World Scientific,1995),p130
7. M.Ohkubo:JAERI-Conf 98-003,p340,
8. M.Ohkubo: JAERI-Conf 2000-005,p325,
9. M.Ohkubo: Phys.Rev.C, 53.1325(1996)
10. A.Bohr and B.Mottelson;Single Particle Motion, Vol.1(Benjamin,London,1968)
11. Landolt-Börnstein New Series Vol 16/B, "Neutron Resonance Parameters", Springer(1998)
12. S.Sukhoruchkin: ISINN-7,Dubna 1998

Table 1 Expansion of E_x by C/n series

^{32}S + n J=1/2 L=0 resonances Table-S32(1)

j	E_n (keV)	E_n^* (keV)	E_x (keV)	Index	LCM	E_{rec} (keV)	R	δ (keV)	δ/E_{rec}
1	102.7	99.6	8741.2	5 30 50	150	230	0.5	15.4	0.067
				5 35 40	280	123.2	1	23.6	0.192
				9 12 17					
2	376.9	365.4	9007.1	4 90	180	191.7	2	17.9	0.093
				5 30 36	180				
				6 15 36	180				
				9 11 17					
3	696.1	675.0	9316.7	4 50	100	345.0	2	15.0	0.044
				5 20 50	100				
				6 12 50	300	115.0	6	15.0	0.130
				9 10 17					
4	1047.5	1015.8	9657.3	4 50 100	100	345	3	19.2	0.056
				5 25 25	25	1380			
				6 14 24	168	205.4	5	11.0	0.054
				8 12 14	168				
5	1065.9	1033.6	9675.2	4 33	132	261.4	4	11.8	0.045
				6 12 33	132				
6	1161.4	1126.2	9767.8	4 30	60	575	2	23.8	0.041
				5 12	60				
				6 12 30	60				
				6 15 20	60				
				8 8 30	240	143.8	8	23.8	
7	1290.0	1250.9	9892.5	4 50 60	300	115	11	14.1	0.123
				5 15 50	150	230	5.5	14.1	0.061
				6 10 50	150				
8	1419.4	1376.3	10018.0	4 42 60	420	82.1	17	20.1	0.244
				5 15 42	210	164.3	8.5	20.1	0.122
				7 10 21	210				
9	1605.6	1556.9	10198.5	4 22	44	784.1	2	11.3	0.014
				4 44 44	44				
				4 40 48	240	143.7	11	24.3	0.169
				5 16 30	240				
				6 12 22	132	261.4	6	11.3	0.043
				8 8 22	88	392.0	4	11.3	0.029
10	1659.4	1609.1	10250.7	4 40 45	360	95.8	17	20.0	0.209
				6 10 33	330	104.5	15.5	11.3	0.108

SI28 TO PB206 16 NUCLIDES 33 SPACINGS

N= 33 NC2= 528

43.2	49.6	73.3	73.7	74.1	77.7
86.1	93.3	156.5	189.3	201.9	213.5
225	226.3	233.9	241	249.1	253.2
277.3	295.2	302.9	308.6	339.3	358.4
365.4	407.8	456.1	478.6	534.9	575.6
634.1	757.5	922.7	0	0	0

ACCURACY + - ,INTMAX, NEIGHBOR .005 20 15

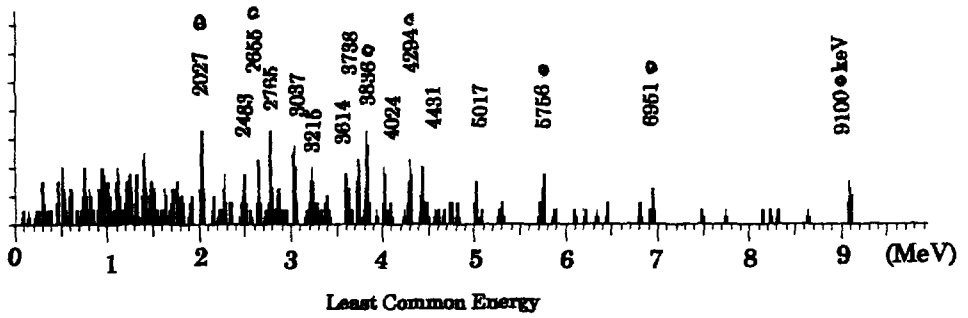

Fig.1 LCE distribution for the Dominant spacings.

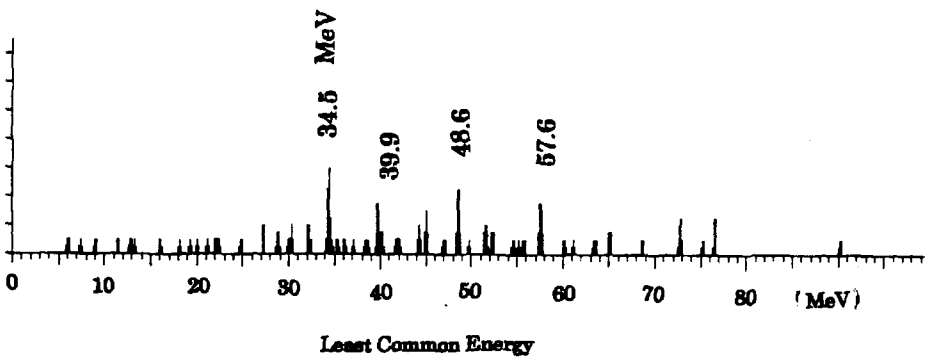

Fig.2 LCE-2 distribution for all labeled peaks in Fig.1

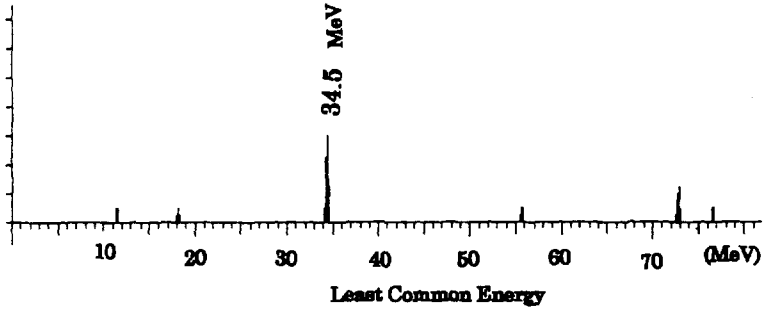

Fig.3 LCE-2 distribution for 7 labeled peaks with circles in Fig.1.

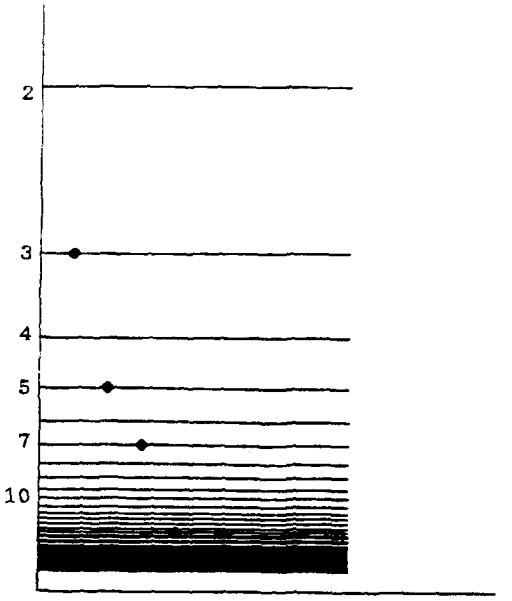

Fig.4 Tentative energy levels for the osillators

JP0150696

3.34

Lumped Group Constants of FP Nuclides for Fast Reactor Shielding Calculation Based on JENDL-3.2

Shiro TABUCHI and Takafumi AOYAMA
Experimental Reactor Division, Irradiation Center, Oarai Engineering Center
Japan Nuclear Cycle Development Institute
4002 Narita, Oarai, Ibaraki 311-1393 JAPAN
E-mail : tabuchi@oec.jnc.go.jp

ABSTRACT

The lumped group constants of FP nuclides used for a fast reactor shielding calculation were computed based on the JENDL-3.2 nuclear data library and were compiled to the JSDJ2/ JFTJ2 set. The effect of FP nuclides on neutron flux calculations was evaluated in the JOYO experimental fast reactor. These tests showed that conventional calculations that ignored FP overestimated neutron flux by about 2%.

Keywords : lumped group constants, FP, fast reactor, JOYO, shielding, JENDL-3.2

1. Introduction

Fission products (FPs) were not considered in conventional fast reactor shielding analyses that were predominantly developed in clean core experiments like the JASPER program [1, 2]. However, in power reactors with high burn-up, the accumulation of FP affects the neutron balance so it cannot be neglected in the neutron flux calculation. In this study, the group constants of FP nuclides were computed based on the JENDL-3.2 [3] nuclear data library and these were compiled to the JSDJ2 [4] set. Using the constants, the effect of the FP nuclides on shielding calculation was evaluated in the JOYO experimental fast reactor.

2. Lumped FP Group Constants

2.1 Selection of FP Nuclides

The flow chart for computing the lumped FP constants is illustrated in Fig. 1.

Initially, FP nuclides need to be considered for the group constants. Generation and depletion for nearly 880 FP nuclides can be computed with the ORIGEN2 [5] burn-up calculation. The calculation uses the specification and material contents of the JOYO Mk-II driver as an example of fast reactor MOX fuel.

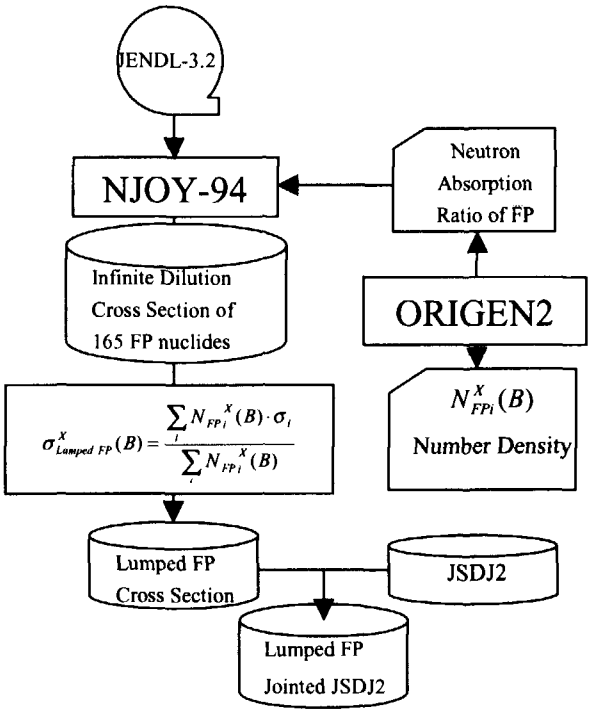

Fig.1 Flow Chart of Computing FP Group Constant

Table.1 The neutron absorption ratio of FP nuclides

	Nuclide	R	A		Nuclide	R	A		Nuclide	R	A		Nuclide	R	A
1	Ru-101	8.93%	8.93%	54	Ce-144	0.18%	96.56%	107	Eu-151	0.01%	99.68%	160	Ag-107	0.00%	99.81%
2	Pd-105	7.90%	16.83%	55	Gd-157	0.18%	96.73%	108	Cd-116	0.01%	99.69%	161	Be-9	0.00%	99.81%
3	Tc-99	7.06%	23.89%	56	Pd-110	0.14%	96.87%	109	Sn-118	0.01%	99.70%	162	Nb-93	0.00%	99.81%
4	Rh-103	6.02%	29.91%	57	Mo-99	0.14%	97.01%	110	Cd-110	0.01%	99.71%	163	Ga-71	0.00%	99.81%
5	Cs-133	5.72%	35.63%	58	Gd-156	0.13%	97.14%	111	Se-78	0.01%	99.72%	164	Li-7	0.00%	99.81%
6	Pd-107	4.65%	40.29%	59	Cd-113	0.11%	97.25%	112	Xe-130	0.01%	99.72%	165	Ga-69	0.00%	99.81%
7	Mo-97	4.54%	44.83%	60	Cs-134	0.11%	97.35%	113	Ba-137	0.01%	99.73%				
8	Sm-149	4.39%	49.21%	61	Eu-154	0.10%	97.46%	114	Gd-160	0.01%	99.74%				
9	Pm-147	3.77%	52.98%	62	Ce-140	0.10%	97.56%	115	Ba-140	0.01%	99.74%				
10	Nd-145	3.37%	56.35%	63	Sb-125	0.10%	97.66%	116	Sn-126	0.01%	99.75%				
11	Cs-135	2.74%	59.09%	64	Tb-159	0.10%	97.75%	117	Te-125	0.01%	99.76%				
12	Nd-143	2.64%	61.73%	65	Sm-154	0.10%	97.85%	118	Sn-120	0.01%	99.76%				
13	Xe-131	2.38%	64.11%	66	Sr-90	0.10%	97.95%	119	Sm-153	0.00%	99.77%				
14	Ru-102	2.21%	66.31%	67	I-131	0.09%	98.04%	120	Mo-96	0.00%	99.77%				
15	Sm-151	2.19%	68.51%	68	Y-89	0.09%	98.12%	121	Cs-136	0.00%	99.77%				
16	Mo-95	2.15%	70.66%	69	Ba-138	0.08%	98.20%	122	Sn-122	0.00%	99.78%				
17	Mo-98	1.89%	72.55%	70	Pr-143	0.08%	98.28%	123	Sn-124	0.00%	99.78%				
18	Ag-109	1.80%	74.35%	71	Br-81	0.08%	98.36%	124	Pm-148	0.00%	99.79%				
19	Ru-104	1.69%	76.04%	72	Te-130	0.08%	98.44%	125	As-75	0.00%	99.79%				
20	Mo-100	1.58%	77.63%	73	In-115	0.08%	98.51%	126	Xe-128	0.00%	99.79%				
21	Eu-153	1.56%	79.19%	74	Te-128	0.07%	98.59%	127	Ba-134	0.00%	99.79%				
22	Zr-93	1.27%	80.45%	75	Cd-112	0.07%	98.65%	128	Xe-135	0.00%	99.80%				
23	Ru-103	1.19%	81.65%	76	Te-129m	0.07%	98.72%	129	Zr-90	0.00%	99.80%				
24	Pr-141	1.03%	82.67%	77	Rb-87	0.06%	98.78%	130	Nd-142	0.00%	99.80%				
25	I-129	0.97%	83.65%	78	Kr-84	0.06%	98.84%	131	Sn-115	0.00%	99.80%				
26	Zr-95	0.88%	84.53%	79	Xe-133	0.05%	98.89%	132	Te-126	0.00%	99.80%				
27	Zr-96	0.75%	85.28%	80	Sb-121	0.05%	98.94%	133	Sr-86	0.00%	99.80%				
28	Nd-146	0.70%	85.98%	81	Te-127m	0.05%	98.99%	134	Gd-154	0.00%	99.80%				
29	Xe-132	0.69%	86.67%	82	Pm-148m	0.05%	99.03%	135	Eu-152	0.00%	99.80%				
30	Pd-108	0.68%	87.35%	83	Se-79	0.05%	99.08%	136	Sb-124	0.00%	99.80%				
31	Nb-95	0.67%	88.02%	84	Rh-105	0.05%	99.13%	137	Te-122	0.00%	99.80%				
32	Ce-141	0.62%	88.63%	85	Sm-150	0.04%	99.17%	138	Kr-82	0.00%	99.80%				
33	Zr-91	0.61%	89.24%	86	Sb-123	0.04%	99.21%	139	Ge-76	0.00%	99.80%				
34	Zr-92	0.48%	89.72%	87	Gd-155	0.03%	99.24%	140	Ge-73	0.00%	99.80%				
35	Xe-134	0.48%	90.20%	88	Sn-117	0.03%	99.28%	141	Sn-116	0.00%	99.80%				
36	Ru-106	0.48%	90.68%	89	Pm-149	0.03%	99.31%	142	Te-124	0.00%	99.80%				
37	Sm-152	0.48%	91.16%	90	Xe-136	0.03%	99.34%	143	Ge-74	0.00%	99.80%				
38	Nd-148	0.46%	91.62%	91	Pd-104	0.03%	99.37%	144	La-138	0.00%	99.80%				
39	Cd-111	0.44%	92.06%	92	Gd-158	0.03%	99.40%	145	Ge-72	0.00%	99.80%				
40	Rb-85	0.43%	92.49%	93	Ru-100	0.03%	99.43%	146	In-113	0.00%	99.80%				
41	I-127	0.42%	92.91%	94	Kr-85	0.03%	99.46%	147	Gd-152	0.00%	99.80%				
42	La-139	0.42%	93.33%	95	Sr-89	0.03%	99.49%	148	Ba-135	0.00%	99.80%				
43	Pd-106	0.41%	93.74%	96	Cd-114	0.02%	99.51%	149	Xe-129	0.00%	99.80%				
44	Eu-155	0.35%	94.08%	97	Sr-88	0.02%	99.54%	150	Se-76	0.00%	99.80%				
45	Zr-94	0.32%	94.40%	98	Sn-119	0.02%	99.56%	151	Ru-99	0.00%	99.81%				
46	Sm-147	0.31%	94.71%	99	Sm-148	0.02%	99.58%	152	Nb-94	0.00%	99.81%				
47	Ce-142	0.29%	95.00%	100	Se-82	0.02%	99.59%	153	Cd-108	0.00%	99.81%				
48	Nd-150	0.28%	95.28%	101	Ba-136	0.02%	99.61%	154	Te-123	0.00%	99.81%				
49	Nd-147	0.26%	95.54%	102	Ag-110m	0.02%	99.62%	155	Sr-87	0.00%	99.81%				
50	Cs-137	0.25%	95.80%	103	Se-77	0.01%	99.64%	156	Kr-80	0.00%	99.81%				
51	Y-91	0.20%	96.00%	104	Kr-86	0.01%	99.65%	157	Br-79	0.00%	99.81%				
52	Nd-144	0.19%	96.19%	105	Eu-156	0.01%	99.66%	158	Sn-114	0.00%	99.81%				
53	Kr-83	0.19%	96.37%	106	Se-80	0.01%	99.67%	159	Li-6	0.00%	99.81%				

R : Absorption ratio of each nuclide
A : Accumulated absorption ratio

About 99.8% of the total FP neutron absorption comes from 165 major nuclides as shown in Table 1. The cross section data for these neutrons are stored in the JENDL-3.2 library. The contributions of other FP nuclides were found to be negligible so the calculation used only these 165 FP nuclides.

2.2 Computing Group Constants

The lumped group constants for the FP nuclides were generated as follows. The 100 group infinite dilution cross section of each individual FP nuclide was computed with the NJOY-94 [6] code. The energy group structure is the same as the JSDJ2 set and the scattering anisotropy is considered up to P3 components of Legendre expansion.

Atomic number densities of the FP nuclides generated from fission nuclides of ^{235}U, ^{238}U, ^{239}Pu and ^{241}Pu were independently computed by ORIGEN2 as a function of fuel burn-up. The lumped FP constants were then obtained as shown in equation (1) by averaging the infinite dilution cross sections with the atomic number densities based on the assumption that one fission produces one lumped FP.

$$\sigma^{X}_{Lamped\ FP}(B) = \frac{\sum_{i} N_{FPi}{}^{X}(B) \cdot \sigma_i}{\sum_{i} N_{FPi}{}^{X}(B)} \qquad (1)$$

Where $N^{X}_{FPi}(B)$ is the amount of FP nuclide i generated from fissile nuclide x (for ^{235}U, ^{238}U, ^{239}Pu and ^{241}Pu) at the burn-up B, and σ_i is the cross section of FP nuclide i. The burn-up of the JOYO Mk-II driver fuel was assumed to be 10, 40, 63 and 90GWd/t. These FP group constants were added to the JSDJ2/JFTJ2 [4] set where the neutron self-shielding factor was set to be unity since the JOYO burn-up value did not affect the neutron self-shielding.

2.3 Verification of FP Constants

To verify the calculated lumped FP constants, the absorption microscopic cross section data was compared with the JFS-3-J3.2 [7] group constants used for the fast reactor core calculation. The lumped group constants for FP nuclides produced from ^{239}Pu fission reaction at the 40GWd/t burn-up level are shown in Fig. 2. Both cross section curves agreed well. There exists little difference in The FP group constants did not vary significantly at four burn-up levels as shown in Fig. 3.

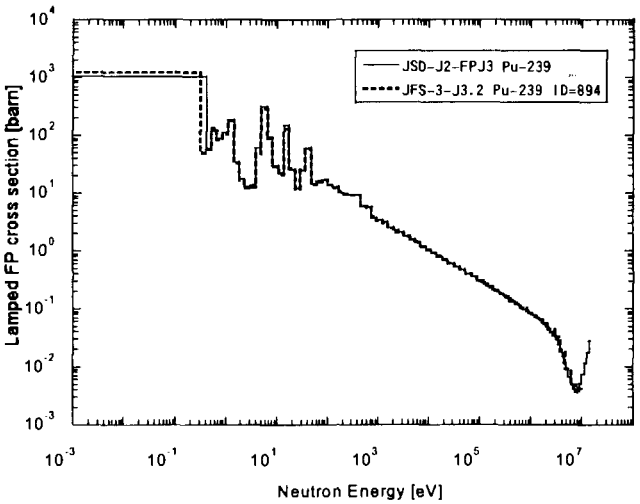

Fig.2 Lumped FP Cross-Section from ^{239}Pu

The macroscopic absorption cross-section of the fuel materials was calculated using the RADHEAT-V3 [8] system. Calculations were done with and without FP. The comparison of the results are shown in Fig. 4. Some difference was observed in the lower energy region. However, both results agreed well above 1keV, which is important for analyzing a small fast reactor like JOYO because the absorption cross-section differed by only about 1 to 3% less than 0.3MeV.

3. The Effect of FP on Shielding Analysis

3.1 Shielding Calculation Method

In order to evaluate the effect of FP nuclides on the JOYO shielding analysis, the neutron flux distribution was calculated using the DORT [9] two-dimensional transport code. Table 2 lists the key elements of the calculation method. The neutron flux distributions were calculated in the RZ and XY-R θ geometry with the fixed source mode and neutron source distribution obtained from the JOYO Mk-II core management code system MAGI [10].

In the XY-R θ calculation, neutron leakage in the axial direction was considered as a pseudo-absorption to calculate the neutron flux distribution in the core center plane. This axial leakage term was obtained using the gradient of the neutron flux by the RZ calculation at 2.5 cm above and below the horizontal surface of the core.

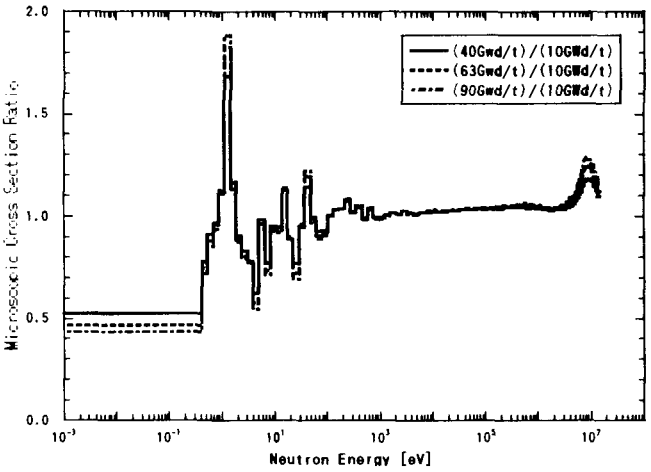

Fig.3 Burn-up Dependency of ^{239}Pu Lumped FP

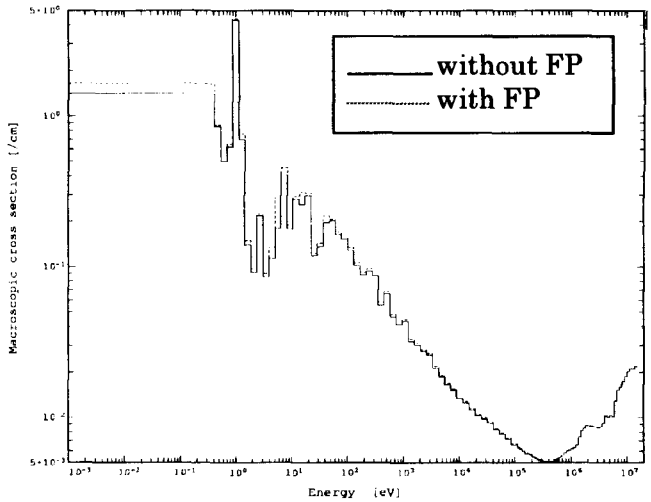

Fig.4 Macroscopic Absorption Cross-Section of Fuel Material

Table 2 Neutron Flux Calculation Conditions

Transport code	DORT
Cross section calculation code	RADHEAT-V3
Neutron cross section set	JSDJ2
Self shielding factor set	JFTJ2
γ -ray production Library	Modified New-POPOP4 [11] (including delayed fission γ -ray)
No. of angular quadratures	S30
Order of scattering anisotropy	P3

3.2 Effect on Neutron Flux

The comparison of the neutron spectra calculated with and without FP in the core center is shown in Fig. 5. The neutron flux above 1MeV decreases by about 2% when considering neutron absorption by FP nuclides. The ratio of total and fast (E>0.1MeV) neutron flux calculated along the core center plane in the RZ geometry with and without FP is shown in Fig. 6. The total neutron flux decreased by about 1.5% in in-vessel storage rack region when considering FP, where moderated neutrons would be captured by FP nuclides.

Note that at the position furthest away from the in-vessel spent fuel storage rack, the total and fast neutron flux decreased by only 2% when considering FP.

4. Conclusion

The fast reactor shielding calculations were improved by including the group constants of FP nuclides that were computed based on the JENDL-3.2 library. The effect of FP nuclides on neutron flux calculations was evaluated in JOYO, which has a hard neutron spectrum. It was found that the conventional calculations that ignored FP overestimated the neutron flux by about 2%.

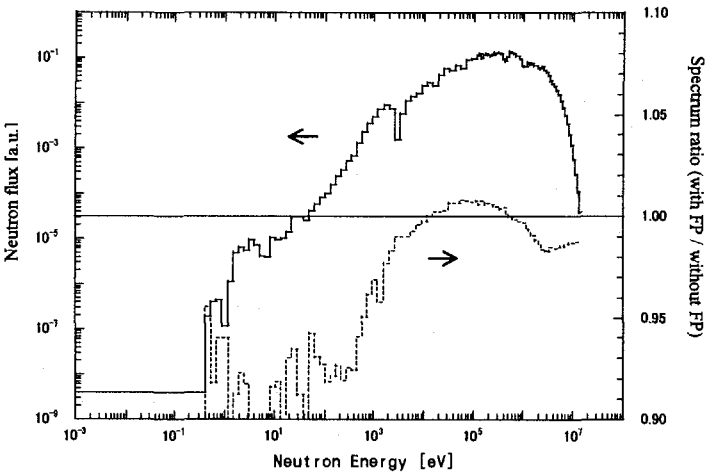

Fig.5 Comparison of Neutron Spectrum in the JOYO Core Center

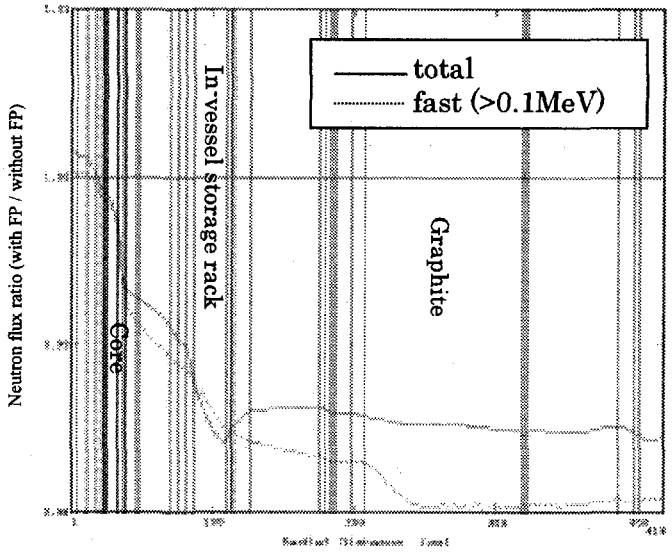

Fig.6 The Ratio of Neutron Flux with and without FP by RZ Calculation

Acknowledgements

The authors would like to appreciate the cooperation and valuable comments by Dr. O.Sato of Mitsubishi Research Institute, Inc. on the ORIGEN2 and DORT calculation.

References

(1) D. Ingersoll, N. Ohtani,: Proc. ANS Topical Conf. Theory and Practices in Radiation Protection and Shielding, Knoxville, Tenn., Apr. 1987, Vol.2, pp.346-353 (1987).
(2) N. Ohtani, S. Suzuki, Proc. ANS Winter Meeting, Wash.D.C., Nov. 1990, pp.89-94 (1990).
(3) T.Nakagawa, et. al.: J. Nucl. Sci. Technol., Vol. 32, 1259 (1995).
(4) M. Takemura, et al.: 1987 Fall Mtg.of the Atomic Energy Society of Japan,A61,Oct (1987) in Japanese.
(5) A.G.Croff, :ORNL/TM-7175 (1980).
(6) R.E.MacFarlane, D.W.Muir,: LA-12740-M (1994).
(7) H.Takano et. al.: JAERI-M 89-141 (1989).
(8) K.Koyama, et. al.: JAERI-M 7155 (1977).
(9) W. A. Rhoades, R. L. Childs,: CCC-484 (1989).
(10) Arii, et al.: J. At. Energy Soc. Japan, Vol.39, No.4, pp.315-325 (1997) in Japanese.
(11) T. Sekine et al.: JNC Technical Review No.6 p.19 (2000) in Japanese.

JP0150697

3.35

Benchmark Experiments on Advanced Breeding Blanket Materials and SiC with 14-MeV Neutrons

F. Maekawa[1], Y. Kasugai[1], C. Konno[1], K. Ochiai[1], M. Wada[2] and H. Takeuchi[1]
[1] *Japan Atomic Energy Research Institute, Tokai-mura, Naka-gun, Ibaraki-ken 319-1195 Japan*
[2] *Startcom Co., Ltd., Nerima-ku, Tokyo, 179-0085 Japan*
e-mail: fujio@fnshp.tokai.jaeri.go.jp

Fusion neutronics benchmark experiments were conducted for a low-activation structural material (SiC) and three advanced tritium breeding blanket materials ($LiAlO_2$, Li_2TiO_3, Li_2ZrO_3). Neutrons and secondary gamma-rays were measured in experimental assemblies with impinging D-T neutrons. Validity of cross section data in recent evaluated nuclear data files were tested by the analyses of the experiment. Serious problems were pointed out in FENDL/E-1.0 for silicon and ENDF/B-VI for zirconium. As far as JENDL Fusion File, JENDL-3.2 and FENDL/E-2.0 were concerned, no significant problems were found for the four materials, and these data could be used adequately for fusion reactor designs.

1. Introduction

In recent designs of fusion reactors, use of advanced tritium breeding materials and low-activation structural materials is indispensable to accomplish technically feasible and attractive fusion reactors. However, benchmark tests of nuclear data for these materials have not been performed sufficiently because of lack of benchmark experimental data. To ameliorate this situation, benchmark experiments on three advanced tritium breeding materials ($LiAlO_2$, Li_2TiO_3, Li_2ZrO_3) and a low-activation structural material (SiC) were conducted by using the 14-MeV neutron source facility FNS in JAERI. A part of the experiments for measurements of neutron and gamma-ray spectra leaking from the experimental assemblies are reported elsewhere [1-3]. This paper deals with in-situ measurement experiments and results of benchmark tests with the experimental data for recent evaluated nuclear data files.

2. Experiment and Analysis

Experimental assemblies were produced by piling up sintered blocks in dimensions shown in Fig. 1. Figure 2 shows experimental assembly made of lithium zirconate in a pseudo-cylinder shape of 457 mm in diameter and 577 mm in thickness. D-T neutrons generated by FNS were impinged into the experimental assembly, and neutrons and gamma-rays were measured at several positions in the assembly. Measured quantities were neutron spectra from 14-MeV down to 0.3 eV, reaction rate distributions, gamma-ray spectra and gamma-ray heating rates. These quantities are measured frequently in similar experiments at FNS, and details of the measurements have been described in Ref. [4].

The continuous energy Monte Carlo transport calculation code MCNP-4B [5] was used for experimental analysis. Evaluated nuclear data files tested were JENDL-3.2 [6], JENDL Fusion File [7] (hereafter, JENDL-FF), ENDF/B-VI [8], FENDL/E-1.0 [9] and FENDL/E-2.0 [10]. Cross section data for some of elements in JENDL Fusion File, and all the data in FENDL/E-1.0 and FENDL/E-2.0 originated in other data sources as shown in Table 1.

3. Results and Discussion

3.1. Silicon Carbide (SiC)

Figure 3 compares measured and calculated neutron spectra at a 432 mm depth in the SiC assembly. Results by JENDL-FF and FENDL/E-2.0 agree satisfactory with the experimental data. The FENDL/E-1.0 calculation gives neutron flux intensity above 10 keV smaller than the measured values. This reason can be attributed to elastic scattering cross section of silicon at ~ 14-MeV as shown in Fig. 4. Total cross section in the three data files are close to each other while elastic scattering cross section in FENDL/E-1.0 at 14-MeV, ~ 0.5 b, is much smaller than the other values, ~ 0.75 b. When a 14-MeV neutron is scattered elastically, a produced secondary neutron is most likely to penetrate toward deep inside of the SiC assembly compared with secondary neutrons produced by other nuclear reactions. This is due to the anisotropic angular distribution of secondary neutrons for the elastic scattering reaction that is enhanced to forward directions. Hence, when the silicon data in FENDL/E-1.0 are used, the 14-MeV neutron flux is calculated smaller as penetration thickness increases compared with other two data files. The experimental results indicate that the elastic scattering cross section in FENDL/E-1.0 is too small.

Another problem is found in the silicon data in FENDL/E-1.0. Neutron fluxes below 1 MeV calculated with FENDL/E-1.0 near the D-T neutron source are larger than the experimental data. Figure 5 compares double differential neutron emission cross section (DDX) of silicon at 14.1 MeV in the three data files with the experimental data [11]. There is a strange peak below 1 MeV in the DDX of FENDL/E-1.0, and this is the reason for the overestimation of neutron fluxes below 1 MeV.

No problem is found in secondary gamma-ray data in all the data files tested.

3.2. Lithium Titanate (Li_2TiO_3)

Since neutron transport cross section for Li_2O has been already validated in previous benchmark studies [12], benchmarking on Li_2TiO_3, Li_2ZrO_3 and $LiAlO_2$ is suitable for testing cross section data for Ti, Zr and Al, respectively. As for secondary gamma-rays, a problem has been pointed out [3] in oxygen data in JENDL-3.2 that the most prominent gamma-ray peak at 6.13 MeV produced by 14-MeV neutron interaction with ^{16}O is given much smaller. This affects on calculated results for gamma-rays for the three blanket materials commonly when the oxygen data in JENDL are used.

Figure 6 compares measured and calculated neutron spectra at a 279 mm depth in the lithium titanate assembly. All the calculations give nearly the same results, and they agree well with the experimental data. The good agreements are consistent with results of the leakage neutron spectrum measurement above 50 keV at FNS [1, 2]. On the other hand, overestimation of calculated neutron fluxes in an energy region of 0.1 - 1 MeV by more than 50 % is reported [12] for the OKTAVIAN pulsed sphere experiment on titanium. The FNS and OKTAVIAN experiments are inconsistent each other, and there might be a problem in the OKTAVIAN experiment on titanium if we rely on the FNS experiments.

3.3. Lithium Zirconate (Li_2ZrO_3)

Neutron spectra at a 177 mm depth in the lithium zirconate assembly measured and calculated are shown in Fig. 7. Figure 8 shows ratios of calculated to experimental reaction rates (C/E values) for the $^{93}Nb(n,2n)^{92m}Nb$, $^{115}In(n,n')^{115m}In$ and $^{235}U(n,fission)$ reactions which are mainly sensitive to 14-MeV, 1 - 10 MeV and eV - keV neutrons, respectively. The calculation with ENDF/B-VI overestimates 14-MeV neutron fluxes with penetration depth increases as indicated in the $^{93}Nb(n,2n)^{92m}Nb$ reaction rate. The reason is that the elastic scattering cross section at 14 MeV for Zr is given larger in ENDF/B-VI. The overestimation of the $^{115}In(n,n')^{115m}In$ reaction rate by ENDF/-VI is attributed to inadequate DDX data at

14-MeV for Zr. Although slight overestimation of neutron fluxes in an energy range from 0.1 to 10 MeV is found in the JENDL-FF and FEND/E-2.0 calculations, it is not so significant. These results for MeV energy neutrons are consistent with the leakage neutron spectrum measurement [1, 2].

Although low energy neutron fluxes are calculated smaller than the experimental values as shown in Fig. 7 and the $^{235}U(n,fission)$ reaction rate in Fig. 8, the reason has not been identified.

3.4. Lithium Aluminate ($LiAlO_2$)

Figure 9 compares measured and calculated neutron spectra at a 279 mm depth in the lithium aluminate assembly. All the calculations give nearly the same results, and they agree almost satisfactory with the experimental data. The good agreements are consistent with results of the leakage neutron spectrum measurement [1, 2] and the OKTAVIAN pulsed sphere experiment [12].

4. Summary

Fusion neutronics benchmark experiments were conducted for a low-activation structural material (SiC) and three advanced tritium breeding blanket materials ($LiAlO_2$, Li_2TiO_3, Li_2ZrO_3). As a result of benchmark tests for cross section data in recent evaluated nuclear data files, serious problems were pointed out in FENDL/E-1.0 for silicon and ENDF/B-VI for zirconium. As far as JENDL Fusion File, JENDL-3.2 and FENDL/E-2.0 were concerned, no significant problems were found for the four materials, and these data could be used adequately for fusion reactor designs.

Acknowledgments

The authors would like to express his sincere gratitude to the operation staffs of FNS.

References

[1] Murata I., et al.: "Benchmark Experiment on $LiAlO_2$, Li_2TiO_3 and Li_2ZrO_3 Assemblies with D-T Neutrons - Leakage Neutron Spectrum Measurement -", to be published in Fusion Eng. Des.

[2] Nishio T., et al..: "Measurement of Leakage Neutron Spectra from Advanced Blanket Materials and Structural Materials Induced by D-T Neutrons", JAERI-Conf 2000-005,, pp. 172-177 (2000).

[3] Nishio T., et al..: "Measurement of Secondary Gamma-ray Spectra from Structural and Blanket Materials Bombarded by D-T Fusion Neutrons", presented in this symposium.

[4] Maekawa F., et al.: "Data Collection of Fusion Neutronics Benchmark Experiment Conducted at FNS/JAERI", JAERI-Data/Code 98-021 (1998).

[5] Briesmeister J. F., (Ed.): "MCNP - A General Monte Carlo N-Particle Transport Code, Version 4B", LA-12625-M, Los Alamos National Laboratory (1997).

[6] Nakagawa T., et al.: J. Nucl. Sci. Technol., 32, pp. 1259-1271 (1995).

[7] Chiba S., Fukahori T., Yu B. and Kosako K.: "Evaluation of the Double-Differential Cross Sections of Medium-Heavy Nuclei for JENDL Fusion File", JAERI-Conf 96-005, pp. 45-54 (1996).

[8] Rose P. F. (Ed.): "ENDF-201 ENDF/B-VI Summary Documentation", BNL-NCS-17541, Brookhaven National Laboratory (1991).

[9] Ganesan S. and McLaughin P. K.: IAEA-NDS-128 (1995).

[10] Pashchenko A. B. and Wienke H.: IAEA-NDS-175 Rev. 3 (1998).

[11] Takahashi A., et al..: OKTAVIAN Report, A-87-03, Osaka University (1987).

[12] Maekawa F., et al.: "Compilation of Benchmark Results for Fusion Related Nuclear Data", JAERI-Data/Code 98-024 (1998).

Table 1 Origin of cross section data for each element in the five evaluated nuclear data files.

Evaluation	Si	C	Li	O	Al	Ti	Zr
JENDL-3.2	J-3.2	J-3.2	J-3.2	J-3.2	J-3.2	J-3.2	J-3.2
JENDL Fusion File	J-FF	J-FF	J-3.2	J-3.2	J-FF	J-FF	J-FF
ENDF/B-VI	B6	B6	B6	B6	B6	B6	B6
FENDL/E-1.0	BROND	B6	B6	B6	J-3.1	J-3.1	BROND
FENDL/E-2.0	B6	J-FF	B6	J-3.2	J-3.1	J-3.1	J-FF

J-3.1: JENDL-3.1 J-3.2: JENDL-3.2 J-FF: JENDL Fusion File
B6: ENDF/B-VI BROND: BROND-2

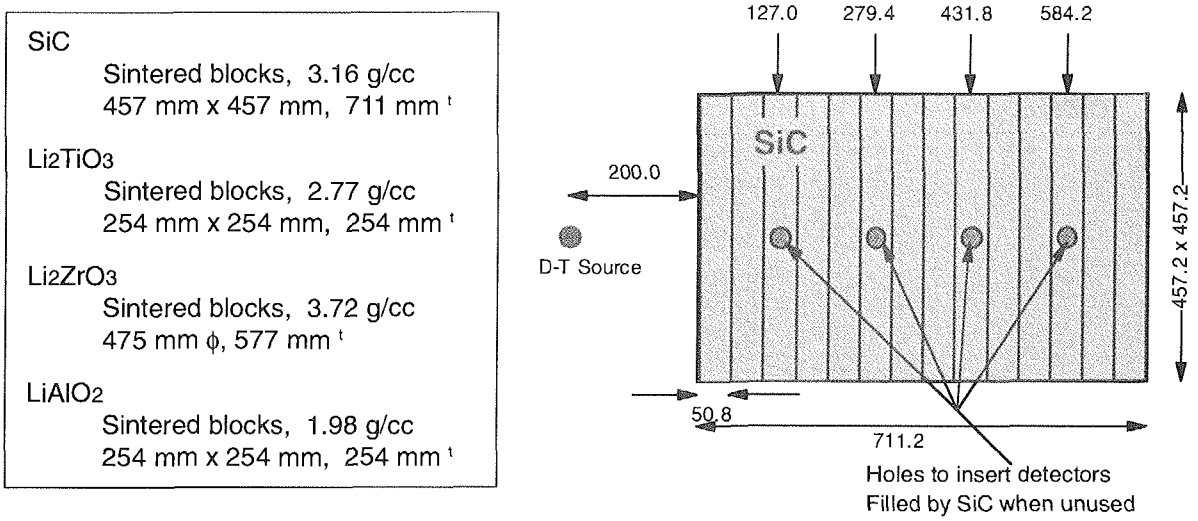

Fig. 1 Specifications for the experimental assemblies (left) and a schematic drawing of the SiC assembly (right).

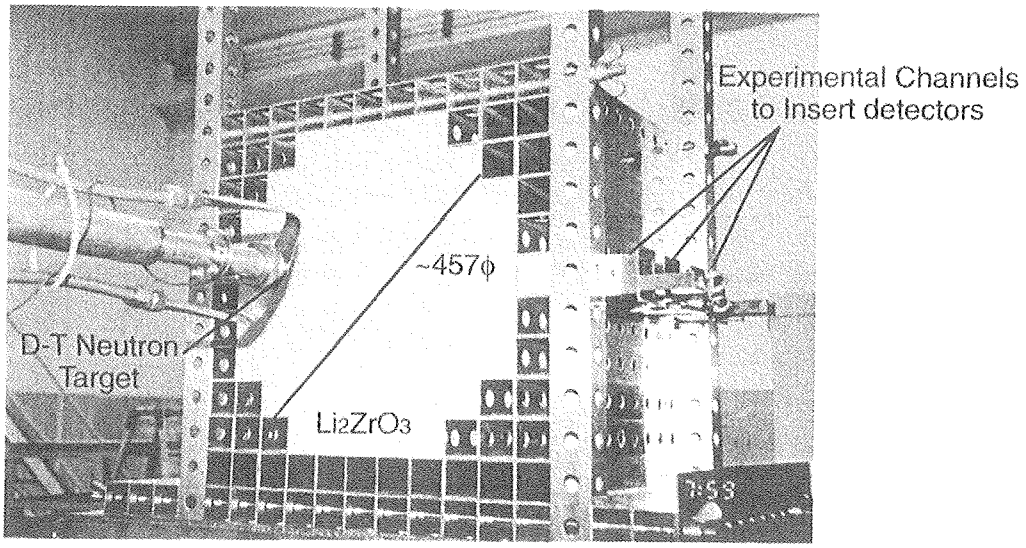

Fig. 2 Experimental assembly made of lithium zirconate.

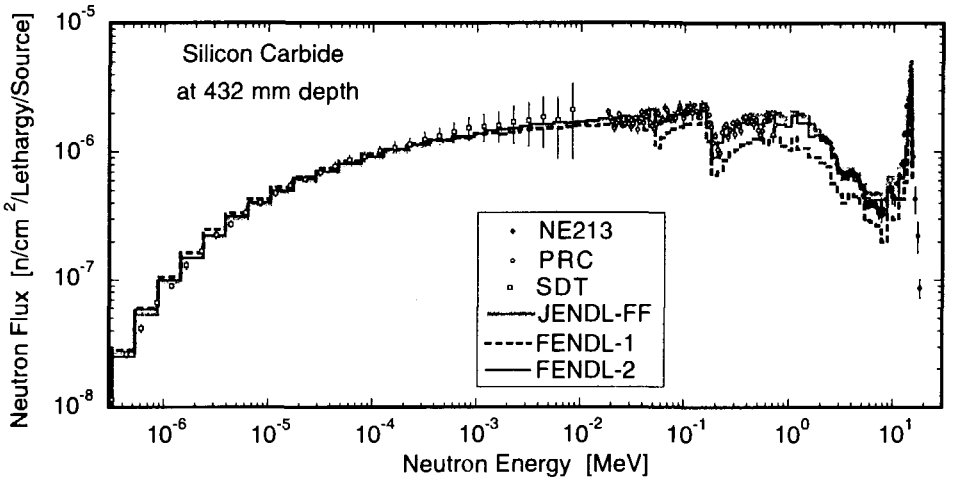

Fig. 3 Neutron spectra in the silicon carbide (SiC) assembly measured and calculated with three cross section files.

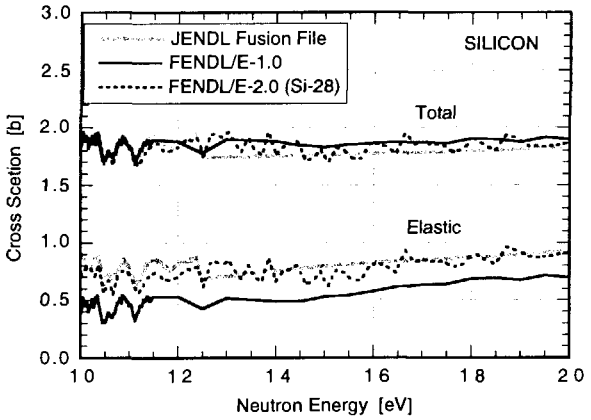

Fig. 4 Total and elastic scattering cross sections of silicon in JENDL Fusion File, FENDL/E-1.0 and FENDL/E-2.0. Data for the main silicon isotope (Si-28, 92.2 %) are plotted for FENDL/E-2.0 instead of silicon data in natural abundance.

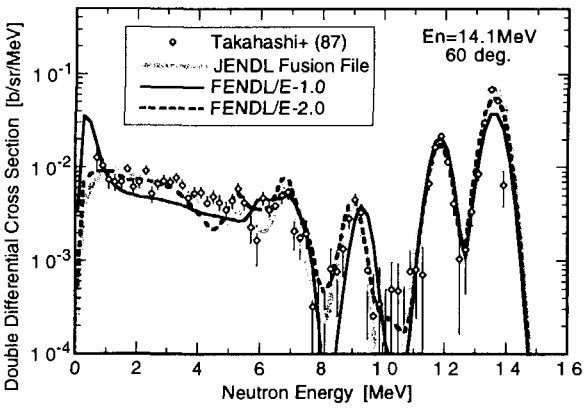

Fig. 5 Double differential neutron emission cross section of silicon at En=14.1 MeV for a scattering angle of 60 degrees measured by Takahashi, et al. [11] and that in the three cross section files .

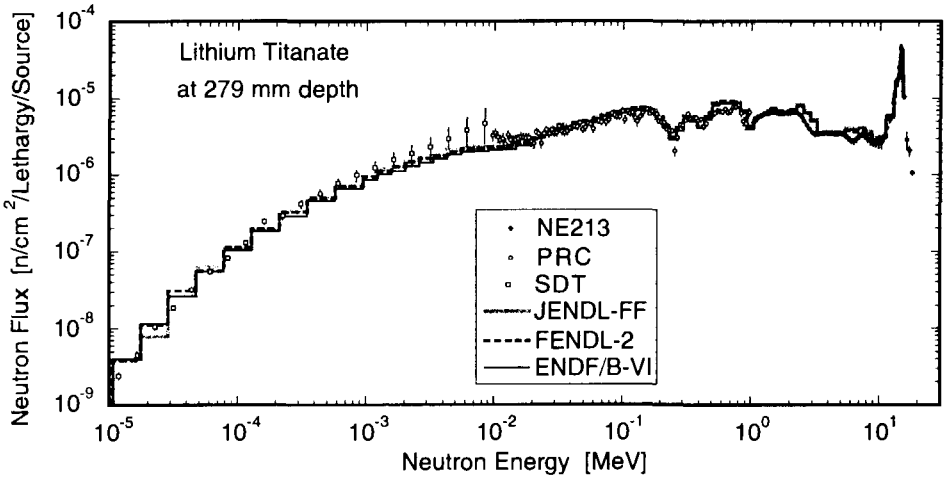

Fig. 6 Neutron spectra in the lithium titanate (Li_2TiO_3) assembly measured and calculated with three cross section files.

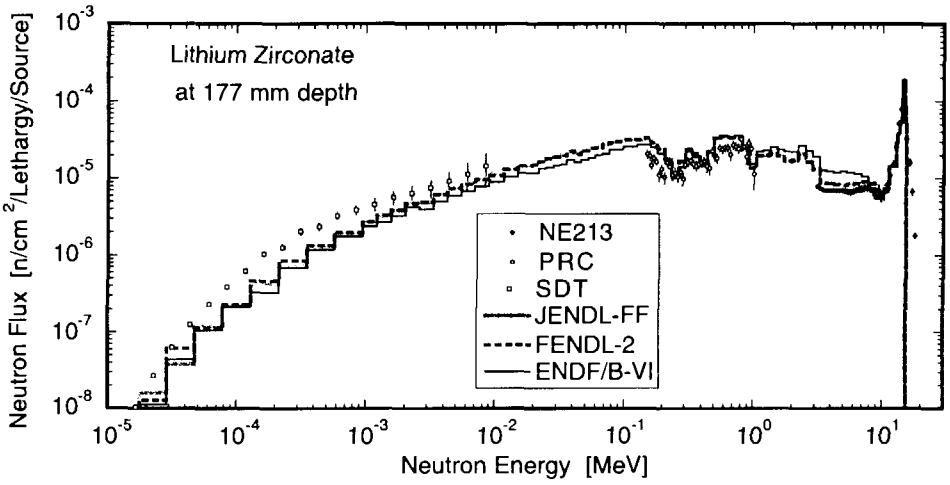

Fig. 7 Neutron spectra in the lithium zirconate (Li_2ZrO_3) assembly measured and calculated with three cross section files.

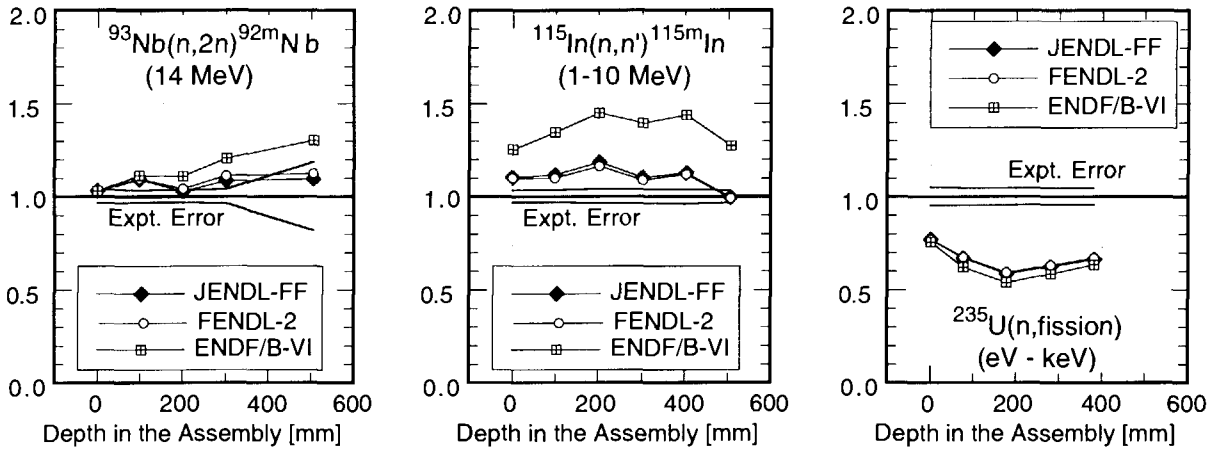

Fig. 8 C/E values for the three reaction rates in the lithium zirconate (Li_2ZrO_3) assembly.

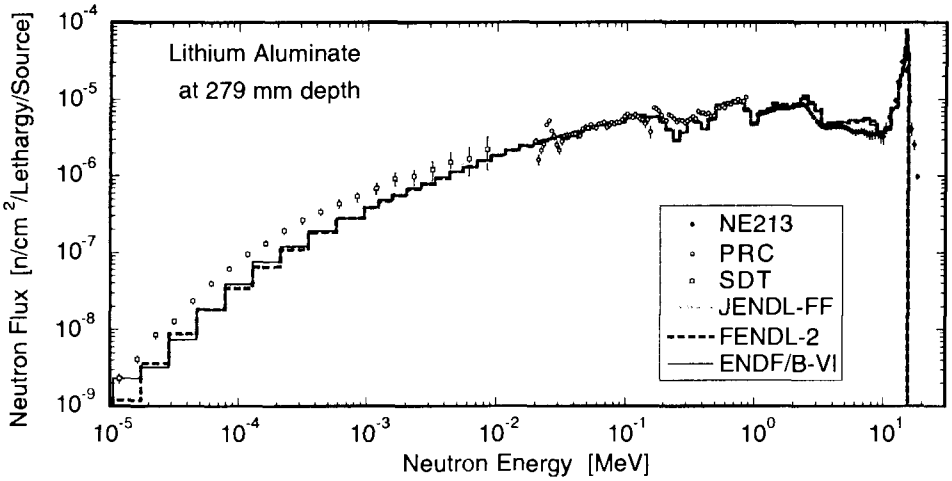

Fig. 9 Neutron spectra in the lithium aluminate ($LiAlO_2$) assembly measured and calculated with three cross section files.

JP0150698

3.36

Nuclear Reactions and Self-Shielding Effects of Gamma-Ray Database for Nuclear Materials

Mitsutane Fujita and Tetsuji Noda
National Research Institute for Metals
1-2-1, Sengen, Tsukuba, Ibaraki 305-0047
E-mail: fujita@nrim.go.jp, WWW: http://inaba.nrim.go.jp/Irrd/

A database for transmutation and radioactivity of nuclear materials is required for selection and design of materials used in various nuclear reactors. The database based on the FENDL/A-2.0 on the Internet and the additional data collected from several references has been developed in NRIM site of "Data-Free-Way" on the Internet. Recently, the function predicted self-shielding effect of materials for γ -ray was added to this database.

The user interface for this database has been constructed for retrieval of necessary data and for graphical presentation of the relation between the energy spectrum of neutron and neutron capture cross section. It is demonstrated that the possibility of chemical compositional change and radioactivity in a material caused by nuclear reactions can be easily retrieved using a browser such as Netscape or Explorer.

1. Introduction

In the data system for nuclear material design and selection used in various reactors, huge material databases and several kinds of tools for data analysis or simulation code of the phenomena under irradiation [1] are required. Thus, a database on transmutation for nuclear materials had been constructed on PC [2]. The database is converted to a system used on Internet [3-5]. As a database for nuclear material design and selection used in various reactors are developed in NRIM site of "Data-Free-Way"[5-8]. A database storing the data on nuclear reaction is needed to calculate the simulation. Using the database, we can retrieve the data of nuclear reaction for material design on the Internet and understand qualitatively the behavior of nuclear reaction such as the transmutation or decay. The database is required for the friendly user-interface for the retrieval of necessary data. In the paper, features and functions of the developed system are described and especially, examples of the easily accessible search of nuclear reactions are introduced

2. Outline of the database on transmutation for nuclear materials

2.1 Database system

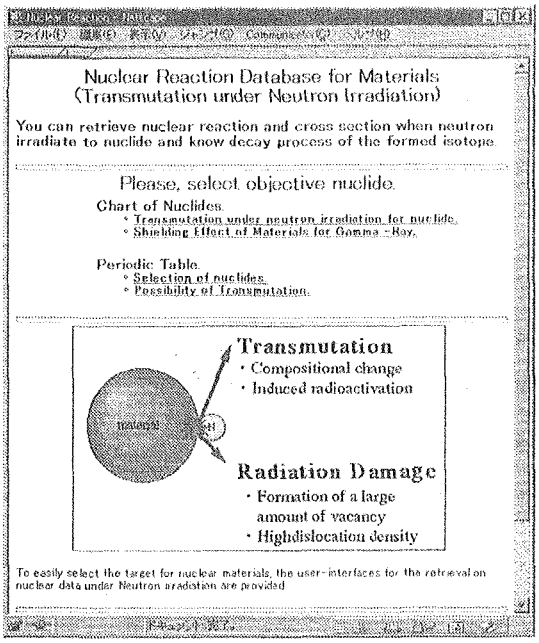

Fig.1 Opening screen of the for transmutation under neutron irradiation.

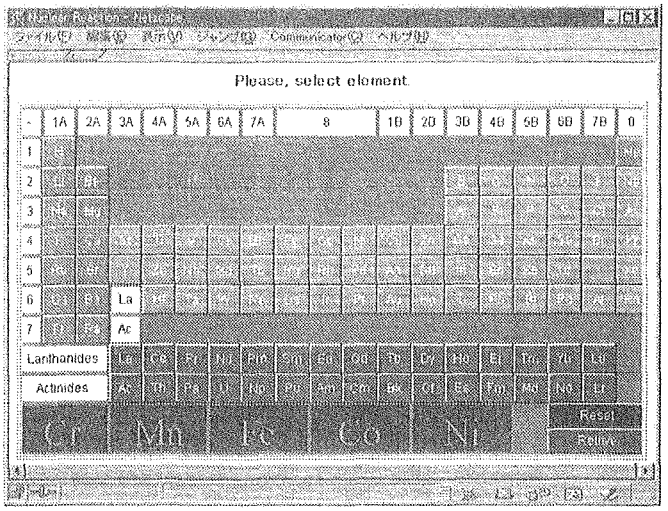

Fig.2 Screen for selection of the nuclide from Periodic table

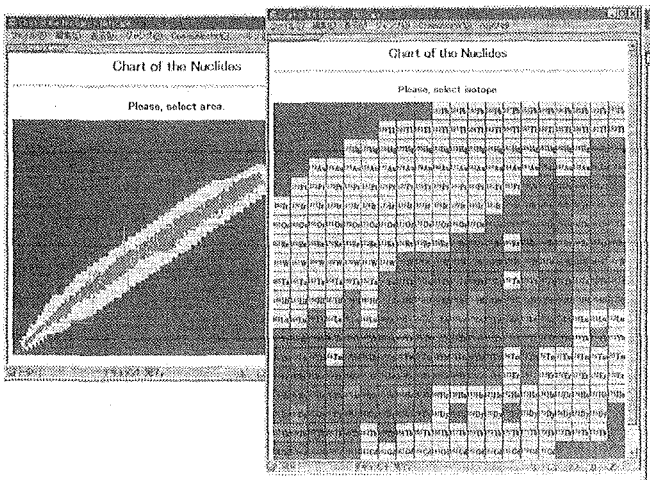

Fig.3 Screen for selection of the nuclide from the chart of the nuclides

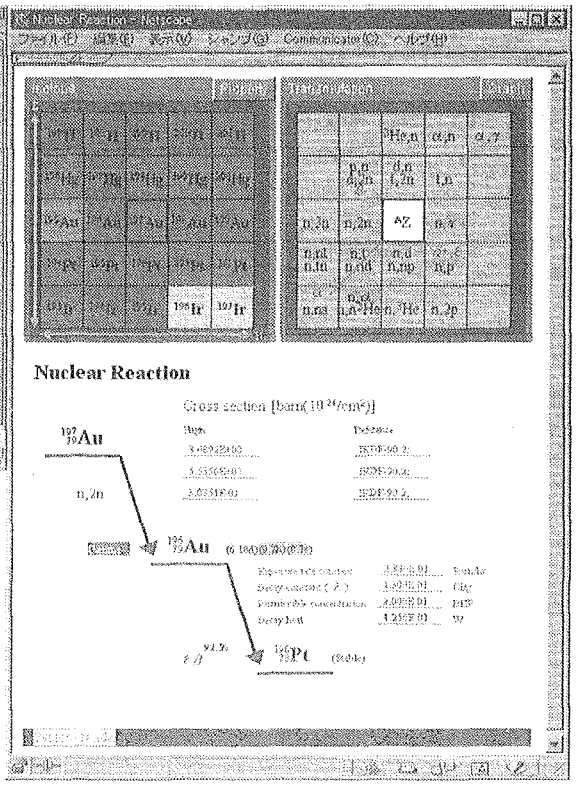

Fig.4 An example of screen to retrieve data on nuclear transmutation of ^{197}Au to ^{196} Au by (n,2n) reaction and decay process of ^{196} Au.

In the database of transmutation for nuclear materials, the data of nuclear reaction for

material design is stored and we can understand qualitatively the behavior of nuclear reaction such as the transmutation or decay. The database is managed by ORACLE where RDBMS (relational database management system) is supported on workstation with UNIX OS. As the RDBMS and WWW were connected, users are able to retrieve necessary data using Netscape or Explorer as a user-interface through the Internet.

Fig. 1 shows the opening screen of the for transmutation which users are accessed the database by selecting the term of " Nuclear Reaction Database" for nuclear materials on transmutation and self-shielding effect of materials for γ -ray under neutron irradiation in the WWW of NRIM site on "Data-Free-Way". Users are able to select various interface for retrieval and obtain the necessary data. Fig.2 shows the screens to select a desired nuclide from periodic table. Fig.3 shows the other screens to select a nuclide form chart of the nuclides

2.2 Data structure

The database consists of five main tables and three supplemental tables. Main tables are element, isotope, spontaneous decay, transmutation and cross section table. The element table has the data such as element name, atomic weight and etc. These data are input values obtained from ordinary periodic table. The data in the isotope table consist of the natural abundance ratio, half-life data, γ -ray or β -ray energy and maximum permissible concentration in air (MPC), which are taken from isotope table. The spontaneous decay table has the data of decay mode and branching ratio. The transmutation table has the data of transmutation process, produced nuclide and etc. The neutron cross-section table stores the data with 42-energy group covering from thermal neutron energy to 15MeV.

2.3 Stored data

Various data, which are required for simulation on nuclear reaction, have been collected from reports as follows;

I. Nuclear data such as neutron cross-section are collected from JAERI's CROSSLIB, ENDF/B- 6, JENDL-3 and FENDL/A-2.0. The number of cross section for nuclear reactions which were stored in the database is 3213 in stable nuclides and 5484 in unstable ones.

II. The data on decay process, γ -ray, isotope and element are collected respectively from

a. "Table of Radioactive Isotopes" E. Browne and R. B. Firestone, 1986, LBLU of C, John Wiley & Sons,

b. "Radiation Data Book", edited by Y. Murakami, H. Danno and A. Kobayashi, 1982, Chijin-Shokan.

c. "Chart of the Nuclides" compiled by Y. Yoshizawa and T. Horiguchi and M. Yamada, 1996, JNDC and NDC in JAERI.

d. "Elsevier's Periodic Table of the Elements", collected by P. Lof, 1987, Elsevier.

3. Self-shielding effects of materials for γ-ray

3.1 Stored Data

Various data, which are required for self-shielding effects have been collected from reports as follows;

Linear Attenuation Coefficient of Materials: Photon Cross-Sections from 1keV to 100MeV for Elements, Nuclear Data Tables A7, (1970) 565.

3.2 Calculation Method

Surface dose rate for given nuclear material is calculated for an unstable nuclide by the following equation.

$$D = K\sum c\frac{\mu_a SB}{2\mu_m} \qquad (1)$$

D: Surface dose rate (Sv/h)

K:constant

C:Conversion factor (Sv/Gy)

B:Build up factor

μ_a: Gamma-ray energy absorption coefficient of air (m^2/kg)

μ_m: Linear attenuation coefficient of material (m^2/kg)

S: Rate of gamma-ray emission (MeV/kg/s)

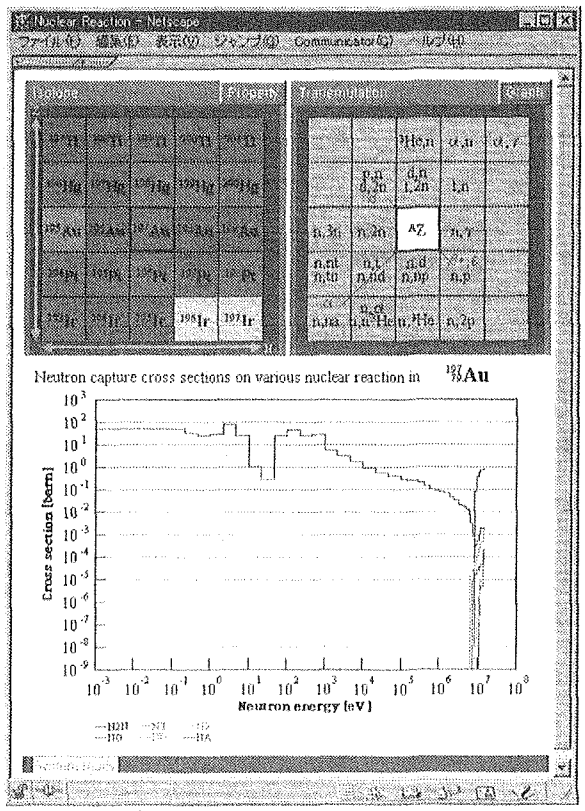

Fig.5 An example of graph of relation between neutron capture cross section for various reaction and neutron energy in ^{197}Au.

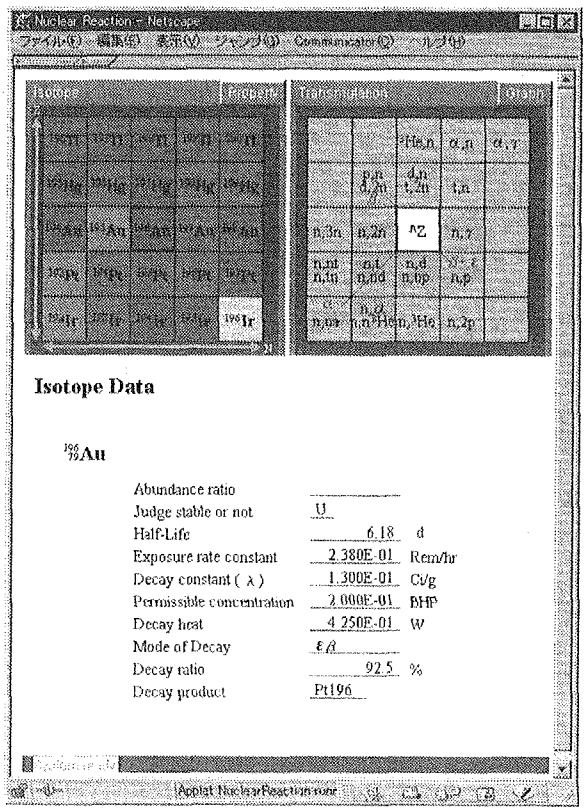

Fig.6 An example of screen to retrieved nuclide data on ^{196}Au formed by nuclear

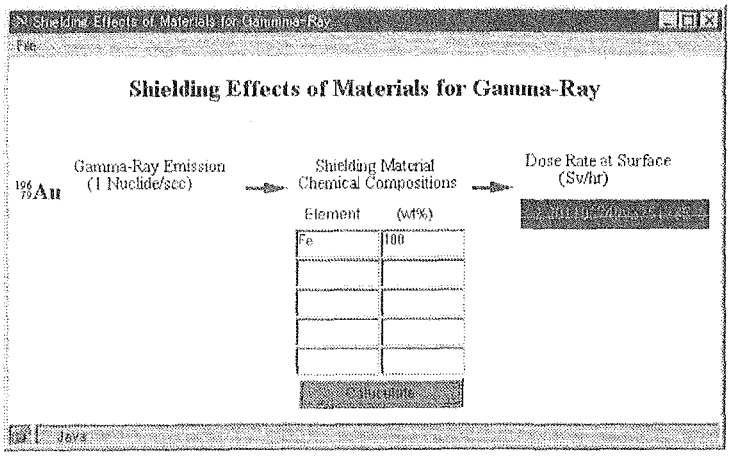

Fig.7 An example of screen of calculator for self-shielding effects of materials for γ -ray from ^{196}Au.

3. Functions and user-interface

3.1 Functions

Fig. 1 shows opening main menu screen of the database. This database has four retrieval functions of nuclear reaction process, properties of radioactive isotope, spontaneous decay of each isotope and decay of produced nuclides after nuclear reaction. We can understand qualitatively the behavior of nuclear reaction such as the transmutation or decay. the function predicted self-shielding effect of materials for γ -ray was added to this database.

3.2 User-interface for retrieval data

Fig. 2 and Fig. 3 show screens of the selection of the isotope or the nuclide from the periodic table and chart of nuclides, respectively. Fig. 4 shows an example of screen to be retrieved ^{197}Au on nuclear transmutation of ^{197}Au to ^{196} Au by (n,2n) reaction and decay process of ^{196} Au by (n,2n) reaction and decay process of ^{196} Au. Fig. 5 shows screen that by selecting the desired nuclear reaction in right folder, user is able to know records on a given transmutation and spontaneous decay in the reaction process. The graph as shown in Fig. 5 appears, if user clicks the graph button in the screen shown Fig. 4 or Fig. 6. The graphs shows the relation between transmutation cross section and neutron energy spectrum on various reactions. The high value of the cross section means that the neutron reaction easily occurs. Fig. 6 shows mass number, the natural abundance ratio, half-life data, to γ -ray or β -ray energy on ^{196}Au formed by ^{197}Au(n,2n)^{196}Au reaction. Moreover, if user clicks the red button indicated (gamma) in Fig. 4, the screen appears as shown in Fig. 7. In the screen, a self-shielding effect of materials for γ -ray formed ^{196} Au is able to calculate. This new function was added to nuclear reaction database for nuclear materials.

4. Summary

1) A database on transmutation for nuclear materials with a user-friendly interface was constructed in WWW server on the Internet. (http://inaba.nrim.go.jp//Irra/)

2) The database consists of mainly four tables storing the information of atomic element, isotope, transmutation and cross section for 42 neutron energy groups.
3) The user interface for this database has been constructed for retrieval of necessary data and for graphical presentation of the relation between the energy spectrum of neutron and neutron capture cross section. It is demonstrated that the possibility of chemical compositional change and radioactivity in a material caused by nuclear reactions can be easily retrieved using a browser such as Netscape or Explorer.

References

[1] T. Noda, H. Araki, F. Abe and M. Okada: Trans. NRIM, 30 (1988) p. 1-31.

[2] M. Fujita and T. Noda: COMP '93, ISIJ (1993) p. 404-409.

[3] Fujita M., M. Utsumi, T. Noda; JAERI-Conf 97-004 (1998) p.208

[4] M. Fujita, M. Utsumi and T. Noda; Proc. of '98 Sympo. on Nuclear Data, (1998), November, JAERI-Conf. 99-002 p.302-307

[5] F. Ueno, S. Kano, M. Fujita, Y. Kurihara, H. Nakajima, N. Yokoyama and S. Iwata; J. Nucl. Sci. Techn., vol.31 (1994) p.1314-1334.

[6] M. Fujita, Y. Kurihara, H. Shindo, N. Yokoyama, F. Ueno, S. Kano, and S. Iwata: ASTM STP 1311, ASTM (1997) p. 249-260.

[7] M. Fujita, M. Utsumi and T. Noda; J. Japan Inst. Metals, Vol.63, No.9 (1999), p.1141-1144.

[8] M. Fujita, J. Kinugawa, H. Tsuji, Y. Kaji, S. Kano, Y. Tachi, K. Shimura, R. Nakajima and S. Iwata; J. Fusion Eng. And Design (2000), in press.

JP0150699

3.37

Study of Retrieval, Utilize and Circulation System for Nuclear Data in Computerized Media

Yosihide OHBAYASI

Meme Media Laboratory, Hokkaido University, Sapporo, Hokkaido 060-8628

We have shown and have developed a new type of nuclear data retrieval system, in which a nuclear reaction data compilation is applied as an example. To get benefits from recent computer and network technologies, we adopt the IntelligentPad architecture as a framework of the present system. We set the future aim of our database system toward the "effective" use of nuclear reaction data: I. "Re-produce, Re-edit, Re-use", II. "Circulation, Evolution", III. "Knowledge discovery". We discuss the appropriate concepts, which fit for the above purpose.

1. Introduction

Recently, we have shown and have developed a new type of nuclear data retrieval system, in which a nuclear reaction data compilation is applied as an example. To get benefits from recent computer and network technologies, we adopt the IntelligentPad architecture as a framework of the present system [1]. This software architecture has many useful features for handling multimedia, media-based system construction, and graphical user interface. IntelligentPad is not only a specific software package, but also the fundamental environment architecture to support the effective utilization of computerized resources.

We designed the client-server retrieval system. The server system is constructed on a relational database, and the client system is constructed on an IntelligentPad software package [2]. Our system is called CONTIP, which is an abbreviation of "Creative, Cooperative and Cultural Objects for Nuclear data and Tools" [3]. The current trial system has mainly two features: i) interactive data visualization and comparison and ii) 2D intuitive data navigation (Figure 1.). We will develop CONTIP to realize effective utilization of nuclear reaction data: I. "Re-production, Re-edit, Re-use", II. "Circulation, Coordination and Evolution", III. "Knowledge discovery".

2. Major concepts for the development

For effective utilization of nuclear data, seamless linkages between measured experimental data and its application should be important. Considering these linkages, it is

essential to link accumulation, evaluation and circulation on the same system. Furthermore, there are interdependences among them: evaluation of accumulated data, circulation of evaluated data, and re-accumulation evaluated data. Therefore, we should consider constructing the framework so as to achieve this continuous cycle. In addition, we should consider integrating the different databases which have different compilation policy or evaluation policy. Using the integrated database, we can retrieve and utilize the various resources concerned with nuclear data (Figure 2).

In order to realize the purpose of the above, we consider the three major concepts for the development. i) Medialization: All utilities are constructed with the synthesis of simple pads. A retrieved data is also introduced as a data pad. Data browsing, Visualization, Comparison, etc., are simultaneously available on this system (Figure 3). ii) Access architecture: Once we have all computational resources on the synthetic media, we should consider to give a so-called 'field', to navigate and share among users. iii) Unified data description format: For the effective re-use of precious information of nuclear data, from compilation stage to the end-user stage, all nuclear data information should be described by something unified description framework.

Once our knowledge for the nuclear data, which include not only numerical experimental data but also the background information of the experiment, evaluation policies, etc., are described by using computational "media" which can be edited by many users and be shared on the net, it will be a strong basis for our knowledge sharing. It is helpful that users who are responsible for the nuclear data use such basis.

3. Current development

With the above background and motivation, current development is underway. In this section, some examples of our development are shown which fit for the above purpose of nuclear data information.

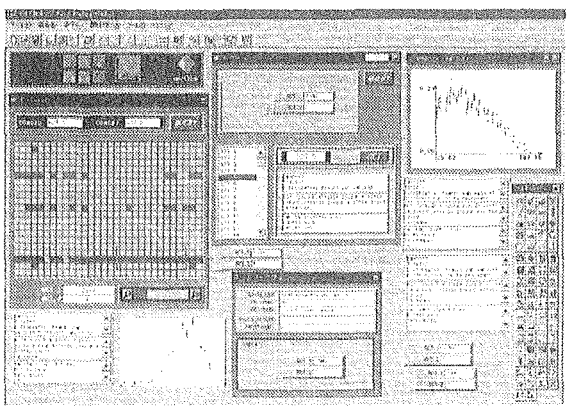

Fig.1. A Snapshot of utilities.

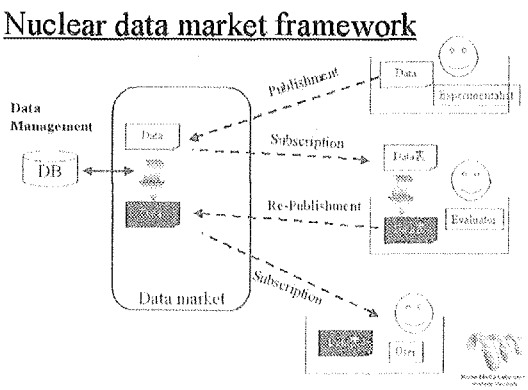

Fig.2 Nuclear data market framework

For the extension of the system, e.g., use of the other application on the system, we can do it by introducing the proxy pad, like Figure 4. In this figure, accession to the database is achieved by using database proxy pad.

On the other hand, Gnuplot proxy is introduced in order to use plotting function for the retrieved data. By dragging and dropping to the Gnuplot proxy, numerical data is transferred to the Gnuplot application, and graphic pad displays plotting image which made by the Gnuplot (Figure 5.).

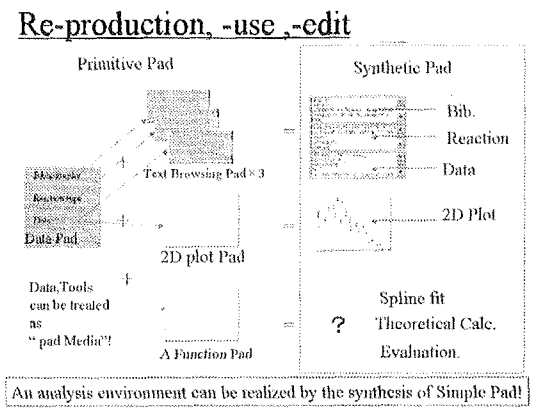

Fig.3. Synthetic description of data and tools.

In addition, it is natural that we have necessity which we should discuss or evaluate some nuclear data for an application via the network. Once the description of each data is unified among whole users, e.g., we adopt the basis of pad description for data and tool; each pad can be distributed via the net with holding the ability of editing. By using PIAZZA technology [4], which gives sharing environment of the pads via the net, as shown in Figure 6 and 7, it is possible to give so-called "interactive information sharing field". In the Figure 6, this snapshot is user A's desktop of the system. User A distributes new data to sharing space via drag and drop operation. On the other hand, as shown in Figure 7., distributed new data is available for user B via the sharing interface. User B can edit the formerly distributed data. In this case, user B adds new data, and re-distributes them.

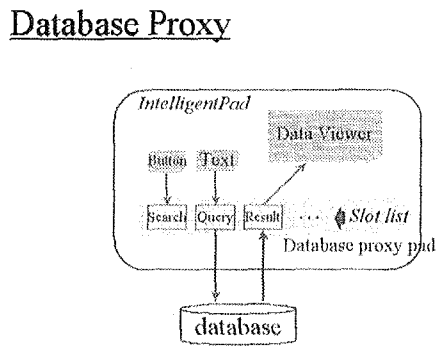

Fig.4. Database proxy. Introducing proxy pad, other application can be used.

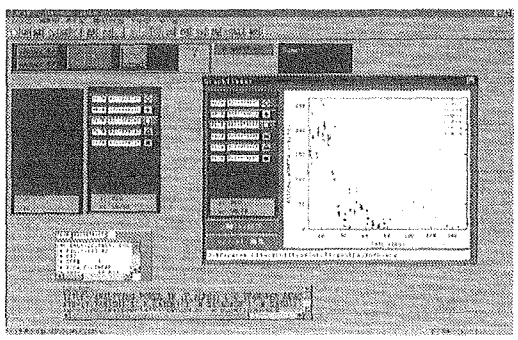

Fig.5. Data plotting interface. Proxy for Gnuplot is introduced.

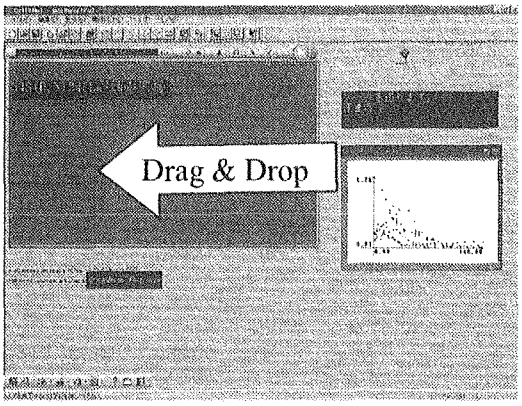

Fig. 6. Example of the information sharing. User A distributes new data to sharing space via drag and drop operation.

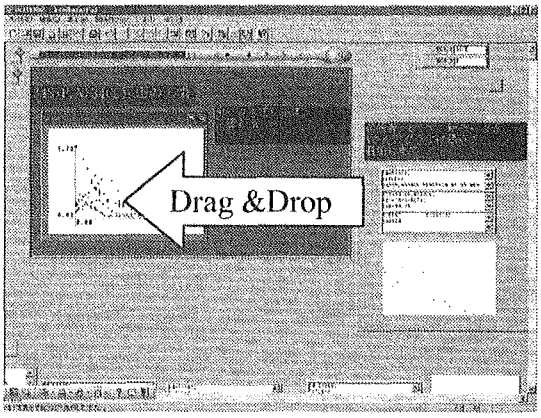

Fig.7. This snapshot is user B's desktop. User B can edit and re-distribute the formerly distributed data.

4. Summary

We discuss and develop the effective utilities for nuclear data. And actually we consider the important concepts such as i) Medialization of nuclear data and tools, ii) Access architecture and iii) Unified data description format. Current IntelligentPad for Windows trial package is available freely via http://www.pads.or.jp/. We are going to release "mile-stone" package for nuclear reaction data retrieval system by using above IntelligentPad, which includes EXFOR data toward the next year.

For the further development, recently, so-called semi-structure description of data likes HTML is familiar to describe for a publication. For example, XML [5] is a recent development of such description format, and by using such format; unified description of nuclear data from author level to end-user level is expected to be available. We will consider the semi-structure description format of nuclear reaction data.

References

[1] Y.Ohbayasi, et al, Jour. of Info. Sci. 26 (1), pp.29-37.
[2] Y. Tanaka, Information and software technology 38(3)1996 201
[3] IntelligentPad consortium. http://www.pads.or.jp/
[4] PIAZZA project is developed under the initiative of Meme Media Laboraotry, Hokkaido University.
[5] XML See http://www.w3c.org/

JP0150700

3.38

Calculation of neutron-induced single-event upset cross sections for semiconductor memory devices

Taketo IKEUCHI*, Yukinobu WATANABE*, SUN Weili+, and Hideki NAKASHIMA*
*Department of Advanced Energy Engineering Science, Kyushu University, Kasuga, Fukuoka 816-8580, Japan
+Department of Applied Quantum Physics and Nuclear Engineering, Kyushu University, Fukuoka 812-8581, Japan
email: watanabe@aees.kyushu-u.ac.jp

Neutron-induced single-event upset (SEU) cross sections for semiconductor memory devices are calculated by the Burst Generation Rate (BGR) method using LA150 data and QMD calculation in the neutron energy range between 20 MeV and 10 GeV. The calculated results are compared with the measured SEU cross sections for energies up to 160 MeV, and the validity of the calculation method and the nuclear data used is verified. The kind of reaction products and the neutron energy range that have the most effect on SEU are discussed.

1. Introduction

In recent years, much attention has been paid to cosmic-ray induced soft errors in semiconductor memory devices used at sea level and in aircrafts as well as in artificial satellites in space[1]. Cosmic rays at sea level consist of mainly neutrons, protons, pions, and muons over a wide energy range from MeV to GeV. These energetic cosmic-ray particles interact with materials used in semiconductor memory devices, and fast heavy ions can be generated via a nuclear reaction with a silicon nucleus. These ions can give rise to local charge burst in a micron volume, which results in upset of the memory cell information quantum that is called "single-event upset (SEU)". This is known as a microscopic picture of the cosmic-ray induced soft errors. Therefore, quantitative estimation of the soft errors requires more reliable nuclear reaction data for silicon in the high-energy range and modeling of charge transport in microelectronics devices.

In the present work, we focus on the soft errors induced by neutrons having about 95% of the cosmic rays at sea level. Neutron-induced SEU cross sections are calculated by the Burst Generation Rate (BGR) method[2] using LA150 data[3] and QMD calculation[4] in the neutron energy range between 20 MeV and 10 GeV. The calculated results are compared with measured SEU cross sections up to 160 MeV[5], and the kind of reaction products and the neutron energy range that are crucial to the SEU are also investigated.

2. A Method of calculating SEU cross sections

2.1 Burst Generation Rate (BGR) model

The SEU rate is defined by

$$\text{SEU rate} = \int \sigma_{SEU}(E_n)\phi(E_n)dE_n , \qquad (1)$$

where $\sigma_{SEU}(E_n)$ is the SEU cross section for a neutron energy, E_n, and $\phi(E_n)$ is the neutron

flux. Using the Burst Generation Rate (BGR) method[2], $\sigma_{SEU}(E_n)$ is given by

$$\sigma_{SEU}(E_n) = C \cdot V \cdot BGR(E_n, Q_c), \quad (2)$$

where C is the charge collection efficiency and V is the sensitive volume per bit. The BGR is defined as the probability that the charged particles and ions with energy more than a critical energy E_r are emitted in the nuclear reaction, and is given as a function of incident neutron energy, E_n and critical charge, Q_c which can be converted into E_r using the relation E_r(MeV) = 22.5 Q_c(pC).

$$BGR(E_n, Q_c) = \sum_i BGR(E_n, Q_c, A_i, Z_i)$$

$$= N_{Si} \sum_i \int\int_{E_r}^{E_{max}^{(i)}} \left(\frac{d^2\sigma}{dEd\Omega} \right)^{(i)} d\Omega dE, \quad (3)$$

where N_{Si} is the number density of silicon atoms, and the index i stands for the kind of reaction product with mass number A_i and atomic number Z_i. $(d^2\sigma/dEd\Omega)^{(i)}$ is the double-differential production cross section of the reaction product i.

In the previous papers related to the BGR model[2], $E_{max}^{(i)}$ was assumed to be the maximum emission energy of the reaction product i. However, this treatment might overestimate the BGR when one considers the energy deposit of ions with high energy in a finite volume. Since the energy deposit in a small volume depends on the linear energy transfer (LET), we newly introduce an "effective depth d " as a parameter for BGR calculations. By taking into account the LET, $E_{max}^{(i)}$ is estimated as the maximum energy of the reaction product i that deposits energy above E_r within the depth d. Note that isotropic angular distribution is assumed for emission of the reaction products for simplicity.

This naïve method does not account for transport of local burst charge in a medium, and therefore corresponds to the zero-order approximation to charge transport. In the present work, the product of C and V is treated as a normalization parameter that can be determined so as to fit experimental $\sigma_{SEU}(E_n)$ data as mentioned below.

2.2 Input data

LA150 nuclear data[3] are used for energies from 20 to 150 MeV. For energies above 150 MeV, the JQMD code[4] based on the QMD plus statistical decay model (SDM) is employed to calculate the energy spectra of reaction products. The default parameters are used in the JQMD calculations. The total reaction cross section calculated by QMD is normalized to a systematics given by Niita[6]. Note that light charged-particles (p, d, t, ^{3}He, and α) and those heavy ions with their atomic numbers less than 5 are not considered in the SEU calculations because the energy deposit by these particles and ions is very small and their effect on SEU is negligible.

The SRIM code[7] is used to calculate the LET necessary to estimate the maximum energy $E_{max}^{(i)}$ in Eq.(3).

3. Results and discussions

Figure 1 shows a comparison of calculations with measured data [5] for SRAMs with 256Kb or 1Mb. The measured data are normalized to the data of Cypress. As can be seen in Fig.1, the measured SEU cross sections shows a weak dependence on chips and have a similar energy dependence. The normalization constant CV in Eq.(2) was determined so as to provide the BGR function calculated with Q_c=0.1pC and d=1μm a best fit to the data of Cypress. The

solid curve with Q_c =0.1pC and d=1μm shows satisfactory agreement with the measured data. Use of a finite effective depth d=1μm leads to a decrease in the calculated SEU cross section with increasing neutron energy, as can be seen from a comparison between the solid curve and the dotted one.

Calculations of the SEU cross section are extended to incident energies above 150 MeV. The QMD plus SDM calculation was used to obtain the relevant nuclear reaction data, *i.e.*, energy spectra of all emitted heavy nuclei. Before the nuclear data are inputted to calculations of SEU cross-sections, one should see to what extent the QMD plus SDM calculation can reproduce experimental differential data. Since there is no experimental data for neutron-induced reactions on ^{28}Si, we have applied the QMD plus SDM calculation to the proton-induced reaction on ^{27}Al at 180 MeV[8] and examined the applicability. Comparisons of the calculation with experimental data are shown in Figs.2 to 4. The calculated results are in good agreement with the experimental data to a similar extent to the AMD calculation[9], except for production of heavy ions with $A < 11$.

Calculated BGR functions with LA150 and QMD nuclear data are plotted for energies up to 10 GeV together with the calculated reaction cross section, σ_R, in Fig.5. A discontinuity of the calculated BGR functions appears at an incident energy of 150 MeV, because the nuclear data used is altered at this energy. For neutron energies above 100 MeV, the BGR function calculated with infinite depth d=∞ shows the energy dependence similar to the reaction cross section that is almost independent of the energy. On the other hand, the BGR function with a finite effective depth d=1μm decreases with an increase in neutron energy. This may be due to an increase in the average kinetic energy of the reaction products, which leads to reduction of the energy deposited in the medium because the LET becomes small. In the energy range less than 100 MeV, the BGR function decreases as the incident energy decreases, while the reaction cross section increases. This opposite behavior can be explained from two main causes. One of them is that major components among the reaction products for lower incident energies are light ions, such as protons and alpha particles, which provide negligible contribution to SEU. Furthermore, the energy spectra of residual heavy nuclei are shifted to the low energy side and the contribution to BGR functions becomes small in a case with rather large Q_c corresponding to high threshold energy E_r. This can be seen from Fig.6 that shows a dependence of Q_c on BGR functions in the case of d=1μm. It is found that the dependence is strong and Q_c affects the shape of the BGR functions at low incident energies.

Using the BGR functions given in Fig.6, the incident energy range having the most effect on the SEU rate has been examined by assuming a neutron flux distribution at sea level given by IBM group[1]. The resultant integrated SEU rate is plotted as a function of the incident neutron energy in Fig.7. A major contribution (up to about 90 %) to the SEU rate comes from neutrons up to 400 MeV for semiconductor memory devices with these Q_c values. Therefore, this means that the relevant nuclear data of silicon with high accuracy are necessary for reliable estimation of the SER rate, particularly, at energies ranging from 20 to 400 MeV.

Finally, we have investigated the kind of reaction products that influence largely the SEU. The result is presented for two incident energies, 150 MeV and 1 GeV, in Fig.8. Both the cases show that production of heavy ions such as Ne, Na, and Mg plays a major role in the SEU because such ions have large LET.

4. Conclusion

The BGR functions were calculated in the neutron energy range between 20 MeV and 10 GeV using the neutron nuclear data of LA150 and the QMD calculation by considering the LET of reaction products. The SEU cross sections obtained using the calculated BGR

functions reproduced well the energy dependence of the experimental ones up to 160 MeV for SRAMs with 256Kb or 1Mb by introducing the finite effective depth d as a parameter. The incident energy range having the most effect on the SEU rate at sea level was found to be 20 to 400 MeV, particularly, for devices with small effective charge Q_c. In addition, it was found that the reaction products that influence the SEU strongly are the heavy ions such as Ne, Na, and Mg having large LET.

This work is the first step towards establishment of a reliable method of evaluating soft errors in semiconductor memory devices. From the point of view of the nuclear reaction data, a new evaluation [10] in JENDL High energy file should be applied to calculations of the neutron-induced SEU cross sections in order to see a dependence of the nuclear data used. In addition, calculations of proton and pion induced SEU cross sections will be interesting to see similarities and differences in effects of neutrons, protons, and pions on the SEU in order to enhance understandings of the mechanisms of soft errors.

Acknowledgements

The authors would like to thank Dr. K. Niita for allowing them to use the JQMD code. One of the authors, SW, is grateful to the JSPS's Postdoctoral Fellowships for Foreign Researchers.

References

[1] J.F. Ziegler et al., IBM J. Res. Develop. **40**, No.1 (1996).
[2] J.F. Ziegler and W. Lanford, Science **206**, 776 (1979).
[3] M.B. Chadwick et al., Nucl. Sci. Eng. **131**, 293 (1998).
[4] K. Niita et al., JQMD code, JAERI-Data/Code 99-042 (1999).
[5] K. Johansson et al., IEEE Trans. Nucl. Sci. **45**, 2519 (1998).
[6] K. Niita, Proc. of the 1999 Nuclear Data Symp, Nov. 18-19, 1999, JAERI, Tokai, Japan; JAERI-Conf 2000-005 (2000), p.98.
[7] J.F. Ziegler, SRIM code (1999).
[8] K. Kwiatkowski et al., Phys. Rev. Lett. **50**, 1648 (1983).
[9] Y. Tosaka et al., Phy. Rev. C **60**, 064613 (1999).
[10] Sun Weili et al, presented at this symposium (2000).

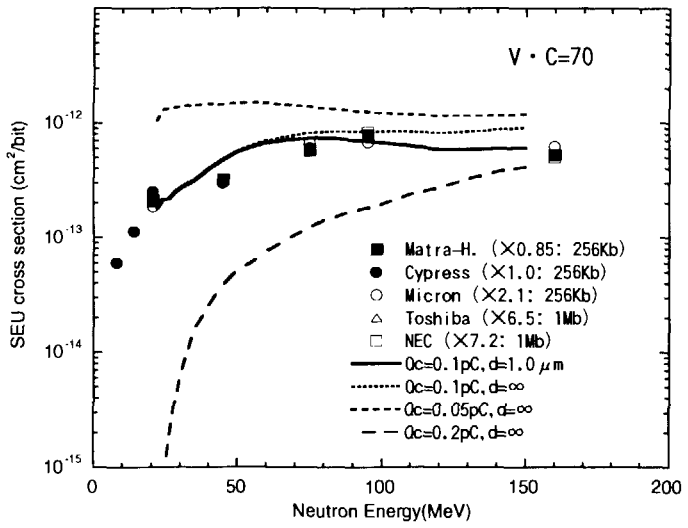

Fig.1 Comparison of the calculated SEU cross sections with the measured ones taken from Ref.[5]. Each measured data is normalized to the data of Cypress.

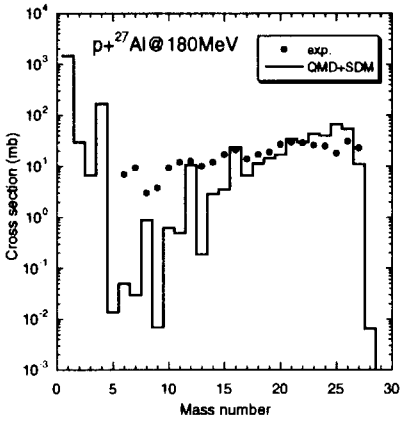

Fig.2 Mass distribution calculated with QMD plus SDM in the proton-induced reaction on ^{27}Al at 180MeV. The experimental data are taken from Ref.[8].

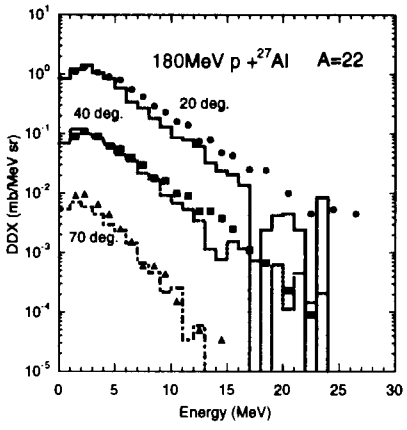

Fig.3 Measured and calculated double-differential production cross sections for fragments with A=22 in the proton-induced reaction on ^{27}Al at 180 MeV. The measured data are taken from Ref.[8]

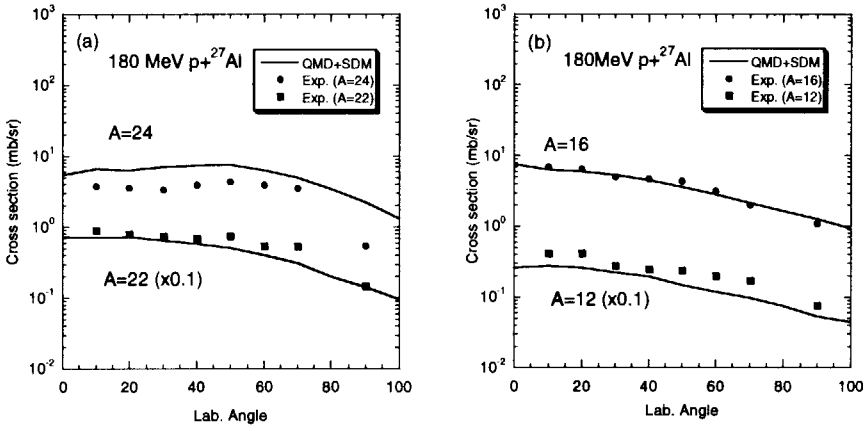

Fig.4 Measured and calculated angular distributions of fragments with (a) A=24 and 22 and with (b) A=16 and 12 in the proton-induced reaction on ^{27}Al at 180 MeV. The measured data are taken from Ref.[8].

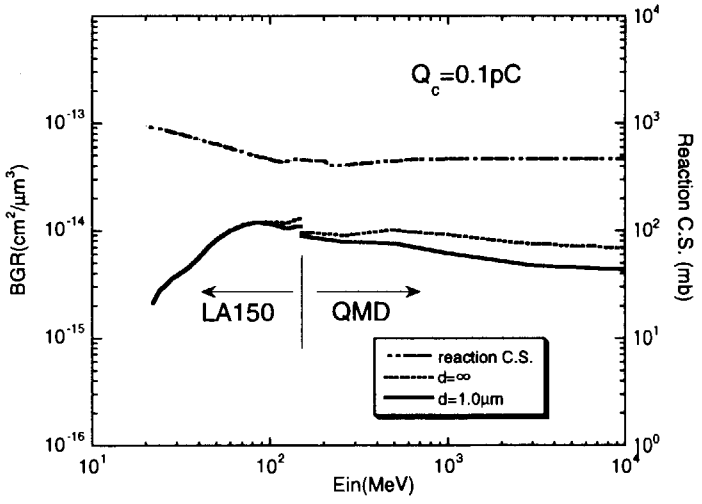

Fig.5 BGR functions calculated with critical charge Q_c=0.1pC and total reaction cross sections.

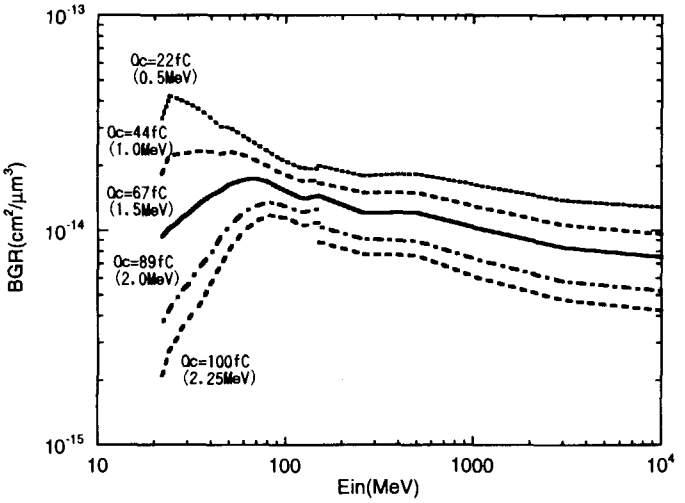

Fig.6 Dependence of BGR functions on critical charge Q_c. The effective depth d is fixed to be 1 μm.

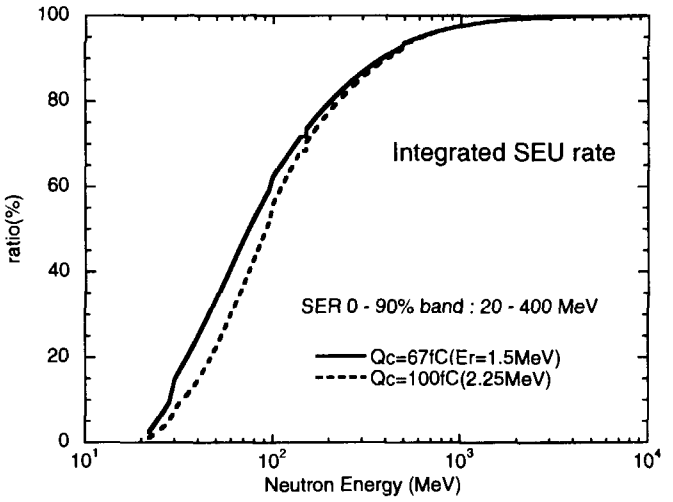

Fig.7 Integrated SEU rate as a function of neutron energy.

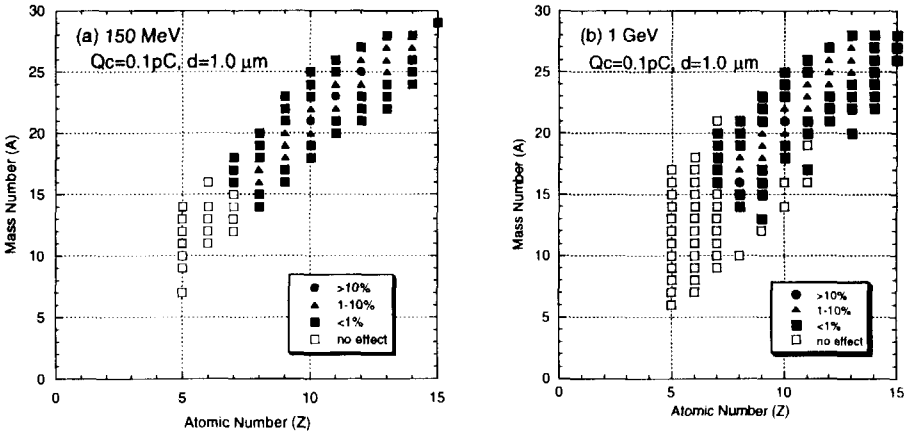

Fig.8 Distribution of the reaction products having effects on SEU for two incident neutron energies of (a) 150 MeV and (b) 1 GeV.

JP0150701

3.39

Preparation of a liquid nitrogen target for measurement of γ-ray in the $^{14}N(n,\gamma)^{15}N$ reaction as an intensity standard in energy region up to 11 MeV

M. Hirano[1], H. Obayashi[1], H. Sakane[2], M. Shibata[2], K. Kawade[2] and A. Taniguchi[3]

[1]*Department of Nuclear Engineering, Nagoya University.*

[2]*Department of Energy Engineering and Science, Nagoya University.*

[3]*Research Reactor Institute, Kyoto University.*

e-mail: h952535b@mbox.media.nagoya-u.ac.jp

For determination of relative γ-ray intensities up to 11 MeV in the $^{14}N(n,\gamma)^{15}N$ reaction, we have developed a liquid nitrogen (N_2) target which contain no hydrogen (H) to improve the accuracy of γ-ray intensities. The ratio of the relative uncertainties for the liquid nitrogen to that for the melamine ($C_3H_6N_6$) widely used was improved by a factor of 2 above 2.2 MeV and a factor of 3 - 6 below 2.2 MeV. It has been shown that the liquid nitrogen target is useful for reduction of the 2.2 MeV γ-ray from the $^{1}H(n,\gamma)^{2}H$ reaction and improvement of statistics.

1 Introduction

The high energy γ-rays are important in the fields of prompt neutron capture γ-ray analysis and nuclear spectroscopy of unstable nuclei. To obtain the γ-ray intensities measured with HPGe detectors, the detection efficiencies in energy region up to 10 MeV are needed. Standard radioactive nuclides such as ^{133}Ba, ^{152}Eu, ^{60}Co and ^{56}Co are used in the energy region below 3.2 MeV, but above 3.2 MeV it is difficult to find suitable radioactive sources that have reasonably long half-lives. Hence, the capture γ-rays emitted from the $^{14}N(n,\gamma)^{15}N$ reaction are used, because of (1) it emits the intense γ-rays which are well spaced in the energy range between 1.7 and 10.8 MeV and (2) the level scheme is relatively simple. The γ-ray intensities in this reaction with accuracy of 1 - 3% were reported by Kennett *et al.*[1)] and Jurney *et al.*[2)]. But there are some discrepancies between them, and re-measurement is strongly desired.

Melamine ($C_3H_6N_6$) has been widely used as a nitrogen target. However, since hydrogen in melamine has large total cross sections, the large attenuation of neutron

fluence rate in the target is serious problem. Moreover, intense γ-ray emitted from the $^{1}H(n,\gamma)^{2}H$ reaction causes increasing of background. In order to resolve these problems, we tried to develop a target system of liquid nitrogen.

2 Experiments

Experiments were carried out by using thermal neutron beam at KUR E-3 neutron guide tube. The neutron fluence rate is about 4×10^{6} n/cm^{2}·s.

The liquid nitrogen target system is shown in Fig. 1. Capture γ-rays emitted from ^{15}N were measured with 22% and 38% HPGe detectors that are located at 10 cm from the target. A target vessel made of polyethylene ($2\times8\times8$ cm^{3}, 20μm thickness) filled with liquid nitrogen is placed on the neutron beam. It is surrounded by enriched ^{6}LiF-box ($10\times10\times10$ cm^{3}, 0.5 cm thickness) that have a neutron incident window (2×10 cm^{2}). The HPGe detectors are shielded with ^{6}LiF-box from scattered neutrons in the target.

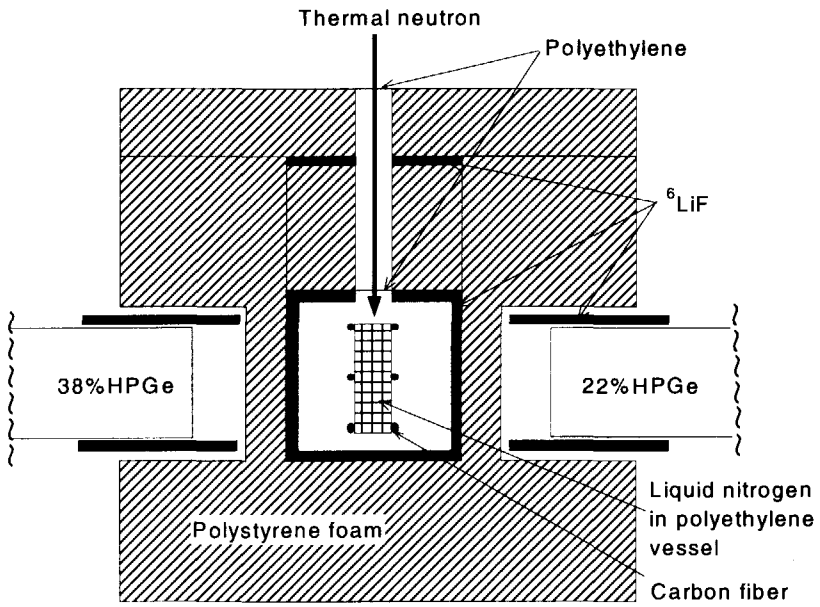

Fig.1 Schematic plane view of a liquid nitrogen target system.

A 5 *l* reservoir vessel is connected to the target vessel and supplies liquid nitrogen to target. The reservoir vessel needs to be filled with liquid nitrogen every 10 hours. A drop-lid divides the reservoir vessel from the target vessel as shown in Fig. 2, and reduces a leak of scattered neutrons to negligible small.

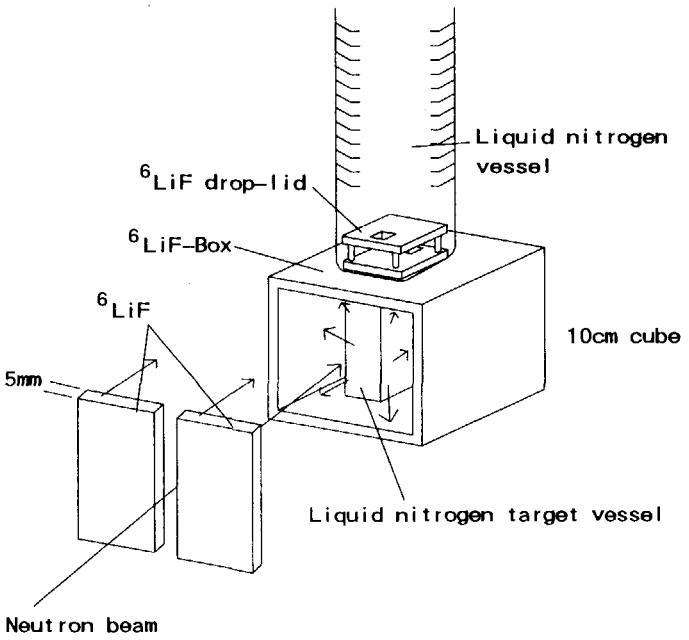

Fig.2 A view of ^{6}LiF-Box and ^{6}LiF drop lid.

The polyethylene foam was used as thermal shield material for suppressing the accumulation of frost around the target. The counting rate of 2.2 MeV γ-ray from ^{2}H was low, but it gradually increased in 70 hours.

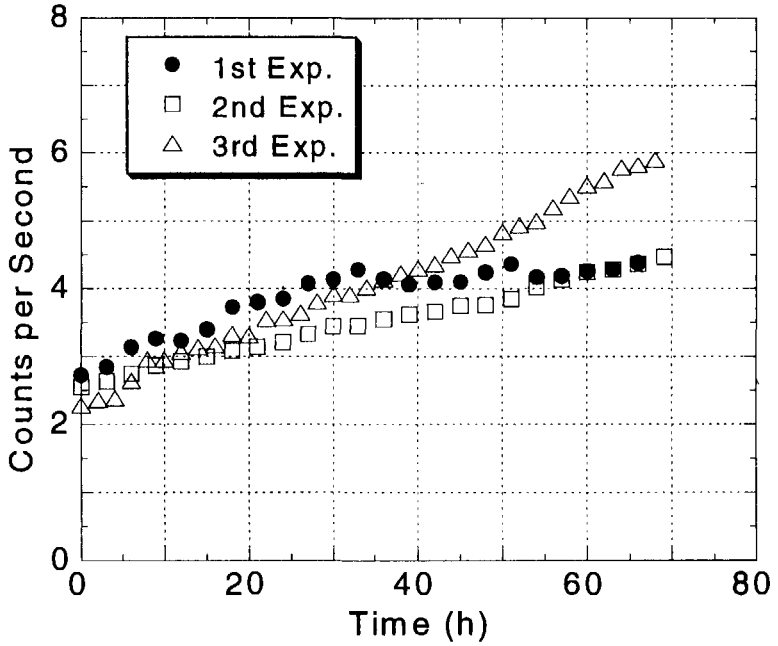

Fig. 3 The peak counting rate of 2.2 MeV γ-ray increased owing to the accumulation of frost around target vessel.

3 Results and discussion

The liquid nitrogen target system well worked for about 70 hours. The singles spectra obtained with the melamine and the liquid nitrogen is shown on liner scale in Fig. 4. The peak counting rate obtained with the liquid nitrogen was 4 times larger than that of the melamine. In the melamine, 2.2 MeV γ-ray emitted from ^{2}H dominated in the total counting rate. In the liquid nitrogen, the γ-ray of 2.2 MeV was reduced to 1/7. The 1.999 MeV γ-ray was clearly observed, which plays an important role in the determination of γ-ray intensities. Moreover, 1.073, 1.988, 2.030, 2.262, 2.293, 3.856 and 8.569 MeV γ-rays were also much clearly observed.

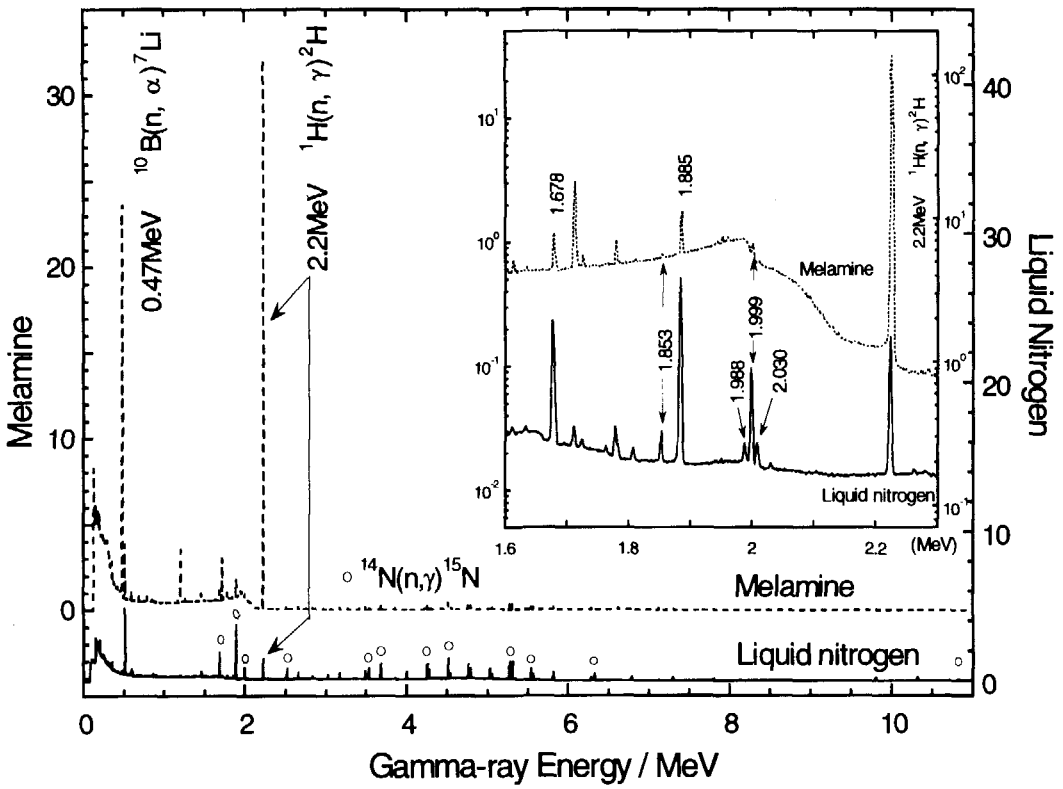

Fig. 4 The γ-ray spectra of liquid nitrogen (right scale) and melamine (left scale) obtained with HPGe detector. The partial figure of the energy region below 2.2MeV are inserted.

Fig. 5 shows the ratios of the relative uncertainties for melamine to that for liquid nitrogen. It was improved by a factor of 2 above 2 MeV and a factor of 3～6 below 2 MeV.

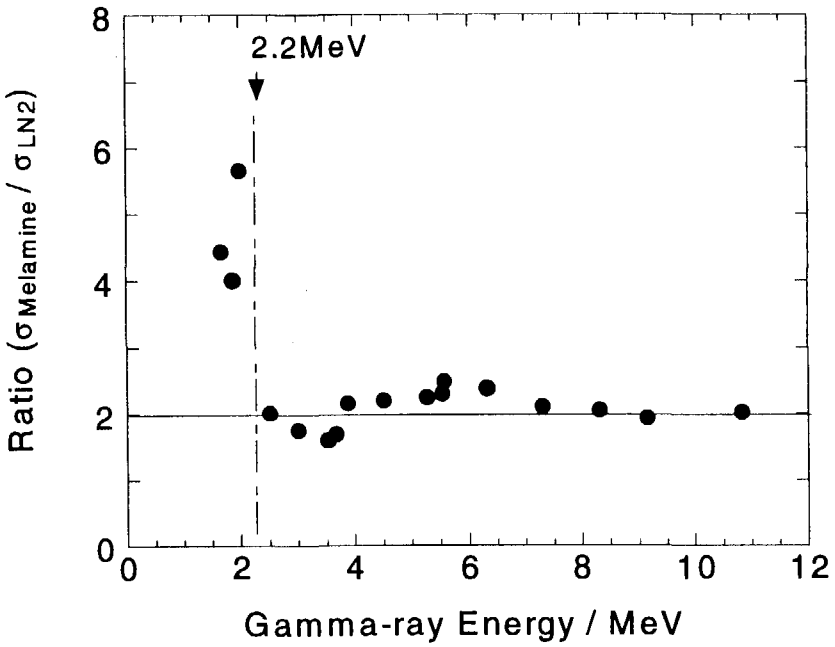

Fig. 5 The ratio of relative uncertainty for melamine to that for liquid nitrogen was improved by a factor of 2 above 2 MeV and a factor of 3-6 below 2 MeV. Dotted line means a position of 2.2 MeV γ-ray from the $^{1}H(n,\gamma)^{2}H$ reaction.

We tentatively determined the γ-ray intensities by the balance method[1], which simultaneously determine the γ-ray intensities and the efficiency function of the detector by requiring an intensity balance for each level. The level scheme that was used in the balance method is shown in Fig. 6. The γ-rays marked with * are those clearly observed in this work.

The comparison of our tentative results obtained from melamine and liquid nitrogen is shown in Fig. 7. It is shown that there are up to about 10% discrepancies between them.

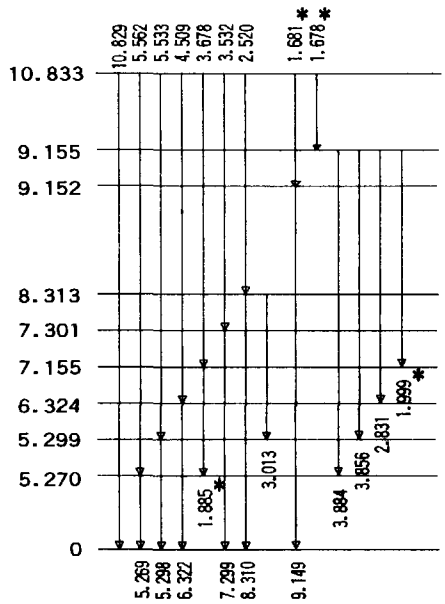

Fig. 6 The level scheme for ^{15}N

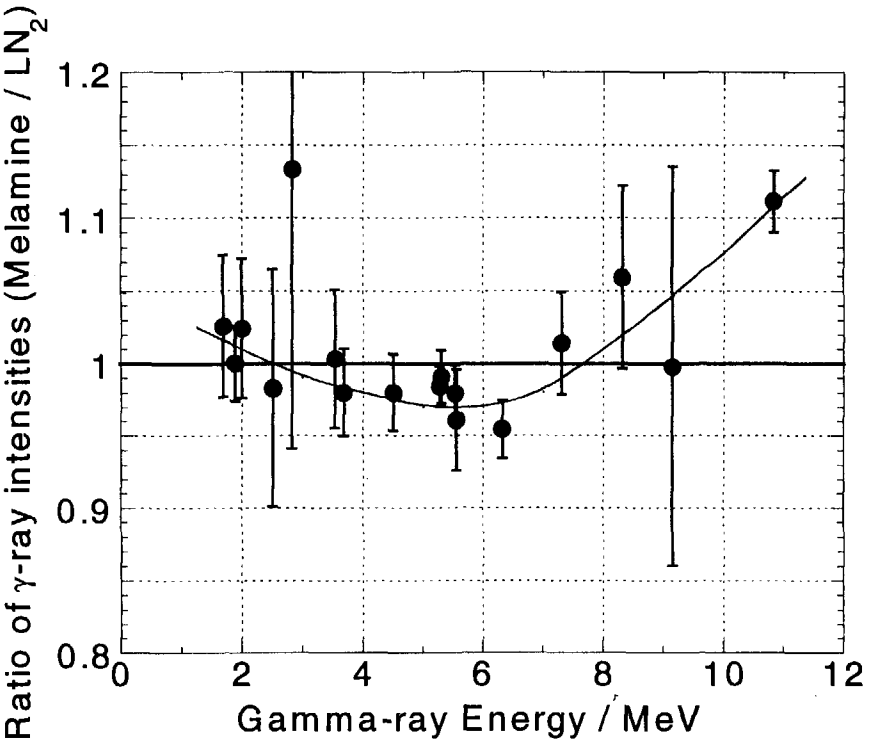

Fig. 7 Comparison of γ-ray intensities determined by melamine and liquid nitrogen. Solid line are given for eye guide.

4 Conclusion

We have proposed the liquid nitrogen target for determination of γ-ray intensities up to 11 MeV in the $^{14}N(n,\gamma)^{15}N$ reaction. It is recognized that the liquid nitrogen target is very useful for improvement of statistics and reduction of the background from $^{1}H(n,\gamma)^{2}H$ reaction.

We are planning to measure capture γ-ray by using thermal neutron at KUR B-4 neutron guide tube (5×10^{7} n/cm^2·s). More statistical improvement is expected.

References

1) T. J. Kennett, W. V. Prestwich and J. S. Tsai, *Nucl. Instr. Meth.*, A249, 366-378, 1986.

2) E. T. Jurney, J. W. Starner, J. E. Lynn and S. Raman, *Phys. Rev.*, C56, 118-134, 1997.

JP0150702

3.40

Nuclear Data Needs for Neutron Spectrum Tailoring at International Fusion Materials Irradiation Facility (IFMIF)

Masayoshi SUGIMOTO
Department of Fusion Engineering Research, Japan Atomic Energy Research Institute
Tokai-mura, Naka-gun, Ibaraki-ken 319-1195
e-mail: sugimoto@ifmif.tokai.jaeri.go.jp

International Fusion Materials Irradiation Facility (IFMIF) is a proposal of D-Li intense neutron source to cover all aspects of the fusion materials development in the framework of IEA collaboration. The new activity has been started to qualifying the important technical issues called Key Element technology Phase since 2000. Although the neutron spectrum can be adjusted by changing the incident beam energy, it is favorable to be carried out many irradiation tasks at the same time under the unique beam condition. For designing the tailored neutron spectrum, neutron nuclear data for the moderator-reflector materials up to 50 MeV are required. The data for estimating the induced radioactivity is also required to keep the radiation level low enough at maintenance time. The candidate materials and the required accuracy of nuclear data are summarized.

1. Introduction

The development of the fusion reactor materials is one of the most important issues for realizing the fusion power as an energy source. The neutron irradiation tests of the candidate materials are the ultimate and unavoidable steps to obtain the enough qualification and licensing. The IFMIF activity has been carried out for these six years under the framework of IEA international collaboration to construct the intense neutron source for fusion materials irradiation tests. The conceptual design was performed through 1995-1999, which consisted of CDA (Conceptual Design Activity) and CDE (Conceptual Design Evaluation) phases and was completed by a cost reduced design and a facility deployment in three stages (50mA/125mA/250mA for beam current) to contribute to the corresponding stages of the fusion power development [1-3]. After the conceptual design study it is recognized that the several essential technology needs to be verified in a separated activity prior to the engineering test phase by using a prototype system. These key technologies, such as high current and stable beam injector operation, steady and safe Li loop behavior, etc., should be investigated in three-years KEP (Key Element technology verification Phase), so that the proper decision of the next phase, EVP (Engineering Validation Phase), can be made. The updated schedule of IFMIF program is shown in Fig. 1 along with the relation to the DEMO (demonstration reactor for power generation) and ITER (International Thermonuclear Experimental Reactor) schedules.

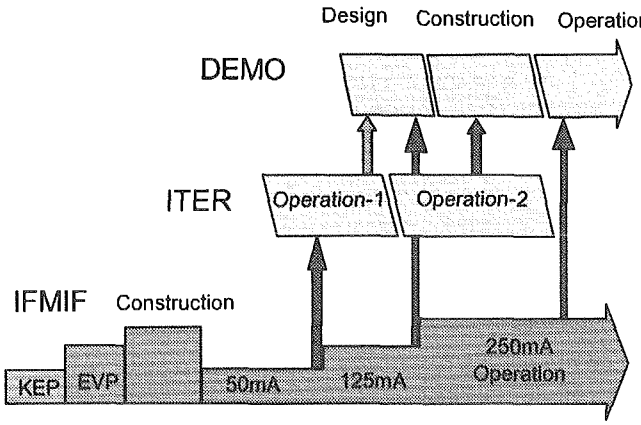

Fig. 1 Staged deployment of IFMIF and relation to DEMO/ITER.

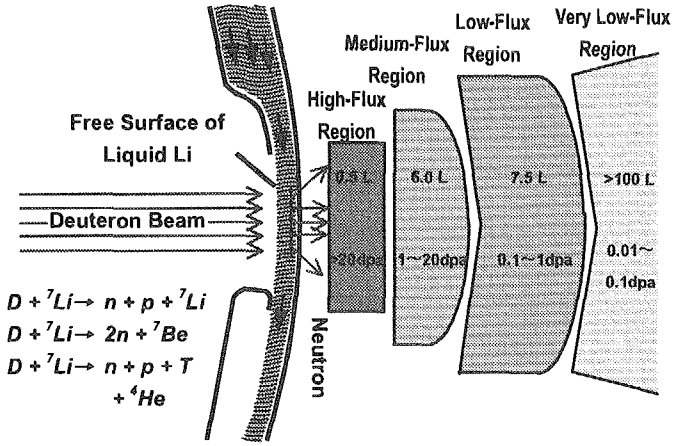

Fig.2 Principle of D-Li neutron source for materials irradiation.

As shown in Fig.2, IFMIF is based on the D-Li neutron source using a high-current deuteron accelerator and a high-speed lithium jet stream target with a free surface on the vacuum side to satisfy the performance requirements (>20dpa for 500cm^3, see Table 1 in details). The limited irradiation volume is effectively utilized by using a small specimen test technology. The main reaction channels producing the neutrons are the stripping and break up processes having the continuous energy spectrum with a broad peak around the half of incident particle energy in the forward direction, which can be adjusted to the desired energy region suitable for simulating the neutron induced effects in the specific materials. Such a tuning method is powerful to simulate the neutron fields of the various materials at the different locations, like first wall materials, tritium breeding materials or ceramics insulator. The idea of simultaneous irradiation with multiple purposes using a spectrum tailoring method is recently stressed for saving the extra time necessary for the experimental arrangement between the irradiation campaigns [4]. The method employs a small block of spectrum converter (moderator/ reflector/ multiplier) to compromise the intensity and spectrum at the test assemblies in the medium-flux regions. It reduces some part of irradiation volume by sharing the space for the test species and the spectrum converter blocks, so that it is essential to optimize the size and position of the converter to maintain both the neutron flux and the irradiation volume. The present report overviews the possible schemes of spectrum tailoring in IFMIF and the required nuclear data for designing them.

Table 1. Requirements of IFMIF neutron field

Accumulated damage	100~200 dpa (displacement per atom)
Irradiation volume	>500 cm^3 with 10^{14}n/s cm^2
Spatial gradient of neutron flux	<10%/cm
Overall machine availability	70 %

2. Possibility of Spectrum Tailoring

A generic scheme of the arrangement of spectrum converters is shown in Fig. 3, where the test area of the most intense neutron field is almost unchanged and the converter blocks are placed around the area behind to approximate the desired neutron field. The distance between the neutron source and the test cell wall is 1.5 m, however all test assemblies are packed together within 0.5 m from the neutron source to achieve the required flux levels. The typical size of converter block would be 5 x 5 x 1 cm^3, made from H, D, Be, O, C, Pb, Bi, U, and other container material elements. The block is necessary to be durable for neutron damage and temperature condition during the irradiation tests. It is also desirable not to produce an excessive radioactivity and decay heat for easy handling after the irradiation tests. The high-energy neutrons are produced in the forward cone of half angle, ~30deg, so that it is effective to place the moderator and multiplier blocks before the spectrum tailored test region. The scattered off neutrons should be reflected back to the test region using the surrounding reflector blocks. If the slower neutron component is desired, the moderator/reflector can be placed behind the test region. The best combination of such converter and reflector blocks in a limited space is a principal design issue to make this method useful.

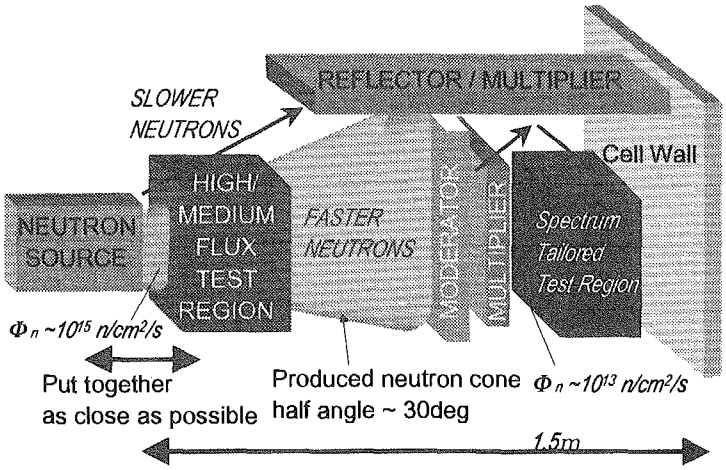

Fig. 3. Schematic configuration of spectrum tailoring in IFMIF

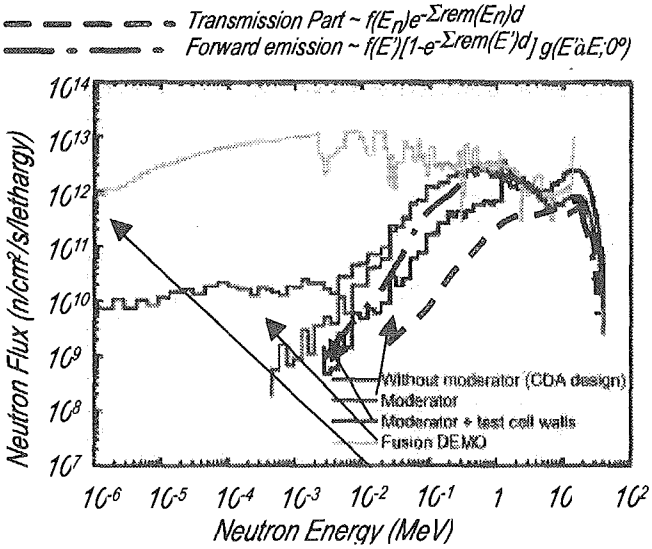

Fig. 4. Comparison of neutron spectra at medium-flux region with/without a Be block after high-flux region (Ref. [4]).

In Fig.4, an example of tailoring is presented to indicate the effectiveness of small piece of spectrum converter. Two Be blocks of 3cm thick are placed before and after the medium flux test region where tritium breeding materials are tested. The original spectrum is mainly modified through the neutron transmission and forward emission by the block close to the target, and the similarity to the fusion reactor spectrum is improved. The lowest energy part can be tailored by using the side reflector blocks as indicated by the calculation including the effect of test cell walls. The drawback of this tailoring method is the reduction of the volume-flux product in the test region, ~50%, so that the best combination of the irradiation

test plans for the flux sensitive and spectrum sensitive properties is important. It is helpful to minimize the occupied space if the extremely high density materials can be available for the converter blocks.

3. Nuclear Data Needs

There are two categories to consider the nuclear data needs for the spectrum tailoring: (1) data for neutron transport calculation in the test cell including the test assemblies and converter blocks, and (2) data for nuclear heating and activation calculation in the converter blocks. The issues specific to the IFMIF are the neutron induced reaction data up to 50 MeV and the double differential neutron yield from source reaction. The latter is a basic information for planning every irradiation experiments and the relative accuracy within 10% is required to satisfy the uniformity of neutron flux in the test assemblies.

(1) Neutron Transport Calculation

The Neutron DDX (especially at low energy and larger scattering angles) data are primarily requested to perform the design of spectrum tailoring. The neutron production reaction processes, e.g. (n,2n), (n,3n) and (n,Xn) where X is a charged particle, are important in the considered energy range.

(2) Nuclear Heating Calculation

The photon production and the charged particle production processes are important.

(3) Activation Calculation

The long-lived radioactive residual production process is important. It is necessary to pay much attention to the sequential multi-step reaction process because of the production of the various charged particles and neutrons in the materials.

The above data are generally required also to investigate the other neutronics problems in IFMIF, however the items in (1) are relatively specific to this issue and the present status is overviewed in table 2. Due to the lack of enough experimental data for each nuclear process, a systematical understanding of the partial DDX information becomes important. The integrity of the nuclear process like energy and particle balance is hard to maintain if only the inclusive DDX data are available. The theoretical calculation support for the systematic analyses is inevitable to reduce the modeling parameters. The continued systematical measurements by using 14 MeV (and other neutron source) facilities are highly appreciated to confirm the theoretical approach.

Table 2. Present status of some neutron production reaction channels up to 50 MeV.

Reaction Type	Status
(n,2n)	Generally good situation except for Be, candidate of multiplier material.
(n,3n)	Generally worse. Heavily relied on model calculations. Experimental consistency check is recommended.
(n,pn)	Situation is better. Systematic measurement to separate (n,d) process is lacked.
(n,αn)	Comparatively worse. No systematic study is found.

The "systematics" at the referenced energy (e.g. 14 MeV) may be valuable for practical use, however

they contain less physical meaning and it is preferred to apply the following channel excitation approach.

• Analysis of reaction channel branching as a function of excitation energy is fruitful generally.

• Trend of channel branch excitation is dominantly ruled by particle transmission in exit channel and level density form. The compoud nuclear process dominancy is assumed..

• Absolute cross sections of these partial channels are normalized to global trend of non-elastic cross section, which is essentially the size of effective interaction area seen by entering neutron. The optical model calculation is precise, however perspective view is lost easily in the complex process. The simpler approach like Diffraction model (Ramsauer model) is one of the solution.

• Charged particle production near threshold is strongly affected by Coulomb field and "preformed" particle density in the compound nucleus. The latter is generally treated using asymmetry factor, (N-Z)/A.

• Relative DDX data are composed of the phase space factor and the nuclear state factor expressing the contribution of direct and pre-equilibrium process.

The accuracy of cross sections is required to be within 10% for integrated data and 20-40% for the DDX data.

4. Conclusion

The IFMIF project is stepped forward to Key Element Technology Phase in 2000 and a development and design refinement will be carried out for three years. One of the important issues of IFMIF neutronics is achievement of both the high flux/large irradiation volume and the spectrum matching for many purposes. This requires spectrum tailoring and the neutron production DDX up to 50 MeV are required to design the spectrum in a specified region. It is recommended to keep the efforts to measure the experimental data and acquire the precise nuclear response in a systematical way, to achieve the designed neutron field.

Acknowledgement

The IFMIF design concepts are contributed by all members of the IFMIF design team. The supports of Drs. S. Matsuda and M. Seki , and Profs. H. Matsui and T. Muroga are gratefully acknowledged.

References

[1] IFMIF CDA Team: "IFMIF International Fusion Materials Irradiation Facility Conceptual Design Activity Final Report", Ed. Martone M., ENEA RT/ERG/FUS/96/11, Dec. 1996.

[2] IFMIF Design Team: "IFMIF International Fusion Materials Irradiation Facility Conceptual Design Evaluation Report", Ed. Möslang A., FZK Report, FZKA 6199 (1999).

[3] IFMIF Team: "IFMIF International Fusion Materials Irradiation Facility Conceptual Design Activity Reduced Cost Report: A supplement to the CDA by the IFMIF team" Eds. Ida M., et al., JAERI-Tech 2000-014 (2000).

[4] Möslang A., private communication.

Appendix: Participant List

AKAOSUGI S.	JAERI
AKINO Fujiyoshi	IRM
ANDO Yoshihira	Toshiba Co.
AOKI Takao	Tohoku Univ.
AOYAMA Takafumi	JNC
ARUGA Takeo	JAERI
ASAI Masato	JAERI
ASAMI Akira	
ASAMI Tetsuo	Data Engineering Inc.
ASANO Yoshihiro	JAERI
BABA Mamoru	Tohoku Univ.
Chakrobortty, T.K.	BAEC
CHIBA Satoshi	JAERI
Csikai, Julius	Univ. of Debrecen
Dietze, Klaus	JNC
ENDO Akira	JAERI
FUJIMURA T.	JAERI
FUJITA Mitsutane	NRIM
FUJIWARA Setsuo	JAERI
FUKAHORI Tokio	JAERI
FUKETA Toyojiro	JMSF
FURIHATA Shiori	MRI
FURUTAKA Kazuyoshi	JNC
GOTO Shinichi	JAERI
Guinyun Kim	PAL
HABA Hiromitsu	JAERI
HAGIWARA Masayuki	Tohoku Univ.
HANDA Hiroyuki	HEC
HARADA Hideo	JNC
HARADA Masahide	JAERI
HARIMA Yoshiko	CRC
Harun-ar-Rashid A.K.M.	Univ. of Chittagong
HASEGAWA Akira	JAERI
HINO Tetsushi	Hitachi Ltd.
HIRANO Masami	Nagoya Univ.
HIROISHI Tsutomu	Tohoku Univ.
HORIGUCHI Takayoshi	Hiroshima Int. Univ.
ICHIHARA Akira	JAERI
IGARASI Sin-iti	
IGASHIRA Masayuki	Tokyo Inst. of Tech.
IGUCHI Tetsuo	Nagoya Univ.
IKEDA Kazumi	MHI
IKEUCHI Taketo	Kyushu Univ.
ISHIBASHI Kenji	Kyushu Univ.
ISHII Kazuya	Hitachi Ltd.
ISHIKAWA Makoto	JNC
ISHIMOTO Shunsuke	Kyushu Univ.
IWAMOTO Akira	JAERI
IWAMOTO Osamu	JAERI
IWASAKI Tomohiko	Tohoku Univ.
KAI Tetsuya	JAERI
KASUGAI Yoshimi	JAERI
KATAKURA Jun-ichi	JAERI
KAWADE Kiyoshi	Nagoya Univ.
KAWAI Masayoshi	KEK
KAWANO Toshihiko	Kyushu Univ.
KAWATA Naoki	Tohoku Univ.
Kim Eunjoo	JAERI
KIMOTO Tatsuya	Nuclear Fuel Industries, Ltd.,
KITAZAWA Hideo	NDA
KITSUKI Hirohiko	Kyushu Univ.
KOBAYASHI Katsuhei	Kyoto Univ.
KOMURO Yuichi	JAERI
KONNO Chikara	JAERI
KOORI Norihiko	Tokushima Univ.
KUNIEDA Satosi	Kyushu Univ.
Liem Peng Hong	NAIS
Liu Ping	CIAE
MAEDA Shigetaka	JNC
MAEKAWA Fujio	JAERI
MAEKAWA Hiroshi	JAERI
MAKI Koichi	Hitachi Ltd.
MARUYAMA Tomoyuki	Nihon Univ.
MATSUNOBU Hiroyuki	DEI
MEIGO Shin-ichiro	JAERI
MINEMOTO K.	VIC
MIURA Takako	Tohoku Univ.
MUKAIYAMA Takehiko	JAERI
MURATA Isao	Osaka Univ.
MURATA Toru	AITEL
Nada Marnada	Nagoya Univ.
NAGAME Yuichiro	JAERI
NAITO Yoshitaka	NAIS
NAKAGAWA Tsuneo	JAERI
NAKAJIMA Ken	JAERI
NAKAMURA Hisashi	
NAKAMURA Shoji	JNC
NAKAMURA Takashi	Tohoku Univ.
NAKAMURA Takeshi	KCC
NAKASHIMA Hiroshi	JAERI
NAUCHI Yasushi	CRIEPI
NEMOTO Makoto	VIC
NISHINAKA Ichiro	JAERI
NISHIO Katsuhisa	JAERI
NISHIO Takashi	Osaka Univ.
NISHITANI Takeo	JAERI
NODA Tetsuji	NRIM
OCHIAI Kentaro	JAERI

OCHIAI Masaaki	JAERI
ODANO Naoteru	JAERI
OHBAYASI Yosihide	Hokkaido Univ.
OHKAWACHI Yasushi	JNC
OHKUBO Makio	SOHONRR
OHSAWA Takaaki	Kinki Univ.
OIGAWA Hiroyuki	JAERI
OKAJIMA Shigeaki	JAERI
OKUNO Hiroshi	JAERI
OYAMATSU Kazuhiro	Aichi Shukutoku Univ.
OZAWA Akira	RIKEN
P. Siangsanan	OAEP
Rong Jian	JAERI
SAIHO Fuminobu	Kyushu Univ.
SAKAMOTO Koh	Kanazawa Univ.
SAKAMOTO Yukio	JAERI
SAKURAI Kiyoshi	JAERI
Sam Yol Lee	Kyoto Univ.
SASAKI Kenji	ARTECH
SASAKI Michiya	Tohoku Univ.
SATO Hisaki	Tohoku Univ.
SATOH Daiki	Kyushu Univ.
SENGOKU Seio	JAERI
Sergey G. Yavshits	KRI
SHIGYO Nobuhiro	Kyushu Univ.
SHIKAZONO Naomoto	IRM
SHIMADA Shoichiro	JAERI
SHIMIZU Toshiaki	Nagoya Univ.
SHONO Akira	JNC
SUGI Teruo	JAERI
SUGIMOTO Masayoshi	JAERI
Sun Weili	Kyushu Univ.
TABUCHI Shiro	JNC
TAHARA Yoshihisa	MHI
TAJI Y.	RIST
TAKADA Hiroshi	JAERI
TAKADA Naoyuki	Nuclear Fuel Industries, Ltd.,
TAKANO Hideki	JAERI
TERADA Yasuaki	Osaka Univ.
TOITA Sentaro	JAERI
TSUJI Masatoshi	TEC
TSUKADA Kazuaki	JAERI
UNO Yoshitomo	JAERI
USUDA Shigekazu	JAERI
WATANABE Yukinobu	Kyushu Univ.
YAMABAYASHI Hisamichi	CTC
YAMAGUCHI Yasuhiro	JAERI
YAMAMOTO Toru	NUPEC
YAMANO Naoki	SAE
Yang Jin An	NAIS
YASHIMA Hiroshi	Tohoku Univ.
YATABE	NAIS
YOSHIDA Tadashi	Musashi Inst. of Tech.
YOSHIZAWA Nobuaki	MRI
ZUKERAN Atsushi	Hitachi Ltd.

国際単位系 (SI) と換算表

表 1　SI 基本単位および補助単位

量	名称	記号
長さ	メートル	m
質量	キログラム	kg
時間	秒	s
電流	アンペア	A
熱力学温度	ケルビン	K
物質量	モル	mol
光度	カンデラ	cd
平面角	ラジアン	rad
立体角	ステラジアン	sr

表 2　SI と併用される単位

名称	記号
分，時，日	min，h，d
度，分，秒	°，′，″
リットル	l，L
トン	t
電子ボルト	eV
原子質量単位	u

1 eV = 1.60218 × 10^{-19} J

1 u = 1.66054 × 10^{-27} kg

表 5　SI 接頭語

倍数	接頭語	記号
10^{18}	エクサ	E
10^{15}	ペタ	P
10^{12}	テラ	T
10^{9}	ギガ	G
10^{6}	メガ	M
10^{3}	キロ	k
10^{2}	ヘクト	h
10^{1}	デカ	da
10^{-1}	デシ	d
10^{-2}	センチ	c
10^{-3}	ミリ	m
10^{-6}	マイクロ	μ
10^{-9}	ナノ	n
10^{-12}	ピコ	p
10^{-15}	フェムト	f
10^{-18}	アト	a

表 3　固有の名称をもつ SI 組立単位

量	名称	記号	他の SI 単位による表現
周波数	ヘルツ	Hz	s^{-1}
力	ニュートン	N	m·kg/s^2
圧力，応力	パスカル	Pa	N/m^2
エネルギー，仕事，熱量	ジュール	J	N·m
工率，放射束	ワット	W	J/s
電気量，電荷	クーロン	C	A·s
電位，電圧，起電力	ボルト	V	W/A
静電容量	ファラド	F	C/V
電気抵抗	オーム	Ω	V/A
コンダクタンス	ジーメンス	S	A/V
磁束	ウェーバ	Wb	V·s
磁束密度	テスラ	T	Wb/m^2
インダクタンス	ヘンリー	H	Wb/A
セルシウス温度	セルシウス度	℃	
光束	ルーメン	lm	cd·sr
照度	ルクス	lx	lm/m^2
放射能	ベクレル	Bq	s^{-1}
吸収線量	グレイ	Gy	J/kg
線量当量	シーベルト	Sv	J/kg

表 4　SI と共に暫定的に維持される単位

名称	記号
オングストローム	Å
バーン	b
バール	bar
ガル	Gal
キュリー	Ci
レントゲン	R
ラド	rad
レム	rem

1 Å = 0.1 nm = 10^{-10} m

1 b = 100 fm^2 = 10^{-28} m^2

1 bar = 0.1 MPa = 10^5 Pa

1 Gal = 1 cm/s^2 = 10^{-2} m/s^2

1 Ci = 3.7 × 10^{10} Bq

1 R = 2.58 × 10^{-4} C/kg

1 rad = 1 cGy = 10^{-2} Gy

1 rem = 1 cSv = 10^{-2} Sv

（注）

1. 表 1 − 5 は「国際単位系」第 5 版，国際度量衡局 1985 年刊行による。ただし，1 eV および 1 u の値は CODATA の 1986 年推奨値によった。
2. 表 4 には海里，ノット，アール，ヘクタールも含まれているが日常の単位なのでここでは省略した。
3. bar は，JIS では流体の圧力を表わす場合に限り表 2 のカテゴリーに分類されている。
4. EC 閣僚理事会指令では bar，barn および「血圧の単位」mmHg を表 2 のカテゴリーに入れている。

換算表

力	N(=10^5 dyn)	kgf	lbf
	1	0.101972	0.224809
	9.80665	1	2.20462
	4.44822	0.453592	1

粘度　1 Pa·s(N·s/m^2) = 10 P(ポアズ)(g/(cm·s))

動粘度　1 m^2/s = 10^4 St(ストークス)(cm^2/s)

圧力	MPa(=10 bar)	kgf/cm^2	atm	mmHg(Torr)	lbf/in^2(psi)
	1	10.1972	9.86923	7.50062 × 10^3	145.038
	0.0980665	1	0.967841	735.559	14.2233
	0.101325	1.03323	1	760	14.6959
	1.33322 × 10^{-4}	1.35951 × 10^{-3}	1.31579 × 10^{-3}	1	1.93368 × 10^{-2}
	6.89476 × 10^{-3}	7.03070 × 10^{-2}	6.80460 × 10^{-2}	51.7149	1

エネルギー・仕事・熱量	J(=10^7 erg)	kgf·m	kW·h	cal(計量法)	Btu	ft·lbf	eV
	1	0.101972	2.77778 × 10^{-7}	0.238889	9.47813 × 10^{-4}	0.737562	6.24150 × 10^{18}
	9.80665	1	2.72407 × 10^{-6}	2.34270	9.29487 × 10^{-3}	7.23301	6.12082 × 10^{19}
	3.6 × 10^6	3.67098 × 10^5	1	8.59999 × 10^5	3412.13	2.65522 × 10^6	2.24694 × 10^{25}
	4.18605	0.426858	1.16279 × 10^{-6}	1	3.96759 × 10^{-3}	3.08747	2.61272 × 10^{19}
	1055.06	107.586	2.93072 × 10^{-4}	252.042	1	778.172	6.58515 × 10^{21}
	1.35582	0.138255	3.76616 × 10^{-7}	0.323890	1.28506 × 10^{-3}	1	8.46233 × 10^{18}
	1.60218 × 10^{-19}	1.63377 × 10^{-20}	4.45050 × 10^{-26}	3.82743 × 10^{-20}	1.51857 × 10^{-22}	1.18171 × 10^{-19}	1

1 cal = 4.18605 J (計量法)

= 4.184 J (熱化学)

= 4.1855 J (15 °C)

= 4.1868 J (国際蒸気表)

仕事率　1 PS (仏馬力)

= 75 kgf·m/s

= 735.499 W

放射能	Bq	Ci
	1	2.70270 × 10^{-11}
	3.7 × 10^{10}	1

吸収線量	Gy	rad
	1	100
	0.01	1

照射線量	C/kg	R
	1	3876
	2.58 × 10^{-4}	1

線量当量	Sv	rem
	1	100
	0.01	1

(86 年 12 月 26 日現在)